FIELD DATA, MODELS AND UNCERTAINTY IN HAZARD ASSESSMENT OF PYROCLASTIC DENSITY CURRENTS AND LAHARS: GLOBAL PERSPECTIVES

EDITED BY: Pablo Tierz, Andrea Bevilacqua, Stuart Mead, Elaine Spiller and Laura Sandri

PUBLISHED IN: Frontiers in Earth Science

frontiers Research Topics

ISSN 1664-8714
ISBN 978-2-88966-866-3
DOI 10.3389/978-2-88966-866-3

About Frontiers

Frontiers is more than just an open-access publisher of scholarly articles: it is a pioneering approach to the world of academia, radically improving the way scholarly research is managed. The grand vision of Frontiers is a world where all people have an equal opportunity to seek, share and generate knowledge. Frontiers provides immediate and permanent online open access to all its publications, but this alone is not enough to realize our grand goals.

Frontiers Journal Series

The Frontiers Journal Series is a multi-tier and interdisciplinary set of open-access, online journals, promising a paradigm shift from the current review, selection and dissemination processes in academic publishing. All Frontiers journals are driven by researchers for researchers; therefore, they constitute a service to the scholarly community. At the same time, the Frontiers Journal Series operates on a revolutionary invention, the tiered publishing system, initially addressing specific communities of scholars, and gradually climbing up to broader public understanding, thus serving the interests of the lay society, too.

Dedication to Quality

Each Frontiers article is a landmark of the highest quality, thanks to genuinely collaborative interactions between authors and review editors, who include some of the world's best academicians. Research must be certified by peers before entering a stream of knowledge that may eventually reach the public - and shape society; therefore, Frontiers only applies the most rigorous and unbiased reviews.
Frontiers revolutionizes research publishing by freely delivering the most outstanding research, evaluated with no bias from both the academic and social point of view. By applying the most advanced information technologies, Frontiers is catapulting scholarly publishing into a new generation.

What are Frontiers Research Topics?

Frontiers Research Topics are very popular trademarks of the Frontiers Journals Series: they are collections of at least ten articles, all centered on a particular subject. With their unique mix of varied contributions from Original Research to Review Articles, Frontiers Research Topics unify the most influential researchers, the latest key findings and historical advances in a hot research area! Find out more on how to host your own Frontiers Research Topic or contribute to one as an author by contacting the Frontiers Editorial Office: frontiersin.org/about/contact

FIELD DATA, MODELS AND UNCERTAINTY IN HAZARD ASSESSMENT OF PYROCLASTIC DENSITY CURRENTS AND LAHARS: GLOBAL PERSPECTIVES

Topic Editors:
Pablo Tierz, The Lyell Centre, United Kingdom
Andrea Bevilacqua, National Institute of Geophysics and Volcanology (INGV), Italy
Stuart Mead, Massey University, New Zealand
Elaine Spiller, Marquette University, United States
Laura Sandri, National Institute of Geophysics and Volcanology (Bologna), Italy

Citation: Tierz, P., Bevilacqua, A., Mead, S., Spiller, E., Sandri, L., eds. (2021). Field Data, Models and Uncertainty in Hazard Assessment of Pyroclastic Density Currents and Lahars: Global Perspectives. Lausanne: Frontiers Media SA.
doi: 10.3389/978-2-88966-866-3

Table of Contents

frontiers in Earth Science

EDITORIAL
published: 15 April 2021
doi: 10.3389/feart.2021.665725

Editorial: Field Data, Models and Uncertainty in Hazard Assessment of Pyroclastic Density Currents and Lahars: Global Perspectives

Pablo Tierz[1]*, *Andrea Bevilacqua*[2], *Stuart Mead*[3], *Elaine Spiller*[4] and *Laura Sandri*[5]

[1]British Geological Survey, The Lyell Centre, Edinburgh, United Kingdom, [2]Istituto Nazionale di Geofisica e Vulcanologia, Sezione di Pisa, Pisa, Italy, [3]Volcanic Risk Solutions, Massey University, Palmerston North, New Zealand, [4]Department of Mathematical and Statistical Sciences, Marquette University, Milwaukee, WI, United States, [5]Istituto Nazionale di Geofisica e Vulcanologia, Sezione di Bologna, Bologna, Italy

Keywords: volcanology, volcanic hazard assessment, uncertainty, pyroclastic density currents (PDCs), lahars

Editorial on the Research Topic

Field Data, Models and Uncertainty in Hazard Assessment of Pyroclastic Density Currents and Lahars: Global Perspectives

Pyroclastic density currents (PDCs, e.g., Sparks et al., 1978; Branney and Kokelaar, 2002; Sulpizio et al., 2014; Dellino et al., 2019) and lahars (e.g., Manville et al., 2009; Vallance and Iverson, 2015; Thouret et al., 2020) are two of the most destructive volcanic phenomena. They can generate enormous losses of life (e.g., Auker et al., 2013; Baxter et al., 2017; Brown et al., 2017), as well as extensive structural damage to buildings and infrastructure within tens of kilometers from their source (e.g., Valentine, 1998; Baxter et al., 2005; Jenkins et al., 2015). Hazard assessments of PDCs and lahars represent the foundation for estimating the substantial risk that these volcanic mass flows pose to the human environment.

Unfortunately, these hazard assessments are complicated by the spatio-temporal complexity associated with the processes of triggering, propagation (including flow transitions) and emplacement of PDCs and lahars (e.g., Iverson, 1997; Pierson and Major, 2014; Dufek et al., 2015; Dufek, 2016). This natural variability (or aleatory uncertainty), alongside incomplete and imperfect knowledge (or epistemic uncertainty, cf. Woo, 1999; Connor et al., 2001; Marzocchi et al., 2004; Sparks and Aspinall, 2004; Marzocchi and Bebbington, 2012) should ideally be incorporated into the mass-flow hazard assessment (e.g., Bayarri et al., 2009, 2015; Sandri et al., 2014, 2018; Spiller et al., 2014; Neri et al., 2015; Mead et al., 2016; Tierz et al., 2016, 2017, 2018; Bevilacqua et al., 2017, 2019; Mead and Magill, 2017; Wolpert et al., 2018; Hyman et al., 2019; Rutarindwa et al., 2019). At the core of any volcanic hazard assessment resides the volcanological knowledge available for the volcano of interest and/or *analogous* ones, including information about the sources of uncertainty (e.g., Newhall and Hoblitt, 2002; Aspinall et al., 2003; Sandri et al., 2012; Pallister et al., 2019; Tierz et al., 2019, 2020; Cioni et al., 2020).

In this Research Topic (RT), we have attempted to gather and showcase volcanological expertise from around the globe, related to any *component* of PDC and lahar hazard assessment: i.e., volcanological field data collection, analysis and interpretation; experimental and/or numerical and/or statistical modeling, including uncertainty quantification. Volcanic systems in 12 countries and 6 continents have been studied (**Figure 1A**). Below, we summarize the main findings of each article, highlighting the most relevant methodological and volcanological aspects.

Zhao et al. provide a thorough description of the characteristics and spatial distribution of PDC lithofacies, including systematic changes with distance from the vent and topography of the volcanic edifice, associated with the VEI 7 Millennium eruption (946 AD) of Tianchi volcano (China-DPR

OPEN ACCESS

Edited and reviewed by:
Valerio Acocella,
Roma Tre University, Italy

***Correspondence:**
Pablo Tierz
pablo@bgs.ac.uk,
orcid.org/0000-0001-8889-9900

Specialty section:
This article was submitted to Volcanology, a section of the journal Frontiers in Earth Science

Received: *08 February 2021*
Accepted: *15 February 2021*
Published: *15 April 2021*

Citation:
Tierz P, Bevilacqua A, Mead S, Spiller E and Sandri L (2021) Editorial: Field Data, Models and Uncertainty in Hazard Assessment of Pyroclastic Density Currents and Lahars: Global Perspectives. Front. Earth Sci. 9:665725. doi: 10.3389/feart.2021.665725

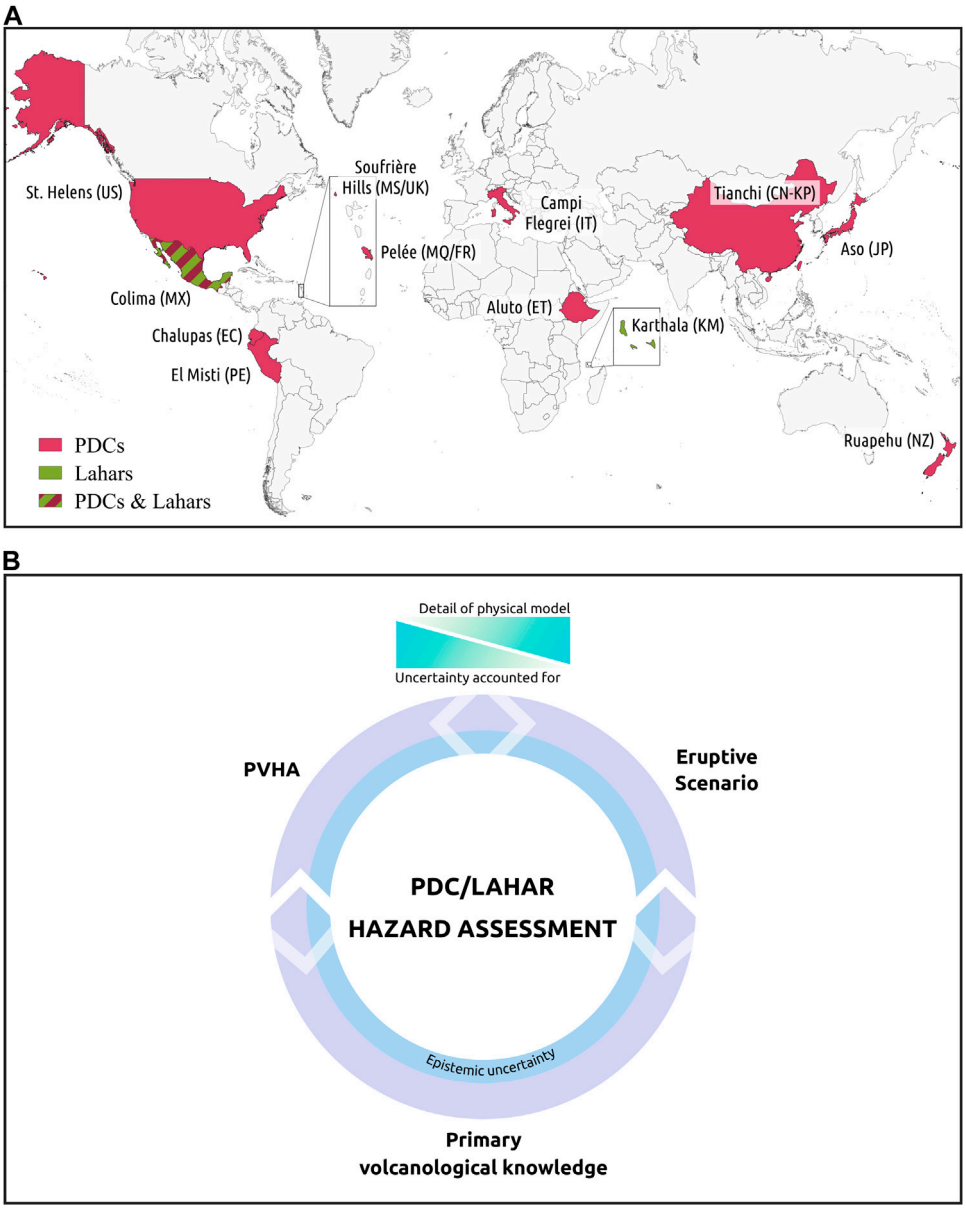

FIGURE 1 | Summary of present and future global perspectives in the field of volcanic hazard assessment of pyroclastic density currents (PDCs) and lahars derived from this Research Topic. **(A)** Global distribution of countries where volcanic systems have been analyzed in the Research Topic, divided according to whether the main object of study were PDCs or lahars (NB. Two different studies, one for PDCs, **Patra et al.**, and another for lahars, **Walsh et al.**, were presented for Volcán de Colima, Mexico). Map generated using Quantum Geographical Information System (QGIS Development Team, 2021), and Eurostat GISCO Geodata (©EuroGeographics for the administrative boundaries, 1:3 Million Scale. Downloaded January 25, 2021). **(B)** Interrelationships between three main approaches commonly used in volcanic hazard assessment of PDCs and lahars. One is based on collating fundamental volcanological knowledge for the volcanic system of interest (and/or analogue volcanoes). Both scenario-based as well as probabilistic volcanic hazard assessments (PVHA) build upon this primary volcanological knowledge. Currently, there is a balance between the degree of physical detail and the uncertainty accounted for that can be achieved with scenario-based and PVHA methods. We argue that the three approaches are complementary and mutually beneficial, and that they should be increasingly merged in future hazard assessments. We also stress the key importance of acknowledging the presence of epistemic uncertainty on all three approaches, and of trying to quantify it as best as possible.

Korea border). The work underlines the significant PDC hazard from past (and future) eruptions at Tianchi, and recalls the notable thermal hazard of PDCs.

Takarada and Hoshizumi re-evaluate the distributions and eruptive volumes of large-scale PDC (up to 166 km runout) and tephra fall deposits derived from the caldera-forming Aso-4 eruption

(87–89 ka) of Aso volcano (Japan). The total eruptive volume of the Aso-4 eruption is about 1.5–3 times larger than the previous estimation, making it now a M8.1–8.4 (VEI 8) super-eruption.

Silleni et al. develop a new isopach-based method to estimate (large-magnitude) ignimbrite volumes, using extrapolations of the pre-eruption topography to better constrain epistemic uncertainty. The method should be reproducible for other topography-controlled ignimbrites and, applied to the M7 Campanian Ignimbrite eruption (~40 ka) of Campi Flegrei caldera (Italy), significantly reduces the epistemic uncertainty in total erupted volume compared to previous estimates.

Gillies et al., by means of a comprehensive field-mapping at Mt. Ruapehu volcano (New Zealand), have identified 12 new PDC deposits from at least 10 previously unknown flows. Concentrated-flow behavior and the approximate age ranges of these flows were inferred from lithofacies, stratigraphy and whole-rock geochemistry. The article highlights the capability of Mt. Ruapehu to generate different sizes and styles of PDCs, a key element for future hazard planning.

Gilbertson et al. propose an alternate mechanism for secondary hydroeruptions in PDC deposits. Analogue experiments suggest hydroeruptions are possible where low-permeability (fine-grained) beds are capped by high-permeability (coarse-grained) beds through a drag-based mechanism. Gas pockets and explosive failure may occur if gas flow supports fluidization of the fine, but not coarse particles. This expands the range of physical mechanisms for a secondary hazard often poorly represented in the geologic record.

Walsh et al. analyze lahar dynamics using a 3-component, broadband seismometer at Volcán de Colima (Mexico). The study argues the merits of utilizing all three seismic components to analyze the spectral content of ground motion parallel to and across the drainage channel. They further relate these seismic analyses to the flow rheology and physical processes of the observed lahars.

Córdova et al. combined fieldwork, laboratory, remote-sensing and numerical-modeling techniques to infer the relation between a hummocky field at Chalupas caldera (Ecuador), and the partial collapse of the post-caldera Buenavista lava dome. The work evidences the advantages of integrating *classical* and modern techniques for the interpretation of volcanological phenomena, and sheds light on the directionality, timing and approximate volume of the associated breccia flow.

Dille et al. tested the effectiveness of two flow models for simulating rain-triggered lahars at Karthala volcano, Grand Comore Island. Karthala has a lower gradient and poorly incised channels that can limit the reliability of models compared to stratovolcanoes. Field methods to improve the Digital Elevation Model (DEM) and constrain inputs improved accuracy of the results. This article demonstrates approaches that may improve hazard assessment accuracy in difficult-to-model settings.

Gueugneau et al. numerically investigate the Mount Pelée May 8th, 1902 pyroclastic current, using a two-phase model that simulates both the block-and-ash flow and the ash-cloud surge. The study discusses conflicting interpretations of the pyroclastic current dynamics, either a blast related to a laterally oriented dome explosion or an ash-cloud surge derived from the block-and-ash flow.

Charbonnier et al. conducted a multi-disciplinary study on the PDCs generated by El Misti volcano (Peru) in its reference eruption for hazard assessment in Arequipa (>1 M residents). Combining new field-mapping with a 2-m resolution DEM, they re-assessed the area invaded by PDCs and their total bulk volume. The latter is used in the VolcFlow model to assess the probability of similar PDCs impacting specific valleys, which is key to understand potential effects of PDCs on Arequipa.

Patra et al. describe an uncertainty-quantification approach to characterize models of geophysical flows (e.g., TITAN2D) and analyze the contribution of each force term (e.g., gravity, bed friction) to the outputs. They present the method by comparing three rheology assumptions, across a wide range of flow regimes, in the case study of a block-and-ash flow propagating on the SW slope of Volcán de Colima (Mexico).

Clarke et al. present a comprehensive procedure for PVHA of PDCs; from primary field-data collection, analysis and interpretation, to the physical/statistical modeling required for uncertainty quantification. The method is applied to Aluto volcano (Ethiopia) but is transferable to other volcanic systems. A basic understanding of past eruptions remains crucial to design and justify the modeling strategy but initial PVHA of PDCs may be possible at data-scarce volcanoes, if supported by data from analogue volcanoes.

Spiller et al. introduce a probabilistic model for the cessation of PDC activity that accounts for the time elapsed from the last PDC. They combine this model with a structured and reproducible uncertainty quantification framework that allows robust, yet rapid, PVHA using observational data for dome-collapse PDCs, numerical simulations of TITAN2D and Gaussian process emulators. The method is applied to a hiatus in volcanic activity, or post-eruption unrest context, at Soufrière Hills Volcano, Montserrat.

In conclusion, we suggest that increased connections between the PDC/lahar scientific communities worldwide will result in further advances in the field. We believe that future hazard assessments will require enhanced multi- and inter-disciplinarity among volcano scientists; continuous communication and mutual learning between *observational* volcanology and physical/statistical modeling aimed at simulating eruptive scenarios and/or quantifying uncertainty in PVHA (**Figure 1B**).

AUTHOR CONTRIBUTIONS

All authors contributed significantly to the writing of the manuscript and approved it for publication. PT generated the figures.

FUNDING

This work has been supported by Global Geological Risk Platform of the British Geological Survey NC-ODA grant NE/R000069/1: Geoscience for Sustainable Futures.

ACKNOWLEDGMENTS

We warmly thank Valerio Acocella for having encouraged us to submit this Research Topic and for all his support throughout.

We are extremely grateful to Eliza Calder for her contributions to the Research Topic before she had to, unfortunately, withdraw from the editing team. We sincerely thank Fabio Dioguardi for his invaluable work as convener of the session at Cities on Volcanoes 10, which directly resulted in the preparation of this Research Topic. We also thank a number of colleagues for very fruitful conversations about the science covered in the aforementioned session and in this Research Topic: Jonathan Procter, Sylvain Charbonnier, Abani Patra, Augusto Neri, Tomaso Esposti Ongaro, Greg Valentine, Sue Loughlin, Ben Clarke, Domenico Doronzo, Sarah Ogburn, Mark Woodhouse, Matteo Trolese and others. Last but not least, we wholeheartedly thank all the authors that have contributed to the Research Topic, all the reviewers and editors that have freely dedicated their precious time to improve the clarity and/or quality of the research presented, and the support team of Frontiers in Earth Science, in particular Ursula Rabar, for supporting us throughout the process of preparing and completing this Research Topic. Published with permission of the Executive Director of British Geological Survey (NERC-UKRI).

REFERENCES

Aspinall, W. P., Woo, G., Voight, B., and Baxter, P. J. (2003). Evidence-based volcanology: application to eruption crises. *J. Volcanol. Geotherm. Res.* 128, 273–285. doi:10.1016/s0377-0273(03)00260-9

Auker, M., Sparks, R., Siebert, L., Crosweller, H., and Ewert, J. (2013). A statistical analysis of the global historical volcanic fatalities record. *J. Appl. Volcanol.* 2, 2. doi:10.1186/2191-5040-2-2

Baxter, P. J., Boyle, R., Cole, P., Neri, A., Spence, R., and Zuccaro, G. (2005). The impacts of pyroclastic surges on buildings at the eruption of the Soufriere Hills volcano, Montserrat. *Bull. Volcanol.* 67, 292–313. doi:10.1007/s00445-004-0365-7

Baxter, P. J., Jenkins, S., Seswandhana, R., Komorowski, J. C., Dunn, K., Purser, D., et al. (2017). Human survival in volcanic eruptions: thermal injuries in pyroclastic surges, their causes, prognosis and emergency management. *Burns* 43, 1051–1069. doi:10.1016/j.burns.2017.01.025

Bayarri, M. J., Berger, J. O., Calder, E. S., Dalbey, K., Lunagomez, S., Patra, A. K., et al. (2009). Using statistical and computer models to quantify volcanic hazards. *Technometrics* 51, 402–413. doi:10.1198/tech.2009.08018

Bayarri, M. J., Berger, J. O., Calder, E. S., Patra, A. K., Pitman, E. B., Spiller, E. T., et al. (2015). Probabilistic quantification of hazards: a methodology using small ensembles of physics-based simulations and statistical surrogates. *Int. J. Uncertain. Quantif.* 5, 297–325. doi:10.1615/Int.J.UncertaintyQuantification.2015011451

Bevilacqua, A., Patra, A. K., Bursik, M. I., Pitman, E. B., Macías, J. L., Saucedo, R., et al. (2019). Probabilistic forecasting of plausible debris flows from Nevado de Colima (Mexico) using data from the Atenquique debris flow, 1955. *Nat. Hazards Earth Syst. Sci.* 19 (4), 791–820. doi:10.5194/nhess-19-791-2019

Branney, M. J., and Kokelaar, B. P. (2002). *Pyroclastic density currents and the sedimentation of ignimbrites*. Piccadilly, United Kingdom: Geological Society of London, Vol. 2.

Brown, S. K., Jenkins, S. F., Sparks, R. S. J., Odbert, H., and Auker, M. R. (2017). Volcanic fatalities database: analysis of volcanic threat with distance and victim classification. *J. Appl. Volcanol.* 6, 1–20. doi:10.1186/s13617-017-0067-4

Cioni, R., Tadini, A., Gurioli, L., Bertagnini, A., Mulas, M., Bevilacqua, A., et al. (2020). Estimating eruptive parameters and related uncertainties for pyroclastic density currents deposits: worked examples from Somma-Vesuvius (Italy). *Bull. Volcanol.* 82, 65. doi:10.1007/s00445-020-01402-7

Connor, C. B., Hill, B. E., Winfrey, B., Franklin, N. M., and Femina, P. C. L. (2001). Estimation of volcanic hazards from tephra fallout. *Nat. Hazards Rev.* 2, 33–42. doi:10.1061/(asce)1527-6988(2001)2:1(33)

Dellino, P., Dioguardi, F., Doronzo, D. M., and Mele, D. (2019). The rate of sedimentation from turbulent suspension: an experimental model with application to pyroclastic density currents and discussion on the grain-size dependence of flow runout. *Sedimentology* 66, 129–145. doi:10.1111/sed.12485

Dufek, J. (2016). The fluid mechanics of pyroclastic density currents. *Annu. Rev. Fluid Mech.* 48, 459–485. doi:10.1146/annurev-fluid-122414-034252

Dufek, J., Esposti Ongaro, T., and Roche, O. (2015). "Pyroclastic density currents: processes and models," in *The encyclopedia of volcanoes*. 2nd Edn. Editors H. Sigurdsson, B. Houghton, S. McNutt, H. Rymer, and J. Stix (Cambridge, United Kingdom: Academic Press), 617–629. doi:10.1016/B978-0-12-385938-9.00035-3

Hyman, D. M., Bevilacqua, A., and Bursik, M. I. (2019). Statistical theory of probabilistic hazard maps: a probability distribution for the hazard boundary location. *Nat. Hazards Earth Syst. Sci.* 19, 1347–1363. doi:10.5194/nhess-19-1347-2019

Iverson, R. M. (1997). The physics of debris flows. *Rev. Geophys.* 35, 245–296. doi:10.1029/97rg00426

Jenkins, S. F., Phillips, J. C., Price, R., Feloy, K., Baxter, P. J., Hadmoko, D. S., et al. (2015). Developing building-damage scales for lahars: application to Merapi volcano, Indonesia. *Bull. Volcanol.* 77, 75. doi:10.1007/s00445-015-0961-8

Manville, V., Németh, K., and Kano, K. (2009). Source to sink: a review of three decades of progress in the understanding of volcaniclastic processes, deposits, and hazards. *Sediment. Geol.* 220, 136–161. doi:10.1016/j.sedgeo.2009.04.022

Marzocchi, W., and Bebbington, M. S. (2012). Probabilistic eruption forecasting at short and long time scales. *Bull. Volcanol.* 74, 1777–1805. doi:10.1007/s00445-012-0633-x

Marzocchi, W., Sandri, L., Gasparini, P., Newhall, C., and Boschi, E. (2004). Quantifying probabilities of volcanic events: the example of volcanic hazard at Mount Vesuvius. *J. Geophys. Res.* 109, B11201. doi:10.1029/2004JB003155

Mead, S. R., and Magill, C. R. (2017). Probabilistic hazard modelling of rain-triggered lahars. *J. Appl. Volcanol.* 6, 8. doi:10.1186/s13617-017-0060-y

Mead, S., Magill, C., and Hilton, J. (2016). Rain-triggered lahar susceptibility using a shallow landslide and surface erosion model. *Geomorphology* 273, 168–177. doi:10.1016/j.geomorph.2016.08.022

Neri, A., Bevilacqua, A., Esposti Ongaro, T., Isaia, R., Aspinall, W. P., Bisson, M., et al. (2015). Quantifying volcanic hazard at Campi Flegrei caldera (Italy) with uncertainty assessment: 2. Pyroclastic density current invasion maps. *J. Geophys. Res. Solid Earth* 120, 2330–2349. doi:10.1002/2014jb011776

Newhall, C., and Hoblitt, R. (2002). Constructing event trees for volcanic crises. *Bull. Volcanol.* 64, 3–20. doi:10.1007/s004450100173

Pallister, J., Papale, P., Eichelberger, J., Newhall, C., Mandeville, C., Nakada, S., et al. (2019). Volcano observatory best practices (VOBP) workshops-a summary of findings and best-practice recommendations. *J. Appl. Volcanol.* 8, 2. doi:10.1186/s13617-019-0082-8

Pierson, T. C., and Major, J. J. (2014). Hydrogeomorphic effects of explosive volcanic eruptions on drainage basins. *Annu. Rev. Earth Planet. Sci.* 42, 469–507. doi:10.1146/annurev-earth-060313-054913

QGIS Development Team (2021). QGIS geographic information system. Available at: http://qgis.osgeo.org Accessed January 27, 2021.

Rutarindwa, R., Spiller, E. T., Bevilacqua, A., Bursik, M. I., and Patra, A. K. (2019). Dynamic probabilistic hazard mapping in the Long Valley volcanic region CA: integrating vent opening maps and statistical surrogates of physical models of pyroclastic density currents. *J. Geophys. Res. Solid Earth* 124, 9600–9621. doi:10.1029/2019jb017352

Sandri, L., Jolly, G., Lindsay, J., Howe, T., and Marzocchi, W. (2012). Combining long- and short-term probabilistic volcanic hazard assessment with cost-benefit analysis to support decision making in a volcanic crisis from the Auckland volcanic field, New Zealand. *Bull. Volcanol.* 74, 705–723. doi:10.1007/s00445-011-0556-y

Sandri, L., Thouret, J. C., Constantinescu, R., Biass, S., and Tonini, R. (2014). Long-term multi-hazard assessment for El Misti volcano (Peru). *Bull. Volcanol.* 76, 1–26. doi:10.1007/s00445-013-0771-9

Sandri, L., Tierz, P., Costa, A., and Marzocchi, W. (2018). Probabilistic hazard from pyroclastic density currents in the Neapolitan area (Southern Italy). *J. Geophys. Res. Solid Earth* 123, 3474. doi:10.1002/2017JB014890

Sparks, R. S. J., and Aspinall, W. P. (2004). Volcanic activity: Frontiers and challenges in forecasting, prediction and risk assessment. *IUGG* 19, 359–373. doi:10.1029/150gm28

Sparks, R. S. J., Wilson, L., and Hulme, G. (1978). Theoretical modeling of the generation, movement, and emplacement of pyroclastic flows by column collapse. *J. Geophys. Res.* 83 (B4), 1727–1739. doi:10.1029/JB083iB04p01727

Spiller, E. T., Bayarri, M. J., Berger, J. O., Calder, E. S., Patra, A. K., Pitman, E. B., et al. (2014). Automating emulator construction for geophysical hazard maps. *SIAM-ASA J. Uncertain. Quantif.* 2, 126–152. doi:10.1137/120899285

Sulpizio, R., Dellino, P., Doronzo, D. M., and Sarocchi, D. (2014). Pyroclastic density currents: state of the art and perspectives. *J. Volcanol. Geotherm. Res.* 283, 36–65. doi:10.1016/j.jvolgeores.2014.06.014

Thouret, J. C., Antoine, S., Magill, C., and Ollier, C. (2020). Lahars and debris flows: characteristics and impacts. *Earth-Sci. Rev.* 201, 103003. doi:10.1016/j.earscirev.2019.103003

Tierz, P. (2020). Long-term probabilistic volcanic hazard assessment using open and non-open data: observations and current issues. *Front. Earth Sci.* 8, 257.

Tierz, P., Loughlin, S. C., and Calder, E. S. (2019). VOLCANS: an objective, structured and reproducible method for identifying sets of analogue volcanoes. *Bull. Volcanol.* 81, 76. doi:10.1007/s00445-019-1336-3

Tierz, P., Sandri, L., Costa, A., Sulpizio, R., Zaccarelli, L., Vito, M. A. D., et al. (2016). "Uncertainty assessment of pyroclastic density currents at Mount Vesuvius (Italy) simulated through the energy cone model," in *Natural hazard uncertainty assessment: modeling and decision support*. Editors P. Webley, K. Riley, and M. P. Thompson (Hoboken, NJ: John Wiley & Sons), 125–145. doi:10.1002/9781119028116.ch9

Tierz, P., Stefanescu, E. R., Sandri, L., Sulpizio, R., Valentine, G. A., Marzocchi, W., et al. (2018). Towards quantitative volcanic risk of pyroclastic density currents: probabilistic hazard curves and maps around Somma-Vesuvius (Italy). *J. Geophys. Res. Solid Earth* 123–383. doi:10.1029/2017JB015383

Tierz, P., Woodhouse, M. J., Phillips, J. C., Sandri, L., Selva, J., Marzocchi, W., et al. (2017). A framework for probabilistic multi-hazard assessment of rain-triggered lahars using bayesian belief networks. *Front. Earth Sci.* 5, 73. doi:10.3389/feart.2017.00073

Valentine, G. A. (1998). Damage to structures by pyroclastic flows and surges, inferred from nuclear weapons effects. *J. Volcanol. Geotherm. Res.* 87, 117–140. doi:10.1016/s0377-0273(98)00094-8

Vallance, J. W., and Iverson, R. M. (2015). "Lahars and their deposits," in *The encyclopedia of volcanoes*. 2nd Edn. Editors H. Sigurdsson, B. Houghton, S. McNutt, H. Rymer, and J. Stix (Cambridge, United Kingdom: Academic Press), 649–664. doi:10.1016/B978-0-12-385938-9.00037-7

Woo, G. (1999). *The mathematics of natural catastrophes*. London, United Kingdom: Imperial College Press.

Conflict of Interest: The authors declare that the research was conducted in the absence of any commercial or financial relationships that could be construed as a potential conflict of interest.

frontiers in Earth Science

ORIGINAL RESEARCH
published: 23 June 2020
doi: 10.3389/feart.2020.00170

Distribution and Eruptive Volume of Aso-4 Pyroclastic Density Current and Tephra Fall Deposits, Japan: A M8 Super-Eruption

Shinji Takarada and Hideo Hoshizumi*

Geological Survey of Japan, National Institute of Advanced Industrial Science and Technology (AIST), Tsukuba, Japan

Estimations of the distribution and eruptive volume of large-scale pyroclastic density current (PDCs) and tephra fall deposits are essential for evaluation of the affected area, long-term volcanic hazards assessments, volcanic activity, and geophysical and petrological quantitative analysis at caldera volcanoes. For this study, the original distributions and eruptive volumes of large-scale PDC (up to 166 km runout distance) and tephra fall deposits derived from the last 87–89 ka caldera-forming eruption (named Aso-4) of Aso volcano in Japan were reevaluated. The original distributions and volumes of PDC deposits just after the eruption were estimated using 3,600 data from geological maps, published research papers, and borehole thickness. The original distributions and volumes of tephra falls were estimated from new isopach maps based on thickness and distribution data of submarine, lacustrine, and subaerial tephra fall deposits. The estimated original volume of the Aso-4 PDC deposits is 340–935 km^3 (5.6–14.8 $\times$ 10^{14} kg). The estimated original volume of the Aso-4 tephra fall deposit is 590–920 km^3 (6.0–9.3 $\times$ 10^{14} kg). The total eruptive volume of the Aso-4 eruption was 930–1,860 km^3 (1.2–2.4 $\times$ 10^{15} kg). This estimation result is about 1.5 to 3 times larger than the previous estimation (>600 km^3). Thus, the Aso-4 eruption is now defined as a M8.1–8.4 (VEI8) super-eruption. The Aso-4 results to be the largest eruption in Japan and the 2nd largest eruption in the world (after the 74 ka Toba eruption) in the last 100 ka.

Keywords: Aso caldera, ignimbrite, co-ignimbrite ash, large-scale eruption, estimation uncertainty, volcanic hazard assessment

OPEN ACCESS

Edited by:
Andrea Bevilacqua, National Institute of Geophysics and Volcanology, Italy

Reviewed by:
Antonio Costa, National Institute of Geophysics and Volcanology, Italy
Greg A. Valentine, University at Buffalo, United States

****Correspondence:***
Shinji Takarada
s-takarada@aist.go.jp

Specialty section:
This article was submitted to Volcanology, a section of the journal Frontiers in Earth Science

Received: *06 April 2020*
Accepted: *04 May 2020*
Published: *23 June 2020*

Citation:
Takarada S and Hoshizumi H (2020) Distribution and Eruptive Volume of Aso-4 Pyroclastic Density Current and Tephra Fall Deposits, Japan: A M8 Super-Eruption. Front. Earth Sci. 8:170. doi: 10.3389/feart.2020.00170

INTRODUCTION

Accurate determinations of the eruptive volumes of large-scale caldera-forming eruptions provide an essential parameter for assessing long-term eruption records, eruption activity evaluations, and quantitative geophysical and petrological investigations. The eruptive volume is also used for developing reliable volume vs. time diagrams and volcanic hazard assessments. Recently, several studies to estimate the eruptive volume of tephra falls derived from large-scale volcanic eruptions were made (e.g., Costa et al., 2014; Kandlbauer and Sparks, 2014). Furthermore, a large number of studies have been published to estimate the eruptive volume of tephra fall deposits (e.g., Pyle, 1989, 1995; Fierstein and Nathenson, 1992; Legros, 2000; Bonadonna and Houghton, 2005;

Sulpizio, 2005; Bonadonna and Costa, 2012; Engwell et al., 2013). However, relatively few studies have reported high-resolution eruptive volume estimates of large-scale caldera-forming pyroclastic density current (PDC) deposits (e.g., Cook et al., 2016).

The 87–89 ka Aso-4 eruption is the largest of the 4 major caldera-forming eruptions from Aso caldera. It is also considered to be one of the largest eruptions in Japan in the last 1 Ma (e.g., Hayakawa, 1995). Here we estimated the original distributions and eruptive volume of the large-scale Aso-4 PDC deposit, based on more than 3,600 boreholes, topography, and outcrop data with a 7 km × 5.5 km mesh interval. The eruptive volume of the co-ignimbrite ash fall deposit derived from the Aso-4 eruption was also estimated using new isopach maps based on thickness data from about 70 locations, including submarine and lacustrine sample data.

GEOLOGY OF ASO-4 PDC DEPOSITS

Aso caldera, 25 km N-S × 18 km E-W, is located in central Kyushu and is one of the largest calderas in Japan (Ono et al., 1977; Ono and Watanabe, 1985). It was formed by four major eruptive events that produced widespread PDC deposits: Aso-1 (ca. 270 ka), Aso-2 (ca. 140 ka), Aso-3 (ca. 120 ka), and Aso-4 (89 ka) PDCs (Ono and Watanabe, 1985; K-Ar ages from Matsumoto et al., 1991). The Aso-4 PDC deposit records the largest eruptive event and is widely distributed in northern and central Kyushu and western Yamaguchi Prefecture (**Figure 1**). The Aso-4 PDCs reached as far as 166 km to NNE from the central caldera (**Figure 1**), one of the largest runout distances ever recorded. For comparison, the runout distances of the 18.8 Ma Peach Spring Tuff, United States, reached as far as 175 km (Roche et al., 2016), the 40 Ma Big Cottonwood Canyon Tuff, United States, reached >150 km (Henry, 2008), and the 186 AD Taupo ignimbrite, New Zealand, reached ca. 80 km (Wilson and Walker, 1985). A large number of studies were made on the Aso-4 PDC deposits such as Ono (1965), Watanabe and Ono (1969), Watanabe (1972, 1978, 1979), Ono et al. (1977), Ono and Watanabe (1983, 1985), Hoshizumi et al. (1988), Suzuki-Kamata and Kamata (1990), Kamata (1997), Saito et al. (2005), and Okumura et al. (2010). Ono and Watanabe (1983) defined the approximate distributions of Aso-1, Aso-2, Aso-3, and Aso-4 PDC deposits. The Aso-1 and Aso-2 PDC deposits are distributed as far as 30 km from the caldera, Aso-3 PDC deposit is distributed as far as 50 km W and 70 km E from the caldera and Aso-4 PDC deposit is distributed widely and as far as 166 km NNE (**Figure 1**; the distribution and volume of the Aso-4 PDC deposits are examined in this study). The distal facies of the Aso-4 PDC deposits in Yamaguchi Prefecture were studied by Matsuo and Takahashi (1974), Matsuo (1978, 1984, 2001), and Matsuo and Kawaguchi (2015). The Aso-4 PDC deposit contains hornblende phenocrysts, which is a marker to distinguish it from the Aso-1, 2, and 3 PDC deposits (e.g., Ono et al., 1977; Ono and Watanabe, 1985; Saito et al., 2005). The Aso-4 PDC deposits within terrace deposits in Miyazaki and Fukuoka Prefectures were reported by Nagaoka (1984), Shimoyama et al. (1984), and Endo and Suzuki (1986).

Aso-4 tephra fall deposits are widely distributed and are one of the most significant marker tephras for volcanological studies throughout Japan (Machida et al., 1985; Machida and Arai, 1988, 2003; Nagahashi et al., 2004, 2007; Aoki, 2008; Tsuji et al., 2018). No preceding Plinian tephra fall deposits have been observed beneath the Aso-4 PDC deposits (Ono et al., 1977; Ono and Watanabe, 1983), suggesting most of the widely distributed tephra fall deposits are derived from the co-ignimbrite ash (Machida et al., 1985; Machida and Arai, 2003). The thickness of the Aso-4 tephra fall deposits is a few cm in Omachi City, Nagano Prefecture, 5 cm in Noshiro City, Akita Prefecture, and 15 cm in Abashiri City, Hokkaido (**Figure 1**; Machida et al., 1985).

The Aso-4 PDC deposits consist of several massive dacite units, which are defined by lithology, facies, and cooling history (e.g., Watanabe, 1978; Hoshizumi et al., 1988; Kamata, 1997). Aso-4A and 4B units were defined by Ono and Soya (1968) and Ono et al. (1977). Aso-4A, Aso-4T, and Aso-4B units were subsequently defined by Hoshizumi et al. (1988) and Kamata (1997) (**Figure 2**). More detailed subdivisions comprise the Oyatsu white pumice flow, Koei ash flow, Hatobira pumice flow, Yame pumice flow, Motoigi gray pumice flow, Benri scoria flow, Tosu orange pumice flow, and Kunomine scoria flow deposits, which were defined by Watanabe (1978) in the western part of the Aso caldera area. The Tosu orange pumice flow (Aso-4T) is a low-aspect ratio ignimbrite, which shows widely distributed ignimbrite-veneer type deposits (Watanabe, 1978; Suzuki-Kamata and Kamata, 1990).

The Aso-4A PDC deposits consist of <100 m-thick, densely to partially welded and non-welded, poorly sorted, and massive ignimbrite containing relatively large amounts of pumice lapilli and blocks (**Figures 2**, **3a**,**b**). The Aso-4A PDC deposits are normally massive, but flow unit boundaries are sometimes observed in a few-meters interval, suggesting that this consists of >10–20 flow units. The upper non-welded facies are sometimes eroded. The lower part of the ignimbrite consists of non-welded grayish white to gray-colored matrix and pumice block and lapilli. The layer 2a (Sparks et al., 1973) is sometimes developed at the base of the non-welded facies. Breccia facies are sometimes developed at the bottom of the Aso-4A PDC deposit (**Figures 2**, **3a**). The breccia facies consist of lithic-rich matrix and boulders, blocks, and lapilli-size dense rocks with a small amount of pumice lapilli. Tuff breccia blocks and boulders are sometimes included in the breccia facies. The densely welded facies consist of a dark gray matrix and black fiamme-rich block and lapilli (**Figures 2**, **3d**). The size of the fiamme is >5 cm (sometimes >20–50 cm). A devitrification zone is developed at the lower part of the welded facies. The partially welded facies consist of gray to dark gray matrix and grayish white flattened pumice blocks and lapilli (**Figure 2**). The welded facies show 1–2 m wide columnar joints (**Figure 3c**). The non-welded facies consist of a grayish white to gray matrix and 15–40 vol. % of pumice blocks and lapilli (**Figures 2**, **3b**). The pumice blocks and lapilli are gray to white with tube-type vesicles and are usually <20 cm in size. The matrix consists of fine glassy ash and <4 mm-size crystal fragments. The Aso-4A PDC deposits are the

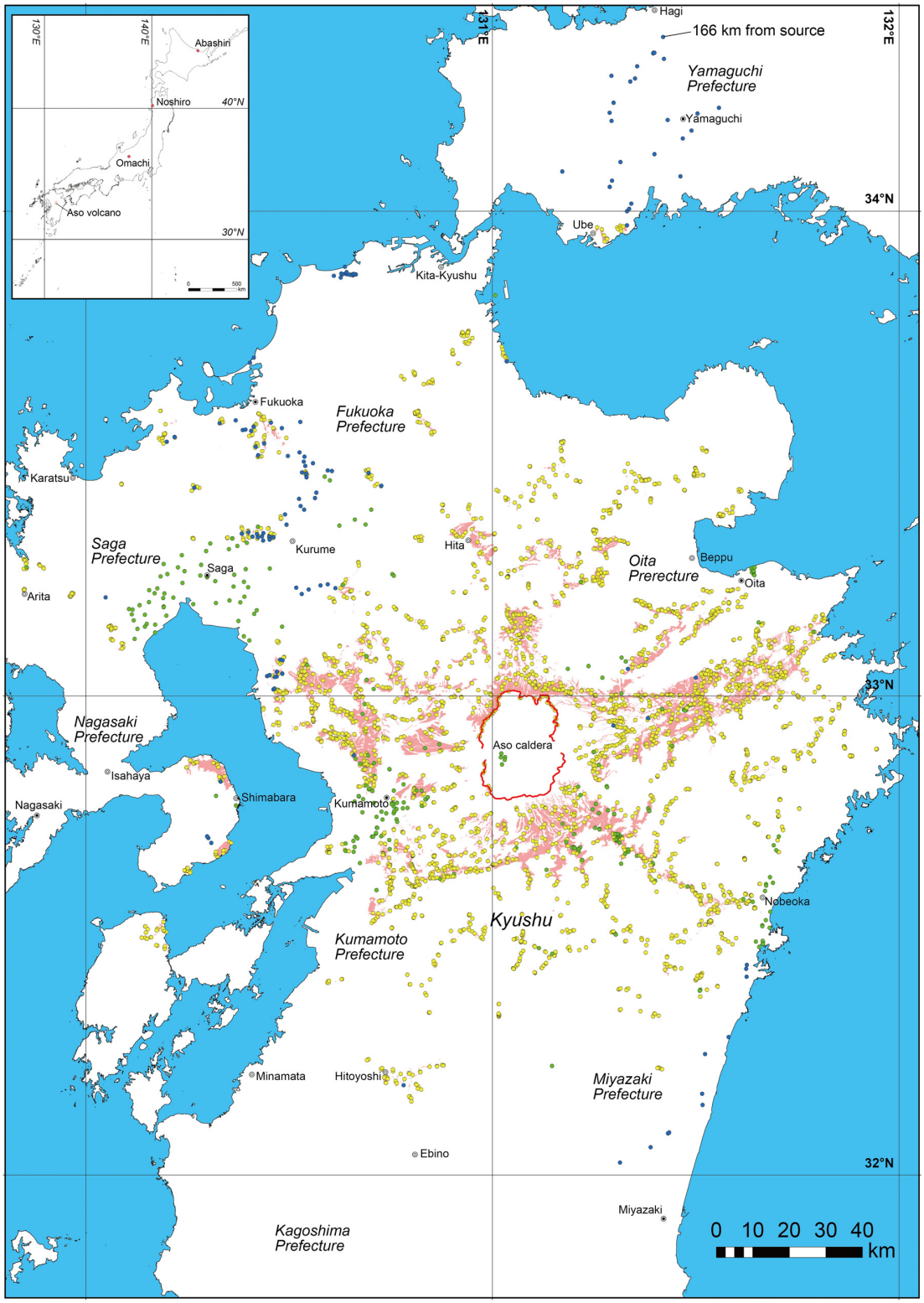

FIGURE 1 | Distribution of current Aso-4 PDC deposit exposures (orange-colored part) and Aso caldera (red line). Circles on the map indicate locations to measure the thickness of PDC deposits based on outcrops (blue circle), borehole (green circle), and topography (yellow circle) sites. The outcrop located at 166 km from the source is shown. The tephra fall outcrop locations at Omachi City, Nagano Prefecture, Noshiro City, Akita Prefecture, and Abashiri City, Hokkaido, are shown in the inset map (upper left corner).

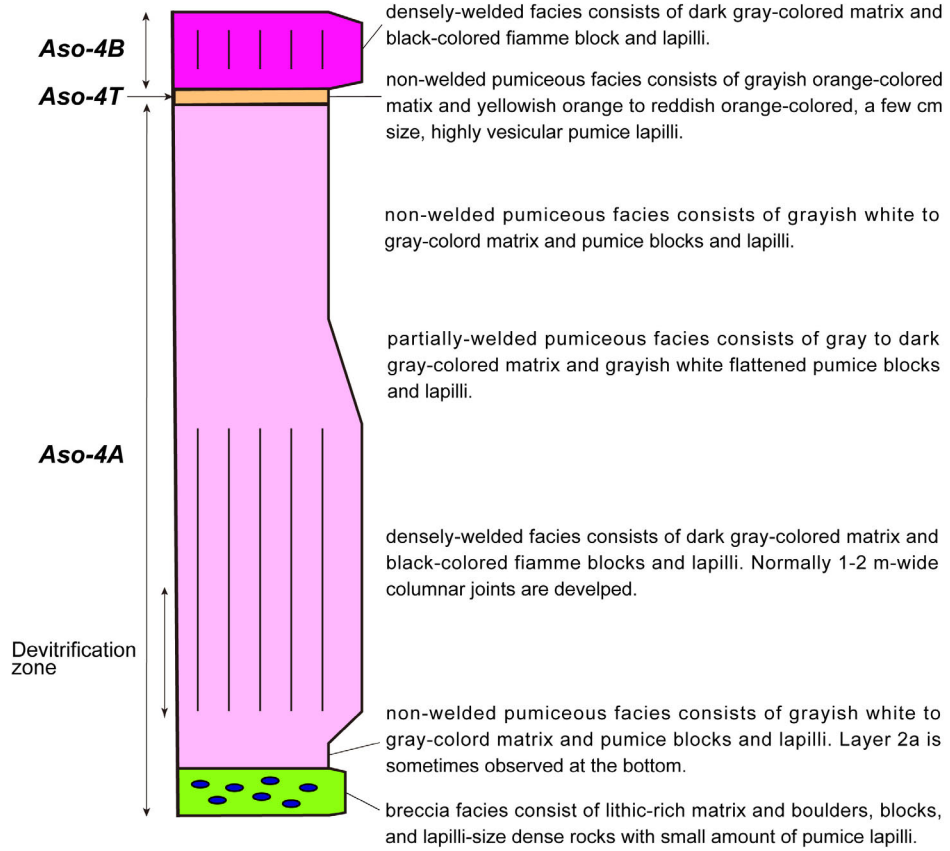

FIGURE 2 | Schematic columnar section of Aso-4 PDC deposit at the north and eastern side of Aso caldera area.

most voluminous of the Aso-4 units. The Aso-4T PDC deposits are relatively thin and distributed locally compared with the Aso-4A PDC deposits (**Figure 2**). The Aso-4T deposits are non-welded and consist of orange-gray matrix and yellowish-orange to reddish-orange-colored highly vesicular pumice lapilli. The size of the pumice clasts is usually less than a few cm. A relatively small amount of <1 cm-size lithic clasts are contained. The Aso-4T unit traveled as far as 166 km from the source. The upper Aso-4B deposits are densely welded and consist of dark-gray matrix and black-colored fiamme block and lapilli (**Figure 2**). The thickness of the Aso-4 PDC deposits decreases in the distal facies (**Figure 3e**). The densely welded ca. 100–400 m-thick intra-caldera Aso-4 PDC deposits are found from the borehole samples at −800 to −1000 m a.s.l. within the steep-sided low-gravity zone (Hoshizumi et al., 1997; Komazawa, 1995; NEDO, 1995).The measured densities of Aso-4 PDC welded facies are 1,690, and 1,810 (partially welded), 2,240, 2,260, and 2,270 (densely welded) kg/m^3 (mean is about 2,000 kg/m^3) and the non-welded facies is about 1,100 kg/m^3. Published values for the measured densities of Aso-4 PDC welded facies range from 1,500–2,450 kg/m^3 (mean is about 2000 kg/m^3; Suzuki and Ono, 1963; Suzuki, 1970; Urai and Tsu, 1986; Yamaguchi et al., 2000) and the non-welded facies is about 1,100 kg/m^3 (e.g., Suzuki, 1970). The degree of welding of Aso-4 PDC deposits ranges between welded rank II (1,250–1,650 kg/m^3) and VI (>2,300 kg/m^3), according to the classification of Quane and Russell (2005).

Petrological studies of Aso-4 PDC deposits were made by Lipman (1967), Watanabe (1978, 1979), Hunter (1998), Kaneko et al. (2007), Miyoshi et al. (2011), and Ushioda et al. (2020). Watanabe (1978, 1979) and Kaneko et al. (2007) showed that the magma of the Aso-4 PDC deposits were derived from homogeneous, voluminous felsic magma sources (SiO_2 = 66–70%) and heterogeneous, low volume mafic magmas (SiO_2 = 50–57%). Kaneko et al. (2007) discussed that the Aso-4 PDC deposits are characterized by two cycles of initial voluminous felsic magmas followed by mafic and mixed magmas.

Matsumoto et al. (1991) and Matsumoto (1996) defined a K-Ar age of 89 ± 7 ka for the Aso-4 deposit. Yoshikawa and Kuwae (2001), Nagahashi et al. (2004, 2007), and Tsuji et al. (2018) similarly defined age of 87 ka (Marine Isotope Stage, MIS5.2) based on tephra correlations with marine tephras. Therefore, the eruption age of the Aso-4 event is considered to be 87–89 ka.

Machida et al. (1985) and Machida and Arai (2003) estimated the volume of Aso-4 PDC deposit at >200 km^3 and Aso-4 tephra fall at >400 km^3. Suto et al. (2007) estimated the total volume of the tephra fall deposit at 1,051 km^3. Yamamoto (2015) estimated the total volume at 384 km^3 in DRE (dense rock equivalent;

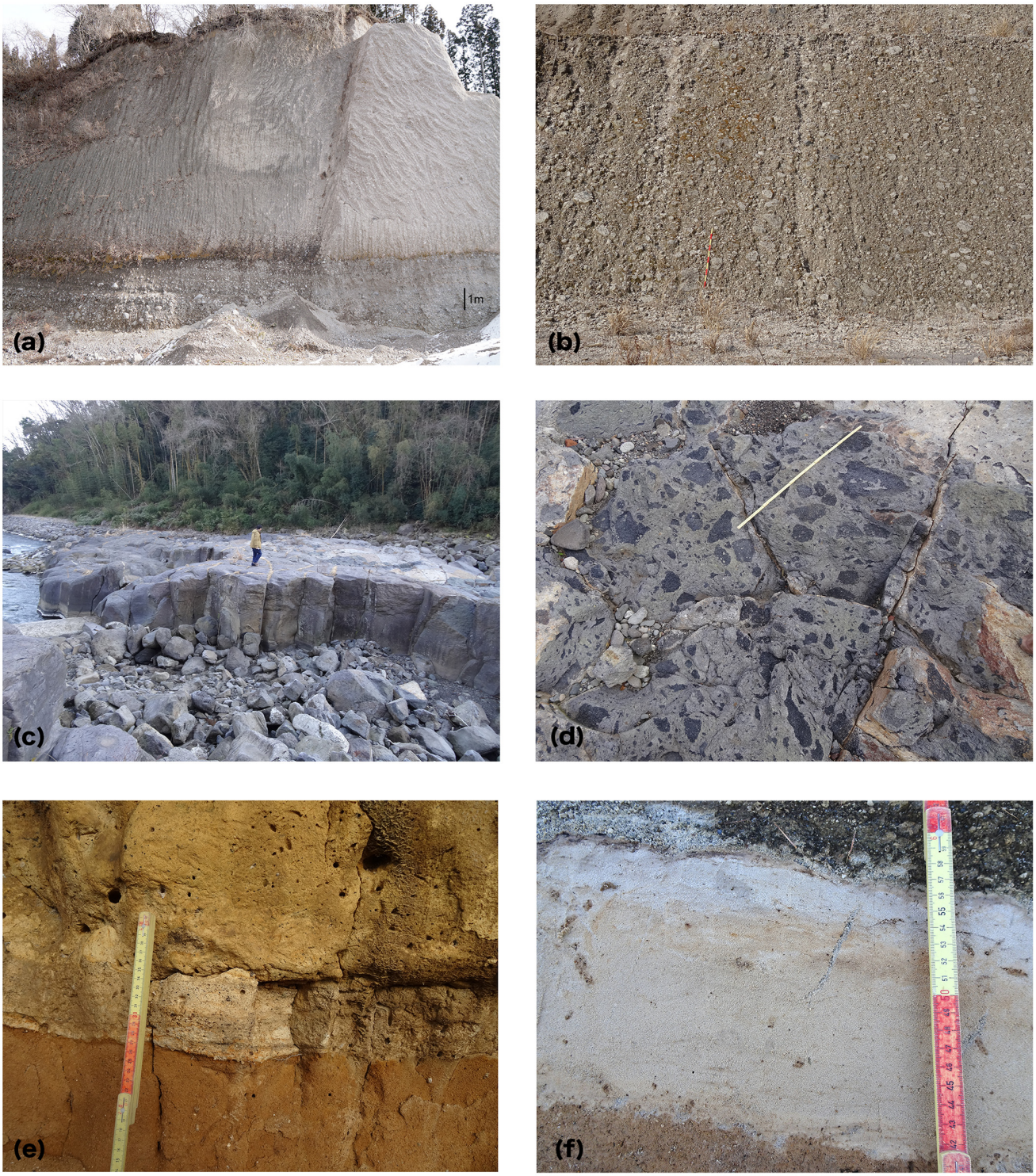

FIGURE 3 | Typical outcrops of Aso-4 PDC and tephra fall deposits. **(a)** Non-welded facies (11 km SE from the source). The lower part is the breccia facies. **(b)** Enlargement of the non-welded facies (30 km N). The scale is 1 m long. **(c)** Welded facies (33 km ENE). **(d)** Enlargement of the welded facies. Note plan view of fiammes [location is the same as **(c)**]. **(e)** Distal facies of the 10–15 cm-thick Aso-4 PDC deposit (white and pale orange-colored part, 117 km NNW). **(f)** A 12 cm-thick Aso-4 tephra fall deposit at Shari Town, Hokkaido (1,695 km NE from the source).

Walker, 1980). Nakajima and Maeno (2015) estimated the total volume at 200 km^3 in DRE.

METHODS AND RESULTS

Distribution and Thickness Estimation of Aso-4 PDC Deposits

The distribution of the current exposure of Aso-4 PDC deposits (**Figures 1**, **4**) was compiled based on geological maps, such as 1:50,000 and 1:200,000 Geological Maps published by Geological Survey of Japan (GSJ), 1:50,000 Surface Geological Maps published by Ministry of Land, Infrastructure and Tourism (MLIT), and maps in published papers. The distribution of the current exposure of Aso-4 PDC deposits was traced using GIS software. The Aso-4 PDC distributions are not shown in areas that have been covered subsequently by thick tephra fall deposits (e.g., the eastern part of Aso caldera) and the younger Kuju volcanic area (30 km NE of Aso caldera).

The original distribution of Aso-4 PDC deposits just after the eruption was estimated by integrating observations and data from current distributions, topographic maps, published papers, and boreholes (**Figures 4–7**). The distal runout distribution limit of Aso-4 PDC deposits in the sea area is assumed to be oval in shape (Machida et al., 1985; Machida and Arai, 2003), as shown in **Figure 5**. The maximum runout distances and apparent friction coefficient (H/L ratio) of Aso-4 PDC deposits are different from the directions, according to the topography of the source region and their pass. For example, the maximum distances of the Aso-4 PDC deposits from the source depend on direction: 166 km (NNE direction), 123 km (WNW), 84 km (SSW), 97 km (SSE), and 80 km (E). Especially, SE to SW side of the Aso caldera is high mountain areas, where the Aso-4 PDC deposits were accumulated within the basins and valleys. Therefore, we think that the oval shape is more reasonable than circular. The Aso-4 PDC deposits were considered to fill the low-land area and valleys. The Aso-4 PDC deposits were assumed to be transferred by turbidity currents and traveled further along the submarine bottom surface topography. However, we considered the Aso-4 PDC that we infer traveled on the surface of the sea, ignoring the submarine processes after entering into submarine seawater. The thin ignimbrite veneer deposits (Walker, 1981) were locally

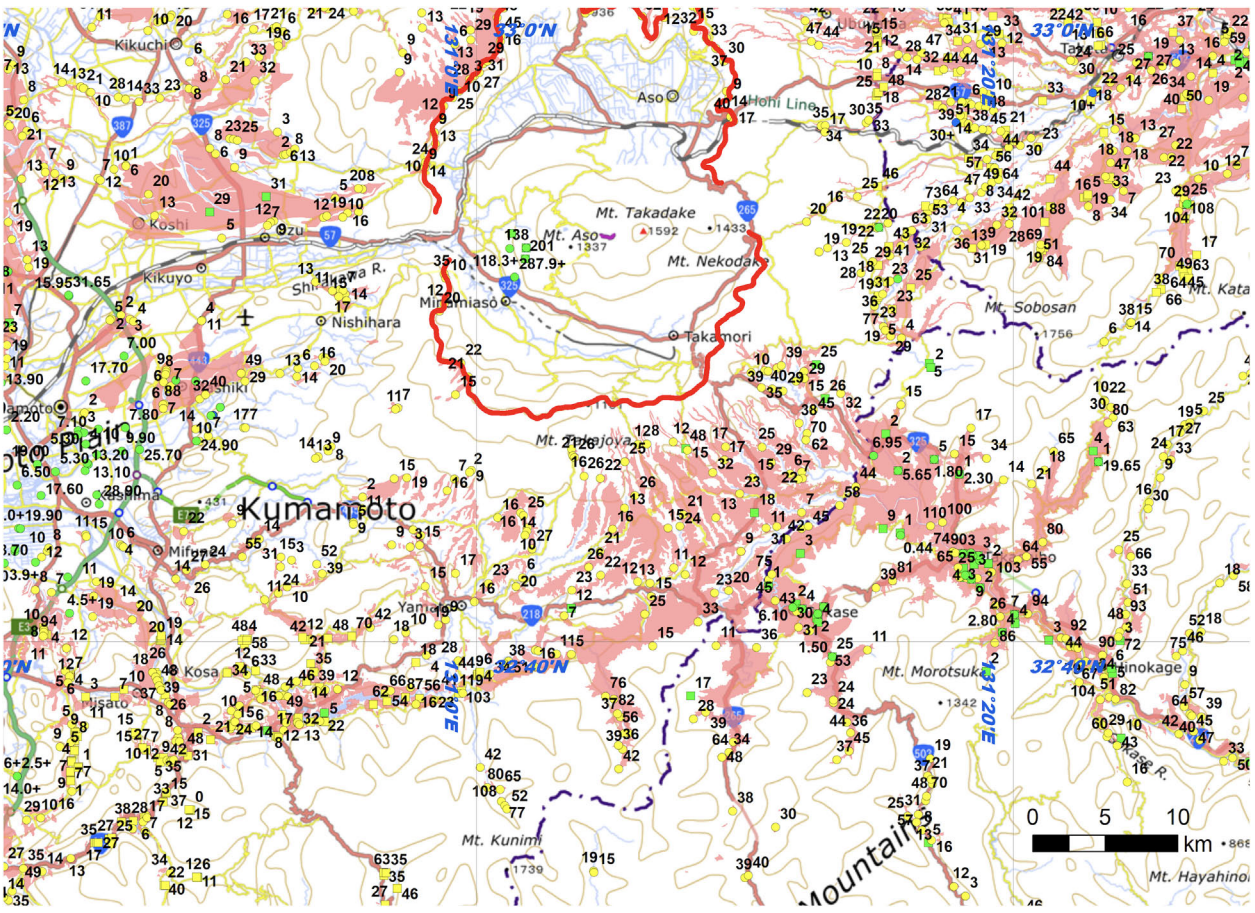

FIGURE 4 | Distribution of Aso-4 PDC deposits and thickness data. The thickness values of the deposits are shown in meters. Circles and squares on the map indicate locations to measure the thickness of PDC deposits based on outcrops (blue), borehole (green), and topography (yellow) sites. The circle marks are non-welded, and the square marks are welded points. The Geospatial Information Authority of Japan (GSI) Tile Map (English) is used as the base map.

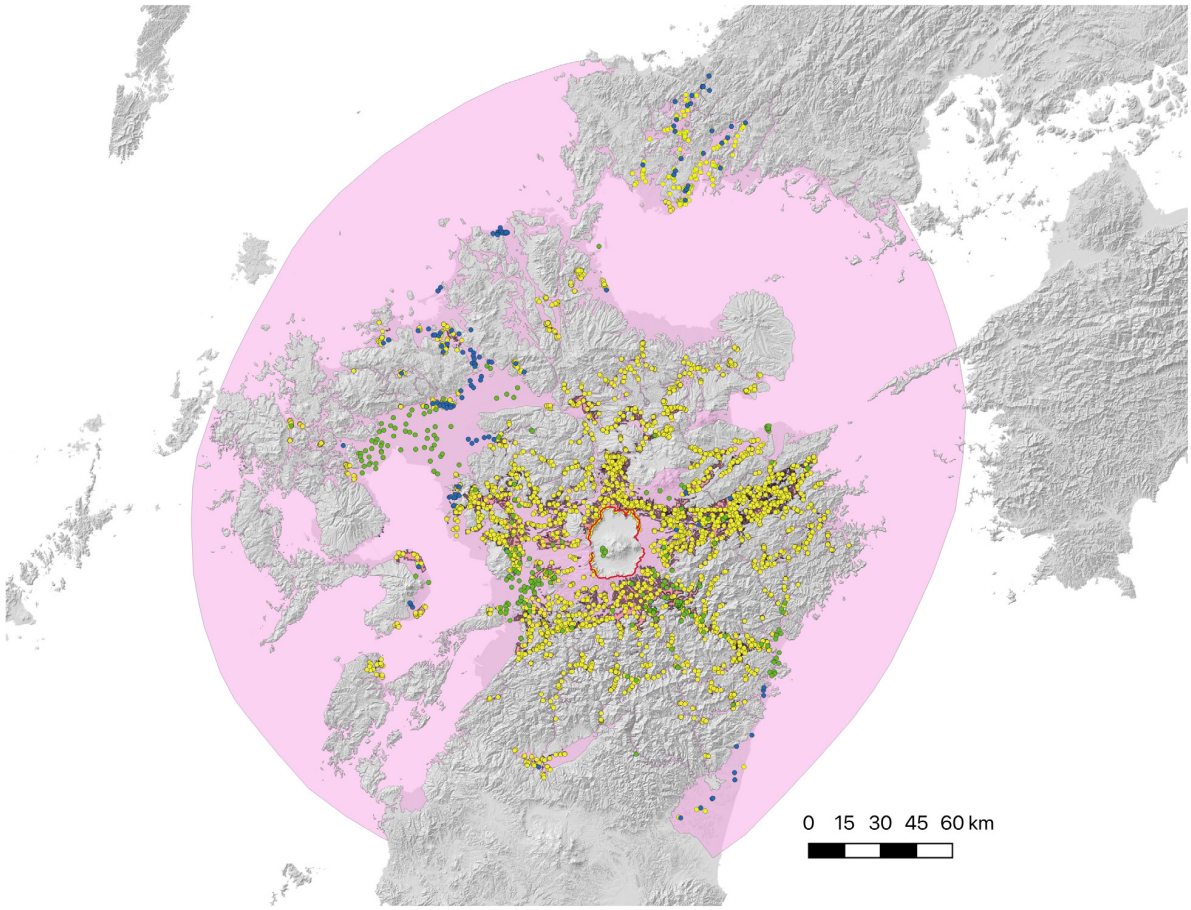

FIGURE 5 | Estimated original distribution of Aso-4 PDC deposit after the emplacement. Legends of circles on the map are the same as in **Figures 1**, **4**. The Geospatial Information Authority of Japan (GSI) Tile Map (Shaded relief map) is used as the base map.

preserved, but not considered on this map because the accurate mapping of such volumetrically minor material was not possible.

The thickness of the Aso-4 PDC deposits was measured using 1:200,000 Geological Maps and 1:50,000 Geological Maps published by GSJ, 1:50,000 Surface Geological Maps published by MLIT, borehole data KuniJiban Database provided by MLIT (MLIT, 2020) and Geo Station Database provided by the National Research Institute for Earth Science and Disaster Prevention (NIED) (NIED, 2020). Location, altitude, and depth of the top and bottom of the deposits in subsurface boreholes and welded (1,070 points) and non-welded (2,541 points) data were compiled (3,611 points in total; **Figures 1**, **4**–**7**). Partially welded facies are classified as non-welded in our compilation. Thickness data at outcrops obtained from published papers were used (blue circles in **Figures 1**, **4**, **5**, **7**). Thickness data were measured from the top and bottom depth of the Aso-4 deposits on the KuniJiban and Geo Station Databases (green circles in **Figures 1**, **4**–**7**; accuracy is about 10 cm). The thickness data were also measured from upper-limit and lower-limit altitudes on geological maps at ignimbrite plateau and measurable points (yellow circles in **Figures 1**, **4**–**7**). The thickness of the deposits within the caldera (118–407 m) was also measured using borehole data (Hoshizumi et al., 1997; Komazawa, 1995; NEDO, 1995). The thickness data were compiled in an excel spreadsheet and plotted using QGIS software.

Volume Estimation of Aso-4 PDC Deposits

The thickness data were analyzed within a 7 km × 5.5 km mesh grid (**Supplementary Table S1**). The maximum (**Figure 6a**), minimum (**Figure 6b**), and average (mean; **Figure 6c**) of each grid cell was calculated and plotted (purple-colored numbers values in **Figure 6**). For example, the 3rd cell from the right in the middle of **Figure 6** contains 6 thickness data of non-welded facies (48.9, 55.2, 34, 37, 9, and 50 m). Hence, the maximum, minimum, and average (mean) thickness are 55.2 m, 9 m, and ca. 39 m, respectively. The thickness was plotted for non-welded facies (**Figures 6**, **7b**) and also welded facies (**Figure 7a**). The grid cells that contain no thickness data were estimated using the ordinary kriging method (geospatial interpolation; Davis, 1986; Yamamoto, 2000). When the thickness value became <0 m, the estimated thickness was assigned to be 0 m. In the sea area, the marginal thickness was set at 0 m (right-lower corner of

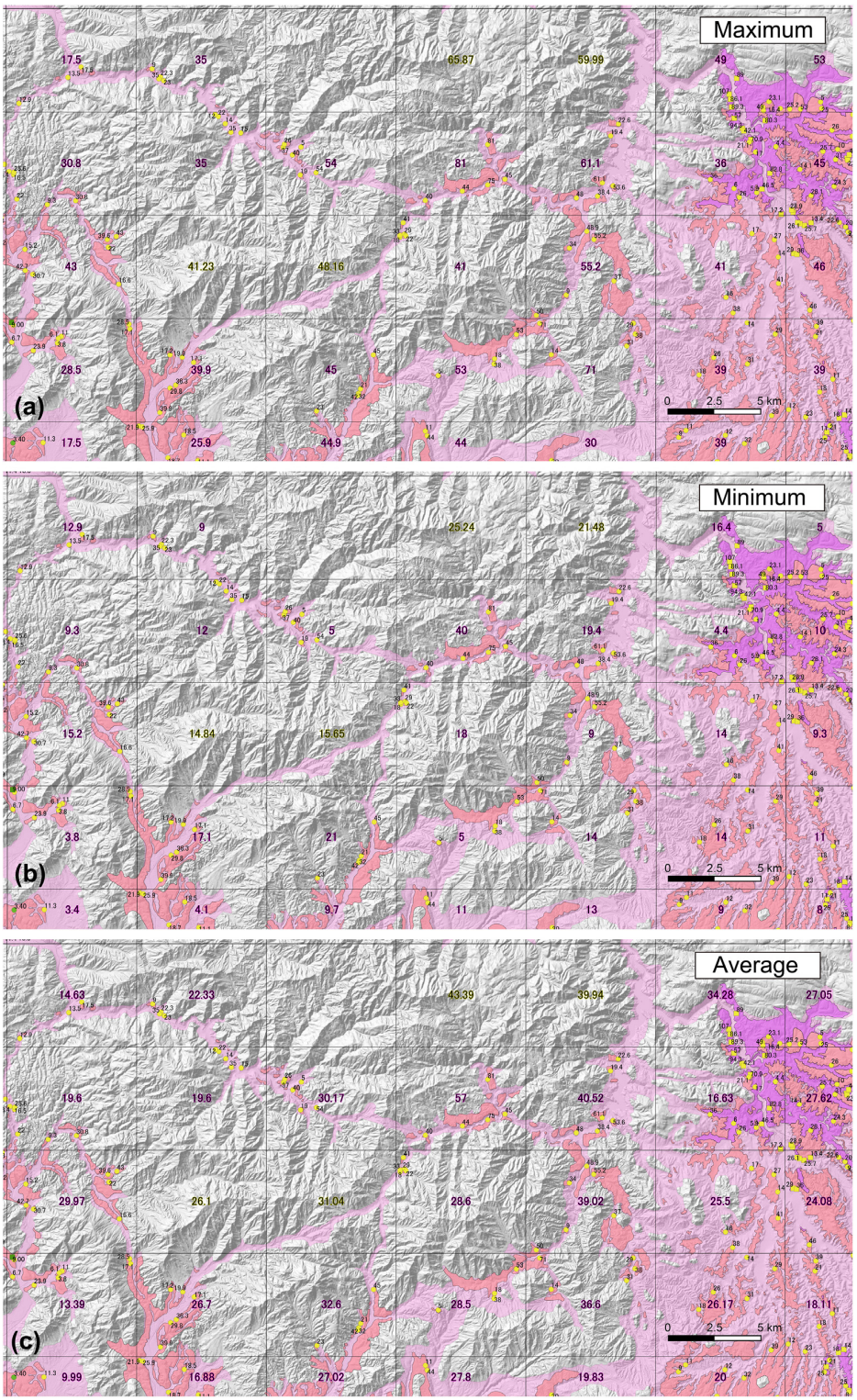

FIGURE 6 | Estimated thickness of non-welded parts of Aso-4 PDC deposits [maximum **(a)**, minimum **(b)**, and average (mean) cases **(c)**] at NW side of Aso caldera. Orange-colored parts are the non-welded facies of Aso-4 PDC deposits (current exposure). Purple-colored parts are the welded-facies (current exposure). Light pink-colored parts are the estimated original distribution of the Aso-4 PDC deposit. Purple-colored rim numbers are the maximum **(a)**, minimum **(b)**, and average **(c)** thickness values (m) of all points data within the cell. Yellow-colored rim numbers are the estimated thickness values using the ordinary kriging method. Circles and Squares on the map indicate locations to measure the thickness of PDC deposits based on borehole (green) and topography (yellow) sites. The circle marks are non-welded, and the square marks are welded points. The Geospatial Information Authority of Japan (GSI) Tile Map (Shaded relief map) is used as the base map.

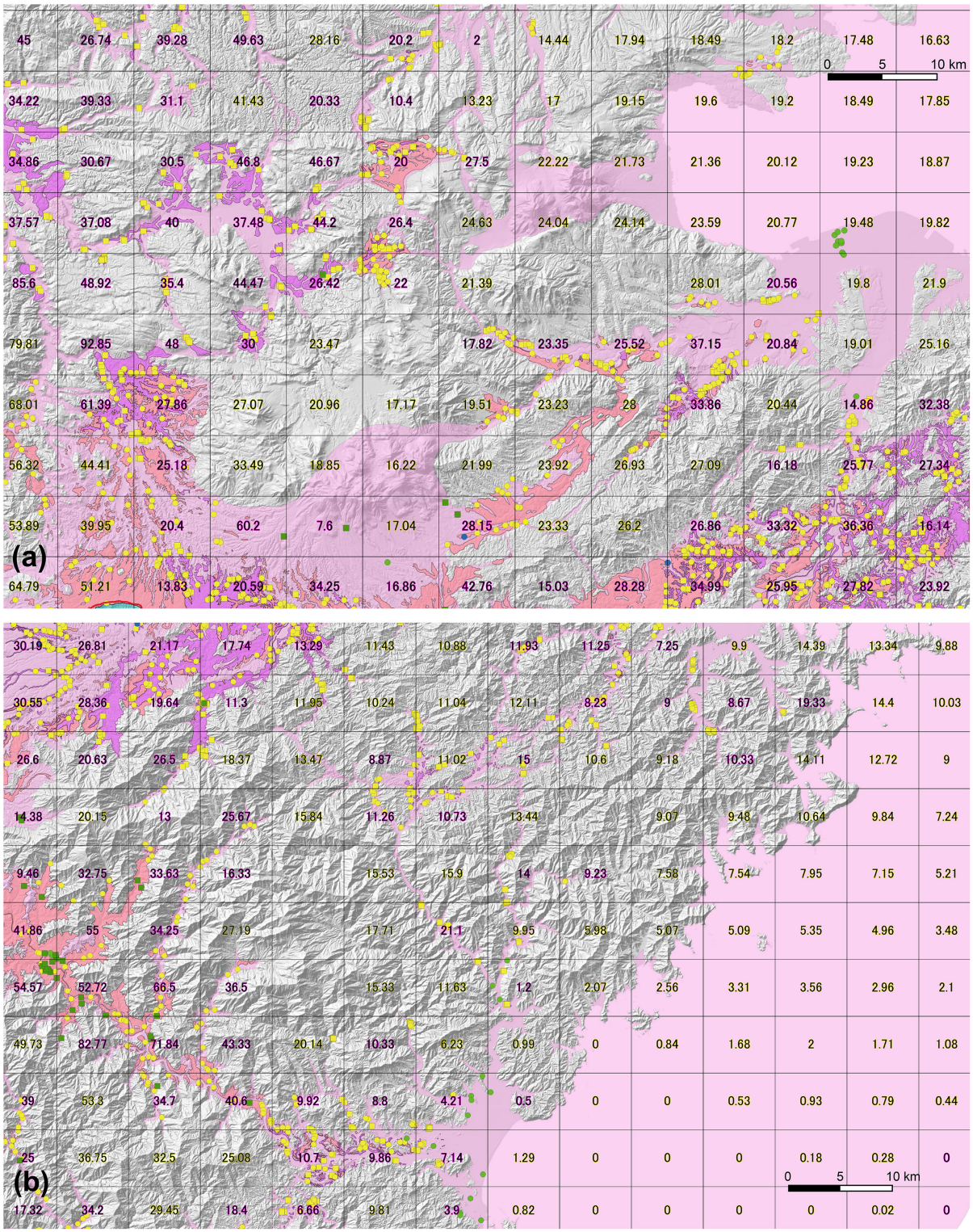

FIGURE 7 | Estimated thickness of Aso-4 PDC deposit. Welded PDC deposits at N and NE side of Aso caldera **(a)** and non-welded PDC deposits at E and SE side of Aso caldera **(b)**. Orange-colored parts are the non-welded facies of Aso-4 PDC deposits (current exposure). Purple-colored parts are the welded-facies (current exposure). Light pink-colored parts are the estimated original distribution of the Aso-4 PDC deposit. Purple-colored rim numbers are the average (mean) thickness of all points data within the cell. Yellow-colored rim numbers are the estimated thickness values using the ordinary kriging method. Symbol colors and type of point data are the same as **Figure 6**. The Geospatial Information Authority of Japan (GSI) Tile Map (Shaded relief map) is used as the base map.

TABLE 1 | Results of the area and volume estimation of Aso-4 PDC deposit (density of the non-welded and unclassified facies is 1,100 kg/m^3, welded facies is 2,000 kg/m^3, and dense rock is 2,500 kg/m^3).

		Area (km^2)	Volume (km^3 Bulk)			Volume (km^3 DRE)		
			Maximum	Minimum	Average	Maximum	Minimum	Average
Current Exposure	Non-welded and unclassified	1,007	37.1	7.6	21.3	16.3	3.4	9.4
	Welded	336	16.6	5.6	10.9	13.3	4.5	8.7
	Subtotal	1,343	53.7	13.2	32.1	29.6	7.8	18.0
Original Distribution (outflow)	Non-welded and unclassified	–	288.9	82.8	173.8	127.1	36.4	76.5
	Welded	–	429.3	163.5	296.7	343.4	130.8	237.4
	Subtotal	34,324	**718.2**	**246.2**	**470.5**	**470.6**	**167.2**	**313.8**
Intracaldera	Non-welded and unclassified	–	145.4	42.3	105.8	64.0	18.6	46.5
	Welded	–	71.9	49.3	64.3	57.6	39.5	51.4
	Subtotal	357	217.4	91.6	170.1	121.5	58.1	98.0
	Total	34,681	**935.6**	**337.9**	**640.5**	**592.1**	**225.3**	**411.8**

The bold numbers values are the most important values (results of our estimation).

Figure 7b), and the thickness of the PDC deposits (above the sea surface) was calculated using the ordinary kriging method. The thickness tends to decrease radially from the source toward the marginal rim in the sea area. The thickness of the deposits in the subaerial area changes according to the local topography. Local thickening of the PDC deposits is observed at the slope change or basin areas (such as the upper right of **Figure 6**, middle left and lower right of **Figure 7a**, and middle left of **Figure 7b**).

The occupied area of the estimated original Aso-4 PDC deposit (i.e., just after the deposition; the light-pink colored area in **Figures 6**, **7**) within each 7 km × 5.5 km grid cell was calculated using QGIS software. The maximum, minimum, and average volumes of each grid cell were calculated by multiplying the estimated thickness and area of the Aso-4 PDC deposit (volumes of non-welded and welded facies were calculated, separately). The total estimated bulk volume (km^3) was calculated by summing up all estimated volumes of grid cells. The DRE volume (**Table 1**) was calculated from the ratio between the average non-welded density (1,100 kg/m^3) and dense rock density (2,500 kg/m^3) and also the ratio between the average welded density (2,000 kg/m^3) and dense rock density (2,500 kg/m^3).

The results of the area and volume estimations of Aso-4 PDC deposits are summarized in **Table 1**. The current exposure area of the Aso-4 PDC deposit is about 1,000 km^2. The estimated original distribution area of the outflow Aso-4 PDC deposit (just after deposition) is about 34,000 km^2. Total volumes of the current exposure of Aso-4 PDC deposits are 13–54 km^3 in bulk (8–30 km^3 in DRE). The estimated original volumes of Aso-4 PDC outflow deposits are 250–720 km^3 (170–470 km^3 in DRE). The estimated original volumes of intracaldera Aso-4 PDC deposits are 90–220 km^3 (58–120 in DRE). The total estimated original volumes of Aso-4 PDC deposit just after deposition are 335–940 km^3 (225–590 km^3 in DRE; 5.6–14.8 × 10^{14} kg) (**Table 1**).

Distribution Estimation of Aso-4 Tephra Fall Deposits

Thickness and location data of Aso-4 tephra fall deposits are recompiled from prior studies, which comprise data for 71 locations of outcrops, lacustrine, submarine, and on-land cores and boreholes (**Supplementary Table S2**). The thickness data were plotted using ArcGIS software, and isopach maps (1, 2, 4, 8, 16, 32, 64, and 128 cm) of Aso-4 tephra deposits were made (**Figure 8**). The thickness of the tephra fall deposit in Eastern Hokkaido is up to 15 cm (**Figure 3f**). This value is relatively high compared to the Honshu area (probably due to local wind effects). Hence, two types of isopach maps were made: (1) Maximum case (**Figure 8a**), using the thickness data of Eastern Hokkaido and assuming erosion in the Honshu area; and (2) Minimum case (**Figure 8b**), for which the thickness data of Eastern Hokkaido were considered to be influenced by local wind disturbance and ignored for drawing.

Volume Estimation of Aso-4 Tephra Fall Deposits

The area of each isopach contour was calculated using ArcGIS software, and the volumes of Aso-4 tephra fall deposits were estimated using the segment integration method (Takarada et al., 2001, 2016). In the maximum case, the volume was calculated by integrating 3 subdivisions (**Figure 8a**; subdivided at 16 and 64 cm isopachs). In each segment, the data were plotted approximately on a straight line using the least square method. The volume was calculated for the area between the caldera rim (5.3 × 10^2 km^2) and the distal limit, for a total area of 10^8 km^2 (0.1 mm in thickness). The thickness of the tephra fall deposit at the caldera rim was assumed at 300 cm from the extrapolation of the trend of 64 and 128 cm isopach data. The average density of the tephra fall deposit was estimated at about 1,000 kg/m^3. The estimated results were 400 km^3 (4.0 × 10^{14} kg) in the area of the distal region (<16 cm isopach data area), 470 km^3 (4.7 × 10^{14} kg) in the medial region (between 16 and 64 cm data area), and 47 km^3 (4.7 × 10^{13} kg) in the area of the proximal region (between 64 and 300 cm data area). The total estimated eruptive mass of the Aso-4 tephra deposit was 920 km^3 (370 km^3 in DRE; 9.2 × 10^{14} kg).

In the minimum case, the volume was calculated by integrating three subdivisions (**Figure 8b**; subdivided at 4 and 64 cm isopach). The volume was also calculated for the area

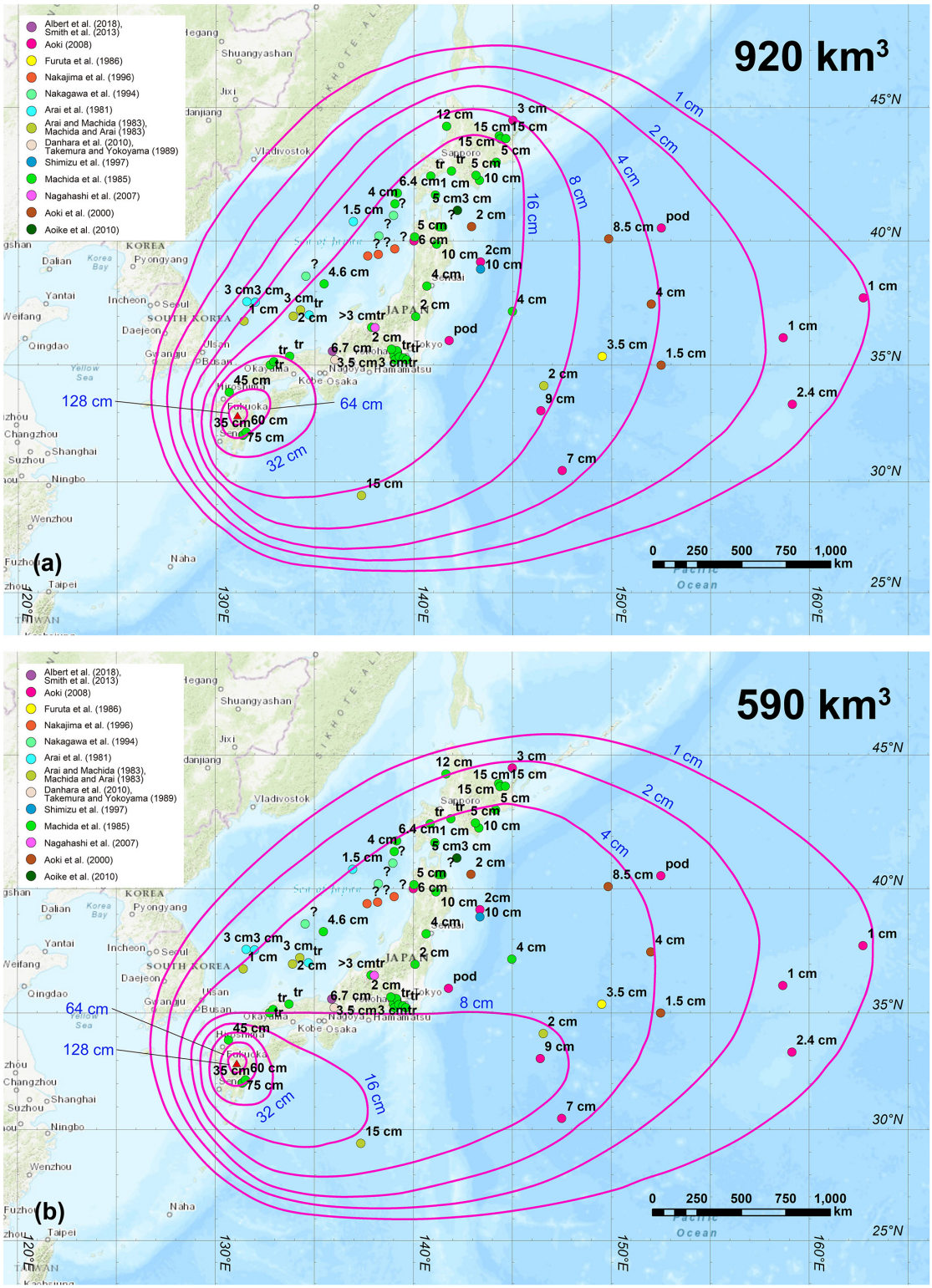

FIGURE 8 | Isopach maps of Aso-4 tephra fall distributions. Maximum case **(a)** and minimum case **(b)**. The data are tephra fall deposit from a borehole at Lake Suigetsu (Albert et al., 2018; Smith et al., 2013) (purple-colored circle), tephra fall deposit from a borehole at Lake Biwa (Takemura and Yokoyama, 1989; Danhara et al., 2010) (pale orange), submarine tephra deposits from Aoki (2008) (pink), Furuta et al. (1986) (yellow), Nakagawa et al. (1994) (light green), Nakajima et al. (1996) (orange), Arai et al. (1981) (light blue), Arai and Machida (1983) and Machida and Arai (1983) (greenish brown), Shimizu et al. (1997) (blue), Machida et al. (1985) (green), Aoki et al. (2000) (brown), and Aoike et al. (2010) (dark green), and on land tephra fall deposits from Machida et al. (1985) (green) and Nagahashi et al. (2007) (red purple).

between the caldera rim (5.3×10^2 km^2) and the distal limit, for a total area of 10^8 km^2. The thickness of the tephra fall deposit at the caldera rim was assumed at 300 cm. The estimated results were 170 km^3 (1.7×10^{14} kg) in the area of the distal region (<4 cm isopach data area), 380 km^3 (3.8×10^{14} kg) in the medial region (between 4 and 64 cm data area), and 45 km^3 (4.5×10^{13} kg) in the area of the proximal region (between 64 and 300 cm data area). The total estimated eruptive mass of the Aso-4 tephra deposit was 590 km^3 (240 km^3 in DRE; 5.9×10^{14} kg).

DISCUSSION

Aso-4 PDC Deposit Distributions and Volume

The original distributions of Aso-4 PDC deposits just after the emplacement were made based on the current distribution of the deposits, borehole data, and topographic data (**Figures 5–7**). This original estimated distribution is one of the most detailed maps of the Aso-4 PDC deposit, which shows the affected areas in this region. The current exposure area of the Aso-4 PDC deposit is about 1,000 km^2 (**Table 1**). The estimated original distribution area of the outflow Aso-4 PDC deposit (just after the emplacement) is about 34,000 km^2. Therefore, the area of estimated distribution is 34 times larger than the current deposit exposure. Most of the deposits were considered to be eroded, as observed for PDC deposits after the eruption of Pinatubo in 1991 (e.g., Major et al., 1996). This new map provides essential information for considering the affected area of the Aso-4 PDC and evaluating potential future eruption scenarios at Aso caldera. We assumed an oval shape for the distal limit of the Aso-4 PDC deposit, as shown in Machida et al. (1985) and Machida and Arai (2003). The estimation of the distal limit of the large-scale PDC is relatively difficult, especially in the sea area. Numerical simulations, such as the energy cone model (Malin and Sheridan, 1982), are one of the solutions.

Maximum, minimum, and average thickness data within each 7 km × 5.5 km mesh grid were calculated based on 3,611 thickness point data (**Figures 6**, **7**). The total estimated eruptive volume of the Aso-4 PDC deposits is 940 km^3 (590 km^3 DRE in maximum), 335 km^3 (225 km^3 DRE in minimum), and 640 km^3 (410 km^3 DRE in average) (**Table 1**). This result is about 1.7–4.7 times larger than the minimum value of the previous estimation at >200 km^3 (Machida and Arai, 2003). The main reason for the larger revised value is that this study was based on a much more detailed estimation of distributions and thicknesses data, including data not exposed on the surface (borehole data). This estimation method used a 7 km × 5.5 km mesh grid, making it one of the most detailed volume estimations of large-scale PDC deposits. This method can be used to accurately estimate the volumes of other caldera-forming large-scale PDC deposits around the world.

Volume estimation method uncertainties are herein considered. Factors that may have increased the upper limit bound are as follows. (1) The upper part of Aso-4 PDC deposits are sometimes eroded due to weathering since 87–89 ka, and thus the measured thickness data from the geological maps may be underestimated. (2) The unclassified point data are included in the non-welded facies. Some of them are considered to be welded facies (increase the DRE volume and eruptive mass). (3) The distribution of the ignimbrite veneer facies in the mountain area is not included in this estimation. The distance from the source to the coast area is about 70 km on average. Therefore, the area to the coast is ca. 1.5×10^4 km^2. The average thickness of the ignimbrite veneer facies is about 2 m (Watanabe, 1986; Suzuki-Kamata and Kamata, 1990). The total estimated volume of the veneer facies is estimated at about 30 km^3. This volume is about 3.2–9 % of the estimated total volume (335–940 km^3) of the Aso-4 PDC deposit.

Factors that may have decreased the lower limit bound are as follows. (1) The distribution limit in the sea area is considered as oval in shape; however, the original runout distance of the Aso-4 PDC deposits may be shorter locally due to the topographical barriers in the subaerial region. (2) The average density of the Aso-4 PDC deposits is decreasing according to the runout distance. The effect of the lower density of the distal facies tends to decrease the total DRE volume.

Another possible factor in changing the upper and lower bounds is the fact that the ordinary kriging method is used for the estimation of no-measured thickness data area by the extrapolation of the surrounding measured area data. This estimation does not integrate the PDC dynamics (e.g., local deposition due to topographic changes such as slope and valley width changes). The thickness may change if the PDC dynamics are included. Future studies such as numerical simulations, including deposition processes from the bottom of the PDC, are needed.

Aso-4 Tephra Fall Distributions and Volume

The estimated volumes of Aso-4 tephra fall (590–920 km^3; 240–370 km^3 in DRE) became larger than the minimum value of the previous estimation (>400 km^3; Machida et al., 1985; Machida and Arai, 2003). The estimation result is about 56–88% volume of the estimation (1,051 km^3) by Suto et al. (2007). The main reasons for the calculation of a larger volume compared to the Machida et al. (1985) and Machida and Arai (2003) in this study are: (1) the isopach map area became much larger than the previous estimation due to the inclusion of more submarine tephra fall data; and (2) the calculation method is different from the previous estimation. Machida et al. (1985) and Machida and Arai (2003) estimated the eruptive volume of the Aso-4 tephra fall using the extended area (>4×10^6 km^2) multiplied by the average thickness of 10 cm. Suto et al. (2007) estimated the eruptive volume of the Aso-4 tephra fall deposits using GIS software and the isopach map published by Machida et al. (1985) and Machida and Arai (2003). However, no details of the calculation methodology were provided in the paper. The purpose of their paper was to make a tephra fall database covering the whole of Japan. The results of such volume estimations are preliminary and tend to have significant errors (e.g., Yamamoto, 2017).

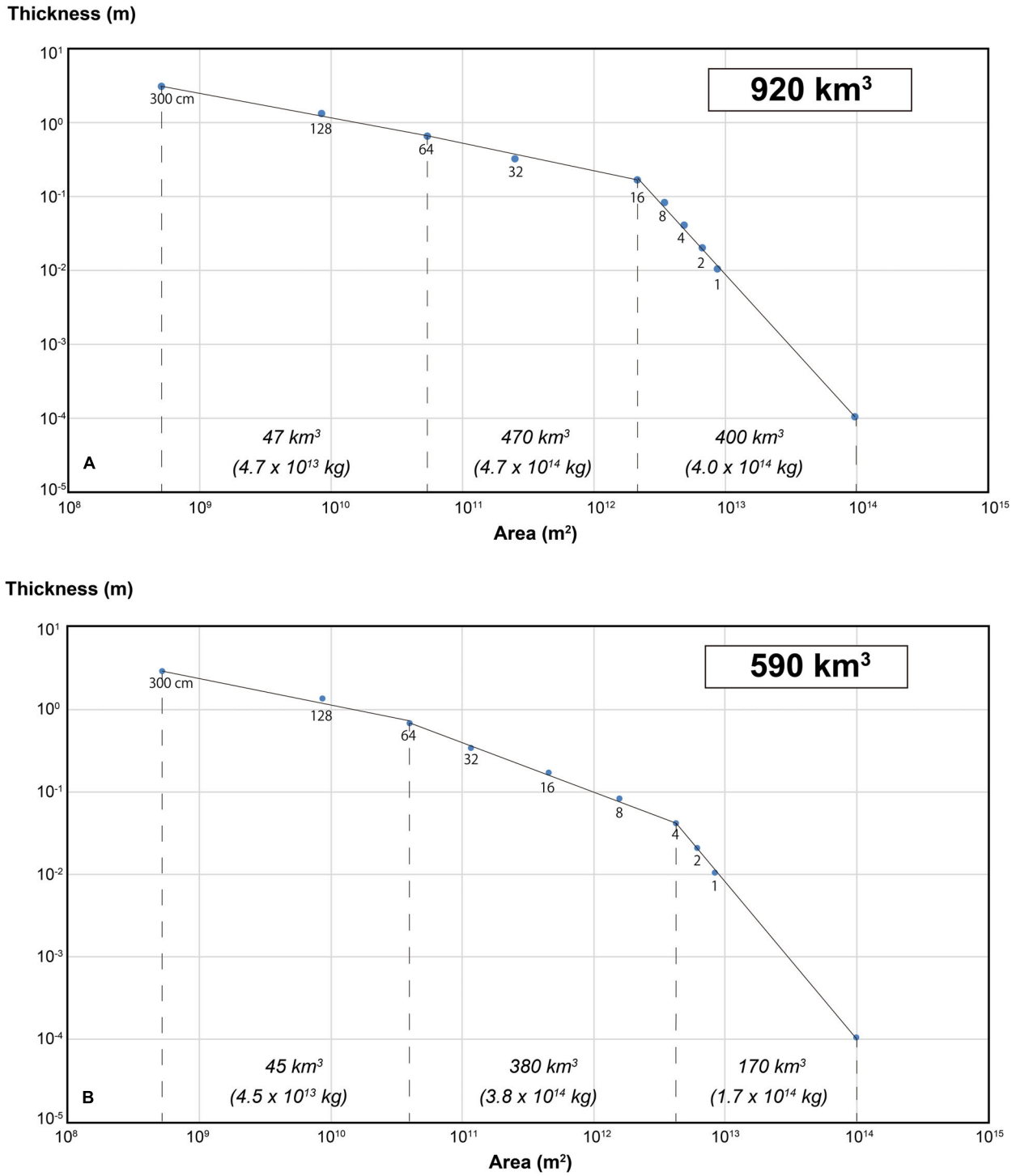

FIGURE 9 | Estimation results of Aso-4 tephra fall deposits using the segment integration method. Maximum case **(A)** and minimum case **(B)**.

Uncertainties in tephra fall volume estimates originate with several factors. Factors that may have increased the upper limit bound are as follows. (1) Especially relatively thin tephra fall deposits in the distal regions are quickly eroded by wind and rainfall. The tephra deposits are preserved only in limited areas such as lakes, swamps, and peatlands. Even if the tephra was deposited in these areas, the original thickness might not be preserved (the original deposit thickness may be thicker than the current thickness). (2) The submarine tephra fall deposits are possibly diffused due to the submarine currents while settling on

the bottom of the sea (other factors than the wind diffusion). (3) In this tephra fall volume estimation, up to 10^8 km^2 areas are calculated (**Figure 9**). Although, cryptotephras derived from the co-ignimbrite tephra falls are possibly distributed more widely as the Earth's surface area, especially for such a large-scale eruption case (e.g., Abbott and Davies, 2012; Davies, 2015). When the cryptotephra distributed to the area as large as on the Earth's surface (5.1×10^8 km^2; five times larger than the current extent), the estimated total tephra volume is 930 km^3 in maximum (extrapolated the decreasing trend of 16 cm to 1 cm isopach maps; **Figure 9A**). The difference is 10 km^3, indicating that the effect of the far distal area is about 1% of the total tephra volume.

The volume ratio of tephra fall deposits in the proximal area (64–300 cm thickness segment) is relatively small compared to the total eruptive volume (45–47 km^3; 5–7%; **Figure 9**). Even if the calculation area is extended up to a vent size (e.g., 0.01 km^2), the result of the total volume is not changed (590–920 km^3). The volume ratio in the proximal area against the total volume is different from other types of eruption. For example, the volume ratio of tephra fall deposits in the proximal area (between 0.45 and 1.5 kg/m^2) against the total volume of the 2014 Ontake phreatic eruption is 38% (4.5×10^8 kg/1.18×10^9 kg) (Takarada et al., 2016). These differences are probably due to the different eruption mechanisms between the two types of tephra falls (large-scale Plinian and small-scale phreatic eruptions).

Factors that may have decreased the lower limit bound are as follows. (1) The Aso-4 PDC deposits are subdivided into eruptive units with cooling unit hiatuses (e.g., Watanabe, 1978), suggesting the duration of the Aso-4 eruption lasted for more than a few days to months. The isopach map may consist of a combination of several isopach maps with the different wind directions. In this case, the total tephra fall volume may be decreased due to a combination of narrow isopach maps. (2) For the tephra fall deposits in the lacustrine and submarine areas, it is possible that the thickness of the deposit is sometimes increased due to reworking by bottom currents in such settings.

Another possible factor to consider in changing the upper and lower bounds is that we used the segment integration method, which enables relatively accurate mathematical calculations (Takarada et al., 2001, 2016). Other tephra fall estimation methods such as Exponential fit (Pyle, 1989), Power-law fit (Bonadonna and Houghton, 2005), and Weibull fit (Bonadonna and Costa, 2012), however, are essential to check our estimation results. Such considerations will be addressed in a subsequent study.

Eruptive Volume of Aso-4 Eruption

The total eruptive volume of the Aso-4 eruption was estimated at 930–1,860 km^3 (465–962 km^3 in DRE; 1.2–2.4 $\times$ 10^{15} kg). This result is about 1.5–3.1 times larger than the minimum volume of the previous estimation by Machida and Arai (2003; >600 km^3), 1.1–2.3 times larger than [Yamamoto (2015); 384 km^3 in DRE], and 2.2–4.5 times larger than Nakajima and Maeno (2015; 200 km^3 in DRE). The reason for the larger revised volume is mainly due to more accurate estimations of distributions and thicknesses based on detailed datasets and different estimation methods. The eruption magnitude [$M = log_{10}$*(erupted mass (kg))-7*; Hayakawa, 1993; Pyle, 2000] is calculated at M8.1–8.4. The Aso-4 caldera-forming eruption is now considered to be one of the M8 (VEI8) class super-eruptions. This is the largest eruption in Japan in the last 100 ka. The eruptive volume of the 30 ka Aira eruption is estimated at 940–1,040 km^3 (380–430 km^3 in DRE; Takarada, 2019). The eruptive volume of the 106 ka Toya eruption is estimated at 230–310 km^3 (100–140 km^3 in DRE; Takarada, 2019; Tomiya and Miyagi, 2020). The Aso-4 eruption is about 0.8–2 times larger than the Aira eruption and about 3–8 times larger than the Toya eruption.

The eruptive volume of the 75 ka Youngest Toba Tuff derived from the Toba caldera is estimated at 13,200 km^3 (5,300 km^3 in DRE) (Costa et al., 2014). The eruptive volume of the 25.4 ka Oruanui eruption in the Taupo Volcanic Zone is estimated at 530 km^3 in DRE (Wilson, 2001; Vandergoes et al., 2013). Thus, the Aso-4 eruption is the 2nd largest eruption in the world in the last 100 ka. The eruptive volume of the 27.8 Ma Fish Canyon Tuff from the La Carita caldera, San Juan Volcanic Field, is estimated at 5,000 km^3 (Lipman et al., 1997; Bachmann et al., 2002). The eruptive volume of the 2.1 Ma Hukleberry Ridge Tuff derived from the Yellowstone caldera is estimated at 2,450 km^3 (Christiansen, 2001; Ellis et al., 2012). The eruptive volume of the 1.6 Ma Otowi Member of Bandelier Tuff derived from the Valles caldera is 216–550 km^3 in DRE (Cook et al., 2016). The Aso-4 eruption is one order smaller compared to the VEI 9 Youngest Toba Tuff (the largest volcanic eruption in the Quaternary), and 0.9–1.8 times larger than the Orunaui eruption in the Taupo Volcanic Zone. The Aso-4 eruption is 12–18% volume of the Fish Canyon Tuff (one of the largest ignimbrites in the world), 40–80% volume of the Hukleberry Ridge Tuff (the largest eruption from the Yellowstone), and slightly larger than the Otowi Member of Bandelier Tuff.

The total eruptive mass is estimated at 1.2–2.4 $\times$ 10^{15} kg. The Aso-4 PDC deposits consist of 8 eruptive units, which sometimes show discontinuities of welding degree and cooling unit hiatuses between them (e.g., Watanabe, 1978); thus, the volume of 1 flow unit (1 event) is on the order of 10^{13}–10^{14} kg. For example, if an event occurred within a period of 10–60 min, the average mass flow rate (MFR) is calculated at 10^9–10^{11} kg/s. The numerical 3D simulation suggests that the expected eruption column height of co-ignimbrite tephra fall would be as high as 40–60 km at this MFR (Costa et al., 2018). A significant global climate and environmental impact would occur from such a large eruption column due to the release of a large amount of volcanic gas (SO_2, HCl, and HF) (e.g., Rampino and Self, 1982; Trenberth and Dai, 2007; Kravitz and Robock, 2011). Long-term catastrophic effects on vegetation and ecosystem would be expected (e.g., Costa et al., 2014). Interaction with rainfall would cause the tephra fall deposits covering Japan to produce abundant lahars over large areas for more than 10 years (e.g., a large number of lahars occurred due to the ca. 10 km^3 1991 Pinatubo eruption for more than 10 years; Major et al., 1996). Therefore, a M8 class super-eruption would cause long-term severe volcanic hazards. Further studies on climate and volcanic hazard assessments are necessary.

The estimated distributions and eruptive volume of the Aso-4 PDC and tephra fall deposits are considered to become an essential dataset for volcanological, geophysical, and petrological

investigations, and volcanic hazard assessments for large-scale super-eruptions. This volume data is also useful to establish a more precise volume vs. time diagram of Aso volcano. The distribution and thickness data are useful for future studies on volcanic hazards. Research efforts on the estimation of the eruptive volume of other large-scale eruptions in Japan, such as Aira, Toya, Kutcharo, and Towada calderas, were made recently (e.g., Takarada et al., 2017, 2018; Takarada, 2019). Reevaluation of the eruptive volumes of major caldera-forming eruptions in other countries is also crucial. The estimation methods outlined in this contribution are applicable to any other large-scale caldera-forming eruptions and will enable the progression of similar volcanological research worldwide.

CONCLUSION

Detailed distributions of 87–89 ka Aso-4 PDC deposits were made based on published papers, geological maps, and borehole data (**Figures 5–7**). Thickness data were compiled from a total of 3,611 outcrops, geological maps, and borehole locations. The volume was calculated using thickness data and area of PDC deposit within each 7 km × 5.5 km mesh grid. The ordinary kriging method was used when no thickness data existed in the mesh grid. The maximum, minimum, and average volumes were calculated. The total eruptive volume of the Aso-4 PDC deposit was estimated at 340–940 km^3 (225–590 km^3 in DRE). The volume of co-ignimbrite Aso-4 tephra fall was estimated using two new isopach maps based on 71 submarine, lacustrine, and subaerial tephra deposits. The estimated volume of the Aso-4 tephra fall was 590–920 km^3 (240–370 km^3 in DRE), using the segment integration method (Takarada et al., 2001, 2016).

The total estimated eruptive volume of the Aso-4 eruption was 930–1,860 km^3 (465–960 km^3 in DRE; 1.2–2.4 × 10^{15} kg). Therefore, the Aso-4 eruption is now considered to have been a M8.1-8.4 (VEI 8) super-eruption. The Aso-4 eruption is the largest volcanic eruption in Japan and considered to be the 2nd largest eruption in the world in the last 100 ka. It is expected that these estimation results will provide essential parameters for long-term eruption forecasting, evaluation of volcanic activities, quantitative geophysical and petrological research work, and future volcanic hazards assessment. The proposed estimation method can be applied to any large-scale caldera-forming eruptions in the world for the reevaluation of eruptive volumes of PDC and tephra fall deposits.

DATA AVAILABILITY STATEMENT

The raw data supporting the conclusions of this article are available in the **Supplementary Material**. We include the data on location, area, measured thickness, estimated thickness (using ordinary kriging method), and original and current exposure volume in each mesh of the Aso-4 PDC deposits (**Supplementary Table S1**). Location, thickness, and references of the Aso-4 tephra fall deposits are also provided (**Supplementary Table S2**).

AUTHOR CONTRIBUTIONS

ST and HH conducted the fieldwork, compiled the data, determined the distribution of the Aso-4 PDC and tephra fall deposits, and undertook data interpretation as well as the refinement of this article.

FUNDING

This study was partly supported by the Secretariat of the Nuclear Regulation Authority, Japan.

ACKNOWLEDGMENTS

We acknowledge valuable discussions with Nobuo Geshi, Takashi Kudo, Teruki Oikawa, Isoji Miyagi, and Akihiko Tomiya of Geological Survey of Japan, AIST, and Yasuo Miyabuchi of Kumamoto University. We thank Sanko Consultant Co., Ltd., for all the support to compile the datasets. We also thank Christopher Conway and Joel Bandibas of Geological Survey of Japan, AIST, for checking the English of the manuscript. We are grateful for the detailed and valuable comments from two reviewers, AC and GV, and chief editor, Valerio Acocella, who allowed us to improve the manuscript.

SUPPLEMENTARY MATERIAL

The Supplementary Material for this article can be found online at: https://www.frontiersin.org/articles/10.3389/feart.2020.00170/full#supplementary-material

REFERENCES

Abbott, P. M., and Davies, S. M. (2012). Volcanism and the Greenland ice-cores: the tephra record. *Earth Sci. Rev.* 115, 173–191. doi: 10.1016/j.earscirev.2012.09.001

Albert, P. G., Smith, V. C., Suzuki, T., Tomlinson, E. L., Nakagawa, T., McLean, D., et al. (2018). Constraints on the frequency and dispersal of explosive eruptions at Sambe and Daisen volcanoes (South-West Japan Arc) from the distal Lake Suigetsu record (SG06 core). *Earth Sci. Rev.* 185, 1004–1028. doi: 10.1016/j.earscirev.2018.07.003

Aoike, K., Nishi, H., Sakamoto, T., Iijima, K., Tsuchiya, M., Taira, A., et al. (2010). Paleoceanographic history of offshore Shimokita Peninsula for the past 800,000 years based on primary analyses on cores recovered by D/V CHIKYU during the shakedown cruises. *KASEKI (Fossils)* 87, 65–81. doi: 10.14825/kaseki.87.0_65

Aoki, K. (2008). Revised age and distribution of ca. 87 ka Aso-4 tephra based on new evidence from the northwest Pacific Ocean. *Quat. Int.* 178, 100–118. doi: 10.1016/j.quaint.2007.02.005

Aoki, K., Yamamoto, H., and Yamauchi, M. (2000). Late quaternary tephrostaratigraphy of marine cores collected during "Mirai" MR98-03 and MR99-K04 cruises. *Report of Japan Marine Science and Technology Center* 41, 49–55. doi: 10.1016/j.envpol.2018.11.018

Arai, F., and Machida, H. (1983). "Deep submarine tephra catalogue around Japan Island," in *Research on Quaternary Volcanic Activities and Climate Change*

Mainly for the Deep Marine Deposits Analysis in and Around Japan. Report of Grant-in-Aid for Co-Operative Research (A) 56390016, ed. H. Machida (Tokyo: Japan Soc. Promotion of Science), 7–34.

Arai, F., Oba, T., Kitazato, H., Horibe, Y., and Machida, H. (1981). Late Quaternary tephrochronology and paleo-oceanography of the sediments of the Japan Sea. *Quat. Res.* 20, 209–230. doi: 10.4116/jaqua.20.209

Bachmann, O., Dungan, M. A., and Lipman, P. W. (2002). The fish canyon magma body, San Juan Volcanic Field, Colorado: rejuvenation and eruption of an upper-crustal Batholith. *J. Petrol.* 43, 1469–1503. doi: 10.1093/petrology/43.8.1469

Bonadonna, C., and Costa, A. (2012). Estimating the volume of tephra deposits: a new simple strategy. *Geology* 40, 415–418. doi: 10.1130/G32769.1

Bonadonna, C., and Houghton, B. F. (2005). Total grain-size distribution and volume of tephra-fall deposits. *Bull. Volcanol.* 67, 441–456. doi: 10.1007/s00445-004-0386-2

Christiansen, R. L. (2001). *The Quaternary and Pliocene Yellowstone Plateau Volcanic Field of Wyoming, Idaho, and Montana. U. S. Geological Survey Professional Paper 729-G*. Reston, VA: USGS. doi: 10.3133/pp729G

Cook, G. W., Wolff, J. A., and Self, S. (2016). Estimating the eruptive volume of a large pyroclastic body: the Otowi Member of the Bandelier Tuff, Valles caldera, New Mexico. *Bull. Volcanol.* 78:10. doi: 10.1007/s00445-016-1000-0

Costa, A., Smith, V. C., Macedonio, G., and Matthews, N. E. (2014). The magnitude and impact of the Youngest Toba Tuff super-eruption. *Front. Earth Sci* 2:16. doi: 10.3389/feart.2014.00016

Costa, A., Suzuki, Y. J., and Koyaguchi, T. (2018). Understanding the plume dynamics of explosive super-eruptions. *Nat. Commun.* 9:654. doi: 10.1038/s41467-018-02901-0

Danhara, T., Yamashita, T., Iwano, H., Takemura, K., and Hayashida, A. (2010). Chronology of the 1400-m core obtained from Lake Biwa in 1982-1983: Re-investigation of fission-track ages and tephra identification. *Quat. Res.* 49, 101–119. doi: 10.4116/jaqua.49.101

Davies, S. M. (2015). Cyrptotephras: the revolution in correlation and precision dating. *J. Quat. Sci.* 30, 114–130. doi: 10.1002/jqs.2766

Davis, J. C. (1986). *Statistic and Data Analysis in Geology -Second Edition*. Hoboken, NJ: Wiley.

Ellis, B. S., Branney, M. J., Barry, T. L., Barfod, D., Bindeman, I., Wolff, J. A., et al. (2012). Geochemical correlation of three large-volume ignimbrites from the Yellowstone hotspot track, Idaho, USA. *Bull. Volcanol.* 74, 261–277. doi: 10.1007/s00445-011-0510-z

Endo, H., and Suzuki, Y. (1986). *Geology of the Tsuma and Takanabe District. Quadrangle Series, 1:50,000*. Tsukuba: Geological Survey of Japan.

Engwell, S. L., Sparks, R. S. J., and Aspinall, W. P. (2013). Quantifying uncertainties in the measurement of tephra fall thickness. *J. Appli. Volcanol.* 2:5. doi: 10.1186/2191-5040-2-5

Fierstein, J., and Nathenson, M. (1992). Another look at the calculation of fallout tephra volumes. *Bull. Volcanol.* 54, 156–167. doi: 10.1007/BF00278005

Furuta, T., Fujioka, K., and Arai, F. (1986). Widespread submarine tephras around Japan-Petrographic and chemical properties. *Mar. Geol.* 72, 125–142. doi: 10.1016/0025-3227(86)90103-9

Hayakawa, Y. (1993). Proposal of eruption magnitude. *Bull. Volcanol. Soc. Japan* 6, 223–226. doi: 10.18940/kazan.38.6_223

Hayakawa, Y. (1995). One million-year chronology of volcanic eruptions in Japan using master tephras. *Bull. Volcanol. Soc. Japan* 40, S1–S15. doi: 10.18940/kazan.40.Special_S1

Henry, C. H. (2008). Ash-flow tuffs and paleovalleys in northeastern Nevada: implications for Eocene paleogeography and extension in the Sevier hinterland, northern great Basin. *Geosphere* 4, 1–35. doi: 10.1130/GES00122.1

Hoshizumi, H., Ono, K., Mimura, K., and Noda, T. (1988). *Geology of the Beppu District. Quadrangle Series, 1:50,000*. Tsukuba: Geological Survey of Japan.

Hoshizumi, H., Watanabe, K., Sakaguchi, K., Uto, K., Ono, K., and Nakamura, T. (1997). The Aso-4 pyroclastic flow deposit confirmed from the deep drill holes inside the Aso caldera. *Program. Abstracts Volcanol. Soc. Jpn* A05:5. doi: 10.18940/vsj.1997.2.0_5

Hunter, A. G. (1998). Intracrustal controls on the coexistence of tholeiitic and calc-alkaline magma series at Aso volcano, SW Japan. *J. Petrol.* 39, 1255–1284. doi: 10.1093/petroj/39.7.1255

Kamata, H. (1997). *Geology of the Miyanoharu District. Quadrangle Series, 1:50,000*. Tsukuba: Geological Survey of Japan.

Kandlbauer, J., and Sparks, R. S. J. (2014). New estimates of the 1815 Tambora eruption volume. *J. Volcanol. Geotherm. Res.* 286, 93–100. doi: 10.1016/j.jvolgeores.2014.08.020

Kaneko, K., Kamata, H., Koyaguchi, T., Yoshikawa, M., and Furukawa, K. (2007). Repeated large-scale eruptions from a single compositionally stratified magma chamber: an example from Aso volcano, Southwest Japan. *J. Volcanol. Geotherm. Res.* 167, 160–180. doi: 10.1016/j.jvolgeores.2007.05.002

Komazawa, M. (1995). Gravimetric analysis of Aso volcano and its interpretation. *J. Geodetic Soc. Jpn.* 41, 17–45. doi: 10.11366/sokuchi1954.41.17

Kravitz, B., and Robock, A. (2011). Climate effects of high-latitude volcanic eruptions: role of the time of year. *J. Geophys. Res.* 116:D01105. doi: 10.1029/2010JD014448

Legros, F. (2000). Minimum volume of a tephra fallout deposit estimated from a single isopach. *J. Volcanol. Geotherm. Res.* 96, 25–32. doi: 10.1016/S0377-0273(99)00135-3

Lipman, P. W. (1967). Mineral and chemical variations within an ash-flow sheet from Aso caldera, south-western Japan. *Cont. Mineral. Petrol.* 16, 300–327. doi: 10.1007/BF00371528

Lipman, P. W., Dungan, M., and Bachmann, O. (1997). Comagmatic granophyric granite in the Fish Canyon Tuff, Colorado: implications for magma-chamber processes during a large ash-flow eruption. *Geology* 25, 915–918. doi: 10.1130/0091-7613(1997)025<0915:CGGITF>2.3.CO;2

Machida, H., and Arai, F. (1983). Extensive ash falls in and around the Sea of Japan from large late Quaternary eruptions. *J. Volcanol. Geotherm. Res.* 18, 151–164. doi: 10.1016/0377-0273(83)90007-0

Machida, H., and Arai, F. (1988). A review of late quaternary deep-sea tephra around Japan. *Quat. Res.* 26, 227–242. doi: 10.4116/jaqua.26.3_227

Machida, H., and Arai, F. (2003). *Atlas of Tephra in and around Japan (Revised Edition)*. Tokyo: University of Tokyo Press.

Machida, H., Arai, F., and Momose, M. (1985). Aso-4 ash: a widespread tephra and its implications to the events of Late Pleistocene in and around Japan. *Bull. Volcanol. Soc. Japan* 30, 49–70. doi: 10.18940/kazanc.30.2_49

Major, J. J., Janda, R. J., and Daag, A. S. (1996). "Watershed disturbance and lahars on the east side of Mount Pinatubo during the mid-June 1991 eruptions," in *Fire and Mud Eruptions and Lahars of Mount Pinatubo, Philippines*, eds C. G. Newhall, and R. S. Punongbayan (Washington, DC: University of Washington Press), 895–919.

Malin, M. C., and Sheridan, M. F. (1982). Computer-assisted mapping of pyroclastic surges. *Science* 13, 637–640. doi: 10.1126/science.217.4560.637

Matsumoto, A. (1996). K-Ar age determinations of young volcanic rocks -correction for initial $^{40}Ar/^{36}Ar$ ratios and its application-. *Chishitsu News* 501, 12–17.

Matsumoto, A., Uto, K., Ono, K., and Watanabe, K. (1991). K-Ar age determination for Aso volcanic rocks -concordance with volcanostratigraphy and application to pyroclastic flows. *Program. Abstracts Volcanol. Soc. Jpn* 1991.2, B3, 73. doi: 10.18940/vsj.1991.2.0_73

Matsuo, S. (1978). The Pleistocene volcanic ash layers in Asahi Village and Ato Town, Abu County. *Nat. Yamaguchi Prefect.* 5, 12–18.

Matsuo, S. (1984). "An emissary from Kyushu," in *Yamaguchi Prefecture Geology Guide*, eds N. Murakami, Y. Nishimura, and Geological Soc. Yamaguchi (Tokyo: Corona Ltd.), 218–222.

Matsuo, S. (2001). Late Pleistocene-Holocene widely distributed volcanic ash in Yamaguchi Prefecture (no. 1) -Aso-4 pyroclastic flow deposit I. *Rep. Geol. Soc. Yamaguchi* 47, 1–12.

Matsuo, S., and Kawaguchi, T. (2015). Ube matsuyama cho volcanic Ash II and Aso pyroclastic flow unit "Aso-4 II". *Rep. Geol. Soc. Yamaguchi* 74, 8–14.

Matsuo, S., and Takahashi, Y. (1974). Discovery of Ube volcanic ash stratigraphy. *Rep. Geol. Soc. Yamaguchi* 7, 15–23.

Miyoshi, M., Shibata, T., Yoshikawa, M., Sano, T., Shinmura, T., and Hasenaka, T. (2011). Genetic relationship between post-caldera and caldera-forming magmas from Aso volcano, SW Japan: constraints from Sr isotope and trace element compositions. *J. Mineral. Petrol. Sci.* 106, 114–119. doi: 10.2465/jmps.101021b

MLIT (2020). *"KuniJiban" National Ground Information Database in Japan*. Tokyo: Ministry of Land, Infrastructure, Transport and Tourism.

Nagahashi, Y., Sato, T., Takeshita, Y., Tawara, T., and Kumon, F. (2007). Stratigraphy and chronology of widespread tephra beds intercalated in the

TKN-2004 Core sediment obtained from the Takano Formation, Central Japan. *Quat. Res.* 46, 305–325. doi: 10.4116/jaqua.46.305

Nagahashi, Y., Yoshikawa, S., Miyakawa, C., Uchiyama, T., and Inouchi, Y. (2004). Stratigraphy and chronology of widespread tephra layers during the past 430 ky in Kinki District and the Yatsugatake Mountains: major element composition of the glass shards using EDS analysis. *Quat. Res.* 43, 15–35. doi: 10.4116/jaqua.43.15

Nagaoka, S. (1984). Late Pleistocene tephrochronology in the region from the Osumi Peninsula to the Miyazaki Plain in South Kyushu, Japan. *J. Geography.* 93, 347–370. doi: 10.5026/jgeography.93.6_347

Nakagawa, M., Fujioka, K., Furuta, T., and Koizumi, S. (1994). Volcanic ash layer in the Leg. 127, 128 core from Japan Sea. *Chikyu Monthly* 16, 691–698.

Nakajima, S., and Maeno, F. (2015). What happen during the catastrophic eruption? *Nikkei Sci.* 45, 4, 32–41.

Nakajima, T., Kikkawa, K., Ikehara, K., Katayama, H., Kikawa, E., Joshima, M., et al. (1996). Marine sediments and late Quaternary stratigraphy in the southeastern part of the Japan Sea -concerning the timing of dark layer deposition-. *J. Geol. Soc. Jpn.* 102, 125–138. doi: 10.5575/geosoc.102.125

NEDO (1995). *Report of Geothermal Development and Promotion, Aso Western Region*, 38. Tokyo: New Energy and Industrial Technology Development Organization.

NIED (2020). *Geo Station*. Available online at: http://www.geo-stn.bosai.go.jp/jps/index.html (accessed April 3, 2020)

Okumura, K., Teraoka, Y., Imai, I., Hoshizumi, H., Ono, K., and Shishido, A. (2010). *Geology of the Nobeoka District. Quadrangle Series, 1:50,000*. Tsukuba: Geological Survey of Japan, AIST.

Ono, K. (1965). Geology of the eastern part of Aso Caldera, central Kyushu, Southwest Japan. *J. Geol. Soc. Jpn.* 71, 541–553. doi: 10.5575/geosoc.71.541

Ono, K., Matsumoto, Y., Miyahisa, M., Teraoka, Y., and Kambe, N. (1977). *Geology of the Taketa District. Quadrangle Series, 1:50,000*. Kawasaki: Geological Survey of Japan.

Ono, K., and Soya, T. (1968). Stratigraphy of pyroclastic flows from Aso Caldera (abstract). *J. Geol. Soc. Jpn.* 74:101.

Ono, K., and Watanabe, K. (1983). Aso Caldera. *Chikyu Monthly* 5, 73–82.

Ono, K., and Watanabe, K. (1985). *Geological Map of Aso Volcano, 1:50,000*. Tsukuba: Geological Survey of Japan.

Pyle, D. M. (1989). The thickness, volume and grainsize of tephra fall deposits. *Bull. Volcanol.* 51, 1–15. doi: 10.1007/BF01086757

Pyle, D. M. (1995). Assessment of the minimum volume of tephra fall deposits. *J. Volcanol. Geotherm. Res.* 69, 379–382. doi: 10.1016/0377-0273(95)00038-0

Pyle, D. M. (2000). "Sizes of volcanic eruptions," in *Encyclopedia of Volcanoes*, eds H. Sigurdsson, B. F. Houghton, S. R. McNutt, H. Rymer, and J. Stix (Cambridge, MA: Academic Press), 257–264.

Quane, S. L., and Russell, J. K. (2005). Ranking welding intensity in pyroclastic deposits. *Bull. Volcanol.* 67, 129–143. doi: 10.1007/s00445-004-0367-5

Rampino, M. R., and Self, S. (1982). Historic eruptions of Tambora (1815), Krakatau (1883), and Agung (1963), their stratospheric aerosols, and climate impact. *Quat. Res.* 18, 127–143. doi: 10.1016/0033-5894(82)90065-5

Roche, O., Buesch, D. C., and Valentine, G. A. (2016). Slow-moving and far-travelled dense pyroclastic flows during the Peach Spring super-eruption. *Nat. Commun.* 7:10890. doi: 10.1038/ncomms10890

Saito, M., Miyazaki, K., Toshimitsu, S., and Hoshizumi, H. (2005). *Geology of the Tomochi District. Quadrangle Series, 1:50,000*. Tsukuba: Geological Survey of Japan, AIST.

Shimizu, A., Torii, M., Shiihara, M., and Oda, M. (1997). Age assignment of the bottom of Core KH94-3 LM8 PC5 based upon a volcanic ash layer in its lowest part. *Mem. Fac. Sci. Kumamoto Univ.* 15, 1–7.

Shimoyama, S., Kameyama, T., Miyata, Y., and Tashiro, Y. (1984). The Quaternary formations of Itoshima coastal plain, Fukuoka Prefecture. *J. Fac. Literature Kitakyushu Univ.* Ser. B 17, 39–58.

Smith, V. C., Staff, R. A., Blockley, S. P. E., Bronk Ramsey, C., Nakagawa, T., Mark, D. F., et al. (2013). Project Members (2013). Identification and correlation of visible tephras in the Lake Suigetsu SG06 sedimentary archive, Japan: chronostratigraphic markers for synchronizing of east Asian/west Pacific palaeoclimatic records across the last 150 ka. *Quat. Sci. Rev.* 67, 121–137. doi: 10.1016/j.quascirev.2013.01.026

Sparks, R. S. J., Self, S., and Walker, G. P. L. (1973). Products of ignimbrite eruptions. *Geology* 1, 115–118. doi: 10.1130/0091-7613(1973)1<115:POIE>2.0.CO;2

Sulpizio, R. (2005). Three empirical methods for the calculation of distal volume of tephra-fall deposits. *J. Volcanol. Geotherm. Res.* 145, 315–336. doi: 10.1016/j.jvolgeores.2005.03.001

Suto, S., Inomata, T., Sasaki, H., and Mukoyama, S. (2007). Database of the volcanic ash fall distribution map of Japan. *Bull. Geol. Surv. Jpn.* 58, 261–321. doi: 10.9795/bullgsj.58.261

Suzuki, T. (1970). The relation between porosity and compressive strength in some welded-tuff. *Bull. Volcanol. Soc. Japan* 15, 132–139. doi: 10.18940/kazanc.15.3_132

Suzuki, T., and Ono, K. (1963). Vertical variation of lithologic characters and intensity of natural remanent magnetization of the Aso pyroclastic flow deposit. *Bull. Volcanol. Soc. Japan* 8, 144–150. doi: 10.18940/kazanc.8.3_144

Suzuki-Kamata, K., and Kamata, H. (1990). The proximal facies of the Tosu pyroclastic-flow deposit erupted from Aso caldera, Japan. *Bull. Volcanol.* 52, 325–333. doi: 10.1007/BF00302046

Takarada, S. (2019). Estimation of eruptive volume of the Aso-4, Aira and Toya eruptions. *Program. Abstracts Volcanol. Soc. Jpn* A3–14:46. doi: 10.18940/vsj.2019.0_46

Takarada, S., Kudo, T., Geshi, N., and Hoshizumi, H. (2017). Distribution and eruptive volume estimation of Ito, Hachinohe and Aso4 pyroclastic flow deposits. *Abstract, JpGU-AGU Joint Meeting*. SVC50-18. Japan Geoscience Union.

Takarada, S., Miyagi, I., and Tomiya, A. (2018). Estimation of distributions and eruptive volumes of Toya and Kutcharo pyroclastic flows. *Program. Abstracts Volcanol. Soc. Jpn* B3-24:116. doi: 10.18940/vsj.2018.0_116

Takarada, S., Oikawa, T., Furukawa, R., Hoshizumi, H., Itoh, J., Geshi, N., et al. (2016). Estimation of total discharged mass from the phreatic eruption of Ontake volcano, central Japan, on September 27, 2014. *Earth Planets Space* 68:138. doi: 10.1186/s40623-016-0511-4

Takarada, S., Yoshimoto, M., Kitagawa, J., Hiraga, M., Yamamoto, T., Kawanabe, Y., et al. (2001). Volcanic ash falls from the Usu 2000 eruption and situation at the source area. *Bull. Geol. Surv. Jpn.* 52, 167–179. doi: 10.9795/bullgsj.52.167

Takemura, K., and Yokoyama, T. (1989). Sedimentary environments inferred from lithofacies of the Lake Biwa 1400 m core sample, Japan. *Jpn. J. Limnol.* 50, 247–254. doi: 10.3739/rikusui.50.247

Tomiya, A., and Miyagi, I. (2020). Age of the Toya eruption. *Bull. Volcanol. Soc. Jpn.* 65, 13–18. doi: 10.18940/kazan.65.1_13

Trenberth, K. E., and Dai, A. (2007). Effects of Mount Pinatubo volcanic eruption on the hydrological cycle as an analog of geoengineering. *Geophys. Res. Letter.* 34:L15702. doi: 10.1029/2007GL030524

Tsuji, T., Ikeda, M., Furusawa, A., Nakamura, C., Ichikawa, K., Yanagida, M., et al. (2018). High resolution record of Quaternary explosive volcanism recorded in fluvio-lacustrine sediments of the Uwa basin, southwest Japan. *Quat. Int.* 471, 278–297. doi: 10.1016/j.quaint.2017.10.016

Urai, M., and Tsu, H. (1986). *Petro-Magnetic Properties in the Hohi Geothermal Region. Report of Geothermal Resources Assessments Technologies in Japan*. Tsukuba: Geological Survey of Japan, 177–225.

Ushioda, M., Miyagi, I., Suzuki, T., Takahashi, E., and Hoshizumi, H. (2020). Preeruptive P-T conditions and H_2O concentration of the Aso-4 silicic end-member magma based on high-pressure experiments. *J. Geophys. Res. Solid Earth* 125:e2019JB018481. doi: 10.1029/2019JB018481

Vandergoes, M. J., Hogg, A. G., Lowe, D. J., Newnham, R. M., Denton, G. H., Southon, J., et al. (2013). A revised age for the Kawakawa/Oruanui tephra, a key marker for the last glacial maximum in New Zealand. *Quat. Sci. Rev.* 74, 195–201. doi: 10.1016/j.quascirev.2012.11.006

Walker, G. P. L. (1980). The Taupo Pumice: product of the most powerful known (ultraplinian) eruption? *J. Volcanol. Geotherm. Res.* 8, 69–94. doi: 10.1016/0377-0273(80)90008-6

Walker, G. P. L. (1981). An ignimbrite veneer deposit: the trail-maker of a pyroclastic flow. *J. Volcanol. Geotherm. Res.* 9, 409–421. doi: 10.1016/0377-0273(81)90047-0

Watanabe, K. (1972). Geology of the western part of Aso Caldera. *Mem. Fac. Educ. Kumamoto Univ. Nat. Sci.* 21, 75–85.

Watanabe, K. (1978). Studies on the Aso pyroclastic flow deposits in the region to the west of Aso Caldera, Southwest Japan, I: Geology. *Mem. Fac. Educ. Kumamoto Univ. Nat. Sci.* 27, 97–120.

Watanabe, K. (1979). Studies on the Aso pyroclastic flow deposits in the region to the west of Aso Caldera, Southwest Japan, II: Petrology of the Aso-4 pyroclastic flow deposits. *Mem. Fac. Educ. Kumamoto Univ. Nat. Sci.* 28, 75–112.

Watanabe, K. (1986). "Flow and Depositional Mechanism of Tosu Orange Pumice Flow from Aso caldera," in *Research on Characteristic and Disasters of Dry Granular Flow Derived From Volcanic Eruptions. Report of Grant-in-Aid for Research (Natural Disasters) 58020012*, ed. S. Aramaki (Tokyo: Japan Soc. Promotion of Science), 115–128.

Watanabe, K., and Ono, K. (1969). Geology of the vicinity of Omine on the western flank of the Aso caldera. *J. Geol. Soc. Jpn.* 75, 365–374. doi: 10.5575/geosoc.75.365

Wilson, C. J. N. (2001). The 26.5 ka Oruanui eruption, New Zealand: an introduction and overview. *J. Volcanol. Geotherm. Res.* 112, 133–174. doi: 10.1016/S0377-0273(01)00239-6

Wilson, C. J. N., and Walker, G. P. L. (1985). The Taupo eruption, New Zealand I. General aspects. *Phil. Trans. R. Soc. Lond. A.* 314, 199–228. doi: 10.1098/rsta.1985.0019

Yamaguchi, H., Oguchi, C., Nishiyama, K., and Matsukura, Y. (2000). A preliminary report on rock properties of Aso pyroclastic flow deposits. *Bull. Terrestrial Environment Research Center, Tsukuba Univ.* 1, 59–65. doi: 10.15068/00146899

Yamamoto, J. K. (2000). An alternative measure of the reliability of ordinary kriging estimates. *Math. Geol.* 32, 489–509. doi: 10.1023/A:1007577916868

Yamamoto, T. (2015). "Cumulative volume step-diagrams for eruptive magma from major Quaternary volcanoes in Japan," in *GSJ Open-File Report*. Tsukuba: Geological Survey of Japan, AIST, 613.

Yamamoto, T. (2017). Quantitative eruption history of Pleistocene Daisen volcano, SW Japan. *Bull. Geol. Surv. Jpn.* 68, 1–16. doi: 10.9795/bullgsj.68.1

Yoshikawa, S., and Kuwae, M. (2001). Last 400 ka high-resolution volcanic ash chronology from lake sediments in Lake Biwa. *Chikyu Monthly* 23, 594–599.

Conflict of Interest: The authors declare that the research was conducted in the absence of any commercial or financial relationships that could be construed as a potential conflict of interest.

frontiers in Earth Science

ORIGINAL RESEARCH
published: 22 July 2020
doi: 10.3389/feart.2020.00279

Dynamics and Impacts of the May 8th, 1902 Pyroclastic Current at Mount Pelée (Martinique): New Insights From Numerical Modeling

Valentin Gueugneau[1,2], Karim Kelfoun[2], Sylvain Charbonnier[1], Aurelie Germa[1] and Guillaume Carazzo[3]*

[1] School of Geosciences, University of South Florida, Tampa, FL, United States, [2] Université Clermont Auvergne, Centre National de la Recherche Scientique (CNRS), Institut de Recherche Pour le Developpement (IRD), Observatoire de Physique du Globe de Clermont (OPGC), Laboratoire Magmas et Volcans, Clermont-Ferrand, France, [3] Université de Paris, Institut de Physique du Globe de Paris, CNRS, Paris, France

The Mount Pelée May 8th, 1902 eruption is responsible for the deaths of more than 29,000 people, as well as the nearly-complete destruction of the city of Saint Pierre by a single pyroclastic current, and is, sadly, the deadliest eruption of the 20th century. Despite intensive field studies on the associated deposit, two conflicting interpretations of the pyroclastic current dynamics (either a *blast* or a simple *ash-cloud surge*) emerged in the 90's and have been paralyzing research ever since, leaving numerous unknowns (i.e., source conditions, volume). This study is the first to investigate numerically the May 8th, 1902 pyroclastic current, using the new two-phase version of VolcFlow that simulates more accurately both parts of pyroclastic currents (i.e., the block-and-ash flow and the ash-cloud surge). Physical flow parameters are either extracted from field data or estimated empirically when no value was found in the literature. Among the two interpretations, only the simple *ash-cloud surge* is tested, generated from a block-and-ash flow initially supplied from the artificially recreated 1902 crater. The block-and-ash flow overflows from the southern V-shaped crater outlet and stays confined into the Rivière Blanche, whereas the ash-cloud surge expands radially and spreads westward, seaward, and eastward, ultimately reaching St Pierre 8 km away, within 330 s. The extent of both parts of the simulated current, as well as the thickness and the direction of the ash-cloud surge are accurately reproduced for a total volume of 32×10^6 m^3, for which a significant part (one third) is deposited in the sea (not recorded in previous studies). Simulations demonstrate that the pear-like shape of the ash-cloud surge deposit is explained by a late surge production along the Rivière Blanche but also that a blast-like event may be required at the initial stage of the explosion, which in some way reconciles the two conflicting past interpretations. Results also highlight the role played by the topography in controlling transport and deposition mechanisms of such pyroclastic currents especially the lateral spreading of the ash-cloud surge. Our study improves the assessment of pyroclastic current-related hazards at Mount Pelée, which could be helpful for future eruptions.

Keywords: Mount Pelée, pyroclastic current, numerical modeling, simulation, surge, blast

OPEN ACCESS

Edited by:
Andrea Bevilacqua, National Institute of Geophysics and Volcanology (INGV), Italy

Reviewed by:
E. Bruce Pitman, University at Buffalo, United States
Michael Manga, University of California, Berkeley, United States

****Correspondence:***
Valentin Gueugneau
vgueugneau@usf.edu

Specialty section:
This article was submitted to Volcanology, a section of the journal Frontiers in Earth Science

Received: *17 April 2020*
Accepted: *17 June 2020*
Published: *22 July 2020*

Citation:
Gueugneau V, Kelfoun K, Charbonnier S, Germa A and Carazzo G (2020) Dynamics and Impacts of the May 8th, 1902 Pyroclastic Current at Mount Pelée (Martinique): New Insights From Numerical Modeling. Front. Earth Sci. 8:279. doi: 10.3389/feart.2020.00279

INTRODUCTION

The 1902–1905 Mount Pelée eruption is a classic example often cited by volcanologists and media to demonstrate the hazards caused by the generation and rapid emplacement of a violent and unpredicted pyroclastic current. On May 8th, 1902, a powerful "nuée ardente" (term used by Lacroix, 1904 to describe the pyroclastic current) coming from the crater traveled down the volcano and nearly destroyed the city of Saint Pierre, 8 km away. On May 20th, a second powerful pyroclastic current occurred in the same area and achieved the total destruction of St Pierre. The two events were responsible for at least 29,000 deaths (Lacroix, 1904), culminating in the deadliest volcanic eruption of the last century. As such, past studies have mainly focused on reconstructing the eruptive sequence in order to better understand the potential hazards of Mount Pelée. One of the first records of this event was compiled by Lacroix (1904), who arrived on Martinique Island 2 months later and described with great detail the features of the May 8th pyroclastic current (i.e., deposit characteristics, damage in St Pierre, and various bodily injuries found in the town). Our understanding of the May 1902 Mount Pelée pyroclastic currents was improved decades later with the 1980 Mount St Helens eruption (Lipman and Mullineaux, 1981) and the subsequent advances the eruption brought to the understanding of explosive dome collapse processes. With new insight from the St. Helens eruption, numerous studies reinterpreted the deposits of the May 1902 eruption (Fisher et al., 1980; Fisher and Heiken, 1982, 1983, 1990; Sparks, 1983; Boudon and Lajoie, 1989; Bourdier et al., 1989; Charland and Lajoie, 1989; Lajoie et al., 1989; Boudon et al., 1990) to better constrain the eruptive source conditions and flow propagation dynamics. Two conflicting interpretations emerged from these studies: (i) St Pierre was destroyed by the ash-cloud surge component of a pyroclastic current derived from a primarily block-and-ash flow (BAF) traveling down the Rivière Blanche (Fisher et al., 1980; Fisher and Heiken, 1982), oriented in the southern direction initiated from a pre-eruption crater outlet (Chrétien and Brousse, 1989; Tanguy, 1994; Tanguy, 2004); (ii) the eruption consisted of a laterally oriented dome explosion, leading to the generation of a blast that traveled directly toward St Pierre destroying the city (Lacroix, 1904; Sparks, 1983; Boudon and Lajoie, 1989; Bourdier et al., 1989; Charland and Lajoie, 1989; Lajoie et al., 1989; Boudon et al., 1990).

The debate, focusing on whether or not a blast occurred during the May 8th, 1902 eruption, (Boudon et al., 1990; Fisher and Heiken, 1990) highlights the difficulties in identifying characteristic features of such a process due in part to large differences with the May 18th, 1980 Mount St Helens blast as well as the lack of a general blast model at that time. Later, Belousov et al. (2007) proposed a broad description of a volcanic blast, based on a review of three well-documented eruptions (Bezymianny, 1956; Mount St. Helens, 1980; Soufrière Hills, 1997): "a violent explosion of a magma body (internal or external) that releases a high energetic flow with high velocities ($>$100 m s^{-1}) that covers a remarkably broad area, causing significant damage." The authors also identified four criteria to distinguish a blast from a simple pyroclastic current: (i) a typical deposit stratigraphy in three layers – unit A, consisting of a mixture of accidental material (substratum rocks, vegetation fragments,. . .) eroded from the passage of the blast; unit B, fine-depleted layer, composed of coarse particles (few millimeters to few centimeters); unit C, laminated, composed of lapilli and ash – together with a debris avalanche deposit, (ii) a broad area of inundation with substantial damage due to high dynamic pressures, (iii) evidence of intense erosion at the base of the blast deposit sequence, and (iv) extreme velocities ($>$100 m s^{-1}). Recent numerical modeling of the Soufrière Hills Volcano (Esposti Ongaro et al., 2008) and Mount St Helens blasts (Esposti Ongaro et al., 2012) show that the dynamics seem to be composed of three main phases: a short *burst phase* at the beginning during which the magma is fragmented and transported by the overpressure of the volcanic gas, a *collapse phase* during which gravity surpasses the pressure and becomes the driving force, and a *PDC phase* in which the flow turns to a pyroclast-laden density current. Several other eruptions have produced pyroclastic currents that share some blast criteria including Mount Unzen in 1991 (Taniguchi and Suzuku-Kamata, 1993), Chaitén in 2008 (Major et al., 2013), Arenal in 1968 (Alvarado et al., 2006), and Merapi in 2010 (Komorowski et al., 2013). Thus, Komorowski et al. (2013) proposed a modified blast description of Belousov (2007) by distinguishing three categories of blast-like flow: (1) very extensive blasts associated with flank collapses (Bezymianny, 1956; Mount St. Helens, 1980; Lipman et al., 1981; Belousov et al., 2007); (2) vertically-directed blasts of intermediate intensity (Lamington, 1951; Taylor, 1958); and (3) low intensity blasts produced by dome collapse (Soufrière Hills, 1997; Sparks et al., 2002; Voight et al., 2002; Merapi, 2010; Komorowski et al., 2013). With this new description of a volcanic blast, we revisit the May 8th, 1902 eruption at Mount Pelée.

Since the debate in the early 90s, no consensus has emerged and consequently some key aspects of the Mt. Pelée eruption remain unclear. The lack of an unambiguous scenario describing the proper source conditions, internal dynamics, and volume of material deposited by the pyroclastic current constitutes an obstacle in the assessment of hazards and risks posed by such flows at the active Mount Pelée volcano.

To provide new insight, this study simulates the May 8th, 1902 pyroclastic current at Mount Pelée using the two-layer version of the numerical model VolcFlow (Kelfoun, 2017). Because of the model framework, only the scenario from which an ash-cloud surge is generated from a block-and-ash flow (Fisher et al., 1980) is simulated. The source and boundary conditions are set according to field data: the pyroclastic current is generated by imposing a mass flux at the Mount Pelée summit crater, reconstructed with a synthetic pre-eruptive morphology (Tanguy, 1994), that overflows through the southern crater outlet into the Rivière Blanche. Quantitative assessment of the modeling results is performed by comparing the simulation outputs to a compilation of field data (Lacroix, 1904; Fisher et al., 1980; Fisher and Heiken, 1982, 1983, 1990; Sparks, 1983; Boudon and Lajoie, 1989; Bourdier et al., 1989; Charland and Lajoie, 1989; Lajoie et al., 1989). The comparison focuses on variation in deposit thickness, areas inundated by the flows, types of deposits, local direction of the current, and dynamic pressure of the ash-cloud

surge. The volume of the simulated flow is adjusted by trial and error in order to obtain the best fit with real deposits. A realistic deposit volume is proposed, and the mass flux of the pyroclastic current that entered the sea is estimated. With the model reliability and eruptive scenario tested, we discuss the source conditions of the eruption, as well as the occurrence of a blast-like event.

This study clarifies some important features of the famous May 8th, 1902 eruption and better explains why Saint Pierre was heavily destroyed by the pyroclastic current on that day. The numerical modeling results give important insights into the dynamics of the pyroclastic current, as well as the general eruptive sequence and improve the assessment of pyroclastic current-related hazards at Mount Pelée, helpful for the mitigation of future eruptive crises. This work also constitutes another validation/confirmation case study for the numerical code VolcFlow, as it has already been conducted for the November 5th, 2010 Merapi eruption (Kelfoun et al., 2017) and for the June 25th, 1997 Soufrière Hills Volcano eruption (Gueugneau et al., 2019).

GEOLOGICAL SETTING

Martinique Island and Mount Pelée

Martinique, in the central part of the Lesser Antilles, emerged about 25 Ma ago, in response to the subduction of the Atlantic plate beneath the Caribbean plate. On the island, volcanism migrated westward and built nine complexes, with compositions ranging from basalts to rhyolites. Plio-pleistocene volcanoes align north-south along the western coast. Mount Pelée, the youngest volcano, is characterized by an evolution from effusive to explosive dynamics since it emerged about 550 ka ago (Germa et al., 2011). The western flank of the volcano was destroyed by three successive collapses, 125, 25, and 9 ka ago (Le Friant, 2003; Boudon et al., 2007; Germa et al., 2011), leaving imbricate horseshoe-shaped structures within which the modern cone sits (dashed lines **Figure 1**). Volcanic activity at Mt. Pelée over the past 5,000 years is characterized by a heterogeneous succession of sub-Plinian/Plinian and dome-forming (Pelean) eruptions (Westercamp and Traineau, 1983; Boudon et al., 2005; Carazzo et al., 2012; Michaud-Dubuy et al., 2019). Among these events, the P6 (4,610 BP) and P4 (2,440 BP) Plinian eruptions produced small explosive fountains associated with pyroclastic currents (Westercamp and Traineau, 1983), whereas the P5 (4,060 BP), P3 (79 cal CE), P2 (280 cal CE) and P1 (1300 cal CE) Plinian eruptions formed 20–30 km high stable Plinian columns that underwent total or partial collapse with associated pyroclastic currents at some stage (Carazzo et al., 2012, 2019, 2020). Numerous eruptions involved formation and/or destruction of lava domes often with a blast-like phase identified, including the P2, P1, 1902–1905 CE (Lacroix, 1904) and the 1929–1932 CE eruptions (Perret, 1935). Historical events at Mt. Pelée volcano also include two minor phreatic eruptions in 1792 CE and 1851 CE (Jaggar, 1903), and at least since the late 19th century recurrent non-eruptive lahars have occurred in the Rivière du Prêcheur valley (Aubaud et al., 2013).

The 1902–1905 CE eruption is well-documented in a series of contemporary reports that describe the eruptive products and their impacts on the towns of St Pierre and Morne-Rouge (Lacroix, 1904). The climactic phase of the eruption on May 8th was followed by major pyroclastic currents on May 20th, 26th, June 6th, July 9th, and August 30th. Then, a dome-forming phase characterized by the great spine and a decrease in activity of explosive events continued until September 1903. Small recurrent pyroclastic currents associated with the lava dome building stage occurred until the end of the eruption but were mostly contained within the Rivière Blanche valley (Lacroix, 1904).

The May 8th, 1902 Explosion: From Precursors to the Pyroclastic Current

According to Roobol and Smith (1975); Chrétien and Brousse (1989), and Lacroix (1904), precursors of the May 1902 eruption began more than 10 years before the eruption, in 1889, when fumaroles were observed in the Etang Sec caldera for the first time. The fumarolic activity slowly intensified until 1902, and on April 23rd to 25th phreatic explosions occurred inside the caldera, releasing ash without showing any sign of magma. This phreatic activity was observed sporadically until May 1st and 2nd when it reached its paroxysm. On May 5th, after a 3 day lull, the caldera, recently filled with hot water and likely weakened by the fumaroles, collapsed sending lahars seaward via the Rivière Blanche, isolating the Le Prêcheur village. The collapse left an empty crater with a south-facing V-shaped outlet. On May 6th, the magmatic activity started with the onset of an explosion marked by a high dark plume accompanied by lightning. Magma had likely reached the surface and a lava dome was visible on May 7th (Chrétien and Brousse, 1989). On May 8th at about 8 am, the newly formed lava dome, clearly visible but topped by a high column of white steam, exploded and a large pyroclastic current, likely exploiting the V-shaped outlet, flowed into the Rivière Blanche. Emerging from the crater, the current flowed seaward expanding laterally leaving the inundated area in the form of a cone-like shape, with the eastern-most and western-most radius at an angle of approximately 90 degrees, reaching St. Pierre 8 km from the summit at 8:02 a.m. **Figures 2C,D** are pictures taken on May 11th from a boat showing the Center and Mouillage districts partially demolished (Lacroix, 1904). Despite the precursors, no evacuation had been ordered. Lacroix (1904) estimated the death toll to be between 28,000 and 29,000, all due to a single pyroclastic current. On May 20th, another strong explosion triggered a large pyroclastic current that traveled the same route, this time completely destroying St Pierre. **Figures 2A,B** show St Pierre, viewed from Morne Abel (A) and Morne d'Orange (B) in August 1902 (Lacroix, 1904), and the consequences of the passage of the May 8th and 20th pyroclastic currents: blown down buildings and only a few partially remaining walls, mostly those parallel to the coastline, in the southern part of the city.

Pyroclastic Current Deposit Characteristics

Several studies have focused on the 1902 pyroclastic current deposits and their sedimentological characteristics, and are

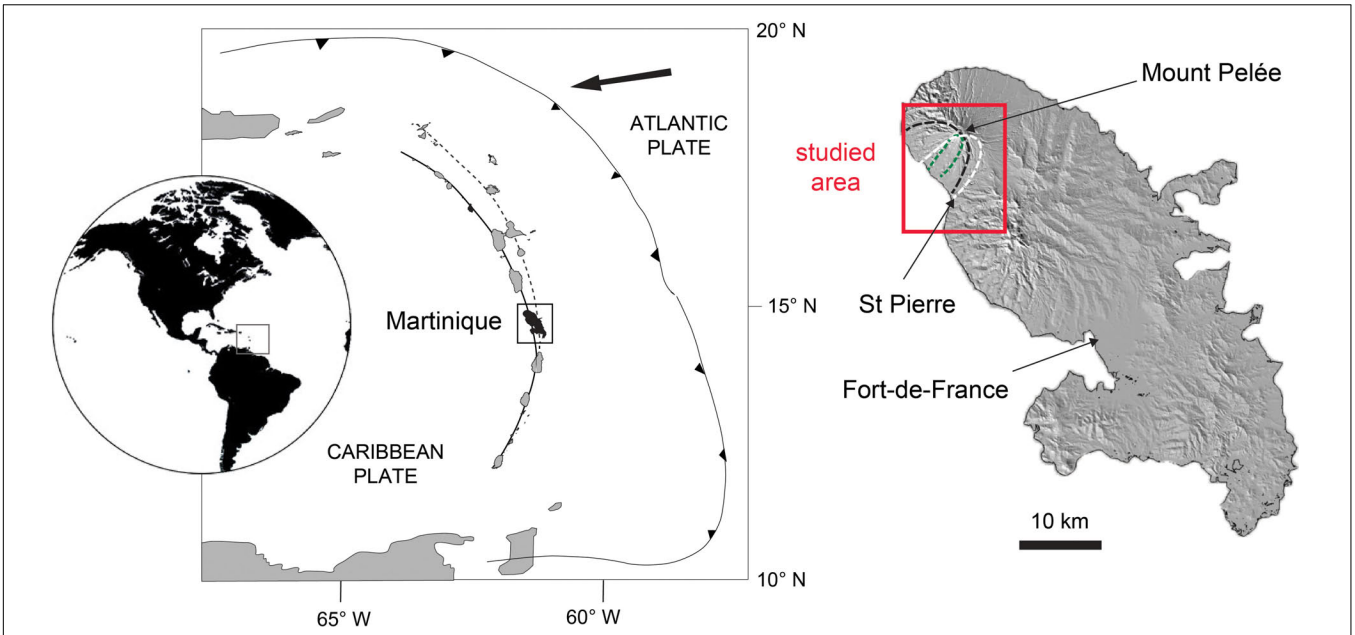

FIGURE 1 | Regional setting of Martinique Island in the central part of the Lesser Antilles. The dashed line north of Martinique represents the Oligocene arc front, the bold line represents the Plio-Pleistocene arc front. The black arrows point in the direction of subduction of the Atlantic plate beneath the Caribbean Plate. The Mount Pelée volcano is located in the northern part of the island, and the study area is within the red rectangle, described in **Figure 2**. The dashed lines within the study area refer to imbricate horseshoe-shaped structures left by flank collapses of the volcano 125, 25, and 9 ka ago (Le Friant, 2003; Boudon et al., 2007; Germa et al., 2011).

compiled in the deposit distribution map of the May 8th, 1902 eruption (**Figure 3**) and also listed in **Table 1**. Two types of pyroclastic current deposits have been identified:

- A several-meter thick, unsorted bed of coarse particles in a fine-grained matrix channelized within the Rivière Blanche, described later as a block-and-ash flow deposit (delimited by the pink area in **Figure 3**) which covers about 3.5 km^2 (Fisher et al., 1980; Fisher and Heiken, 1982; Boudon and Lajoie, 1989; Bourdier et al., 1989; Charland and Lajoie, 1989; Lajoie et al., 1989). The deposit is massive, with weak grading and poor clast organization/segregation, and seemingly filled the entire valley (Lacroix, 1904).
- A thin, stratified bed of finer particles (lapilli-ash) covering a large area (delimited in **Figure 3** by the white line), corresponding to the devastated area outlined in Lacroix's map (black line, p. 223, 1904). Roobol and Smith (1975) estimated the devastated area at 58 km^2, but using a geo-referenced digital elevation model we obtained a value of 51.2 km^2. This deposit surrounds the crater to the north for about 1 km and extends 500 m past St Pierre to the south and to St Philomène to the west. Fisher et al. (1980); Fisher and Heiken (1982), Bourdier et al. (1989), and Lajoie et al. (1989) identified three principal units in this deposit: (i) a lower unit composed of coarse, dark-gray lithic clasts, often normally graded and fine-depleted at the base (**Figure 4**) and composed of numerous degassing pipes in the upper part (called *secondary block-and-ash flow deposit* by Fisher and Heiken, 1982), (ii) a middle unit generally massive but locally laminated (**Figure 4**) composed of lapilli and ash (called *secondary ash-cloud surge deposit* by Fisher and Heiken, 1982), and (iii) a thin upper unit not continuous within the deposit area (unit is missing in St Pierre, **Figure 4**) composed of ash and accretionary lapilli (called *airfall tuff* by Fisher and Heiken, 1982). The mean grain size is relatively homogeneous in each of the three units and varies between 0 and 2 ϕ (2–0.25 mm). Total thickness of this stratified bed varies by more than a meter at Fond Canonville to a few millimeters south of St Pierre. The cumulated thickness of the 3 units, measured from twenty different locations by Bourdier et al. (1989), are presented in **Table 1** and reported on the map in **Figure 3**. One striking feature is the sharp decrease in deposit thickness from the Rivière Sèche valley (locations 9–11 in **Figure 3**) to the edge of the devastated area (locations 14–20 in **Figure 2**) in the eastern part of St Pierre. All studies attribute this deposit to a turbulent ash-cloud surge (Fisher et al., 1980; Fisher and Heiken, 1982; Sparks, 1983; Bourdier et al., 1989; Boudon and Lajoie, 1989; Charland and Lajoie, 1989; Lajoie et al., 1989). The debated and confusing terminology used by Fisher and Heiken (1982) (called "*secondary block-and-ash flow*") was later clarified by Fisher and Heiken (1990) with the term "single ash-cloud surge" deposit.

Using a variety of indicators, the local direction of propagation of the ash-cloud surge was reconstructed. Lacroix (1904) estimated the direction of the ash-cloud surge to be parallel to

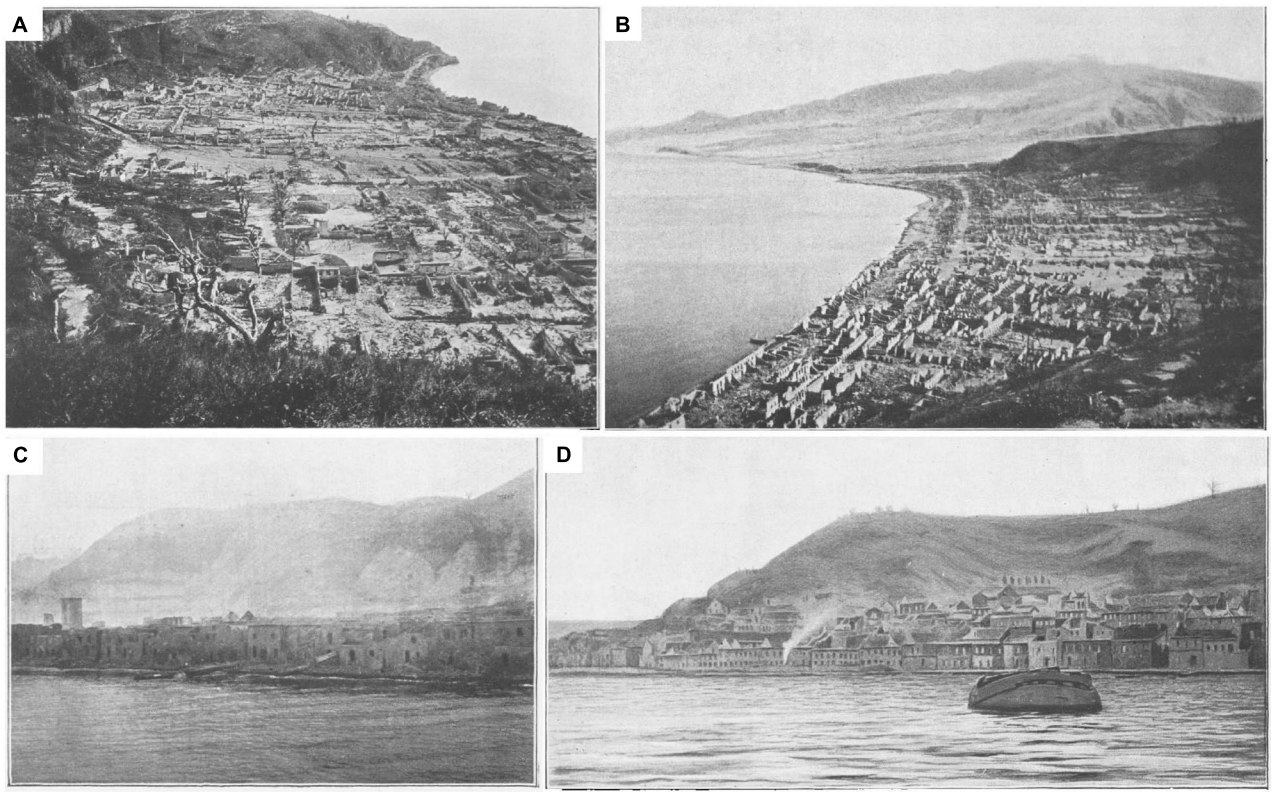

FIGURE 2 | Pictures of St Pierre after the eruption, from Lacroix (1904). **(A,B)** Were taken in August 1902 from Morne Abel looking south **(A)** and from Morne d'Orange looking north **(B)**. **(C,B)** Were taken in May 11th, 1902, 3 days after the passage of the pyroclastic current, from a boat a few hundred meters off the coast. It shows the Mouillage and Center districts only partially destroyed. See **Figure 9** for a closer view of St Pierre city map.

Victor Hugo Street in St Pierre (red line in **Figure 3**) using the N-S orientation of the remaining standing walls and the N-S alignment of the dead bodies in the streets. From measurements in cross-bedded deposits, Fisher et al. (1980); Lajoie et al. (1989), and Charland and Lajoie (1989) identified flow directions in Fond Canonville and on the east of the Rivière Blanche, close to the coast (red arrows in **Figure 3**). However, authors disagreed on the direction, either being from north to south or from the block-and-ash flow to the southwest. Using twisted iron bars from the passage of both the May 8th and 20th pyroclastic currents through Fort Cemetery in St Pierre, Boudon and Lajoie (1989) measured the mean direction of N200° supporting the flow direction measurement of Charland and Lajoie (1989) pointing to the crater.

The dynamic pressure of the ash-cloud surge can be estimated from its effects on buildings, especially in St Pierre, following the study of Jenkins et al. (2013). The pressure in the proximal zone of the Rivière Blanche was very high; Lacroix (1904) mentions a total destruction and disappearance of houses and factories along the coast at Fond Coré. Comparing the damage at Merapi volcano (Jenkins et al., 2013), the dynamic pressure likely exceeded 10 kPa in this area. Pressure decreased away from the Rivière Blanche to the periphery of the devastated area, attested by the partial damage observed on infrastructure located in this peripheral zone, especially in St Pierre. Based on the dynamic pressure calculation method of Jenkins et al. (2013) for brick walls (their equation **Figure 6B**) we can infer that the northern part of the city (i.e., Fort district), for which walls are almost completely destroyed, was exposed to a dynamic pressure greater than 2 kPa. The rest of the city, only partially damaged, was exposed to a dynamic pressure less than 2 kPa, as deduced from the presence of standing walls in the Center and Mouillage districts, and then pressure drops under 1 kPa in the southernmost part of the city attested by the standing cathedral towers in **Figures 3C,D**. The 2 kPa limit can be approximated by the "annihilation line" of Hill (1902) (represented in **Figure 3** by the black dashed line).

Interpretations of the Source Conditions and Dynamics of the Pyroclastic Current

Following these extensive field studies, various interpretations of the May 8th, 1902 pyroclastic current source conditions and its internal dynamics have been inferred. We regroup them in two main theories:

– *Highly turbulent ash-cloud surge coming from the crater, the blast*: Based on eye-witness accounts (p. 248), Lacroix (1904) interpreted the origin of the pyroclastic current as coming from the collapse of a dark/gray plume above the crater, exiting the crater through the V-shaped outlet. Lacroix's interpretation was revised by Sparks (1983), after

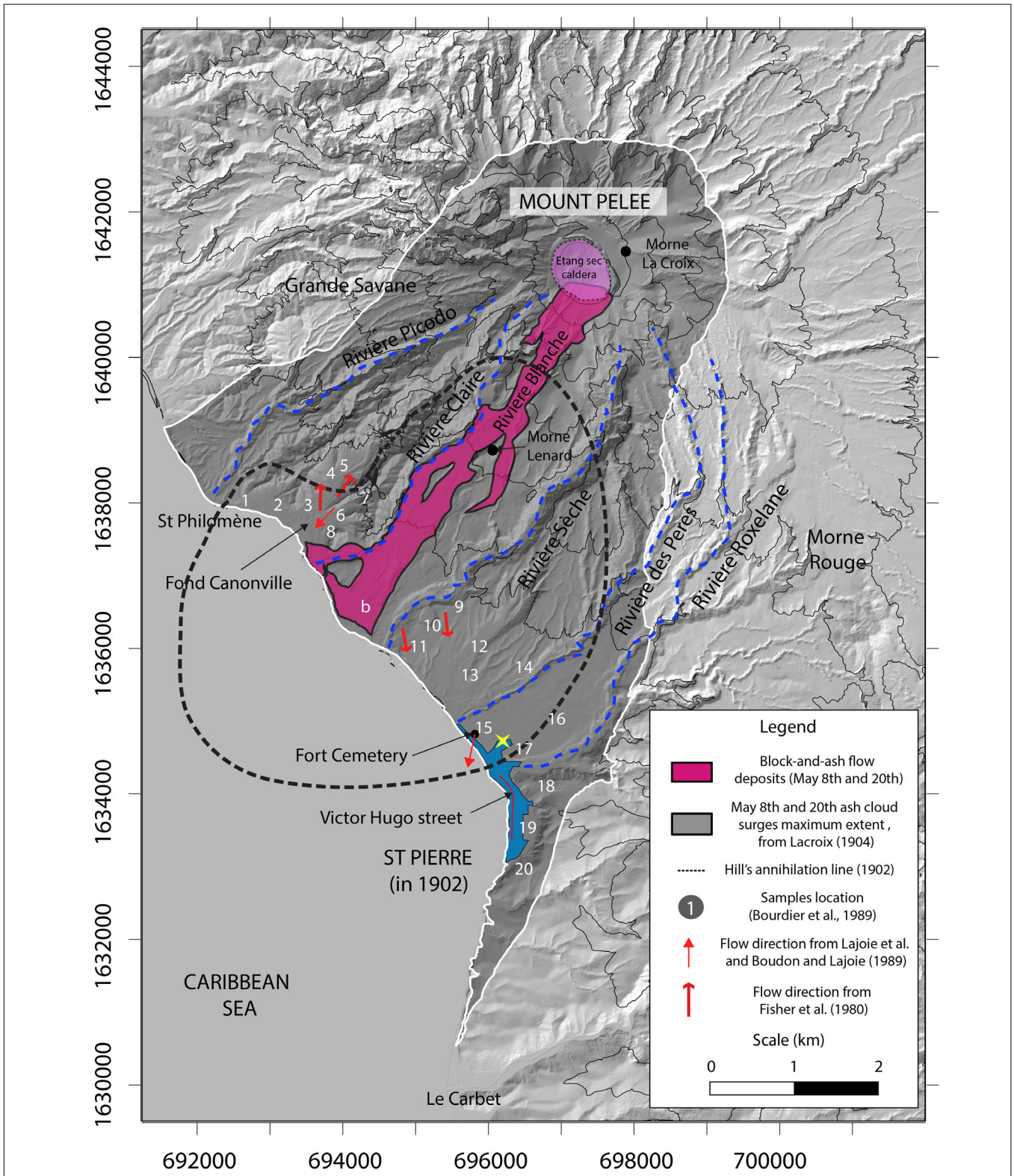

FIGURE 3 | Distribution map of the May 8th, 1902 eruption, with the ash-cloud surge and the block-and-ash flow inundated areas shown in gray and pink, respectively (modified after Bourdier et al., 1989; Hill, 1902; Lacroix, 1904; and BRGM Geological map). Main rivers are marked by blue dashed lines. The Hill's annihilation line is represented by a black dotted circle. The pre-eruptive extent of the city of St Pierre is represented by the blue area. Current direction from Fisher and Heiken (1982), and Boudon and Lajoie (1989) – Lajoie et al. (1989) are represented by thick and thin red arrows, respectively. The location of samples used in this study are represented by the white numbers (from Bourdier et al., 1989).

TABLE 1 | Compilation of field data of the May 8th, 1902 eruption at Mount Pelée. Sample locations refer to the white numbers in **Figure 1**.

	Sample locations	Deposits thickness (m)	Velocity (m s^{-1})	Runout (km)	Area covered (km^2)
BAFs	B	3–10	No data	6.3	3.5
	1	0.57			
	2	0.14			
	3	0.79			
	4	4.00			
	5	0.07			
	6	0.57			
	7	0.43			
	8	0.71			
	9	0.79			
Ash-cloud	10	2.86	55 (Fisher et al., 1980)	10.9	51.2
surge	11	1.50	150 (Lacroix, 1904)		
	12	2.00			
	13	2.29			
	14	0.43			
	15	0.43			
	16	0.43			
	17	0.36			
	18	0.07			
	19	0.04			
	20	0.03			

*Data from Lacroix (1904); Fisher et al. (1980), Fisher and Heiken (1982); Sparks (1983), and Bourdier et al. (1989). Runout and area covered (taking into account the topography) have been calculated by digitizing the outlines in **Figure 1**.*

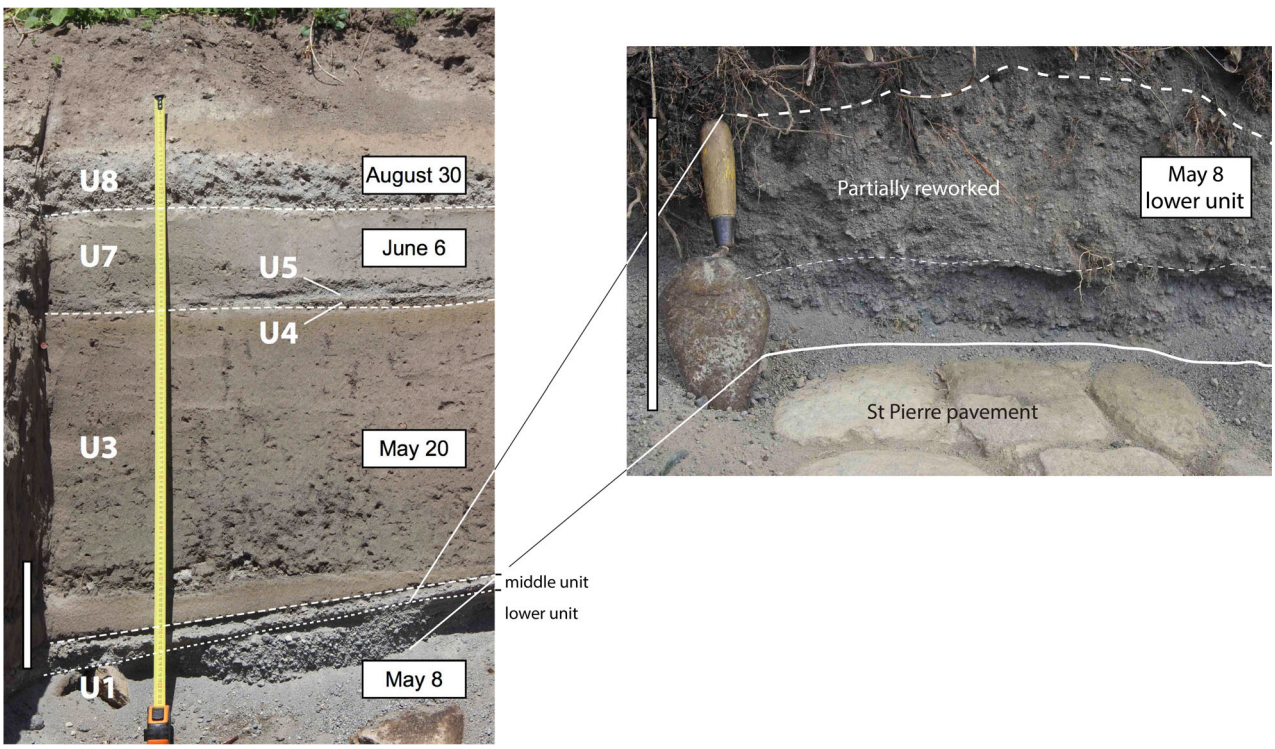

FIGURE 4 | Fine-grained facies of the May 8th, May 20th, June 6th, and August 30th deposits in the Fort district (St Pierre). Units U1 to U8 are from Bourdier et al. (1989). Unit U1, corresponds to the May 8th deposit, separated in three layers, i.e., the lower, middle and upper unit (see text for description). Only the middle and lower unit are visible at St Pierre. The picture on the right is a closer view of the U1 lower layer, sampled in the northern part of St Pierre (yellow star in **Figure 2**) where the deposit is directly in contact with the pavement of the city. The white scale bar is 20 cm long.

the 1980 Mount St Helens eruption, as a laterally-oriented dome explosion leading to a blast flow, an interpretation that was confirmed a few years later by Boudon and Lajoie (1989); Bourdier et al. (1989), Charland and Lajoie (1989); Lajoie et al. (1989), and Boudon et al. (1990). The blast hypothesis is based on: (1) estimated velocities > 100 m s^{-1} (Lacroix, 1904; Lajoie et al., 1989); (2) the unusually large size of pyroclasts (several centimeters) transported by the surge (Bourdier et al., 1989; Lajoie et al., 1989; Boudon et al., 1990); (3) the 90° spreading angle of the deposits in a cone-like shape (Sparks, 1983); and 4) the direction of the current in a straight line from the crater outlet (Boudon and Lajoie, 1989; Charland and Lajoie, 1989; Lajoie et al., 1989).

– *Ash-cloud surge derived from the block-and-ash flow*: a second group championed the idea that St Pierre was destroyed by an ash-cloud surge derived from the block-and-ash-flow. This concentrated flow is thought to have been generated from the collapse of a short column formed by an intra-crater vertical explosion (Fisher et al., 1980; Fisher and Heiken, 1982, 1983, 1990), and then, due to the shape of the crater, was transported into the outlet downstream toward the south. This idea came from Hill (1902) who initially located the source to be approximately at Morne Lenard (2.8 km SW from the current vent, see **Figure 3**). Later, Fisher et al. (1980) and Fisher and Heiken (1982) re-examined this model finding that the source identified by Hill (1902) corresponds to the source of the ash-cloud surge rather than the source of the block-and-ash flow, which is confirmed by the measurement of cross-bedded flow directions pointing to the Rivière Blanche instead of the crater (thick red arrows, **Figure 3**). The authors also defended a roll-back movement of the ash-cloud surge around Fond Canonville, where they inferred that the ash-cloud surge flowed up-valley in the opposite direction of the rest of the flow, after being confined in the Rivière Blanche valley by a high ridge (see **Figure 3** in Fisher et al., 1980), following flow direction measurements in the cross-bedded deposit (**Figure 3**).

Missing and Unclear Data

Because of the two differing interpretations outlined above, the exact nature of the eruption source conditions (i.e., lateral dome explosion or column collapse) and the dynamics of the dilute part of the pyroclastic current (i.e., blast or surge) remain unclear and need further clarification in order to better understand the May 8th, 1902 eruption.

Moreover, despite insightful descriptions of the 1902 pyroclastic current deposits, the total deposit volume is still missing. No study has estimated the volume of each separate current (May 8th and 20th, June 6th, or August 30th) as the field studies conducted following the eruption compiled the effects of the individual currents. Tanguy (2004) estimated the lava dome volume, which may have filled the Etang Sec caldera prior to the eruption, at 18–23 × 10^6 m^3. Nevertheless, the total volume of the May 8th pyroclastic current, as well as the volume portions of the block-and-ash flow and ash-cloud surge components, are still unknown.

NUMERICAL MODELING

VolcFlow

The numerical model used in this study is the newer two-layer version of VolcFlow, which was developed to more accurately simulate the dynamics and extent of pyroclastic currents (Kelfoun, 2017). This version was used to simulate: (i) block-and-ash flows and ash-cloud surges at Merapi Volcano (Kelfoun et al., 2017), (ii) surge-derived pyroclastic flows at Soufrière Hills Volcano in Montserrat (Gueugneau et al., 2019), and (iii) for probabilistic hazard assessment at Misti Volcano in Peru (Charbonnier et al., 2020, this issue). The code is based on two coupled, depth-averaged currents: one for the basal concentrated flow (also called block-and-ash flow in this study) and one for the overriding ash-cloud surge. The dynamics of each current are modeled using depth-averaged equations of mass and momentum balance in the x and y directions. The ash-cloud surge requires an additional equation, as density varies in time and space due to loss of mass through sedimentation. The two layers are then coupled and exchange mass and momentum following two exchanges laws (arrows in **Figure 5**). The complete description of the physical model, the equations, and all the parameters used in VolcFlow are summarized in **Supplementary Material**. The reader can also refer to Kelfoun (2017) and Gueugneau et al. (2019, **Supplementary Material**) for detailed code description.

To simulate stresses applied to the concentrated flow during transport using a depth-averaged approach, the plastic rheological law is used, involving a constant retarding stress T (see **Supplementary Material**). Despite the lack of physical explanation for applying this rheology to pyroclastic currents, several studies have demonstrated the ability of the constant retarding stress to reproduce various features of such currents and their deposits (Kelfoun et al., 2009, 2017; Kelfoun, 2011; Charbonnier and Gertisser, 2012; Ogburn and Calder, 2017; Gueugneau et al., 2019). The ash-cloud surge is simulated as a turbulent continuum that loses momentum due to turbulent drag stresses.

Topography

To perform the numerical simulations, the Observatoire Volcanologique et Sismologique de Martinique provided a 5 m resolution LiDAR DEM of Martinique Island, constructed in 2012, that was down-sampled to 10 m to save computational time. The original DEM was also cropped to the southwest corner of Mount Pelée volcano, including the crater, the coastline and the city of St Pierre, with an area of 15 × 11 km (red rectangle in **Figure 1**). Despite the passage of more than a hundred years between the eruption and the DEM acquisition, the topography does not seem to have changed much in this area when compared to Lacroix's topographic map (p. 223, 1904), with the exception of the summit and the Rivière Blanche valley, which were rapidly filled with the 1902-05 and 1929-32 deposits. Intense erosion

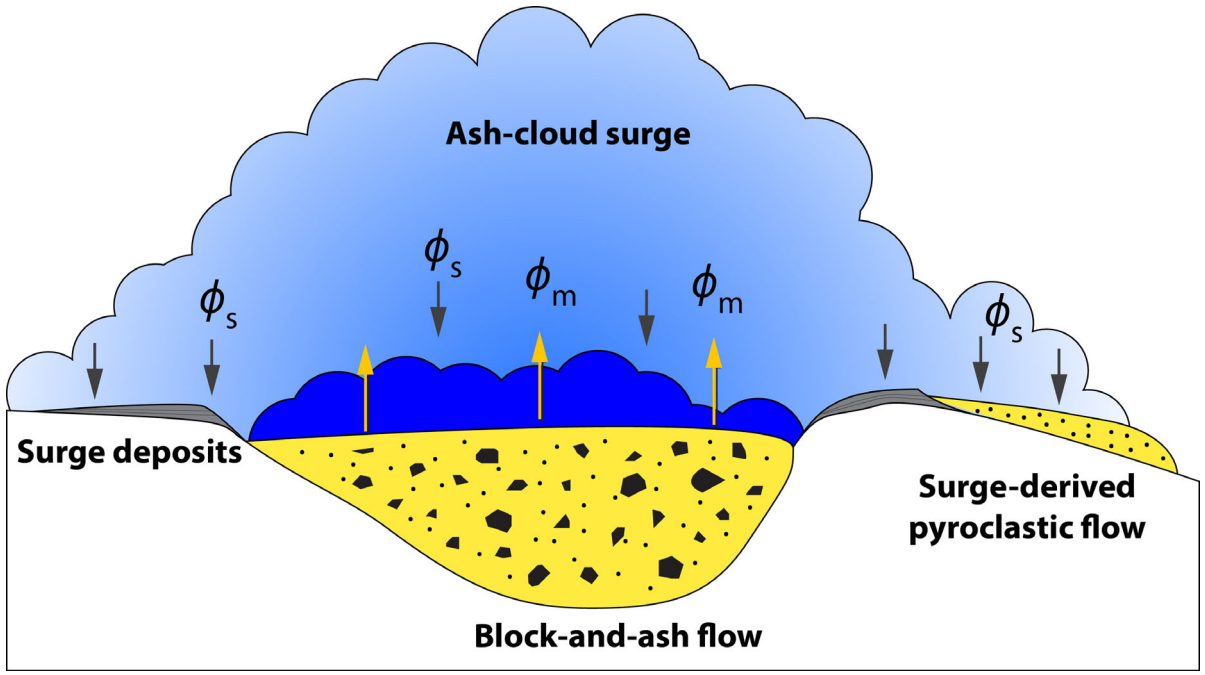

FIGURE 5 | Sketch of the general model of the two-phase version of VolcFlow (Kelfoun, 2017). The first layer simulating the block-and-ash flow feeds the second layer simulating the ash-cloud surge through the mass flux ϕ_m. The second layer can either settle on the ground to form deposits or surge-derived pyroclastic flows, or incorporate back into the block-and-ash flow following the settling law ϕ_s.

by the Rivière Blanche has carved a new channel through the soft pyroclastic deposit, deepening the valley floor to a pre-1902 depth.

Source Conditions and Input Parameters

Despite the current debate regarding the source conditions that generated the May 8th pyroclastic current (i.e., either column collapse or dome collapse), a common feature of both scenarios is that all the pyroclastic current volume was constrained within crater outlet. The crater shape seems to have reoriented the expansion of the fragmented material into this V-shaped outlet. In order to numerically reproduce these source conditions as accurately and realistically as possible, the DEM of the summit area was artificially modified to reproduce the topography of the Etang Sec caldera, as estimated by Lacroix (1904), Chrétien and Brousse (1989), and Tanguy (1994). This caldera is approximated in the DEM by a bowl-shape of 860 m wide for 300 m deep, and centered roughly on the 1929 lava dome, as illustrated in **Figure 6**. With this modification, the outlet on the southern part of the crater rim is reconstructed at the same location as it was prior to May 1902 (**Figure 6**). Because of all the uncertainties related to the source conditions during the May, 8th 1902 eruption, the source of our simulation was simplified to a constant volume rate supplied for a duration Δt directly into the synthetic crater. This simplified source can thus model the collapse of either a short column or a lava dome. The volume rate is calculated by dividing the total volume of material supplied in the crater V_{ini} by the duration Δt (**Figure 6C**, orange curve). Consequently, the mass accumulates in the crater until its level reaches the lowest elevation point of the crater rim, the V-shaped outlet (**Figure 6**), and overflows, leading to the formation of the block-and-ash flow channelized in the Rivière Blanche valley. The resulting overflow is self-regulated and dependent on the supply rate in the crater, as illustrated in **Figure 6C** (blue curve). Since the total volume of the eruption is unknown, the input values for the initial volume of material V_{ini} and the supply duration Δt (ranges shown in **Table 2**) were explored by trial and error to determine the most realistic value, following the calibration procedure described in the next section. Because of the synthetic crater, a large part of the deposit volume remains stuck inside the depression and does not feed the simulated pyroclastic current. Therefore, we distinguished the volume of material supplied in the crater V_{ini} to the total volume of deposit V that escaped through it to constitute the pyroclastic current. The best-fit simulation was obtained with an initial volume of material supplied in the crater $V_{ini} = 45 \times 10^6$ m^3 during $\Delta t = 200$ s yielding a total deposit volume $V = 32 \times 10^6$ m^3 and a volume of material remaining in the crater of 13×10^6 m^3.

Only the scenario of Fisher et al. (1980) was tested, with the ash-cloud surge generated solely by the block-and-ash flow coming from the crater outlet, and its feasibility and realism in reproducing the real flows is assessed. The formation and development of the simulated ash-cloud surge is dictated by the surge production law [ϕ_m (Eq. 9), **Supplementary Material**], which is a function of the velocity of the concentrated flow. Consequently, the higher the block-and-ash flow velocity, the higher the surge production. The simulated ash-cloud surge then evolves with its own dynamics and spreads laterally around the

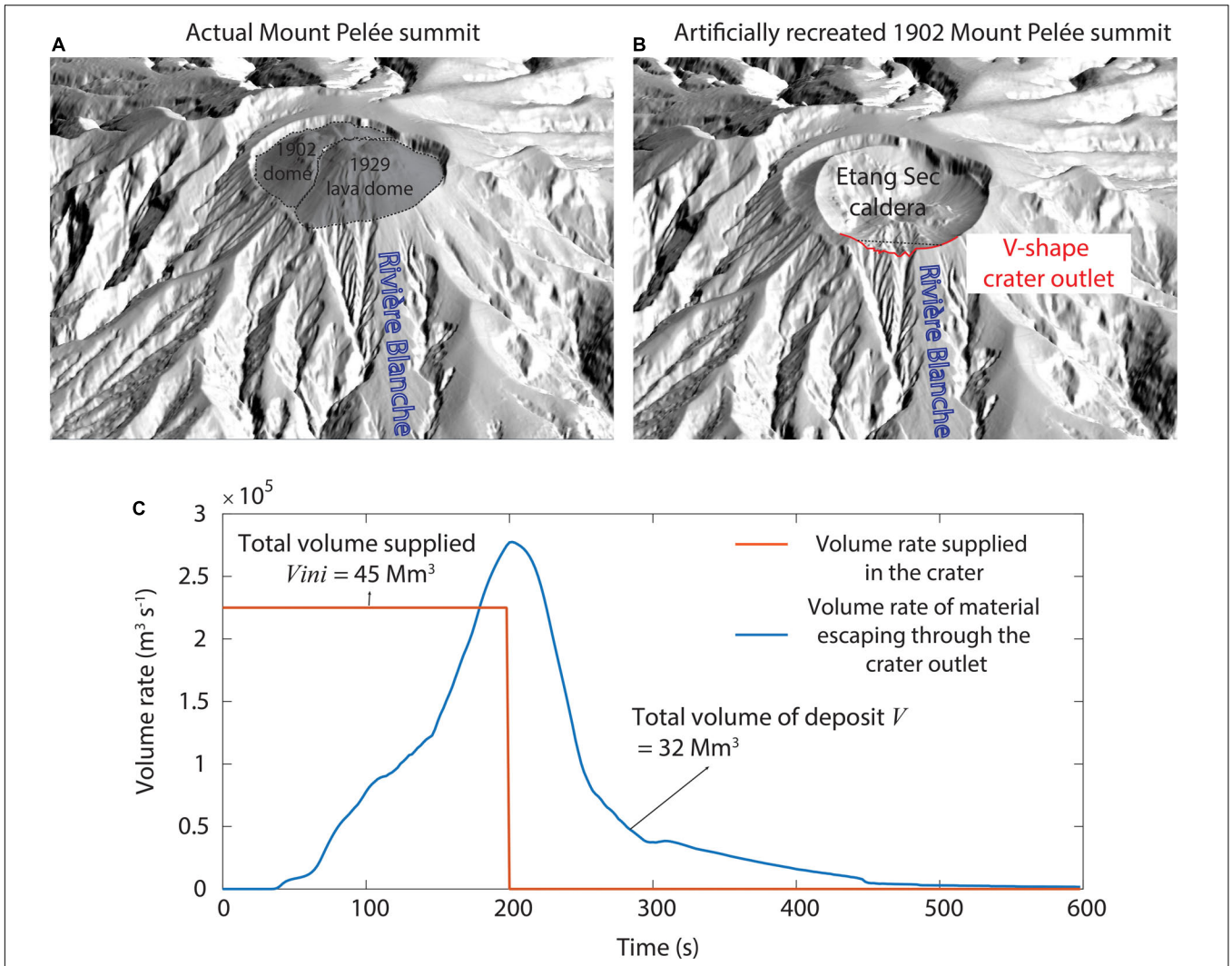

FIGURE 6 | Illustration of the digital topographic modifications performed for this study between the actual Mount Pelée summit **(A)** and the DEM used in the simulations with the new synthetic 1902 Etang Sec caldera topography **(B)**. The red line in B highlights the position of the newly formed V-shape crater outlet. **(C)** Illustrates the variation of the volume rate supplied in the crater (red line) and the resulting volume rate of block-and-ash flow that overflows to the Rivière Blanche through the crater outlet (blue line) during the VolcFlow simulations.

Rivière Blanche as it is less sensitive to the topography than the valley-confined concentrated flow. To model such complex dynamics of the pyroclastic current, the code requires 11 input parameters for each simulation (see **Supplementary Material**). Six parameters were extracted from field data or the literature: particle density ρ_p, atmosphere density ρ_a, concentrated flow density ρ_d, gas surge density ρ_g, particle mean diameter d, and Voellmy drag stress c_1 (values presented in **Table 2**) (see Gueugneau et al., 2019). The other five parameters, the initial volume, the surge production parameter c_3, the constant retarding stress of the concentrated flow T, the density of the mixture transferred from the concentrated flow to the surge ρ_m, the surge drag stress c_2, and the particle drag coefficient C_d, are empirical or unconstrained from field data and must be adjusted by trial and error. Each of these parameters has a clear influence on the morphology of the simulated flows and on the resulting deposit footprint, which makes it relatively easy to estimate the best fit. To better see the influence of each parameter on the model dynamics, the reader can refer to Kelfoun et al. (2017) and Gueugneau et al. (2019, **Supplementary Material**) for two examples of a comparative table highlighting the sensitivity of simulated flows to each of these parameters, for similar small-volume pyroclastic currents.

Quantification of the Differences Between Model and Observed Data

To quantitatively evaluate the simulation results and to identify a best fit simulation, the differences between simulated and observed flows are calculated using validation metrics, which compare areas inundated by the simulation (*Asim*) to the real deposit (*Aobs*). The matching area between simulated and

TABLE 2 | Input parameters for the best-fit VolcFlow simulation presented in **Figure 7**.

	Symbols	Literature	Simulations
Input parameters from literature			
Particle density	ρ_p	2400 kg m^{-3}	2400 kg m^{-3}
Atmosphere density	ρ_a	1–1.2 kg m^{-3}	1 kg m^{-3}
Concentrated flow density	ρ_d	1600 kg m^{-3}	1600 kg m^{-3}
Gas surge density	ρ_g	0.6 kg m^{-3}	0.8 kg m^{-3}
Particle mean diameter	d	0–2 ϕ	2 ϕ
Voellmy drag stress coefficient	c_1	0.01	0.01
	Symbols	**Explored range**	**Best value**
Estimated parameters using the best fit			
Total volume	V	13–64 × 10^6 m^3	32 × 10^6 m^3
Supply duration	Δt	50–500 s	200 s
Mixture density	ρ_m	1–50 kg m^{-3}	15 kg m^{-3}
Surge production coefficient	c_3	10^{-4} to 10^{-1}	0.008
Particle drag coefficient	C_d	1–40	35
Yield stress	T	1500–3500 Pa s	3000 Pa s
Surge drag stress coefficient	c_2	0.1–0.025	0.3

The first section of the table refers to input parameters extracted from field data and literature. The second part refers to input parameters estimated by trial and error, showing the range of value explored and the best values associated to the best fit simulation.

observed flows is called true positive (TP), the over-simulated area is called false positive (FP) and the missing simulated area is called false negative (FN). Three coefficients were used:

(1) the Jaccard similarity coefficient (R_J) uses TP and the union of areas inundated by observed and simulated flows:

$$R_J = \frac{|Aobs \cap Asim|}{|Aobs \cup Asim|} \times 100 = \frac{TP}{TP + FN + FP} \times 100 \quad (1)$$

(2) the model sensitivity (R_{MS}) uses TP and the area inundated by simulated flows:

$$R_{MS} = \frac{|Aobs \cap Asim|}{|Asim|} \times 100 = \frac{TP}{TP + FP} \times 100 \quad (2)$$

(3) the model precision (R_{MP}) uses TP and the area inundated by observed flows:

$$R_{MP} = \frac{|Aobs \cap Asim|}{|Aobs|} \times 100 = \frac{TP}{TP + FN} \times 100 \quad (3)$$

The reader can refer to Charbonnier et al. (2018) for a more detailed description of these metrics. Values obtained for the best-fit simulation are included in **Table 3**.

For more than a hundred simulations of 10–20 h each, seven unconstrained input parameters (**Table 2**) were adjusted to obtain a combination of highest possible values for the three metrics, obtained for the 90th simulation. The volume of material in the crater and the supply duration are first adjusted by matching the general aerial distribution and thicknesses of the simulated deposits to the real one. Then, the surge characteristics (production and sedimentation parameters) as well as the constant retarding stress of the concentrated flow are adjusted to find the combination of highest values for the three metrics for the area covered by the ash-cloud surge only. The choice to focus primarily on the ash-cloud surge was motivated by the fact that: (1) its extent and limits, as extracted from the field, are based on robust evidence and therefore only contain small uncertainties, and (2) it covered a much larger area than the block-and-ash flow, restricted to valleys. In addition, other flow/deposit parameters like deposit thicknesses, flow velocities and runouts are compared to those measured in the field (**Table 1**).

Volcflow SIMULATION RESULTS

Extent and Thickness

Overall the fit was good between the area covered by the simulated ash-cloud surge and the real one (**Figure 7**), as shown by the high values obtained for all three metrics used (>75% for the ash-cloud surge Jaccard fit, **Table 3**). However, the maximum runout in the south of St Pierre is underestimated where the simulated ash-cloud surge traveled 600 m less that the real flow. Also, a large part of the area inundated by the ash-cloud surge around the northern part of the crater is not reproduced by the simulations. Since the location of the initial mass flux in the simulations was set to be in the southern crater outlet, the simulated ash-cloud surge derived from the block-and-ash flow in the proximal area was unable to spread northward and inundate that part of the crater.

Comparisons between the simulated surge deposit thicknesses with those measured at 20 locations in the field (Bourdier et al., 1989) show relatively good agreement (**Table 3**). Apart from some model overestimations in Fond Canonville area (locations 2–6), simulated surge thicknesses are less than ±50% of error. Surge

TABLE 3 | Values of validation metrics used for evaluating the best-fit simulation.

Metrics	Sample locations	Thickness (m)	Velocity (m/s)	Runout (km)	Volume (10^6 m^3)	Surface (km^2)
BAFs	b	4.3 0%	19	6.3 0%	7.8	4.4 + 29%
	1	0.53 -7%				
	2	0.55 +100%				
	3	3.14 +100%				
	4	3.82 –4.5%				
	5	3.10 +100%				
	6	2.99 +100%				
	7	0.29 -32%				
	8	0.81 +14%				
	9	1.02 +29%				
Ash-cloud	10	2.67 -8%	45–10% (Fisher et al., 1980)	10.1 -10%	11.4	43.1 -16%
surge	11	1.17 -22%	or -66% (Lacroix, 1904)			
	12	2.57 +28%	22 when hits St Pierre			
	13	1.20 -48%				
	14	0.36 -16%				
	15	0.43 0%				
	16	0.23 -49%				
	17	0.25 -30%				
	18	0.12 -71%				
	19	0.05 +25%				
	20	0.02 -33%				

Quantification	Jaccard fit (R_J)	Sensitivity (R_{MS})	Precision (R_{MP})
BAFs	43.5%	55.2%	67.4%
Ash-cloud surge	74.5%	93.4%	78.7%

*The simulated thicknesses were measured at the same locations as those presented in **Table 1** and **Figure 2**. The misfits between simulation results and field data are reported as percentages of error next to each value. The Jaccard fit R_J, the model sensitivity R_{MS}, and the model precision R_{MP} coefficients were calculated for both the block-and-ash flow and the ash-cloud surge. See text for explanation.*

velocities are either in good agreement or underestimated by a factor of 3, depending on the reference value taken (**Table 3**) but are within the typical range of 40–90 m s^{-1} for ash-cloud surge estimations elsewhere (Calder et al., 1999; Cronin et al., 2013; Ogburn et al., 2014). The simulated surge requires 330 s to reach St Pierre, more than twice Lacroix's estimation (around 120 s), and travels through the entire city in roughly 200 s (see **Figures 7A–D**).

The block-and-ash flow simulation also provides a relatively good fit (**Figure 7**), although the values obtained for the three validation metrics are lower than for the surge (between 43 and 67%). Indeed, the simulated flow inundated an area similar to the real flow (with a model precision coefficient of 67.4%) but with a few false positives, leading to a total surface 30% larger and therefore to a lower Jaccard fit coefficient (43%). Nevertheless, four important block-and-ash flow features observed in the field and reproduced in the simulation paradoxically highlight the success of the simulation: (i) the confinement of the block-and-ash flow in the Rivière Blanche, (ii) the divergence of the flow into two branches at the passage of Morne Lenard, (iii) the presence of two deposit-free pockets on the southwest of Morne Lenard and on the east of the Rivière Blanche valley along the coast, and (iv) a relatively constant average deposit thickness of a few meters along the inundated area that increases close to the sea and gives a delta-like shape to the deposit. The simulated block-and-ash flow travels at an average velocity of 19 m s^{-1}, relatively common for this type of flow, as described elsewhere (Calder et al., 1999; Ogburn et al., 2014).

Surge Dynamic Pressure and Direction

Figure 8 presents the maximum dynamic pressure and the mean direction of the ash-cloud surge extracted from the best-fit simulation. In VolcFlow, the dynamic pressure P_{dyn} is calculated following Valentine (1998):

$$P_{dyn} = \frac{1}{2}\rho_s v^2 \quad (4)$$

where v is the velocity of the simulated surge and ρ_s its density. Because the ash-cloud surge is generated from the block-and-ash flow during its transport downstream, the variation of its dynamic pressure follows the path of the Rivière Blanche. Values gradually decrease from more than 5 kPa toward the block-and-ash flow to a few Pa only toward the edges. This gradual pressure decrease is not linear and accelerates with distance from the Rivière Blanche, indicated by the presence of clustered isobar lines from 3 to 1 kPa over a few hundred meters which contrasts with those < 1 kPa that spread over an area 2 or 3 times larger (**Figure 8**). This pattern was also observed at Merapi volcano by Jenkins et al. (2013) and Kelfoun et al. (2017). The mean direction of the simulated surge is radially dispersed around the block-and-ash flow and perfectly matches the direction measured in the field by Fisher et al. (1980) to the east of the Rivière Blanche and those measured by Charland and Lajoie (1989) to the west. However,

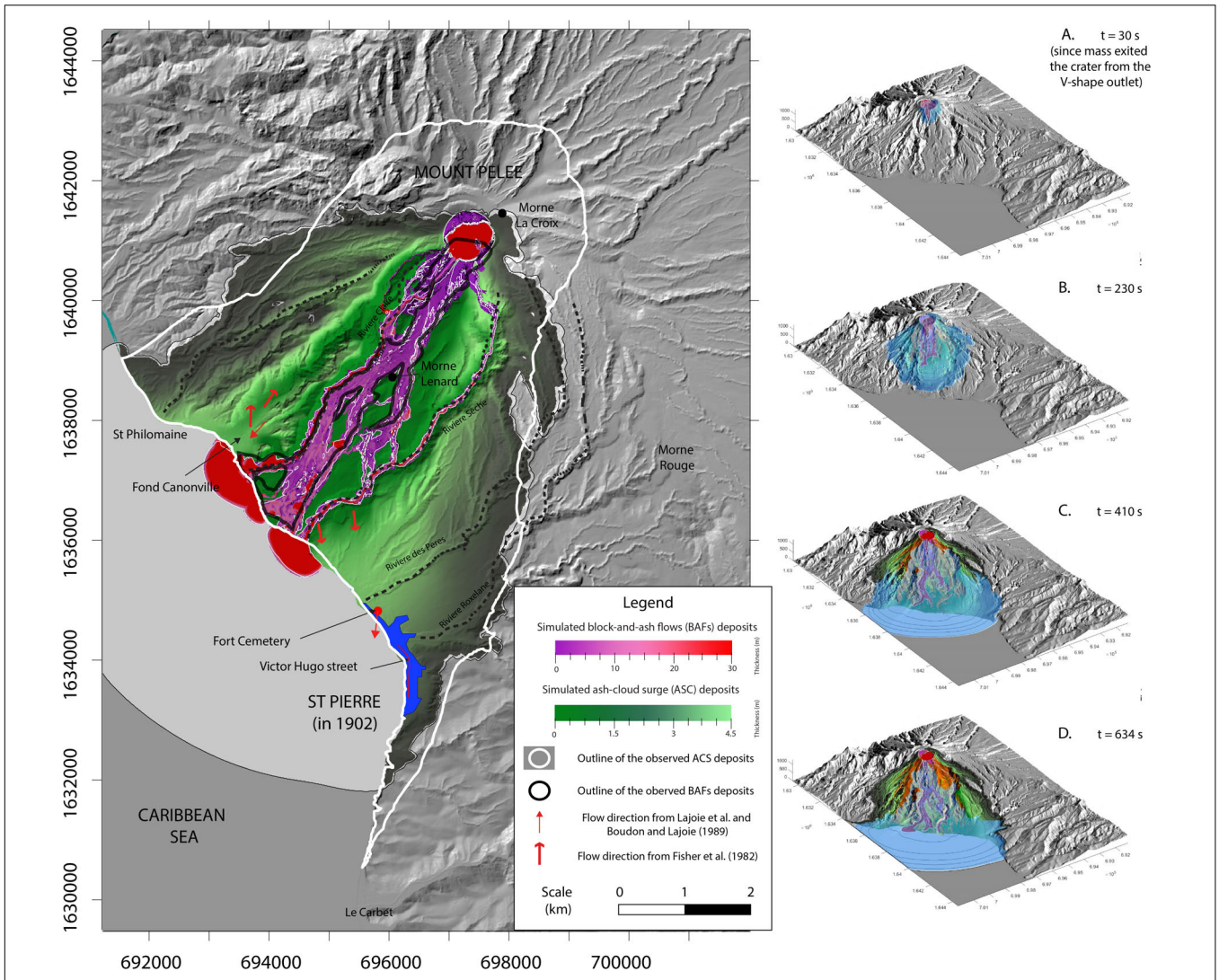

FIGURE 7 | Results of the best fit simulation obtained using the input parameters presented in **Table 2**. **(A)** Final distribution of the simulated deposits from the best-fit simulation, which include the extent of the simulated ash-cloud surge (green color scale for the thickness) and the simulated block-and-ash flow (pink color scale). For ease of comparison, outlines of the observed ash-cloud surge and block-and-ash flow, as extracted from the field, have been added with a white and black outline, respectively. **(B–E)** Sequence of four snap shots of the best-fit simulation at 30, 230, 410, and 634 s after the mass starts to overflow through the crater outlet, showing the propagation of the flows overlain on the DEM.

the model does not match the backward direction measured by Fisher et al. (1980) at Fond Canonville. Toward the east, especially in the St Pierre area, flow directions slowly change from south to southeast as the simulated surge expanded eastward. The same observation can be made on the western side of the area inundated by the surge with a flow direction that changes from southwest to west. The passage of the simulated ash-cloud surge over the flat sea surface promotes its lateral spreading as it covers a larger area to the west of St. Philomène and to the south toward St Pierre, giving a pear-like shape to the inundated area.

To better investigate the behavior of the simulated ash-cloud surge toward St Pierre, **Figure 9A** shows a snapshot of the simulated flow dynamics in this area over the DEM while **Figure 9B** superimposes these simulation results and field observations over the topographic map of St Pierre in 1902 from Lacroix (1904). The external, low dynamic pressure zone of the simulated surge (with a maximum pressure of 1.5 kPa) reaches only the northern part of the city, whereas field estimations made in 1902 give values of more than 2 kPa at this location. In **Figure 9B**, the Hill's annihilation line should roughly correspond to the 2 kPa dynamic pressure field, but our simulations give a maximum dynamic pressure of only 1 kPa at this location (blue line in **Figure 8**). Thus, the dynamic pressure in St Pierre seems to be underestimated by the model compared to field observations. Concerning the surge direction toward St Pierre, we notice that the western deflection of the current by the sea seems to be counterbalanced by the topographic barrier to the east of the city, from Morne Abel to Morne d'Orange (**Figure 9A**). In this

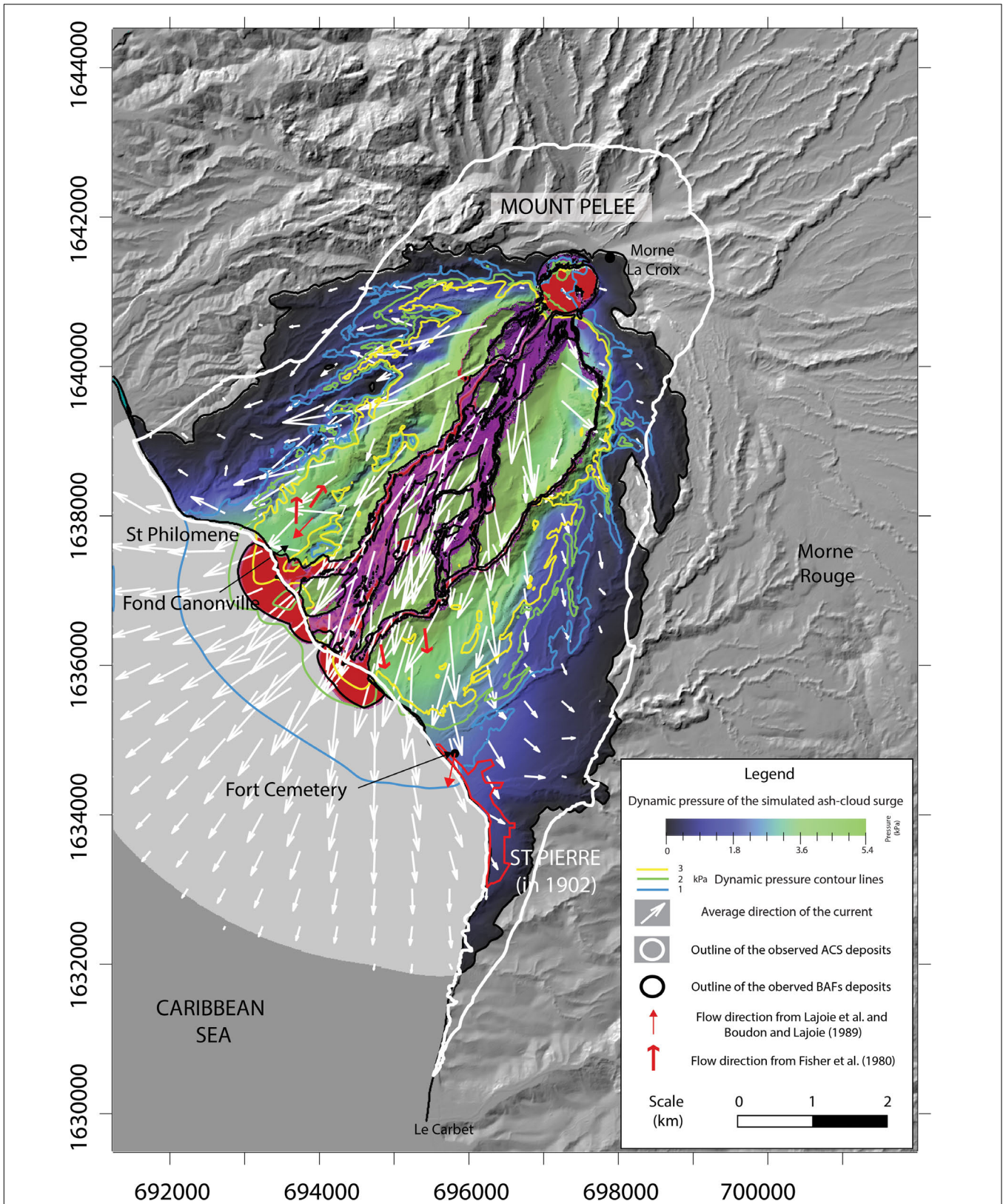

FIGURE 8 | Map of the maximum dynamic pressure and a mean direction of the ash-cloud surge from the best fit simulation. The distribution of the dynamic pressure is shown as a color scale, and isobar lines indicate the 1,2 and 3 kPa (blue, green and yellow lines, respectively) pressure fields. The average direction of the current is represented by white arrows, whose lengths correspond to the velocity of the ash-cloud surge, calculated from the center of the arrow.

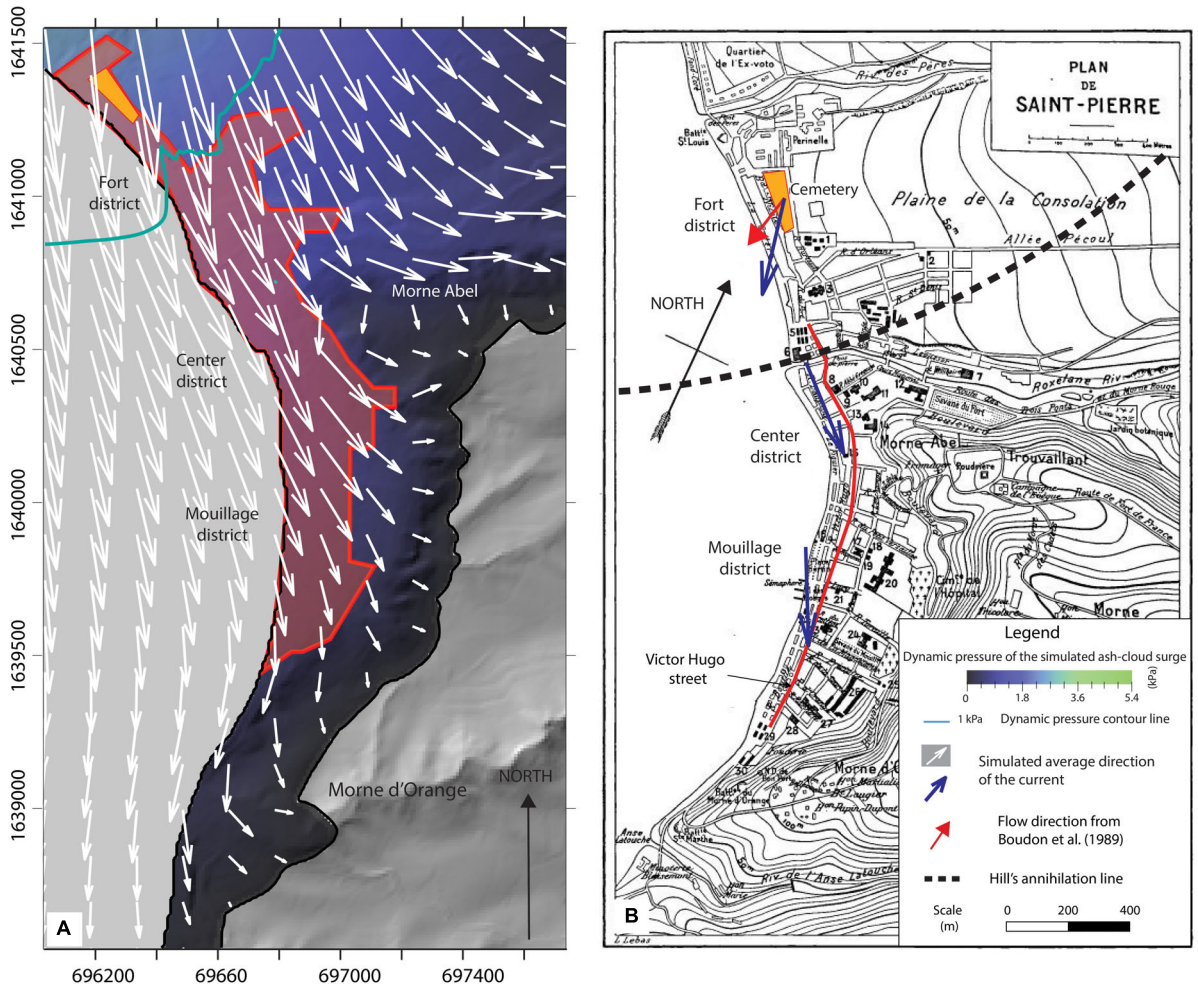

FIGURE 9 | Zoom of St Pierre's area showing the maximum dynamic pressure and the mean direction of the ash-cloud surge from the best-fit simulation: (A) superimposed over the DEM and polygon of the city as mapped by Lacroix (1904), (B) superimposed over the topographic map of the city, showing directions of the simulated current (blue arrows) facing Victor Hugo street (red line).

area, the surge direction changes from southeast to south as it propagates toward the southern part of the city (**Figures 7A,B**), matching approximately the direction of the Victor Hugo street (red line) as observed by Lacroix (1904). However, the mean direction of the simulated surge does not match the surge direction measured in Fort Cemetery by Boudon and Lajoie (1989). In summary, after entering the sea at Fort district, the simulated surge is first deflected to the east toward St Pierre, and then further deflected to the south by the hills on the east of St Pierre (south of Morne Abel, **Figure 8**). The direction of the simulated surge seems to be highly variable when it passes through St Pierre due to high turbulence induced by the complex pattern of the city infrastructures.

Flow Volumes: Total Mass Flux and Mass Flux Released in the Sea

When the simulated block-and-ash flow entered the sea, it formed unrealistic thick and large lobes (**Figure 7**). Because the sea corresponds to a planar surface of 0 m elevation in the DEM, it causes a brutal break in slope at the coastline and a strong deceleration of the block-and-ash flow, artificially increasing the flow thickness in the coastal area around the Rivière Blanche, the Rivière Claire and the Rivière Sèche. At the end of the simulation, the total volume deposited on land represents 19×10^6 m^3, whereas the volume accumulated offshore is 13×10^6 m^3, representing more than a third of the total deposit volume. The offshore volume was deposited within ∼1000 s, with an estimated average volumetric rate of material of 13,000 m^3 s^{-1} carried offshore.

INTERPRETATION: NEW INSIGHTS TO THE ERUPTIVE MODEL

Reproduction of the First-Order Dynamics and Deposit Characteristics

The good fit obtained between our simulations and the May 8th, 1902 pyroclastic current deposits seems consistent with

a depositional model where a channelized block-and-ash flow emplaced in the Rivière Blanche progressively filled the valley with thick deposits, together with an unconfined ash-cloud surge that spread laterally to produce a relatively thin deposit that thinned away from its source. Focusing all the mass through the crater outlet as the primary source condition for our simulations, as previous workers have commonly hypothesized from field observations, results in good correlations with the real event. The resulting self-regulated volume rate (**Figure 6**), generated by passive overflowing of the mass through the lowest elevated part of the crater rim, produces a realistic simulated pyroclastic current. The direction of the ash-cloud surge seems to corroborate quite well with the field direction measurements and the damage in St Pierre. However, simulations did not reproduce the up-valley movement of the surge at Fond Canonville, inferred by Fisher et al. (1980). The simulated ash-cloud surge was not confined in the Rivière Blanche valley and inundated the Fond Canonville area with a north-east to south-west direction, consistent with the measurements of Charland and Lajoie (1989) and Lajoie et al. (1989). Charland and Lajoie (1989) questioned the reliability of the flow directions measured by Fisher et al. (1980), pointing out that directions measured in a cross-bedded deposit are strongly dependent on the methodology used. But beyond these conflicting measurements, the landward flow direction obtained by Fisher et al. (1980) could also be explained by the rapid thermal expansion of the surge entering the sea, flashing seawater into steam and generating a landward dilute current, as described by Herd et al. (2005) at Montserrat, or by Dufek and Bergantz (2007) for the Kos Plateau Tuff eruption. Unfortunately, if such a process had occurred, our simulations did not capture it because VolcFlow does not model such flow temperature and energy variations.

While the deposit extent and paleo-current directions are well reproduced by our simulations, the dynamic pressure seems to be underestimated. Given the equation used here to calculate the dynamic pressure (Eq. 4), either the velocity of the simulated surge v or its density ρ_s are underestimated. Simulated flow velocities seem to be accurate if we compare them with the field estimations from Fisher et al. (1980) but are underestimated compared to the estimated value of 150 m s^{-1} given by Lacroix (1904). Underestimation of the dynamic pressure could also be explained by an underestimation of the surge density at the base of the flow. In fact, the shallow-water modeling approach used in VolcFlow implies the use of an averaged density across the entire current depth, which provides accurate reproduction of the general surge dynamics but constitutes an important simplification from natural density-stratified surges (Valentine, 1987). Therefore, the actual density at the base of surges (the part that interacts with buildings) is much higher than a depth-averaged value. This density difference could potentially explain the resulting underestimation of the dynamic pressures in our simulations.

In order to reproduce the actual runout of the ash-cloud surge, the particle drag coefficient C_d used in our simulations had to be set to an unrealistically high value (see **Table 2**). In fact, the chosen value of 35 does not match any previous estimation of this coefficient for volcanic particles (0.47–1; Dellino et al., 2005) and is overestimated by a factor of at least 30. C_d has been tuned in our model because it is the only parameter linked to the settling velocity (Eq. 11, **Supplementary Material**) that can be modified to change the sedimentation rate, with the mean grain size d already considered the smallest value recorded in the deposit (2ϕ). With a smaller settling velocity, the simulated ash-cloud surge settles much slower, keeping particles in suspension for a longer time, and subsequently covers a larger area before becoming buoyant. Therefore, some process seems to have hindered sedimentation in the May 8th pyroclastic current. A similar process has already been inferred for the simulation of the November 5th, 2010 pyroclastic current at Merapi by Kelfoun et al. (2017) for which the occurrence of a blast-like phase is also discussed (Charbonnier et al., 2013; Komorowski et al., 2013). However, no such issue arises when a similar approach was used to simulate the June 25th, 1997 pyroclastic currents at Soufrière Hills Volcano (Gueugneau et al., 2019), where no blast-like phase is mentioned. Different hypotheses are proposed to explain the hindering of the sedimentation: (i) if the base of the May 8th, 1902 ash-cloud surge was relatively dense, as suggested by the high dynamic pressures obtained from field observations, particle settling in the density-stratified surge could have been reduced and particles transported further away (i.e., hindered settling, Druitt, 1995). The factor of 30 obtained for the best-fit value of C_d could be applied to the surge density instead, thus giving similar modeling results. (ii) the air entrainment and subsequent thermal expansion of the ash-cloud surge, neglected in VolcFlow, can also reduce the sedimentation and increase the runout of the current, as suggested by Bursik and Woods (1996); Doyle et al. (2008) and demonstrated numerically by Benage et al. (2016). With the inability to reproduce thermal effects in our model, neglecting air entrainment might be limiting, especially at Mount Pelée where the presence of high ridges can enhance air entrainment, as Andrews and Manga (2011) have demonstrated experimentally. Moreover, the resuspension of soft material (i.e., ash), deposited with the onset of the 1902 eruptive phase, can also enhance air entrainment in the surge. Further model development is needed to include air entrainment in VolcFlow and to investigate whether this process has a significant influence on the dynamics of two-layer, depth-averaged simulated currents, as recently proposed by Shimizu et al. (2005) with their model.

Despite such approximations and simplifications made in the model, the VolcFlow simulations allow us to discuss the first-order dynamics controlling the main behavior of the May 8th, 1902 Mount Pelée pyroclastic current. The model of Fisher et al. (1980) tested in this study, inferring a surge formation from the concentrated flow, seems adequate to reproduce the pear-like shape of the area inundated. This proves that most of the surge production has to be initiated outside of the crater, along the Rivière Blanche, with a peak after Morne Lenard, as discussed by Fisher and Heiken (1982). To illustrate the importance of generating a surge along the Rivière Blanche, an additional VolcFlow simulation was performed, in which the surge production from the block-and-ash flow is suppressed. Instead, the two different layers of the simulated pyroclastic current (i.e., ash-cloud surge and block-and-ash flow) are supplied independently into the synthetic crater, with the same

duration and volumes as those obtained from the best-fit simulation outlined above (i.e., 11.4×10^6 m^3 for the ash-cloud surge and 20.8×10^6 m^3 for the block-and-ash flow, including the 13×10^6 m^3 stuck in the crater). Results of this complementary simulation (**Figure 10**) show that without a surge production along the Rivière Blanche valley, the ash-cloud surge is unable to reach St Pierre. Indeed, the simulated surge spreads radially around the crater without following the southward spreading of the block-and-ash flow. The development of a significant portion of the surge in the Rivière Blanche is likely facilitated by the crater outlet. Moreover, the shape of the simulated ash-cloud surge area differs from the pear-like shape characterizing our best-fit simulation as well as the May 8th, 1902 surge area (**Figure 8**). The progressive generation of an ash-cloud surge during the southward propagation of the main block-and-ash flow seems to be the more suitable process to explain both the shape of the inundated area and maximum runout of the surge toward St Pierre, as inferred by previous field investigations (Fisher et al., 1980; Fisher and Heiken, 1982). Thus, this also shows that simulating only one of the two conflicting scenarios to investigate the dynamic of the May 8th, 1902 pyroclastic current was satisfactory. Indeed, regarding our results, simulating the pyroclastic current as a blast flow appears to be unnecessary since a blast is exclusively formed in the crater, as the complementary simulation, and would probably have been unable to reproduce the pear-like shape of the surge deposit.

Another interesting outcome of the complementary simulation (**Figure 10**) is that the vertical mass flux in the crater generated a surge covering the northern part of the crater, although it does not accurately match Lacroix's outline. A source with an initial vertical component, like an explosion, that collapses and spreads volcanic products radially around the crater seems to be required in order to inundate this area. This corroborates witnesses' accounts of the eruption collected by Hill (1902) and Lacroix (1904) from the Morne Rouge village. If an explosion had occurred on May 8th 1902, it was most likely from the sudden decompression of a dome, resulting in a block-and-ash flow deposit similar to those described at Merapi (Charbonnier et al., 2013; Komorowski et al., 2013), Colima (Macorps et al., 2018), Soufrière Hills Volcano (Calder et al., 1999; Loughlin et al., 2002), or Unzen (Ui et al., 1999). Thus, we hypothesize that the source of the May 8th, 1902 pyroclastic current was most likely an explosive dome collapse, during which the shape of the crater enhanced the lateral spreading of the pyroclastic current by redirecting the products of the explosion through the crater outlet to the south. The remaining portion of the vertical jet formed during the explosion collapsed, providing enough lateral momentum for a dilute current to form and overflow the northern rim of the crater, inundating a small area downslope before rapidly stopping and becoming buoyant.

May 8th Pyroclastic Current Dynamics: The Blast Discussion

The occurrence of a blast during the May 8th, 1902 eruption has been strongly debated (Fisher and Heiken, 1983, 1990; Sparks, 1983; Boudon et al., 1990). The idea of a blast like Mount St Helens was first rejected by Fisher and Heiken (1983, 1990), mainly from field evidence (i.e., discordant flow directions, slower flow velocities, differences in deposit facies between the 1902 surge deposit and the blast deposit from May 18th, 1980 at Mount St Helens) but later supported by Boudon and Lajoie (1989); Bourdier et al. (1989), Lajoie et al. (1989), and Boudon et al. (1990) (using a different stratigraphy, flow directions and velocities). When using the more recent blast description of Belousov et al. (2007), the May 8th, 1902 pyroclastic current appears to be clearly different from the Mount St Helens blast: the debris avalanche deposit as well as layer A are missing in the stratigraphy, the area covered is one order of magnitude lower (51 km^2 instead of 623 km^2 for Mount St Helens, Lipman and Mullineaux, 1981), the flow volume is much smaller (32×10^6 m^3 instead of 94×10^6 m^3, Lipman and Mullineaux, 1981) and the shape of the area is relatively different too.

Paradoxically, discarding the hypothesis of a violent decompressive phase as a source condition for the May 8th, 1902 pyroclastic current is limiting. In fact, the May 8th, 1902 pyroclastic current exhibits remarkable features that can be attributed to a decompressive blast-like event as described nowadays:

- The northern part of the crater requires a source with an initial vertical component to be inundated, compatible with a short *burst phase*.
- The ash-cloud surge deposit facies from May 8th, 1902 at Mount Pelée is similar to the deposit facies of units U1L1 and U1L2 from the November 5th, 2010 Merapi unconfined deposit, which was interpreted as a low intensity blast by Komorowski et al. (2013). The lower unit in the May 8th deposit is composed of relatively coarse particles, which require a high level of turbulence to be sustained in suspension for a long time (Lajoie et al., 1989) and is fine-depleted, as is the unit U1L1 at Merapi. Moreover, even if the deposit stratigraphy does not match the blast stratigraphy of Belousov et al. (2007) exactly, the lower and middle unit of the May 8th, 1902 deposit (and the U1L1 and U1L2 units at Merapi) are in fact relatively close to their B and C units.
- The mass flux of material released at the source and needed to correctly simulate the May 8th, 1902 pyroclastic current is comparable to mass fluxes calculated during previous blast-like events. The average volume rate of overflowing material calculated from the blue curve in **Figure 6C** is 64×10^3 m^3 s^{-1} with a density $\rho_d = 1600$ kg m^{-3} yielding a mass flux of 10^8 kg s^{-1}, similar to the 10^8 kg s^{-1} deduced at Soufrière Hills Volcano for the December 26th, 1997 event (Sparks et al., 2002) or to the 10^7–10^8 kg s^{-1} calculated at Merapi for the November 5th, 2010 eruption (Komorowski et al., 2013; Kelfoun et al., 2017), and much higher than the average mass rate for a regular dome-collapse pyroclastic current at Soufrière Hills in June 25th, 1997, estimated at 8×10^6 kg s^{-1} (Loughlin et al., 2002; Gueugneau et al., 2019).

In summary, a few arguments support the fact that the initiation of the May 8th, 1902 pyroclastic current could have been partially driven by a decompressive blast-like phase,

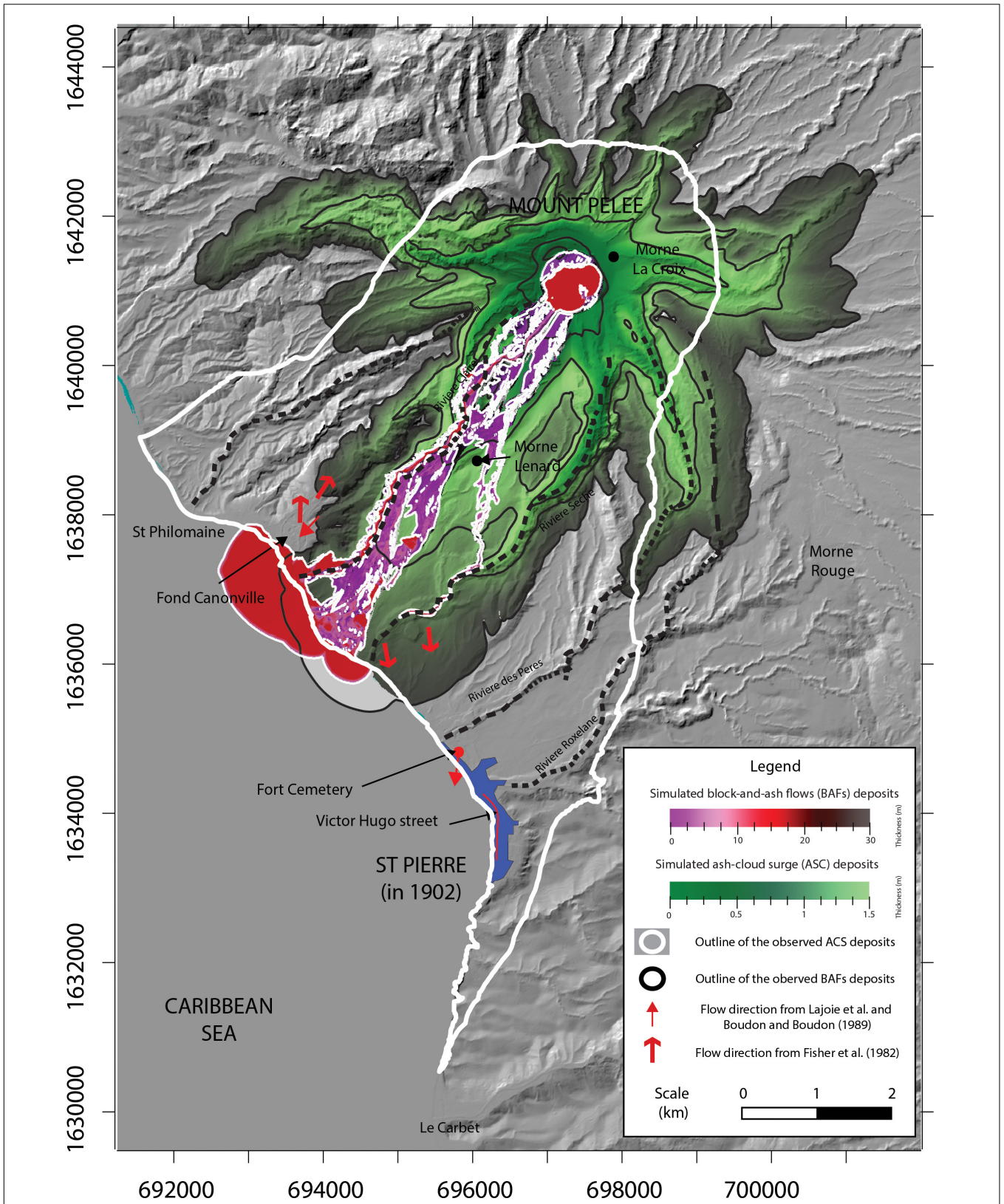

FIGURE 10 | Result of a complementary simulation with the ash-cloud surge and the block-and-ash flow supplied directly into the crater, without any surge production from the block-and-ash flow during the transport. The source conditions are adapted to supply 11.4 × 10^6 m^3 of ash-cloud surge and 20.8 × 10^6 m^3 of block-and-ash flow for the same duration (i.e., 200 s).

however, most of the characteristics of the current and its deposits are accurately reproduced by an ash-cloud surge generated from the block-and-ash flow, for which the surge production increases gradually with the spreading of the concentrated flow. Since our model is currently unable to simulate a laterally-directed blast and its associated initial *burst phase*, our results show instead that: (i) such a lateral explosion was not a compulsory component of the source conditions needed to correctly reproduce the characteristics of the May 8th pyroclastic current numerically, and (ii) the May 8th events can be modeled with relatively simple physics, commonly attributed to small-scale eruptions generating small-volume pyroclastic currents. A sudden decompression of the lava dome with a small vertical component could have likely taken place in the first few seconds of the eruption, explaining the presence of surge deposits on the northern part of the upper flank of the volcano, as well as the coarser nature of the basal layer in the deposit sequence, likely responsible for the high dynamic pressure of the distal surge. However, this potential initial blast-like phase at Mount Pelée does not compare with the May 18th, 1980 Mount St Helens blast sequence. Moreover, with such a short period between the May 20th pyroclastic current and the May 8th event with similar characteristics, it seems unlikely and too complex for a new pressurized and voluminous lava dome to grow and generate another blast (the pressurized phase was estimated at a few months at Soufrière Hills, 1997; Sparks et al., 2002). The May 8th, 1902 pyroclastic current may fit instead inside a spectrum between a blast (i.e., Belousov et al., 2007 definition) and an ash-cloud surge commonly associated with small-volume pyroclastic currents, most likely within the low-intensity, third group of blast-like events as defined by Komorowski et al. (2013). The physical behavior of such a blast is likely not dissimilar to one of a simple ash-cloud surge. This idea is reinforced by the work of Esposti Ongaro et al. (2008, 2012) demonstrating that, even if the December 26th, 1997 Soufrière Hills blast and the May 18th, 1980 Mount St Helens blast started with a decompression phase (*burst phase*), they quickly collapsed and transformed into powerful turbulent ash-cloud surges (*PDC phase*) in only a few tens of seconds.

Estimating the Total Volume of the Pyroclastic Current Deposit

Using results from our numerical simulations, we found 32×10^6 m^3, including 19×10^6 m^3 on land, to be the best input value for total deposited volume needed to reproduce the extent and thickness of the observed deposits. This corresponds, to our knowledge, to the first estimation of the total volume of the May 8th, 1902 pyroclastic current deposit. Nevertheless, because of the simplified physics used in our model, this value should be considered with caution and rather corresponds only to a first-order estimation. A rounded value of 30×10^6 m^3 can be used as an order of magnitude for comparison. Nevertheless, the relatively good correlations of the best-fit simulation with the observed deposit in terms of thickness distribution and repartition (**Figure 7** and **Table 3**) support the validity of the total deposit volume proposed here. This volume corresponds to almost one and a half times the total volume of extruded lave dome prior to the May 8th eruption, estimated at $18–23 \times 10^6$ m^3 by Tanguy (2004). This indicates that the volume of the dome in the crater prior to the May 8th eruption was smaller than the volume of the May 8th event alone, somewhat supporting the theory of Fisher and Heiken (1982, 1983) of an initial explosion of the superficial magma plug/dome that opened the magma conduit and supplied fresh magma during the May 8th eruption. This is also supported by the componentry analysis by Bourdier et al. (1989) with an average of only 5–10% of non-juvenile clasts. Modeling results also show that the volume of simulated block-and-ash flow deposit that reached the sea represents an important part of the total volume of the deposit (13×10^6 m^3), yielding a ratio of about one third. Again, this ratio must be taken with caution due to simplifications made in the model to simulate the sea surface. Nevertheless, measuring only the volume deposited on land to estimate the total volume of the eruption is too restrictive and underestimates the value.

New Insights for Hazards Assessment

Results of simulations highlight the important role that topography played in promoting the spreading of the May 8th, 1902 pyroclastic current in the direction of St Pierre. First of all, due to the proximity of the sea from the Mount Pelée crater, which acts as a flat and smooth surface, any surge produced by a block-and-ash flow, that propagates mostly southward, will be diverted when material flows over the sea surface. Secondly, the plains and gentle slopes to the north of St Pierre (**Figure 8**) allow the surge to keep its momentum for a long period of time in the eastern direction. Finally, the ridge on the eastern part of St Pierre (**Figure 8**) redirects the flow from eastward to southward. These observations corroborate with numerous studies showing the high sensitivity of small-volume pyroclastic currents to the topography at Unzen (Yamamoto et al., 1993), Merapi (Charbonnier and Gertisser, 2008; Lube et al., 2011; Gertisser et al., 2012; Kelfoun et al., 2017), Montserrat (Ogburn et al., 2014; Gueugneau et al., 2019), or Colima (Macorps et al., 2018).

The key input parameters used for the best-fit simulations (i.e., surge production, mixture density, constant retarding stress) are similar to those used in previous studies for modeling small-volume pyroclastic currents from June 25th, 1997 eruption at Soufrière Hills Volcano, Montserrat (Gueugneau et al., 2019) and those from November 5th, 2010 at Merapi Volcano in Indonesia (Kelfoun et al., 2017). This demonstrates that the May 8th, 1902 pyroclastic current at Mount Pelée was more likely a relatively common phenomenon that can be modeled at first-order as a regular small-volume pyroclastic current. This also demonstrates that the city of St Pierre cannot be exclusively destroyed by eruptions involving catastrophic phenomenon, like a Plinian column collapse or a laterally-directed blast explosion, but also by pyroclastic currents coming from the sudden decompression of a lava dome with dimensions similar to the one formed during the 1902-05 eruption. The probability of an occurrence of a destructive pyroclastic current in St Pierre then becomes higher than previously stated. In the last 5,000 years of activity, the occurrence of a blast-like event at Mt Pelée is currently estimated at one every 500 years (Westercamp and Traineau, 1983; Carazzo

et al., 2012), but the probability increases to one every 300 years if we combine these events with more frequent eruptions associated with small-volume block-and-ash flows. With such an increased probability of a similar pyroclastic current reaching St Pierre during future eruptions at Mount Pelée, the increased risk should be revised accordingly and included in short-term mitigation plans at this volcano.

CONCLUSION

The numerical simulation of the Mount Pelée May 8th, 1902 pyroclastic current confirmed numerous inferred flow and deposit characteristics previously suggested by various field studies. The model reproduced accurately both the block-and-ash flow and the associated ash-cloud surge component of the current, for an estimated total deposit volume of $\sim 32 \times 10^6$ m^3, with $\sim 19 \times 10^6$ m^3 on land and $\sim 13 \times 10^6$ m^3 deposited in the sea. The tested scenario, an ash-cloud-surge produced from the emplacement of a block-and-ash flow in the Rivière Blanche, seems realistic and opens some discussion about the internal dynamics of the current. Our study brings new evidence to support the occurrence of such a scenario:

- The pear-like shape of the surge inundated area seems to be associated with the late formation of the ash-cloud surge during the southward propagation of the block-and-ash flow.
- The computed directions of the simulated currents that show an initial southward propagation of both the block-and-ash flow and surge, and late diversion of the surge toward the east, correlate with most of the measured flow directions obtained in the field.

However, a few claims support the presence of a decompressive blast-like event:

- The surge deposit facies is similar to those described for the November 5th, 2010 Merapi blast-like deposits (fine-depleted and coarse nature of the basal layer).
- The surge propagation in the northern part of the upper flank could be associated with a short explosion at the beginning of the eruption, analogous to a "low-intensity" burst phase.

Based on results obtained from our VolcFlow simulations and previous field data, the May 8th eruption can be interpreted as a sudden decompression of the lava dome growing in the crater, leading to a small vertical column that quickly collapsed into a powerful pyroclastic current, focused mainly by the shape of the southern crater outlet. Immediately after, a dense block-and-ash flow developed in the Rivière Blanche and generated an overriding ash-cloud surge during its southward propagation. The surge became more and more voluminous and powerful as it moved seaward and spread westward and eastward. When both currents reached the sea, the ash-cloud surge traveled over the northern plains of St Pierre and sea, promoting its lateral spreading. Moving eastward, it reached St Pierre and was progressively diverted southward through the city.

Results of simulations also highlights the important role played by the main topographic features of the southern flank of Mount Pelée during the eruption, which enhanced the lateral spreading of the surge, further exposed St Pierre to the path of the flow. With similar characteristics as in previous case studies elsewhere, the May 8th, 1902 event is considered as a small-scale explosive event for this volcano, associated with high-energy, small-volume pyroclastic currents for which the probability of occurrence is higher than a catastrophic blast event (one every 300 years). Thus, our study subsequently improves the assessment of hazards posed by pyroclastic currents at Mount Pelée, helpful for future eruptions, and can be replicated for similar pyroclastic currents elsewhere on Earth where the dynamic is also debated (i.e., Merapi, Indonesia; Unzen, Japan; Chaiten, Chile; Arenal, Costa Rica). It finally brings new claims supporting that the generation of the ash-cloud surge in small-volume pyroclastic currents is mostly coming from the block-and-ash flow.

DATA AVAILABILITY STATEMENT

The raw data supporting the conclusions of this article will be made available by the authors, without undue reservation, to any qualified researcher.

AUTHOR CONTRIBUTIONS

VG performed the simulations, interpreted the data, and drafted the work. SC helped to interpret the data and revised thoroughly the whole manuscript. AG wrote the Martinique Island geological history and revised the work. GC wrote the Mount Pelée recent eruptive history, provided the deposits pictures at St Pierre, and revised the work. KK helped to interpret the data and revised the work, mostly the numerical modeling, results, and discussion sections. VG, KK, and SC designed the work. All authors contributed to the article and approved the submitted version.

FUNDING

The development of the numerical code was funded by the Domerapi-ANR (French Agence Nationale de la Recherche) Project (ANR-12-BS06-0012). This research was supported by the National Science Foundation CAREER award #1751905. This research was also partly supported by the French Government Laboratory of Excellence initiative no. ANR-10-LABX-0006, the Région Auvergne and the European Regional Development Fund. This was Laboratory of Excellence ClerVolc contribution number 423. GC was partially funded by the PREST Interreg Project.

ACKNOWLEDGMENTS

We thank the editor and the two reviewers who have contributed to improve this work with their insightful

comments and suggestions. We would like also to thank Judy McIlrath for having kindly revised the English of the manuscript and subsequently greatly improved it. We finally acknowledge the Observatoire Volcanologique et Sismologique de Martinique for having provided us the DEM of the Martinique Island.

SUPPLEMENTARY MATERIAL

The Supplementary Material for this article can be found online at: https://www.frontiersin.org/articles/10.3389/feart.2020.00279/full#supplementary-material

REFERENCES

Alvarado, G. E., Soto, G. J., Schmincke, H.-U., Bolge, L. L., and Sumita, M. (2006). The 1968 andesitic lateral blast eruption at Arenal volcano, Costa Rica. *J. Volcanol. Geotherm. Res.* 157, 9–33. doi: 10.1016/j.jvolgeores.2006.03.035

Andrews, B. J., and Manga, M. (2011). Effects of topography on pyroclastic density current runout and formation of coignimbrites. *Geology* 39, 1099–1102. doi: 10.1130/G32226.1

Aubaud, C., Athanase, J. E., Clouard, V., Barras, A. V., and Sedan, O. (2013). A review of historical lahars, floods, and landslides in the Prêcheur river catchment (Montagne Pelée volcano, Martinique island, Lesser antilles). *Bull. Soc. Geol. Fr.* 184, 137–154. doi: 10.2113/gssgfbull.184.1-2.137

Belousov, A., Voight, B., and Belousova, M. (2007). Directed blasts and blast-generated pyroclastic density currents: a comparison of the Bezymianny 1956, Mount St Helens 1980, and Soufrière Hills, Montserrat 1997 eruptions and deposits. *Bull. Volcanol.* 69, 701–740. doi: 10.1007/s00445-006-0109-y

Benage, M. C., Dufek, J., and Mothes, P. A. (2016). Quantifying entrainment in pyroclastic density currents from the Tungurahua eruption, Ecuador: Integrating field proxies with numerical simulations. *Geophys. Res. Lett.* 43, 6932–6941. doi: 10.1002/2016GL069527

Boudon, G., and Lajoie, J. (1989). The 1902 Peleean deposits in the Fort Cemetery of St . Pierre, Martinique : a model for the accumulation of turbulent nuees ardentes. *J. Volcanol. Geotherm. Res.* 38, 113–129. doi: 10.1016/0377-0273(89)90033-90034

Boudon, G., Bourdier, J. L., Gourgaud, A., and Lajoie, J. (1990). The may 1902 eruptions of mount pelée: high-velocity directed blasts or column-collapse nuées ardentes? *J. Volcanol. Geotherm. Res.* 43, 359–364. doi: 10.1016/0377-0273(90)90062-K

Boudon, G., Le Friant, A., Komorowski, J.-C., Deplus, C., and Semet, M. P. (2007). Volcano flank instability in the Lesser Antilles Arc: Diversity of scale, processes, and temporal recurrence. *J. Geophys. Res.* 112:B08205. doi: 10.1029/2006JB004674

Boudon, G., Le Friant, A., Villemant, B., and Viode, J. P. (2005). "Martinique," in *Volcanic Atlas of the Lesser Antilles*, ed. J. M. Lindsay, (Jamaica: University of the West Indies), 65–102.

Bourdier, J. L., Boudon, G., and Gourgaud, A. (1989). Stratigraphy of the 1920 and 1929 nuée-ardente deposits. Mt. Pelée, Martinique. *J. Volcanol. Geotherm. Res.* 38, 77–96. doi: 10.1016/0377-0273(89)90031-0

Bursik, M. I., and Woods, A. W. (1996). The dynamics and thermodynamics of large ash flows. *Bull. Volcanol.* 58, 175–193. doi: 10.1007/s004450050134

Calder, E. S., Cole, P. D., Dade, W. B., Druitt, T. H., Hoblitt, R. P., Huppert, H. E., et al. (1999). Mobility of pyroclastic flows and surges at the Soufriere Hills Volcano. *Montserrat. Geophys. Res. Lett.* 26, 537–540. doi: 10.1029/1999GL900051

Carazzo, G., Tait, S., and Kaminski, E. (2019). Marginally stable recent Plinian eruptions of Mt. Pelée volcano (Lesser Antilles): the P2 AD 280 eruption. *Bull. Volcanol.* 81, 1–17. doi: 10.1007/s00445-018-1265-1266

Carazzo, G., Tait, S., Kaminski, E., and Gardner, J. E. (2012). The recent Plinian explosive activity of Mt. Pelée volcano (Lesser Antilles): The P1 AD 1300 eruption. *Bull. Volcanol.* 74, 2187–2203. doi: 10.1007/s00445-012-0655-654

Carazzo, G., Tait, S., Michaud-Dubuy, A., Fries, A., and Kaminski, E. (2020). Transition from stable column to partial collapse during the 79 cal CE P3 Plinian eruption of Mt. Pelée volcano (Lesser Antilles). *J. Volcanol. Geotherm. Res.* 392:106764. doi: 10.1016/j.jvolgeores.2019.106764

Charbonnier, S. J., Connor, C. B., Connor, L. J., Sheridan, M. F., Oliva Hernández, J. P., and Richardson, J. A. (2018). Modeling the October 2005 lahars at Panabaj (Guatemala). *Bull. Volcanol.* 80:4. doi: 10.1007/s00445-017-1169-x

Charbonnier, S. J., Germa, A., Connor, C. B., Gertisser, R., Preece, K., Komorowski, J. C., et al. (2013). Evaluation of the impact of the 2010 pyroclastic density currents at Merapi volcano from high-resolution satellite imagery, field investigations and numerical simulations. *J. Volcanol. Geotherm. Res.* 261, 295–315. doi: 10.1016/j.jvolgeores.2012.12.021

Charbonnier, S. J., and Gertisser, R. (2008). Field observations and surface characteristics of pristine block-and-ash flow deposits from the 2006 eruption of Merapi Volcano, Java, Indonesia. *J. Volcanol. Geotherm. Res.* 177, 971–982. doi: 10.1016/j.jvolgeores.2008.07.008

Charbonnier, S. J., and Gertisser, R. (2012). Evaluation of geophysical mass flow models using the 2006 block-and-ash flows of Merapi Volcano, Java, Indonesia: Towards a short-term hazard assessment tool. *J. Volcanol. Geotherm. Res.* 23, 87–108. doi: 10.1016/j.jvolgeores.2012.02.015

Charbonnier, S. J., Thouret, J-C., Gueugneau, V., and Constantinescu, R. (2020). New insights into the c.2070 yr BP pyroclastic currents at El Misti volcano (Peru) from field observations, optical imagery and probabilistic modeling. *Front. Earth Sci.*

Charland, A., and Lajoie, J. (1989). Characteristics of Pyroclastic Deposits At the Margin of Fond-Canonville, Martinique, and Implications for the Transport of the 1902 Nuees-Ardentes of Mt Pelee. *J. Volcanol. Geotherm. Res.* 38, 97–112. doi: 10.1016/0377-0273(89)90032-90032

Chrétien, S., and Brousse, R. (1989). Events preceding the great eruption of 8 May, 1902 at Mount Pelée. *Martinique. J. Volcanol. Geotherm. Res.* 38, 67–75. doi: 10.1016/0377-0273(89)90030-90039

Cronin, S. J., Lube, G., Dayudi, D. S., Sumarti, S., Subrandiyo, S., and Surono, A. (2013). Insights into the October–November 2010 Gunung Merapi eruption (Central Java, Indonesia) from the stratigraphy, volume and characteristics of its pyroclastic deposits. *J. Volcanol. Geotherm. Res.* 261, 244–259. doi: 10.1016/j.jvolgeores.2013.01.005

Dellino, P., Mele, D., Bonasia, R., Braia, G., La Volpe, L., and Sulpizio, R. (2005). The analysis of the influence of pumice shape on its terminal velocity. *Geophys. Res. Lett.* 32, 1–4. doi: 10.1029/2005GL023954

Doyle, E. E., Hogg, A. J., Mader, H. M., and Sparks, R. S. J. (2008). Modeling dense pyroclastic basal flows from collapsing columns. *Geophys. Res. Lett.* 35:L04305. doi: 10.1029/2007GL032585

Druitt, T. H. (1995). Settling behaviour of concentrated dispersions and some volcanological applications. *J. Volcanol. Geotherm. Res.* 65, 27–39. doi: 10.1016/0377-0273(94)00090-94

Dufek, J., and Bergantz, G. W. (2007). Dynamics and deposits generated by the Kos Plateau Tuff eruption: Controls of basal particle loss on pyroclastic flow transport. *Geochem. Geophys. Geosyst.* 8:Q12007. doi: 10.1029/2007GC001741

Esposti Ongaro, T., Clarke, A. B., Neri, A., Voight, B., and Widiwijayanti, C. (2008). Fluid dynamics of the 1997 Boxing Day volcanic blast on Montserrat. *West Indies. J. Geophys. Res.* 113:B03211. doi: 10.1029/2006JB004898

Esposti Ongaro, T., Clarke, A. B., Voight, B., Neri, A., and Widiwijayanti, C. (2012). Multiphase flow dynamics of pyroclastic density currents during the May 18, 1980 lateral blast of Mount St. Helens. *J. Geophys. Res. Solid Earth* 117:B06208. doi: 10.1029/2011JB009081

Fisher, R. V., and Heiken, G. (1982). Mt. Pelée, Martinique: May 8 and 20, 1902, pyroclastic flows and surges. *J. Volcanol. Geotherm. Res.* 13, 339–371. doi: 10.1016/0377-0273(83)90132-90134

Fisher, R. V., and Heiken, G. (1983). Mt. Pelée, Martinique: May 8 and 20, 1902, pyroclastic flows and surges — Reply. *J. Volcanol. Geotherm. Res.* 19, 180–184. doi: 10.1016/0377-0273(83)90132-90134

Fisher, R. V., and Heiken, G. (1990). Discussion of four papers in the Mount Pel6e Special Issue (J . Volcanol Geotherm . tinique, by J . L . Bourdier, G . Boudon and A . Gourgaud . 2 . Characteristics of pyroclastic deposits at the margin of Fond Canonville, Martinique, and implications. *J. Volcanol. Geotherm. Res.* 43, 353–364.

Fisher, R. V., Smith, A. L., and Roobol, M. J. (1980). Destruction of St. Pierre, Martinique, by ash-cloud surges, May 8 and 20, 1902. *Geology* 8:472. doi: 10.1130/0091-761319808<472

Germa, A., Quidelleur, X., Labanieh, S., Chauvel, C., and Lahitte, P. (2011). The volcanic evolution of Martinique Island: Insights from K–Ar dating into the Lesser Antilles arc migration since the Oligocene. *J. Volcanol. Geotherm. Res.* 208, 122–135. doi: 10.1016/j.jvolgeores.2011.09.007

Gertisser, R., Cassidy, N. J., Charbonnier, S. J., Nuzzo, L., and Preece, K. (2012). Overbank block-and-ash flow deposits and the impact of valley-derived, unconfined flows on populated areas at Merapi volcano. Java, Indonesia. *Nat. Hazards* 60, 623–648. doi: 10.1007/s11069-011-0044-x

Gueugneau, V., Kelfoun, K., and Druitt, T. (2019). Investigation of surge-derived pyroclastic flow formation by numerical modelling of the 25 June 1997 dome collapse at Soufrière Hills Volcano. *Montserrat. Bull. Volcanol.* 81:25. doi: 10.1007/s00445-019-1284-y

Herd, R. A., Edmonds, M., and Bass, V. A. (2005). Catastrophic lava dome failure at soufrière hills volcano, montserrat, 12–13 July 2003. *J. Volcanol. Geotherm. Res.* 148, 234–252. doi: 10.1016/j.jvolgeores.2005.05.003

Hill, R. T. (1902). A study of Pelée: impressions and conclusions of a trip to Martinique. *Century Magazine* 64, 764–785.

Jaggar, T. A. Jr. (1903). The eruption of Mount Pelée, 1851. *Am. Nat.* 38, 51–73. doi: 10.1086/278377

Jenkins, S., Komorowski, J. C., Baxter, P. J., Spence, R., Picquout, A., Lavigne, F., et al. (2013). The Merapi 2010 eruption: An interdisciplinary impact assessment methodology for studying pyroclastic density current dynamics. *J. Volcanol. Geotherm. Res.* 261, 316–329. doi: 10.1016/j.jvolgeores.2013.02.012

Kelfoun, K. (2011). Suitability of simple rheological laws for the numerical simulation of dense pyroclastic flows and long-runout volcanic avalanches. *J. Geophys. Res.* 116, 1–14. doi: 10.1029/2010JB007622

Kelfoun, K. (2017). A two-layer depth-averaged model for both the dilute and the concentrated parts of pyroclastic currents. *J. Geophys. Res. Solid Earth* 122, 1–19. doi: 10.1002/2017JB014013

Kelfoun, K., Gueugneau, V., Komorowski, J.-C., Cholik, N., and Merciecca, C. (2017). Simulation of block-and-ash flows and ash-cloud surges of the 2010 eruption of Merapi volcano with a two-layer model. *J. Geophys. Res. Solid Earth* 122, 1–16. doi: 10.1002/2017JB013981

Kelfoun, K., Samaniego, P., Palacios, P., and Barba, D. (2009). Testing the suitability of frictional behaviour for pyroclastic flow simulation by comparison with a well-constrained eruption at Tungurahua volcano (Ecuador). *Bull. Volcanol.* 71, 1057–1075. doi: 10.1007/s00445-009-0286-286

Komorowski, J. C., Jenkins, S., Baxter, P. J., Picquout, A., Lavigne, F., Charbonnier, S., et al. (2013). Paroxysmal dome explosion during the Merapi 2010 eruption: Processes and facies relationships of associated high-energy pyroclastic density currents. *J. Volcanol. Geotherm. Res.* 261, 260–294. doi: 10.1016/j.jvolgeores.2013.01.007

Lacroix, A. (1904). La Montagne Pelée et ses éruptions. *Bull. Am. Geogr. Soc.* 38, 60–62.

Lajoie, J., Boudon, G., and Bourdier, J. (1989). Depositional mechanics of the 1902 pyroclastic nuee-ardente deposits of Mr. Pelee, Martinique. *J. Volcanol. Geotherm. Res.* 38, 131–142. doi: 10.1016/0377-0273(89)90034-6

Le Friant, A. (2003). Numerical simulation of the last flank-collapse event of Montagne Pelée, Martinique, Lesser Antilles. *Geophys. Res. Lett.* 30, 3–6. doi: 10.1029/2002GL015903

Lipman, P. W., Moore, J. G., and Swanson, D. A. (1981). Bulging of the north flank before the May 18 eruption: Geodetic data. *US Geol. Surv. Prof. Pap.* 1250, 143–155.

Lipman, P. W., and Mullineaux, D. R. (1981). *The 1980 eruptions of Mount St. Helens, Washington. Geological*. Washington, DC: US Government Printing Office.

Loughlin, S. C., Calder, E. S., Clarke, A., Cole, P. D., Luckett, R., Mangan, M. T., et al. (2002). Pyroclastic flows and surges generated by the 25 June 1997 dome collapse, soufrière hills volcano, *Montserrat. Geol. Soc. London, Mem.* 21, 191–209. doi: 10.1144/GSL.MEM.2002.021.01.09

Lube, G., Cronin, S. J., Thouret, J. C., and Surono, S. (2011). Kinematic characteristics of pyroclastic density currents at merapi and controls on their avulsion from natural and engineered channels. *Bull. Geol. Soc. Am.* 123, 1127–1140. doi: 10.1130/B30244.1

Macorps, E., Charbonnier, S. J., Varley, N. R., Capra, L., Atlas, Z., and Cabré, J. (2018). Stratigraphy, sedimentology and inferred flow dynamics from the July 2015 block-and-ash flow deposits at Volcán de Colima. Mexico. *J. Volcanol. Geotherm. Res.* 349, 99–116. doi: 10.1016/j.jvolgeores.2017.09.025

Major, J. J., Pierson, T. C., Hoblitt, R. P., and Moreno, H. (2013). Pyroclastic density currents associated with the 2008-2009 eruption of Chaitén Volcano (Chile): Forest disturbances, deposits, and dynamics. *Andean Geol.* 40, 324–358. doi: 10.5027/andgeoV40n2-a09

Michaud-Dubuy, A., Carazzo, G., Tait, S., Le Hir, G., Fluteau, F., and Kaminski, E. (2019). Impact of wind direction variability on hazard assessment in Martinique (Lesser Antilles): The example of the 13.5 ka cal BP Bellefontaine Plinian eruption of Mount Pelée volcano. *J. Volcanol. Geotherm. Res.* 381, 193–208. doi: 10.1016/j.jvolgeores.2019.06.004

Ogburn, S. E., and Calder, E. S. (2017). The relative effectiveness of empirical and physical models for simulating the dense undercurrent of pyroclastic flows under different emplacement conditions. *Front. Earth Sci.* 5:83. doi: 10.3389/feart.2017.00083

Ogburn, S. E., Calder, E. S., Cole, P. D., and Stinton, A. J. (2014). The effect of topography on ash-cloud surge generation and propagation. *Geol. Soc. Lond. Mem.* 39, 179–194. doi: 10.1144/M39.10

Perret, F. (1935). *The Eruption of Mt. Pelée, 1929-1932*. Washington, DC: Carnegie institution of Washington.

Roobol, M. J., and Smith, A. L. (1975). A comparison of the recent eruptions of Mt. Pelée, Martinique and Soufrière, St. Vincent. *Bull. Volcanol.* 39, 214–240. doi: 10.1007/BF02597829

Shimizu, H. A., Koyaguchi, T., and Suzuki, Y. J. (2019). The run-out distance of large-scale pyroclastic density currents: a two-layer depth-averaged model. *J. Volcanol. Geotherm. Res.* 381, 168–184. doi: 10.1016/j.jvolgeores.2019.03.013

Sparks, R. S. J. (1983). Mont Pelee, Martinique: may 8 and 20, 1902, pyroclastic flows and surges - discussion. *J. Volcanol. Geotherm. Res.* 19, 175–184.

Sparks, R. S. J., Barclay, J., Calder, E. S., Herd, R. A., Komorowski, J.-C., Luckett, R., et al. (2002). Generation of a debris avalanche and violent pyroclastic density current on 26 December (Boxing Day) 1997 at Soufriere Hills Volcano, Montserrat. *Geol. Soc. London, Mem.* 21, 409–434. doi: 10.1144/GSL.MEM.2002.021.01.18

Tanguy, J.-C. (2004). Rapid dome growth at Montagne Pelée during the early stages of the 1902-1905 eruption: a reconstruction from Lacroix's data. *Bull. Volcanol.* 66, 615–621. doi: 10.1007/s00445-004-0344-z

Tanguy, J.-C. C. (1994). The 1902-1905 eruptions of Montagne Pelée, Martinique: anatomy and retrospection. *J. Volcanol. Geotherm. Res.* 60, 87–107. doi: 10.1016/0377-0273(94)90064-90067

Taniguchi, H., and Suzuku-Kamata, K. (1993). Direct measurement of over pressure of volcanic blast on the June 1991 eruption at Unzen volcano. Japan. *Geophys. Res. Lett.* 20, 89–92. doi: 10.1029/92gl02720

Taylor, G. A. (1958). The 1951 eruption of Mount Lamington, Papua. *Aust. Bur. Miner. Resour. Geol. Geophys. Bull.* 38, 1–117.

Ui, T., Matsuwo, N., Sumita, M., and Fujinawa, A. (1999). Generation of block and ash flows during the 1990-1995 eruption of Unzen Volcano. Japan. *J. Volcanol. Geotherm. Res.* 89, 123–137. doi: 10.1016/S0377-0273(98)00128-120

Valentine, G. A. (1987). Stratified flow in pyroclastic surges. *Bull. Volcanol.* 49, 616–630. doi: 10.1007/BF01079967

Valentine, G. A. (1998). Damage to structures by pyroclastic flows and surges, inferred from nuclear weapons effects. *J. Volcanol. Geotherm. Res.* 87, 117–140. doi: 10.1016/S0377-0273(98)00094-98

Voight, B., Komorowski, J.-C., Norton, G. E., Belousov, A. B., Belousova, M., Boudon, G., et al. (2002). The 26 December (Boxing Day) 1997 sector collapse and debris avalanche at Soufriere Hills Volcano, Montserrat. *Geol. Soc. London, Mem.* 21, 363–407. doi: 10.1144/GSL.MEM.2002.021.01.17

Westercamp, D., and Traineau, H. (1983). The past 5,000 years of volcanic activity at Mt. Pelée Martinique (F.W.I): Implications for assessment of volcanic hazards. *J. Volcanol. Geotherm. Res.* 57, 159–185. doi: 10.1017/CBO9781107415324.004

Yamamoto, T., Takarada, S., and Suto, S. (1993). Pyroclastic flows from the 1991 eruption of Unzen volcano, Japan. *Bull. Volcanol.* 55, 166–175. doi: 10.1007/BF00301514

Conflict of Interest: The authors declare that the research was conducted in the absence of any commercial or financial relationships that could be construed as a potential conflict of interest.

frontiers in Earth Science

ORIGINAL RESEARCH
published: 28 July 2020
doi: 10.3389/feart.2020.00275

Comparative Analysis of the Structures and Outcomes of Geophysical Flow Models and Modeling Assumptions Using Uncertainty Quantification

Abani Patra[1,2], *Andrea Bevilacqua*[1,3,4]*, *Ali Akhavan-Safaei*[5], *E. Bruce Pitman*[6], *Marcus Bursik*[3] and *David Hyman*[3,7]

[1] Computational Data Science and Engineering, University at Buffalo, Buffalo, NY, United States, [2] Tufts University, Data Intensive Sciences Center, Medford, MA, United States, [3] Department of Earth Sciences, University at Buffalo, Buffalo, NY, United States, [4] Istituto Nazionale di Geofisica e Vulcanologia, Sezione di Pisa, Pisa, Italy, [5] Department of Mechanical and Aerospace Engineering, University at Buffalo, Buffalo, NY, United States, [6] Department of Materials Design and Innovation, University at Buffalo, Buffalo, NY, United States, [7] Cooperative Institute for Meteorological Satellite Studies, UW, Madison, WI, United States

OPEN ACCESS

Edited by:
Chong Xu,
China Earthquake Administration, China

Reviewed by:
José Pedro Matos,
Stucky SA, Switzerland
Jia-wen Zhou,
Sichuan University, China

***Correspondence:**
Andrea Bevilacqua
andrea.bevilacqua@ingv.it

Specialty section:
This article was submitted to Geohazards and Georisks, a section of the journal Frontiers in Earth Science

Received: 28 October 2019
Accepted: 16 June 2020
Published: 28 July 2020

Citation:
Patra A, Bevilacqua A, Akhavan-Safaei A, Pitman EB, Bursik M and Hyman D (2020) Comparative Analysis of the Structures and Outcomes of Geophysical Flow Models and Modeling Assumptions Using Uncertainty Quantification. Front. Earth Sci. 8:275. doi: 10.3389/feart.2020.00275

We advocate here a methodology for characterizing models of geophysical flows and the modeling assumptions they represent, using a statistical approach over the full range of applicability of the models. Such a characterization may then be used to decide the appropriateness of a model and modeling assumption for use. We present our method by comparing three different models arising from different rheology assumptions, and the output data show unambiguously the performance of the models across a wide range of possible flow regimes. This comparison is facilitated by the recent development of the new release of our TITAN2D mass flow code that allows choice of multiple rheologies. The quantitative and probabilistic analysis of contributions from different modeling assumptions in the models is particularly illustrative of the impact of the assumptions. Knowledge of which assumptions dominate, and, by how much, is illustrated in the topography on the SW slope of Volcán de Colima (MX). A simple model performance evaluation completes the presentation.

Keywords: depth averaged models, uncertainty quantification (UQ), Colima (Mexico), block and ash flows, computer models, volcanic hazard assessment, pyroclastic flows

1. INTRODUCTION

This paper describes an uncertainty quantification driven approach to analyze total models and individual assumptions that are composed into models of geophysical mass flows. This is especially relevant when the observations/measurements are not adequate to characterize the behavior of the system which is modeled. Observational data inadequacy is rarely characterized even for verified and validated models.

Since models actualize a hypothesis, it follows that a model articulates a belief about the data. Thus a model will always have some uncertainty in prediction, since the subjectivity of the belief can never be completely eliminated (Higdon et al., 2004; Kennedy and O'Hagan, 2011), nor is the data at hand usually enough to characterize its behavior at the desired prediction. Principles like

"Occam's razor" and Bayesian statistics (Farrell et al., 2015) provide some guidance, but *robust and quantitative approaches that allow the testing of model components for fitness* need to be developed. In related work, we have shown that the application of the empirical falsification principle (Popper, 1959) over an arbitrarily wide envelope of possible inputs reduces the subjectivity and uncertainty in a case study where the available data was not adequate (Bevilacqua et al., 2019).

There are usually numerous models for representing complex systems with sparse observations, like large scale geophysical mass flows (Kelfoun, 2011). It is often difficult to decide which of these models are appropriate for a particular analysis. Nevertheless, ready availability of many models as reusable software tools makes it the user's burden to select one appropriate for their purpose. For example, the 4th release of TITAN2D[1], already adopted in Bevilacqua et al. (2019), offers multiple rheology options in the same code base (Simakov et al., 2019). The availability of different models for similar or the same phenomena in the same tool provides us the ability to directly compare outputs and internal variables in all the models while controlling for difficult to quantify effects like numerical solution procedures, input ranges and computer hardware. This can improve the process for integrating information from multiple models (Bongard and Lipson, 2007). Given a particular problem for which predictive analysis is planned, the information generated and its comparison to available observational data can be used to guide model choice and input space refinement (Bevilacqua et al., 2019). However, as we have discovered, such comparison requires a careful understanding of each model and its constituents and a well-organized process like that which we describe here for such a comparison. In this study, we focus on the comparison between models, more than on the input space refinement problem.

A modeling assumption is essentially a simple postulate framing direct relationships among quantities under study. Models are compositions of many such assumptions. The study of models is, thus, a study of these assumptions and their composability and applicability. For complex systems good models may contains needless assumptions that may be removed or a good assumption could greatly improve a different model. In practice, these are usually subjective choices, not data driven. Moreover, assumptions needed may change as the system evolves, making *model choice* more difficult (Patra et al., 2018a).

In this study, we analyze the general features that differ among models in a probabilistic framework, oriented to extrapolation and forecast. More significantly, we describe and compare them using newly introduced concepts of dominance factors and expected contributions. This type of analysis, enabled by our approach, allows us to quantitatively evaluate modeling assumptions and their relative importance.

2. METHODS AND DATA SOURCES

The statistically driven method introduced in this study for analyzing complex models provides extensive and quantitative information. Geophysical flow modeling usually compares simulation to observation, and fits the model parameters using the solution of a regularized inverse problem. Nevertheless, this is not always sufficient to solve forecasting problems, in which the range of possible flows might not be limited to a single type and scale of flow. Our approach is different, and evaluates the statistics of a range of flows, produced by the couple $(M, \mathcal{P}_M)$—i.e., a model M and a probability distribution for its parameters $\mathcal{P}_M$. New quantitative information can solve classical qualitative problems, either model-model or model-observation comparison. The mean plot represents the average behavior of flows in the considered range, and provides the same type of output that is provided by a single simulation. Moreover, the uncertainty ranges generate additional pieces of information that often highlight the differences between the models.

2.1. Analysis Process

Following the approach in Patra et al. (2018a) and Bevilacqua et al. (2019), we define $\left(M(A), \mathcal{P}_{M(A)}\right)$, where A is a set of assumptions, $M(A)$ is the model composed of those assumptions, and $\mathcal{P}_M$ is a probability measure in the input space of M. In this study we are considering a measure $\mathcal{P}_M$ defined through a prior choice of the input domain. In general, $\mathcal{P}_M$ could be obtained after a calibration step, or become a single value after the solution of an inverse problem for the optimal reconstruction of a particular flow. This could reduce the predictive capabilities of the model, where we have to investigate the outcomes over a non-trivial and relatively wide input space. However, our approach can be easily implemented after a more careful input space refinement (e.g., Bevilacqua et al., 2019).

Our problem cannot be solved using classical sensitivity analysis (e.g., Saltelli et al., 2010; Weirs et al., 2012), which decomposes the variance of model output with respect to the input parameters. Indeed, model assumptions cannot be seen as input parameters, because they are related to the terms in the governing equations. These terms can be seen as random variables depending on the inputs, but they have an unknown probability distribution and are not independent. In the sequel we will define the new concepts of dominance factors and expected contributions to cope with this problem. Essentially, if the assumptions represent the atomic elements constituting the models, then the dominance factors will tell us which atomic element is the *most important* in the model, and the contributing variables will quantitatively determine the full atomic decomposition of the model, through space and time.

The investigation of contributing variables illustrates the impact of modeling assumptions. Furthermore, understanding which assumptions dominate, and by how much, is a key step toward enabling the construction of more efficient models for desired inputs. We summarize our analysis process in two steps.

Stage 1: Setup of Parameter Ranges
In this study, we assume:

$$\mathcal{P}_M\left(p_1, \ldots, p_{N_M}\right) \sim \bigotimes_{i=1}^{N_M} Unif(a_{i,M}, b_{i,M}),$$

[1] Available online at: vhub.org.

where N_M is the number of parameters of M. This is not restrictive, and in case of correlation between the commonly used parameters $(\hat{p}_j)_{j=1,\hat{N}_M}$, or non-uniform distributions, we can always define a function g such that $g[(p_i)_{j=1,N_M}] = (\hat{p}_j)_{j=1,\hat{N}_M}$, and the (p_i) are independent and uniformly distributed. In particular, we choose these parameter ranges trough an explorative testing for physical consistency of model outcomes and range of inputs/outcomes of interest, and using information collected from the literature. This step is critical, because if the statistical comparison is dominated by trivial macroscopic differences, it cannot focus on the rheology details. In the preparation of hazard analysis, expert elicitation processes can be used to ensure that the studies correctly account for all anticipated and possible flow regimes.

Stage 2: Simulations and Output Data Gathering
For each model M, we produce datasets of *model inputs*, *contributing variables* and *model outputs*. These concepts are introduced in Patra et al. (2018a), and briefly reported in Bevilacqua et al. (2019). The *model outputs* could be flow height, lateral extent, area, velocity, acceleration, and derived quantities such as Froude number Fr. In general they include any explicit outcome of the flow calculations. Instead, the *contributing variables* include quantities that are related to individual assumptions A_i, typically not observed in the outputs of the model. For example these could be values of different source terms in momentum balances of complex flow calculations, or dissipation terms, or inertia terms. We base our analysis on a Monte Carlo simulation, sampling the model inputs and producing a family of graphs for the expectation of the contributing variables and model outputs. We also include their 5th and 95th percentiles. The sampling technique of the input variables follows Patra et al. (2018a). It is based on the Latin Hypercube Sampling idea (McKay et al., 1979; Stein, 1987; Owen, 1992a; Ranjan and Spencer, 2014; Ai et al., 2016), and in particular, on the improved space-filling properties of the orthogonal array-based Latin Hypercubes (Owen, 1992b; Tang, 1993). The volume of output data generated is likely to be large but modern computing and data handling equipment readily available to most modeling researchers[2] in university and national research facilities are more than adequate.

2.2. Monte Carlo Process and Statistical Analysis

In this study, like in Bevilacqua et al. (2019), the flow range is defined by establishing boundaries for inputs like flow volume or rheology coefficients characterizing the models. Latin Hypercube Sampling is performed over $[0,1]^d$ where d depends on the number of input parameters. Those scale-less samples are thus linearly transformed to span the required intervals. Section 3.2 provides examples of Latin Hypercube design in the three models that are targets of this study, with respect to their commonly used parameters.

[2]We thank the University at Buffalo Center for Computing Research.

Through the Monte Carlo simulation, we calculate data for each sample run and each output or contributing variable $f(\underline{\mathbf{x}}, t)$ described as a function of time on the elements of the computational grid. This analysis produces very large volume of data which then has to be processed utilizing statistical methods for summative impact.

We devise many statistical measures for analyzing the data, following the definitions in Patra et al. (2018a) reported in this study for the sake of completeness. In particular, let $(F_i(\underline{\mathbf{x}}, t))_{i=1,\dots,k}$ be an array of force terms, where $\underline{\mathbf{x}} \in \mathbf{R}^d$ is a spatial location, and $t \in T$ is a time instant. The degree of contribution of those force terms to the flow dynamics can be significantly variable in space and time, and we define the *dominance factors* $[P_j(\underline{\mathbf{x}}, t)]_{j=1,\dots,k}$, i.e., the probability of each $F_j(\underline{\mathbf{x}}, t)$ to be the dominant force. Those probabilities provide insight into the dominance of a particular source or dissipation term on the model dynamics. We remark that we focus on the modulus of the forces and hence we cope with scalar terms. It is also important to remark that all the forces depend on the input variables, and they can be thus considered as random variables. Furthermore, these definitions are general and could be applied to any set of contributing variables, and not only to the force terms.

Definition 1 (Dominance factors). *Let* $(F_i)_{i=1,\dots,k}$ *be random variables on* $(\Omega, \mathcal{F}, \mathcal{P}_M)$. *Then,* $\forall i$, *the dominant variable is defined as*:

$$\Phi := \max_i |F_i|.$$

In particular, for each $j = 1, \dots, k$, *the dominance factors are defined as*:

$$P_j := \mathcal{P}_M \left\{ \Phi = |F_j| \right\}.$$

We remark that the dominant variable Φ is also a random variable, and in particular it is a stochastic process parameterized in time and space. Moreover, we define the *random contributions*, an additional tool that we use to compare the different force terms, following a less restrictive approach than the dominance factors. They are obtained dividing the force terms by the dominant force Φ, and hence belong to $[0, 1]$.

Definition 2 (Expected contributions). *Let* $(F_i)_{i=1,\dots,k}$ *be random variables on* $(\Omega, \mathcal{F}, \mathcal{P}_M)$. *Then,* $\forall i$, *the random contribution is defined as*:

$$C_i := \begin{cases} \frac{F_i}{\Phi}, & \text{if } \Phi \neq 0; \\ 0, & \text{otherwise.} \end{cases}$$

where Φ *is the dominant variable. Thus,* $\forall i$, *the expected contributions are defined by* $E[C_i]$.

Thus, for a particular location x, time t, and parameter sample ω, we have $C_i(\underline{\mathbf{x}}, t, \omega) = 0$ if there is no flow or all the forces are null. The expectation of C_i is reduced by the chance of F_i being small compared to the other terms, or by the chance of having no flow in $(\underline{\mathbf{x}}, t)$. Expected contributions are obtained after diving

the force terms by the dominant variable Φ, which is an unknown quantity depending on time, location, and input parameters. We provide an additional result, further explaining the meaning of those contributions through the conditional expectation. The proof is an easy consequence of the rule of chain expectation.

Proposition 3. *Let $(F_i)_{i=1,\dots,k}$ be random variables on $(\Omega, \mathcal{F}, \mathcal{P})$. For each i, let C_i be the random contribution of F_i. Then we have the following expression:*

$$E[C_i] = \sum_j P_j \mathbb{E}\left[\frac{F_i}{|F_j|} \;\middle|\; \Phi = |F_j|\right],$$

where $P_j := \mathcal{P}\left\{\Phi = |F_j|\right\}$.

2.3. Modeling of Geophysical Mass Flows

Models that are computationally tractable are rarely able to capture the physics of the complex flow class of large scale dense granular avalanches. In addition, very often the only actual information available is the a posteriori deposit left by the flow, with sparse data and significant uncertainty affecting the mechanisms of flow initiation and propagation. This modeling task is challenging and the subject of continuing research. Due to intrinsic mathematical, physical, or numerical issues, models that appear to reproduce well the flows in certain conditions, may turn out to be poor in others. However, because of the high consequences of such flows, several models composed of different assumptions have been proposed. For example in (Iverson, 1997; Denlinger and Iverson, 2001, 2004; Iverson and Denlinger, 2001; Pitman et al., 2003; Iverson et al., 2004; de' Michieli Vitturi et al., 2019), the depth-averaged model was applied in the simulation of test geophysical flows in large scale experiments. Several studies were specifically devoted to the modeling of volcanic mass flows (Bursik et al., 2005; Kelfoun and Druitt, 2005; Macías et al., 2008; Kelfoun et al., 2009; Charbonnier et al., 2013). In fact, volcanos are great sources for a rich variety of geophysical flow types and provide field data from past flow events.

We first assume that the laws of mass and momentum conservation hold for properly defined system boundaries. After this, because these flows are typically very long and wide with small depth we assume their *shallowness* (Savage and Hutter, 1989). This enables the calculation of simpler and more computationally tractable equations, by integrating through the flow depth. Both these assumptions, conservation laws and shallowness, could be investigated with the procedure defined above. Nevertheless, there is much evidence in the literature for their validity and we do not test them in this study.

The depth-averaged Saint-Venant equations that result are:

$$\begin{aligned}
\frac{\partial h}{\partial t} + \frac{\partial}{\partial x}(h\bar{u}) + \frac{\partial}{\partial y}(h\bar{v}) &= 0 \\
\frac{\partial}{\partial t}(h\bar{u}) + \frac{\partial}{\partial x}\left(h\bar{u}^2 + \frac{1}{2}kg_z h^2\right) + \frac{\partial}{\partial y}(h\bar{u}\bar{v}) &= S_x \qquad (1)\\
\frac{\partial}{\partial t}(h\bar{v}) + \frac{\partial}{\partial x}(h\bar{u}\bar{v}) + \frac{\partial}{\partial y}\left(h\bar{v}^2 + \frac{1}{2}kg_z h^2\right) &= S_y
\end{aligned}$$

Like in Patra et al. (2005), here the Cartesian coordinate system is aligned such that z is normal to the surface; h is the flow height in the z direction; $h\bar{u}$ and $h\bar{v}$ are respectively the components of momentum in the x and y directions; and the earth pressure coefficient k relates the lateral stress components, $\bar{\sigma}_{xx}$ and $\bar{\sigma}_{yy}$, to the normal stress component, $\bar{\sigma}_{zz}$. We remark that $\frac{1}{2}kg_z h^2$ is the contribution of depth-averaged pressure to the momentum fluxes. S_x and S_y are the sum local stresses: as described in Patra et al. (2018a) they include the gravitational driving forces, the basal friction force resisting to the motion of the material, and additional forces specific of rheology assumptions.

The class of assumptions that we specifically test in this study are the assumptions on the rheology of the flows. In particular they model the different dissipation mechanisms embedded in S_x, S_y, and that cause an abundance of models with much controversy on the most suitable model.

We will define our approach and illustrate it using three models for large scale mass flows incorporated in our large scale mass flow simulation framework TITAN2D (Patra et al., 2005, 2006; Yu et al., 2009; Aghakhani et al., 2016). The description of the models is summarized from Bevilacqua et al. (2019) and reported in this study for the sake of clarity. So far, TITAN2D has been successfully applied to the simulation of different geophysical mass flows with specific characteristics (Sheridan et al., 2005, 2010; Rupp et al., 2006; Charbonnier and Gertisser, 2009; Norini et al., 2009; Procter et al., 2010; Sulpizio et al., 2010; Capra et al., 2011). Several studies involving TITAN2D were also directed toward a statistical study of geophysical flows, focusing on uncertainty quantification (Dalbey et al., 2008; Dalbey, 2009; Stefanescu et al., 2012a,b), or on the more efficient production of hazard maps (Bayarri et al., 2009, 2015; Spiller et al., 2014; Ogburn et al., 2016; Tierz et al., 2018; Bevilacqua et al., 2019; Hyman et al., 2019; Rutarindwa et al., 2019).

In the three following sections, we summarize *Mohr-Coulomb* (MC), *Pouliquen-Forterre* (PF) and *Voellmy-Salm* (VS) models. Models based on additional heterogeneous assumptions are possible, either more complex (Pitman and Le, 2005; Iverson and George, 2014) or more simple (Dade and Huppert, 1998). We decided to focus on these three because of their popularity. Moreover, if the degree of complexity in the models is significantly different, model comparison should take that into account, but this is outside the purpose of this study (Farrell et al., 2015).

2.3.1. Mohr-Coulomb Model

Based on the long history of studies in soil mechanics (Rankine, 1857; Drucker and Prager, 1952), the Mohr-Coulomb rheology (MC) was developed and used to represent the behavior of geophysical mass flows (Savage and Hutter, 1989).

Shear and normal stress are assumed to obey Coulomb friction equation, both within the flow and at its boundaries. In other words,

$$\tau = \sigma \tan\phi, \qquad (2)$$

where τ and σ are respectively the shear and normal stresses on failure surfaces, and ϕ is a friction angle. This relationship does not depend on the flow speed.

We can summarize the MC rheology assumptions as:

- *Basal Friction* based on a constant friction angle.
- *Internal Friction* based on a constant friction angle.
- *Earth pressure coefficient* formula depends on the Mohr circle (it can be 0 or ±1).
- Velocity based *curvature effects* are included into the equations.

MC equations

As a result, we can write down the source terms of the Equation (1):

$$\begin{aligned} S_x &= g_x h - \frac{\bar{u}}{\|\underset{\sim}{\bar{\mathbf{u}}}\|}\left[h\left(g_z + \frac{\bar{u}^2}{r_x}\right)\tan(\phi_{bed})\right] \\ &\quad -hk_{ap}\,\mathrm{sgn}\left(\frac{\partial \bar{u}}{\partial y}\right)\frac{\partial(g_z h)}{\partial y}\sin(\phi_{int}) \\ S_y &= g_y h - \frac{\bar{v}}{\|\underset{\sim}{\bar{\mathbf{u}}}\|}\left[h\left(g_z + \frac{\bar{v}^2}{r_y}\right)\tan(\phi_{bed})\right] \\ &\quad -hk_{ap}\,\mathrm{sgn}\left(\frac{\partial \bar{v}}{\partial x}\right)\frac{\partial(g_z h)}{\partial x}\sin(\phi_{int}) \end{aligned} \tag{3}$$

Where, $\underset{\sim}{\bar{\mathbf{u}}} = (\bar{u}, \bar{v})$, is the depth-averaged velocity vector, r_x and r_y denote the radii of curvature of the local basal surface. The inverse of the radii of curvature is usually approximated with the partial derivatives of the basal slope, e.g., $1/r_x = \partial\theta_x/\partial x$, where θ_x is the local bed slope.

In our study, sampled input parameters are ϕ_{bed}, and $\Delta\phi := \phi_{int} - \phi_{bed}$. In particular, we assumed $\Delta\phi \in [2^\circ, 10^\circ]$ (Dalbey et al., 2008).

2.3.2. Pouliquen-Forterre Model

The scaling properties for granular flows down rough inclined planes led to the development of the Pouliquen-Forterre rheology (PF), assuming a variable frictional behavior as a function of Froude Number and flow depth (Pouliquen, 1999; Forterre and Pouliquen, 2002, 2003; Pouliquen and Forterre, 2002).

PF rheology assumptions can be summarized as:

- *Basal Friction* is based on an interpolation of two different friction angles, based on the flow regime and depth.
- *Internal Friction* is neglected.
- *Earth pressure coefficient* is equal to one.
- Normal stress is modified by a *pressure force* linked to the thickness gradient.
- Velocity based *curvature effects* are included into the equations.

An empirical friction law $\mu_b(\|\underset{\sim}{\bar{\mathbf{u}}}\|, h)$ is defined in the whole range of velocity and thickness. The expression changes depending on two flow regimes, according to a parameter β and the Froude number $Fr = \|\underset{\sim}{\bar{\mathbf{u}}}\|/\sqrt{hg_z}$. The critical angles ϕ_1 and ϕ_2, and the quantities $\mathcal{L}, \beta$ are the parameters of the model. In particular, $\mathcal{L}$ is the characteristic depth of the flow over which a transition between the angles ϕ_1 to ϕ_2 occurs. More details can be found in Bevilacqua et al. (2019).

PF equations

The depth-averaged Equation (1) source terms thus take the following form:

$$\begin{aligned} S_x &= g_x h - \frac{\bar{u}}{\|\underset{\sim}{\bar{\mathbf{u}}}\|}\left[h\left(g_z + \frac{\bar{u}^2}{r_x}\right)\mu_b(\|\underset{\sim}{\bar{\mathbf{u}}}\|, h)\right] + g_z h\frac{\partial h}{\partial x} \\ S_y &= g_y h - \frac{\bar{v}}{\|\underset{\sim}{\bar{\mathbf{u}}}\|}\left[h\left(g_z + \frac{\bar{v}^2}{r_y}\right)\mu_b(\|\underset{\sim}{\bar{\mathbf{u}}}\|, h)\right] + g_z h\frac{\partial h}{\partial y} \end{aligned} \tag{4}$$

In our study, sampled input parameters are ϕ_1, $\Delta\phi_{12} := \phi_2 - \phi_1$, and β. In particular, we assumed $\Delta\phi_{12} \in [10^\circ, 15^\circ]$, and $\beta \in [0.1, 0.85]$. Moreover, $\mathcal{L}$ is equal to $1dm$ (Pouliquen and Forterre, 2002; Forterre and Pouliquen, 2003).

2.3.3. Voellmy-Salm Model

The theoretical analysis of dense snow avalanches led to the VS rheology (VS) (Voellmy, 1955; Salm et al., 1990; Salm, 1993; Bartelt et al., 1999). Dense snow or debris avalanches consist of mobilized, rapidly flowing ice-snow mixed to debris-rock granules (Bartelt and McArdell, 2009). The VS rheology assumes a velocity dependent resisting term in addition to the traditional basal friction, ideally capable of including an approximation of the turbulence-generated dissipation. Many experimental and theoretical studies were developed in this framework (Gruber and Bartelt, 2007; Kern et al., 2009; Christen et al., 2010; Fischer et al., 2012).

The following relation between shear and normal stresses holds:

$$\tau = \mu\sigma + \frac{\rho\|\underset{\sim}{\mathbf{g}}\|}{\xi}\|\underset{\sim}{\bar{\mathbf{u}}}\|^2, \tag{5}$$

where, σ denotes the normal stress at the bottom of the fluid layer and $\underset{\sim}{\mathbf{g}} = (g_x, g_y, g_z)$ represents the gravity vector. The two parameters of the model are the bed friction coefficient μ and the velocity dependent friction coefficient ξ.

We can summarize VS rheology assumptions as:

- *Basal Friction* is based on a constant coefficient, similarly to the MC rheology.
- *Internal Friction* is neglected.
- *Earth pressure coefficient* is equal to one.
- Additional *turbulent friction* is based on the local velocity by a quadratic expression.
- Velocity based *curvature effects* are included into the equations, following a different formulation from the previous models.

VS equations

Therefore, the final source terms take the following form:

$$\begin{aligned} S_x &= g_x h - \frac{\bar{u}}{\|\underset{\sim}{\bar{\mathbf{u}}}\|}\left[h\left(g_z + \frac{\|\underset{\sim}{\bar{\mathbf{u}}}\|^2}{r_x}\right)\mu + \frac{\|\underset{\sim}{\mathbf{g}}\|}{\xi}\|\underset{\sim}{\bar{\mathbf{u}}}\|^2\right], \\ S_y &= g_y h - \frac{\bar{v}}{\|\underset{\sim}{\bar{\mathbf{u}}}\|}\left[h\left(g_z + \frac{\|\underset{\sim}{\bar{\mathbf{u}}}\|^2}{r_y}\right)\mu + \frac{\|\underset{\sim}{\mathbf{g}}\|}{\xi}\|\underset{\sim}{\bar{\mathbf{u}}}\|^2\right]. \end{aligned} \tag{6}$$

In our study, sampled input parameters are μ, and ξ. In particular, ξ uniform sampling is accomplished in log-scale. In fact, values of ξ between 250 and 4,000 m/s^2 have been described for snow avalanches (Salm, 1993; Bartelt et al., 1999; Gruber and Bartelt, 2007).

2.4. Contributing Variables

For analysis of modeling assumptions we need to record and classify the results of different modeling assumptions. In our case study, we focus on the right-hand side terms in the momentum equation and we call them RHS forces, or, more simply, the force terms. They are internal to the computation and rarely visible as a system output.

$$\boldsymbol{RHS_1} = [g_x h, g_y h], \tag{7}$$

it is the gravitational force term, it has the same formulation in all models.

The expression of **basal friction force** $\boldsymbol{RHS_2}$ depends on the model:

$$\begin{aligned}
\boldsymbol{RHS_2} &= -\, h g_z \tan(\phi_{bed}) \left[\frac{\bar{u}}{\|\underset{\sim}{\bar{\mathbf{u}}}\|}, \frac{\bar{v}}{\|\underset{\sim}{\bar{\mathbf{u}}}\|} \right], \text{ in MC model.} \\
\boldsymbol{RHS_2} &= -\, h g_z\, \mu_b(\|\underset{\sim}{\bar{\mathbf{u}}}\|, h) \left[\frac{\bar{u}}{\|\underset{\sim}{\bar{\mathbf{u}}}\|}, \frac{\bar{v}}{\|\underset{\sim}{\bar{\mathbf{u}}}\|} \right], \text{ in PF model.} \\
\boldsymbol{RHS_2} &= -\, h g_z \mu \left[\frac{\bar{u}}{\|\underset{\sim}{\bar{\mathbf{u}}}\|}, \frac{\bar{v}}{\|\underset{\sim}{\bar{\mathbf{u}}}\|} \right], \text{ in VS model.}
\end{aligned} \tag{8}$$

The expression of the force related to the **topography curvature**, $\boldsymbol{RHS_3}$, also depends on the model:

$$\begin{aligned}
\boldsymbol{RHS_3} &= -\, h \tan(\phi_{bed}) \left[\frac{\bar{u}^3}{r_x \|\underset{\sim}{\bar{\mathbf{u}}}\|}, \frac{\bar{v}^3}{r_y \|\underset{\sim}{\bar{\mathbf{u}}}\|} \right], \text{ in MC model.} \\
\boldsymbol{RHS_3} &= -\, h\, \mu_b(\|\underset{\sim}{\bar{\mathbf{u}}}\|, h) \left[\frac{\bar{u}^3}{r_x \|\underset{\sim}{\bar{\mathbf{u}}}\|}, \frac{\bar{v}^3}{r_y \|\underset{\sim}{\bar{\mathbf{u}}}\|} \right], \text{ in PF model.} \\
\boldsymbol{RHS_3} &= -\, h \mu \left[\frac{\bar{u}\|\underset{\sim}{\bar{\mathbf{u}}}\|}{r_x}, \frac{\bar{v}\|\underset{\sim}{\bar{\mathbf{u}}}\|}{r_y} \right], \text{ in VS model.}
\end{aligned} \tag{9}$$

All the three models have an additional force term, having a different expressions and different meaning in the three models:

$$\begin{aligned}
\boldsymbol{RHS_4} &= -\, h k_{ap} \sin(\phi_{int}) \left[\operatorname{sgn}\left(\frac{\partial \bar{u}}{\partial y}\right) \frac{\partial (g_z h)}{\partial y}, \operatorname{sgn}\left(\frac{\partial \bar{v}}{\partial x}\right) \frac{\partial (g_z h)}{\partial x} \right], \\
&\quad \text{in MC model.} \\
\boldsymbol{RHS_4} &= g_z h \left[\frac{\partial h}{\partial x}, \frac{\partial h}{\partial y} \right], \text{ in PF model.} \\
\boldsymbol{RHS_4} &= -\, \frac{\|\underset{\sim}{\mathbf{g}}\|}{\xi} \|\underset{\sim}{\bar{\mathbf{u}}}\|^2 \left[\frac{\bar{u}}{\|\underset{\sim}{\bar{\mathbf{u}}}\|} \frac{\bar{v}}{\|\underset{\sim}{\bar{\mathbf{u}}}\|} \right], \text{ in VS model.}
\end{aligned} \tag{10}$$

These contributing variables can be analyzed locally and globally for discriminating among the different modeling assumptions. We remark that a complete representation of the model functional should include also the left hand side (LHS) terms. For instance, the lateral stress component k_{ap} could be influenced by bed and internal frictional coefficients, and it appears in the LHS terms (Gray et al., 1999; Pirulli et al., 2007). Our statistical approach could be easily extended to the LHS terms. We did not focus on them for the sake of simplicity.

Finally, we also study the spatial integrals defined by $F(t) = \int_{\mathbb{R}^k} f(\underline{\mathbf{x}}, t) d\underline{\mathbf{x}}$, where $d\underline{\mathbf{x}}$ is the area of the mesh elements. This provides a global view of the results and is complementary to the observations taken locally. For instance, by integrating the scalar product of source terms in the momentum balance and velocity we can compare the relative importance of modeling assumptions when we seek accuracy on global quantities.

3. CASE STUDY AND RESULTS

Our case study is a pyroclastic flow down the SW slope of Volcán de Colima (MX)—an andesitic stratovolcano that rises to 3,860 m above sea level, situated in the western portion of the Trans-Mexican Volcanic Belt (**Figure 1**). Volcán de Colima has historically been the most active volcano in México (la Cruz-Reyna, 1993; González et al., 2002; Zobin et al., 2002).

Pyroclastic flows generated by explosive eruptions and lava dome collapses of Volcán de Colima are a well-studied topic (Martin Del Pozzo et al., 1995; Sheridan and Macías, 1995; Saucedo et al., 2002, 2004, 2005; Sarocchi et al., 2011; Capra et al., 2015). The presence of a change in slope and multiple ravines characterize the SW slope of the volcano. Volcán de Colima has been used as a case study in several research papers involving the Titan2D code (Rupp, 2004; Rupp et al., 2006; Dalbey et al., 2008; Yu et al., 2009; Sulpizio et al., 2010; Capra et al., 2011; Aghakhani et al., 2016). On July 10th-11th, 2015, the volcano underwent its most intense eruptive phase since its Subplinian-Plinian 1913 AD eruption (Saucedo et al., 2010; Zobin et al., 2015; Capra et al., 2016; Reyes-Dávila et al., 2016; Macorps et al., 2018). We assume the flow to be generated by the gravitational collapse of a lava dome represented by a material pile placed close to the summit area—at 644956N, 2157970E UTM13 (Rupp et al., 2006; Aghakhani et al., 2016). A lava dome collapse occurs when there is a significant amount of recently-extruded highly-viscous lava piled up in an unstable configuration. Further extrusion and/or externals forces can cause the still hot dome of viscous lava to collapse, disintegrate, and avalanche downhill (Bursik et al., 2005; Wolpert et al., 2016; Hyman and Bursik, 2018). The volcano produced several pyroclastic flows of this type, called Merapi style flows (Macorps et al., 2018). The hot, dense blocks in this "block and ash" flow (BAF) will typically range from centimeters to a few meters in size.

The rheology of volcanic rock avalanches and dense pyroclastic flows is complex, and it is difficult to constrain the physics of the processes. A priori predictive ability of the known block and ash flow models is limited by inability to tune without knowledge of flow character (Patra et al., 2005). Since these dense flows are constituted of blocks, ash and gas, friction between the particles during emplacement could confer a Coulomb behavior

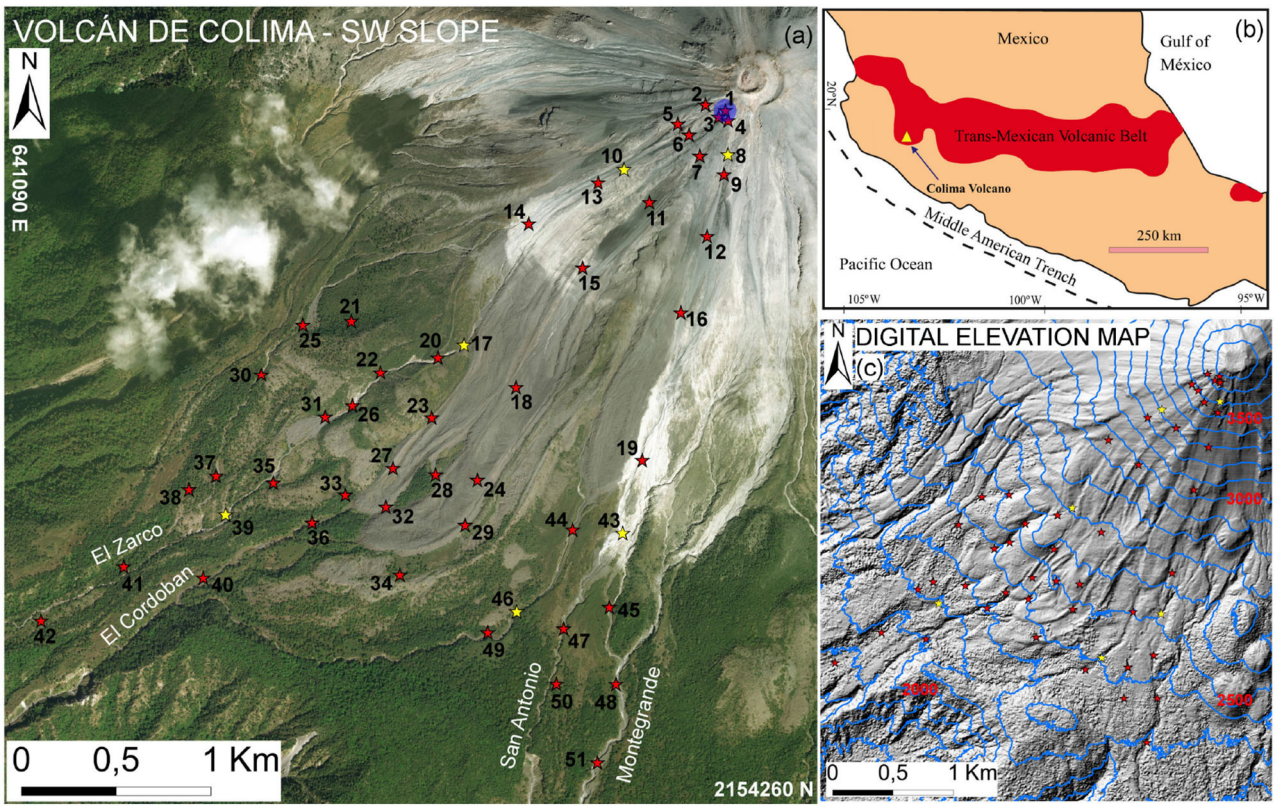

FIGURE 1 | (a) Volcán de Colima (México) overview, including 51 numbered locations (stars) and major ravines. Initial pile is marked by a blue dot. Coordinates are in UTM zone 13N. **(b)** Regional geology map. **(c)** Digital elevation map. Six preferred locations are colored in yellow. Elevation isolines are displayed in blue, elevation values in red.

to the whole flow. So, the Mohr Coulomb model was often considered appropriate, sometimes associated with a velocity or volume-dependent term (Spiller et al., 2014). However, a simple Coulomb behavior is not ideal, whatever the value of friction angle used. A friction angle that varies according to the velocity and thickness of the flows has also been assumed in the simulations of natural flows (Kelfoun, 2011). For these reason all three models, MC, VS and PF, are a priori appropriate but not ideal for a block and ash flow. Our new quantitative approach provides a tool in the evaluation of what model best characterizes the flow.

Our computations were performed on a DEM of 5m-pixel resolution, obtained from Laser Imaging Detection and Ranging (LIDAR) data acquired in 2005 (Davila et al., 2007; Sulpizio et al., 2010). We placed 51 locations along the flow inundated area to accomplish local testing. After evaluating the results in all the locations, six of them are adopted as preferred locations, being representative of different flow regimes.

3.1. Preliminary Consistency Testing of the Input Ranges

In this same setting, Dalbey et al. (2008) assumed $\phi_{bed} = [15°, 35°]$, while Capra et al. (2011) adopted $\phi_{bed} = 30°$. Then, Spiller et al. (2014) Bayarri et al. (2015), and Ogburn et al. (2016) found a statistical correlation between flow size and effective basal friction inferred from field observation of geophysical flows. A BAF at the scale of our simulations would possess $\phi_{bed} = [13°, 18°]$ according to their estimates. Small changes in the parameter ranges do not change significantly the results.

Figure 2 displays the maps of maximum flow height observed in the extreme cases tested. Simulation options are - max_time = 7,200 s (2 h), height/radius = 0.55, length_scale = 4 km, number_of_cells_across_axis = 50, order = first, geoflow_tiny = 1.0×10^{-4} (Patra et al., 2005; Aghakhani et al., 2016). Initial pile geometry is paraboloid. Even if the maximum runout is matched between the models, they display significantly different macroscopic features. In particular, MC displays a further distal spread before entering the ravines, PF shows a larger angle of lateral spread at the initiation pile, and stops more gradually than MC with more complex inundated area boundary lines. VS is less laterally extended and the material reaches higher thickness. The flow generally looks significantly channelized, and displays several not-inundated spots due to minor topographical coulées.

- **Material Volume:** $[2.08, 3.12] \times 10^5\ m^3$, i.e., average of $2.6 \times 10^5\ m^3$ and uncertainty of ±20%.
- **Rheology models' parameters:**

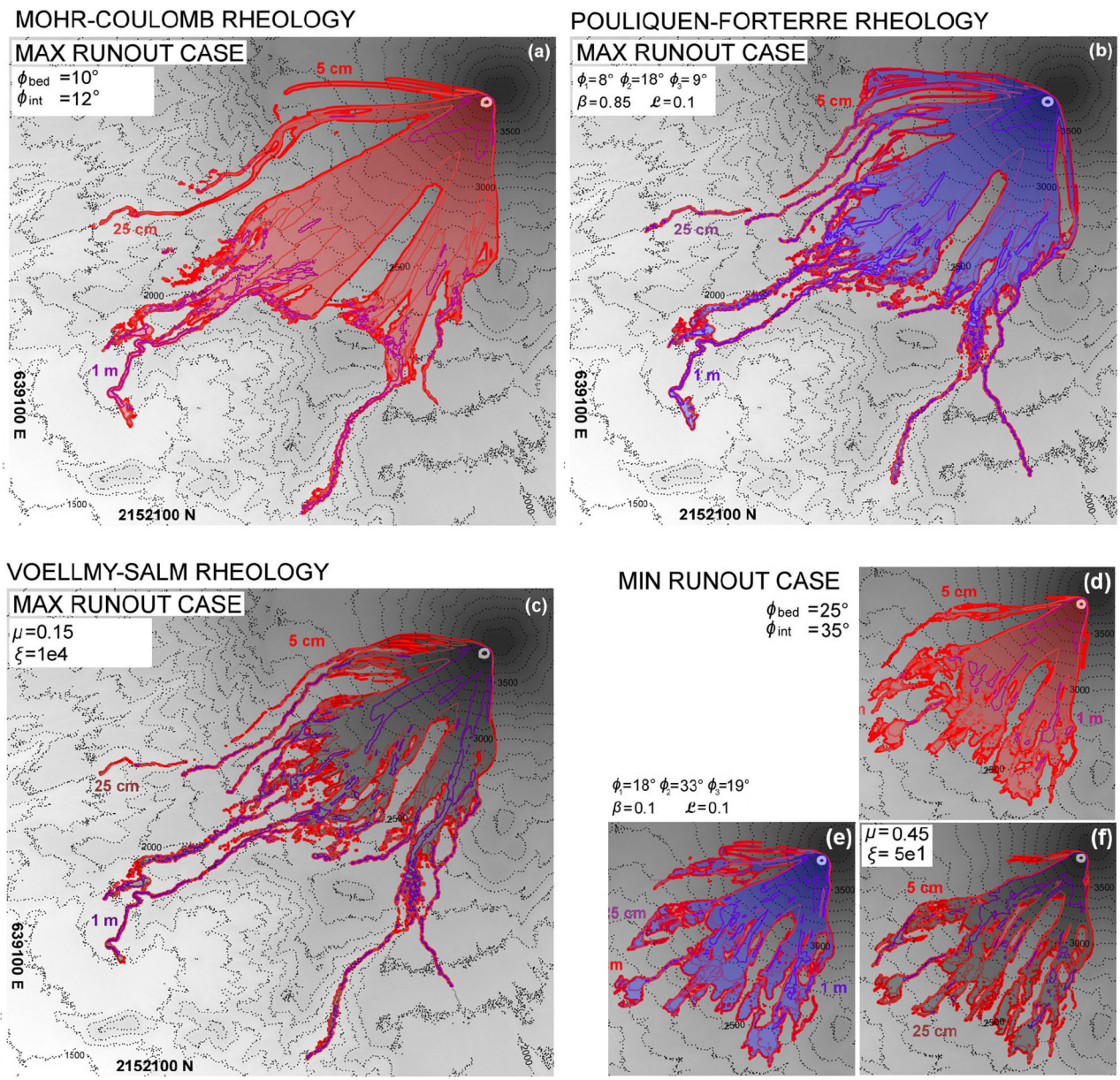

FIGURE 2 | Volcán de Colima—comparison between *max flow height* maps of simulated flow, assuming MC **(a,d)**, PF **(b,e)**, and VS **(c,f)** models. Extreme cases—**(a–c)** ***max. volume–min. resistance*** and **(d–f)** ***min. volume–max. resistance***.

MC - $\phi_{bed} \in [10°, 25°]$.

PF - $\phi_1 \in [8°, 18°]$.

VS - $\mu \in [0.15, 0.45]$, $\log(\xi) \in [1.7, 4]$.

We adopt a Latin Hypercube Sampling based on an orthogonal array $OA(s^d, d, s, d)$ (Patra et al., 2018b). We take $s = 8$ for the 3-dimensional designs over the parameter space of Mohr-Coulomb and Voellmy-Salm models, i.e., 512 points; we took $s = 6$ for the 4-dimensional designs over the more complex parameter space of the Pouliquen-Forterre model, i.e., 1,296 points.

3.2. Exploring Flow Limits

Figures 3A–C illustrates the sampling design of our simulations. **Figures 3D–I** show examples of the contributions obtained assuming parameter values at the extremes of their range.

Data is inherently discontinuous due to the mesh modification, and it is reported with colored dots. If the mesh element which contains the considered spatial location changes, then the force term is calculated on a different region and suddenly changes too. This can also affect the dominant variable, and more than one random contribution can incorrectly appear to be at unity at the same time. However, it is evident

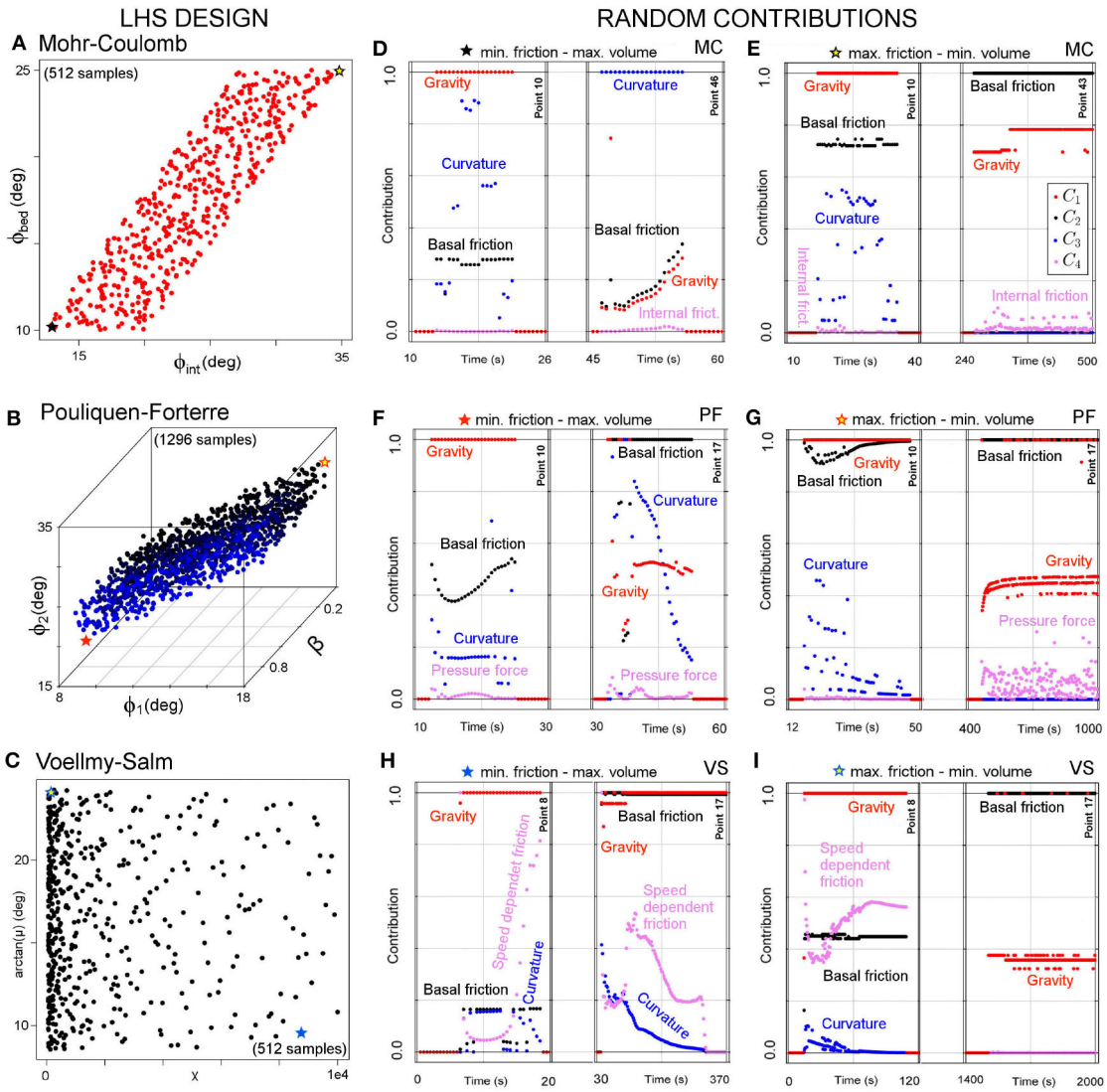

FIGURE 3 | (A–C) Example of Latin Hypercube Sampling design, Volcán de Colima case study. Colored stars mark the values producing the minimum and maximum friction. The parameter values are projected with respect to their volume value. **(D–I)** Plots of random contributions at specific locations, obtained with **(D,E)** MC, **(F,G)** PF, and **(H,I)** VS model. Each plot includes two graphs. One refers to a proximal location to the initial pile (left), and the other to a more distal location (right). The dominant variable is expressed by the dots on the top line, $C_i = 1$. Point numbers refer to **Figure 5**. Different colors correspond to different force terms.

that the dynamics and its temporal scale is evolving, and that the contributions can reveal a large amount of information about it. We remark that, $\forall i$, the calculation of $\mathbb{E}[C_i]$ with respect to $\mathcal{P}_M$ removes the effects of data discontinuity, and hence this is a fundamental step in our further analysis. We note that the above choices are easily changed, and if we are interested for instance in the performance of the models for very large or very small flows, a suitable volume range can be chosen and the procedure re-run.

3.3. Observable Outputs

The number of spatial locations is significantly high. We placed 51 points to span the entire inundated area, in search of different flow regimes, as displayed in **Figure 1**. These locations have an explorative purpose, whereas the six preferred locations will describe distinct flow regimes. We remark that all the distances reported in the following are measured in vertical projection, thus without considering the differences in elevation.

Figure 4 shows the mean flow height, $h(L, t)$, at the 51 spatial locations of interest, according to MC. In **Figure 4A**, the only location is set on the center of the initial pile. The height profile is bell-shaped, starting from zero and then waning back to zero in $\sim$ 20 s. All the dynamics occur during the first minute. In **Figures 4F–J**, points are set where the slope reduces, and the flow can channelize, and typically leaves a deposit. The distance from the initial pile is $\sim 2 - 3$ km.

In general is either observed an initial short-lasting bulge followed by a slow decrease lasting for several minutes and asymptotically tending to a positive height, or a steady increase

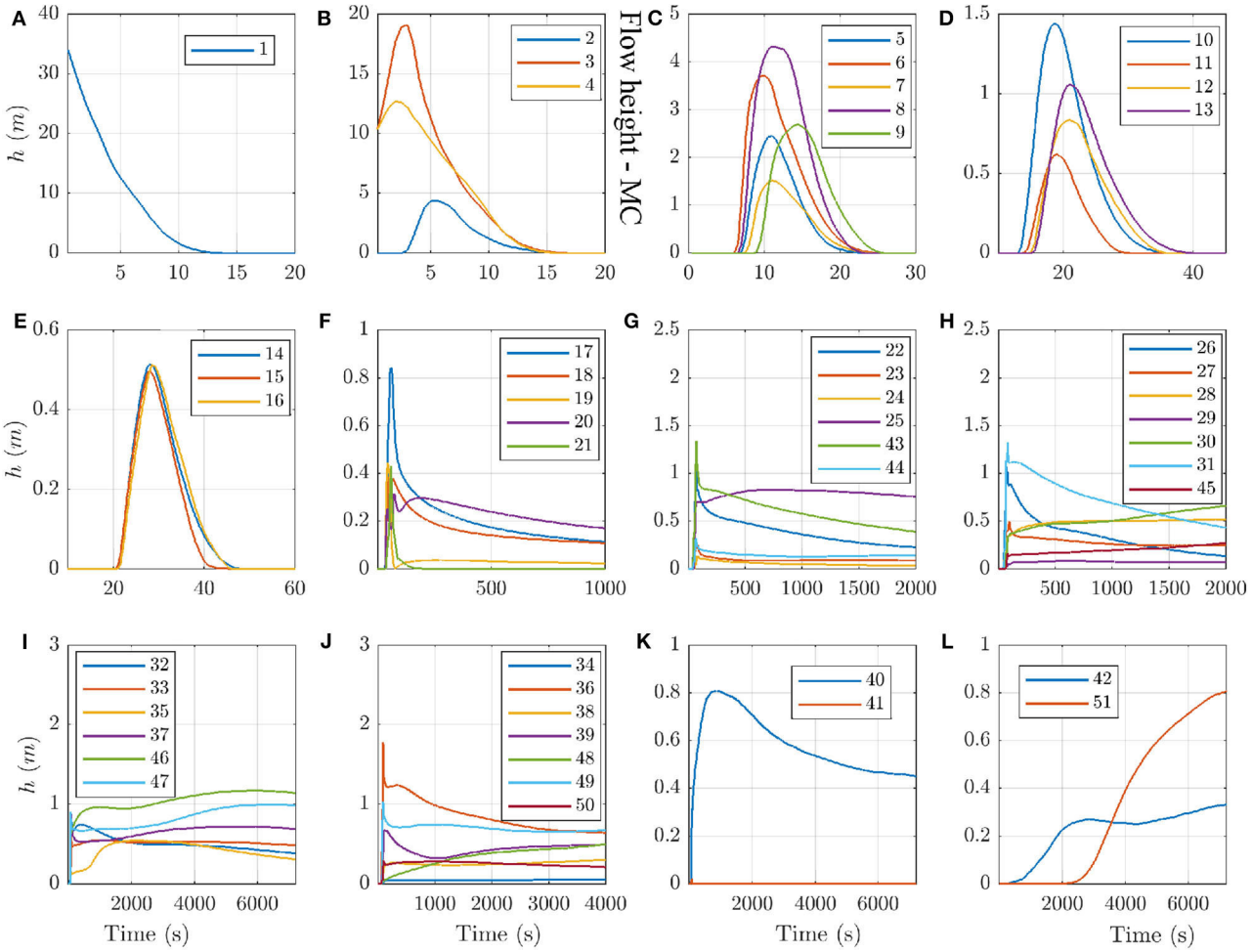

FIGURE 4 | MC model, mean flow height $h(L, t)$ in 51 numbered locations (**Figure 1**). Plots **(A–L)** have different scales on either time and space axes.

of material height tending to a positive height. In both cases it is sometimes observed a bimodal profile in the first 5 min. Finally, **Figures 4K,L** focus on three points set at about the runout distance of the flow, in the most important ravines, at $\sim 4-5$ km from the initial pile.

3.3.1. Flow Height in Six Locations

We select six preferred locations, illustrative of a range of flow regimes. They are $[L_8, L_{10}, L_{17}, L_{39}, L_{43}, L_{46}]$, as displayed in **Figure 5**. The first two points, L_8 and L_{10}, are both proximal to the initiation pile. Points L_{17} and L_{43} are placed where the slope is reducing and the ravines are evident, and L_{39} and L_{46} are placed in the channels, further down-slope. In particular, L_8, L_{43}, and L_{46} are at the western side of the inundated area, whereas L_{10}, L_{17}, and L_{39} are at the eastern side.

Figure 6 shows the flow height, $h(L, t)$, at the points $(L_i)_{i=8,10,17,39,43,46}$. Distances from the initial pile are in vertical projection. In **Figures 6A,B**, we show the flow height in points L_8 and L_{10}, $\sim 200m$ and $\sim 500m$ from the initial pile, respectively. Models MC and PF display similar profiles, positive for less than $15s$ and bell-shaped. VS requires a significantly longer time to decrease, particularly in point L_{10}, where the average flow height is still positive after $\sim 200s$. Peak average values in L_8 are $3.4m$ in *PF*, $4.3m$ in MC, $4.7m$ in VS. Uncertainty is about $\pm 2m$, halved on the lower side in *MC*, and *PF*. In L_{10}, models MC and PF are very similar, with peak height at $1.4m$ and uncertainty $\pm 0.5m$. Model VS, in contrast, has a maximum height of $1.1m$ lasting for $50s$, and 95^{th} percentile reaching $3.7m$.

In **Figures 6C,E**, we show the flow height in points L_{17} and L_{43}, both at $\sim 2km$ from the initial pile. All the models show a fast spike during the first minute, followed by a slow decrease. There is still material after $1800s$. VS has a secondary rise peaking at $\sim 450s$, which is not observed in the other models. This produces higher values for the most of the temporal duration, but similar deposit thickness after more than 1 h. Maximum values are $1m$ for MC, $2m$ for PF, and $1.5m$ for VS, in both locations. The 5^{th} percentile is zero in all the models, meaning that the parameter range does not always allow the flow to reach these locations. The 95^{th} percentile is above $5m$, except for VS in point L_{17}. In **Figures 6D,F**, we show the flow height in points L_{39} and L_{46},

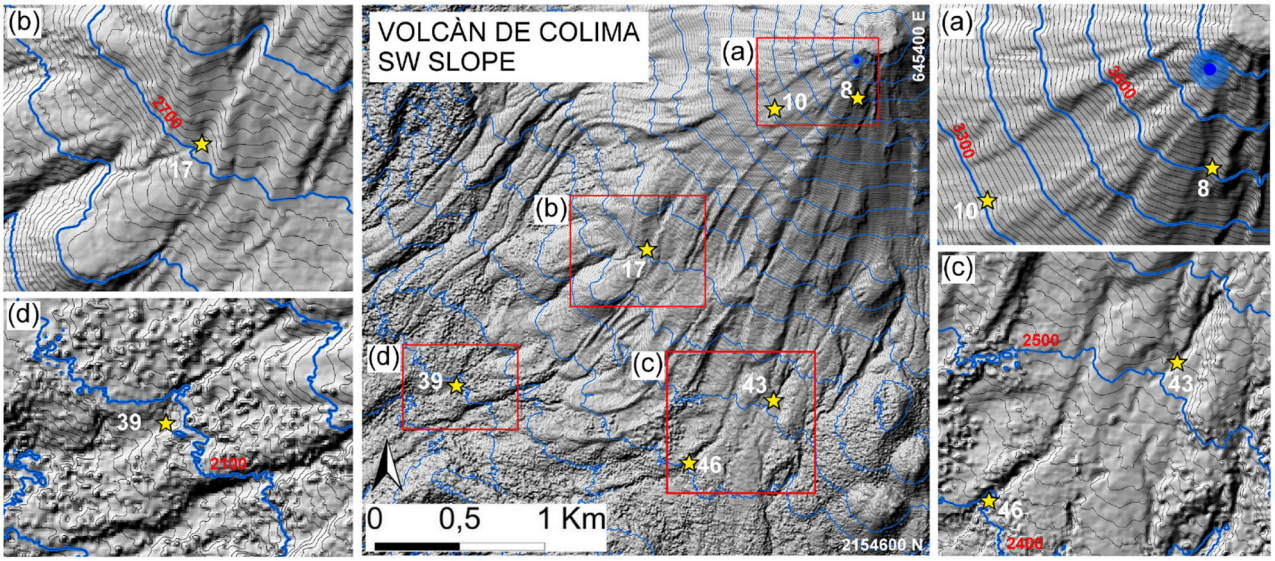

FIGURE 5 | Volcán de Colima (México) overview, including six numbered locations (stars). In panels **(a–d)** are enlarged the proximal topographic features to those locations. Initial pile is marked by a blue dot. Reported coordinates are in UTM zone 13N. Elevation isolines at every 10*m* are displayed in black, at every 100*m* in bold blue. Elevation values in red.

both placed at more than 3*km* from the initial pile. The three models all show a monotone profile except for MC in point L_{39}, which instead displays an initial spike and a decrease before to rise again. A similar thing is observed in the 95^{th} percentiles of all the models. It is significant that the 5^{th} percentile of PF becomes positive after $\sim 5,400s$, meaning that almost surely the flow has reached that location. Deposit thickness in point L_{39} is $\sim 0.5m$ for all the models, whereas in point L_{46} it is $1.7m$ in VS, $1.6m$ in PF, and $1.2m$ in MC.

We note that VS is temporally stretched compared to the other models, and material arrives later and stays longer in all the sample points. This is a consequence of the speed dependent term reducing flow velocity.

4. ANALYSIS AND DISCUSSION

4.1. Contributing Variables Proximal to the Initial Pile

Figure 7 shows the dominance factors $(P_i)_{i=1,\dots,4}$ of the RHS terms modulus, in the three proximal points L_8, L_{10}, and L_{17}, all closer than 1 km to the initial pile. This Figure is modified from Patra et al. (2018a) and its description is reported in this study for the sake of completeness.

The plots **7A–C** and **7D–F** are related to point L_8 and L_10, respectively. They are significantly similar. The gravitational force $\boldsymbol{RHS_1}$ is the dominant variable with a very high chance, $P_1 > 90\%$. In MC and PF there is a small probability, $P_3 = 5 - -30\%$, of $\boldsymbol{RHS_3}$ being the dominant variable for $\sim 5s$. In VS it is observed a $P_4 = 5\%$ chance of $\boldsymbol{RHS_4}$ being dominant, just for a few seconds. **Figures 7G–I** concern the relatively more distal point L_{17}. They are split in two sub-frames at different time scale. In all the models, $\boldsymbol{RHS_2}$ is the most probable dominant variable, and its dominance factor has a bell-shaped profile. In all the models, also $\boldsymbol{RHS_1}$ has a small chance of being the dominant variable. In MC this chance is more significant, at most $P_1 = 30\%$ for $\sim 20s$, and again $P_1 = 2\%$ in $[100, 7, 200]s$. In PF $P_1 = 15\%$ in two peaks, one short lasting at about $55s$, and the second extending in $[100, 500]s$. Also in VS, $P_1 = 15\%$ at $[300, 500]s$. Its profile is unimodal in time and becomes $P_1 < 2\%$ after $2,000s$. In MC and PF, $\boldsymbol{RHS_3}$ has a dominance factor $P_3 = 10\%$ at $[30, 50]s$ and $[40, 50]s$, respectively.

In summary, gravitational force is dominant with a very high chance until the no-flow probability becomes large. In MC and PF curvature related forces can also be dominant for a short time. In VS gravitational force is dominant for a larger time span than in the other models, because of the longer presence of the flow. The speed dependent friction can be dominant with a small probability at the beginning of the dynamics.

Figure 8 shows the corresponding expected contributions $\mathbb{E}[C_i]_{i=1,\dots,4}$. $\forall i$, C_i is related to the force term $\boldsymbol{RHS_i}$. The contributions in points L_8 and L_{10} are shown in **Figures 8A–F**, respectively. The plots related to the same model are similar. In all the models C_1 is significantly larger than C_2 and C_3, which are almost equivalent in MC and PF, while $C_2 > C_3$ in VS. C_4 always gives a negligible contribution, except in VS, where it is comparable to C_2. In L_8, following PF, C_3 is bimodal, whereas it is unimodal in MC and VS. This is not observed in L_{10}. In L_8, C_3 is greater than in L_{10}, compared to the other forces. VS always shows a slower decrease of the plots. In plots **Figures 8G–I** are shown the expected contributions in L_{17}. The plots are split in two sub-frames at different time scale. Initial dynamics is dominated by C_2, except for in MC, and only for a short time, $[30, 40]s$. In MC there is an initial peak of C_2 which is not observed in the other models. C_3 has a significant size, in MC

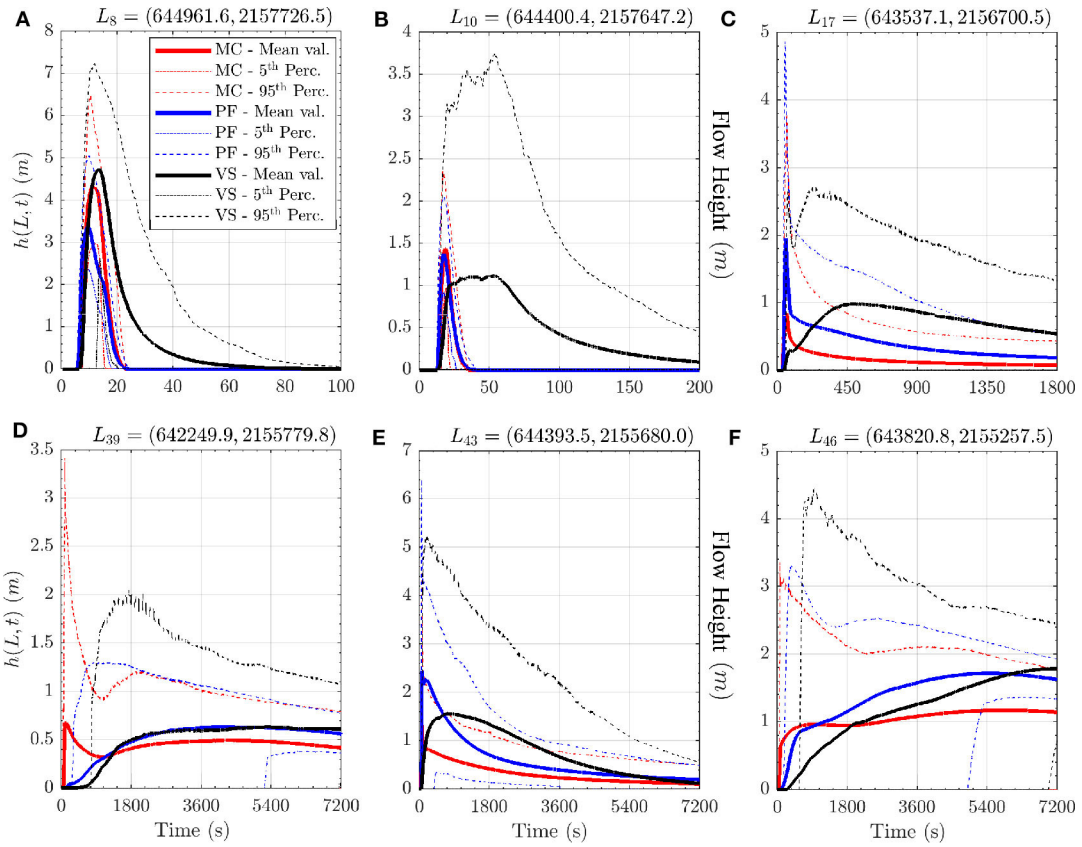

FIGURE 6 | Flow height in six locations. Bold line is mean value, dashed/dotted lines are 5th and 95th percentile bounds. Different models are displayed with different colors. Plots **(A–F)** show different locations and are at different scale, for simplifying lecture.

and PF, and unimodal profile. In PF, after C_3 wanes, at about 60*s* also C_4 becomes not negligible for $\sim$ 40*s*. The second part of the temporal domain is characterized by a slow decrease of $C_2 > C_1$.

4.2. Contributing Variables Distal From the Initial Pile

Figure 9 shows the dominance factors $(P_i)_{i=1,\dots,4}$ in the three distal points L_{39}, L_{43}, and L_{46}, all more than 2 km far from the initial pile. **Figures 9A–C** and L_{39} are dominated by $\boldsymbol{RHS_1}$. In all the models P_1 is increasing and $P_1 > 90\%$ at the end of the simulation. In MC, P_1 shows a plateau at $\sim$ 40% in $[90, 2,000]s$ preceded and followed by steep increases, while in the other models it rises gradually. $P_2 > 0$ after $\sim$ 500 and 3,600*s*, respectively, but is never greater than 2%. In MC $P_3 \approx 10\%$ at $[50, 70]s$. No-flow probability becomes zero in PF and VS, while stops at 20% in MC. **Figures 9D–F** are related to point L_{43}, and are remarkably complex. In MC, either P_1 and P_2 are $\sim$ 35% in the first 200*s*. Then, P_2 increases, and $\boldsymbol{RHS_2}$ becomes the only dominant variable after 3,600*s*. The no-flow probability is never below 30%. $P_3 = 35\%$ in $[40, 60]s$. Instead, in PF $P_1 > 90\%$ until 3,600*s*, and P_2 rises only in the very last amount of time, reaching $P_2 = P_1 = 40\%$. The no-flow probability is very low during the most of the temporal window, rising at 20% only at 7,200*s*. Both P_3 and P_4 show short peaks, $\sim$ 10%, at $[50, 60]s$.

In VS the no-flow probability is never below 20%, and the dominance factors are broadly equivalent to MC, although P_1 is the greatest up to 4,000*s*, and $P_3 \equiv 0$. **Figures 9G–I** are related to point L_{46} and they are similar to those recorded at point L_{17}, but $P_2 > 90\%$ and the no-flow probability decreases to zero in the second half of the simulation. Moreover, in all the models P_1 does not show any initial peak and instead increases slowly, reaching $P_1 = 10\%$ after more than 3,600*s*.

In summary, only the gravity or the basal friction are dominant with high probability. Some of the points have a deposit at the end with a high chance, some other not, depending on the slope. In general, in MC the no-flow probability tends to be larger than in the other models, because some flow samples stops earlier, or completely leaves the site. Again, curvature can have a small chance to be dominant in MC and PF, particularly when the speed is high. Point L_{43} deserves a specific discussion. It is not proximal to the initiation, but the no-flow probability is increasing at the end, meaning that all the material tends to leave the site. Moreover, the dominating force can be the gravity or the basal friction depending on the time and the model. In MC and VS both the two forces have similar chances to be dominant for most of the time of the simulation. In PF, only the gravitational force is dominant with a high chance. This is probably because

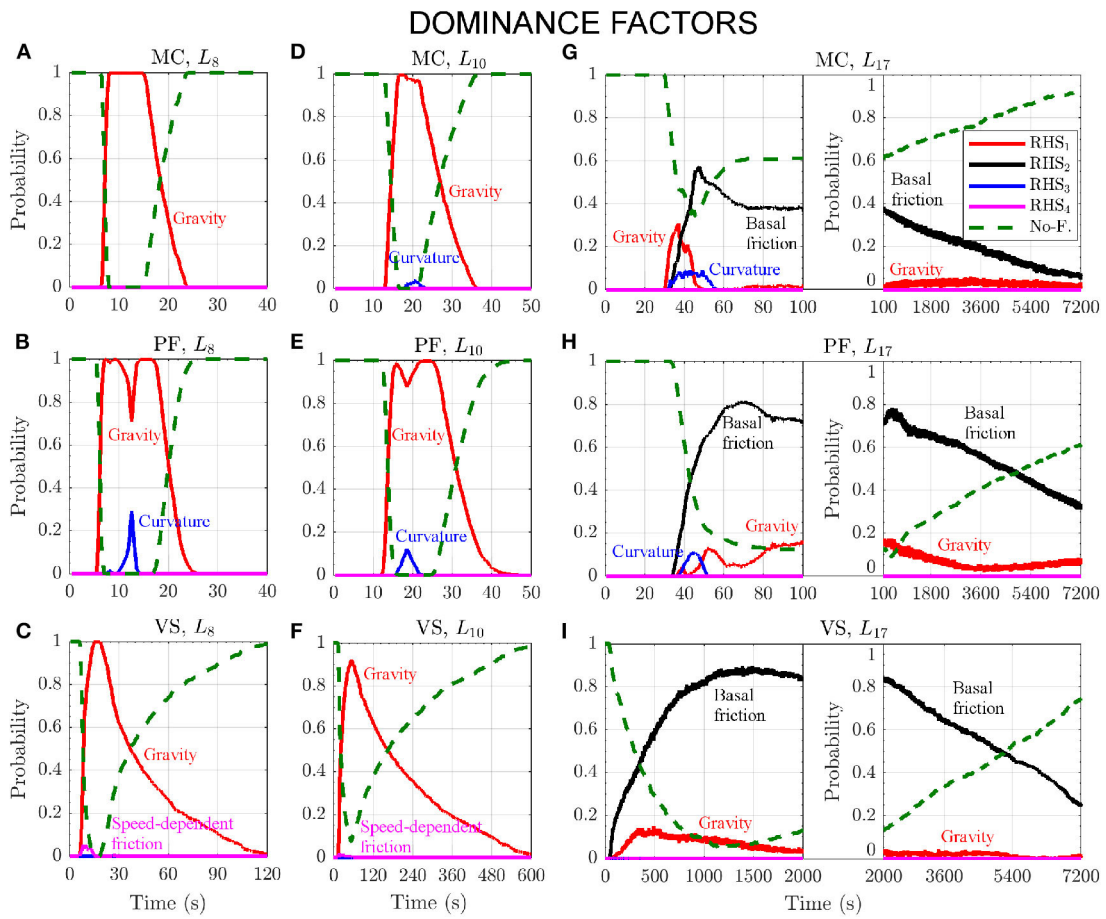

FIGURE 7 | Dominance factors of the forces in three locations in the first km of runout. Different models are plotted separately: **(A,D,G)** assume MC; **(B,E,H)** assume PF; **(C,F,I)** assume VS. Different colors correspond to different force terms. No-flow probability is displayed with a green dashed line.

point L_{43} is situated downhill of a place where a significant amount of material stops.

Figure 10 shows the expected contributions in the distal points. In general, it is worth noting that the remarkable diversity in the dominance factors between the different locations can be the consequence of even a small imbalance between gravity and basal friction. All the plots are dominated by C_1 and C_2, and the remarkable differences observed in the dominance factors depend on which contribution is the greatest. In general these two contributions have similar profiles. **Figures 10A–C** are related to point L_{39} and $C_1 > C_2$. In MC, also is $C_3 > 0$ for a short time. In MC and PF also $C_4 > 0$, but it is significantly lower than the previous contributions, almost negligible in MC. **Figures 10D–F** concern point L_{43}. In MC $C_1 < C_2$, in PF $C_1 > C_2$, in VS they C_1 decreases and crosses C_2 at $\sim 3,600s$. The two contributions form a plateau in MC, in $[90, 200]s$. In MC and PF $C_3 > 0$ for a few seconds, and also $C_4 > 0$ with an initial spike at $\sim 60s$. In particular, C_4 reaches ~ 0.05 at point L_{43}, and in **Figure 3E** we showed that the force contribution can also be at 0.1 in that location, depending on the input values chosen. This means that RHS4 can be about 10% of the dominant force. In PF it shows a long lasting plateau, while becomes negligible in MC. **Figures 10G–I** are related to point L_{46}. In all the models $C_1 < C_2$, and these force contributions are monotone increasing. Only in MC $C_3 > 0$ shortly, and $C_4 > 0$, but almost negligible.

4.3. Flow Extent and Spatial Integrals

Figure 11 shows the volumetric average of speed and Froude Number. It also shows the inundated area as a function of time. Spatial averages and inundated area have smoother plots than local measurements, and most of the details observed in local measurements are not easy to discern. In **Figure 11A**, the speed shows a bell-shaped profile in all the models, but the maximum speed is $\sim 60m/s$ in MC, $\sim 50m/s$ in PF, $\sim 20m/s$ in VS, on average. Uncertainty is $\pm 18m/s$ in MC, similar, but skewed, in VS, and $\pm 10m/s$ in PF.

In **Figure 11B**, the *Fr* profile is very similar to the speed, but the difference between VS and the other models is accentuated. Maximum values are ~ 50 in MC, ~ 38 in PF, ~ 5 in VS, whereas uncertainty is ± 10 in MC, ± 7 in PF, and skewed $[-5, +10]$ in VS. In **Figure 11C**, inundated area has a first peak in MC and PF, both at $\sim 1.15km^2$, followed by a decrease to 0.55 and $0.7km^2$,

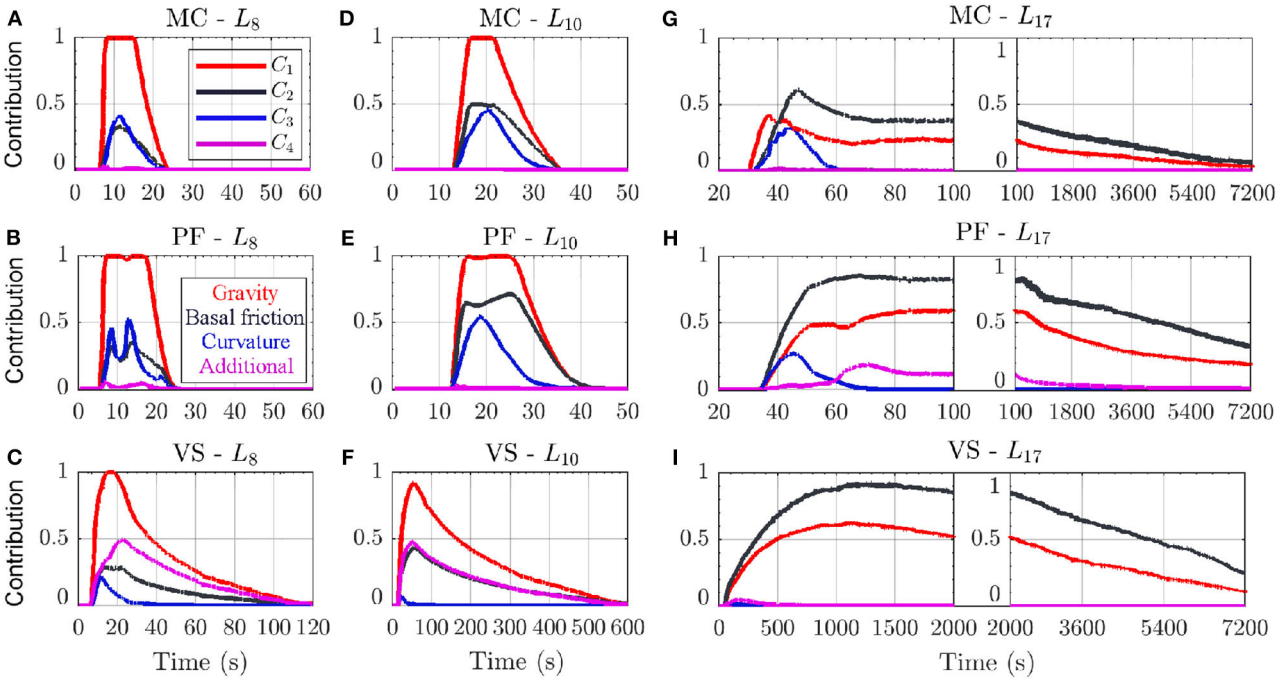

FIGURE 8 | Expected contributions of the forces in three locations in the first km of runout. Different models are plotted separately: **(A,D,G)** assume MC; **(B,E,H)** assume PF; **(C,F,I)** assume VS. Different colors correspond to different force terms.

respectively, and then a slower increase up to a flat plateau at 0.9 and $1.5km^2$, respectively. Uncertainty is $\sim \pm 0.2km^2$ in both MC and PF until $\sim$ 100*s*, and then it increases at $\pm 0.3km^2$ and $[-0.5, +0.4]km^2$, respectively. In MC this increase in uncertainty is concentrated at $\sim$ 100*s*, while it is more gradual in PF. VS has a different profile. The initial peak is only significant in the 95^{th} percentile values, and occurs later, at $\sim$ 100*s*. The peak is of $\sim$ $1km^2$ on the average, but up to $\sim$ $1.8km^2$ in the 95^{th} percentile. The decrease after the peak is very slow and the average inundated area never goes below $0.85km^2$, and eventually reaches back to $\sim 1km^2$. Uncertainty is $[-0.3, +0.2]km^2$.

4.4. Power Integrals

Figure 12 shows the spatial sum of the powers. The estimates in this section assume $\rho = 1,800kg/m^3$ as a constant scaling factor. Corresponding plots of the force terms are included in Patra et al. (2018b). The scalar product of force with velocity imposes the bell-shaped profile. In general, gravity term is larger in VS, because a portion of the flow lingers on the higher slopes for a long time. Basal friction has a higher peak in PF compared to the other models, due to the interpolation of the two basal friction angles.

In **Figure 12A**, the power of $\boldsymbol{RHS_1}$ starts from zero and rises up to 1.4×10^{11} *W* in MC, 1.2×10^{11} *W* in PF, 6.5×10^{10} *W* in VS. Uncertainty is $\pm 4.0 \times 10^{10}$ *W* in MC, $\pm 3.0 \times 10^{10}$ *W* in PF, $[-4.0, 5.0] \times 10^{10}$ *W* in VS. The decrease of gravitational power is related to the slope reduction, and this decrease is more gradual in VS than in the other models. In **Figure 12B**, the power of $\boldsymbol{RHS_2}$ is always negative and peaks to -6.5×10^{10} *W* in MC, -5.0×10^{10} *W* in PF, -2.0×10^{10} *W* in VS. In VS this dissipative power is significantly more flat than in the other models. MC and PF show negligible powers after $\sim$ 100*s*, VS after $\sim$ 200*s*. Uncertainty is $\pm 2.0 \times 10^{10}$ *W* in MC, $\pm 1.5 \times 10^{10}$ *W* in PF, $[-2.0, 1.0] \times 10^{10}$ *W* in VS. In PF, the plot starts from stronger values than in the other models, but it is also the faster to wane. In **Figure 12C**, the power of $\boldsymbol{RHS_3}$ shows a negative peak at -7.0×10^{10} *W* in MC, -4.5×10^{10} *W* in PF, -0.5×10^{10} *W* in VS. Uncertainty on the peak value is $[-4.5, 3.5] \times 10^{10}$ *W* in MC, $[-2.5, 2.0] \times 10^{10}$ *W* in PF, $[-1.0, 0.5] \times 10^{10}$ *W* in VS. The three models all show a bell-shaped profile, MC and PF waning to zero at 90*s*, VS at $\sim$ 30*s*. In **Figure 12D**, the power of $\boldsymbol{RHS_4}$ has a different meaning in the three models. In MC it is the internal friction term, and it only has almost negligible ripple visible in the first second. In PF it is a depth averaged pressure force linked to the thickness gradient, and has a very small effect limited to the first second of simulation, at 0.5×10^{10} *W*. It becomes null at $\sim$ 10*s*. In VS, instead, it is a speed dependent term, and has a very relevant effect. The plot shows a bell-shaped profile, with a peak of -3.5×10^{10} *W*, $[-2.0, 1.0] \times 10^{10}$ *W*. After that, this dissipative power gradually decreases, and becomes negligible at 200*s*.

4.5. Example of Model Performance Calculation

Finally, we give an example of model performance evaluation of the couple $(M, \mathcal{P}_M)$ according to a specific observation. In past work (Patra et al., 2005), MC rheology was tuned to match

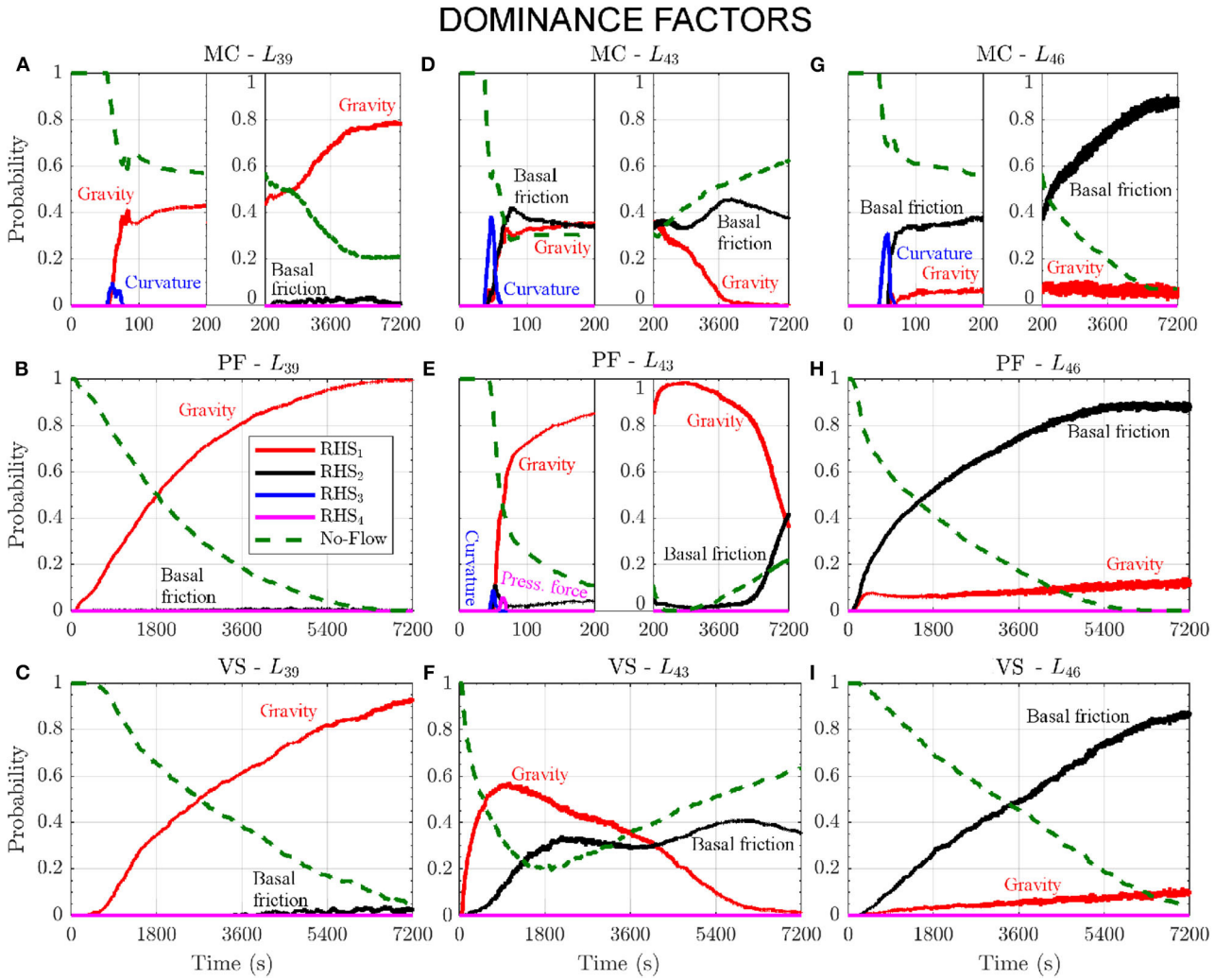

FIGURE 9 | Dominance factors of the forces in three locations after 2 km of runout. Different models are plotted separately: **(A,D,G)** assume MC; **(B,E,H)** assume PF; **(C,F,I)** assume VS. Different colors correspond to different force terms. No-flow probability is displayed with a green dashed line.

deposits for known block and ash flows, but *a priori* predictive ability was limited by inability to tune without knowledge of flow character. The new procedure developed in this study enables an enhanced quantification of model performance, i.e., the similarity of the outputs and real data. We remark that the measured performance refers to the couple $(M, \mathcal{P}_M)$, and that different parameter ranges can produce different performances (Tierz et al., 2016; Sandri et al., 2018). This is in contrast with traditional performance analysis based on particular, albeit calibrated, simulations (Charbonnier and Gertisser, 2012).

Our example concerns the Volcán de Colima case study, and in particular we compare the inundated region in our simulations to the deposit of a BAF occurred 16 April 1991 (Rupp, 2004; Saucedo et al., 2004; Rupp et al., 2006). In addition to modeling uncertainty, other uncertainty sources affect this evaluation. For example, our digital elevation map may be different from the exact topography encountered by the real flow, and the inundated region may have been different from the extent of the deposit found in the field. The inundated region is defined as the points in which the maximum flow height H is greater than $10cm$. A similar procedure may be applied to any observed variable produced by the models, if specific data become available.

Let $\mathcal{M} : \mathcal{C}(\mathbb{R}^2) \to [0, 1]$ be a similarity index defined on the compact subsets of the real plane, i.e., the closed and bounded sets. An equivalent definition can be based on the pseudo-metric $1 - \mathcal{M}$. For example, we define

$$\mathcal{M}_1 := \frac{\int_{\mathbb{R}^2} 1_D(\mathbf{x})d\mathbf{x}}{\int_{\mathbb{R}^2} 1_{S\cup D}(\mathbf{x})d\mathbf{x}}, \quad \mathcal{M}_2 := \frac{\int_{\mathbb{R}^2} 1_{S\cap D}(\mathbf{x})d\mathbf{x}}{\int_{\mathbb{R}^2} 1_D(\mathbf{x})d\mathbf{x}},$$
$$\mathcal{J} := \mathcal{M}_1 \cdot \mathcal{M}_2,$$

where $S \subset \mathbb{R}^2$ is the inundated region, and $D \subset \mathbb{R}^2$ is the recorded deposit.

In particular, $\mathcal{M}_1$ is the area of the deposit over the area of the union of inundated region and deposit, $\mathcal{M}_2$ is the area of the intersection of inundated region and deposit over the area of the

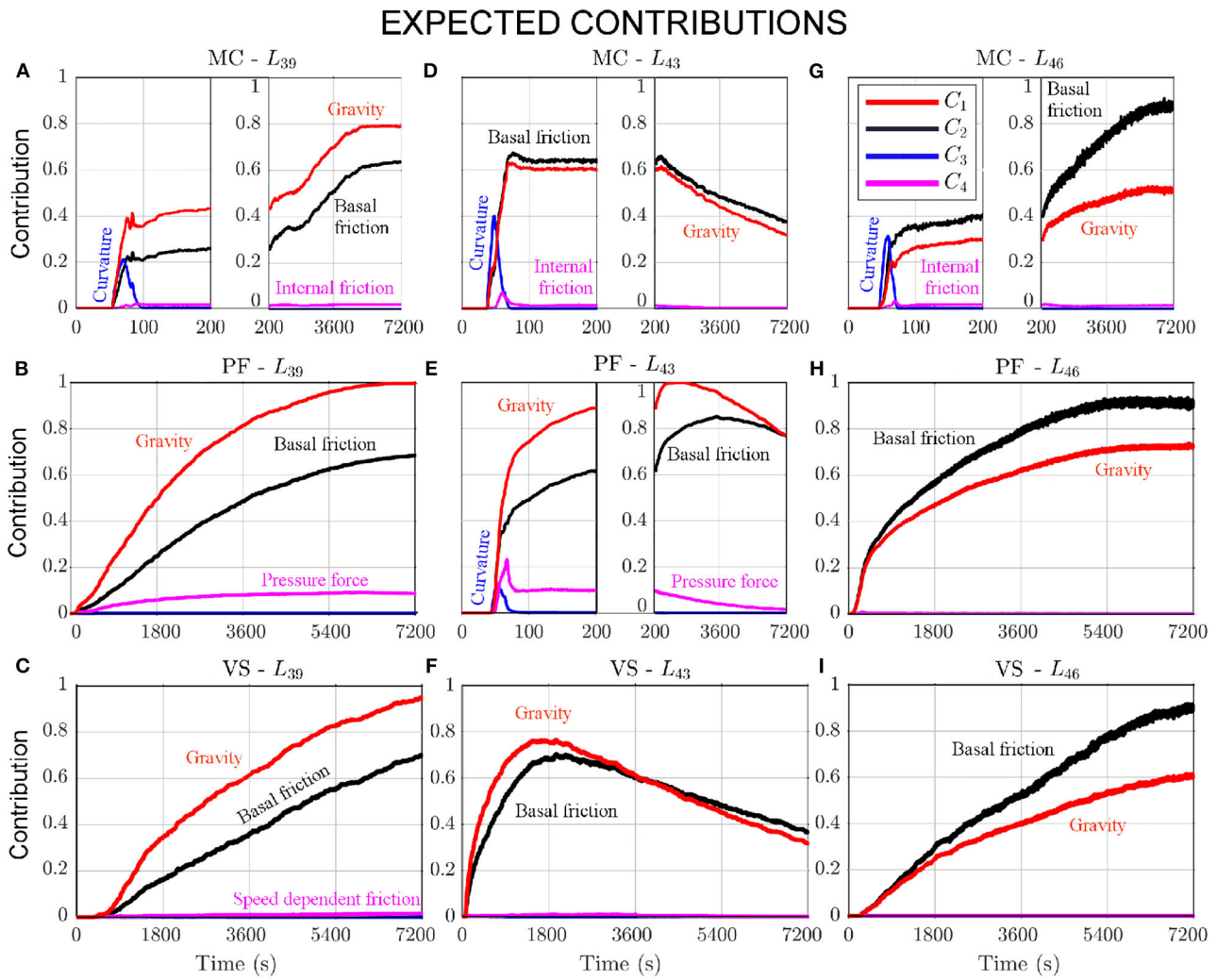

FIGURE 10 | Expected contributions of the forces in three locations after 2 km of runout. Different models are plotted separately: **(A,D,G)** assume MC; **(B,E,H)** assume PF; **(C,F,I)** assume VS. Different colors correspond to different force terms.

deposit, $\mathcal{J}$ is the product of the previous, also called Jaccard Index (Jaccard, 1901). **Figure 13** shows the probability distribution of the similarity indices, according to the uniform probability $\mathcal{P}_M$ on the parameter ranges defined in this study. Different metrics can produce different performance estimates, for example MC inundates most of the deposit, but overestimates the inundated region, while VS relatively reduces the inundated region outside of the deposit boundary, but also leaves several not-inundated spots inside it.

Let $g : [a, b] \rightarrow [0, 1]$ be a score function defined over the percentile range of the similarity index. The global 5^{th} and 95^{th} percentile values $[a, b]$ are defined assuming to select the model randomly with equal chance, and are also shown in **Figures 13A–C**.

Then the performance score G_g of model $(M, \mathcal{P}_M)$ is defined as:

$$G_g\,(M, \mathcal{P}_M) = \int_{[a,b]} g(x) df_M(x),$$

where f_M is the pdf related to the model. Possible score functions include a step function at the global median, a linear or quadratic function, a sigmoid function. **Table 1** shows alternative performance scores, according to changing similarity indices and score functions.

5. CONCLUSIONS

In this study, we have described a statistically driven method for investigating the constituents of complex models. We implemented three different models composed of different assumptions about rheology in geophysical mass flows to illustrate the approach. The data objectively shows the

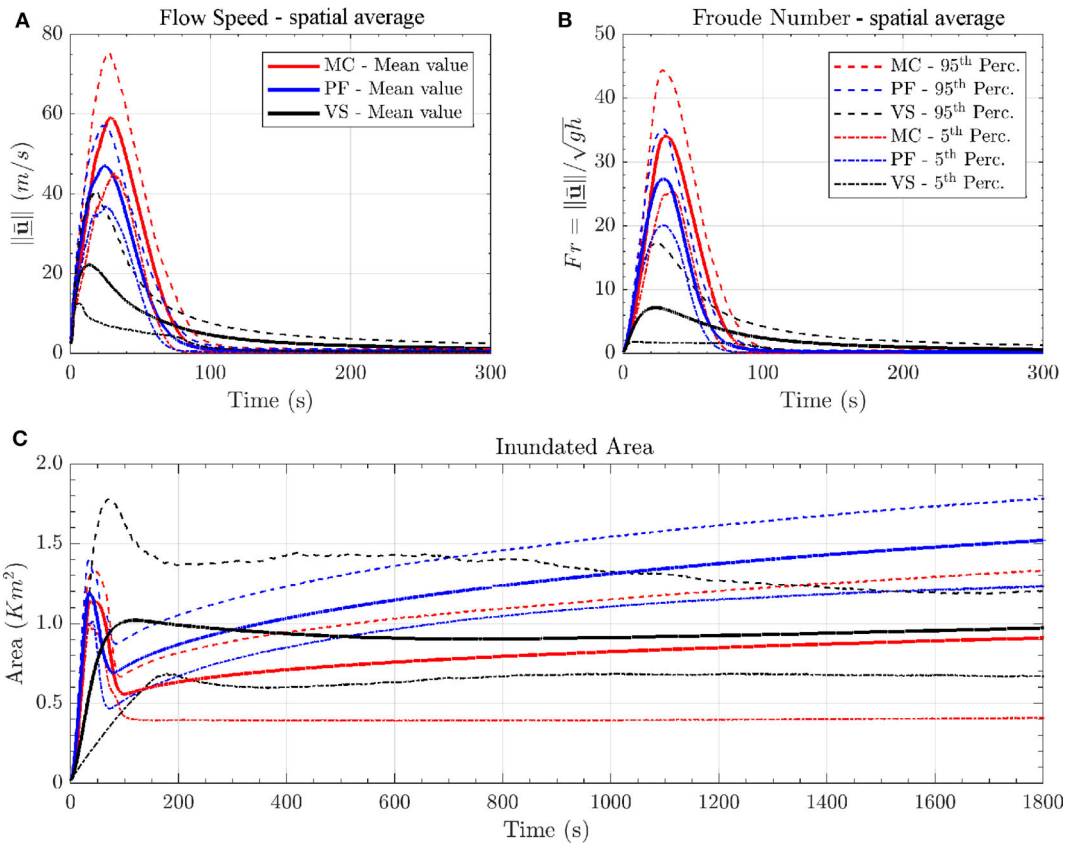

FIGURE 11 | Comparison between spatial averages of **(A)** flow speed, and **(B)** Froude Number, in addition to the **(C)** inundated area, as a function of time. Bold line is mean value, dashed/dotted lines are 5th and 95th percentile bounds. Different models are displayed with different colors. Figure modified from Patra et al. (2018a).

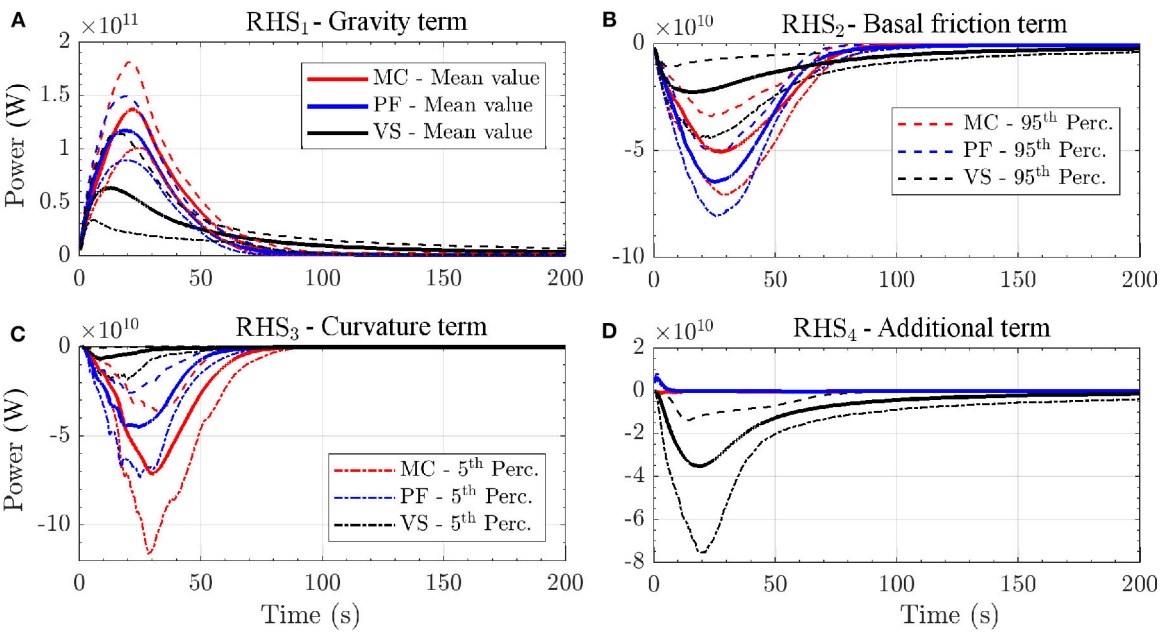

FIGURE 12 | Spatial integrals of the powers. Bold line is mean value, dashed lines are 5th and 95th percentile bounds. Model comparison on the mean value is also displayed. Plots **(A–D)** show different RHS terms and are at different scale, for simplifying lecture.

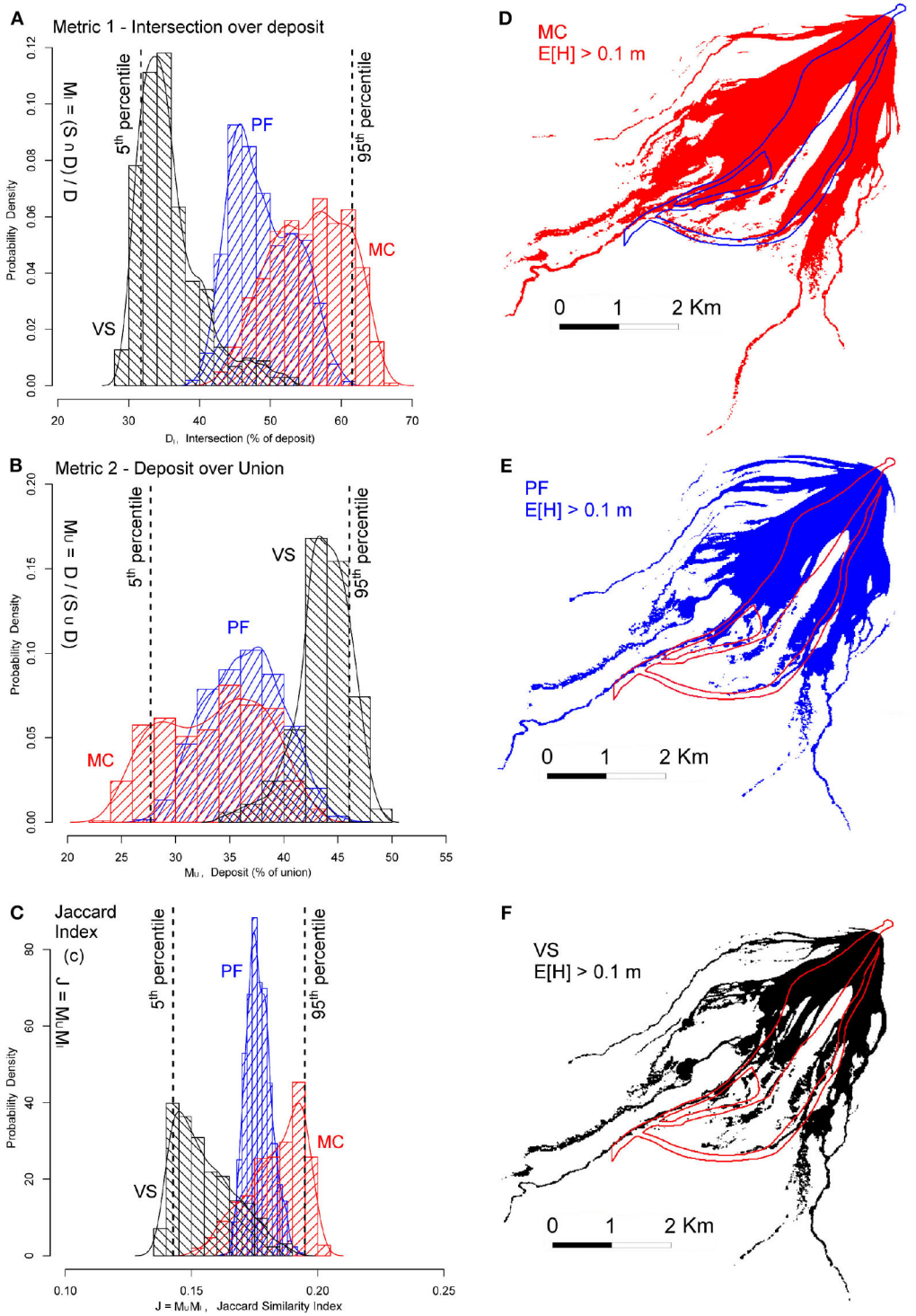

FIGURE 13 | Volcán de Colima. Pdf of the similarity index of inundated regions and a real BAF deposit. Panel **(A)** is based on $\mathcal{M}_I$, **(B)** on $\mathcal{M}_U$, **(C)** on $\mathcal{J}$. The models are MC (red), PF (blue), VS (black). Data histograms are displayed in the background. Global 5th and 95th percentile values are indicated with dashed lines. Plots **(D–F)** display the average inundated region $\{x : E[H(x)] > 10cm\}$. The boundary of the real deposit is marked with a colored line.

performance of the models over many possible flow regimes and topographies. The analysis of contributing variables illustrates the impact of several modeling assumptions. Understanding which assumptions dominate, and by how much, is a key step toward the construction of more efficient models for desired inputs. Such model composition is the subject of ongoing and

TABLE 1 | Performance scores as a function of model, performance metric, and score function.

Score function	Step function			Linear			Quadratic			Sigmoid		
	$y = 1_{\{x>0.5\}}$			$y = x$			$y = x^2$			$y = \exp(-2(1-x)^2)$		
Metric/Model	MC (%)	PF (%)	VS (%)	MC (%)	PF (%)	VS (%)	MC (%)	PF (%)	VS (%)	MC (%)	PF (%)	VS (%)
M1=D/(S∪D)	16.11	26.67	57.23	19.61	28.41	51.98	13.72	21.92	64.36	21.40	29.80	48.80
M2=(S∩D)/D	58.96	38.63	2.41	52.32	38.42	9.27	62.01	34.11	3.87	48.95	38.55	12.50
J=(S∩D)/(S∪D)	43.61	48.36	8.04	46.44	38.99	14.57	54.25	36.49	9.26	43.67	39.64	16.70

Different colors mark different models.

future work, with the purpose of bypassing the search for a unique best model, and going beyond a simple mixture of alternative models.

In summary, our new method enabled us to break down the effects of the different physical assumptions in the dynamics, providing an improved understanding of what characterizes each model. The procedure was applied to the Digital Elevation Map (DEM) of the SW slope of Volcán de Colima (MX). In particular, we presented:

- A short review of the assumptions characterizing three commonly used rheologies of Mohr-Coulomb, Poliquenne-Forterre, Voellmy-Salm. This included a qualitative list of such assumptions, and a breaking down of the different terms in the differential equations.
- A new statistical framework, processing the mean and the uncertainty range of either observable or contributing variables in the simulations. The new concepts of dominance factors and expected contributions enabled a simplified description of the local dynamics. These quantities were analyzed at selected sites, and spatial integrals were calculated, which illustrate the characteristics of the entire flow.
- The contribution coefficients C_i and dominance factors P_i introduced here allow us to quantify and compare in a probabilistic framework the effect of modeling assumptions based on the full range of flows explored using statistically rigorous ensemble computations.
- A final discussion, explaining all the observed features in the results in light of the known physical assumptions of the models, and the evolving flow regime in space and time. This included an example of the model performance estimation method, which depends on the metric and the cost function adopted.

Our analysis uncovered the following main features of the different geophysical models used in the example analysis:

- Compared to the standard MC model, the lack of internal friction in the PF model produces an accentuated lateral spread. The spread is increased by the uninhibited internal pressure force, which briefly pushes the flow ahead and laterally during the initial collapse. That force can also have some minor effects in the accumulation of the final deposit. The interpolation between the smaller bed friction angle ϕ_1 and the larger value ϕ_2 in the PF model suddenly stops the flow if it is thin compared to its speed. This mechanism suppresses large peaks in flow speed.
- In VS, the speed-dependent friction has a great effect in reducing lateral spread and producing channelized flow even where there are otherwise minor ridges and adverse slopes in the topography. The flow tends to be significantly slower and more stretched out in the downslope direction. The effects of different formulations of the curvature term have less impact than do the effects of lower basal friction and speed.
- In our case study the internal friction term in the MC model has a relatively small impact on the dynamics of the flow. Neglecting the term will be a meaningful choice if workload reduction is required in future analyses.

Furthermore, we can make the following statements about the technique in terms of its use on models in general:

- It gives information not only on which forces in the equations of motion are dominating the flow, but also shows where these forces are greatest and gives insight into why they locally peak and vary, and into the impacts of the dominating forces on the model flow outputs,
- It provides a new, quantitative technique to evaluate the most important forces or phenomena acting in a particular model domain, which can supplement, provide insight and guidance into, and generate quantitative information for, the more typical methods used in force analysis of intuition and Similarity Theory.

Additional research concerning other case studies, and different parameter ranges, might reveal other flow regimes, and hence differences in the consequences of the modeling assumptions under new circumstances.

DATA AVAILABILITY STATEMENT

The datasets generated for this study are available on request to the corresponding author.

AUTHOR'S NOTE

An extended version of this manuscript has been released at https://arxiv.org/abs/1805.12104 (Patra et al., 2018b). In particular, Patra et al. (2018b) includes a further analysis of the additional case study of a small scale flow on inclined

plane and flat runway, as well as additional details on the latin hypercubes based on orthogonal arrays, and supplementary datasets including estimates of local Froude Numbers and spatial integrals of force terms.

AUTHOR CONTRIBUTIONS

AP and AB conceived the main conceptual ideas. AB and AA-S implemented and performed the simulations and optimization calculations. AB and AP interpreted the computational results and wrote the paper. All authors discussed the results, commented on the manuscript, provided critical feedback, and gave final approval for publication.

FUNDING

We would like to acknowledge the support of NSF awards 1521855, 1621853, and 1339765.

REFERENCES

Aghakhani, H., Dalbey, K., Salac, D., and Patra, A. K. (2016). Heuristic and Eulerian interface capturing approaches for shallow water type flow and application to granular flows. *Comput. Methods Appl. Mech. Eng.* 304, 243–264. doi: 10.1016/j.cma.2016.02.021

Ai, M., Kong, X., and Li, K. (2016). A general theory for orthogonal array based Latin hypercube sampling. *Stat. Sin.* 26, 761–777. doi: 10.5705/ss.20 2015.0029

Bartelt, P., and McArdell, B. (2009). Granulometric investigations of snow avalanches. *J. Glaciol.* 55, 829–833. doi: 10.3189/002214309790152384

Bartelt, P., Salm, B., and Gruber, U. (1999). Calculating dense-snow avalanche runout using a Voellmy-fluid model with active/passive longitudinal straining. *J. Glaciol.* 45, 242–254. doi: 10.1017/S002214300000174X

Bayarri, M. J., Berger, J. O., Calder, E. S., Dalbey, K., Lunagomez, S., Patra, A. K., et al. (2009). Using statistical and computer models to quantify volcanic hazards. *Technometrics* 51, 402–413. doi: 10.1198/TECH.2009.08018

Bayarri, M. J., Berger, J. O., Calder, E. S., Patra, A. K., Pitman, E. B., Spiller, E. T., et al. (2015). Probabilistic quantification of hazards: a methodology using small ensembles of physics-based simulations and statistical surrogates. *Int. J. Uncertain. Quant.* 5, 297–325. doi: 10.1615/Int.J.UncertaintyQuantification.2015011451

Bevilacqua, A., Patra, A. K., Bursik, M. I., Pitman, E. B., Macías, J. L., Saucedo, R., et al. (2019). Probabilistic forecasting of plausible debris flows from Nevado de colima (Mexico) using data from the atenquique debris flow, 1955. *Nat. Hazards Earth Syst. Sci.* 19, 791–820. doi: 10.5194/nhess-19-791-2019

Bongard, J., and Lipson, H. (2007). Automated reverse engineering of nonlinear dynamical systems. *Proc. Natl. Acad. Sci. U.S.A.* 104, 9943–9948. doi: 10.1073/pnas.0609476104

Bursik, M., Patra, A., Pitman, E., Nichita, C., Macias, J., Saucedo, R., et al. (2005). Advances in studies of dense volcanic granular flows. *Rep. Prog. Phys.* 68:271. doi: 10.1088/0034-4885/68/2/R01

Capra, L., Gavilanes-Ruiz, J. C., Bonasia, R., Saucedo-Giron, R., and Sulpizio, R. (2015). Re-assessing volcanic hazard zonation of Volcán de Colima, Mexico. *Nat. Hazards* 76, 41–61. doi: 10.1007/s11069-014-1480-1

Capra, L., Macís, J., Cortés, A., Dávila, N., Saucedo, R., Osorio-Ocampo, S., et al. (2016). Preliminary report on the July 10-11, 2015 eruption at Volcán de Colima: pyroclastic density currents with exceptional runouts and volume. *J. Volcanol. Geotherm. Res.* 310(Suppl. C), 39–49. doi: 10.1016/j.jvolgeores.2015.11.022

Capra, L., Manea, V. C., Manea, M., and Norini, G. (2011). The importance of digital elevation model resolution on granular flow simulations: a test case for Colima volcano using TITAN2D computational routine. *Nat. Hazards* 59, 665–680. doi: 10.1007/s11069-011-9788-6

Charbonnier, S., Germa, A., Connor, C., Gertisser, R., Preece, K., Komorowski, J.-C., et al. (2013). Evaluation of the impact of the 2010 pyroclastic density currents at Merapi volcano from high-resolution satellite imagery, field investigations and numerical simulations. *J. Volcanol. Geotherm. Res.* 261(Suppl. C), 295–315. doi: 10.1016/j.jvolgeores.2012.12.021

Charbonnier, S., and Gertisser, R. (2012). Evaluation of geophysical mass flow models using the 2006 block-and-ash flows of Merapi volcano, Java, Indonesia: towards a short-term hazard assessment tool. *J. Volcanol. Geotherm. Res.* 231–232:87–108. doi: 10.1016/j.jvolgeores.2012.02.015

Charbonnier, S. J., and Gertisser, R. (2009). Numerical simulations of block-and-ash flows using the Titan2D flow model: examples from the 2006 eruption of Merapi Volcano, Java, Indonesia. *Bull. Volcanol.* 71, 953–959. doi: 10.1007/s00445-009-0299-1

Christen, M., Kowalski, J., and Bartelt, P. (2010). RAMMS: Numerical simulation of dense snow avalanches in three-dimensional terrain. *Cold Regions Sci. Technol.* 63, 1–14. doi: 10.1016/j.coldregions.2010.04.005

Dade, W. B., and Huppert, H. E. (1998). Long-runout rockfalls. *Geology* 26, 803–806. doi: 10.1130/0091-7613(1998)026<0803:LRR>2.3.CO;2

Dalbey, K., Patra, A. K., Pitman, E. B., Bursik, M. I., and Sheridan, M. F. (2008). Input uncertainty propagation methods and hazard mapping of geophysical mass flows. *J. Geophys. Res. Solid Earth* 113, 1–16. doi: 10.1029/2006JB004471

Dalbey, K. R. (2009). *Predictive simulation and model based hazard maps* (Ph.D. thesis). University at Buffalo, Buffalo, NY, United States.

Davila, N., Capra, L., Gavilanes-Ruiz, J., Varley, N., Norini, G., and Vazquez, A. G. (2007). Recent lahars at Volcán de Colima (Mexico): drainage variation and spectral classification. *J. Volcanol. Geotherm. Res.* 165, 127–141. doi: 10.1016/j.jvolgeores.2007.05.016

de' Michieli Vitturi, M., Esposti Ongaro, T., Lari, G., and Aravena, A. (2019). Imex_sflow2d 1.0: a depth-averaged numerical flow model for pyroclastic avalanches. *Geosci. Model Dev.* 12, 581–595. doi: 10.5194/gmd-12-581-2019

Denlinger, R. P., and Iverson, R. M. (2001). Flow of variably fluidized granular masses across three-dimensional terrain: 2. Numerical predictions and experimental tests. *J. Geophys. Res.* 106, 553–566. doi: 10.1029/2000JB900330

Denlinger, R. P., and Iverson, R. M. (2004). Granular avalanches across irregular three-dimensional terrain: 1. Theory and computation. *J. Geophys. Res.* 109:F01014. doi: 10.1029/2003JF000085

Drucker, D. C., and Prager, W. (1952). Soil mechanics and plastic analysis for limit design. *Q. Appl. Math.* 10, 157–165. doi: 10.1090/qam/48291

Farrell, K., Tinsley, J., and Faghihi, D. (2015). A Bayesian framework for adaptive selection, calibration, and validation of coarse-grained models of atomistic systems. *J. Comput. Phys.* 295, 189–208. doi: 10.1016/j.jcp.2015.03.071

Fischer, J., Kowalski, J., and Pudasaini, S. P. (2012). Topographic curvature effects in applied avalanche modeling. *Cold Regions Sci. Technol.* 74–75:21–30. doi: 10.1016/j.coldregions.2012.01.005

Forterre, Y., and Pouliquen, O. (2002). Stability analysis of rapid granular chute flows: formation of longitudinal vortices. *J. Fluid Mech.* 467, 361–387. doi: 10.1017/S0022112002001581

Forterre, Y., and Pouliquen, O. (2003). Long-surface-wave instability in dense granular flows. *J. Fluid Mech.* 486, 21–50. doi: 10.1017/S0022112003 004555

González, M. B., Ramírez, J. J., and Navarro, C. (2002). Summary of the historical eruptive activity of Volcán De Colima, Mexico 1519-2000. *J. Volcanol. Geotherm. Res.* 117, 21–46. doi: 10.1016/S0377-0273(02)00233-0

Gray, J. M. N. T., Wieland, M., and Hutter, K. (1999). Gravity-driven free surface flow of granular avalanches over complex basal topography. *Proc. R. Soc. Lond. Ser. A Math. Phys. Eng. Sci.* 455, 1841–1874. doi: 10.1098/rspa.1999.0383

Gruber, U., and Bartelt, P. (2007). Snow avalanche hazard modelling of large areas using shallow water numerical models and GIS. *Environ. Modell. Softw.* 22, 1472–1481. doi: 10.1016/j.envsoft.2007.01.001

Higdon, D., Kennedy, M., Cavendish, J. C., Cafeo, J. A., and Ryne, R. D. (2004). Combining field data and computer simulations for calibration and prediction. *SIAM J. Sci. Comput.* 26, 448–466. doi: 10.1137/S1064827503426693

Hyman, D., and Bursik, M. (2018). Deformation of volcanic materials by pore pressurization: analog experiments with simplified geometry. *Bull. Volcanol.* 80:19. doi: 10.1007/s00445-018-1201-9

Hyman, D. M., Bevilacqua, A., and Bursik, M. I. (2019). Statistical theory of probabilistic hazard maps: a probability distribution for the hazard boundary location. *Nat. Hazards Earth Syst. Sci.* 19, 1347–1363. doi: 10.5194/nhess-19-1347-2019

Iverson, R. M. (1997). The physics of debris flows. *Rev. Geophys.* 35, 245–296. doi: 10.1029/97RG00426

Iverson, R. M., and Denlinger, R. P. (2001). Flow of variably fluidized granular masses across three-dimensional terrain: 1. Coulomb mixture theory. *J. Geophys. Res.* 106:537. doi: 10.1029/2000JB900329

Iverson, R. M., and George, D. L. (2014). A depth-averaged debris-flow model that includes the effects of evolving dilatancy. I. Physical basis. *Proc. R. Soc. Lond. A Math. Phys. Eng. Sci.* 470:2170. doi: 10.1098/rspa.2013.0819

Iverson, R. M., Logan, M., and Denlinger, R. P. (2004). Granular avalanches across irregular three-dimensional terrain: 2. Experimental tests. *J. Geophys. Res. Earth Surface* 109:F01015. doi: 10.1029/2003JF000084

Jaccard, P. (1901). Distribution de la flore alpine dans le bassin des Dranses et dans quelques régions voisines. *Bull. Soc. Vaudoise Sci. Nat.* 37, 241–272.

Kelfoun, K. (2011). Suitability of simple rheological laws for the numerical simulation of dense pyroclastic flows and long-runout volcanic avalanches. *J. Geophys. Res.* 116:B08209. doi: 10.1029/2010JB007622

Kelfoun, K., and Druitt, T. H. (2005). Numerical modeling of the emplacement of Socompa rock avalanche, Chile. *J. Geophys. Res. Solid Earth* 110:B12. doi: 10.1029/2005JB003758

Kelfoun, K., Samaniego, P., Palacios, P., and Barba, D. (2009). Testing the suitability of frictional behaviour for pyroclastic flow simulation by comparison with a well-constrained eruption at Tungurahua volcano (Ecuador). *Bull. Volcanol.* 71, 1057–1075. doi: 10.1007/s00445-009-0286-6

Kennedy, M. C., and O'Hagan, A. (2011). Bayesian calibration of computer models. *J. R. Stat. Soc. Ser. B Stat. Methodol.* 63, 425–464. doi: 10.1111/1467-9868.00294

Kern, M., Bartelt, P., Sovilla, B., and Buser, O. (2009). Measured shear rates in large dry and wet snow avalanches. *J. Glaciol.* 55, 327–338. doi: 10.3189/002214309788608714

la Cruz-Reyna, S. D. (1993). Random patterns of occurrence of explosive eruptions at Colima Volcano, Mexico. *J. Volcanol. Geotherm. Res.* 55, 51–68. doi: 10.1016/0377-0273(93)90089-A

Macías, J., Capra, L., Arce, J., Espíndola, J., García-Palomo, A., and Sheridan, M. (2008). Hazard map of El Chichón volcano, Chiapas, México: constraints posed by eruptive history and computer simulations. *J. Volcanol. Geotherm. Res.* 175, 444–458. doi: 10.1016/j.jvolgeores.2008.02.023

Macorps, E., Charbonnier, S. J., Varley, N. R., Capra, L., Atlas, Z., and Cabré, J. (2018). Stratigraphy, sedimentology and inferred flow dynamics from the July 2015 block-and-ash flow deposits at Volcán de Colima, Mexico. *J. Volcanol. Geotherm. Res.* 349, 99–116. doi: 10.1016/j.jvolgeores.2017.09.025

Martin Del Pozzo, A. M., Sheridan, M. F., Barrera, M., Hubp, J. L., and Selem, L. V. (1995). Potential hazards from Colima Volcano, Mexico. *Geofisica Int.* 34, 363–376.

McKay, M. D., Beckman, R. J., and Conover, W. J. (1979). A comparison of three methods for selecting values of input variables in the analysis of output from a computer code. *Technometrics* 21, 239–245. doi: 10.1080/00401706.1979.10489755

Norini, G., De Beni, E., Andronico, D., Polacci, M., Burton, M., and Zucca, F. (2009). The 16 November 2006 flank collapse of the south-east crater at Mount Etna, Italy: study of the deposit and hazard assessment. *J. Geophys. Res. Solid Earth* 114:B02204. doi: 10.1029/2008JB005779

Ogburn, S. E., Berger, J., Calder, E. S., Lopes, D., Patra, A., Pitman, E. B., et al. (2016). Pooling strength amongst limited datasets using hierarchical Bayesian analysis, with application to pyroclastic density current mobility metrics. *Stat. Volcanol.* 2, 1–26. doi: 10.5038/2163-338X.2.1

Owen, A. B. (1992a). A central limit theorem for Latin hypercube sampling. *J. R. Stat. Soc.* 54, 541–551. doi: 10.1111/j.2517-6161.1992.tb01895.x

Owen, A. B. (1992b). Orthogonal arrays for computer experiments, integration and visualization. *Stat. Sin.* 2, 439–452.

Patra, A., Bevilacqua, A., and Akhavan-Safaei, A. (2018a). "Analyzing complex models using data and statistics," in *Computational Science-ICCS 2018*, eds Y. Shi, H. Fu, Y. Tian, V. V. Krzhizhanovskaya, M. H. Lees, J. Dongarra, and P. M. A. Sloot (Cham: Springer International Publishing), 724–736. doi: 10.1007/978-3-319-93701-4_57

Patra, A., Bevilacqua, A., Akhavan-Safaei, A., Pitman, E., Bursik, M., and Hyman, D. (2018b). Comparative analysis of the structures and outcomes of geophysical flow models and modeling assumptions using uncertainty quantification. *arXiv [preprint] arXiv:*1805.12104. Available online at: https://arxiv.org/abs/1805.12104

Patra, A., Nichita, C., Bauer, A., Pitman, E., Bursik, M., and Sheridan, M. (2006). Parallel adaptive discontinuous Galerkin approximation for thin layer avalanche modeling. *Comput. Geosci.* 32, 912–926. doi: 10.1016/j.cageo.2005.10.023

Patra, A. K., Bauer, A. C., Nichita, C. C., Pitman, E. B., Sheridan, M. F., Bursik, M., et al. (2005). Parallel adaptive numerical simulation of dry avalanches over natural terrain. *J. Volcanol. Geotherm. Res.* 139, 1–21. doi: 10.1016/j.jvolgeores.2004.06.014

Pirulli, M., Bristeau, M.-O., Mangeney, A., and Scavia, C. (2007). The effect of the earth pressure coefficients on the runout of granular material. *Environ. Modell. Softw.* 22, 1437–1454. doi: 10.1016/j.envsoft.2006.06.006

Pitman, E. B., and Le, L. (2005). A two-fluid model for avalanche and debris flows. *Philos. Trans. Ser. A Math. Phys. Eng. Sci.* 363, 1573–1601. doi: 10.1098/rsta.2005.1596

Pitman, E. B., Nichita, C. C., Patra, A., Bauer, A., Sheridan, M., and Bursik, M. (2003). Computing granular avalanches and landslides. *Phys. Fluids* 15:3638. doi: 10.1063/1.1614253

Popper, K. R. (1959). *The Logic of Scientific Discovery*. London; New York, NY: Routledge. doi: 10.1063/1.3060577

Pouliquen, O. (1999). Scaling laws in granular flows down rough inclined planes. *Phys. Fluids* 11, 542–548. doi: 10.1063/1.869928

Pouliquen, O., and Forterre, Y. (2002). Friction law for dense granular flows: application to the motion of a mass down a rough inclined plane. *J. Fluid Mech.* 453, 133–151. doi: 10.1017/S0022112001006796

Procter, J. N., Cronin, S. J., Platz, T., Patra, A., Dalbey, K., Sheridan, M., et al. (2010). Mapping block-and-ash flow hazards based on Titan 2D simulations: a case study from Mt. Taranaki, NZ. *Nat. Hazards* 53, 483–501. doi: 10.1007/s11069-009-9440-x

Ranjan, P., and Spencer, N. (2014). Space-filling Latin hypercube designs based on randomization restrictions in factorial experiments. *Stat. Probabil. Lett.* 94(Suppl. C):239–247. doi: 10.1016/j.spl.2014.07.032

Rankine, W. J. M. (1857). On the stability of loose earth. *Philos. Trans. R. Soc. Lond.* 147, 9–27. doi: 10.1098/rstl.1857.0003

Reyes-Dávila, G. A., Arámbula-Mendoza, R., Espinasa-Perena, R., Pankhurst, M. J., Navarro-Ochoa, C., Savov, I., et al. (2016). Volcan de Colima dome collapse of July, 2015 and associated pyroclastic density currents. *J. Volcanol. Geotherm. Res.* 320(Suppl. C), 100–106. doi: 10.1016/j.jvolgeores.2016.04.015

Rupp, B. (2004). *An analysis of granular flows over natural terrain* (Master's thesis). University at Buffalo, Buffalo, NY, United States.

Rupp, B., Bursik, M., Namikawa, L., Webb, A., Patra, A. K., Saucedo, R., et al. (2006). Computational modeling of the 1991 block and ash fows at Colima Volcano, México. *Geol. Soc. Am. Spcl. Pap.* 402, 223–237. doi: 10.1130/2006.2402(11)

Rutarindwa, R., Spiller, E. T., Bevilacqua, A., Bursik, M. I., and Patra, A. K. (2019). Dynamic probabilistic hazard mapping in the long valley volcanic region ca: integrating vent opening maps and statistical surrogates of physical models of pyroclastic density currents. *J. Geophys. Res. Solid Earth* 124, 9600–9621. doi: 10.1029/2019JB017352

Salm, B. (1993). Flow, flow transition and runout distances of flowing avalanches. *Ann. Glaciol.* 18, 221–226. doi: 10.1017/S0260305500011551

Salm, B., Burkard, A., and Gubler, H. (1990). *Berechnung von Fliesslawinen: eine Anleitung f¨ur* Praktiker mit Beispielen. Mitteilungen des Eidgenössische Institutes für Schnee- und Lawinenforschung, 47.

Saltelli, A., Annoni, P., Azzini, I., Campolongo, F., Ratto, M., and Tarantola, S. (2010). Variance based sensitivity analysis of model output. Design and estimator for the total sensitivity index. *Comput. Phys. Commun.* 181, 259–270. doi: 10.1016/j.cpc.2009.09.018

Sandri, L., Tierz, P., Costa, A., and Marzocchi, W. (2018). Probabilistic hazard from pyroclastic density currents in the Neapolitan area (southern Italy). *J. Geophys. Res. Solid Earth* 123, 3474–3500. doi: 10.1002/2017JB014890

Sarocchi, D., Sulpizio, R., Macías, J., and Saucedo, R. (2011). The 17 July 1999 block-and-ash flow (BAF) at Colima Volcano: New insights on volcanic granular flows from textural analysis. *J. Volcanol. Geotherm. Res.* 204, 40–56. doi: 10.1016/j.jvolgeores.2011.04.013

Saucedo, R., Macías, J., Bursik, M., Mora, J., Gavilanes, J., and Cortes, A. (2002). Emplacement of pyroclastic flows during the 1998-1999 eruption of Volcán de Colima, México. *J. Volcanol. Geotherm. Res.* 117, 129–153. doi: 10.1016/S0377-0273(02)00241-X

Saucedo, R., Macías, J., Gavilanes, J., Arce, J., Komorowski, J., Gardner, J., and Valdez-Moreno, G. (2010). Eyewitness, stratigraphy, chemistry, and eruptive dynamics of the 1913 Plinian eruption of Volcán de Colima, México. *J. Volcanol. Geotherm. Res.* 191, 149–166. doi: 10.1016/j.jvolgeores.2010.01.011

Saucedo, R., Macías, J., Sheridan, M., Bursik, M., and Komorowski, J. (2005). Modeling of pyroclastic flows of Colima Volcano, Mexico: implications for hazard assessment. *J. Volcanol. Geotherm. Res.* 139, 103–115. doi: 10.1016/j.jvolgeores.2004.06.019

Saucedo, R., Macías, J. L., and Bursik, M. (2004). Pyroclastic flow deposits of the 1991 eruption of Volcán de Colima, México. *Bull. Volcanol.* 66, 291–306. doi: 10.1007/s00445-003-0311-0

Savage, S. B., and Hutter, K. (1989). The motion of a finite mass of granular material down a rough incline. *J. Fluid Mech.* 199:177. doi: 10.1017/S0022112089000340

Sheridan, M., Stinton, A., Patra, A., Pitman, E., Bauer, A., and Nichita, C. (2005). Evaluating Titan2D mass-flow model using the 1963 Little Tahoma Peak avalanches, Mount Rainier, Washington. *J. Volcanol. Geotherm. Res.* 139, 89–102. doi: 10.1016/j.jvolgeores.2004.06.011

Sheridan, M. F., and Macías, J. L. (1995). Estimation of risk probability for gravity-driven pyroclastic flows at Volcan Colima, Mexico. *J. Volcanol. Geotherm. Res.* 66, 251–256. doi: 10.1016/0377-0273(94)00058-O

Sheridan, M. F., Patra, A. K., Dalbey, K., and Hubbard, B. (2010). "Probabilistic digital hazard maps for avalanches and massive pyroclastic flows using TITAN2D," in *Stratigraphy and Geology of Volcanic Areas*, eds G. Groppelli and L. Viereck-Goette (Boulder, CO: Geological Society of America), 281. doi: 10.1130/2010.2464(14)

Simakov, N. A., Jones-Ivey, R. L., Akhavan-Safaei, A., Aghakhani, H., Jones, M. D., and Patra, A. K. (2019). "Modernizing TITAN2D, a parallel AMR geophysical flow code to support multiple rheologies and extendability," in *International Conference on High Performance Computing* (Frankfurt: Springer), 101–112. doi: 10.1007/978-3-030-34356-9_10

Spiller, E. T., Bayarri, M. J., Berger, J. O., Calder, E. S., Patra, A. K., Pitman, E. B., et al. (2014). Automating emulator construction for geophysical hazard maps. *SIAM/ASA J. Uncertain. Quant.* 2, 126–152. doi: 10.1137/120899285

Stefanescu, E. R., Bursik, M., Cordoba, G., Dalbey, K., Jones, M. D., Patra, A. K., et al. (2012a). Digital elevation model uncertainty and hazard analysis using a geophysical flow model. *Proc. R. Soc. Lond. A Math. Phys. Eng. Sci.* 468, 1543–1563. doi: 10.1098/rspa.2011.0711

Stefanescu, E. R., Bursik, M., and Patra, A. K. (2012b). Effect of digital elevation model on Mohr-Coulomb geophysical flow model output. *Nat. Hazards* 62, 635–656. doi: 10.1007/s11069-012-0103-y

Stein, M. (1987). Large sample properties of simulations using Latin hypercube sampling. *Technometrics* 29, 143–151. doi: 10.1080/00401706.1987.10488205

Sulpizio, R., Capra, L., Sarocchi, D., Saucedo, R., Gavilanes-Ruiz, J., and Varley, N. (2010). Predicting the block-and-ash flow inundation areas at Volcán de Colima (Colima, Mexico) based on the present day (February 2010) status. *J. Volcanol. Geotherm. Res.* 193, 49–66. doi: 10.1016/j.jvolgeores.2010.03.007

Tang, B. (1993). Orthogonal array-based Latin hypercubes. *J. Am. Stat. Assoc.* 88, 1392–1397. doi: 10.1080/01621459.1993.10476423

Tierz, P., Sandri, L., Costa, A., Zaccarelli, L., Di Vito, M. A., Sulpizio, R., and Marzocchi, W. (2016). Suitability of energy cone for probabilistic volcanic hazard assessment: validation tests at Somma-Vesuvius and Campi Flegrei (Italy). *Bull. Volcanol.* 78:79. doi: 10.1007/s00445-016-1073-9

Tierz, P., Stefanescu, E. R., Sandri, L., Sulpizio, R., Valentine, G. A., Marzocchi, W., et al. (2018). Towards quantitative volcanic risk of pyroclastic density currents: probabilistic hazard curves and maps around somma-vesuvius (Italy). *J. Geophys. Res. Solid Earth* 123, 6299–6317. doi: 10.1029/2017JB015383

Voellmy, A. (1955). Über die Zerstörungskraft von Lawinen. *Schweiz Bauzeitung* 73, 159–165, 212-217, 246-249, 280-285.

Weirs, V. G., Kamm, J. R., Swiler, L. P., Tarantola, S., Ratto, M., Adams, B. M., et al. (2012). Sensitivity analysis techniques applied to a system of hyperbolic conservation laws. *Reliabil. Eng. Syst. Saf.* 107, 157–170. doi: 10.1016/j.ress.2011.12.008

Wolpert, R., Ogburn, S., and Calder, E. (2016). The longevity of lava dome eruptions. *J. Geophys. Res. Solid Earth* 121, 676–686. 2015JB012435. doi: 10.1002/2015JB012435

Yu, B., Dalbey, K., Webb, A., Bursik, M., Patra, A. K., Pitman, E. B., et al. (2009). Numerical issues in computing inundation areas over natural terrains using Savage-Hutter theory. *Nat. Hazards* 50, 249–267. doi: 10.1007/s11069-008-9336-1

Zobin, V., Arámbula, R., Bretón, M., Reyes, G., Plascencia, I., Navarro, C., et al. (2015). Dynamics of the January 2013-June 2014 explosive-effusive episode in the eruption of Volcán de Colima, México: insights from seismic and video monitoring. *Bull. Volcanol.* 77:31. doi: 10.1007/s00445-015-0917-z

Zobin, V., Luhr, J., Taran, Y., Bretón, M., Cortés, A., De La Cruz-Reyna, S., et al. (2002). Overview of the 1997-2000 activity of Volcán de Colima, México. *J. Volcanol. Geotherm. Res.* 117, 1–19. doi: 10.1016/S0377-0273(02)00232-9

Conflict of Interest: The authors declare that the research was conducted in the absence of any commercial or financial relationships that could be construed as a potential conflict of interest.

frontiers in Earth Science

ORIGINAL RESEARCH
published: 07 August 2020
doi: 10.3389/feart.2020.00323

Pyroclastic Density Current Facies in the Millennium Eruption of Tianchi Volcano, Northeast China: Insights From Topography, Stratigraphy, Granulometry, and Petrography

Bo Zhao[1,2], Jiandong Xu[1,2], Hongmei Yu[1,2] and Zhengquan Chen[1,2]*

[1] National Observation and Research Station of Jilin Changbaishan Volcano, Institute of Geology, China Earthquake Administration, Beijing, China, [2] Key Laboratory of Seismic and Volcanic Hazards, Institute of Geology, China Earthquake Administration, Beijing, China

Large-scale pyroclastic density currents (PDCs) produce inhomogeneity of distributions, thicknesses, stratigraphic structures, and temperatures, thereby causing poor understanding of PDC emplacement processes. Millennium Eruption (ME) of Tianchi volcano in 946 A.D. produced masses of PDCs, covering an area of more than 1570 km^2 around the caldera in the Chinese territory. To understand PDC emplacement processes, we examine the proximal to distal variations in the PDC facies during the ME by analyzing the topography, stratigraphy, granulometry, and petrography. The topography of Tianchi volcano has different slopes, including the cone (> 6°), lava shield (2–5°) and lava plateau (< 1°), which affected the PDC emplacement during the ME. The shape of the PDC deposits radiates outward from the caldera, and the periphery has two pyroclastic aprons. The proximal strata (< 10 km) are less than 4 m thick and consist of eutaxitic and lava-like structures in the gullies of the cone. The medial strata (10–20 km) are 10–60 m thick, with columnar joints, pumice-rich layers, and lithic-rich layers in the valleys of the shield. The distal strata (> 20 km) are less than 10 m thick, with coarse-tail layers, ground surge layers, climbing layers, and carbonized woods in the plateau. From the proximal to the distal strata, the emplacement temperature of the PDCs decreased from 740 to 280°C. The medial layers indicate a gravitational differentiation effect and weakened transportation, which led to the formation of thick beds. The distal PDCs demonstrate fluidization characteristics and a density lower than that of the proximal and medial strata, which exhibit clear stratification. Grain size data (< 64 mm) show that the median diameters decreases with increasing distance from the caldera. Rhyolitic and trachytic pumice were found and are assumed to be associated with the composition of the magma chamber. Magmatic mixing structures were confirmed through microscope observations. The volume of the PDCs in the Chinese territory is approximately 7 km^3. Our results assist in unraveling some PDCs emplacement processes, marked by a high level of topography confinement, about 50 km runout distance, 280–750°C emplacement temperatures, and more than 7 km^3 volume, which provide insights of the PDCs destruction during the ME.

Keywords: Tianchi volcano, Millennium Eruption, PDCs, facies, topography

OPEN ACCESS

Edited by:
Pablo Tierz,
The Lyell Centre, United Kingdom

Reviewed by:
Sonia Calvari,
National Institute of Geophysics and Volcanology, Italy
Micol Todesco,
Istituto Nazionale di Geofisica e Vulcanologia (INGV), Italy

****Correspondence:***
Bo Zhao
zhaobo@ies.ac.cn

Specialty section:
This article was submitted to Volcanology, a section of the journal Frontiers in Earth Science

Received: *17 February 2020*
Accepted: *13 July 2020*
Published: *07 August 2020*

Citation:
Zhao B, Xu J, Yu H and Chen Z (2020) Pyroclastic Density Current Facies in the Millennium Eruption of Tianchi Volcano, Northeast China: Insights From Topography, Stratigraphy, Granulometry, and Petrography. Front. Earth Sci. 8:323. doi: 10.3389/feart.2020.00323

INTRODUCTION

Large-scale eruptions, characterized by volcanic explosivity index (VEI) $\geq$ 7, always produce masses of pyroclastic density currents (PDCs), which are one of the most hazardous eruptive phenomena owing to their complex emplacement processes. These PDC deposits are always inhomogeneous in their distributions, thicknesses, stratigraphic structures, and temperatures from the eruptive center to the distal (Branney and Kokelaar, 2002). The emplacement processes of PDCs from large-scale eruptions are still not well understood because these eruptions have not been observed in historic times (Lesti et al., 2011). A useful approach to understanding the emplacements of PDCs from large-scale eruptions is to build a facies model.

Tianchi volcano (also known as Changbaishan or Baitoushan) is a giant intraplate stratovolcano (Wei et al., 1997) that is located on the border between China and North Korea and the Hunchun-Yalu River tectonic fault zone (**Figure 1A**; Liu et al., 1998). The Tianchi caldera has an irregular shape, is 4.4 km from north to south, and 3.3 km from east to west. The highest peak, named Baitou or Jiangjun, has an elevation of 2749 m and is located in North Korea. In 946 A.D., Tianchi volcano experienced a VEI 7 eruption (Xu et al., 2013; Oppenhimer et al., 2017; Pan et al., 2017a) that is known as the Millennium Eruption (ME), which is considered to be one of the largest eruptions on Earth in the last 2000 years (Horn and Schmincke, 2000; Liu, 2000; Wei et al., 2004a). The ME resulted in massive PDCs with a volume of 8.5 km^3 and flowing at a distance of 50 km (Liu and Xiang, 1997a). Historical records suggest that Tianchi volcano may have erupted again in 1199–1200, 1668, 1702, and 1903 after the ME (Jin and Cui, 1999). Currently, the Tianchi caldera lake has stored nearly 2 billion cubic meters of water and has a gap in its northern reaches, which are located in the Chinese territory (**Figure 1B**).

Tianchi volcano has experienced shield-forming, cone-forming, and ignimbrite-forming stages (Liu, 2000; Fan et al., 2006; Wei, 2014). The shield-forming products of Tianchi volcano mainly consists of a basaltic lava plateau around the volcano, formed in 1.2–2 Ma. The cone-forming eruption stage was dominated by trachyte magma, which erupted between 0.1 and 1 Ma. Previous studies generally determined the positions of the cone, lava shield, and lava plateau according to lithological features, leading to different views. Liu (2000) suggested the cone base at an altitude greater than 1600 m. Luan (2008) reported that an altitude of the Tianchi volcanic cone base was more than 1500 m. whereas Wei (2014) stated that a cone base altitude was between 1000 and 1900 m. This discrepancy is caused because different positions of trachytes at the base of the cone were used in these studies. In the last 100,000 years, numerous explosive eruptions have occurred (Jin and Zhang, 1994), with the ME being the best known. The magma is mainly composed of rhyolite. The ME of Tianchi volcano was a Plinian eruption that had an eruption column estimated to be as high as 35 km according to eruption dynamics (Wei et al., 1998). Volcanic ash drifted 1000 km eastward to Japan (Machida and Arai, 1983; Yu et al., 2013), and the eruption column collapsed to form PDCs that cover 2180 km^2 in China (Liu and Xiang, 1997a). Horn and Schmincke (2000) estimated that the magma volume of the eruption was 25 $\pm$ 5 km^3, and divided the ME into an early large-scale eruption (95% volume) and a late small-scale eruption (5% volume), with a 25 km high column of the former. The above information suggests that the ME had a large scale and was complex.

Monitoring data from 2003 to 2006 showed unrest (Ji et al., 2009; Stone, 2010; Liu et al., 2011; Xu et al., 2012; Wei et al., 2013). The background value of the seismic events was 2 per month in Tianchi volcano before 2003 (Liu et al., 1992, 2011; Li and Sun, 1996; Xu et al., 2012). The number increased to 72 per month from 2003 to 2006, with a maximum of 243 in 1 month. The annual average horizontal displacements away from the caldera were 19.6 mm/yr from 2002 to 2003, 10.2 mm/yr from 2003 to 2004, and 8.6 mm/yr from 2004 to 2005. The average $^3He/^4He$ ratio of a hot spring in the Changbaishan valley, 3.57 km away from the center of the caldera lake, was approximately 6.5 between 2003 and 2006, which is higher than before 2003 (average ratio of 5.35). After 2006, the monitoring data showed a return to the level before 2003. This monitoring evidence shows the potential of a future eruption at Tianchi volcano. PDCs are the most hazardous volcanic phenomena for the population living near the volcano due to their large dynamic pressure, fast velocity, long run-out distance and high temperature (e.g., Druitt, 1998; Branney and Kokelaar, 2002; Sulpizio et al., 2014; Dufek et al., 2015). Loose deposits of PDCs are also the main particle sources for secondary lahars, which can occur during non-eruptive periods (e.g., Blong, 1996; Pierson and Major, 2014). Therefore, it is important to identify lithofacies characteristics, such as the spatial distribution, thickness, grain size, and stratigraphic structures of PDCs produced during the ME, to better understand the eruption dynamics and provide a reference for emergency plans to reduce casualties and property loss.

Researchers have investigated the chronology of the ME PDCs (Liu and Wang, 1982; Liu et al., 1989, 1997; Liu and Xiang, 1997a,b; Cui et al., 1997, 2000; Yin et al., 2005, 2012; Xu et al., 2012; Oppenhimer et al., 2017), their stratigraphy (Yang et al., 1996, 2007; Liu, 2006; Wang et al., 2013, 2019; Zhao et al., 2013), geochemistry (Fan et al., 1999, 2006, 2007; Sui et al., 2007; Wei, 2010; Tang et al., 2014; Liu et al., 2015; Zhang et al., 2015; Chen et al., 2017; Pan et al., 2017a,b) and hazard (Wei et al., 1998, 2004b; Horn and Schmincke, 2000; Yu et al., 2013) since the 1980s. Previous investigations of the ME PDCs that focused on chronology and geochemistry found that the eruption occurred around 946 A.D, and indicated that there is a magma chamber at possibly 5–10 km depth below Tianchi volcano containing a mixture of rhyolites and trachytes (Machida and Arai, 1983; Liu, 1999; Fan et al., 2006, 2007; Wu et al., 2007; Wei, 2010; Xu et al., 2012; Kyong-Song et al., 2016; Chen et al., 2017; Oppenhimer et al., 2017; Pan et al., 2017a,b). However, relatively few stratigraphic studies have been conducted on the ME PDCs, and the ME facies model remains to be established.

To better understand emplacement processes, we investigate the PDCs emplaced during the ME in the Chinese territory

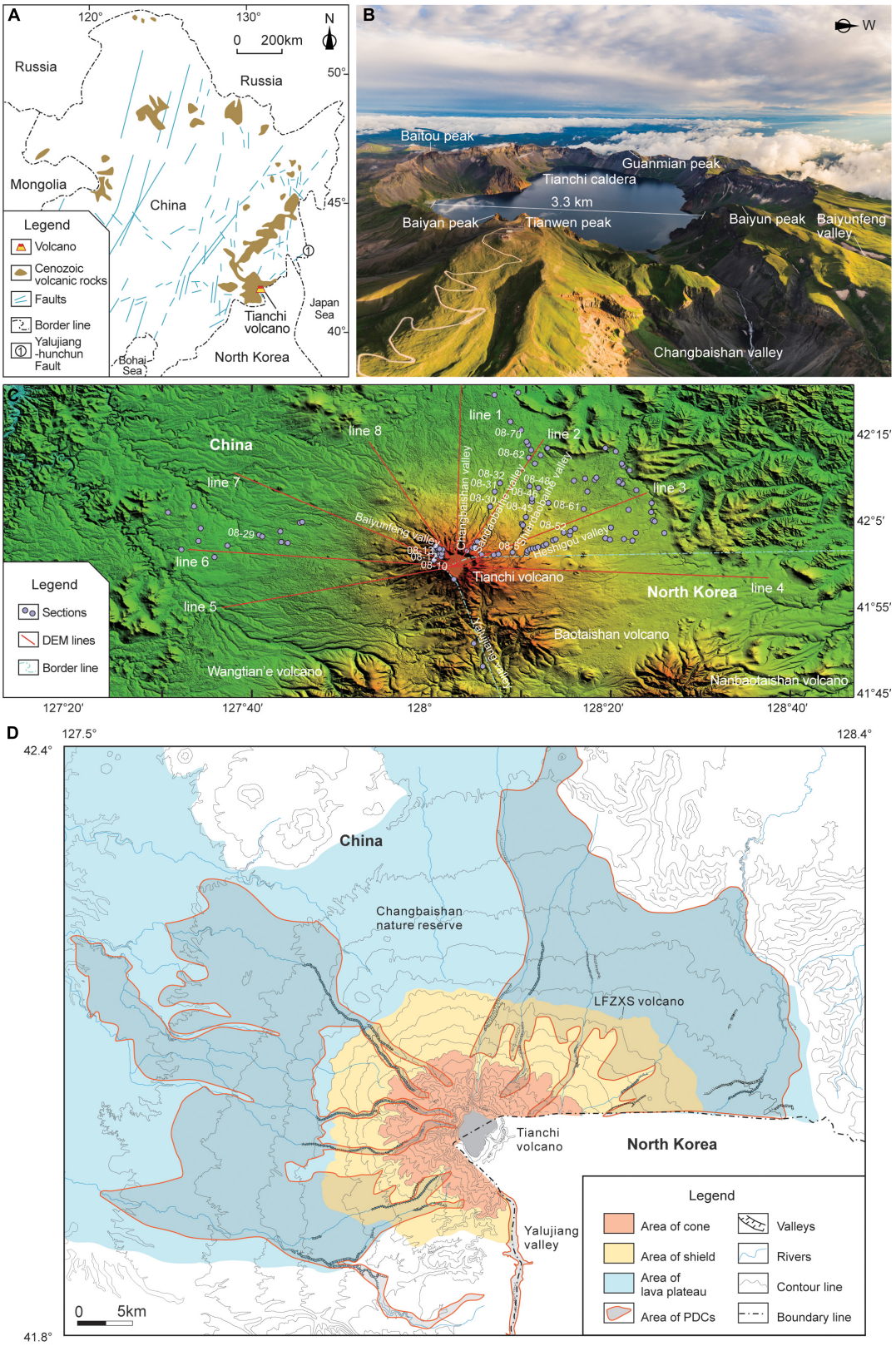

FIGURE 1 | (A) Location of Tianchi volcano, Cenozoic volcanic rocks and tectonic location in Northeast China (revised after Liu, 1999). **(B)** Aerial photograph of Tianchi caldera (photographed from north to south). **(C)** Digital elevation model (DEM) survey line and profile location of Tianchi volcano (DEM data from Alos30, Japan). **(D)** PDCs distribution of ME, and relationship with the area of the cone, the shield and the lava plateau (revised after Zhao et al., 2013).

via five aspects, i.e., the topography of Tianchi volcano, its stratigraphic, granulometric, and microscopic characteristics, and whole-rock composition, so as to establish the facies model of the PDCs during the ME.

MATERIALS AND METHODS

Topographic Analysis

The purpose of the DEM analysis was to study the characteristics of the PDC deposits emplaced during the ME in different landforms. Most of the primitive topography before the ME, including the lava plateau, shield and a part of the cone, has been preserved during the ME. Over the last 1000 years, the topographic changes have not been significant. Therefore, using the modern-day topography to analyze the PDC emplacement during the ME is still justifiable. The topographic data were obtained using Japan's Alos30 Digital Elevation Model (DEM) with a resolution of 30 m. The Global mapper was used with the Tianchi caldera as the center, to identify eight topography sections (**Figure 1C**) for the slope analysis of Tianchi volcano. This analysis was used to identify the Tianchi volcanic cone, lava shield, and lava plateau. The length of line 1, 2, 3, 4, 5, 6, 7, and 8 was 41, 30, 31, 45, 37, 41, 38, and 29 km, respectively.

Field Geological Survey

A geological field survey was conducted to collect samples and detail the stratigraphy of the PDC emplaced during the ME. Geological surveys, with a total of 104 working points and cross profiles, were performed along the Changbaishan, Shierdaobaihe, and Sandaobaihe valley on the northern slope, the Baiyunfeng valley on the western slope, and the Yalujiang valley on the southern slope near the cone and lava shield (**Figure 1C**; lacking data in North Korea's territory in the east). The purpose of focusing on the valleys was to ensure the continuity of the cross profile for a full comprehension of their attributes. Well-exposed outcrops on the lava plateaus were selected for mapping and sampling.

Granulometry

A grain size analysis was conducted on loose samples collected in the field. The measured grain diameter (d) ranged from 0.0625 to 64 mm (0.0625, 0.125, 0.25, 0.5, 1, 2, 4, 8, 16, 32 and 64 mm) and included 11 size grades from 4 to −6 phi (φ) (where $\varphi = -\log_2 d$, 4, 3, 2, 1, 0, −1, −2, −3, −4, −5, −6, respectively). The weight of the samples was typically 500 g, and a vibrating screen was used for screening. Inman (1952) has put forward the concepts of median diameter (Md_φ), which indicates the central size tendency and graphical standard deviation (σ_φ), which is a measure of sorting. The relevant formulae are: $Md_\varphi = \varphi_{50}$; $\sigma_\varphi = (\varphi_{84}-\varphi_{16})/2$, where φ_{50}, φ_{84} and φ_{16}, respectively represent the grain size of 50, 84, and 16% cumulative weight percentage, respectively.

The weight percentage of each grain size was measured, a histogram established, and the median phi value (M_φ) and graphical standard deviation (σ_φ) obtained. This method was used to compare the grain sizes of the samples collected at different locations to examine changes in the flow direction and transport mechanisms of the PDCs.

Microanalysis

The morphological characteristics of the PDC deposits were investigated at the microscopic level using microanalysis. This study used rock slice identification to examine the microstructure of the strongly welded rocks and large-particle pumices, and scanning electron microscope (SEM) to examine the surface characteristics of the small particle pumices. Microscopic analysis was used to identify the dynamic processes of the pyroclasts. A Carl Zeiss Axioskop 40 Polarizing Microscope was used to observe thin sections (magnification ranging from X5 to X150) in the CEA Key Laboratory of Seismic and Volcanic Hazards, Institute of Geology, CEA. Samples were analyzed using JEOL JSM-5610LV scanning electron microscope (SEM) in the SEM Laboratory of the Institute of Geology, Chinese Academy of Geological Sciences. The operation parameters included a 15 kV acceleration voltage, 10 μA electron current, and a magnification ranging from X100 to X2000. The SEM was operated between 15 and 25°C.

Whole-Rock Analysis

A whole-rock analysis was conducted to understand the geochemical composition of the pumices in the PDCs. Black and gray-white pumices were selected. The samples were tested in the laboratory of the Institute of Regional Geology and Mineral Resource Investigation in Hebei province, China. The instruments included an Axios^{max} X-ray fluorescence spectrometer, a P124S Electronic analytical balance, and Burettes. The analyses were conducted between 18 and 27°C.

Estimation of PDC Volume (V) in the Chinese Territory During the ME

The results of the topographic analysis and geological field survey around Tianchi volcano were based on the distribution of the PDCs. The PDCs were divided into four parts that include the plateau, shield, cone, and Yalujiang valley (**Figure 1D**). The area (A) and average thickness (AT) were calculated using the following equations:

(1) $V_{plateau} = A_{plateau} * AT_{plateau}$,
(2) $V_{shield} = A_{shield} * AT_{shield}$,
(3) $V_{cone} = A_{cone} * AT_{cone}$,
(4) $V_{Yalujiang} = A_{Yalujiang} * AT_{Yalujiang}$, and
(5) $V_{total} = V_{plateau} + V_{shield} + V_{cone} + V_{Yalujiang}$.

The above-mentioned formulas were used to calculate the PDCs volume during the ME in the Chinese territory.

RESULTS

Geomorphological Characteristics of Tianchi Volcano

The characteristics of the PDC deposits during the ME are closely related to the original geomorphology of Tianchi volcano. This

section explores the topography of Tianchi volcano and PDC deposits in different landforms.

Slope Characteristics of the Cone, the Lava Shield, and the Lava Plateau

The cone, lava shield, and lava plateau differ in slope because of different causes of formation. This study distinguishes between these three using the slope difference.

At least four eruptions occurred in the cone-forming stage of Tianchi volcano (Liu, 2000; Fan et al., 2006; Wei, 2014) and formed composite cones. The terrain of the cone fluctuates significantly, with a gentle slope at the bottom of the cone, reaching 30° near the caldera, and an average slope generally greater than 6° (**Figure 2**). The altitude of the cone base is above 1500 m, which is consistent with Luan (2008) and has an average distance of less than 10 km from the caldera.

The lava shield terrain is less undulating, with an average slope of 2–5° and an altitude of 1000–1500 m (**Figure 2**). The average distance between the lava shield and the center of the caldera is 10–20 km, while outliers reach 25 km.

The lava plateau has a gentle terrain, with the distance to the center of the caldera that is typically greater than 20 km, an average slope less than 1°, and an altitude typically less than 1000 m (**Figure 2**).

Distribution of the PDCs on the Cone, Lava Shield, and Lava Plateau

The gully-type deposits on the cone are within 0–10 km from the center of the caldera. Furthermore, the deposits are mainly distributed in radial canyons near the cones, such as the Changbaishan, Sandaobaihe, and Shierdaobaihe valley on the northern slope, the Baiyunfeng valley on the western slope, and the Yalujiang valley on the southern slope (**Figure 1C**). PDC deposits were observed in the upper reaches of the Shiderdaobaihe valley (**Figure 3A**) and have a thickness between 1 and 4 m (**Figure 4**), whereas massive continuous PDC deposits were rarely observed on the surrounding mountain slopes.

Valley-type deposits on the volcanic shield are 10–20 km away from the center of the caldera. Furthermore, PDCs that were deposited in the valleys of the lava shield have an exposed

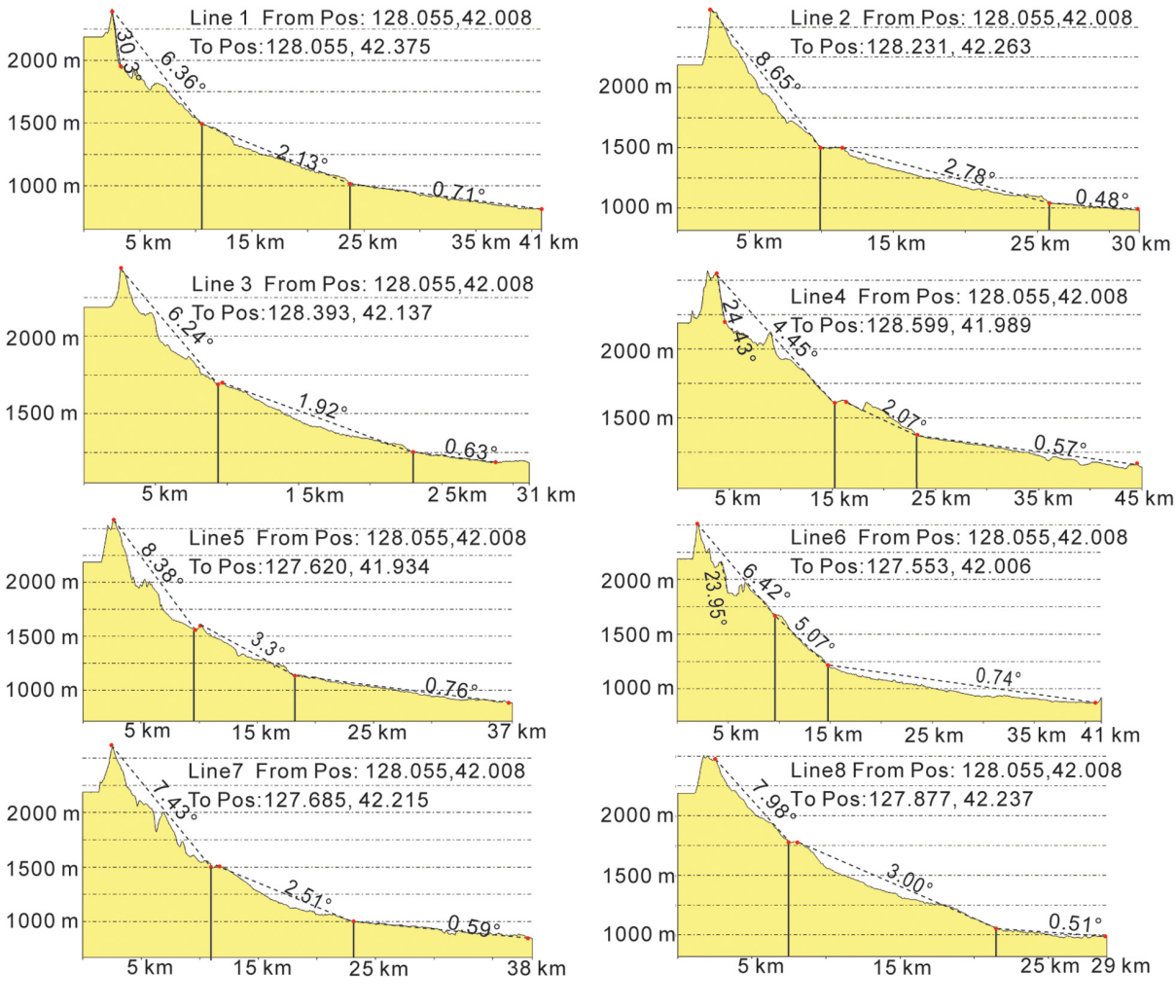

FIGURE 2 | Digital Elevation Model profile of the Alos30 image of the Tianchi volcanic cone, lava shield, lava plateau, and slopes (from line 1 to line 8).

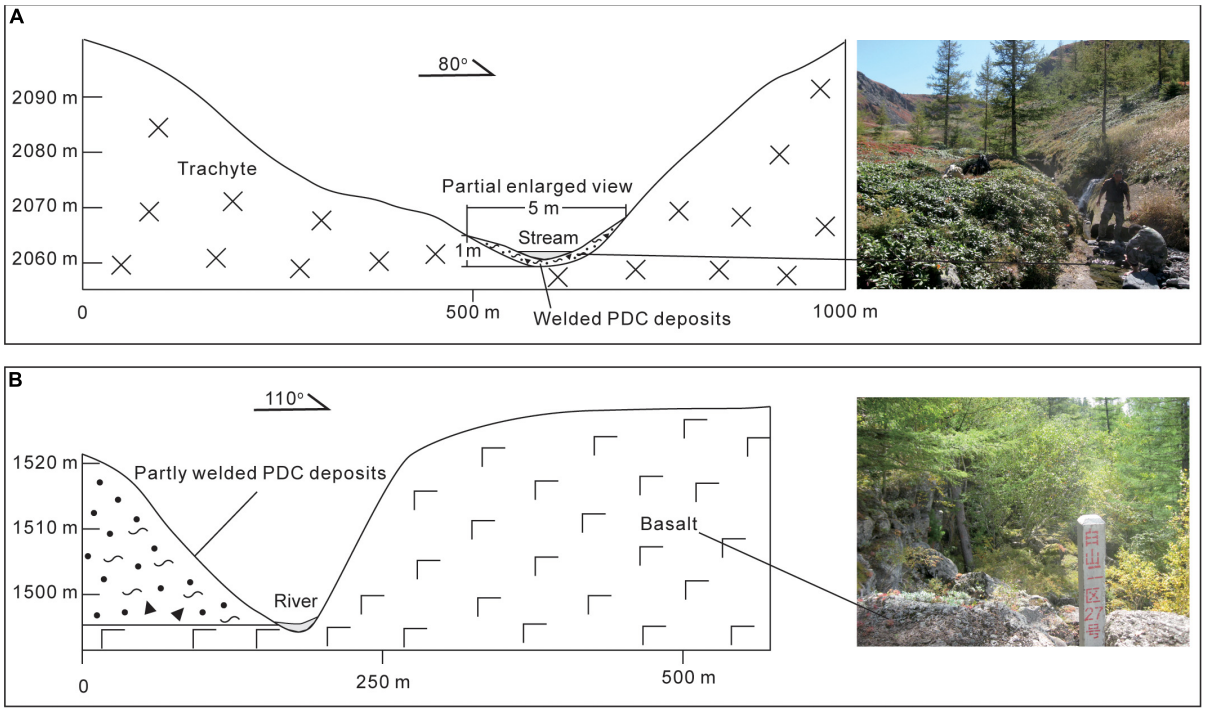

FIGURE 3 | (A) Schematic of the Shierdaobaihe gully-type deposits. **(B)** Schematic of Shierdaobaihe basalt valley deposits.

thickness between 10 and 20 m (**Figure 4**), whereas no massive PDC deposits were found on the basalt shield, at the top of the cliff (**Figure 3B**).

The lava plateaus constitute an area of open terrain and gentle slope. Fan-shaped deposits on the lava plateau are more than 20 km away from the center of the caldera, including two large fan-shaped deposits on the northeast and west sides. PDC deposits are typically less than 10 m thick in the exposed low land or river profiles (**Figure 4**).

The existence of volcanoes such as Wangtian'e and Baotaishan (**Figure 1C**) causes the landform in the southern part of Tianchi volcano to be more uneven than those in the northern and western slope, featuring numerous canyons. Influenced by the original terrain of the volcanoes on the southern slope, the PDC in the Yalujiang valley has valley branch-type deposits that have a maximum exposed thickness of 60 m.

In summary, PDC deposits are controlled by the original topography of Tianchi volcano. The thickest deposits were found in the lava shield, and thin deposits were found in the cones and lava plateaus. The PDCs rushed out of the canyon channel to form fan-shaped deposits in the lava plateau. The distribution of the PDCs during the ME shows that the PDC deposits radiate outwards from the center caldera, the periphery has a pyroclastic apron with at least two fan-shaped deposits, and the branch-type valley deposits are joined in a near-circular shape.

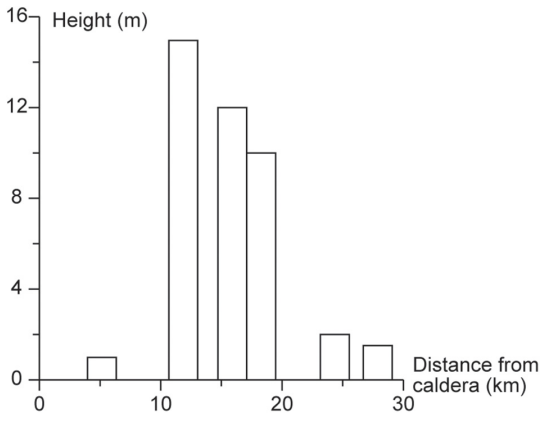

FIGURE 4 | Distribution of stratum thickness in the Shierdaobaihe valley.

Stratigraphic Characteristics of the PDCs in the ME

The preliminary analysis is divided according to the characteristics of the volcanic topography, PDC distribution patterns, and the PDC strata. Therefore, the ME PDC deposits were divided into three types: proximal deposits in the cone (0–10 km), medial deposits in the shield (10–20 km), and distal deposits in the lava plateau (> 20 km). This profile explores the structures of the proximal, medial, and distal PDC deposits.

Characteristics of the Proximal Strata

Proximal ME PDC deposits cover the peaks around the Tianchi caldera, parts of the mountain slopes that surround the cone, and the valleys.

(1) Stratigraphic characteristics of ME deposits in Tianchi volcano peaks

Fallout and spatter deposits are exposed at the different Tianchi volcano peaks. The stratigraphic characteristics of the Tianwen Peak and Baiyan peak on the northern slope, Baiyun Peak on the western slope, and Guanmian Peak on the southern slope are examined.

Tianwen Peak and Baiyan Peak are on the north side of the Tianchi caldera. Pumice strata can be seen at the Tianwen Peak, with colors from bottom to top ranging from gray, yellow, gray-white, to black (**Figure 5A**). Among them, gray and yellow pumices are considered to be eruptive products from 5,000 years ago (Liu et al., 1998; Yu et al., 2012). The gray-white pumices are ME rhyolites with a thickness of 10–20 m (Liu et al., 1998; Liu, 2000; Fan et al., 2005; Wei et al., 2007; Yu et al., 2012). The black trachyte pumices are considered to be the product of the 1702 eruption (**Figure 5B**; Liu et al., 1996; Liu, 2000; Wei et al., 2007). Baiyanfeng has a similar stratigraphic sequence (**Figures 5C,D**).

Fan-shaped gray-white pumice deposits, with an exposed thickness of 2–4 m exist on the outer slope of the Baiyun Peak which is located on the west side of Tianchi volcano (**Figure 5E**). The fan-shaped deposits are surrounded by alpine meadows, and the gray-black ME deposits can be seen in the gullies on the edge of the meadows (**Figure 5F**).

Fallout ME pumice strata are observed at the Guanmian Peak with a gentle slope on the south side of Tianchi volcano and the outer sections (**Figure 5G**), which covered larger areas than that on the northern and western slope. The thickness of the exposed formation is 0.5–2 m. The primary composition of the formation consisted of gray-white pumices and a small amount of gray-black trachyte lithic (**Figure 5H**).

(2) Stratigraphic characteristics of the ME PDCs in the gullies near the Tianchi cone

The gullies that are within 10 km from the center of the Tianchi caldera and have ME PDC thicknesses between 1 and 4 m consist of three types of structures (i.e., eutaxitic and lava-like structures). Large-scale continuous PDC deposits rarely occur on the mountain slope surrounding the cone.

The PDC deposits are distributed in the stream gully at the bottom of the Shierdaobaihe valley on the northern slope of Tianchi volcano (profile point 08-5 on the Chinese-North Korean border, 42.029829°, 128.125317°). The PDC deposits are approximately 5.1 km away from the center of Tianchi volcano and extend roughly 1 km northward into China. However, this is not the case in North Korea. The stratum is typically 1–2 m thick and appears to be mostly gray, with a high degree of welding and eutaxitic structures (**Figures 6A,B**). The eutaxitic structures are mainly composed of gray, gray-black magma fragments, and brick-red lithic fragments. The magma fragments are stretched and directional (**Figure 6B**).

Profile 08-10 (42.013284°, 128.015645°) is located at Baiyunfeng valley on the western slope of Tianchi volcano and is 3.38 km away from the center of Tianchi volcano. The ME deposits have an uneven thickness and extend steadily along the gully. The stratum has lag breccias (**Figure 6C**) formed during the ME. Profile 08-10 is completely gray-black, has an exposed thickness of 3–4 m, has high volumes of lag breccias, a semi-angular shape, a particle-supporting structure, a typical grain size of 60 cm, and maximum values reaching 1 m.

Profile 08-12 is located 100 m west of profile 08-10 and display different stratigraphic characteristics. The formation is completely gray-black and has a thickness between 4 and 5 m (**Figure 6D**). The stratum is divided into three parts. The upper part is 2–3 m thick and comprises welded tuffs containing breccias. The middle part is approximately 1 m thick and has parallel beddings with plastic flow characteristics (**Figure 6E**). There are bends in certain locations that were possibly caused by the secondary flow of fragmented magma falling to the ground, which serves as high temperature near the caldera. Under the parallel beddings there is a gray-black pumice-rich layer with bombs that have a gray-white fresh surface which is uncovered when smashed with a hammer (**Figure 6F**). The lower part consists of gray-black breccia tuffs that have a thickness of 1–2 m.

Profile 08-13 is located 30 m west of profile 08-12, without the intermediate bedding of profile 08-12 (**Figure 6G**). A stalactite-like structure has been found in the pumice-rich layer cavity (**Figure 6H**). The Stalactite-like structure hangs upside down, with a thick feature on the top and a thin feature on the bottom. The surface is rough. This is similar to stalactite. It is not common in the proximal deposits. Compared with lava stalactites (Corsaro et al., 2005), the structure has a rough surface, does not originate from the lava flow, and is probably related to volcanic ash dribbling in the cavity.

Characteristics of the Medial Strata

In the canyons 10–20 km away from the center of the Tianchi caldera, the medial strata generally have thick-bed deposits, irregular columnar joints, lithic-rich layers, pumice-rich layers, and welded layers.

(1) Columnar joints

Columnar joints developed in the Sandaobiahe valley on the northern slope of Tianchi volcano. Profile 08-31 (42.137471°, 128.128201°) is 15.5 km from the center of Tianchi volcano and is a PDC river island formed as a result of river incision (exposed thickness of 4–5 m). The Sandaobaihe River runs along the west edge of the river island (**Figure 7D**). On the eastern edge of the river island (**Figure 7E**) the river channel has dried up. Columnar joints developed on both sides of the river island and have a strong degree of welding and weakening on both sides. Profile 08-30 shows that the river flows through the fissures or columnar joints formed during medial PDC cooling, thereby forming a river channel. Profile 08-32 (**Figure 7C**) is 500 m north of profile 08-31 and has an overall thickness between 8 and 10 m. The top layer consists of gray-yellow tephra. The middle part has irregular columnar joints, and the lower part has a groove that has been eroded by rivers. The columnar joints are narrower in the upper part and wider in the middle and lower parts. The degree of welding weakens from the middle to the upper and lower sides.

Profile 08-30 (42.125156°, 128.118694°) is located approximately 14 km away from the center of Tianchi

FIGURE 5 | Tianchi volcano peaks and strata. **(A)** Tianwen Peak on the northern slope. **(B)** White and black pumice at Tianwen Peak. **(C)** Baiyan Peak on the northern slope. **(D)** Stratigraphic profile of Baiyan Peak. **(E)** Gray-white pumice on the outer slope of Baiyun Peak. **(F)** welded agglomerate at the outer slope of Baiyun Peak. **(G)** Guanmian Peak on the southern slope. **(H)** pumice deposits at Guanmian Peak on the southern slope.

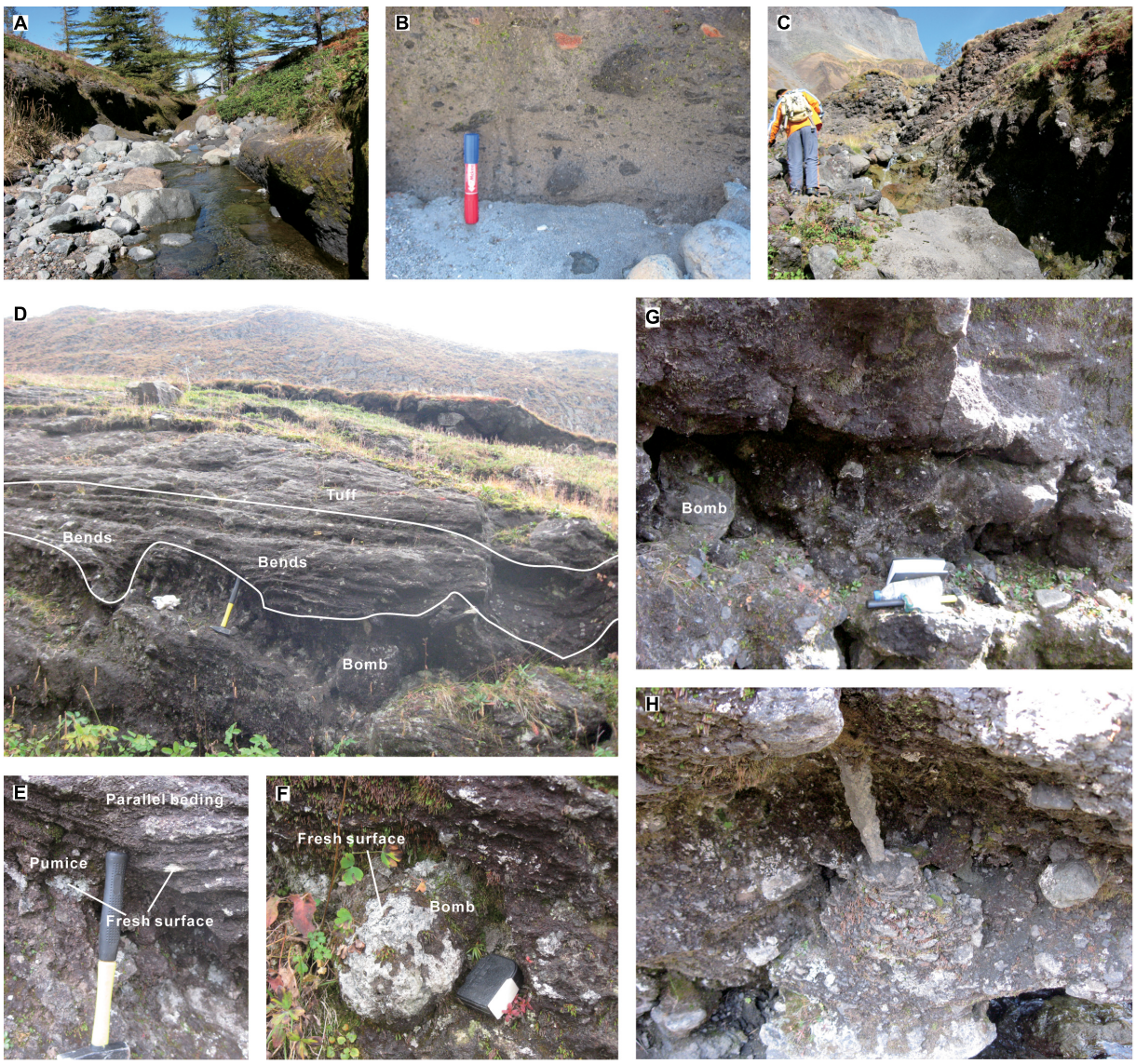

FIGURE 6 | (A) Deposits in the gullies of Shierdaobaihe valley. **(B)** PDC eutaxitic structures. **(C)** Profile 08-10 of Baiyunfeng valley. **(D)** profile 08-12 and plastic layers of Baiyunfeng valley. **(E)** Parallel bedding of profile 08-12. **(F)** Bombs in the profile 08-12. **(G)** Profile 08-13 of Baiyunfeng valley. **(H)** 08-13 stalactite-like structure.

volcano in the Sandaobaihe valley and has block structures with irregular shapes and different sizes, typically ranging from 0.4 to 1 m (**Figure 7A**). In the tracing process, we found that the block structures were formed through collapsed and strongly welded strata (i.e., columnar joints) because of the subsequent impact of the river and weathering (**Figure 7B**). The block structures are secondary features of the ME PDCs.

(2) Lithic-rich layers, pumice-rich layers, and welded layers

Profile 08-52 of Heishigou valley (42.058599°, 128.257290°) is located on the northern slope of Tianchi volcano and is 16.7 km away from the center of the caldera. The bottom of the PDCs is rich in lithic (**Figure 8A**). This formation is 30–40 cm thick, has no welding, and is supported by the tephra matrix. This formation has a massive amount of basalt and trachyte lithics. The grain size of a few lithics reaches 30 cm, and the long axis of the lithics typically points to one direction.

Profile 08-45 (42.134839°, 128.2°) of the Shierdaobaihe valley is located on the northern slope of Tianchi volcano and is 18.5 km away from the caldera. The formation is approximately 15 m thick. A lenticular pumice-rich layer (**Figure 8B**) was found at the base with a thickness of approximately 2 m. The lens contains gray-black pumice and a little black ash that was probably obtained from the top deposits. The size of pumice is typically between 6 and 8 cm, with the largest particles reaching approximately 12 cm. Profile 08-46 is located 200 m north of

FIGURE 7 | (A) Block tuff structures in profile 08-30. **(B)** Irregular columnar joints and block tuff structures at the top of profile 08-30. **(C)** Irregular columnar joints in profile 08-32. **(D)** Columnar joints at the west edge of the River Island in profile 08-31. **(E)** Columnar joints at the east edge of the River Island in profile 08-31.

profile 08-45 and shows different stratigraphic characteristics. The stratum developed at least five welded layers (**Figure 8C**) that are common in the Yalujiang valley.

Profile 08-48 (42.16922°, 128.189882°) of Shierdaobaihe valley is located on the northern slope of Tianchi volcano and is 19.6 km away from the caldera. The compacted formation is completely gray-black. A long-strip pumice-rich layer (**Figure 8D**) exists in the middle of the profile and has an uneven thickness distribution of 0.5–1 m.

In summary, the stratigraphic structure of the medial PDC deposits has the following characteristics. (a) Columnar joints in the middle and upper reaches of the medial PDCs. The formation in the lower reaches of the medial PDCs has no welding. The degree of PDC welding decreases with distance from the caldera. (b) The development of lithic-rich layers and pumice-rich layers shows a gravitational differentiation effect.

Characteristics of the Distal Strata

The distal strata of the lava plateau mainly consist of loose deposits of gray and gray-white pumices. The stratigraphic structures mainly include climbing layers, coarse-tail layers, and ground surge layers. Additionally, reworked pyroclastic deposits occur in this area.

Profile 08-61 (42.111016°, 128.218616°) is located on the northern slope of Tianchi volcano and is 17.48 km from the center of the caldera. The PDCs cover the slope of Laofangzixiaoshan (LFZXS) volcano and form a climbing layer (**Figure 9A**). Profile 08-61 is ash cloud surge deposits supported

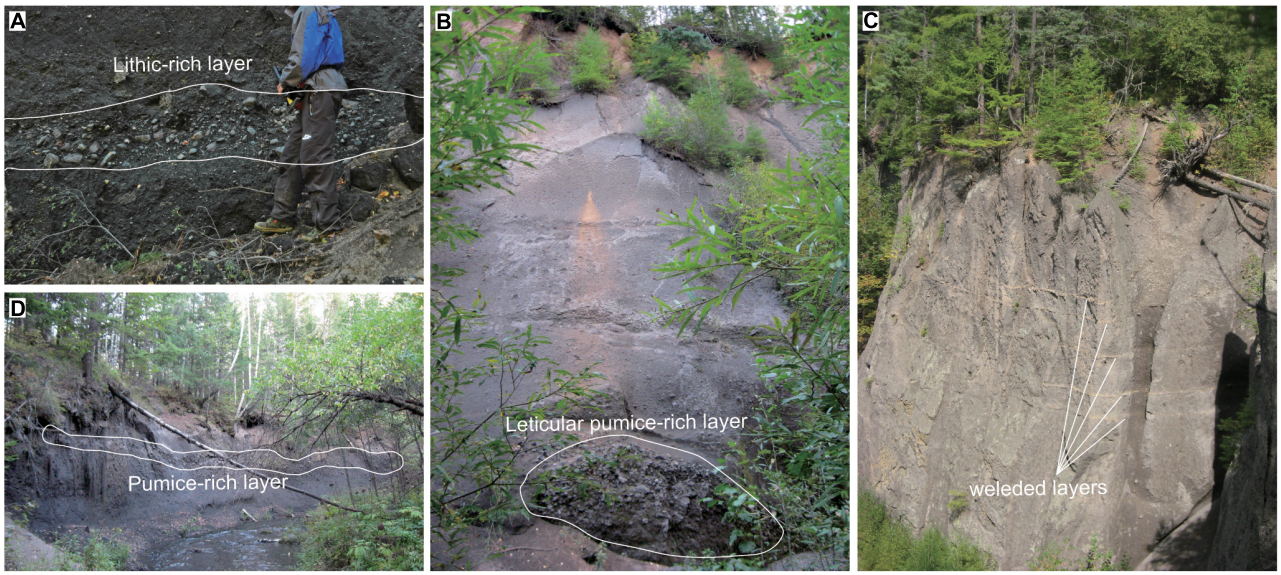

FIGURE 8 | (A) Profile 08-52 of lithic-rich layers. **(B)** Profile 08-45 of lenticular pumice-rich layers. **(C)** Profile 08-46 of welded layers. **(D)** Profile 08-48 of long-strip pumice-rich layers.

by a tephra matrix. The grain size is well sorted. Coarse-grained pumices are partially exposed, and have a size of approximately 3–4 cm. The stratum under the ash cloud is composed of brick red spatter deposits of LFZXS volcano. A definite boundary exists between the gray ash cloud layer and the ejected stratum of LFZXS volcano. The ash cloud climbed over LFZXS volcano.

Profile 08-62 (42.189783°, 128.227088°) is located on the northern slope of Tianchi volcano and is 24.8 km from the center of the caldera. Profile 08-62 has a typical coarse-tail layer (**Figure 9B**) with an exposed thickness of approximately 2 m. Profile 08-62 is completely supported by a gray-white matrix of ash that is roughly divided into 4 layers, from top to bottom. The first layer is rich in large-particle pumices and contains several plant roots. The size of the lithic is typically 6–8 cm in the upper part and gradually decreases to a grain size of 2–4 cm in the lower part. This shows the characteristics of a reverse graded bedding, with relatively concentrated coarse-grained pumices. The second layer consists of tephra deposits with a gas escape structure. The third layer consists of pumice deposits supported by the tephra matrix, which have typical pumice sizes of 2–4 cm. The fourth layer consists of tephra and contains a small amount of large-particle pumices, which have a larger grain size of approximately 3 cm.

Profile 08-29 (42.054684°, 127.659861°) of the distal PDCs is located to the west of Tianchi volcano, is approximately 33 km away from the center of the caldera, and shows cross and diagonal bedding (**Figure 9C**). The lower part is a layer rich in coarse-grained pumices with a thickness of approximately 50 cm and a long axis of 6–8 cm in length. Loose tephra is filled between the pumice layers.

Profile 08-70 (42.262282°, 128.168213°) is located on the northern slope of Tianchi volcano, is approximately 30 km from the center of the caldera and is a reworked pyroclastic layer. Profile 08-70 is similar to the base-surge stratum and has a parallel bedding and pumice-rich layer (**Figure 9D**). The pumice-rich layer has a granular structure, contains no ash, and has a high degree of roundness. The bottom of the pumice-rich layer contains a 0.5 cm thick yellow-brown soil layer, which extends smoothly. The lower part of the soil layer is the original PDC stratum.

Additionally, carbonized wood is common in the distal part. The largest outcrop of carbonized wood in the PDCs is on the southern slope, which has become a scenic spot for tourists to visit (**Figure 9E**).

In summary, the deposits in the distal strata are lighter in color (gray-white) and have loose deposits.

Granulometry

The grain-size distribution is essential when characterizing PDCs. In this study, the comparison of stratigraphic profiles, medial values, and histograms of the medial and distal PDCs of the Shierdaobaihe valley was established to investigate the variation in grain size and clastic composition. The strata analysis covered most of the PDC deposits, such as ash cloud, ground surge, and pumice-rich layers.

The histograms of the main flow unit of the PDCs, except for the ash clouds and ground surges, show a multimodal distribution (**Figure 10**). The median phi size (Md_{φ}) is between −2.5 and 3.25, and the histogram shows a non-uniform distribution. The sorting coefficient (σ_{φ}) is typically greater than 2 and includes poor sorting that has a skew-normal data range between −1.15 and 1.48, but no apparent total skewness. The kurtosis is mostly less than 1.

The histograms of the ash cloud are characterized by a unimodal distribution (**Figure 10**). The median phi size (Md_{φ})

FIGURE 9 | (A) Profile 08-61 of climbing layers. **(B)** Profile 08-62 of coarse-tail layers. **(C)** Profile 08-29 of ground surge layers. **(D)** Profile 08-70 of reworked PDC strata. **(E)** Outcrop of carbonized woods in PDCs.

is typically greater than 3, which indicates a concentration approaching that of fine particles. The sorting coefficient (σ_φ) is typically less than 2 and has an overall good sorting despite the poor sorting of individual cases, which may be caused by large-particle pumices in the bottom layer. Skewness values ranging between −0.23 and 0.2 demonstrate an overall negatively skewed distribution approaching that of fine particles. Most kurtoses are greater than 1 and have a higher spread ratio than that of the main flow unit of PDCs.

The histogram distribution of the ground surge layers is similar to that of the ash cloud deposits (**Figure 10**). The median phi size (Md_φ) is greater than 3, and the sorting coefficient (σ_φ) is less than 2. An adequate overall sorting is observed with a skew-normal data range between −0.23–0.2 and an overall negatively skewed distribution slightly approaching that of fine particles. The kurtosis is greater than 1.

The histograms of the pumice-rich layers show two protruding ends and a receding center (**Figure 10**). The pumice-rich layers are characterized by a dominant percentage of coarse grains and relatively large amounts of volcanic ash, rather than small amounts of medium-sized particles.

Microscopic Morphological Analysis

Microstructure Analysis

(1) Microstructure analysis of proximal pyroclasts

The internal structure of the pumices of the ME at the Tianwen Peak on the northern slope of Tianchi volcano is characterized by vesicular structures. Some pumice vesicles are heavily elongated and appear as thin lines with a parallel orientation (**Figure 11A**). Some vesicles are less elongated and appear in a lenticular shape (**Figure 11B**). A mixed structure was also observed that macroscopically appears as gray-white pumices, containing black lumps and microscopically appears as black pumices blended into gray-white pumices (**Figure 11C**). The boundary between the black part and the surrounding light-colored part is unclear, probably because of magma mixing.

FIGURE 10 | Profile, vertical medial, and histogram variation of medial and distal PDCs of Tianchi volcano.

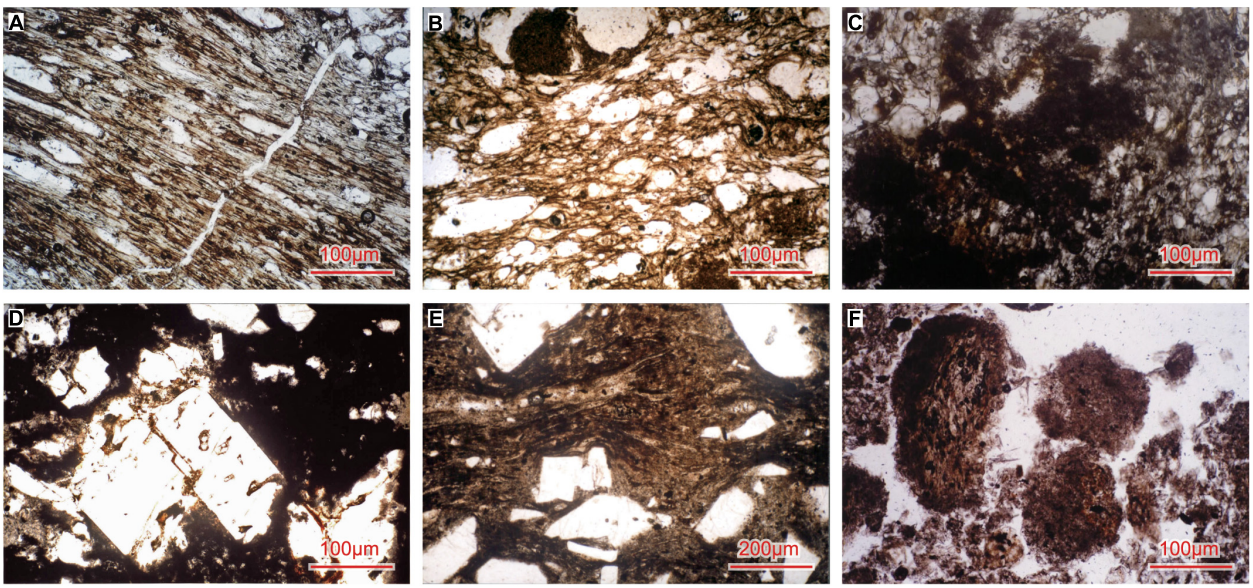

FIGURE 11 | (A) Stretched vesicular structure. **(B)** Lenticular-shaped stretched vesicular structure. **(C)** Welded structure of gray-white and black pumice. **(D)** Lava structure. **(E)** Tuffaceous structure. **(F)** Mud mass structure.

A sample of profile 08-5 of the ME PDC on the northern slope of Tianchi volcano shows breccia lava structures under a microscope (**Figure 11D**). This indicates that the proximal PDC deposits were partially formed by interstitial melt.

(2) Microstructure analysis of medial pyroclasts

Tuffaceous structures are typically developed in the medial strata (**Figure 11E**). The corrosion degree of crystal fragments is usually weak. The cementation consists of extremely fine ash, which is vitreous and different from lava cementation. This cementation is not as even as that of fast-cooling lava and demonstrates fibrous and needle-like vitreous forms under the microscope. The cementation of some samples shows curved directional strips.

(3) Microstructure analysis of distal pyroclasts

Mud masses are developed in the ash cloud layer of profile 08-61 on the northern slope of Tianchi volcano (**Figure 11F**). The strata appear to be earthy gray owing to the existence of mud masses (**Figure 9A**). Therefore, profile 08-61 has a different color from that of other distal profiles. Two reasons may account for the formation of mud masses: the first is *in situ* weathering, and the second is secondary transportation. The stratigraphic profiles indicate that the mud masses in profile 08-61 were formed as a result of *in situ* weathering.

Morphological Analysis

Samples for this ME morphological analysis were derived from profiles 08-45 and 08-62, 08-29, 08-70 of the PDCs, ground surge layers, and secondary pyroclastic strata, respectively. The SEM was used to observe the impact craters, cracks, and a large number of attachments on the surface of the PDC particles.

A "petal-shaped" impact crater was observed on the particle surface of the PDC profile 08-62 (**Figure 12A**). The fragmentation caused by the impact on the original surface has sunken into the interior of the particles, with appendages in the center and radial cracks spreading outwards. As the impact intensified, the fragments fell off and formed a near-circular impact crater (**Figure 12B**).

Fracture textures that formed as a result of quenching were observed on the clastic surface of the PDC and ground surge profiles. Cracks in the PDCs have a "linear" or "Y" shape (**Figure 12C**). Cracks in the ground surge layers resemble turtle shells (**Figure 12D**), consisting of a smooth surface, which turns outwards and almost covers the entire clast surface. Different shapes of cracks suggest an increasing quenching effect, which starts from "linear" to "Y" and progresses to a "turtle shell."

Volcanic ash in the PDCs has sharp edges, sharp corners, and numerous small particles attached to the surface (**Figure 12E**). The reworked ash is sub-angular in shape, and some samples appear rounded, with a few appendages on their relatively clean surface (**Figure 12F**).

Whole-Rock Analysis

A whole-rock analysis was used in to examine the composition of the black and gray-black pumices (magma fragment samples) from the proximal and medial strata and the gray-white pumice samples from the distal strata.

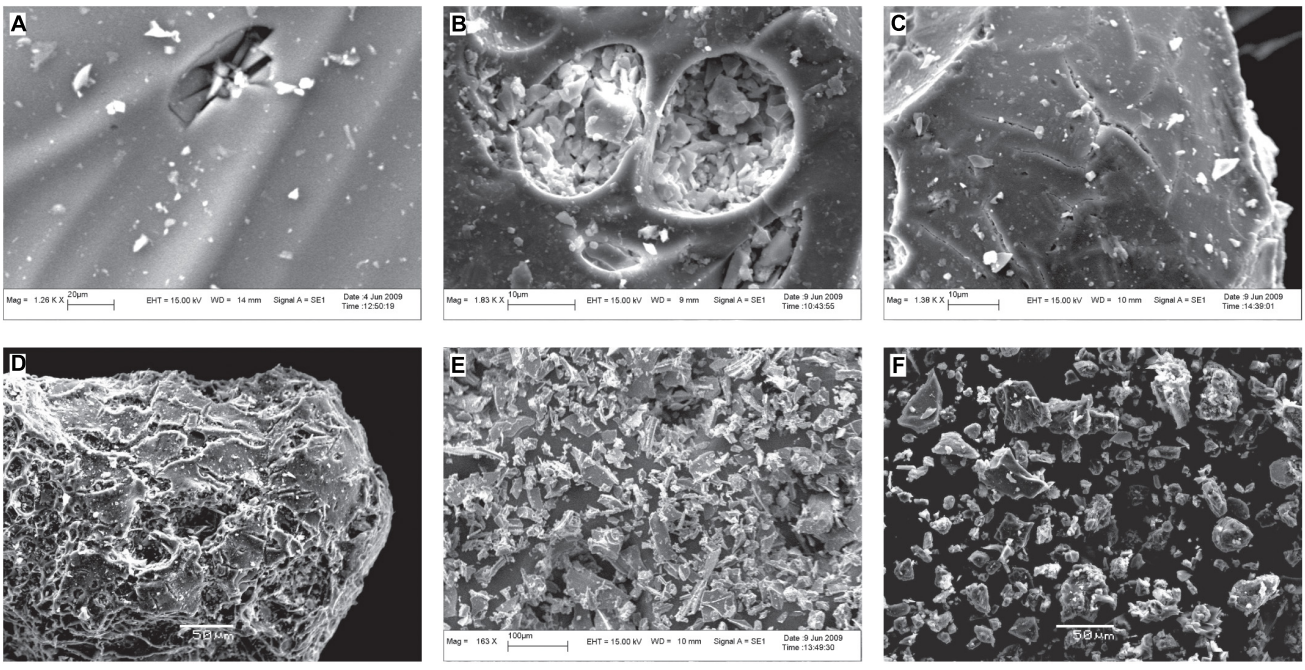

FIGURE 12 | (A) "Petal-shaped" impact crater. **(B)** Circular impact craters and appendages. **(C)** "Linear"- and "Y"-shaped cracks. **(D)** "Turtle shell" crack structure. **(E)** Ash morphology of PDCs. **(F)** Ash morphology of reworked deposits.

The total alkali-silica (TAS) diagram shows that the components of the gray-black pumice (magma fragment strips in the gray white pumice) at points 08-5, 08-45, and 08-52 in the Shierdaobaihe valley are projected in the trachyte zone. However, the components of the distal strata 08-29, 08-60, and 08-62 are projected in the pantellerite zone (**Figure 13** and **Table 1**). Shi et al. (2005) suggested that the white pumices that erupted during the ME are rhyolitic, and the black pumices are trachytic. Fan et al. (2005) proposed that the gray-black and gray-white ME pumices are the ejected products of the trachytic basaltic magma. The results of the TAS diagram in this study and the ME samples of Fan et al. (2005) and Shi et al. (2005) correspond well.

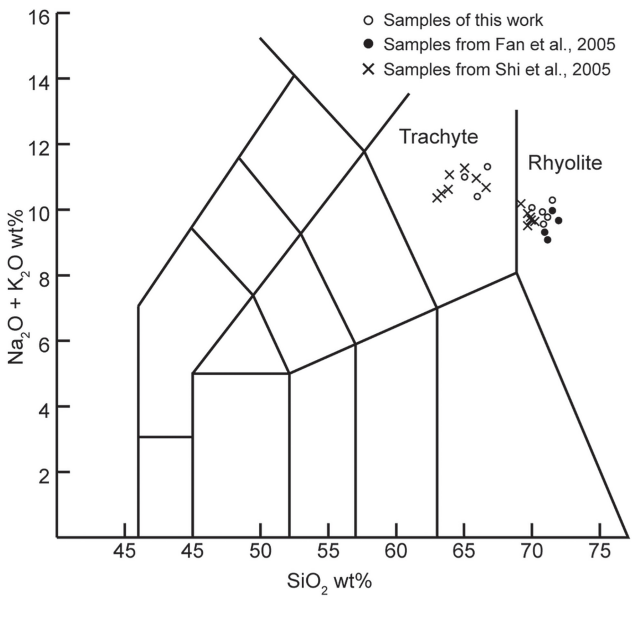

FIGURE 13 | Total alkali-silica diagram of pyroclastic rocks from the ME of Tianchi Volcano (Le Maitre, 1989).

TABLE 1 | Datasheet of the whole-rock test.

Major element	08-5	08-29	08-45	08-52	08-60	08-62
SiO_2	66.46	69.88	65.86	64.86	71	70.6
Al_2O_3	14.96	11.28	13.67	14.28	10.94	11.28
TiO_2	0.36	0.29	0.36	0.34	0.24	0.3
Fe_2O_3	2.11	1.91	2.37	2.29	1.81	2.06
FeO	2.37	2.71	2.68	2.73	2.56	2.63
CaO	1.04	0.77	1.23	1.12	0.5	0.58
MgO	0.19	0.15	0.19	0.18	0.11	0.14
K_2O	5.52	4.64	5.37	5.33	4.49	4.56
Na_2O	5.73	5.36	5.01	5.63	5.23	5.32
MnO	0.126	0.096	0.123	0.13	0.089	0.091
P_2O_5	0.06	0.09	0.08	0.11	0.06	0.07
H_2O^+	0.25	1.92	2.52	2.12	2.08	1.78
H_2O^-	0.25	0.36	0.45	0.18	0.34	0.28
Loss	0.4	2.65	2.92	2.52	2.65	2.38
Total	99.33	99.83	99.86	99.52	99.68	100.01

Volume Estimation

The PDCs deposited during the ME contain two fan-shaped and valley deposits in the Yalujiang valley. The PDC areas were divided into four parts, including the plateau, shield, cone, and Yalujiang valley. The area and average thickness of these four parts were calculated and are listed in **Table 2**. The estimated volume of PDCs deposits in the Chinese territory during the ME was calculated to be approximately 7 km^3.

DISCUSSION

The volume of the PDCs in the Chinese territory is estimated at approximately 7 km^3. This value is close to the result of 8.5 km^3 from Liu and Xiang (1997a), but it is smaller than the result of 19.2 ± 2.6 km^3 from Horn and Schmincke (2000). The difference between this work and Horn and Schmincke results is probably due to two factors. Firstly, according to Horn and Schmincke (2000), the volume estimate probably included the PDC and proximal tephra deposits in North Korea. Secondly, Horn and Schmincke (2000) reported that the PDC covered a half area to the north around the caldera. However, according to our field work, the distribution of PDC is just like a fan shape in the north, which is smaller. The volume estimations of fallout tephra during ME vary from 83 to 120 km^3 (Liu and Xiang, 1997a; Horn and Schmincke, 2000; Yu et al., 2012). Although a big difference in the tephra volume estimations exists, it is widely accepted that the total volume is about 100 km^3 (Wei, 2010; Yu et al., 2012; Pan et al., 2017a). The 1991 eruption of the Pinatubo volcano produced 3.3–4.4 km^3 tephra and was ranked among the five largest eruptions of the 20th century (Paladio-Melosantos et al., 1996). The 2010 eruption of the Merapi volcano produced 0.04 km^3 of PDC deposits and reached a distance of 16 km from the crater (Bignami et al., 2013). Therefore, the scale of the ME is much larger than that of these eruptive events.

The distribution of the PDCs during the ME shows that the palaeotopography influenced the emplacement of the PDCs (i.e., valley-filled deposits). Valley-filled PDC emplacements are common and have also been observed in the 2007 Soufrière volcano eruption (Wadge et al., 2014) and the 2010 Merapi volcano eruption (Bignami et al., 2013). Branney and Kokelaar (2002) proposed that PDCs from a large-volume eruption are minimally affected by the original surface topography, such as the Matahina ignimbrite volume of 120 km^3 of the Taupo volcanic zone (Bailey and Carr, 1994). The volume of the PDCs during the ME is approximately 7 km^3 in the Chinese territory, far less than the volume of the Matahina ignimbrite. Therefore, when considering volume, the PDC emplacement during ME did not get rid of the influence of the original

TABLE 2 | Parameters of the plateau, shield, cone, and Yalujiang valley.

Location	Plateau	Shield	Cone	Yalujiang valley	Total
A (km^2)	1366	152.5	45.8	8.4	1572.7
AT (km)	0.003	0.014	0.002	0.06	
V (km^3)	4.098	2.135	0.0916	0.504	6.9806

topography. The stratigraphic evidence shows that the ash cloud during the ME climbed over LFZXS volcano (**Figure 1D**). Ash clouds are turbulent, represent low-density flows, and can move independently (Cas and Wright, 1987). The unimodal distribution of the histogram shows a single transportation process of ash cloud deposits that was primarily in the form of a suspended transportation. The suspended transport of ash clouds floated over the LFZXS volcano and a part of it emplaced on the hill during the ME.

Temperature is an important physical parameter for PDCs. Blong (1996) proposed that the PDC temperature ranged from 100 to 900°C. The stratigraphic evidence shows that carbonized woods developed in the distal deposits during the ME. The carbonization temperature of wood is above 280°C. Columnar joints were discovered in the medial strata. Through the remanent magnetization analyses of lithic clasts, Wright et al. (2011) estimated the Cerro Galán PDC formation temperature of columnar joints to be above 630°C but below the glass transition temperature. Plastic behavior occurred in the proximal deposits. Zou et al. (2010) reported that the rhyolite magma of Tianchi volcano has a temperature of 740 ± 40°C. Therefore, the temperature of the PDCs during the ME probably ranged between 280 and 740°C, from the distal to the proximal deposits, respectively. In the 1997 Soufrière volcano eruption, the dilute and slow PDCs did not have enough kinetic energy to destroy the weaken buildings (Loughlin et al., 2002). However, the hot ash (> 300–400°C) set off the fire in the buildings and caused lethal burns on direct contact with the skin (Baxter et al., 2005). The same happened again in the 2010 eruption of Merapi volcano. People in the buildings did not survive in the relatively low temperature PDCs (250–300°C), partly because of the hot ash, floating into the buildings' interior through the vent (Jenkins et al., 2013). The run-out distances of PDCs in these two historical eruptive events did not exceeded 16 km (Loughlin et al., 2002; Jenkins et al., 2013). Temperatures above 280°C were maintained beyond 20 km from the Tianchi caldera; thus, the destruction potential of the PDCs associated with the ME must have been remarkable.

The fallout tephra and spatter deposits from the ME remained at the Tianchi Peaks in Chinese borders and have a relatively low thicknesses, which is probably due to three factors. Firstly,

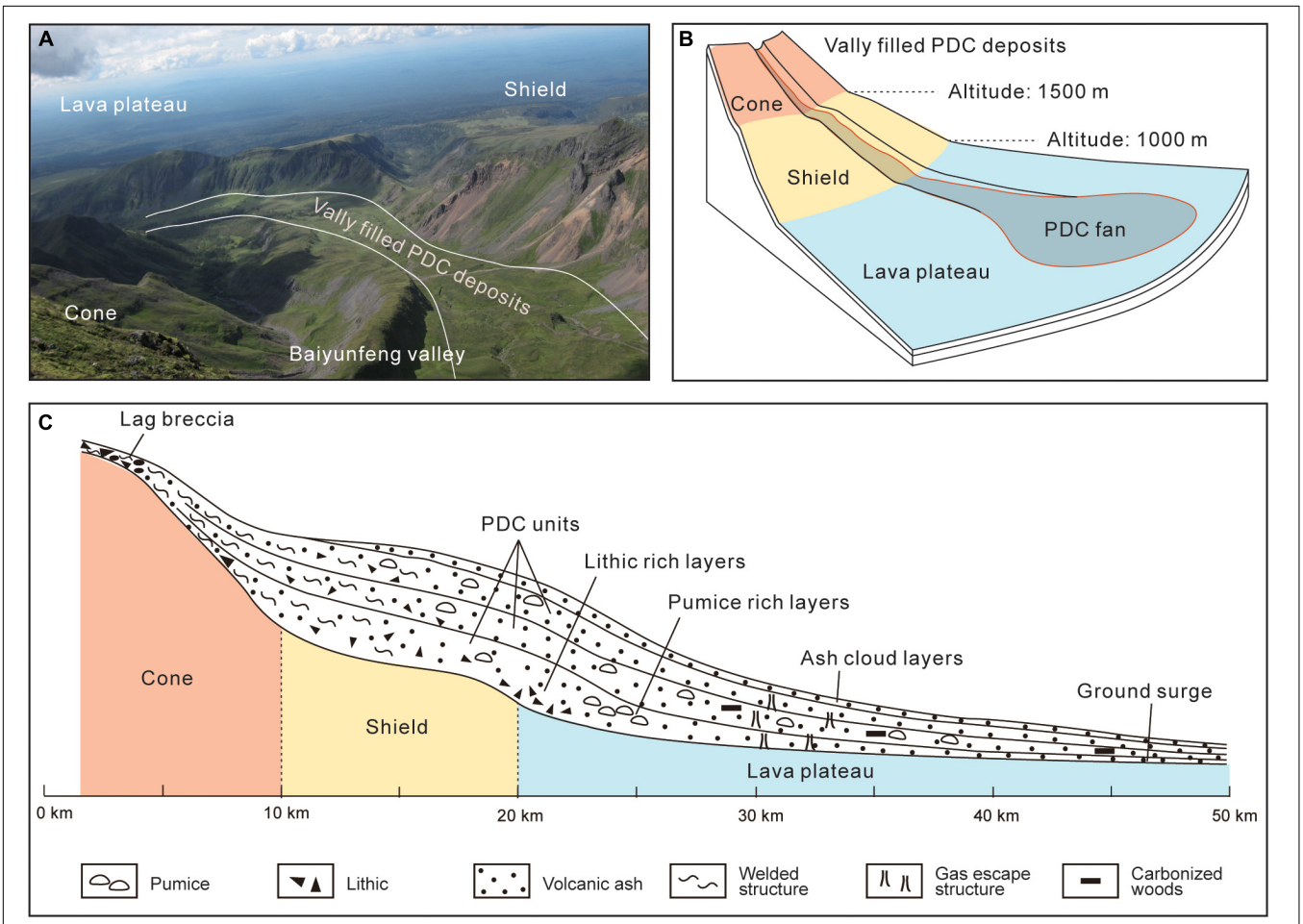

FIGURE 14 | (A) Picture of Baiyunfeng valley. **(B)** Schematic of the PDCs deposition in different terrains of Tianchi volcano. **(C)** PDC facies model of the ME of Tianchi volcano.

the wind was primarily directed toward the east, with a season-dependent intensity (Yu et al., 2013). Fallout tephra heavily accumulated in North Korea because of the wind direction. Secondly, the inclined eruption column could result in an uneven thickness. Thirdly, numerous eruptions occurred, where later eruptions eroded the material and mountain peaks of the earlier ones.

The black pumice at Tianwen Peak was supposed to be the product of the 1702 eruption (Liu et al., 1996). However, Pan et al. (2017a) proposed that the black pumice strata are from the ME. The stratigraphic evidence shows that no apparent discontinuity exists between the gray-white pumice and the black pumice strata at the Tianwen peak (**Figures 5B–D**). The stratum in Baiyunfeng valley near the caldera turns from welded tuff to plastic beddings, then turning to welded tuff with bombs (**Figure 6D**). This stratigraphic evidence indicates a change during the ME, possibly with two eruption stages. The high-precision carbonized ages have been identified using the wiggle-match method, namely, A.D. 938–939 and 946 ± 3 (Yin et al., 2012; Xu et al., 2013). The carbonized woods reported in Yin et al. (2012) are from the north and south slopes, and carbonized wood reported in Xu et al. (2013) is from the west slope. The high-precision dating results also indicate a possibility that the strata of the carbonized wood are from different eruptive stages during the ME. The medial deposits have magma mixture characteristics (magma fragment strips in the gray-white pumice). However, most of the distal deposits are gray-white rhyolite, lacking evidence for a magma mixture. The above evidences show that the ME is likely to have at least two eruptive stages.

The grain-size distribution of the medial and distal strata in the PDCs shows a decrease in the median phi size (Md_{φ}) from top to bottom (**Figure 10**). Layers rich in lithics and large-particle pumices are mostly developed in the middle and lower parts (**Figures 8A–C**), which supports this result. However, this trend is affected by the physical properties of the clasts and the fluid properties of the PDCs. Pyroclasts with a high density and small particles are generally heavily affected by gravitational differentiation and are deposited at the bottom, such as lithic-rich layers. Pumices with a low density and large particles accumulate at the middle and upper parts in the distal stratum (**Figure 9B**). The turbulent movement of the ash cloud can carry large-particle pumices to the upper part. Lithic clasts increase when the thickness increases, while that of crystal clasts and glass clasts decreases. When the distance from the caldera increases, the content of lithics shows a decreasing trend (**Figure 10**). The changes in the content of lithics correlate with the vertical gravitational differentiation and the variation in the PDC density from the medial to the distal.

The PDCs during the ME, characterized by a large volume (approximately 7 km^3 in the Chinese territory), a high temperature (280–740°C), long run-out distances (50 km), and the ability to climb hills, experienced at least two stages, including an early rhyolite stage and a late trachyte stage. Magma mixing is common in the pumice. In China, Tianchi volcano is a famous scenic spot. Within 50 km around the volcano, there are three towns near the rivers with about 111,000 inhabitants (Ji, 2015). In 2019, about 2.47 million tourists visited Tianchi volcano park (Li, 2020). The strata of Tianwen Peak keep the evidence of several explosive eruptions (**Figure 5A**). Previous researchers proposed the ignimbrites forming stage of Tianchi volcano have occurred during the last 100,000 years (Jin and Zhang, 1994; Liu and Song, 1998; Liu, 2000). Although most of these eruptions lack clear age evidences, it is likely that the ignimbrite eruptions have some cycles. Nakada (2000) proposed that areas previously impacted by PDCs would be probably affected again in similar future eruptions. Therefore, the establishment of the PDC facies during the ME can guide the local government in construction planning and reducing hazardous affection of PDCs of potential future eruptions.

CONCLUSION

The ME PDCs form a pyroclastic apron that is thin at both ends and thick in the middle. When using the Tianchi caldera as the center, gully-type deposits formed within 0–10 km, valley-type deposits formed within 10–20 km, and fan-shape deposits formed within 20–50 km (**Figures 1D**, **14A,B**).

Stratigraphically, the PDC facies have the following characteristics. The proximal PDC deposits have eutaxitic and lava-like structures. The medial PDC strata include thick layer deposits, lithic-rich layers, pumice-rich layers, and columnar joints. The distal PDCs strata include coarse-tail layers, climbing layers, and ground surge layers. Gas escape structures also developed, among other structures. The degree of welding decreases with an increase in distance away from the caldera. The entire proximal strata are strongly welded in the vertical profiles, with a few being lava-like. The middle part of the medial strata is strongly welded and has a weakening welding degree at the upper and lower ends. The distal strata consist of loose deposits. Some of the distal deposits have been changed in to secondary lahar deposits by river flows.

The specific granulometric manifestation of the PDC facies are as follows: from the medial to distal strata, the change in media phi (Md_{φ}) indicates a decrease in the particle grain size; the reduction of the pyroclast content from the medial to distal strata demonstrates the gravitational differentiation of the PDCs.

The vertically lithofacies characteristics of the ME PDCs include (**Figure 14C**): lithofacies changes from welded tuffs of gray-black rhyolite with black trachytic components in the proximal deposits to partially welded tuffs of gray-black rhyolite (containing black trachytic components) in the medial deposits, followed by loose gray-white rhyolite in the distal PDC deposits.

The above results show that the PDC was a high-dense, high-energy fluid in the proximal strata with a low thickness. The PDC density decreases in the medial strata and had a weakened transportation that led to the formation of thick layers. An increasingly apparent gravitational differentiation effect was observed as the distance increases. The distal PDCs demonstrate strong fluidization characteristics and a density far lower than that of the proximal and medial strata, which shows a clear stratification.

The establishment of the PDC facies model assists in unraveling some PDCs emplacement processes, marked by a high

level of topography confinement, about 50 km runout distance, 280–750°C emplacement temperatures, and more than 7 km^3 volume, which provide insights of the PDCs destruction during the ME. In order to prevent potential PDCs hazard, newly constructed residential areas and tourism-related structures near Tianchi volcano should be at least 50 km away from the caldera, considering the effect of high temperatures and fire.

DATA AVAILABILITY STATEMENT

The raw data supporting the conclusions of this article will be made available by the authors, without undue reservation, to any qualified researcher.

AUTHOR CONTRIBUTIONS

BZ and JX: designing work plan. BZ and ZC: field geological survey and sampling. HY: microscopic rock slice identification and whole-rock analysis. BZ: scanning electron microscope (SEM) analysis. All authors contributed to the article and approved the submitted version.

FUNDING

This manuscript is jointly supported by the National Natural Science Foundation of China (41402299 and 41861144025) and the Fundamental Scientific Research Project of the Institute of Geology, China Earthquake Administration (IGCEA1516).

ACKNOWLEDGMENTS

The authors gratefully acknowledge the considerable effort by the editor and reviewers. Their valuable comments and constructive suggestions improved the manuscript substantially. The authors thank Professor Haiquan Wei and Professor Qingfu Yang for their guidance, the staff of Changbaishan Volcano Station and Longgang Volcano Station for their assistance in the field investigations, and Xiaomin Liao for the help of drawing.

REFERENCES

Bailey, R. A., and Carr, R. G. (1994). Physical geology and eruptive history of the Matahina Ignimbrite, Taupo volcanic zone, North Island, New Zealand. *J. Geol. Geophys.* 37, 319–344. doi: 10.1080/00288306.194.9514624

Baxter, P. J., Boyle, R., Cole, P., Neri, A., Spence, R., and Zuccaro, G. (2005). The impacts of pyroclastic surges on buildings at the eruption of the Soufrière Hills volcano, Montserrat. *Bull. Volcanol.* 67, 292–313. doi: 10.1007/s00445-004-0365-7

Bignami, C., Ruch, J., Chini, M., Neri, M., Buongiorno, M. F., Hidayati, S., et al. (2013). Pyroclastic density current volume estimation after the 2010 Merapi volcano eruption using X-band SAR. *J. Volcanol. Geotherm. Res.* 261, 236–243. doi: 10.1016/j.jvolgeores.2013.03.023

Blong, R. J. (1996). "Volcanic hazard risk assessment," in *Monitoring and Mitigation of Volcano Hazards*, eds R. Scarpa and R. I. Tilling (Berlin: Springer-Verlag), 675–698.

Branney, M. J., and Kokelaar, P. (2002). Pyroclastic density currents and the sedimentation of ignimbrite. *Lond. Memo. Geol. Soc.* 29–31, 115–118.

Cas, R. A. F., and Wright, J. V. (1987). *Volcanic Successions: Modern And Ancient*. London: Allen and Unwin.

Chen, X. W., Wei, H. Q., Yang, L. F., and Chen, Z. Q. (2017). Petrological and mineralogical characteristics of Tianchi Volcano, Changbai Mountain: implications for crystallization differentiation and magma mixing. *Acta Geoscientia Sin.* 38, 177–192. doi: 10.3975/cagsb.2017.02.11

Corsaro, R. A., Calvari, S., and Pompilio, M. (2005). Formation of lava stalactites in the master tube of the 1792-1793 flow field, Mt. Etna (Italy). *Am. Mineral.* 90, 1413–1421. doi: 10.2138/am.2005.1760

Cui, Z. X., Jin, D. C., and Li, N. (2000). The historical record discovery of 1999-1200 AD large eruption of Changbaishan tianchi volcano and its significance. *Acta Petrol. Sin.* 16, 191–193. doi: 10.3969/j.issn.1000-0569.2000.02.007

Cui, Z. X., Zhang, S. H., and Tian, J. (1997). The study on volcanic eruption and forest conflagration since Holocene in Changbai MT. *Geograph. Res.* 16, 92–97. doi: 10.11821/yj199701001

Druitt, T. H. (1998). Pyroclastic density currents. *Geol. Soc. Lond. Spec. Public.* 145, 145–182. doi: 10.1144/gsl.sp.1996.145.01.08

Dufek, J., Ongar, T. E., and Roche, O. (2015). "Pyroclastic density currents: processes and models," in *Encyclopedia of Volcanoes*, eds H. Sigurdsson, B. Houghton, S. R. McNutt, H. Rymer, and J. Stix (London: Academic Press), 617–629. doi: 10.1016/b978-0-12-385938-9.00035-3

Fan, Q. C., Liu, R. X., Wei, H. Q., Sui, J. L., and Li, N. (1999). Petrogeochemical characteristics of holocene eruption of Tianchi volcano, Changbai mountains. *Geol. Rev.* 45(Suppl.1), 263–271.

Fan, Q. C., Sui, J. L., Sun, Q., Li, N., and Wang, T. H. (2005). Preliminary research of magma mixing and explosive mechanism of the millennium eruption of Tianchi volcano. *Acta Petrol. Sin.* 21, 1703–1708. doi: 10.3321/j.issn:1000-0569.2005.06.017

Fan, Q. C., Sui, J. L., Wang, T. H., Li, N., and Sun, Q. (2006). Eruption history and magma evolution of the trachybasalt in Tianchi volcano, Changbaisha. *Acta Petrol. Sin.* 22, 1449–1457. doi: 10.3321/j.issn:1000-0569.2006.06.001

Fan, Q. C., Sui, J. L., Wang, T. H., Li, N., and Sun, Q. (2007). History of volcanic activity,magma evolution and eruptive mechanism s of the Changbai Volcanic Province. *Geol. J. China Univers.* 13, 175–190. doi: 10.3969/j.issn.1006-7493.2007.02.004

Horn, S., and Schmincke, H. U. (2000). Volatile emission during the eruption of Baitoushan Volcano (China/North Korea) ca. 969 AD. *Bull. Volcanol.* 61, 537–555. doi: 10.1007/s004450050004

Inman, D. L. (1952). Measures for describing the size distribution of sediments. *J. Sedimentol. Petrol.* 22, 125–145.

Jenkins, S., Komorowski, J. C., Baxter, P. J., Spence, R., Picquout, A., Lavigne, F., et al. (2013). The Merapi 2010 eruption: an interdisciplinary impact assessment methodology for studying pyroclastic density current dynamics. *J. Volcanol. Geotherm. Res.* 261, 316–329. doi: 10.1016/j.jvolgeores.2013.02.012

Ji, L. Y., Xu, J. D., Lin, X. D., and Luan, P. (2009). Application of satellite thermal infrared remote sensing in monitoring Changbaishan tianchi volcano activity. *Seismol. Geol.* 31, 617–627. doi: 10.3969/j.issn.0253-4967.2009.04.005

Ji, W. N. (2015). *The Evacuation Planning Research For The Millennium Eruption In Tianchi Volcano, Changbai, Mountains*. Master's thesis, Ocean University of China, Qingdao.

Jin, B. L., and Zhang, X. Y. (1994). *Researching Volcanic Geology In Mount Changbai*. Yanbian: Korean Ethnic Education Press.

Jin, D. C., and Cui, Z. X. (1999). A study of volcanic eruptions in Tianchi volcano, Changbai Mountains recorded in historical documents. *Geol. Rev.* 45(Suppl.1), 304–307.

Kyong-Song, R., Hammond, J. O. S., Chol-Nam, K., Hyok, K., Yong-Gun, Y., Gil-Jong, P., et al. (2016). Evidence for partial melt in the crust beneath Mt. Paektu (Changbaishan), democratic people's republic of Korea and China. *Sci. Adv.* 2:e1501513. doi: 10.1126/sciadv.1501513

Le Maitre, R. W. (1989). *A Classification Of Igneous Rocks And Glossary Of Terms*. Oxford: Blackwell Scientific Publications.

Lesti, C., Porreca, M., Giordano, G., Mattei, M., Cas, R. A. F., Wright, H. M. N., et al. (2011). High-temperature emplacement of the Cerro Galán and Toconquis group ignimbrites (Puna plateau, NW Argentina) determined by TRM analyses. *Bull. Volcano.* 73, 1535–1565. doi: 10.1007/s00445-011-0536-2

Li, J. T., and Sun, G. M. (1996). Recent volcanic activity in Changbaishan and regional earthquakes. *Seismol. Geomagnet. Observ. Res.* 17, 31–38.

Li, L. (2020). *Jilin Changbaishan Mountain Protection Development Management Committee*. Available online at: http://www.changbaishan.gov.cn/shjj/tjxx/202001/t20200102_145727.html (accessed January 15, 2020).

Liu, G. M., Sun, H. Y., and Guo, F. (2011). The newest monitoring information of Changbaishan volcano, NE China. *Acta Petrol. Sin.* 27, 2905–2911.

Liu, J. Q., Chen, S. S., Guo, W. F., Sun, C. Q., Zhang, M. L., and Guo, Z. F. (2015). Research advances in the Mt. Changbai volcano. *Bull. Mineral. Petrol. Geochem.* 34, 710–723. doi: 10.3969/j.issn.1007-2802.2015.04.005

Liu, J. Q., and Wang, S. S. (1982). The formation age of Changbaishan Tianchi volcano. *Sci. Bull.* 21, 1312–1315.

Liu, R. X. (2000). *Active Volcanoes in China*. Beijing: Seismological Press.

Liu, R. X., Fan, Q. C., Zheng, X. S., Zhang, M., and Li, N. (1998). "The products of the recent eruption from Tianchi volcano," in *The Recent Eruption of Tianchi Volcano, Changbaishan*, ed. R. X. Liu (Beijing: Science Press), 40–82.

Liu, R. X., Li, J. T., Wei, H. Q., Xu, D. M., and Zhen, X. S. (1992). Volcano at tianchi lake, Changbaishan MT. - a modern volcano with potential danger of eruption. *Acta Geophys. Sin.* 35, 661–665.

Liu, R. X., Qiu, S. H., Cai, L. Z., Wei, H. Q., Yang, Q. F., Xi, Z., et al. (1997). A study on the last major eruption of Tianchi volcano in Changbai Mountain and its significance. *Sci. China* 27:437. doi: 10.3321/j.issn:1006-9267.1997.05.005

Liu, R. X., and Song, S. R. (1998). "The eruptive history of Tianchi volcano," in *the recent eruption of Tianchi volcano, Changbaishan*, ed. R. X. Liu (Beijing: Science Press), 40–82.

Liu, R. X., Wei, H. Q., Tang, J., Song, S. R., and Li, X. D. (1996). Progress of the study on Tianchi volcano, Changbaishan, China. *Seismol. Geomagnet. Observ. Res.* 17, 2–11.

Liu, X. (1999). Tectonic control of cenozoic volcanism in Northeastern China. *World Geol.* 2, 23–29.

Liu, X. (2006). Sequence and distribution of the pyroclastic deposits of the greatest Eruption of Changbaishan volcano during the period of history. *J. Changchun Univer. Sci. Technol.* 36, 313–318. doi: 10.3969/j.issn.1671-5888.2006.03.001

Liu, X., and Xiang, T. Y. (1997a). *Cenozoic Volcanoes In Northeast China and Their Hazards Of Pyroclastic Deposits*. Changchun: Jilin University Press.

Liu, X., and Xiang, T. Y. (1997b). "Observation on the pyroclastic deposits from the 1000 years ago eruption of Tianchi volcano," in *The Volcanism And Human Environment*, ed. R. X. Liu (Beijing: Seismological Press), 14–20.

Liu, X., Xiang, T. Y., and Wang, X. K. (1989). Episodes of cenozoic volcanism in the Changbai Mountains area. *Jilin Geol.* 3, 30–41.

Loughlin, S. C., Calder, E. S., Clarke, A., Cole, P. D., Luckett, R., Mangan, M. T., et al. (2002). Pyroclastic flows and surges generated by the 25 June 1997 dome collapse, Soufrière Hills Volcano, Montserrat. *Geol. Soc. Lond. Mem.* 21, 191–209. doi: 10.1144/gsl.mem.2002.021.01.09

Luan, P. (2008). *A Study on Characteristics of Remote Sensing Images of Eruptive Products from the Tianchi Volcano in the Changbai Mountains*. Master's thesis, Institute of Geology, China Earthquake Administration, Beijing.

Machida, H., and Arai, F. (1983). Extensive ash falls in and around the Sea of Japan from large late quaternary eruptions. *J. Volcanol. Geotherm. Res.* 18, 151–164. doi: 10.1016/0377-0273(83)90007-0

Nakada, S. (2000). "Hazards from pyroclastic flows and surges," in *Encyclopedia Of Volcanoes*, ed. H. Sigurdsson (San Diego: Academic Press), 945–956.

Oppenhimer, C., Wacker, L., Xu, J. D., Diego Galván, J., Stoffel, M., Guillet, S., et al. (2017). Mult-proxy dating the 'millennium eruption' of Changbaishan to late 946 CE. *Q. Sci. Rev.* 158, 164–171. doi: 10.1016/j.quascirev.2016.12.024

Paladio-Melosantos, M. L. O., Solidum, R. U., Scott, W. E., Quiambao, R. B., Umbal, J. V., Rodolfo, K. S., et al. (1996). "Tephra falls of the 1991 eruptions of mount Pinatubo," in *Fire and Mud: Eruptions and Lahars of Mount Pinatubo, Philippines*, eds C. G. Newhall and R. S. Punongbayan (Seattle: University of Washington Press), 513–535.

Pan, B., De Silva, S. L., Xu, J. D., Chen, Z., Miggins, D. P., Wei, H., et al. (2017a). The VEI-7 Millennium eruption, Changbaishan-Tianchi volcano, China /DPRK: new field, petrological, and chemical constraints on stratigraphy, volcanology, and magma dynamics. *J. Volcanol. Geotherm. Res.* 343, 45–59. doi: 10.1016/j.jvolgeores.2017.05.029

Pan, B., Fan, Q. C., Xu, J. D., Wu, C. Z., Chen, Z. Q., and Guo, F. (2017b). Magmatic processes of the Millennium eruption at Changbaishan Tianchi volcano, China/North Korea. *Acta Petrol. Sin.* 33, 163–172.

Pierson, T. C., and Major, J. J. (2014). Hydrogeomorphic effects of explosive volcanic eruptions on drainage basins. *Annu. Rev. Earth Planet. Sci.* 42, 469–507. doi: 10.1146/annurev-earth-060313-054913

Shi, L. B., Chen, X. D., Yang, Q. F., Wei, H. Q., and Lin, C. Y. (2005). Petrochemistry of pumices of various colors produced by eruption of Changbaishan Tianchi volcano at 1000 years ago. *Seismol. Geol.* 27, 73–82. doi: 10.3969/j.issn.0253-4967.2005.01.008

Stone, R. (2010). Is China's riskiest volcano stirring or merely biding its time? *Science* 329, 498–499. doi: 10.1126/science.329.5991.498-a

Sui, J. L., Fan, Q. C., Liu, J. Q., and Guo, Z. F. (2007). Mantle heterogeneity beneath Changbaishan volcanic province: evidence from geochemical study on trace elements and isotopes. *Acta Petrol. Sin.* 23, 1512–1520.

Sulpizio, R., Dellino, P., Doronzo, D. M., and Sarocchi, D. (2014). Pyroclastic density currents: state of the art and perspectives. *J. Volcanol. Geotherm Res.* 283, 36–65. doi: 10.1016/j.jvolgeores.2014.06.014

Tang, Y., Obayashi, M., Niu, F. G., Grand, S. P., Chen, Y. J., Kawakatsu, H., et al. (2014). Changbaishan volcanism in Northeast China linked to subduction-induced mantle upwelling. *Nat. Geosci.* 7, 470–475. doi: 10.1038/ngeo2166

Wadge, G., Voight, B., Sparks, R. S. J., Cole, P. D., Loughlin, S. C., and Robertson, R. E. A. (2014). "An overview of the eruption of Sourfrière Hills Volcano, Montserrat from 2000 to 2010," in *The Eruption of Sourfrière Hills Volcano, Montserrat from 2000 to 2010*, eds G. Wadge, R. E. A Robertson, and B. Voight (London: Geological Society, London, Memoirs), 39, 1–39.

Wang, P. J., Jian, Y., Chen, C. Y., and Wang, Y. Q. (2013). Volcano-stratigraphy and volcanic architecture of the Changbaishan volcanos, NE China. *J. Jilin Univers.* 43, 319–339. doi: 10.13278/j.cnki.jjuese

Wang, Y. Q., Yu, H. M., Xu, J. D., Chen, Z. Q., and Zhao, B. (2019). A comparative study on the characteristics of two fallout pumices deposits from the millennium eruption of Tianchi volcano in Changbaishan area. *Seismol. Geol.* 41, 208–217. doi: 10.3969/j.issn.0253-4967.2019.01.014

Wei, H. Q. (2010). Magma upmoving process within the magma prism beneath the Changbaishan volcano. *Earth Sci. Front.* 17, 11–23.

Wei, H. Q. (2014). *Tianchi Volcano in the Changbai Mountains*. Beijing: Seismological Press.

Wei, H. Q., Hong, H., Sparks, R. S. J., Walder, J. S., and Bin, H. A. N. (2004a). Potential hazards of eruptions around the Tianchi Caldera lake, China. *Acta Geol. Sin.* 78, 790–794. doi: 10.3321/j.issn:1000-9515.2004.03.024

Wei, H. Q., Jin, B. L., and Liu, Y. S. (2004b). Some advance in the study of volcanic geology and a hazard analysis of Tianchi volcano. *Acta Petrol. Mineral.* 23, 305–312. doi: 10.3969/j.issn.1000-6524.2004.04.008

Wei, H. Q., Liu, G., and Gill, J. (2013). Review of eruptive activity at Tianchi volcano, Changbaishan, Northeast China: implications for possible future eruptions. *Bull. Volcanol.* 75, 1–14. doi: 10.1007/s00445-013-0706-5

Wei, H. Q., Liu, R. X., and Li, X. D. (1997). Ignimbrite-forming eruptions from Tianchi volcano and their climate effect. *Earth Sci. Front.* 4, 253–266.

Wei, H. Q., Liu, R. X., and Yang, Q. F. (1998). "Recovery of the dynamic process of ignimbrite formation in Tianchi volcano," in *The Recent Eruption of Tianchi Volcano, Changbaishan*, ed. R. X. Liu (Beijing: Science Press), 83–107.

Wei, H. Q., Wang, Y., Jin, J. Y., Gao, L., Yun, S. H., and Jin, B. L. (2007). Timescale and evolution of the intracontinental Tianchi volcanic shield and ignimbrite-forming eruption, Changbaishan, Northeast China. *Lithos* 96, 315–324. doi: 10.1016/j.lithos.2006.10.004

Wright, H. M. N., Lesti, C., Cas, R. A. F., Porreca, M., Viramonte, J. G., Folkes, C. B., et al. (2011). Columnar jointing in vapor-phase-altered, non-welded Cerro Galán Ignimbrite, Paycuqui, Argentina. *Bull. Volcano.* 73, 1567–1582. doi: 10.1007/s00445-011-0524-6

Wu, J. P., Ming, Y. H., Zhang, H. R., Liu, G. M., Fang, L. H., Su, W., et al. (2007). Earthquakes swarm acitivity in Changbaishan Tianchi volcano. *Chin. J. Geophys.* 50, 1089–1096.

Xu, J. D., Liu, G. M., Wu, J. P., Ming, Y. H., Wang, Q. L., Cui, D. X., et al. (2012). Recent unrest of Changbaishan volcano, Northeast China: a precursor of a future eruption? *Geophys. Res. Lett.* 39:L16305. doi: 10.1029/2012GL052600

Xu, J. D., Pan, B., Liu, T. Z., Hajdas, I., Zhao, B., Yu, H. M., et al. (2013). Climatic impact of the Millennium eruption of Changbaishan volcano in China: new insights from high-precision radiocarbon wiggle-match dating. *Geophys. Res. Lett.* 40, 54–59. doi: 10.1029/2012GL054246

Yang, Q. F., Li, J. T., Liu, R. X., and Sun, G. J. (1996). Physical mechanism of 750~960AD pumice-flow transport and deposit of Tianchi volcano, Changbajshan. *Seismol. Geomagnet. Observat. Res.* 7, 11–19.

Yang, Q. F., Shi, L. B., Zhang, Y., Chen, B., and Chen, X. D. (2007). Grain-size characteristics of the millennium pyroclastic flow deposits of Tianchi volcano and their geological implications. *Seismol. Geol.* 29, 480–491. doi: 10.3969/j.issn.0253-4967.2007.03.004

Yin, J. H., Timoth Jull, A. J., Burr, G. S., and Zheng, Y. G. (2012). A wiggle-match age for the millennium eruption of Tianchi volcano at Changbaishan, Northeastern China. *Q. Sci. Rev.* 47, 150–159. doi: 10.1016/j.quascirev.2012.05.015

Yin, J. H., Zheng, Y. G., and Liu, Y. X. (2005). The radiocarbon age of carbonized wood in Tianchi volcano, Changbaishan mountains and its implication. *Seismol. Geol.* 27, 83–88. doi: 10.3969/j.issn.0253-4967.2005.01.009

Yu, H. M., Wu, J. P., Xu, J. D., Lin, C. Y., Shi, L. B., and Chen, X. D. (2012). Microstructural characteristics of the Holocene pumice erupted from Changbaishan Tianchi volcano and their volcanological implications. *J. Jilin Univer.* 42(Suppl.3), 132–144.

Yu, H. M., Xu, J. D., Luan, P., Zhao, B., and Pan, B. (2013). Probabilistic assessment of tephra fallout hazard at Changbaishan volcano, Northeast China. *Nat. Hazards* 69, 1369–1388. doi: 10.1007/s11069-013-0683-1

Zhang, M. L., Guo, Z. F., Cheng, Z. H., Zhang, L. H., and Liu, J. Q. (2015). Late Cenozoic intraplate volcanism in Changbai volcanic field, on the border of China and North Korea: insights into deep subduction of the Pacific slab and intraplate volcanism. *J. Geol. Soc.* 172, 648–663. doi: 10.1144/jgs2014-080

Zhao, B., Xu, J. D., and Lin, C. Y. (2013). Study of distal pyroclastic-flow stratum from Tianchi volcano in 1215(±15)eruption: pyroclastic-flow over water. *Acta Geol. Sin.* 87, 73–81. doi: 10.1111/1755-6724.12031

Zou, H. B., Yang, Q. F., and Zhang, H. F. (2010). Rapid development of the great Millennium eruption of Changbaishan (Tianchi) volcano, China/North Korea: Evidence from U-Th zircon dating. *Lithos* 119, 289–296. doi: 10.1016/j.lithos.2010.07.006

Conflict of Interest: The authors declare that the research was conducted in the absence of any commercial or financial relationships that could be construed as a potential conflict of interest.

frontiers in Earth Science

ORIGINAL RESEARCH
published: 31 August 2020
doi: 10.3389/feart.2020.00348

Probabilistic Volcanic Hazard Assessment for Pyroclastic Density Currents From Pumice Cone Eruptions at Aluto Volcano, Ethiopia

Ben Clarke[1,2]*, *Pablo Tierz*[1,3], *Eliza Calder*[1] and *Gezahegn Yirgu*[4]

[1] School of GeoSciences, University of Edinburgh, Edinburgh, United Kingdom, [2] School of Geography, Earth & Environment, University of Leicester, Leicester, United Kingdom, [3] British Geological Survey, The Lyell Centre, Edinburgh, United Kingdom, [4] School of Earth Sciences, Addis Ababa University, Addis Ababa, Ethiopia

OPEN ACCESS

Edited by:
Derek Keir, University of Southampton, United Kingdom

Reviewed by:
Domenico M. Doronzo, Istituto Nazionale di Geofisica e Vulcanologia (INGV), Italy
Guillaume Carazzo, UMR7154 Institut de physique du globe de Paris (IPGP), France

***Correspondence:**
Ben Clarke
bac13@leicester.ac.uk

Specialty section:
This article was submitted to Volcanology, a section of the journal Frontiers in Earth Science

Received: *30 April 2020*
Accepted: *27 July 2020*
Published: *31 August 2020*

Citation:
Clarke B, Tierz P, Calder E and Yirgu G (2020) Probabilistic Volcanic Hazard Assessment for Pyroclastic Density Currents From Pumice Cone Eruptions at Aluto Volcano, Ethiopia. Front. Earth Sci. 8:348. doi: 10.3389/feart.2020.00348

Aluto volcano, in the Main Ethiopian Rift, is a peralkaline caldera system, which comprises conglomerations of rhyolite (obsidian) lavas and enigmatic pumice cones. Recent work at Aluto has found that pumice cone eruptions are highly unsteady, and form convective eruption plumes that frequently collapse to generate pyroclastic density currents (PDCs). We develop a methodology and present results for the first probabilistic volcanic hazard assessment (PVHA) for PDCs at a pumice cone volcano. By doing so, we estimate the conditional probability of inundation by PDCs around Aluto volcano, incorporating the aleatory uncertainty in PDC hazard. We employ a Monte Carlo energy cone modeling approach, which benefits from parameterization informed by field investigations and volcanic plume modeling. We find that despite the relatively modest eruptions that are likely to occur, the wide distribution of past vent locations (and thus the high uncertainty of where future vents might open), results in a broad area being potentially at risk of inundation by PDCs. However, the aleatory uncertainty in vent opening means that the conditional probabilities are lower (≤ 0.12), and more homogeneous, over the hazard domain compared to central-vent volcanoes (where conditional probabilities are often ≤ 1 close to the vent). Despite this, numerous settlements, amenities, and economically valuable geothermal infrastructure, lie within the most hazardous ($P(PDC|eruption) \geq 0.05$) regions of Aluto caldera. The Monte Carlo energy cone modeling approach provides a quantitative, accountable and defendable background and long-term PVHA for PDCs from Aluto. These results could be combined in the future with hazard assessments relating to tephra fall and/or lava to develop a comprehensive volcanic hazard map for the caldera. Following appropriate parameterization, the approach developed here can also be used to compute a PDC PVHA at other volcanoes where vent location is uncertain.

Keywords: PVHA, pyroclastic density current, hazard, energy cone, Monte Carlo, Ethiopia

1. INTRODUCTION

Pumice cone eruptions are some of the least studied forms of volcanic activity on Earth, yet represent the typical eruptive style at caldera volcanoes along the Main Ethiopian rift valley (Fontijn et al., 2018). They have also been documented on Mayor Island, New Zealand (Houghton and Wilson, 1989), and are characteristic of the more recent volcanism on Pantelleria, Italy (Orsi et al., 1989). Contrary to previous interpretations, the eruption of pumice cones has been found to be relatively intense, generating convective eruption plumes (Fontijn et al., 2018; McNamara et al., 2018; Clarke et al., 2019) that are liable to collapse and produce pyroclastic density currents (PDCs) (Hutchison et al., 2016c; Fontijn et al., 2018; Clarke, 2020). These eruptions are tentatively estimated to range from violent-strombolian or vulcanian, to sub-Plinian in intensity (McNamara et al., 2018; Clarke et al., 2019), but column heights, eruption volumes and eruption durations are still very poorly constrained for pumice cone eruptions (e.g., Fontijn et al., 2018). In Ethiopia, a rapidly expanding population (UNDP, 2018), in excess of 1 million people, live within 10 km of volcanoes (Aspinall et al., 2011). Many of these volcanoes have been associated with pumice cone eruptions, so in this setting, these are key eruption types to understand. Additionally, valuable economic and geothermal infrastructure is being developed near these sites (World Bank, 2016). The increasingly high exposure to volcanic hazards in Ethiopia (Vye-Brown et al., 2016), and the recent recognition of the potential hazards at these volcanoes (Fontijn et al., 2018; Clarke et al., 2019; Clarke, 2020), evokes an urgent need for quantitative, accountable, and defendable volcanic hazard assessment (e.g., Connor et al., 2001; Newhall and Hoblitt, 2002; Marzocchi et al., 2010; Calder et al., 2015).

Aluto is a peralkaline rhyolite caldera volcano in the Main Ethiopian Rift. Aluto lies 7 km SE of the town of Ziway, 5 km NE of Bulbulla town, and hosts a diffuse but significant population living on and around its edifice (**Figure 1**). Within the caldera itself, there is a school, and a developing geothermal power station (Teklemariam and Kebede, 2010; World Bank, 2016). To the west of the caldera, sits one of the world's largest rose farms (AfriFlora and Sher Ethiopia, 2017); which provides much of the employment in the area. There is an estimated 415,000 people living within 30 km of Aluto, but there is currently no mandated group responsible for the monitoring of volcanic activity in Ethiopia (Vye-Brown et al., 2016). Although the volcano has been the focus of some recent research activity (Biggs et al., 2011; Hutchison, 2015; Hutchison et al., 2015, 2016a,b,c; Samrock et al., 2015; Braddock et al., 2017; Gleeson et al., 2017; Iddon et al., 2017; Wilks et al., 2017; Fontijn et al., 2018; Hübert et al., 2018; McNamara et al., 2018; Clarke et al., 2019; Clarke, 2020; Iddon and Edmonds, 2020), and has recently shown signs of volcanic unrest (Biggs et al., 2011), there is currently no existing hazard assessment or hazard map for Aluto which could be used to mitigate risk during future episodes of unrest and/or eruptions. The most recent volcanism at Aluto, since at least 60 ka, is dominated by pumice cone eruptions, with the most recent known eruption at 400 $\pm$ 50 years ago (Hutchison et al., 2016c). In this work, we identify 96 vents which are visible at the surface on and around the Aluto edifice and, therefore, there is a wide area from which hazardous volcanic processes, such as PDCs or tephra fallout, could be sourced during future eruptions. These eruptions could impact proximal to medial ($< \sim$10 km) sectors around the volcano, endangering many of the aforementioned sites. PDCs are the dominant cause of fatalities during volcanic eruptions, particularly from 5 to 15 km from the vent (Brown et al., 2017). This, and the near ubiquitous presence of [qualitatively small-volume ($\ll$0.01 km^3)] ignimbrites within pumice cone eruption deposits (Clarke, 2020), emphasizes the need for a PDC hazard assessment for Aluto volcano.

By their nature, PDCs are complex and dynamic processes, and the final footprint that they inundate (one potential measure of their hazard) is the product of a large number of interacting variables; both internal (collapse height, volume, granulometry, temperature etc.), and external (topography, nature of the substrate etc.) (e.g., Branney and Kokelaar, 2002; Sulpizio et al., 2014). This complexity makes hazard assessment of PDCs very challenging, and is compounded by aleatory and epistemic uncertainty (e.g., Spiller et al., 2014; Neri et al., 2015; Tierz et al., 2016b, 2018; Sandri et al., 2018). Aleatory uncertainty (the uncertainty associated with the natural variation of processes from one event to the next. For example, tossing a coin), is inherent to all volcanic systems and processes. The distributed nature of vents at Aluto, and therefore uncertainty in the location of the next eruption, contributes to this aleatory uncertainty. Epistemic uncertainty (the uncertainty associated with a lack of knowledge of how a system operates. E.g., is the coin fair?) is, to a lesser or greater extent, present in our understanding of any volcanic system. This is particularly important for pumice cone eruptions, which we know relatively little about. Pumice cone eruptions at Aluto have only recently been studied in detail (e.g., Fontijn et al., 2018; McNamara et al., 2018; Clarke et al., 2019; Clarke, 2020), and their eruption has never been observed. Consequently, there are only semi-quantitative estimates of eruption magnitude (vulcanian to sub-Plinian; Fontijn et al., 2018; McNamara et al., 2018), in addition to qualitative assessments of eruption styles and processes (unsteady eruptions that frequently generate convective eruption columns and PDCs; Fontijn et al., 2018; Clarke et al., 2019). In order to account for and quantify such uncertainties, probabilistic volcanic hazard assessment (PVHA) (e.g., Newhall and Hoblitt, 2002; Aspinall et al., 2003; Marzocchi et al., 2004, 2010; Bayarri et al., 2009; Wolpert et al., 2018) is widely used, as it provides a more complete and accurate quantification of volcanic hazard compared to single-scenario, deterministic approaches. The aim of this work is to develop a PVHA of PDCs at Aluto, by using newly collected information on the nature of its PDCs (Clarke et al., 2019; Clarke, 2020) to constrain and develop upon some established quantitative methods previously applied to other volcanic systems (e.g., Tierz et al., 2016a,b; Sandri et al., 2018). More broadly, we aim to develop a methodology, which with appropriate parameterization, may be used at similar volcanoes world wide.

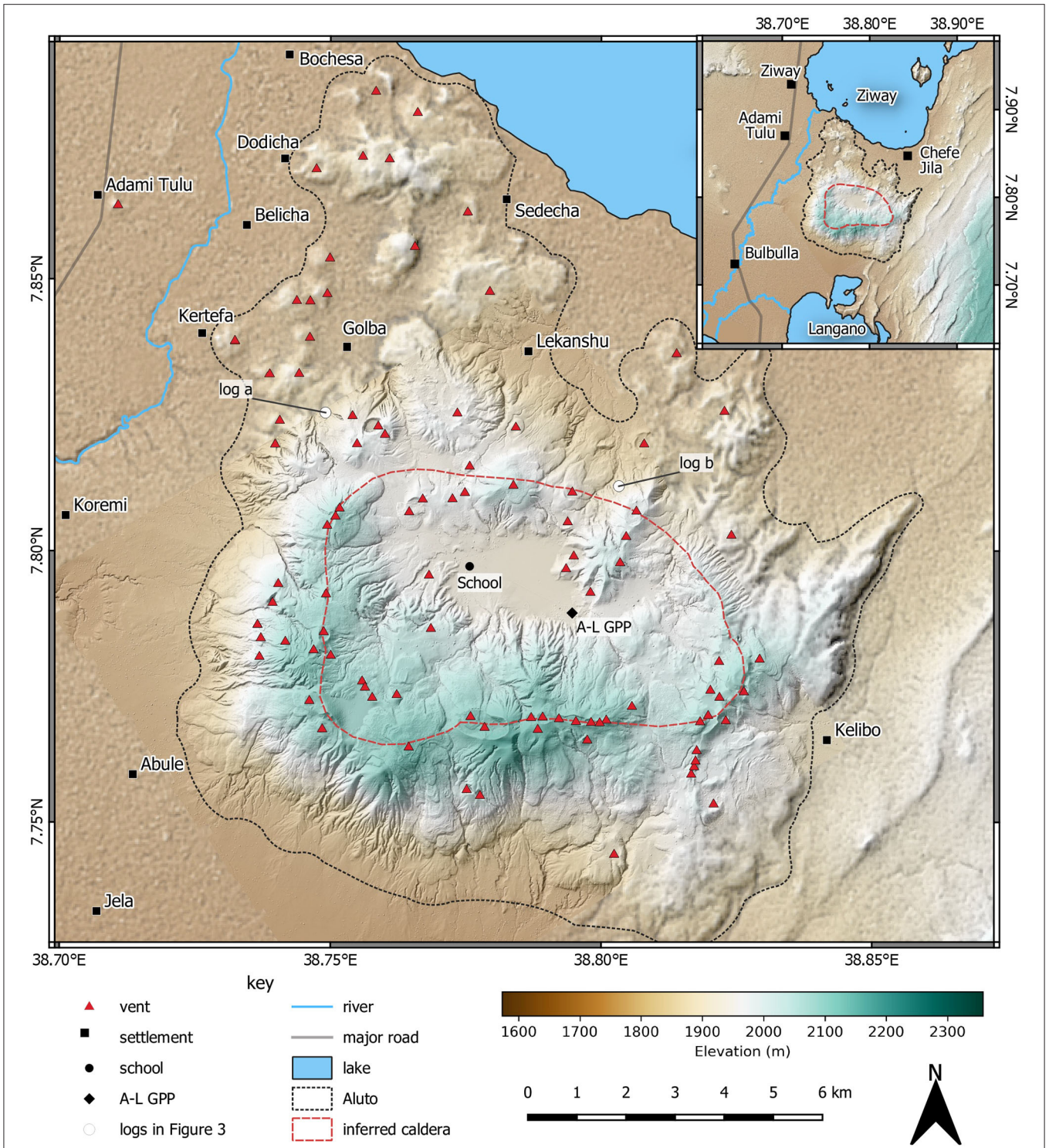

FIGURE 1 | Topographic and regional maps of Aluto volcano showing the location of the 96 pumice cone vents visible at the surface in context. The vents are most concentrated around the inferred caldera ring fault, and cross-cutting regional faults (not shown) around Aluto (Hutchison et al., 2015). The vents were identified from the LiDAR model of Hutchison et al. (2014) and field investigations detailed in Clarke (2020). Named settlements according to regional mapping data are provided, but are by no means exhaustive. "A-L GPP" = Aluto-Langano Geothermal Power Plant. Geodetic system/projection: WGS84/UTM Zone 37N (ESPG:32637).

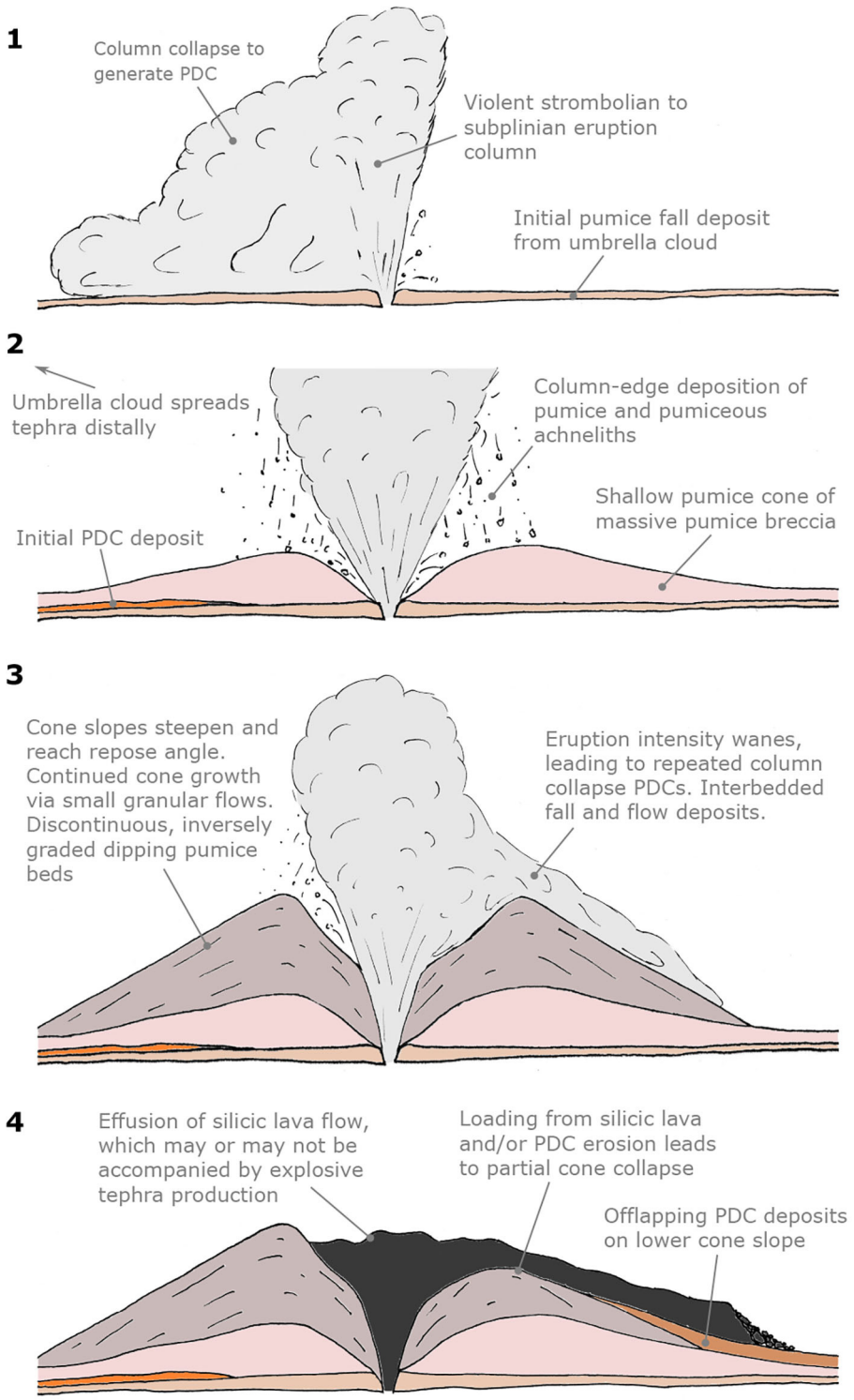

FIGURE 2 | A generalized sequence of a pumice cone eruption at Aluto constructed from the record of nine distinct, but similar, eruptions. Some eruptions begin with the generation of a convective plume producing relatively widespread tephra fall deposits that transition into PDC deposits as the column collapses. Most pumice cone forming eruptions at Aluto begin at stage 2, where a convective eruption plume is generated, and an increasingly steep-sided pumice cone is deposited around the vent from tephra falling from the column-edge, and ballistic deposition (Clarke et al., 2019; Clarke, 2020). As the eruption wanes, the column becomes unsteady, often generating multiple intercalated tephra fall and PDC deposits. The end of the eruption is marked by the emplacement of a silicic lava flow, which may or may not be accompanied by explosive tephra production. Column collapse PDCs are likely to be generated at stages 1 and 3. *After* Clarke (2020).

2. METHODOLOGICAL RATIONALE AND OVERVIEW

At Aluto, pumice cone eruptions have been found to undergo self-similar eruption sequences (**Figure 2**). Pumice cone eruptions at Aluto begin with an intense eruption plume-forming phase, during which the bulk of the pumice cone is deposited as tephra fall from the edge of the convective column, and from the accumulation of ballistic material around the vent (Clarke et al., 2019; Clarke, 2020). This is followed by a waning eruption intensity, and repeated column collapse, producing PDCs (**Figure 3**). This is shown by the frequent interbedding of PDC and fall deposits above the massive angular, clast-supported, cone-forming fall deposits. All the PDC deposits found so far at Aluto are consistent with generation by column-collapse (Clarke, 2020): PDC deposits are typically associated with underlying tephra fall deposits (**Figure 3**), comprise lithologically diverse lithic populations (indicating fragmentation at depth), and do not contain large dense blocks of fragmented lava-dome or plug (e.g., Fisher and Schmincke, 1984). PDC deposits at Aluto are almost exclusively massive lapilli tuffs (Clarke, 2020), indicating they were deposited from granular fluid based PDCs, where high particle density at the base suppresses turbulence and reduces the tendency to develop sedimentary structures (Branney and Kokelaar, 2002). PDC deposits are found proximally, in gullies cut into the sides of pumice cones, as well as further from the pumice cones themselves (found up to 5 km from the nearest possible source-cone). Here, PDC deposits are often present as gorge-filling deposits, and occasionally as sheet-like deposits with an areal coverage on the scale of a few km^2 (Clarke, 2020). The deposits are only sporadically exposed, and outcrops often intersect the reworked shores of palaeolake Langano, meaning that maximum PDC run-out and areal coverage are often minimum values. In summary, we can conclude that the PDCs typical of this phase of pumice cone eruptions are relatively low volume, granular fluid based pyroclastic density currents generated by eruption column-collapse, that are often valley-confined but occasionally spread laterally, and that often reach at least 5 km from the vent. The deposits of PDCs are found on or around most pumice cones that have been investigated at Aluto (Hutchison et al., 2016c; Fontijn et al., 2018; Clarke, 2020), and so as a conservative approach, we assume that all pumice cone eruptions at Aluto generate at least one column-collapse derived PDC, in other words: $P(PDC|eruption) = 1$. The final phase of pumice cone eruptions at Aluto [and at many pumice cones world wide; (e.g., Houghton et al., 1992; Dellino and Volpe, 1995; Gioncada and Landi, 2010)] is typified by the emplacement of a silicic (obsidian) lava flow from the central pumice cone vent. The source of the lava flow can be ascertained by the convergence of surface folds (ogives) to a bulls eye like distribution around the vent, usually accompanied by a dip or bump on the scale of $\leq$ 20 vertical meters, and $\leq$ 100 m in diameter. This is likely to be a surface expression of the underlying vent geometry, caused by the final effusion of an up-heaved dome or spine (bump), or a drain-back or foam-collapse into the conduit (dip) (e.g., Fink, 1983; Griffiths and Fink, 1993). The duration of pumice cone eruptions is poorly understood (Fontijn et al., 2018). Pyroclastic deposits from a single eruption at Aluto often grade continuously into one another (with the notable exception of the transition from pyroclastics to silicic lava flows), and where sharper transitions do occur, there is little evidence for the development of a significant erosional surface. This implies relatively continuous (though unsteady) eruptions; if the eruption is continuous at a violent-strombolian to sub-Plinian intensity, it is likely to last for a matter of hours or days, rather than months or years (Pyle, 2015). Duration of these eruptive episodes is clearly important from a hazard perspective, but this level of detail has rarely been incorporated into PVHA (e.g., Wolpert et al., 2018; Bebbington and Jenkins, 2019).

Though eruptions of pumice cones at Aluto appear to follow a similar sequence, they clearly span a range of magnitudes, producing pumice cones from 10 to 100s of meters tall (Hutchison et al., 2016c; Clarke, 2020), and depositing tephra fall to greater and lesser distances (Fontijn et al., 2018; McNamara et al., 2018). Additionally, distributed pumice cone eruption vents have been identified on and around Aluto (**Figure 1**) using the LiDAR digital terrain model (DTM) from Hutchison et al. (2014). Field evidence indicates that all of the 9 pumice cones investigated here are the product of single eruptions (Clarke, 2020). This means that recent silicic pumice cone eruptions at Aluto behave in a somewhat similar manner to a monogenetic field, where vent locations are expected to change from one eruption to the next and, therefore, the location of the next eruption is highly uncertain. These uncertainties (poorly constrained eruption magnitudes and intensities, and uncertain vent location) need to be robustly accounted for in the PVHA. Taking such first-order observations into account to produce a PVHA in a robust and quantitative manner is challenging, but nonetheless necessary, even for poorly studied volcanic systems. Often, hazard assessments and maps for such [and many other] volcanoes are based upon the geological foot print of prior hazardous phenomena, or the product of a modest number of deterministic numerical simulations based on a limited number of scenarios (Calder et al., 2015). Though these methods may represent a key starting point to estimate volcanic hazard, they fail to fully evaluate the aleatory and epistemic uncertainty, which are pervasive in volcanic systems (e.g., Marzocchi et al., 2010; Spiller et al., 2014; Tierz et al., 2016a,b). To generate a full PVHA of PDCs, there must be a sufficient number of PDC simulations to approximate the diversity and distribution of scenarios in nature. This presents a technical challenge, as often-used PDC simulation tools such as Titan2D (Patra et al., 2005), and VolcFlow (Kelfoun and Druitt, 2005; Kelfoun et al., 2017) are computationally expensive, allowing only a relatively limited number of runs to be performed in a reasonable time frame. Therefore, performing PVHA with such models requires the use of complex uncertainty quantification techniques such as Polynomial Chaos Quadrature (Dalbey et al., 2008; Tierz et al., 2018) or Gaussian Process emulators (Bayarri et al., 2009, 2015; Spiller et al., 2014; Wolpert et al., 2018; Rutarindwa et al., 2019). An alternative approach is to use a simple, less computationally expensive model that requires fewer assumptions to be made about the nature of the eruption. Such a model can then be applied in a Monte Carlo

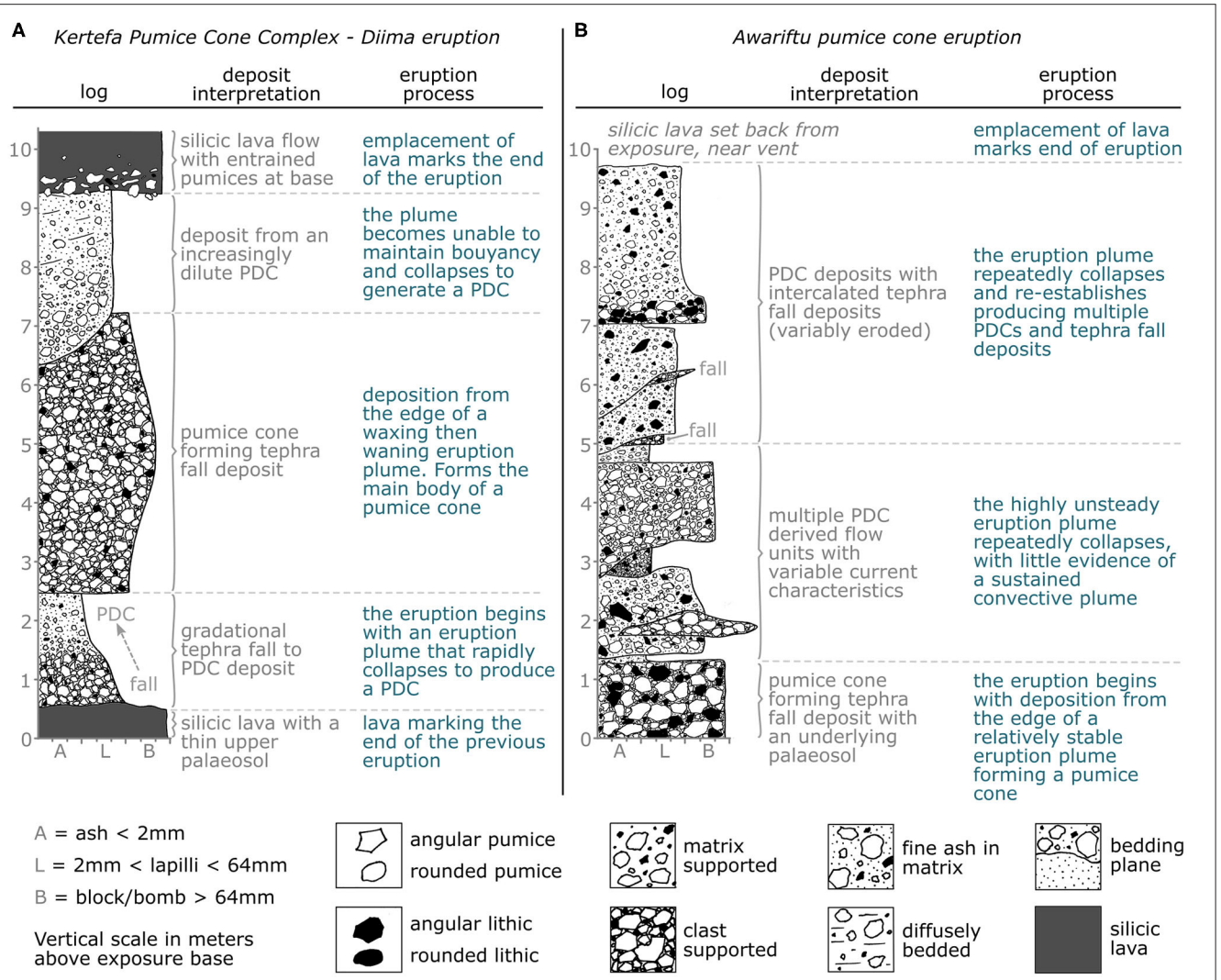

FIGURE 3 | Pyroclastic logs and interpretations from two of the 9 Aluto pumice cones investigated in Clarke (2020). **(A)** The deposits of the Diima eruption, part of the Kertefa Pumice Cone Complex. **(B)** Deposits of the Awariftu pumice cone on the northern flank of the caldera. The PDC deposits, and their close association with tephra fall deposits, are consistent with those often produced during eruption column collapse events. Interpretations from these, and the other 7 eruption reconstructions were used to develop the generalized pumice cone eruption scenario depicted in **Figure 2**.

fashion, covering the parameter space at every potential vent location in a computationally realistic time frame. Afterwards, importance sampling can be applied, where the knowledge and assumptions we make about the systems are used to "weight" the PDC model outputs according to how their respective likelihood is considered. This has the advantage of allowing the PVHA to be updated as knowledge improves, without necessarily having to re-run the PDC models. This is an approach which is also central to the work using statistical emulators, first proposed in Bayarri et al. (2009). A useful final product can be a map of the conditional probability of PDC inundation given an eruption. If the chosen PDC model produces some continuous measure of intensity, such as flow thickness or dynamic pressure, a hazard curve could be generated for each cell in a cartesian grid (e.g., Tonini et al., 2015; Tierz et al., 2018). However, for PDCs, hazard intensity is often considered to be binary (inundation vs. no inundation); owing to their almost ubiquitously destructive and deadly nature. Such a probability map, with a binary "intensity," is useful; as it displays the most important hazard metric for human survival from PDCs (inundation vs. no inundation). Whatever the intensity measure, such a map can be combined with exposure data, such as population distribution, or locations of interest or importance. Additionally, if the conditional probability of PDC inundation is combined with a temporal probability of eruption, and the probability of a PDC being produced given an eruption: the non-conditional probability of PDC inundation within a given time window can be calculated (e.g., Sandri et al., 2014, 2018; Bevilacqua et al., 2017; Rutarindwa et al., 2019). This, combined with the exposure data, allows the calculation of the non-conditional risk

(probability of asset X being lost due to PDC inundation over time period Y).

3. VARIABILITY IN VENT LOCATION

The wide distribution of vents around Aluto is evidence that eruptions are not restricted to a single central vent, and that the location of the next eruption is highly uncertain. This uncertainty must be reflected in the PVHA. If we can estimate the probability of the next eruption occurring at each cell of a grid of potential vent locations, this can be used to incorporate such uncertainty into the Monte Carlo outputs of a PDC model, which describe the uncertainty in PDC generation and propagation (e.g., Tierz et al., 2016a,b; Sandri et al., 2018). The distribution of existing vents at Aluto is not homogeneous, and collectively the vents indicate the presence of a caldera ring fault and cross-cutting region faults (Hutchison et al., 2015, 2016c).

We take a two-dimensional kernel density estimation approach, often applied to basaltic monogenetic fields, and based on the locations of existing vents (Connor and Hill, 1995; Weller et al., 2006; Marti and Felpeto, 2010; Cappello et al., 2012; Bevilacqua et al., 2015). The method assumes that the likelihood of an eruption occurring at any location should be proportional to its proximity to vents from previous eruptions. From any past vent, the probability of a new vent opening near it can be characterized by an isotropic two-dimensional kernel function, centered on the past vent, and which needs to integrate to 1 (i.e., it is a bivariate, Easting-Northing, PDF) (e.g., Connor and Hill, 1995; Weller et al., 2006). The kernel describes how the probability "decays" at progressively greater distances from each vent, in this case equally in all directions. For any point within the hazard domain (i.e., the grid of possible vent-location points) the probability of vent-opening associated with the kernel function of each existing vent is summed and normalized by the number of vents (N). This is in order to ensure that the probability of vent opening over the entire hazard domain is a PDF itself and, thus, integrates to 1. In other words, it is assumed that the conditional probability (given eruption) of a vent opening from one of the vents within the hazard domain is equal to 1 (e.g., Weller et al., 2006; Selva et al., 2012). The probability of an eruption occurring in a particular location is known as the relative "spatial intensity" of volcanism at that point ($\hat{\lambda}_s$); calculated using Equation (1):

$$\hat{\lambda}_s(x,y) = \frac{1}{2\pi N h^2} \sum_{i=1}^{N} \exp\left(-\frac{1}{2}\left[\frac{d_i}{h}\right]^2\right) \quad (1)$$

where N is the total number of existing vents, h is the bandwidth of the kernel, and d_i is the distance between existing vent i and point (x, y). The key variable that characterizes any volcanic field is therefore the bandwidth of the kernel. The model assumes that there is a characteristic spacing of vents at Aluto, which can be fitted by a Gaussian kernel (Connor and Hill, 1995; Weller et al., 2006). Within reason, the choice of kernel shape is relatively inconsequential (Wand and Jones, 1994; Weller et al., 2006), but the bandwidth of the kernel is very important. Following the procedure of Weller et al. (2006), we fit a Gaussian cumulative distribution function (CDF) to an empirical CDF of the nearest neighbor distances of existing vents at Aluto. Qualitatively, the Gaussian fit is good, and provides a bandwidth of 0.716 km, which means that approximately 68% of vents are within 0.716 km of their closest vent. However, it is likely that the closer a vent is to another, the greater the probability of its burial and obscuration, meaning it is less likely to be identified. This introduces an "exposure bias," and implies that the CDF of nearest neighbor distances presented here may under-represent the real proportion of vents at lesser distances. This is a source of epistemic uncertainty in this form of analysis.

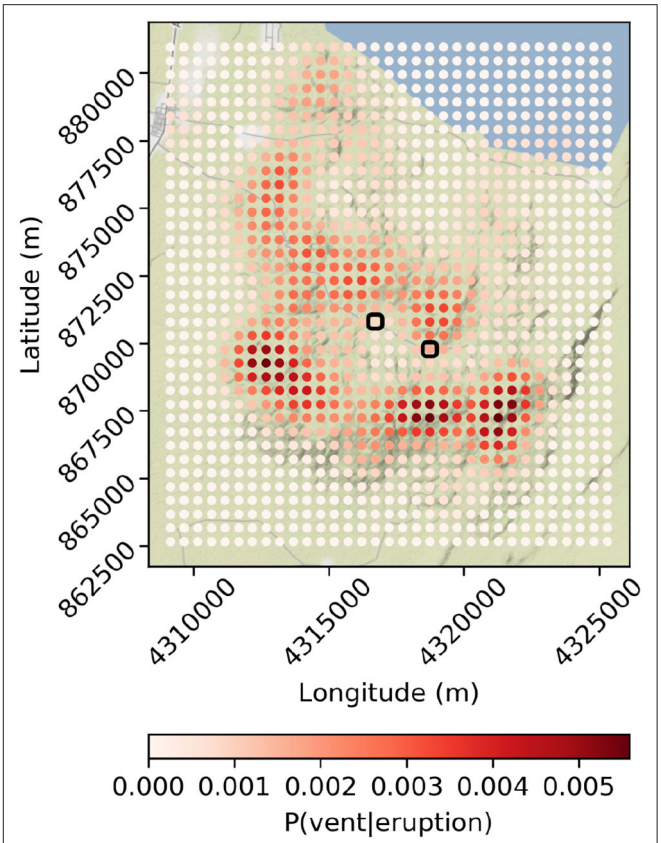

FIGURE 4 | The conditional probability of vent opening at each of the 1,221 simulated vent locations, where color is mapped to *P*(*vent*|*eruption*), using the kernel density estimation method of Connor and Hill (1995). The small black boxes mark the approximate locations of the school **(left)** and geothermal power station **(right)**. Coordinates are in meters, web mercator projection (ESPG: 3857).

We evaluate Equation (1) over the (x, y) locations of vents distributed in a regular 500 m cartesian grid across Aluto (1,221 vents), to calculate the probability of the next volcanic eruption occurring at each. The conditional probability of a vent opening at each point in this grid, given the next eruption at Aluto [$P(vent_i|eruption)$] is presented in **Figure 4**. The code used to do this is available as a fully reproducible Jupyter notebook (Zenodo/GitHub: https://doi.org/10.5281/zenodo.3778328). The sum of these probabilities is 0.995, meaning there is a 0.5%

probability that the next vent will open somewhere beyond these points. This map indicates that the southern and northern rims of the caldera, as well as a diffuse region to the NW of the caldera, are the most probable regions to host the next vent at Aluto. These probabilities are only for the *next* eruption at Aluto, as for subsequent eruptions, analyses will also have to consider the location of the new vents. These values of probability are used directly as weighting factors in the importance sampling of the Monte Carlo PDC model outputs later. Due to Aluto's proximity to Lake Ziway, some of these vents are located within the lake. The average water depth of Lake Ziway is about 2.5 m (Hengsdijk and Jansen, 2006). This is clearly below proposed thresholds of water depth (i.e. pressure) related to the suppression of subaerial pyroclastic products (e.g., Koyaguchi and Woods, 1996; Lindsay et al., 2010; Sandri et al., 2012, 2018). Therefore, we consider that all vent locations on the lake can generate column collapse derived PDCs. Moreover, even though we acknowledge that eruption dynamics of eruptive vents opening on the lake will likely be different than those on land (Mastin and Witter, 2000; Houghton et al., 2015) for the sake of simplicity in this first approach to PVHA of PDCs at Aluto, we model the PDCs from vents on the lake using the same PDC model parameter space as for the other subaerial vents.

4. VARIABILITY IN PDC INUNDATION

4.1. The Energy Cone Model

We choose the energy cone model (Malin and Sheridan, 1982) to evaluate binary PDC inundation footprints for the range of pumice cone eruptions at Aluto. This approach is suitable as it requires few input parameters (suitable for volcanoes where there is high epistemic uncertainty), and is computationally light, meaning that the full parameter space can be thoroughly explored to account for aleatory uncertainty, at a reduced computational cost. Monte Carlo energy cone analysis has been applied to other volcanic systems to produce PVHAs of PDCs, such as Campi Flegrei and Vesuvius (Tierz et al., 2016a,b; Sandri et al., 2018). The energy cone model (**Figure 5**) assumes a source (vent) location, a height from which the PDC collapses (H_c), and a single mobility parameter (ϕ) which in effect describes how rapidly the potential energy from column collapse is consumed during horizontal PDC propagation. In reality, the mobility of a PDC changes in space and time and is dependent on a large number of interacting phenomena; including, for example, the density current granulometry (e.g., Roche et al., 2006), degree of flow fluidization (e.g., Wilson, 1980; Breard et al., 2018; Smith et al., 2018), the development of co-ignimbrite plumes (e.g., Calder et al., 1997; Andrews and Manga, 2011), and the development of stratified and [in-part] decoupled mechanical/flow regimes within the current (e.g., Fisher, 1995; Branney and Kokelaar, 2002; Breard and Lube, 2017). In the energy cone model, all of these phenomena are integrated into a single (empirically defined) angle (ϕ). This angle can be conceptualized as the dip of a line connecting the PDC collapse source and the most distal reach of the PDC, where a more mobile PDC will have a shallower angle. One can then imagine projecting this line from the PDC source at every degree of azimuth, forming a surface

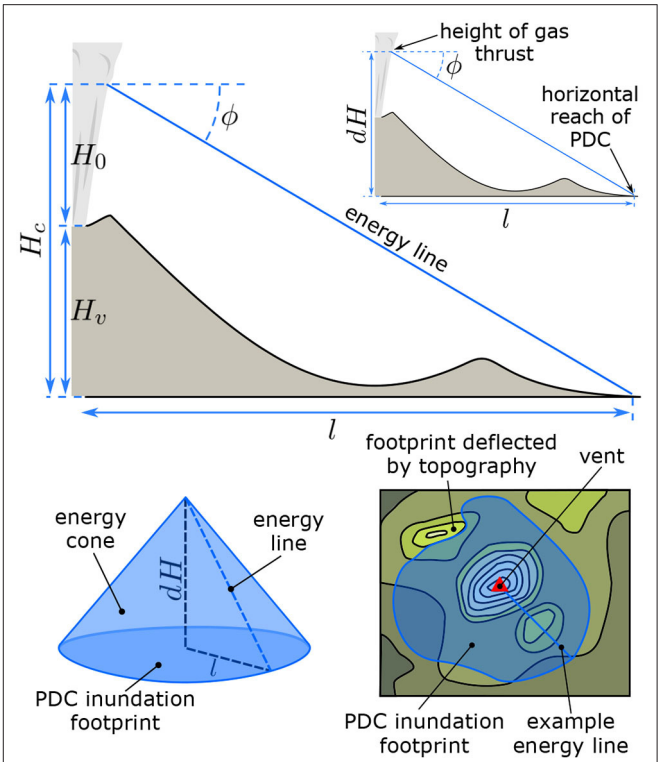

FIGURE 5 | The energy cone model of Malin and Sheridan (1982). Each PDC possesses a particular mobility (ϕ), derived empirically from dH and l of previous PDCs, and a estimated collapse height H_c, derived from the height of the vent (H_v) and the height of the gas thrust region (H_0). The point at which an energy line dipping at mobility angle ϕ intersects the ground marks the expected distal reach of the PDC at that degree of azimuth. This process is repeated at every degree of azimuth around the vent to form an energy cone and a radial PDC inundation footprint. The footprint is perfectly circular on a flat surface, but is irregular where it meets irregular topography.

or "energy cone." Where this line first intersects the surrounding topography marks the outer reach of potential PDC inundation, and the space within this polygon is the maximum potential PDC foot print. It essentially represents an aggregated foot print for flows in any direction, rather than a foot print for an individual flow. PDCs with a taller collapse height, and a greater mobility, have the potential to travel further. An important caveat of the energy cone model, given that is does not attempt to represent an individual flow footprint, is that it does not consider flow channelization of PDCs, which is known to be an important factor controlling the footprint of smaller volume, drainage-confined, concentrated PDCs (e.g., Calder et al., 1999; Douillet et al., 2013; Di Roberto et al., 2014; Saucedo et al., 2019). Density current channelization processes are considered in more complex models such as Titan 2D and VolcFlow, but for reasons already outlined, such models are not preferred in this situation.

The energy cone model must be suitably parameterized to capture the aleatory uncertainty of PDC collapse height and mobility at the volcano in question. This implies choosing and parameterizing probability density functions (PDFs); which describe the expected distribution of each parameter in nature (Rougier et al., 2013; Tierz et al., 2016b). A lack of real

observational data from eruptions at Aluto means that these must be informed by other means. Ultimately, the suitable "target" PDFs will be used later for importance sampling, but uninformative uniform PDFs spanning the range of these PDFs will be used to sample 10,000 pairs of collapse height and mobility for energy cone simulations at each vent (NB. we assume that the aleatory uncertainty in PDC generation does not vary spatially).

4.2. Parameterizing PDC Collapse Height

The collapse height of the PDC in the case of dome forming eruptions is simple, as the PDC is sourced from the surface elevation at the source vent, which can be derived from the DTM. For column collapse events, such as those at Aluto (Clarke et al., 2019; Clarke, 2020), the collapse height (H_c) is considered to be the sum of the altitude of the vent (H_v), and the height above the vent from which collapse initiates (H_0). H_v can be derived from the DTM for each vent during energy cone simulation. The maximum H_0 has been commonly assumed to correspond with the top of the gas thrust region of the column (Tierz et al., 2016a,b; Sandri et al., 2018). Within the gas thrust region, a dense mixture of gas and pyroclasts is transported upwards mainly by momentum linked to explosive fragmentation. Given that the density of this mixture is higher than the surrounding atmosphere, it may collapse gravitationally upon loss of momentum, generating PDCs (e.g., Sparks, 1997; Doronzo et al., 2011; Dellino et al., 2014). If the eruption column entrains enough surrounding air as to become buoyant, a convective region of the column is developed above the top of the gas-thrust region (Sparks, 1997; Dellino et al., 2014). The top of the gas thrust region is therefore a good approximation of H_0. The height of the gas thrust region for the range of volcanic plumes at Aluto was estimated using the PlumeRise model of Woodhouse et al. (2013), by a methodology detailed in Clarke (2020).

A summary of the method to determine the height of collapse from the gas thrust regions is provided here. The method is based on the premise that column collapse occurs at the point when eruption conditions are no longer capable of sustaining a convective eruption plume (Sparks, 1997). The boundary between a convective and collapsing column can be mapped out using PlumeRise, where the critical parameters controlling the fate of the column are gas mass fraction (volatile content of the magma), mass eruption rate ($\dot{m}$), and vent radius (**Table 1**). Clarke (2020) found that by taking the initial parameters for, and assessing the height of the top of the gas thrust region (defined by local minima in plume velocity; e.g., Trolese et al., 2019) for columns at the convective-column/collapsing-column transition: H_0 at the onset of collapse can be estimated; given a vent radius and water content of the magma (Equation 2).

$$H_0 = a \cdot H_2O^b \cdot r^c \tag{2}$$

where H_0 is the height of the gas thrust region in meters, H_2O is the water content of the magma in wt% and r is the vent radius in meters. a, b and c are regression coefficients related to the location of the convecting/collapsing eruption column boundary within the parameter space. For eruption columns produced during pumice cone eruptions at Aluto, maximum-likelihood estimation yields: $a = 12.78$, $b = -0.61$ and $c = 1.1$. These values are appropriate within the parameter space explored using PlumeRise (**Table 1**). Evaluation of the PlumeRise model parameter space also allows the mass eruption rate at the point of collapse ($\dot{m}_c$, kg/s) to be estimated given r and H_2O, by Equation (3):

$$\dot{m}_c = (d \cdot H_2O^e + f) \cdot r^{(g \cdot H_2O + h)} \tag{3}$$

where d, e, f, g, h are regression coefficients estimated through maximum likelihood of the PlumeRise simulation outputs. For Aluto: $d = 809$, $e = -1.01$, $f = -50.6$, $g = -0.014$, and $h = 2.54$.

Since we know, from field evidence, that column collapse occurs at Aluto, we know that eruption conditions pass through those at the boundary between stable and collapsing columns. If we can estimate a fixed gas mass fraction (magmatic water content) and a vent radius at the point of collapse, there is a unique value of H_0 and $\dot{m}_c$ determined by Equations (2) and (3). Equations (2) and (3) were evaluated iteratively (2×10^6 times) for the expected distribution of vent radii and magmatic water

TABLE 1 | Parameters used in the PlumeRise model to locate the stable/collapsing column boundary in mass eruption rate/vent radius/gas mass fraction parameter space.

Parameter	Value (range)	Units	Rationale (reference)
Vent elevation (H_v)	2,025	m (asl)	Mean altitude for vents at Aluto[a]
Vent radius (r)	(10–1,000)	m	Exceeds measured range at Aluto[a]
Gas mass fraction (H_2O)	(0.01–0.1)	fraction	Covers range of H_2O concentrations in published pantellerite melt inclusion data[b–h]
Source temperature	1023.15	K	Estimated magmatic storage temperature at Aluto[i]
Pyroclast density	1,200	kg/m^3	Recommended mean density of pyroclast mixture[j]
Entrainment coefficient	0.09		Recommended value[j]
Wind direction	n/a	degrees	Assuming no-wind atmosphere
Wind velocity	0	m/s	Assuming no-wind atmosphere
Source mass flux ($\dot{m}$)	(10^3–10^{10})	kg/s	Range required to locate stable/collapse boundary for the range of other PlumeRise parameters
Atmospheric model	standard atmosphere		Standard atmosphere modeled by PlumeRise for relevant H_v

The regression coefficient values derived from the model outputs (section 4.2) are therefore appropriate for the range of eruption condition parameters within this table. The location of the boundary between collapsing and stable eruption columns was determined to a precision of 0.1 log units of mass eruption rate. [a]*Clarke (2020);* [b]*Lowenstern and Mahood (1991);* [c]*Wilding et al. (1993);* [d]*Webster et al. (1993);* [e]*Horn and Schmincke (2000);* [f]*Neave et al. (2012);* [g]*Field et al. (2012);* [h]*Iddon and Edmonds (2020);* [i]*Gleeson et al. (2017);* [j]*Woodhouse et al. (2013).*

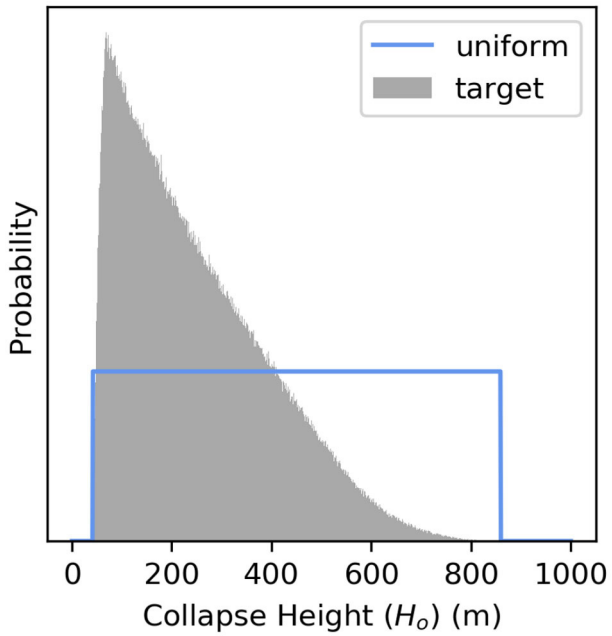

FIGURE 6 | Normalized histogram (gray) showing the expected "target" distribution of collapse heights (H_o) above the vent, based on iterative evaluation of Equation (2) assuming the estimated distribution of vent radii and magmatic water contents at Aluto. A uniform PDF (blue) is fitted to this data and was used for sampling the H_0 parameter during energy cone simulation. In importance sampling, the histogram is used as a target PDF to weight the simulation outputs.

contents at Aluto. Vent radii were measured from the DTM and fitted with a simple triangular distribution (between 10 and 100 m), that extends beyond the dataset to include the possibility of larger events in the future. Water contents were estimated from a review of melt inclusion data in peralkaline rhyolites globally, though because the data set is limited, and the likely distribution of these water contents is uncertain, we assume an uninformative uniform distribution between 4 and 8 wt% H_2O. These values are appropriate for the typical high water contents of pantellerite melts (e.g., Lowenstern and Mahood, 1991; Webster et al., 1993; Wilding et al., 1993; Horn and Schmincke, 2000; Field et al., 2012; Neave et al., 2012), and are consistent with melt inclusion data from Aluto (Iddon and Edmonds, 2020). The product is a histogram of expected H_0 for Aluto (**Figure 6**), which can be combined with H_v during the energy cone simulations at each vent to give H_c, where $H_c = H_0 + H_v$.

Though not required for the energy cone model, the $\dot{m}_c$ calculated in Equation (3) is a useful incidental parameter. We note that for the PlumeRise parameterization (**Table 1**), and expected distributions of r and H_2O at Aluto, $\dot{m}_c$ ranges from 10^4 kg/s to 5×10^6 kg/s. This is consistent with violent-strombolian to sub-Plinian intensity eruptions (Pyle, 2015) tentatively estimated from tephra fall deposits (Fontijn et al., 2018; McNamara et al., 2018) and some proximal deposit constraints (Clarke et al., 2019). This provides confidence that our estimates of eruption conditions are within the correct orders of magnitude for Aluto.

An alternative approach to estimate H_0 is to treat the plume at the point of column collapse as a simple turbulent fountain (e.g., Kaye and Hunt, 2006; Carazzo et al., 2010), where the height of the fountain (H_0) can be estimated by the vent radius, entrainment coefficient and, in volcanic plumes, the dimensionless Richardson number (Ri). The transition between a stable plume and collapsing column occurs at a critical Ri ($\sim$ 0.3) (Kaminski et al., 2005; Degruyter and Bonadonna, 2013; Aubry and Jellinek, 2018), and so H_0 can be approximated as $\sim$ $6.4r$. Though this method is less adapted to the specific volcano, it is more generalizable, and does not require estimation of the gas mass fraction of the magma. Within the range of vent radii expected at Aluto (10–100 m), this parameterization of H_0 is broadly consistent with the PlumeRise-based methodology that we employ in this work, and so is a viable alternative (see **Supplementary Material**). If the turbulent fountain-based methodology is used, a Monte Carlo approach can be used to produce a PDF of H_0, based on the expected distribution of vent radii only. For importance sampling, this H_0 PDF can be used identically to that derived from the PlumeRise-based methodology.

4.3. Parameterizing PDC Mobility

In the energy cone model, PDC mobility is empirically defined from the dH/l ratio, where dH is the measured vertical height drop of the PDC (H_c minus the measured altitude of the PDC deposit toe), and l is the PDC horizontal run out (measured horizontally from the vent to the most distal reach of the deposit) (Malin and Sheridan, 1982). The mobility of the PDC, or angle of the energy line (ϕ) is then (Equation 4):

$$\phi = tan^{-1}\frac{dH}{l} \tag{4}$$

In our Monte Carlo energy cone model, ϕ is iteratively sampled from a uniform distribution, and combined with a sampled H_0. Later, importance sampling can be used to adapt this sample to the expected distribution of ϕ and H_0 in nature. The model is therefore contingent on a realistic distribution of ϕ. Ideally, this would be measured at the volcano in question, but at many volcanoes, including Aluto, such data are very hard to obtain, and/or has not been collected yet. We utilize the FlowDat database (Ogburn, 2012) of PDC data, which includes published dH and l values for a large number of PDCs world wide. As the values in the FlowDat dataset are sourced from numerous workers, the ways in which dH and l are measured in the field vary; from observed eruption column collapse and deposit measurement, to approximating dH as the difference between H_v and the altitude of the PDC deposit toe (thus ignoring H_0, and overestimating ϕ). Because of this, values within the FlowDat dataset are each known to greater or lesser degrees of confidence and precision. This is an additional source of uncertainty, which remains unaccounted for in our assessment. Nonetheless, it has been previously observed (Pablo Tierz, unpublished data) that the impact of H_0 uncertainty on the estimates of ϕ values in the FlowDat database is small. We filter the FlowDat data set, excluding PDCs not representative of Aluto, so that those

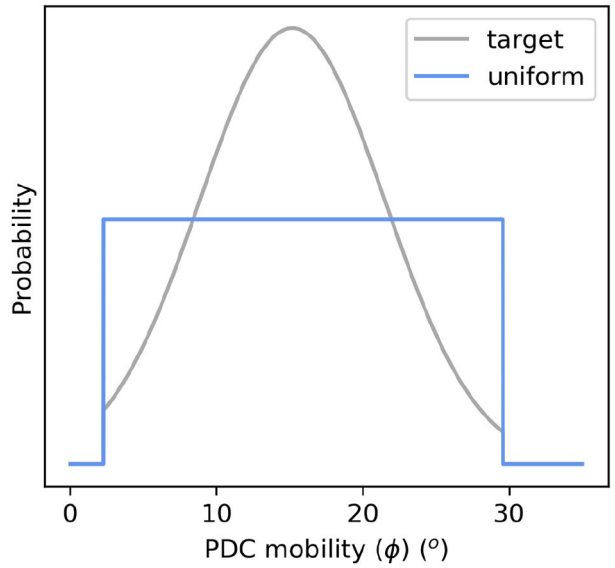

FIGURE 7 | The truncated Gaussian "target" PDF (gray) showing the expected distribution of PDC mobilities (ϕ) at Aluto in nature. The uniform PDF (blue) was used to sample the ϕ parameter during energy cone simulation. In importance sampling, the target PDF was used to weight the simulation outputs.

remaining only include those from column collapse events, and also excluding those produced during caldera forming eruptions or by lateral blasts. Details of the analog data used can be found in the **Supplementary Materials**. This provides 59 values of ϕ to which we fit a truncated Gaussian distribution ($\mu = 15.18$, $\sigma = 6.3$, lower limit = 2, upper limit = 30) (**Figure 7**), in accordance with the observed Gaussian distribution of PDC mobilities (Sheridan and Macías, 1995; Tierz et al., 2016a,b). The Gaussian PDF is truncated to avoid extreme and physically inconsistent mobilities (including zero and negative values) that would otherwise be sampled in the upper and lower tails of a standard Gaussian distribution (Tierz et al., 2016a,b). The locations of the truncation points are the closest integers to the highest and lowest values of ϕ in the filtered FlowDat dataset. This truncated Gaussian PDF is used for the importance sampling later, but a uniform PDF between 2 and 30 degrees is used for initially sampling the parameter pairs for simulation.

5. COMPUTING PROBABILITIES OF PDC INUNDATION

5.1. Energy Cone Modeling

The energy cone model was iterated across the regular grid of 1,221 potential vents, with 10,000 PDC simulations at each vent; each time sampling the same list of input parameter pairs (H_0 and ϕ). H_0 and ϕ pairs were randomly sampled from uniform distributions entirely independent from one another, and so we implicitly assume that these parameters are independent. We justify this as there is no clear relationship between collapse height and mobility in the FlowDat dataset (Tierz et al., 2016a). Ten thousand simulations is generally considered to be statistically representative (e.g., Tierz et al., 2016a,b; Sandri et al., 2018), and provides a precision of 0.01, or 1% ($precision = \frac{1}{\sqrt{n}}$, where n is the number of iterations). The energy cone analysis was conducted using a modified version of the Matlab script developed for Somma-Vesuvius and Campi Flegrei (Tierz et al., 2016a,b), and a 30 m resolution DTM re-sampled from Hutchison et al. (2014). Each simulation produces a footprint over a grid of 30 m cells, where each inundated cell is given a value of "1," and cells which were not inundated are given a value of "0." Though individually each simulation is computationally light, the computational expense of the 12×10^6 necessary energy cone simulations is still high. However, as each simulation is independent, the task can be readily divided across a computing cluster, minimizing the total run time. The analysis was conducted on the EDDIE cluster at the University of Edinburgh Compute and Data Facility, producing 10,000 PDC inundation footprints from each potential vent. Collectively, the results represent uniformly distributed input parameters of vent location, collapse height, and mobility across the range of expected values for each.

5.2. Importance Sampling

In the next phase of the assessment, each grid of results from an energy cone simulation is multiplied by a "weight factor," in a process known as "importance sampling"; placing greater importance on the results of simulations we consider more likely, and less importance on those we consider less likely. Once this is done, the weighted results of all simulations are summed. Grid cells with the highest values are those which are the most prone to inundation by the type and source location of PDCs we expect to see at Aluto. This value is the conditional inundation probability [$P(PDC|eruption)$]; our PVHA.

Firstly, the importance, or "weight factor" (W), associated with the H_0 and ϕ used for each simulation (k) must be calculated (Equation 5). This is done by taking the product of the probability of H_0 and ϕ from their expected, or "target," PDFs calculated earlier [$f(H_k)$ and $f(\phi_k)$]. This is then divided by the product of the sampled probabilities of H_o and ϕ, taken from the uniform PDFs [$g(H_k)$ and $g(\phi_k)$]. A graphical representation of this process, with a worked example, is provided in **Figure 8**. The weight associated with each simulation parameter pair is shown in **Figure 9**.

$$W_k = \frac{f(H_k) \times f(\phi_k)}{g(H_k) \times g(\phi_k)} \tag{5}$$

The probability of PDC inundation in grid cell j, given an eruption of vent i [$P(PDC_j|vent_i)$], can then be calculated as Equation (6):

$$P(PDC_j|vent_i) = \frac{1}{S} \times \sum_{k=1}^{N} (W_k \times s_k) \tag{6}$$

where S is the total number of simulations from vent i (in this case, 10,000), k is the identity of each simulation, and s is a binary 1 or 0 within each grid cell noting inundation vs. no inundation. Effectively, this counts the proportion of weighted simulations in

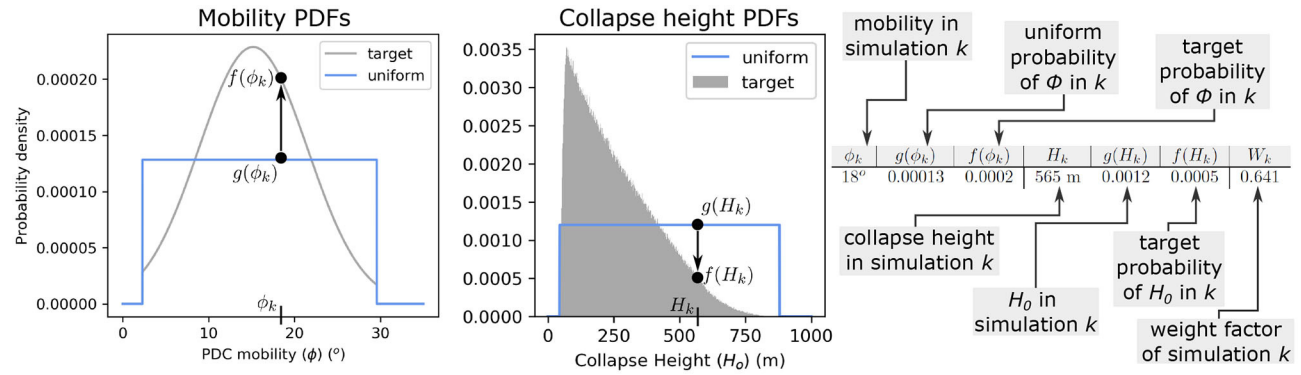

FIGURE 8 | Graphical explanation of the methodology to calculate the weight factor (W) for simulation k. The values for the probability of the collapse height (H_o), and PDC mobility (ϕ), from the target (f) and uniform (g) probability density functions (PDFs) are evaluated at the value of ϕ and H_o used in simulation k. W_k can then be calculated by Equation (5). In this example, $W_k = 0.641$, meaning that grid cells in the output of this simulation will be multiplied by 0.641, lowering their relative importance.

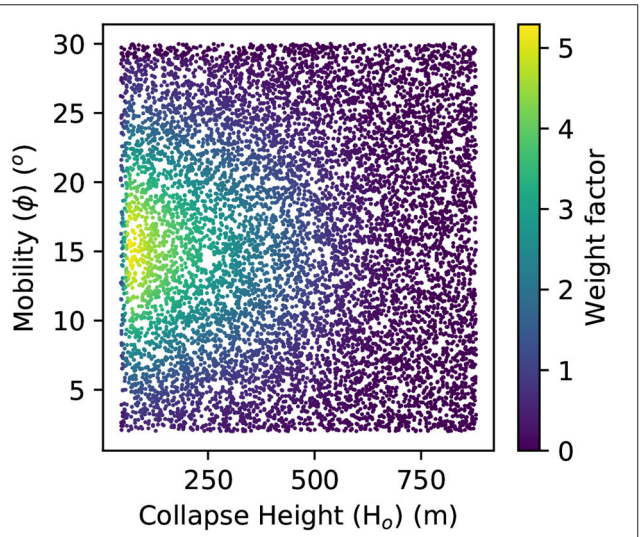

FIGURE 9 | Weighting factors associated with each of the 10,000 collapse height-mobility parameter pairs for energy cone simulations at Aluto. Uniformly distributed parameter pairs are simulated in the energy cone model at each vent, and then the desired weighting can be applied retrospectively. This allows updated collapse height and mobility distributions to be included in future PVHAs without having to re-run the time consuming energy cone model.

which a PDC inundated cell j from vent i. The final step is to also consider the probability of the PDCs being sourced from each vent; this gives the probability of inundation in grid cell j given an eruption $[P(PDC_j)]$, by Equation (7).

$$P(PDC_j) = \sum_{i=1}^{N} P(PDC_j|vent_i) \times P(vent_i) \quad (7)$$

where $P(vent_i)$ is the probability of vent i being the source of the next eruption; calculated in Equation (1). Equation (7) is applied to every grid cell, producing a map of $P(PDC|eruption)$. Importance sampling was conducted using Python, and a fully reproducible exemplar Jupyter notebook with sample energy-cone model data can be found in the via Zenodo/Github (https://doi.org/10.5281/zenodo.3778328).

6. A PVHA OF PDCS AT ALUTO VOLCANO

The main result of the Monte Carlo energy cone PVHA is presented as a map (**Figure 10**), showing the contoured conditional probability of PDC indundation given an eruption from Aluto $[P(PDC|eruption)]$ at a 30 m resolution (this probability map is available as a georeferenced ".Tiff" in the **Supplementary Material**). The 0.01 (1%) probability contour circles the volcano at a 5 km distance from the break in slope at the edge of the edifice, though is somewhat closer on the Eastern flank where it meets steeper topography nearing the edge of the Main Ethiopian Rift. In general, the probability increases toward the edifice, but is particularly high on the outer flanks of the volcano in the SE (between O'Itu Woshe and Kelibo), and the W and NW (between Abule and Sedecha). The caldera floor has the highest probability of PDC inundation with a maximum conditional probability just exceeding 0.12 (12%). This maximum probability is in the eastern region of the caldera floor, which happens to be the location of the geothermal power station. Despite being the most probable location of the next vent (**Figure 4**), the highest topography on the volcano (just beyond the southern edge of the caldera floor) represents the lowest probability of PDC inundation on the edifice.

7. DISCUSSION

7.1. PDC Hazard Around Aluto

The map presented in **Figure 10** indicates the areas that are most likely to be inundated during the next pumice cone eruption at Aluto volcano. The highest probabilities are in low lying regions close to, and on, the edifice. The wide area of possible vent locations around Aluto means that the probability of PDC inundation is spread broadly around the edifice. This means that a wider region may potentially be affected by any given PDC,

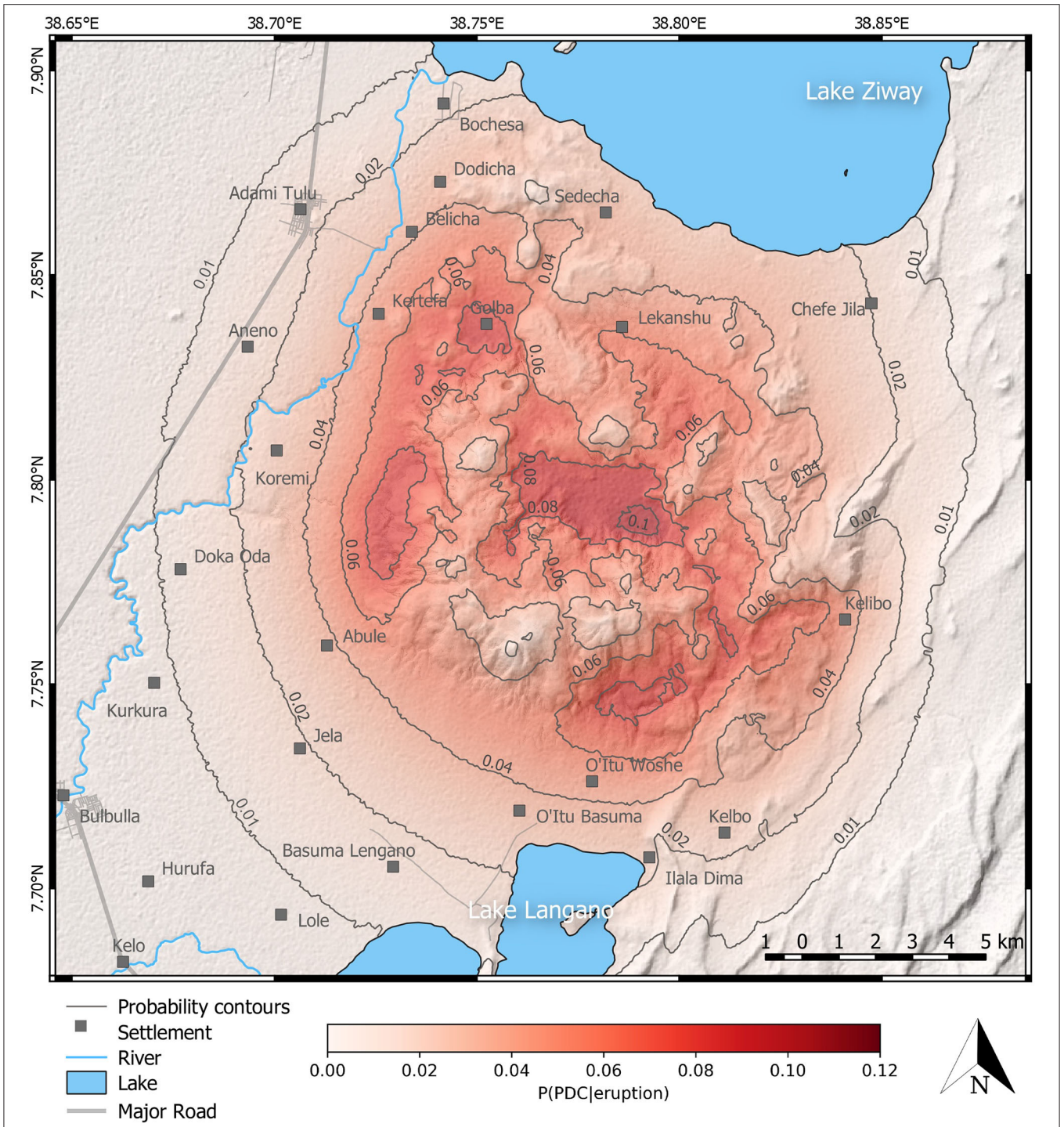

FIGURE 10 | Result of the energy cone modeling showing the conditional probability of PDC inundation around Aluto given an eruption P(PDC|eruption). Probability is provided at a 30 m resolution and has a precision of 0.01 (1%). Apart from the bounding 0.01 (1%) contour, contours of probability are in increments of 0.02 (2%). Settlements names and locations are sourced from the Ethiopian mapping agency. Roads are sourced from OpenStreetMap. High resolution (2 m) LiDAR DTM of Aluto is from Hutchison et al. (2014). Lower resolution (1 arc second) STRM DTM of surrounding regions is from NASA (2014).

but that probability of inundation is more homogeneous across the hazard domain. This "dissipating effect" has been observed at other caldera systems (e.g., Campi Flegrei, Italy; Neri et al., 2015; Sandri et al., 2018), although the computed probability map of PDC inundation may still strongly depend on the vent-opening model used (e.g., Long Valley caldera, USA; Rutarindwa et al.,

2019). By Comparison, at "central-vent" volcanoes, conditional (or even absolute temporal) PDC inundation probabilities approach 1 close to the vent [e.g., Somma-Vesuvius, Italy; (Tierz et al., 2016a,b); Soufrière Hills, Montserrat; (Dalbey, 2009)]. In any case, Aluto is more geomorphologically complex than the two cases just illustrated; with many connected prominences, a central caldera depression, and a diversity of eruptive centers. This means that topographically high regions on the edifice itself, despite being the most probable source location of PDCs, are amongst the least likely to be inundated. This is because their high elevation renders them accessible only to PDCs that originate locally, as opposed to basins around the volcano which are susceptible to inundation by PDCs from a far wider range of potential vents. The caldera is therefore the most likely region to be inundated, as it represents a basin surrounded on all sides by regions with a high vent opening probability. This result is particularly relevant from a risk perspective, as the caldera hosts a school, small settlements, and a geothermal power station. Away from the volcano, flat lying plains to the NE, S, and W provide little impedance to PDCs, whereas topographically complex regions to the E provide barriers that shelter regions comparatively closer to the edifice. It is also important to consider that the maximum area inundated during simulations also strongly depends on the choice of widest vent radius and minimum gas mass fraction (thus tallest H_0), and the most mobile PDC (smallest ϕ); so that the results are a direct consequence of decisions made in the model parameterization.

Despite Ziway's (the main town in the region) proximity to a region of high vent opening probability (the hills between Sedecha and Dodicha), the conditional probability of PDC inundation given an eruption there is relatively low. This is because Ziway sits on the NW edge of the hazard domain, and so is only susceptible to inundation by locally generated PDCs; mostly those from the Sedecha-Dodicha hills, which represent a small subset of those simulated in the entire analysis. However, if the vent opening probability was conditioned so that the vent opened in the region of these hills, the probability of PDC inundation in Ziway would be higher. With the results of the Monte carlo energy cone model at Aluto, it is possible to conduct the importance sampling such that particular scenarios (such as an eruption from somewhere in the region of the Sedicha-Dodicha hills) can be assessed. These scenarios could be useful during a volcanic crisis, where monitoring information (seismic swarms, ground deformation etc.) may indicate the probable location of the vent (e.g., Sandri et al., 2012; Sigmundsson et al., 2015).

7.2. The Use of Field Data to Parameterize Energy Cone Models

To generate a robust PVHA, the model parameterization must reflect the range and distribution of processes that occur at the particular volcano in question (e.g., Connor et al., 2001; Newhall and Hoblitt, 2002; Marzocchi et al., 2004; Bebbington, 2014). This presents a significant challenge for volcanoes which are poorly studied, or behave in a manner distinct to other volcanoes. As far as the authors are aware, this work represents the first PVHA for PDCs at any African volcano, and is certainly the first for pumice-cone style eruptions globally. For any volcano, it is essential to understand the behavior of the system in order to tailor the methodology for PVHA to (1) minimize epistemic uncertainty; gaining the most precise picture possible; and (2) to evaluate aleatory uncertainty, to present a result that reflects an inherently uncertain volcanic system. This understanding is gained through field, laboratory and remote sensing investigations (e.g., Tierz, 2020). In the case of this work, such investigations played a central role, they:

1. Indicated that pumice cone eruptions frequently generate PDCs, and suggested that they were generated by a column collapse mechanism.
2. Showed that at Aluto pumice cone eruptions occur in distinct locations, and that individual vents tend only to be active during one eruption. Which was essential information to quantify the vent-opening probability.
3. Provided evidence to quantify the mass flux, gas mass fraction and vent radius just prior to column collapse, and in turn estimate the height of the gas thrust region (therefore the collapse height of PDCs) (Clarke, 2020).
4. Provided criteria for filtering the FlowDat PDC dataset.

However, there are problems inherent in the use of such data. The first is that they only represent events that have occurred in the past, and so do not necessarily represent the range of events that could occur in the future (e.g., Marzocchi et al., 2012). In order to consider such eventualities, it may be appropriate to extend model parameter distributions. At Aluto, we did this for the vent radius, extending beyond the measured range taking a precautionary, or conservative, approach to consider the possibility of more intense events in the future.

Characterizing a particular eruption style for a volcano is also problematic, as volcanoes often change their behavior over time, and current activity unavoidably represents a "snap-shot" in the geological history of the volcano. Aluto, for example, first existed as a trachytic shield volcano, dominated by trachyte lava flows and tuffs (Hutchison et al., 2016c). Later it generated a caldera during one or two large-magnitude eruptions generating ignimbrite sheets (Hutchison et al., 2016c). Most recently, eruptions are dominated by the relatively modest magnitude peralkaline rhyolite pumice cones modeled here (Fontijn et al., 2018; Clarke et al., 2019; Clarke, 2020). We assume that the most recent pumice cone eruptions at Aluto are the most likely to be representative of the next eruption at Aluto, and so our PVHA does not consider the possibility of a different eruption style. Such caveats need to be clearly communicated to ensure that decisions made upon the PVHA are well informed.

Sampling issues must also be considered when using field data. The field investigations of pumice cones at Aluto focused on 9 pumice cone eruptions, out of 96 vents visible at the surface, and doubtless many more buried vents (Clarke, 2020). It is therefore important to question how much confidence should be placed on eruption scenarios based on these data. Field investigations are also limited by both exposure and preservation. Small events, or events that produce deposits which are more susceptible to erosion, for example, are likely to be

under-represented in the geological record (e.g., Brown et al., 2014; McNamara et al., 2018). It is therefore possible that the larger, perhaps more hazardous, events are over represented in the energy cone models. The fact that new deposits cover older ones also presents a bias in the data set, where more recent events are the most likely to be exposed and therefore excessively influence the conceptual model of eruptions. However, if we assume stationarity of post-caldera volcanism (i.e., future eruptions will behave similarly to the post-caldera eruptions that were investigated), this bias is not necessarily problematic, and is implicit in the stationarity assumption. These issues are not unique to Aluto, and are important caveats to PVHA. Because of these limitations, careful and transparent extrapolation from the existing data set is required. Without extrapolation, there is a risk that the modeled parameter range is insufficient to truly reflect the natural variability. However, excessive extrapolation risks an overly-cautious and pessimistic PVHA, which might unduly influence decision making. Ultimately, decisions surrounding extrapolation are subjective, and so it is essential that a PVHA clearly and transparently communicates the scope, limitations and caveats of the assessment.

7.3. Scope, Limitations, and Caveats of Our Assessment

1. The PVHA presented here provides a conditional probability of PDC inundation around Aluto during its next eruption, assuming that the next eruption is similar to previous dry (not phreatomagmatic) post caldera eruptions at Aluto.
2. The intensity of eruptions (mass eruption rate: ultimately relating to H_0; Clarke, 2020) modeled here exceeds the range of intensities based purely on *measured* vent radii and assumed water contents of the magma. To be cautious, we assume potential vent radii (<100 m) are capable of reaching roughly twice the largest measured vent radii. This increases the top-end of H_0 to reflect the potential for more intense eruptions in the future.
3. The energy cone model does not consider eruption magnitude (total erupted mass), or the volume of any resulting PDCs. PDC volume is positively correlated to mobility (e.g., Hayashi and Self, 1992; Ogburn, 2012), and so volume remains an uncontrolled variable that may influence ϕ at Aluto. Considering the relatively low magnitudes of post-caldera eruptions at Aluto in the past (Fontijn et al., 2018; Clarke et al., 2019; Clarke, 2020), it is possible that some of the higher mobilities sampled here exceed those likely to occur naturally at Aluto.
4. The energy cone model does not consider PDC channelization, and so an increase in effective mobility within drainages is not considered.
5. The energy cone model assumes a radial PDC footprint around the vent, this can be unrealistic for PDCs with a strong directionality (e.g., Charbonnier and Gertisser, 2012; Tierz et al., 2016a,b; Ogburn and Calder, 2017). However, it does provide a cautious estimation of areas that *could* be inundated by a given PDC. It is also important to note that directionality of PDCs can be related to transient controlling mechanisms (Wolpert et al., 2018), and so assuming a radial footprint removes this bias (though admittedly does not address the uncertainty in directionality).
6. The PDC inundation footprint from the energy cone model is contingent on an accurate digital terrain model, even though it has been shown that uncertainty linked to DTM resolution is the lowest contribution to total epistemic uncertainty at other volcanoes (Somma-Vesuvius; Tierz et al., 2016b). However, terrain changes over time, particularly in dynamic volcanic-tectonic systems. For example, the generation of fault scarps, volcanic edifice collapses, or channel/basin-filling during eruptions may all influence the final PDC inundation footprint. Such potential changes are not considered in this assessment. The DTM acquisition dates are 2014 on the edifice, and for the wider region (Hutchison et al., 2014, NASA STRM, 2014).
7. The behavior of PDCs when they enter water is complex, and poorly understood (e.g., Branney and Kokelaar, 2002; Dufek et al., 2009; Sulpizio et al., 2014). The energy cone model does not consider the influence of the substrate on flow mobility, and therefore the footprint over water is highly uncertain (Sandri et al., 2018). For this reason, the PDC inundation probability map is clipped to exclude Lake Ziway in the north, and Lake Langano in the south.
8. As the understanding of Aluto's physical volcanology is in its early stages, and there has not been an observed eruption of the volcano, this model relies heavily on proxy and modeled data. This situation is quite common for many volcanoes around the world (e.g., Loughlin et al., 2015), but obviously introduces epistemic uncertainty into the PVHA results (e.g., Marzocchi et al., 2004). This epistemic uncertainty can be in part reduced using the recently developed VOLCANS methodology to more objectively select the most appropriate volcano analogs based on relatively first-order characteristics of the target volcano (Tierz et al., 2019).

8. CONCLUSIONS

By informing a Monte Carlo energy cone model with field constraints, volcanic plume modeling and global proxy data sets, we have developed the first PVHA for a pumice cone volcano. We find that at Aluto volcano (Ethiopia), the wide spread of potential vent locations means that despite the modest eruption columns that are likely to occur during pumice cone eruptions (Fontijn et al., 2018; McNamara et al., 2018; Clarke et al., 2019; Clarke, 2020), there is a wide area with a probability of PDC inundation equal or >5%, in the event of a pumice cone eruption. Given the aleatory uncertainty in vent opening, the probabilities tend to be more homogeneous and lower than those typically computed at "central-vent" stratovolcanoes (e.g., Bayarri et al., 2009; Tierz et al., 2016a,b, 2018). The highest conditional probability of PDC inundation is 12% within the caldera floor. Other relatively hazardous regions are the western and the south eastern flanks. This probability decays to 1% at around 5 km from the break in slope surrounding the edifice. This area encompasses numerous settlements, and the highest risk region, the caldera floor, hosts

a school and geothermal infrastructure. Though the Monte Carlo energy cone modeling method comes with important caveats, this work now provides a robust background on which further PVHA (for PDCs and other volcanic hazards) at Aluto volcano can be developed. The work also provides a transferable methodology which could be applied to quantify PDC hazards at other caldera systems worldwide; particularly at peralkaline caldera systems, where volcanism is often dominated by pumice cone eruptions.

DATA AVAILABILITY STATEMENT

All datasets generated for this study are included in the article/**Supplementary Material**. The code and files used to generate the energy cone model outputs for this study are available from the authors by request. A series of explanatory Jupyter notebooks and supporting files are available, which provide step-by-step explanations and examples of: (1) calculating the weights associated with input parameters, (2) calculating the vent opening probabilities across a grid of points based on the locations of existing vents, and (3) using this data to conduct importance sampling on a subset of the energy cone model outputs from Aluto, and export the results to a GIS-compatible file. These, including an example data set from Aluto, can be found in via Zenodo/Github at: https://doi.org/10.5281/zenodo.3778328.

AUTHOR CONTRIBUTIONS

BC and PT authored the manuscript. BC conducted fieldwork and carried out all analyses under supervision of PT and EC, who also conducted fieldwork, helped to develop methodologies, and edited the manuscript. GY edited the manuscript, facilitated the research in Ethiopia, and was instrumental in developing the RiftVolc project. All authors contributed to the article and approved the submitted version.

FUNDING

This work is a contribution to the Natural Environment Research Council (NERC) funded RiftVolc project (NE/L013932/1, Rift volcanism: past, present and future) through which PT, EC, and GY are supported. In addition, BC was funded by a NERC doctoral training partnership grant (NE/L002558/1), and PT was also supported by Global Geological Risk Platform of the 350 British Geological Survey NC-ODA grant NE/R000069/1: Geoscience for Sustainable Futures.

ACKNOWLEDGMENTS

We thank Karen Fontijn, Firawalin Dessalegn, Vicki Smith, Sam Engwell, and Amdemichael Zafu for their help and discussions in the field. Particular thanks go to our drivers in the field: Solomon and Zelalem, who helped immensely to make the field expeditions run smoothly and enjoyably. We thank the numerous residents of Aluto who provided assistance, company and passage around Aluto. We also thank Elaine Spiller, Sue Loughlin, and Charlotte Vye-Brown for fruitful conversations about some aspects of this manuscript, and Ashley Smith for his assistance to improve the efficiency of the importance sampling code. Laura Sandri and Lucia Zaccarelli are greatly thanked for the development of the initial version of the Matlab code used to run the energy cone model. We thank Domenico Doronzo, and Guillaume Carazzo for their in-depth and constructive reviews, which greatly improved the manuscript. We also thank Derek Keir and Valerio Acocella for their editorial handling, and additional suggestions which further improved the manuscript. Published with permission of the Executive Director of British Geological Survey (NERC-UKRI).

SUPPLEMENTARY MATERIAL

The Supplementary Material for this article can be found online at: https://www.frontiersin.org/articles/10.3389/feart.2020.00348/full#supplementary-material

The analog PDC mobility data is provided as "**Data Sheet 1**," and the georeferenced PDC inundation probability map is provided as "**Supplementary Figure**" (EPSG:32637). A **Supplementary Figure** "**Presentation 1**," that compares the collapse heights calculated by the alternative PlumeRise and turbulent fountain-based methodologies, is also provided.

REFERENCES

AfriFlora and Sher Ethiopia (2017). *AfriFlora - About Us*.

Andrews, B. J., and Manga, M. (2011). Effects of topography on pyroclastic density current runout and formation of coignimbrites. *Geology* 39, 1099–1102. doi: 10.1130/G32226.1

Aspinall, W., Auker, M., Crosweller, S., Hincks, T. K., Mahony, S., Nadim, F., et al. (2011). *Volcano Hazard and Exposure in Track II Countries and Risk Mitigation Measures - GFDRR Volcano Risk Study*. Bristol University Cabot Institute and NGI Norway for the World Bank: NGI Report 20100806; 309pp.

Aspinall, W. P., Woo, G., Voight, B., and Baxter, P. J. (2003). Evidence-based volcanology: application to eruption crises. *J. Volcanol. Geotherm. Res.* 128, 273–285. doi: 10.1016/S0377-0273(03)00260-9

Aubry, T. J., and Jellinek, A. M. (2018). New insights on entrainment and condensation in volcanic plumes: constraints from independent observations of explosive eruptions and implications for assessing their impacts. *Earth Planet. Sci. Lett.* 490, 132–142. doi: 10.1016/j.epsl.2018.03.028

Bayarri, M. J., Berger, J. O., Calder, E. S., Dalbey, K., Lunagomez, S., Patra, A. K., et al. (2009). Using statistical and computer models to quantify volcanic hazards. *Technometrics* 51, 402–413. doi: 10.1198/TECH.2009.08018

Bayarri, M. J., Berger, J. O., Calder, E. S., Patra, A. K., Pitman, E. B., Spiller, E. T., et al. (2015). Probabilistic quantification of hazards: a methodology using small ensembles of physics-based simulations and statistical surrogates. *Int. J. Uncertain. Quantif.* 5, 297–325. doi: 10.1615/Int.J.UncertaintyQuantification.2015011451

Bebbington, M. S. (2014). Long-term forecasting of volcanic explosivity. *Geophys. J. Int.* 197, 1500–1515. doi: 10.1093/gji/ggu078

Bebbington, M. S., and Jenkins, S. F. (2019). Intra-eruption forecasting. *Bull. Volcanol.* 81:34. doi: 10.1007/s00445-019-1294-9

Bevilacqua, A., Isaia, R., Neri, A., Vitale, S., Aspinall, W. P., Bisson, M., et al. (2015). Quantifying volcanic hazard at Campi Flegrei caldera (Italy) with

uncertainty assessment: 1. Vent opening maps. *J. Geophys. Res*. 120, 2309–2329. doi: 10.1002/2014JB011775

Bevilacqua, A., Neri, A., Bisson, M., Ongaro, T. E., Flandoli, F., Isaia, R., et al. (2017). The effects of vent location, event scale, and time forecasts on pyroclastic density current hazard maps at campi flegrei caldera (Italy). *Front. Earth Sci*. 5:72. doi: 10.3389/feart.2017.00072

Biggs, J., Bastow, I. D., Keir, D., and Lewi, E. (2011). Pulses of deformation reveal frequently recurring shallow magmatic activity beneath the Main Ethiopian Rift. *Geochem. Geophys. Geosyst*. 12, 1–11. doi: 10.1029/2011GC003662

Braddock, M., Biggs, J., Watson, I. M., Hutchison, W., Pyle, D. M., and Mather, T. A. (2017). Satellite observations of fumarole activity at Aluto volcano, Ethiopia: implications for geothermal monitoring and volcanic hazard. *J. Volcanol. Geotherm. Res*. 341, 70–83. doi: 10.1016/j.jvolgeores.2017.05.006

Branney, M. J., and Kokelaar, P. (2002). *Pyroclastic Density Currents and the Sedimentation of Ignimbrites, Vol. 27*. Bath: Geological Society of London Special Publications.

Breard, E. C., Dufek, J., and Lube, G. (2018). Enhanced mobility in concentrated pyroclastic density currents: an examination of a self-fluidization mechanism. *Geophys. Res. Lett*. 45, 654–664. doi: 10.1002/2017GL075759

Breard, E. C., and Lube, G. (2017). Inside pyroclastic density currents-uncovering the enigmatic flow structure and transport behaviour in large-scale experiments. *Earth Planet. Sci. Lett*. 458, 22–36. doi: 10.1016/j.epsl.2016.10.016

Brown, S. K., Crosweller, H. S., Sparks, R. S. J., Cottrell, E., Deligne, N. I., Guerrero, N. O., et al. (2014). Characterisation of the Quaternary eruption record: analysis of the Large Magnitude Explosive Volcanic Eruptions (LaMEVE) database. *J. Appl. Volcanol*. 3, 1–22. doi: 10.1186/2191-5040-3-5

Brown, S. K., Jenkins, S. F., Sparks, R. S. J., Odbert, H., and Auker, M. R. (2017). Volcanic fatalities database: analysis of volcanic threat with distance and victim classification. *J. Appl. Volcanol*. 6, 1–20. doi: 10.1186/s13617-017-0067-4

Calder, E. S., Cole, P. D., Dade, W. B., Druitt, T. H., Hoblitt, R. P., Huppert, H. E., et al. (1999). Mobility of pyroclastic flows and surges at the Soufriere Hills volcano, Montserrat. *Geophys. Res. Lett*. 26, 537–540. doi: 10.1029/1999GL900051

Calder, E. S., Sparks, R. S., and Woods, A. W. (1997). Dynamics of co-ignimbrite plumes generated from pyroclastic flows of Mount St. Helens (7 August 1980). *Bull. Volcanol*. 58, 432–440. doi: 10.1007/s004450050151

Calder, E. S., Wagner, K., and Ogburn, S. E. (2015). "Chapter 20: Volcanic hazard maps," in *Global Volcanic Hazards and Risk, 1st Edn* eds S. Loughlin, S. Sparks, S. K. Brown, S. F. Jenkins, C. Vye-Brown (Cambridge: Cambridge University Press), 335–341. doi: 10.1017/CBO9781316276273.022

Cappello, A., Neri, M., Acocella, V., Gallo, G., Vicari, A., and Del Negro, C. (2012). Spatial vent opening probability map of Etna volcano (Sicily, Italy). *Bull. Volcanol*. 74, 2083–2094. doi: 10.1007/s00445-012-0647-4

Carazzo, G., Kaminski, E., and Tait, S. (2010). The rise and fall of turbulent fountains: a new model for improved quantitative predictions. *J. Fluid Mech*. 657, 265–284. doi: 10.1017/S002211201000145X

Charbonnier, S. J., and Gertisser, R. (2012). Evaluation of geophysical mass flow models using the 2006 block-and-ash flows of Merapi Volcano, Java, Indonesia: towards a short-term hazard assessment tool. *J. Volcanol. Geotherm. Res*. 231–232, 87–108. doi: 10.1016/j.jvolgeores.2012.02.015

Clarke, B., Calder, E. S., Dessalegn, F., Fontijn, K., Cortés, J. A., Naylor, M., et al. (2019). Fluidal pyroclasts reveal the intensity of peralkaline rhyolite pumice cone eruptions. *Nat. Commun*. 10, 1–10. doi: 10.1038/s41467-019-09947-8

Clarke, B. A. (2020). *Post-caldera eruptions and pyroclastic density current hazard in the Main Ethiopian Rift* (Ph.D.). University of Edinburgh, Edinburgh, Scotland.

Connor, B., and Hill, E. (1995). Three nonhomogeneous Poisson models for the probability of basaltic volcanism: application to the Yucca Mountain region, Nevada. *J. Geophys. Res*. 100, 107–117. doi: 10.1029/95JB01055

Connor, B. C. B., Hill, B. E., Winfrey, B., Franklin, N. M., and Femina, P. C. L. (2001). Estimation of volcanic hazards from tephra fallout. *Nat. Hazards Rev*. 2, 33–42. doi: 10.1061/(ASCE)1527-6988(2001)2:1(33)

Dalbey, K. (2009). *Predictive simulation and model based hazard maps of geophysical mass flows* (Ph.D. thesis). University at Buffalo, Buffalo, NY, United States.

Dalbey, K., Patra, A. K., Pitman, E. B., Bursik, M. I., and Sheridan, M. F. (2008). Input uncertainty propagation methods and hazard mapping of geophysical mass flows. *J. Geophys. Res*. 113:B05203. doi: 10.1029/2006JB004471

Degruyter, W., and Bonadonna, C. (2013). Impact of wind on the condition for column collapse of volcanic plumes. *Earth Planet. Sci. Lett*. 377–378, 218–226. doi: 10.1016/j.epsl.2013.06.041

Dellino, P., Dioguardi, F., Mele, D., D'Addabbo, M., Zimanowski, B., Büttner, R., et al. (2014). Volcanic jets, plumes, and collapsing fountains: evidence from large-scale experiments, with particular emphasis on the entrainment rate. *Bull. Volcanol*. 76, 1–18. doi: 10.1007/s00445-014-0834-6

Dellino, P., and Volpe, L. L. (1995). Fragmentation versus transportation mechanisms in the pyroclastic sequence of Monte Pilato-Rocche Rosse (Lipari, Italy). *J. Volcanol. Geotherm. Res*. 64, 211–231. doi: 10.1016/0377-0273(94)00084-T

Di Roberto, A., Bertagnini, A., Pompilio, M., and Bisson, M. (2014). Pyroclastic density currents at Stromboli volcano (Aeolian Islands, Italy): a case study of the 1930 eruption. *Bull. Volcanol*. 76, 1–14. doi: 10.1007/s00445-014-0827-5

Doronzo, D. M., de Tullio, M. D., Dellino, P., and Pascazio, G. (2011). Numerical simulation of pyroclastic density currents using locally refined Cartesian grids. *Comput. Fluids* 44, 56–67. doi: 10.1016/j.compfluid.2010.12.006

Douillet, G. A., Pacheco, D. A., Kueppers, U., Letort, J., Tsang-Hin-Sun, E., Bustillos, J., et al. (2013). Dune bedforms produced by dilute pyroclastic density currents from the August 2006 eruption of Tungurahua volcano, Ecuador. *Bull. Volcanol*. 75, 1–20. doi: 10.1007/s00445-013-0762-x

Dufek, J., Wexler, J., and Manga, M. (2009). Transport capacity of pyroclastic density currents: experiments and models of substrate-flow interaction. *J. Geophys. Res*. 114, 1–13. doi: 10.1029/2008JB006216

Field, L., Blundy, J., Brooker, R. A., Wright, T., and Yirgu, G. (2012). Magma storage conditions beneath Dabbahu Volcano (Ethiopia) constrained by petrology, seismicity and satellite geodesy. *Bull. Volcanol*. 74, 981–1004. doi: 10.1007/s00445-012-0580-6

Fink, J. H. (1983). Structure and emplacement of a rhyolitic obsidian flow, Little Glass Mountain, North California. *Geol. Soc. Am. Bull*. 94, 362–380. doi: 10.1130/0016-7606(1983)94<362:SAEOAR>2.0.CO;2

Fisher, R. V. (1995). Decoupling of pyroclastic currents: hazards assessments. *J. Volcanol. Geotherm. Res*. 66, 257–263. doi: 10.1016/0377-0273(94)00075-R

Fisher, R. V., and Schmincke, H.-U. (1984). *Pyroclastic Rocks, 1st Edn*. Berlin: Springer-Verlag. doi: 10.1007/978-3-642-74864-6

Fontijn, K., McNamara, K., Zafu Tadesse, A., Pyle, D. M., Dessalegn, F., Hutchison, W., et al. (2018). Contrasting styles of post-caldera volcanism along the Main Ethiopian Rift: implications for contemporary volcanic hazards. *J. Volcanol. Geotherm. Res*. 356, 90–113. doi: 10.1016/j.jvolgeores.2018.02.001

Gioncada, A., and Landi, P. (2010). The pre-eruptive volatile contents of recent basaltic and pantelleritic magmas at Pantelleria (Italy). *J. Volcanol. Geotherm. Res*. 189, 191–201. doi: 10.1016/j.jvolgeores.2009.11.006

Gleeson, M., Stock, M., Pyle, D. M., Mather, T. A., Hutchison, W., Yirgu, G., et al. (2017). Constraining magma storage conditions at a restless volcano in the Main Ethiopian Rift using phase equilibria models. *J. Volcanol. Geotherm. Res*. 337, 44–61. doi: 10.1016/j.jvolgeores.2017.02.026

Griffiths, R. W., and Fink, J. H. (1993). Effects of surface cooling on the spreading of lava flows and domes. *J. Fluid Mech*. 252, 667–702. doi: 10.1017/S0022112093003933

Hayashi, J., and Self, S. (1992). A comparison of pyroclastic flow and debris avalanche mobility. *J. Geophys. Res*. 97, 9063–9071. doi: 10.1029/92JB00173

Hengsdijk, H., and Jansen, H. (2006). *Agricultural Development in the Central Ethiopian Rift Valley: A Desk-Study on Water-Related Issues and Knowledge to Supporta Policy Dialogue*. Wagningen University & Research.

Horn, S., and Schmincke, H.-U. (2000). Volatile emission during the eruption of Baitoushan Volcano (China/North Korea) ca. 969 AD. *Bull. Volcanol*. 61, 537–555. doi: 10.1007/s004450050004

Houghton, B. F., Weaver, S. D., Wilson, C. J., and Lanphere, M. A. (1992). Evolution of a Quaternary peralkaline volcano: Mayor Island, New Zealand. *J. Volcanol. Geotherm. Res*. 51, 217–236. doi: 10.1016/0377-0273(92)90124-V

Houghton, B. F., White, J. D., and Van Eaton, A. R. (2015). "Chapter 30: Phreatomagmatic and related eruption styles," in *Encyclopedia of Volcanoes 2*, eds H. Sigurdsson, B. Houghton, S. R. McNutt, H. Rymer, J. Stix (London: Springer), 538–552. doi: 10.1016/B978-0-12-385938-9.00030-4

Houghton, B. F., and Wilson, C. J. (1989). A vesicularity index for pyroclastic deposits. *Bull. Volcanol.* 51, 451–462. doi: 10.1007/BF01078811

Hübert, J., Whaler, K., and Fisseha, S. (2018). The electrical structure of the central main ethiopian rift as imaged by magnetotellurics: implications for magma storage and pathways. *J. Geophys. Res.* 123, 6019–6032. doi: 10.1029/2017JB015160

Hutchison, W. (2015). *Past, present and future volcanic activity at restless calderas in the Main Ethiopian Rift* (Ph.D. thesis). University of Oxford, Oxford, United Kingdom.

Hutchison, W., Biggs, J., Mather, T. A., Pyle, D. M., Lewi, E., Yirgu, G., et al. (2016a). Causes of unrest at silicic calderas in the East African Rift: new constraints from InSAR and soil-gas chemistry at Aluto volcano, Ethiopia. *Geochem. Geophys. Geosyst.* 17, 2825–2834. doi: 10.1002/2016GC006395

Hutchison, W., Fusillo, R., Pyle, D. M., Mather, T. A., Blundy, J. D., Biggs, J., et al. (2016b). A pulse of mid-Pleistocene rift volcanism in Ethiopia at the dawn of modern humans. *Nat. Commun.* 7, 1–12. doi: 10.1038/ncomms13192

Hutchison, W., Mather, T. A., Pyle, D. M., Biggs, J., and Yirgu, G. (2015). Structural controls on fluid pathways in an active rift system: a case study of the Aluto volcanic complex. *Geosphere* 11, 542–562. doi: 10.1130/GES01119.1

Hutchison, W., Pyle, D. M., Mather, T. A., Biggs, J., and Yirgu, G. (2014). 2012 Aluto LiDAR data. *Figshare, Dataset*. doi: 10.6084/m9.figshare.1261646.v2

Hutchison, W., Pyle, D. M., Mather, T. A., Yirgu, G., Biggs, J., Cohen, B. E., et al. (2016c). The eruptive history and magmatic evolution of Aluto volcano: new insights into silicic peralkaline volcanism in the Ethiopian rift. *J. Volcanol. Geotherm. Res.* 328, 9-33. doi: 10.1016/j.jvolgeores.2016.09.010

Iddon, F., and Edmonds, M. (2020). Volatile-rich magmas distributed through the upper crust in the Main Ethiopian Rift. *Geochem. Geophys. Geosyst.* 21, 1–24. doi: 10.1029/2019GC008904

Iddon, F., Edmonds, M., Jackson, C., Hutchison, W., Mather, T. A., Pyle, D. M., et al. (2017). "Reservoir architecture beneath peralkaline volcanoes, Main Ethiopian Rift," in *Volcanic and Magmatic Studies Group Conference* (Liverpool), 118.

Kaminski, E., Tait, S., and Carazzo, G. (2005). Turbulent entrainment in jets with arbitrary buoyancy. *J. Fluid Mech.* 526, 361–376. doi: 10.1017/S0022112004003209

Kaye, N. B., and Hunt, G. R. (2006). Weak fountains. *J. Fluid Mech.* 558, 319–328. doi: 10.1017/S0022112006000383

Kelfoun, K., and Druitt, T. H. (2005). Numerical modeling of the emplacement of Socompa rock avalanche, Chile. *J. Geophys. Res.* 110, 1–13. doi: 10.1029/2005JB003758

Kelfoun, K., Gueugneau, V., Komorowski, J. C., Aisyah, N., Cholik, N., and Merciecca, C. (2017). Simulation of block-and-ash flows and ash-cloud surges of the 2010 eruption of Merapi volcano with a two-layer model. *J. Geophys. Res.* 122, 4277–4292. doi: 10.1002/2017JB013981

Koyaguchi, T., and Woods, A. W. (1996). On the formation of eruption columns following explosive mixing of magma and surface-water. *J. Geophys. Res.* 101, 5561–5574. doi: 10.1029/95JB01687

Lindsay, J., Marzocchi, W., Jolly, G., Constantinescu, R., Selva, J., and Sandri, L. (2010). Towards real-time eruption forecasting in the Auckland Volcanic Field: Application of BET_EF during the New Zealand National Disaster Exercise 'Ruaumoko'. *Bull. Volcanol.* 72, 185–204. doi: 10.1007/s00445-009-0311-9

Loughlin, S. C., Vye-brown, C., Sparks, R., Brown, S., Barclay, J., Calder, E. S., et al. (2015). *Global Volcanic Hazards and Risk, Summary Background Paper for the UN-ISDR Global Assessment Report on Disaster Risk Reduction 2015*. Technical report, Global Volcano Model and International Association of Volcanology and Chemistry of the Earth's Interior.

Lowenstern, J. B., and Mahood, G. (1991). New data on magmatic H2O contents of pantellerites, with implications for petrogenesis and eruptive dynamics at Pantelleria. *Bull. Volcanol.* 54, 78–83. doi: 10.1007/BF00278208

Malin, M. C., and Sheridan, M. F. (1982). Computer-assisted mapping of pyroclastic surges. *Science* 217, 637–640. doi: 10.1126/science.217.4560.637

Marti, J., and Felpeto, A. (2010). Methodology for the computation of volcanic susceptibility. An example for mafic and felsic eruptions on Tenerife (Canary Islands). *J. Volcanol. Geotherm. Res.* 195, 69–77. doi: 10.1016/j.jvolgeores.2010.06.008

Marzocchi, W., Garcia-Aristizabal, A., Gasparini, P., Mastellone, M. L., and Ruocco, A. D. (2012). Basic principles of multi-risk assessment: a case study in Italy. *Nat. Hazards* 62, 551–573. doi: 10.1007/s11069-012-0092-x

Marzocchi, W., Sandri, L., Gasparini, P., Newhall, C., and Boschi, E. (2004). Quantifying probabilities of volcanic events: the example of volcanic hazard at Mount Vesuvius. *J. Geophys. Res.* 109, 1–18. doi: 10.1029/2004JB003155

Marzocchi, W., Sandri, L., and Selva, J. (2010). BET_VH: a probabilistic tool for long-term volcanic hazard assessment. *Bull. Volcanol.* 72, 705–716. doi: 10.1007/s00445-010-0357-8

Mastin, L. G., and Witter, J. B. (2000). The hazards of eruptions through lakes and seawater. *J. Volcanol. Geotherm. Res.* 97, 195–214. doi: 10.1016/S0377-0273(99)00174-2

McNamara, K., Cashman, K. V., Rust, A. C., Fontijn, K., Chalié, F., Tomlinson, E. L., et al. (2018). Using lake sediment cores to improve records of volcanism at aluto volcano in the main ethiopian rift. *Geochem. Geophys. Geosyst.* 19, 3164–3188. doi: 10.1029/2018GC007686

Neave, D. A., Fabbro, G., Herd, R. A., Petrone, C. M., and Edmonds, M. (2012). Melting, differentiation and degassing at the pantelleria volcano, Italy. *J. Petrol.* 53, 637–663. doi: 10.1093/petrology/egr074

Neri, A., Bevilacqua, A., Ongaro, T. E., Isaia, R., Aspinall, W. P., Bisson, M., et al. (2015). Quantifying volcanic hazard at Campi Flegrei caldera (Italy) with uncertainty assessment: 2. Pyroclastic density current invasion maps. *J. Geophys. Res.* 120, 1605–1622. doi: 10.1002/2014JB011776

Newhall, C., and Hoblitt, R. (2002). Constructing event trees for volcanic crises. *Bull. Volcanol.* 64, 3–20. doi: 10.1007/s004450100173

Ogburn, S. (2012). *FlowDat: Mass Flow Database v2.2*. Available online at: https://vhub.org/groups/massflowdatabase.

Ogburn, S. E., and Calder, E. S. (2017). The relative effectiveness of empirical and physical models for simulating the dense undercurrent of pyroclastic flows under different emplacement conditions. *Front. Earth Sci.* 5:83. doi: 10.3389/feart.2017.00083

Orsi, G., Ruvo, L., and Scarpati, C. (1989). The Serra della Fastuca Tephra at Pantelleria: physical parameters for an explosive eruption of peralkaline magma. *J. Volcanol. Geotherm. Res.* 39, 55–60. doi: 10.1016/0377-0273(89)90020-6

Patra, A. K., Bauer, A. C., Nichita, C. C., Pitman, E. B., Sheridan, M. F., Bursik, M., et al. (2005). Parallel adaptive numerical simulation of dry avalanches over natural terrain. *J. Volcanol. Geotherm. Res.* 139, 1–21. doi: 10.1016/j.jvolgeores.2004.06.014

Pyle, D. M. (2015). "Chapter 13: Sizes of volcanic eruptions," in *Encyclopedia of Volcanoes 2*, eds H. Sigurdsson, B. Houghton, S. R. McNutt, H. Rymer, J. Stix (Springer), 257-264. doi: 10.1016/B978-0-12-385938-9.00013-4

Roche, O., Gilbertson, M. A., Phillips, J. C., and Sparks, R. S. (2006). The influence of particle size on the flow of initially fluidised powders. *Powder Technol.* 166, 167–174. doi: 10.1016/j.powtec.2006.05.010

Rougier, J., Sparks, S., and Hill, L. J. (2013). *Risk and Uncertainty Assessment for Natural Hazards, 1st Edn*. Cambridge: Cambridge University Press. doi: 10.1017/CBO9781139047562

Rutarindwa, R., Spiller, E. T., Bevilacqua, A., Bursik, M. I., and Patra, A. K. (2019). Dynamic probabilistic hazard mapping in the long valley volcanic region ca: integrating vent opening maps and statistical surrogates of physical models of pyroclastic density currents. *J. Geophys. Res.* 124, 9600–9621. doi: 10.1029/2019JB017352

Samrock, F., Kuvshinov, A., Bakker, J., Jackson, A., and Fisseha, S. (2015). 3-D analysis and interpretation of magnetotelluric data from the Aluto-Langano geothermal field, Ethiopia. *Geophys. J. Int.* 202, 1923–1948. doi: 10.1093/gji/ggv270

Sandri, L., Jolly, G., Lindsay, J., Howe, T., and Marzocchi, W. (2012). Combining long- and short-term probabilistic volcanic hazard assessment with cost-benefit analysis to support decision making in a volcanic crisis from the Auckland Volcanic Field, New Zealand. *Bull. Volcanol.* 74, 705–723. doi: 10.1007/s00445-011-0556-y

Sandri, L., Thouret, J. C., Constantinescu, R., Biass, S., and Tonini, R. (2014). Long-term multi-hazard assessment for El Misti volcano (Peru). *Bull. Volcanol.* 76, 1–26. doi: 10.1007/s00445-013-0771-9

Sandri, L., Tierz, P., Costa, A., and Marzocchi, W. (2018). Probabilistic hazard from pyroclastic density currents in the Neapolitan Area (Southern Italy). *J. Geophys. Res.* 123, 3474–3500. doi: 10.1002/2017JB014890

Saucedo, R., Macías, J. L., Gavilanes-Ruiz, J. C., Bursik, M. I., and Vargas-Gutiérrez, V. (2019). "Pyroclastic density currents at volcán de Colima," in *Volcan de Colima*, eds N. Varley,

C. B. Connor (Springer), 111–139. doi: 10.1007/978-3-642-25911-1_11

Selva, J., Orsi, G., Di Vito, M. A., Marzocchi, W., and Sandri, L. (2012). Probability hazard map for future vent opening at the Campi Flegrei caldera, Italy. *Bull. Volcanol.* 74, 497–510. doi: 10.1007/s00445-011-0528-2

Sheridan, M. F., and Macías, J. (1995). Estimation of risk probability for gravity-driven pyroclastic flows at Volcan Colima, Mexico. *J. Volcanol. Geotherm. Res.* 66, 251–256. doi: 10.1016/0377-0273(94)00058-O

Sigmundsson, F., Hooper, A., Hreinsdóttir, S., Vogfjörd, K. S., Ófeigsson, B. G., Heimisson, E. R., et al. (2015). Segmented lateral dyke growth in a rifting event at Bárdarbunga volcanic system, Iceland. *Nature* 517, 191–195. doi: 10.1038/nature14111

Smith, G. M., Williams, R., Rowley, P. J., and Parsons, D. R. (2018). Investigation of variable aeration of monodisperse mixtures: implications for pyroclastic density currents. *Bull. Volcanol.* 80, 1–12. doi: 10.1007/s00445-018-1241-1

Sparks, R. (1997). *Volcanic Plumes, 1st Edn*. Chichester: Wiley.

Spiller, E. T., Bayarri, M. J., Berger, J. O., Calder, E. S., Patra, A. K., Pitman, E. B., et al. (2014). Automating emulator construction for geophysical hazard maps. *SIAM/ASA J. Uncertain. Quantif.* 2, 126–152. doi: 10.1137/120899285

Sulpizio, R., Dellino, P., Doronzo, D. M., and Sarocchi, D. (2014). Pyroclastic density currents: state of the art and perspectives. *J. Volcanol. Geotherm. Res.* 283, 36–65. doi: 10.1016/j.jvolgeores.2014.06.014

Teklemariam, M., and Kebede, S. (2010). "Strategy for geothermal resource exploration and development in Ethiopia," in *Proceedings: World Geothermal Congress* (Bali).

Tierz, P. (2020). Long-term probabilistic volcanic hazard assessment using open and non-open data: observations and current issues. *Front. Earth Sci.* 8:257. doi: 10.3389/feart.2020.00257

Tierz, P., Loughlin, S. C., and Calder, E. S. (2019). VOLCANS: an objective, structured and reproducible method for identifying sets of analogue volcanoes. *Bull. Volcanol.* 81, 1–22. doi: 10.1007/s00445-019-1336-3

Tierz, P., Sandri, L., Costa, A., Sulpizio, R., Zaccarelli, L., Vito, M. A. D., et al. (2016a). "Uncertainty assessment of pyroclastic density currents at Mount Vesuvius (Italy) simulated through the energy cone model," in *Natural Hazard Uncertainty Assessment: Modeling and Decision Support, 1st Edn*, eds K. Riley, P. Webley, and M. Thompson (Hoboken, NJ: John Wiley & Sons, Inc.), 125–145. doi: 10.1002/9781119028116.ch9

Tierz, P., Sandri, L., Costa, A., Zaccarelli, L., Di Vito, M. A., Sulpizio, R., et al. (2016b). Suitability of energy cone for probabilistic volcanic hazard assessment: validation tests at Somma-Vesuvius and Campi Flegrei (Italy). *Bull. Volcanol.* 78:79. doi: 10.1007/s00445-016-1073-9

Tierz, P., Stefanescu, E. R., Sandri, L., Sulpizio, R., Valentine, G. A., Marzocchi, W., et al. (2018). Towards quantitative volcanic risk of pyroclastic density currents: probabilistic hazard curves and maps around somma-vesuvius (Italy). *J. Geophys. Res.* 123, 6299–6317. doi: 10.1029/2017JB015383

Tonini, R., Sandri, L., and Anne Thompson, M. (2015). PyBetVH: A Python tool for probabilistic volcanic hazard assessment and for generation of Bayesian hazard curves and maps. *Comput. Geosci.* 79, 38–46. doi: 10.1016/j.cageo.2015.02.017

Trolese, M., Cerminara, M., Esposti Ongaro, T., and Giordano, G. (2019). The footprint of column collapse regimes on pyroclastic flow temperatures and plume heights. *Nat. Commun.* 10, 1–10. doi: 10.1038/s41467-019-10337-3

UNDP (2018). *Human Development Reports - Ethiopia*. Technical report, UN.

Vye-Brown, C., Sparks, R. S. J., Lewi, E., Mewa, G., Asrat, A., Loughlin, S. C., et al. (2016). Ethiopian volcanic hazards: a changing research landscape. *Geol. Soc. Lond. Spec. Publ.* 420, 355–365. doi: 10.1144/SP420.16

Wand, M. P., and Jones, M. C. (1994). *Kernel Smoothing, 1st Edn*. London: Champan & Hall. doi: 10.1201/b14876

Webster, J. D., Taylor, R. P., and Bean, C. (1993). Pre-eruptive melt composition and constraints on degassing of a water-rich pantellerite magma, Fantale volcano, Ethiopia. *Contrib. Mineral. Petrol.* 114, 53–62. doi: 10.1007/BF00307865

Weller, J. N., Martin, A. J., Connor, C. B., Connor, L. J., and Karakhanian, A. (2006). "Chapter 7: Modelling the spatial distribution of volcanoes: an example from Armenia," in *Statistics in Volcanology, 1st Edn*, eds H. M. Mader, S. G. Coles, C. B. Connor, and L. J. Connor (London: Geological Society of London Special Publications), 77–87. doi: 10.1144/IAVCEI001.7

Wilding, M. C., Macdonald, R., Davies, J. E., and Fallick, A. E. (1993). Volatile characteristics of peralkaline rhyolites from Kenya: an ion microprobe, infrared spectroscopic and hydrogen isotope study. *Contrib. Mineral. Petrol.* 114, 264–275. doi: 10.1007/BF00307761

Wilks, M., Kendall, J. M., Nowacki, A., Biggs, J., Wookey, J., Birhanu, Y., et al. (2017). Seismicity associated with magmatism, faulting and hydrothermal circulation at Aluto Volcano, Main Ethiopian Rift. *J. Volcanol. Geotherm. Res.* 340, 52–67. doi: 10.1016/j.jvolgeores.2017.04.003

Wilson, C. J. N. (1980). The rolde of fluidization in the emplacement of pyroclastic flows: an experimental approach. *J. Volcanol. Geotherm. Res.* 8, 231–249. doi: 10.1016/0377-0273(80)90106-7

Wolpert, R. L., Spiller, E. T., and Calder, E. S. (2018). Dynamic statistical models for pyroclastic density current generation at Soufriére Hills Volcano. *Front. Earth Sci.* 6:55. doi: 10.3389/feart.2018.00055

Woodhouse, M. J., Hogg, A. J., Phillips, J. C., and Sparks, R. S. (2013). Interaction between volcanic plumes and wind during the 2010 Eyjafjallajökull eruption, Iceland. *J. Geophys. Res.* 118, 92–109. doi: 10.1029/2012JB009592

World Bank (2016). *Ethiopia Geothermal Development Project*.

Conflict of Interest: The authors declare that the research was conducted in the absence of any commercial or financial relationships that could be construed as a potential conflict of interest.

frontiers in Earth Science

ORIGINAL RESEARCH
published: 02 September 2020
doi: 10.3389/feart.2020.00369

Modeling Lahars on a Poorly Eroded Basaltic Shield: Karthala Volcano, Grande Comore Island

Antoine Dille[1,2], Sam Poppe[1], Sophie Mossoux[1], Hamid Soulé[3] and Matthieu Kervyn[1]*

[1] Department of Geography, Earth System Science, Vrije Universiteit Brussel, Brussels, Belgium, [2] Department of Earth Sciences, Royal Museum for Central Africa, Tervuren, Belgium, [3] Centre National de Documentation et de Recherche Scientifique, Observatoire Volcanologique du Karthala, Moroni, Comoros

Lahars impose significant secondary hazards on highly populated volcanic islands by remobilizing volcanic ash deposits. Karthala, on Grande Comore Island, is a relatively young and poorly eroded basaltic shield volcano with sporadic occurrence of ash-forming phreatic eruptions. In 2005, two mildly explosive episodes emplaced tephra blankets on the summit area. Heavy precipitation subsequently triggered the repetitive occurrence of small-volume secondary lahars up to 2012. These lahars damaged roads and hundreds of houses, affecting thousands of inhabitants at the foot of Karthala volcano, but were poorly documented at the time of their occurrence. Their future hazard remains unclear as well. This study aims at gaining insights into the main characteristics of these lahars, as well as testing and comparing the effectiveness of two numerical tools to simulate the extent of these small-volume lahars. To understand the physical characteristics of the lahars, we first documented the spatial extent and characteristics of the debris deposits at the foot of Karthala volcano and in the ravines that guided the flows. Our observations suggest that the debris were emplaced by small-scale (volumes $\leq 10^5$ m^3), rain-triggered and predominantly low sediment concentration lahars. The spatial extent of the deposits served to calibrate and compare numerical lahar simulations from the widely used volume-limited LaharZ model with simulations from Q-LavHA, a probabilistic flow model originally developed for lava flows. Q-LavHA mitigates some limitations of LaharZ, such as its ability to simulate flow bifurcations and the transition from constrained to unconstrained flow but comparison demonstrates that Q-LavHA typically yielded lower simulation accuracies compared to LaharZ simulations. The obtained accuracy values represent a rather poor performance for both models compared to existing studies on larger-volume lahars on stratovolcanoes, and are inferred to result mostly from difficulties in delineating lahar flow paths on the smooth, poorly eroded topography of the volcanic edifice. We therefore also evaluated the potential to increase simulation accuracy by updating a 10 m resolution Digital Elevation Model (DEM) with channel topography measurements. By using such updated DEMs, the correctly delineated area improved for both models. This approach, however, did not prevent simulations to sometimes miss the hazard-prone position of settlements which were actually affected by the hazard in the past. Our study shows the limitations of numerical volcanic flow simulation strategies on young and poorly eroded volcanic

OPEN ACCESS

Edited by:
Stuart Mead,
College of Sciences, Massey University, New Zealand

Reviewed by:
Jon J. Major,
United States Geological Survey (USGS), United States
Claudio Scarpati,
University of Naples Federico II, Italy

***Correspondence:**
Antoine Dille
antoine.dille@vub.be;
antoine.dille@gmail.com

Specialty section:
This article was submitted to Volcanology, a section of the journal Frontiers in Earth Science

Received: *24 October 2019*
Accepted: *10 August 2020*
Published: *02 September 2020*

Citation:
Dille A, Poppe S, Mossoux S, Soulé H and Kervyn M (2020) Modeling Lahars on a Poorly Eroded Basaltic Shield: Karthala Volcano, Grande Comore Island. Front. Earth Sci. 8:369. doi: 10.3389/feart.2020.00369

edifices, such as active basaltic shields. The results indicate that accurate topographic representations and detailed documentation of spatial extent of the impacted area and lahar deposit thickness are needed to produce accurate lahar simulations, as well as the further adaptation of existing numerical simulation tools to better suit these particular environmental settings.

Keywords: volcano-hydrologic hazards, small-scale lahars, field observation, LaharZ, Q-LavHA, tropical Africa, Digital Elevation Model, Comoros

INTRODUCTION

Lahars are sudden and highly mobile mixtures of water, sediment and rock debris originating from volcano slopes (Smith and Lowe, 1991). Since lahars are fundamentally unsteady flows and experience temporal and spatial transformation while flowing downstream (Pierson and Scott, 1985), the term has commonly a genetic connotation rather than referring to a particular flow behavior or sediment concentration (Vallance, 2005; Manville et al., 2009; Vallance and Iverson, 2015). Lahars are defined as primary when syn-eruptive and secondary when occurring after the volcanic activity. Secondary lahars can notably be triggered by heavy precipitation events. They represent a significant and persistent volcanic hazard, capable of impacting downstream infrastructures and settlements years to decades after an eruption (Vallance, 2005; Mothes and Vallance, 2015; Jones et al., 2017). A critical requirement for the formation of a lahar is the availability of erodible material in the rainwater accumulation zone or along the flow path, allowing an increase of both the initial lahar volume and a multiplication of the discharge by several times while flowing downstream (Scott et al., 2005; Doyle et al., 2011; Vallance and Iverson, 2015). This volume increase process is known as bulking and can lead to intensive channel and bank erosion upstream and incremental infilling of channels downstream of break-in-slope. By reducing the channel conveyance capacity, the infilling can induce overflows during, but also after the event(s) if no action is undertaken to improve the channel conveyance capacity (Pierson, 2005).

Lahars are major volcanic hazards, particularly in tropical and warm temperate volcanic regions where high-intensity rainstorms are common (Mothes and Vallance, 2015). The reduction of the risks related to lahar hazards and the determination of proper mitigation measures require delimiting potential lahar runout and extent as well as understanding the triggering factors (Rodolfo, 2000; Huggel et al., 2008; Darnell et al., 2012). Delineation of lahar hazard zones has traditionally been based on field identification of the inundation limit and the review of past records (Scott, 1988; Lavigne et al., 2000; Perrotta et al., 2006), but now computer models are used as part of lahar hazard assessment to overcome the absence of, or complement historic and geologic records of past lahars (e.g., Canuti et al., 2002; Macías et al., 2008; Darnell et al., 2012; Pistolesi et al., 2014; Castruccio and Clavero, 2015). These models commonly fall into different categories, ranging from empirical models lacking explicit flow physics (e.g., MSF, Huggel et al., 2003; LaharZ, Iverson et al., 1998) to complex models based on computational fluid dynamics (e.g., FLO-2D, O'Brien et al., 2007 or Titan2D, Pitman and Le, 2005; Manville et al., 2012; Mead et al., 2016; Córdoba et al., 2018).

Accurate numerical simulation of topography-driven mass flows requires adequate representation of topography (e.g., Wechsler, 2007; Huggel et al., 2008; Boreggio et al., 2018). However, virtual representations of the topography in a Digital Elevation Model (DEM) are not exempt of errors and uncertainties, for example associated to data acquisition method, local environmental condition, spatial resolution or simply time since their acquisition. Those uncertainties can propagate into the output of volcanic flow simulations, reducing overall model accuracies (Stevens et al., 2003; Hubbard et al., 2007; Darnell et al., 2010; Deng et al., 2019). To increase the performance of flow models, some authors use enhanced versions of the original DEM in which field measurements of the channel morphology are implemented (Muñoz-Salinas et al., 2008, 2009; Darnell et al., 2012; Deng et al., 2019). Such updates to a DEM commonly allow for more realistic simulations and extraction of topographic information, but were mainly tested on steep stratovolcanoes with deeply incised ravines (Muñoz-Salinas et al., 2008, 2009; Darnell et al., 2012; Deng et al., 2019).

This work focuses on a series of lahars which affected Grande Comore Island for nearly a decade after the occurrence of two mildly explosive eruptive phases of Karthala volcano in 2005. These flows affected thousands of inhabitants living in settlements situated at the foot of Karthala, becoming one of the main hazards linked to the volcano (IFRC, 2013; Morin et al., 2016). Despite the relatively extensive impact of these lahars, only the impact of these flows on the surrounding population was investigated (Morin et al., 2009, 2016; Morin, 2012), the characteristics of the lahars, as well as the future hazard they represent remaining largely overlooked. Hence, we first describe the physical characteristics and map the spatial extent of the debris deposited by the flows that affected Grande Comore Island. While the repetitive occurrence of these lahars over populated terrain favored important impacts, these events were relatively small-scale compared to the ones commonly occurring on stratovolcanoes (e.g., Vallance, 2005; Mothes and Vallance, 2015). The smooth surface topography of the basaltic shield volcano contributes to further challenge the numerical simulation of the lahar inundation susceptibility, because the narrow ravines that guided the flows are poorly incised in the surroundings and barely represented in the existing digital topographic data. Therefore, we aimed at testing the ability of a recent probabilistic flow model (Q-LavHA; Mossoux et al., 2016) to reproduce these lahars numerically, compared to a standard volume-limited lahar model (LaharZ; Iverson et al., 1998; Schilling, 2014). The mapped

lahar deposits served to calibrate and compare numerical lahar simulations through the use of fitness indices. Uncertainties in the original DEM associated with the limited erosion of the volcanic edifice yielded to an unclear modeled drainage pattern, and ultimately introduced important errors in the estimation of the lahar-prone areas. Therefore, we also evaluated the simulation accuracy by updating the digital topography with ravine geometries measured in the field.

STUDY AREA: KARTHALA VOLCANO, GRANDE COMORE

Grande Comore Island or Ngazidja is part of the Comoros archipelago, located in the northern part of the Mozambique Channel, between East-Africa and Madagascar (**Figure 1**). The archipelago is under the influence of a tropical humid climate composed of two seasons: a hot and wet season from October to April during which most of the lahars occurred, and a relatively cool and dry season from May to September. The highest precipitations on a yearly basis, 6000–9000 mm, occur close to the summit of Karthala volcano, compared to 2700 mm per year on average at sea level (Morin, 2012). Despite the high amounts of rainfall, the runoff experienced on the island is generally limited to an estimated 5% of rainfall annually. This is due to important infiltration in the permeable lava and scoria that make up the bulk of the volcano (Bourhane et al., 2016) and the dense tropical vegetation cover on the flanks of the volcano. As a result, there is no permanent river on the island.

Karthala volcano (11.75°S, 43.35°E; 2361 m a.s.l.) forms the southern two-thirds of Grande Comore Island (**Figure 1**). It is a typical, relatively young (formations of the western flank date 0.1 ± 0.1 Ma) basaltic shield volcano constructed primarily by successive lava flows and therefore erosion is limited (Bachelery and Coudray, 1993). Karthala's eruptive style is primarily effusive, but sporadic ash-forming phreatic eruptions also occurred from the summit crater at times when a permanent crater lake was present (Bachèlery et al., 2016). Two, mildly explosive, eruptions occurred in 2005 and each emplaced more than 50 × 10^6 m^3 of loose volcanic material on Grande Comore Island (Morin et al., 2009). Centimeter-deep tephra fall deposits have affected between two-thirds (April 2005) and half (November–December 2005) of the island, with meter-deep deposits being measured at the summit of Karthala volcano (Smietana et al., 2007; Morin et al., 2009). Following these eruptions and until 2012, the recurrent formation of lahars from the summit area of the volcano was

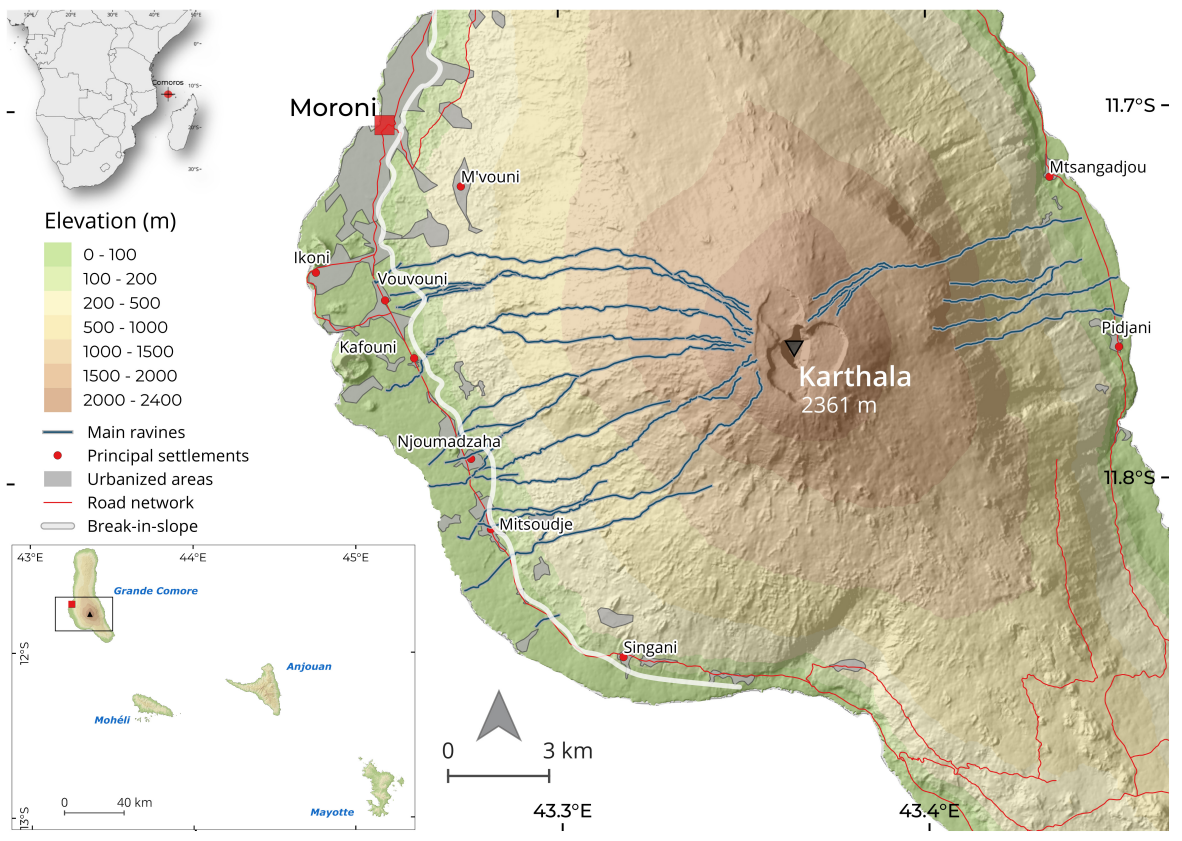

FIGURE 1 | Grande Comore Island and the Comoros Archipelago (insert). The location of the main ravines present on the flanks of Karthala Volcano (southern half of Grande Comore Island) as well as the location of the main settlements are indicated. Note that most of the settlements are sited at the foot of the volcano and their limits often intersect the path of one or multiple ravine(s). Eight ravines on the western flank and one on the eastern flank source from the summit of Karthala where important tephra fallouts were deposited during the 2005 explosive eruptive phases.

observed. These lahars were guided alongside the flanks of the volcanic edifice by small-scale ravines. The decrease in slope gradient and loss of confinement at the foot of the volcano favored overflow and the emplacement of large quantities of sediments within the narrow coastal zone. The majority of the events were documented on the western flank of the volcano. This zone coincides with the most densely populated area on the island, that for a large part concentrates over the coastal zone at the foot of the western flank of Karthala (Mossoux et al., 2018, 2019). At present, the central summit crater holds no permanent lake.

MATERIALS AND METHODS

Survey of Lahar Deposits

A field survey of the lahar deposits was completed in September 2015 to assess the nature of lahars on Karthala volcano. We delineated the extent of the deposits in the area downstream of the break-in-slope (i.e., the aggradation area within the coastal zones, **Figure 1**) by using participative mapping with local communities and extensive field survey. The impacts of the different lahars in each village were discussed with inhabitants and the affected area was collectively delineated on printed satellite views (Google Earth images from 2012). In addition, areas affected by lahars in the villages and their surroundings were visited with local inhabitants. A systematic characterization of deposit thickness and granulometry could not be obtained any longer due to erosion and commercial excavation during the lag time between the event occurrence and the field observations. Instead, a general picture of the characteristics of the deposits (e.g., overall grain size, sorting, thickness, etc.) at different sites over the aggradation area was obtained in man-made trenches where lahar deposits are commercially excavated. The lahar deposits were mapped in September 2015 and therefore integrate material from several events. Yet, they best represent the 2012 lahars which were the last and largest-scale events.

Update of the DEM With Field Measurements of Ravine Morphology

Many of our preliminary lahar simulations at Karthala volcano poorly simulated the hazard-prone position of infrastructures and settlements actually affected by lahar events (see "Results" section). Adequate representation of the topography in a DEM being a fundamental parameter for numerical simulation of mass flows such as lahars (Wechsler, 2007; Huggel et al., 2008; Darnell et al., 2010), we suspected that poor simulation results were caused by lack of representation of small-scale ravines in the DEM. Those ravines guiding the flows over the otherwise smooth topography of the flanks of Karthala, their inaccurate representation resulted in errors in flow path calculations. In an effort to increase simulation accuracies, we updated the available high-resolution DEM [a 10 m TanDEM-X (from 2011 TDX images)] by using field measurements of ravine morphology (**Figure 2**). This DEM was produced by EADS-ASTRIUM with expected absolute horizontal and vertical accuracies < 10 m and relative vertical accuracies < 4 m (Wessel, 2018).

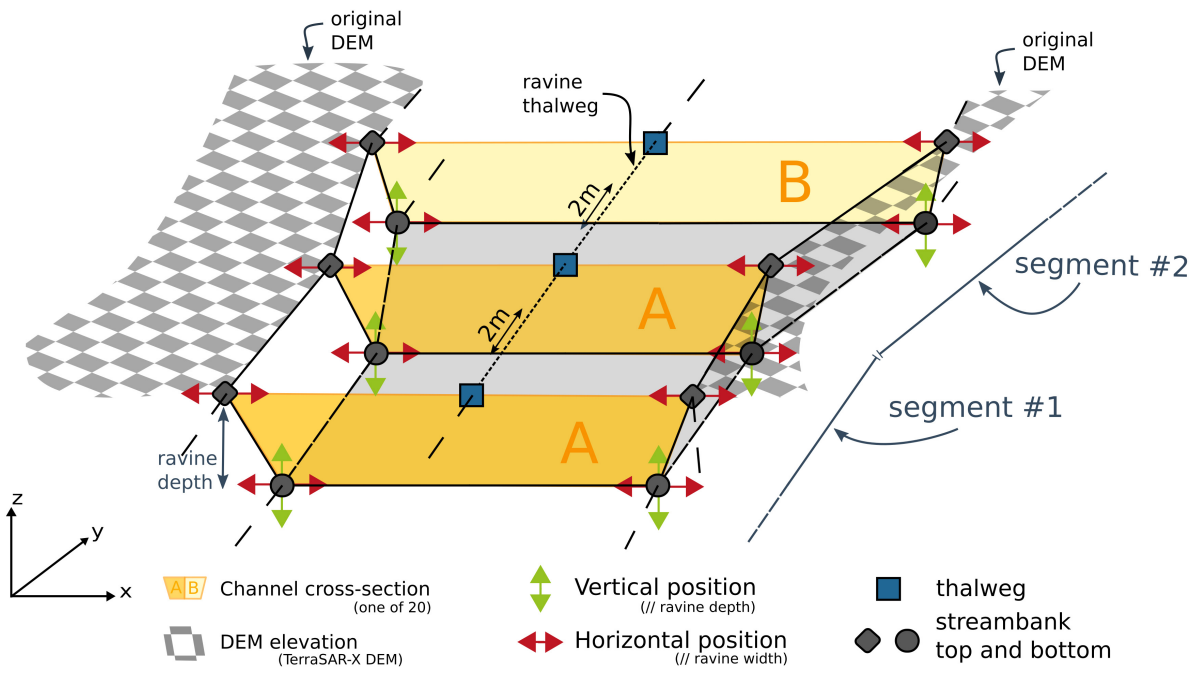

FIGURE 2 | Schematic representation of the method used to implement channel cross-sections in the DEM. Two different channel cross-section geometries (A and B) are presented, corresponding to two different ravine representative segments (#1 and #2). Their characteristics (width, depth, and steepness of streambanks) are derived from field observations for each segment of the ravine.

The method used for the survey of ravine morphologies was adapted from Muñoz-Salinas et al. (2008) and Maerker et al. (2015). It aimed at a rapid and accurate survey of many ravines in a limited amount of time. For each ravine, we recorded the position (x-, y- coordinates) of the thalwegs using a hand-held GPS device with a 2–5 m precision. Measurements of the channel geometry (width and depth) were collected using a measuring tape each time a change in the morphology of the ravine's cross-section was encountered. Not all ravines located on the flanks of Karthala were surveyed and none on its entire length due to access difficulties (e.g., dense vegetation, high cliffs, steep slopes, etc.). A priority was given to ravines which are most important by their size, the quantity of material transported to the coastal area and/or by their probability to affect a village.

The collected information concerning ravine geometry then served as basis to update the DEM, adapting the methods developed by Muñoz-Salinas et al. (2008). To limit the overall complexity of implementing a very large number of different channel cross-sections, we first grouped all different ravine segments into 20 groups (later called representative segments) based on their observed channel geometry (width and depth; **Supplementary Figure 1**). For segments where no field measurements could be collected (about 50% of the combined ravine length on Karthala western flank), the position of the thalweg was deduced from high-resolution Pléiades images (2013) and the channel characteristics were assigned based on known segments having similar elevation, distance from summit and/or slope characteristics.

The implementation of the ravine channel in the DEM was started by creating points along the thalweg (i.e., the middle of the ravine channel) at 2 m intervals (**Figure 2**). At the position of each of these points, we schematically drew a ravine channel cross-section (perpendicular to the thalweg line) by defining four points representing the top and the bottom of each stream bank (see Muñoz-Salinas et al., 2008; **Figure 2**). Both width and depth of the cross-sections were defined based on the values of the representative segment derived from field observations. The elevation of the top the streambanks is simply determined from the original elevation at this location (derived from the DEM). The elevation of the bottom of the streambanks corresponds to the depth of the ravine, therefore subtracted from the original elevation at this location (**Figure 2**). To allow the implementation of these 4 points representing the cross-section along the ravines, the TDX DEM was fully converted into a point feature, where we replaced the points located in the ravine with these newly created cross section points. Because the 10 m resolution of the DEM is not adequate to represent the small ravine dimensions, the initial elevation points were resampled to 5 m resolution using a bilinear interpolation resampling technique in a GIS environment. The final DEM was then interpolated using the ANUDEM method developed by Hutchinson (1989) and Hutchinson et al. (2011). The result is a raster DEM at 5 m resolution where the ravine channels, previously imperceptible to both the eye and flow models, are now present in the DEM representation of the surface topography.

Models for Lahar Flow Simulations

Two simple models were used to reproduce the lahars documented on the flanks of Karthala volcano. Both models are topography driven and do not require the input of hydraulic parameters.

LaharZ (Iverson et al., 1998; Schilling, 2014) is one of the most widely applied models for lahar hazard zonation (Manville et al., 2012; Castruccio and Clavero, 2015). This semi-empirical model is based on relationships derived from the compilation of data from ∼30 lahars worldwide, which provides a correlation between the lahar volume V (m^3), the channel cross-sectional area filled by the flow A (m^2), and planimetric inundation area B (m^2):

$$A = CV^{\frac{2}{3}} \quad (1)$$

$$B = KV^{\frac{2}{3}} \quad (2)$$

where C and K are constants commonly set at 0.05 and 200 for lahars, respectively (Schilling, 2014). These values may not be accurate for all environments (Carranza and Castro, 2006), and some authors (e.g., Worni et al., 2012; Castruccio and Clavero, 2015) have modified those to fit more closely to the characteristics of the flows studied. Given the relatively small scale of the lahars generated on Karthala compared to those included in the dataset of Iverson et al. (1998), we recalibrated the constants using our estimates for the lahars of Karthala (**Table 1**) and data for events of similar scale in the dataset of Iverson et al. (i.e., lahars with volumes less than or equal to 1.5×10^6 m3). From this set combining 16 small-scale lahars, we obtained values for C and K coefficients of 0.04 and 100. We evaluated the potential increase in accuracy provided by the recalibrated constants by comparing to simulation outputs obtained with the values commonly used for lahars (C = 0.05 and K = 200; Schilling, 2014). Simulations were performed for flows with four volumes ranging from 0.5×10^6 m^3 (average estimated volume from the study of the lahar deposits (section "Description of Flow Deposits") to 5×10^6 m^3, that is ca. 3 times the largest estimated volume for a lahar at Karthala volcano.

In LaharZ the onset of the inundation area is usually defined by the intersection of a theoretical cone and the real topography. This so-called H/L cone is known as the proximal hazard zone boundary (PHZB). Owing to the convex shape of Karthala's volcanic edifice (shield volcano), the automatic location of the PHZB was found unrealistic. Similar limitations have already been encountered on other edifices (e.g., Canuti et al., 2002; Pistolesi et al., 2014). Hence, the location of simulation onsets was here manually defined based on the reconnaissance fieldwork, with onsets located between 600 and 800 m a.s.l. on the flank of Karthala. This position is located directly downslope of the lowermost flank section steeper than 20° (hereafter called Onset-L), where ravines are less incised and overflows (i.e., deposition of material outside the ravine channel) were documented. This position might best represent the point where the lahars reached their maximum volume through runoff accumulation and bulking. To assess the capability of LaharZ to also simulate propagation of lahars on steep, erosive section of the ravines

TABLE 1 | Extent and estimation of volume of lahar deposits mapped in the field in September 2015 for the ravines draining the western flank of Karthala volcano.

Settlements	Fine-grained deposits (10^5 m^2)	Bouldery deposits (10^5 m^2)	Total deposits volume (10^5 m^3)	Flow volume estimates for 2012 event (10^5 m^3)
Vouvouni and Mde	11 ± 1.5	0.7 ± 0.07	6 ± 1.0	8 ± 1.6
Kafouni	5.2 ± 0.5	1.3 ± 0.15	3 ± 0.6	5 ± 1.0
Selea	6.5 ± 0.7	1.5 ± 0.16	4 ± 0.8	6 ± 1.2
Nioumadzaha	10 ± 1.0	4.5 ± 0.5	7 ± 1.1	10 ± 2.0
Mitsoudje and Salimani	3.5 ± 0.4	2.0 ± 0.2	3 ± 0.6	4 ± 0.8
Bandani	5.5 ± 0.6	1.5 ± 0.2	4 ± 0.8	5 ± 1.0
Bangoi	2.6 ± 0.3	0.8 ± 0.08	2 ± 0.4	3 ± 0.6
Total	44 ± 5.2	12 ± 1.4	29 ± 5.3	41 ± 8.2

*A discrimination between the extent of fine-grained and bouldery deposits is made and total volumes of sediment are provided for each ravine (named by the closest settlement). Estimates are provided for the deposits mapped in the low-lying coastal area below the break-in-slope at foot of Karthala (see **Figure 4**). An evaluation of potential flow volumes for the April 2012 event is provided by considering that 60% of the total volume of sediment documented in the field were emplaced at this date (coherent with testimonies and field observations). From this estimation of the volume of material transported by the flows, an estimation of the total volume of the lahars (water and sediments) is provided, assuming the lahars had a mean sediment concentration of 40% of the volume (e.g., Lavigne and Thouret, 2003).*

such as performed by Q-LavHA, simulations were also performed from the summit of the volcano (>2200 m) where the lahars were initiated (Onset-H).

Q-LavHA is an open-source plugin that combines existing probabilistic and deterministic models to simulate flow invasion probability based on a DEM (Mossoux et al., 2016). Although the complete plugin was initially designed to model lava flows, the probabilistic approach proposed – because simply constrained by the steepest slope – is relevant to model any other topographically controlled gravity-driven mass flow. Its utilization for modeling lahars is evaluated in this study. With this approach, flow path simulations are iterated from a predefined source point to calculate the probability of inundation of every pixel of the area, with iterations allowing to mimic lateral spread and flow bifurcations. To define where the flow will propagate, the model analyses at each step the elevation of the eights surrounding pixels, allocating to each the following probability to host the flow (Mossoux et al., 2016):

$$P_i^2 = \frac{(\Delta h_i)^2}{\sum_{j=1}^{8}(\Delta h_j)^2},\ i = 1,\ 2,\ \ldots,\ 8 \qquad (3)$$

where Δh_i is the difference in altitude between the pixel where the flow is located (central pixel) and each of the eight surrounding pixels. The probability of each pixel to be inundated by the flow is then calculated by computing several random paths by means of a Monte Carlo algorithm and calculating which proportion of these paths passes through any given pixel. The use of the second power increases the probability of the selection of the steepest flow path and reduces the flow width (Mossoux et al., 2016). This parameter is certainly important for lahars which are more constrained by gravity and more confined in the channel because of their lower overall viscosity with respect to lava flows. To the elevation of the central pixel, the user may decide to add two topographic correction factors (H_c and H_p) that allow the flow to overcome small obstacles and split in several branches. H_c is always added to the elevation of the central pixel before calculating Δh_i and represents the average thickness of the flow (in meters). H_p factor is designed to represent the maximum flow thickness (in meters). By filling small cavities and allowing to overcome small topographical obstacles when H_c is not sufficient, it also influences the degree of lateral spread of the flow. We tested a conservative range of values for H_c (mean flow thickness; 0–4 m) and H_p (maximal flow thickness; 0–6 m). These values seem appropriate in light of the maximum inundation depth reported by eyewitnesses in the villages affected by the lahars, and relationships from the literature stating that lahar flow thickness can be 4–5 times the deposit thickness (Thouret et al., 2020). For each ravine are defined two simulation onsets: Onset-H located over the summit of Karthala where the lahars were initiated (>2200 m a.s.l.) and Onset-L, defined for LaharZ simulations and located where the lahars reached their maximum volume through runoff accumulation and bulking (∼600–800 m a.s.l.). While LaharZ simulations are volume limited, in Q-LavHA, the length of the simulated lahar is simply limited to a maximum length defined by the user. We here provided input lengths (∼30–120 km) that preliminary tests showed sufficient for the simulated lahars to reach the coastal area at the foot of the volcano but that are actually largely exceeding the actual (∼10–14 km) distance between Karthala summit and the coastal area. Accuracies of simulations using four different runout length values were compared. The set-up of the Q-LavHA model, including interdependencies between simulated flow length and DEM resolution, is described in detail in Mossoux et al. (2016).

Three different DEMs were used in the simulations: the original TDX 10 m DEM, an original TDX DEM resampled to 5 m resolution and an updated version of the 5 m resolution DEM that considers the detailed ravine geometry (see section "Update of the DEM With Field Measurements of Ravine Morphology"). The use of these different DEMs allow discrimination of the effect of resampling and of the implementation of the ravine morphology on the simulation outputs.

Different inundation scenarios were tested, to allow parameter calibration and therefore compare the outputs of the most accurate LaharZ and Q-LavHA simulations. For both models, we ran a range of simulation scenarios with the different combination of input parameters that can be tuned in the models (i.e., C, K coefficients and volumes for LaharZ and H_c, H_p and flow length values for Q-LavHA). This was done for simulations over the three ravines draining the western flank of Karthala

that experienced the largest documented lahar flows. In addition, those simulation scenarios were replicated for the two different simulation onsets (Onset-L and Onset-H) and the three different DEMs. The accuracy of each simulation scenario is assessed by use of fitness indices (FI), where the simulated flow is compared to the spatial extent of the deposits mapped in the field (e.g., Favalli et al., 2009; Mossoux et al., 2016). For each ravine, we selected based on the fitness indices the simulations with the highest accuracies for comparison with the best simulations from the other model (best-fit scenario). Detailed fitness indices are provided for the simulations with the highest accuracy for each model, ravine, onset and DEM in **Supplementary Table 2**.

Three different fitness indices are calculated. The true positive (TP) assesses the fit between the simulated inundation area (A_{sim}) and the area mapped in the field (A_{field}). Also referred to as the Jaccard similarity coefficient (Levandowsky and Winter, 1971), it is calculated by dividing the overlapping area between the simulated flow and the actual flow by the net total area covered by the simulated and actual event (Eq. 4).

$$true\ positive\ = \frac{A_{sim} \cap\ A_{field}}{A_{sim} \cup\ A_{field}} \tag{4}$$

The false positive (FP) measures overestimation of the actual inundated area. It therefore represents the fraction of the simulated inundation area that was not mapped as inundated in field (Eq. 5).

$$false\ positive = \frac{A_{sim} - (A_{sim} \cap\ A_{field})}{A_{sim} \cup\ A_{field}} \tag{5}$$

Finally, the false negative (FN), measures the underestimation of the actual inundated area, representing the fraction of the inundation area mapped in the field that is not simulated by the model (Eq. 6).

$$false\ negative = \frac{A_{field} - (A_{sim} \cap\ A_{field})}{A_{sim} \cup\ A_{field}} \tag{6}$$

The three indices being divided by the total area covered by the two flows, their sum equals one (see Mossoux et al., 2016). Note that we consider that high accuracy simulation must both have high true positive values (area correctly delineated) and very low false negative values (area underestimated), both indices being crucial for effective use in risk management (Mossoux et al., 2016). Since Q-LavHA outputs provide probability-related values indicating areas more or less likely to be inundated, a probability value of 0.01% was chosen to classify Q-LavHA simulation pixels into the same two categories as the binary outputs of LaharZ (inundated or not inundated) to allow comparison with the latter. Finally, note that the fitness indices are calculated only over the area downstream of the concave break-in-slope found at the foot of the volcano (**Figure 1**). This allows comparing the two models despite their different strategies in the positioning of the simulation onset.

CHARACTERISTICS OF LAHARS

Karthala Ravines

The majority of the ravines on the Karthala edifice have their origin close to the volcano summit (**Figure 1**), where important tephra fall deposits (up to 2 m thick) were emplaced during the 2005 eruptions (Smietana et al., 2007; see **Figure 3a**). Ravines' width ranges from 5 to 20 m and depth from 1 to 20 m. These values vary greatly, both among ravines and within a single ravine as a function of elevation along the volcano flank. As expected, while most are narrow and shallow close to the fairly flat Karthala summit, they deepen with increase in slope gradient. On the steep flanks, these ravines cross a series of resistant lava flows separated by weaker layers of scoriaceous rubble, sporadic ash or soil. We observed many collapsed streambanks probably formed by undercutting of the weaker layers by intense flows (**Figure 3b**).

Not all ravines reach the shoreline. Many exhibit significant reduction in depth or even total disappearance in the low-lying area after the concave break-in-slope at the foot of Karthala volcano (**Figure 1**). There, debris-fans represent most of the lahar deposits (**Figures 3c,d**). Most of these debris fans are occupied by settlements.

Description of the Flow Events

Ash fallouts associated with the two 2005 explosive eruptions damaged or killed Karthala summit vegetation (depending on the distance from the summit crater). Locally up to meters-thick, a fine ash blanket greatly modified the infiltration capacity of the soil through the formation of an impermeable crust. The combined effect of poor vegetation and decreased permeability increased runoff on the upper slopes of Karthala during heavy precipitation episodes. Surface runoff was able to erode the surface crust, conveying large quantities of loose volcanic material from the summit area by converging into the pre-existing ravines. The first lahars occurred in April 2005 and were described as relatively cohesive hyperconcentrated flows composed of 20–60% of fine to very fine ash (Morin, 2012). Following the limited reestablishment of the vegetation and the relative depletion of unconsolidated volcanic material over the summit area, the sediment concentration of the flows tended to decrease, particularly after 2008 when most of the flows could be considered as normal streamflow (Morin, 2012). However, the two largest and most destructive series of lahar events were experienced in April 2009 and April 2012. This last sequence was of unprecedented volume and debris content and led to significant damages over the densely inhabited south-west part of the island, disrupting the ecology and human activity in the area for months while destroying kilometers of roads and hundreds of houses (Direction Générale de la Sécurité Civile [DGSC], 2012; IFRC, 2013). The complete series of events (2005–2012) is not known due to the scarcity in archive sources, but at least ten sequences were documented (**Supplementary Table 1**).

Rainfall data could aid understanding of the formation processes of the observed lahar events. The quality of *in situ* precipitation measurements available (Agence nationale de l'Aviation Civile de la Météorologie [ANACM], 2015) is

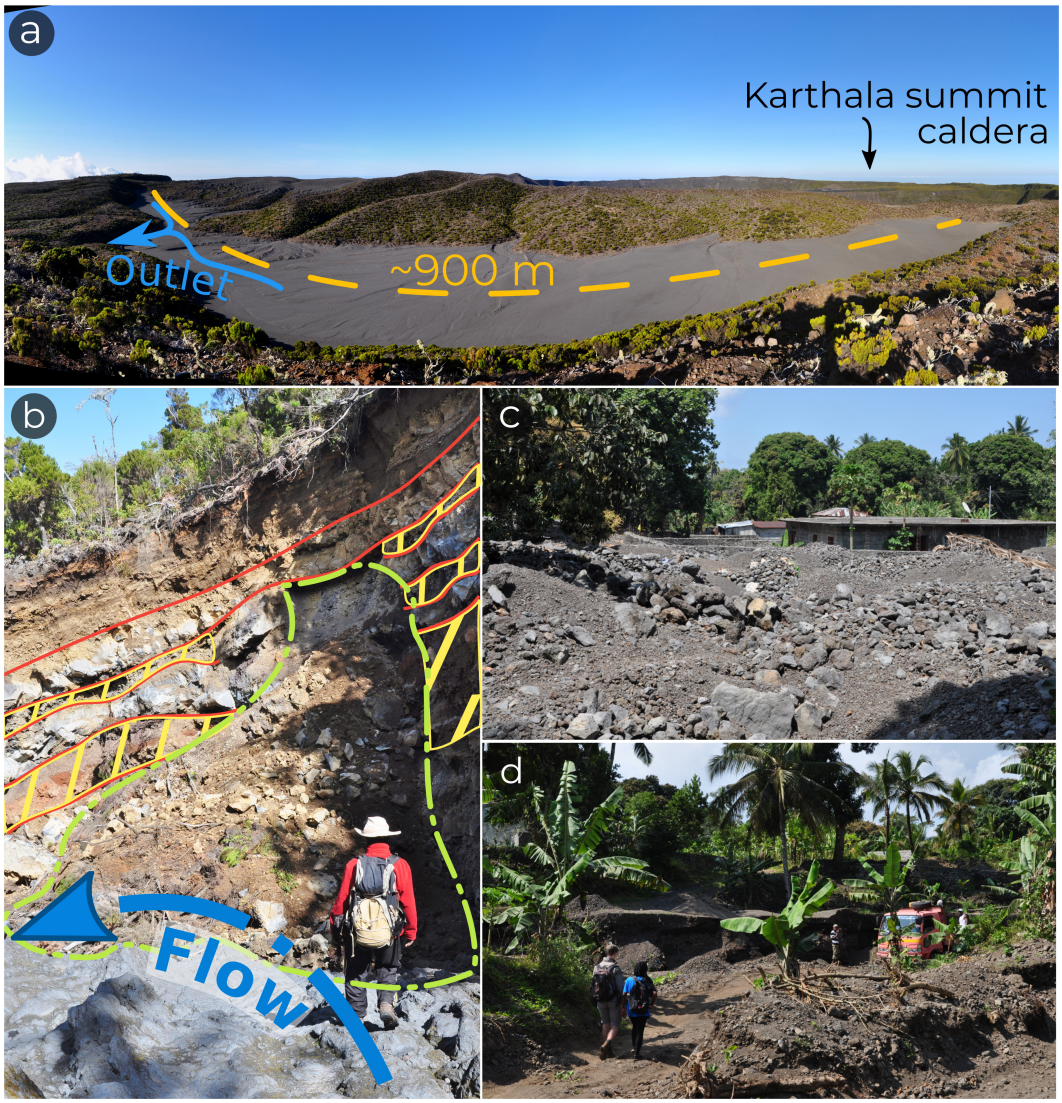

FIGURE 3 | (a) Tephra accumulation zone at the edge of the caldera rim of Karthala (September 2015). The blue arrow represents the outlet of a ravine located on Karthala' western flank. **(b)** Example of streambank collapse. Massive lava flow cores (outlined in red) are separated by weaker layers of scoriaceous rubble (yellow hatching). Once competent lava layers are damaged, the weaker underlying layers are easily undercut. Streambank may then collapse during large water discharge and produce debris with various sizes (up to 5 m), mainly made up from the more competent lava cores. Erosion processes can also take place in the ravine bed. Example of **(c)** boulder-supported and **(d)** fine-grained lahar deposits found at the foot of Karthala volcano. Notice the proximity of housing (built after the 2012 lahar events) and the use of the deposits as construction material.

nevertheless inconsistent for the period of interest (2005–2012). Considering the quality of new global satellite precipitation measurements (e.g., Dezfuli et al., 2017; Skofronick-Jackson et al., 2017), we processed data from version 6 of the Integrated Multi-satellite Retrievals for Global Precipitation Measurement (IMERG; Huffman et al., 2019) to retrieve rainfall estimates (**Supplementary Figure 2**). We investigated the period 2001–2018 for two IMERG pixels located over the center and the western coastal area of Grande Comore Island. These measurements highlight the exceptional rainfall during the lahars of April 2009 and 2012. Respectively 145 and 290 mm of rain were recorded over the center of the island (i.e., Karthala volcano) on 6 and 7 April 2009. Surprisingly, the lahars were reported to have occurred on 15 and 16 April (**Supplementary Table 1**), nearly 10 days after this major rainfall event but coeval with a second, lower magnitude rainfall episode (150 mm in 2 days). The complete series of 10-day cumulative rain measured between 7 and 16 April 2009 shows values that are, by far, ranked as the highest for the 2001–2018 period. Precipitation was less concentrated in April 2012, with measured daily maxima up to 70 mm/day over the coastal area, and 50 mm/day over the center of the island. However, the 10-day cumulative precipitation series for the coastal area (up to 450 mm) is ranked as the highest for the period 2001–2018. During the 2012 event, lahars were

reported to occur between 20 and 25 April. This suggests that the lahars occurred after 10 days of nearly continuous moderate to heavy rainfall.

Description of Flow Deposits

Most of the lahar deposits mapped over the two flanks were observed in the low-lying areas below the concave break-in-slope found at the foot of the volcano (**Figure 4**). There, a decrease in slope gradient and loss of confinement favored incremental infilling of the ravine channels by repetitive deposition from sediment-laden flows. The deposits mapped in September 2015 therefore integrate material from the recurrent sequences of small-scale secondary lahars that followed the 2005 eruptive phases. Yet, their outline probably best represents the April 2012 sequence, which was the last and largest recorded over the island. The mapped deposits cover an area of about 4.4 ± 0.5 km^2 over the western flank of Karthala (**Table 1**) and 0.8 ± 0.1 km^2 over the eastern flank.

As expected, lateral and distal thinning of deposit thicknesses and diminishing grain sizes are observed with increasing distance from the break-in-slope. Deposits found near the foot of Karthala are mostly composed of coarse clasts [angular to rounded boulders (0.25–2.0 m diameter) and large gravels] and poorly sorted sediment, sandy (and smaller) sediments being present in relatively low quantity (estimated < ∼30%, **Figure 3c**). Similar coarse clasts were found at all altitudes during the survey of the ravines suggesting that these clasts originate from scouring and undercutting of the ravine beds and streambanks. In total, about a quarter (1.2 ± 0.2 km^2) of the area mapped over the western flank of Karthala is dominated by such bouldery deposits (**Table 1**). Farther downstream, the presence of large clasts decreases, and an overall more fine-grained matrix composed of coarse sand, sand and silt, is prevalent. These deposits were likely emplaced by low-concentration streamflow resulting from the dilution of hyperconcentrated flows (Lavigne and Thouret, 2003). Layering is observed, sometimes with an important change in the average clast size suggesting the occurrence of multiple deposition events. The composition of these sandy deposits is similar to that found on the summit area of Karthala and therefore probably represent eroded tephra-fall material associated to the 2005 eruptions.

From these observations, rough estimates of volcanic material volumes remobilized by the lahars can be estimated for each ravine. Assuming a typical thickness of 1 m for the zones dominated by boulders and 0.5 m for the remainder, debris volumes range from 3 ± 0.6 10^5 m^3 to 7 ± 1.1 10^5 m^3 for each individual ravine. By summing up, a total remobilized volume of 2.9 ± 0.5 10^6 m^3 is estimated for all the ravines of the western

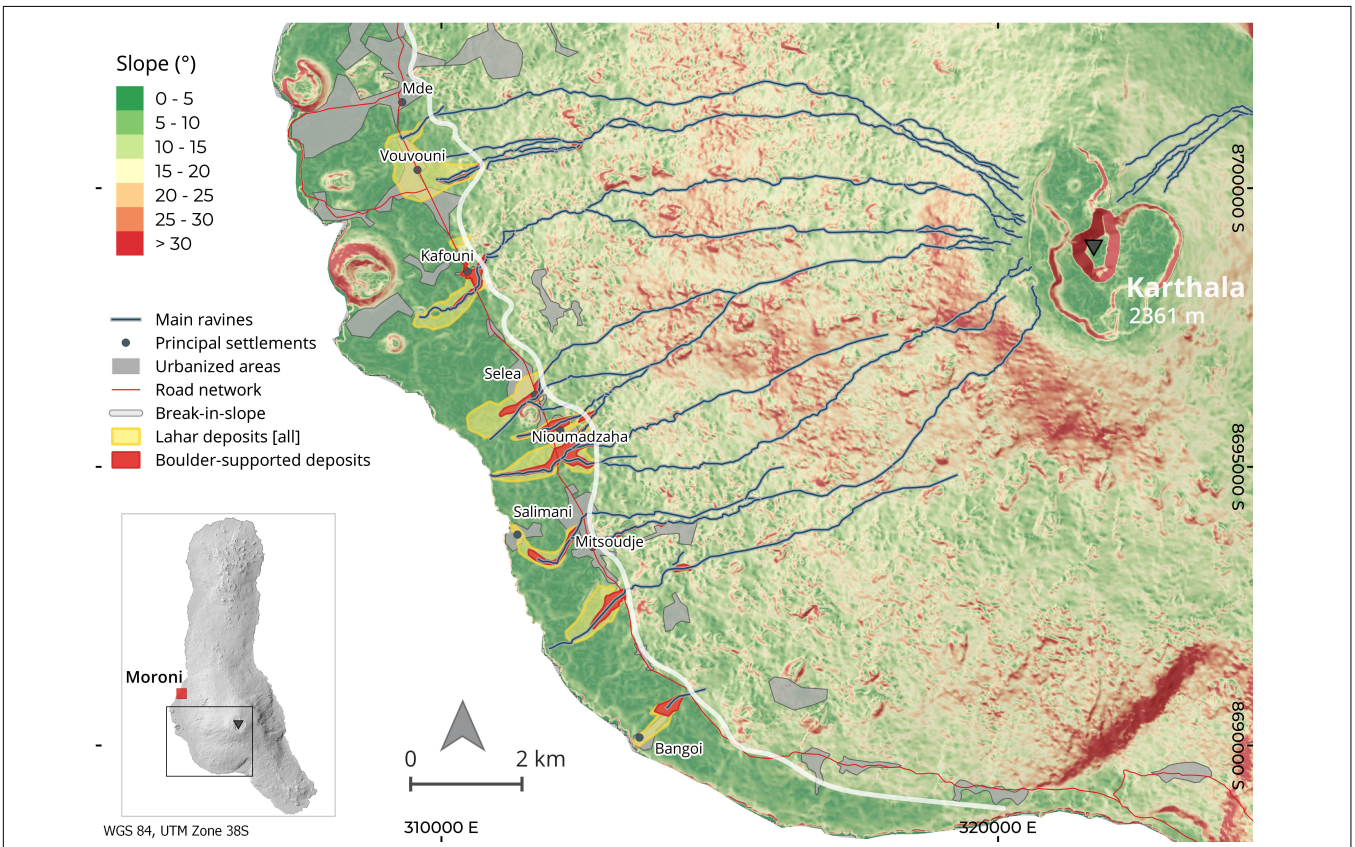

FIGURE 4 | Extent of lahar deposits on the western flank of Karthala Volcano as mapped in the field in September 2015. The extent of zones characterized by boulder-supported deposits is highlighted in red. Notice the frequent overlaps between the settlements and the lahar deposits. The background slope map highlights the position of the break-in-slope. Sectors characterized by large boulder-supported deposits are observed at the foot of ravines crossing the steepest slopes.

flank of Karthala. This estimation yields a mean deposit depth of 0.6 m, which is coherent with field observations. Testimonies and our study of the deposits support that a large fraction of this total volume is associated with the April 2012 flows. Investigation of the lahar deposits also showed that the pattern and scale of lahars varied from catchment to catchment. Bouldery deposits are for instance mostly absent (**Figure 3d**) in the northern ravines that originate from the less steep catchments (**Figure 4**).

NUMERICAL MODELING

Lahar Simulations

Figure 5 displays LaharZ and Q-LavHA simulations with the highest accuracies on the western flank of Karthala. Significant differences are observed in the general spatial pattern of the inundation areas provided by the two models. LaharZ exhibits a single flow unit for each ravine with ragged lateral limits offering binary discrimination between "affected" and "non-affected" zones. Q-LavHA, on the other hand, highlights the probability of inundation of every pixel of the area (DEM). It simulates bifurcations in the flow path and provides a relatively smoother (less ragged) edge of the extent of inundation compared to LaharZ. Comparison of the simulation outputs also shows discrepancies in the lateral extent of the upstream inundation area (before the break-in-slope). While it is kept within a few tens of meters with Q-LavHA, LaharZ simulates widths up to hundreds of meters. Field observations have shown that the actual flows were confined within the ravines over most of the channels' lengths, with lateral overflows limited to a few dozens of meters width (<25 m) over the flatter slope sections. In the low-lying area following the break-in-slope, both codes capture the increase in the lateral extent of the inundation area expected from the loss of confinement and the general decrease of the slope, predicting inundation areas that roughly fit field observations.

Overall, the calculated model accuracies are relatively low, with a median true positive (TP) below the break-in-slope for the three ravines of 0.40 with LaharZ and 0.37 with Q-LavHA (**Table 2**). Importantly, a generally higher fraction of false negative (FN) is observed with Q-LavHA (median value of 0.30 compared to 0.06 for LaharZ simulations). The location (elevation) chosen for the origin of the simulation greatly impacted the calculated accuracy of the outputs of both models. Except for one LaharZ simulation set over the northern ravine, the highest accuracies were always obtained with the lower simulation onset (Onset-L; see **Supplementary Table 2**).

Calibration procedure to obtain best-fit scenarios (most accurate simulations for each DEM, onset and ravine are shown in **Supplementary Table 2**) shows no significant variations of LaharZ simulation outputs with a modification of the C constant. The best-fit value for the planimetric coefficient K depends on the location of the simulation onsets. Simulations performed with a K value of 100 gave the most accurate results for simulations from Onset-L; while a K value of 200 provided the highest accuracies for simulation from Onset-H (Karthala summit). Simulation with volumes in the high spectrum of the range provided the highest accuracies (i.e., $3 \times 10^6\ m^3 - 5 \times 10^6\ m^3$). For Q-LavHA, corrective factors providing the most accurate simulations were 2 m for H_c and 2–4 m for H_p in function of the ravine. These values seem appropriate in light of the maximum inundation depth reported by eyewitnesses in the villages affected by the lahars. Usually, very high runout length values (between 30 and 120 km) gave the most accurate simulations in Q-LavHA (**Figure 5** and **Supplementary Table 2**).

Impact of DEM Update on Flow Simulations

The highest simulation accuracies were generally obtained with the use of the updated DEM (**Figure 5** and **Table 2**). The modifications of the DEM impacted the flow trajectory (particularly for LaharZ), sometimes allowing for the correct identification of the hazard prone-position of settlements otherwise missed with the use of the original DEM. However, the implementation of an accurate drainage system into the DEM did not fully prevent flow simulations from bifurcating to ravines that correspond to another catchment.

Figure 6 displays averaged quality indices over the three ravines using distinct DEMs. Comparison of the fitness indices for the different simulations shows slight improvements for LaharZ and more significant changes with Q-LavHA. On average over the three ravines, the true positives (TP) increased for the two models, from 1 to 10% with LaharZ and from 13 to 77% with Q-LavHA. False negative (FN) values, on the other hand, decreased 7–40% with LaharZ, but increased up to 120% for Q-LavHA in comparison to the use of the original DEM. This

TABLE 2 | Fitness indices for simulations with the highest accuracies obtained by LaharZ and Q-LavHA for the three different ravines.

	True positive		False positive		False negative	
Ravines	**LaharZ**	**Q-LavHA**	**LaharZ**	**Q-LavHA**	**LaharZ**	**Q-LavHA**
Vouvouni	0.40 ± 0.06^{C}	0.37 ± 0.08^{C}	0.45 ± 0.01^{C}	0.30 ± 0.11^{C}	0.16 ± 0.07^{C}	0.33 ± 0.08^{C}
Kafouni	0.38 ± 0.01^{C}	0.44 ± 0.04^{C}	0.57 ± 0.01^{C}	0.44 ± 0.09^{C}	0.06 ± 0.00^{C}	0.12 ± 0.05^{C}
Nioumadzaha	$0.63 \pm 0.01^{A,B}$	0.35 ± 0.05^{C}	$0.31 \pm 0.00^{A,B}$	0.33 ± 0.13^{C}	$0.06 \pm 0.01^{A,B}$	0.32 ± 0.09^{C}
Average	0.47 ± 0.12	0.38 ± 0.04	0.44 ± 0.10	0.36 ± 0.06	0.09 ± 0.05	0.26 ± 0.10

The exponent indicates the DEM with which the highest accuracies were obtained [original 10 m TDX DEM (A), unsampled original TDX DEM at 5 m (B) and the updated TDX DEM at 5 m (C)]. Standard deviation is used to highlight the variation in simulation accuracy depending on the DEM. All the simulations present simulations were performed using the lower simulation onset site (Onset-L). Fitness indices are calculated on the low-lying area below the break-in-slope where most of the lahar deposits were mapped.

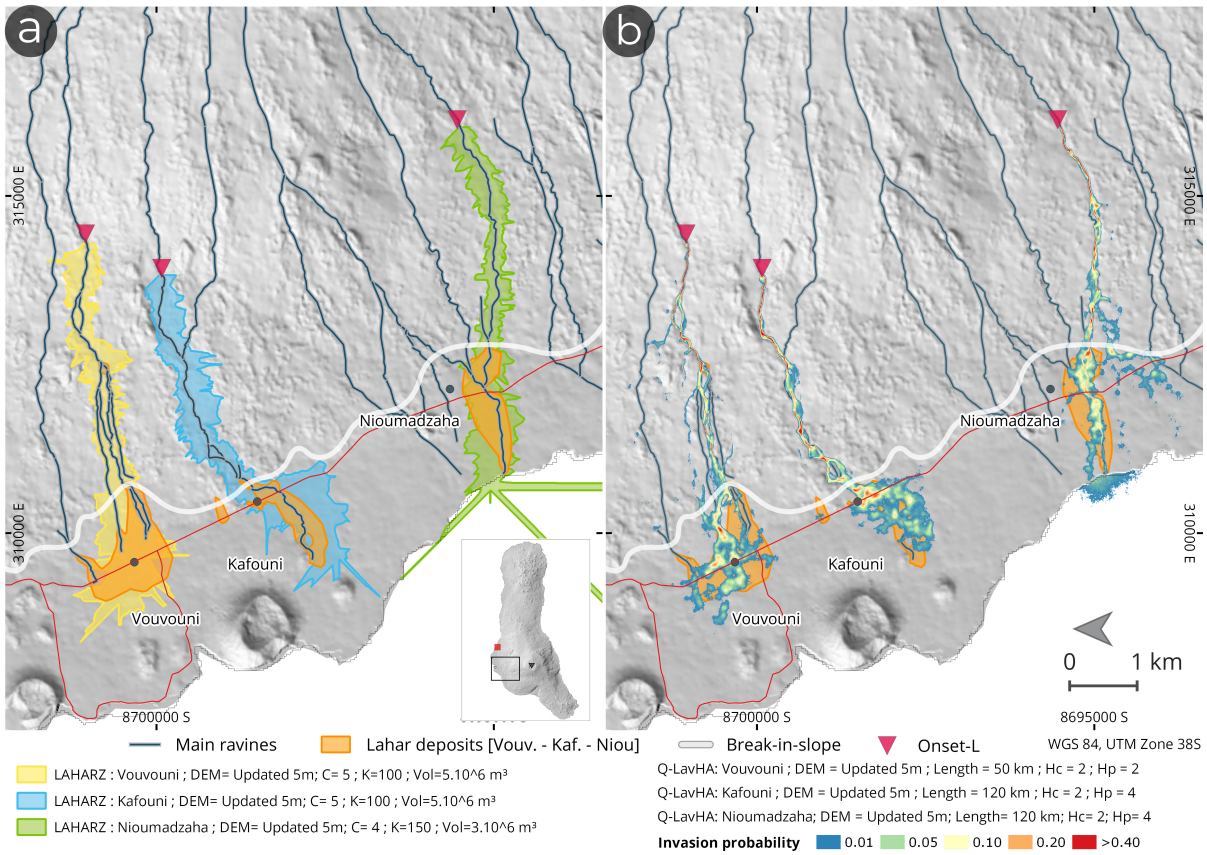

FIGURE 5 | Lahar simulations on Karthala western flank with **(a)** LaharZ and **(b)** Q-LavHA. Simulations with the highest accuracies for the three ravines are shown. The inundation area modeled is compared to the extent of lahar deposits mapped in the field in September 2015 and indicated in orange. The triangles represent the locations of the onsets used for the simulation. All area having an invasion probability lower than 1% in Q-LavHA outputs were filtered out.

increase of false negatives with Q-LavHA simulations is reduced when compared to the upsampled original DEM (**Figure 6**).

DISCUSSION

Lahars Following the 2005 Karthala Eruption

Destruction of vegetation and loss of infiltration capacity by deposition of a meter-thick ash blanket greatly increased surface runoff at the summit of Karthala. Since the summit also represents the origin of most of the ravines draining the flanks of the volcano, it is not surprising that these changes provoked important disturbances to the drainage dynamics. The geomorphic responses included an increase in the frequency, magnitude and spatial extent of seasonal floods, adjustments of the ravine morphology and a strong rise in sediment yield. While common for the aftermath of explosive volcanic eruptions (e.g., Pierson and Major, 2014; Jones et al., 2017), this is unusual for basaltic shield volcanoes. It was here made possible by the deposition of fine ash associated with two phreatic eruptions in 2005, as well as the relative steep flanks and very high rainfall intensity around the volcano summit. Altogether, the documented series of sediment-laden flows are considered as secondary lahars such as defined by Vallance (2000) and Pierson (2005). The study of lahar deposits and eyewitness testimonies illustrate both variations in total discharge volume and sediment concentration across different lahar sequences. Overall, flow magnitudes were probably constrained by catchment characteristics (small and densely vegetated), with recurrent formation of small-scale secondary lahars having volumes of about 10^4–10^5 m^3 and peak discharges in the order of a few 10 m^3/s.

Material from both the volcano summit and ravine channels was found in the aggradation zones over the coastal area, illustrating that flow sediment concentration and mean particle size were increased by bulking. This process led to significant channel and bank erosion upstream of the break-in-slope and incremental infilling of the ravine channels downstream. Incremental filling promoted further reductions of the conveyance capacities of the lower channel reaches, facilitating overflow and the emplacement of large quantities of sediments over adjacent low-lying slopes. This process was certainly favored by the relatively small scale of the ravines in a context of absence of perennial streams. The locations of the villages, almost all located near the break-in-slope, situate them in

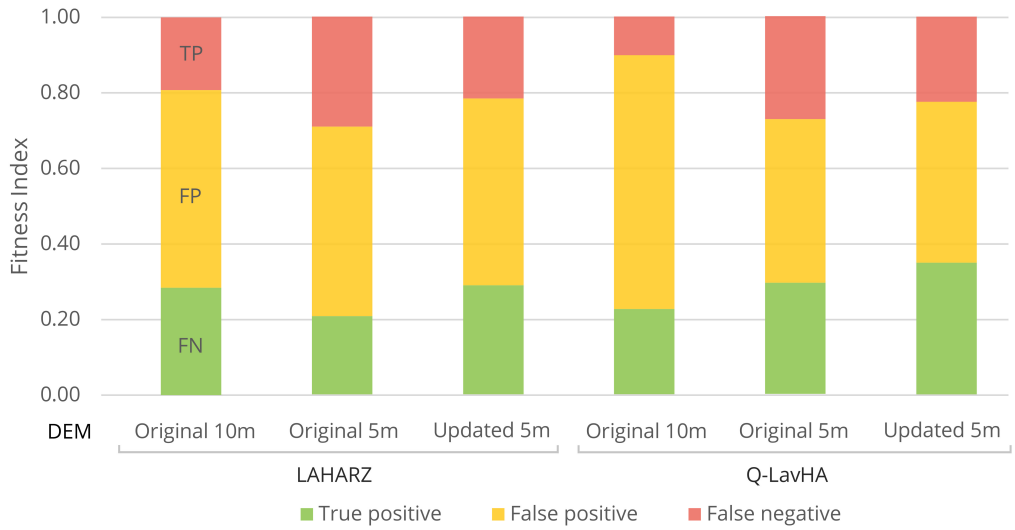

FIGURE 6 | Averaged accuracy indices for simulations using different DEMs for LaharZ (left) and Q-LavHA (right). These indices show the average for results of simulations with an origin located at both onsets (H and L). The use of the updated DEM does not provide significant improvements in LaharZ simulation accuracies. With Q-LavHA, it allows for an important increase of the true positives (TP), which, however, comes at the expense of a rise in false negatives (FN) due to the increased simulation resolution.

this zone of overflow. The local socio-economic conditions also made the inhabitants highly vulnerable by preventing mitigation measures from being implemented (Morin et al., 2009; Direction Générale de la Sécurité Civile [DGSC], 2012; Mossoux et al., 2018, 2019). Reestablishment of channel conveyance capacity between flow sequences and channelizing flows through construction of dykes are measures that otherwise could have reduced the impact of recurring flow sequences (Blong, 2000; Pierson, 2005). However, it must be underscored that the lahars have initially not only been considered a threat by the inhabitants but also as an economic opportunity in the form of extractable construction materials their deposits offer (Morin et al., 2009).

A decrease in sediment concentration with time after tephra deposition is rather common for secondary lahars. It is commonly associated with depletion in erodible material and re-establishment of vegetation (e.g., Vallance and Iverson, 2015; Major et al., 2016). However, the largest lahars on Karthala occurred in April 2009 and 2012, respectively, 4 and 7 years after the initial tephra emplacement. The 2012 lahar sequence also accounts for most of the debris deposits found at the foot of Karthala, reflecting its unprecedented volume and debris content. The absence of perennial flows on the flanks of the volcano strongly couple flow discharge with precipitations intensity, causing large variations in flow competence from one flow to another. We therefore suggest that, if most small-scale events probably had the capacity to trigger bank and bed erosion, many may have had insufficient competence to transport the largest scoured clasts downstream. This material would ultimately be transported by larger-scale events which would thus have unusually high solid load. This may explain the 4–7 years offset between the volcanic eruptions and the occurrence of the largest lahars (that were associated with exceptional rainfalls (section "Description of the Flow Events"). At the daily scale, the apparent delay between the onset of intense rainfall episodes and the timing of the documented lahars [occurring after a few days of important precipitations for both April 2009 and 2012 (**Supplementary Figure 2**)] is difficult to explain. A 1- or 2-day(s) offset may be associated with uncertainty in the (incomplete) testimonies documented, but up to a 10 days offset is recorded in April 2009. An explanation may lie in the high permeability of volcanic material (when not cover by fine ash), that could accommodate first rains through infiltration, while prolonged rainfall would lead to saturation and high surface runoff. Whether the small overall transport capacity of the ravines could in addition be responsible for a relatively "slow" erosion and transport of material downstream remains to be understood. Although no clear evidence has been found in the field, another explanation may lie in the occurrence of landslides on the tephra-covered forested hillslopes. The time needed to the ground to saturate and pore water pressure to rise to a level potentially triggering slope failure would in this case explain the apparent delay (Korup et al., 2019).

No lahars have occurred since April 2012, suggesting that infiltration capacity and quantity of easily mobilized volcanic material have returned to normal, decreasing the probability of lahar events. However, our study helps understanding the effect potential future (mildly) explosive eruptions may have to renew the conditions for the occurrence of similar new lahar events.

Modeling of Lahars

Flow modeling commonly aims for the delineation of potential lahar extent to evaluate the hazard exposure of assets such as settlements or infrastructure (Rodolfo, 2000; Huggel et al., 2008; Anderson et al., 2016). Our simulations benefited from

the collection and integration of extensive field measurements and observations allowing calibration of mass flow model input parameters and evaluation of the output accuracies. As shown, however, none of the simulations performed here captured the full spatial pattern of the documented flood areas. Apparently restricted both by the relative small scale of the lahars (that e.g., changes relationships between volume, cross-sectional and planimetric inundation area compared to large-volume lahars; Schilling, 2014) and by the complex topographic settings (smooth topography with unclear drainage pattern that leads to errors in the simulation of the flow path), the proportion of false negatives in simulation outputs is never negligible (from 0.06 to 0.16 for LaharZ and 0.12 to 0.33 for Q-LavHA). False positive (overestimation), however, commonly represents the largest proportion of the modeled inundation area (**Figure 6**). Such a high proportion of false negative is a major flaw for the effective use of simulation outputs in risk management. While simulations often represent a key aspect of lahar hazard assessment – especially in the rather common circumstances where no direct field observations of previous events are available – these results demonstrate the need for careful investigation and evaluation of simulation outputs before their dissemination. We expect that similar simulations on a rougher topography (e.g., at a stratovolcano, where ravines are commonly deeply incised in the volcano edifice) would obtain higher accuracies (e.g., Castruccio and Clavero, 2015; Charbonnier et al., 2018). Our study therefore highlights a limiting case in the use of numerical models for lahar hazard assessment where reliable, detailed input data lack.

The ash blanket emplaced by the 2005 eruptive sequence at Karthala volcano has been largely depleted over the past decade. Future phreatic eruptions may nevertheless emplace new tephra material, after which renewed periods of increased lahar hazard may be expected. In this perspective, our calibration data and study of models limitations provides insights to better evaluate future lahar hazard, key for improving the risk mitigation strategies on this highly populated volcanic island (Mossoux et al., 2018).

Comparison of Flow Models

This study also aimed to investigate the relevance of Q-LavHA for numerical modeling of lahars and compare it to the widely used LaharZ code. Important disparities between the simulated and affected areas are observed with both models, but LaharZ generally achieves higher simulation accuracies than Q-LavHA. Fitness indices and visual investigation of the outputs show that LaharZ is able to both limit the underestimated area (FN) and constrain overestimation of the inundated area (FP) after the break-in-slope. Q-LavHA, on the other hand, has a stronger tendency to underestimate the area affected by the flow (higher FN).

Our results also illustrate the difference in the type of model outputs, with a probability of inundation of each individual grid cell calculated by Q-LavHA to be compared to the planimetric inundation area for given flow volumes in LaharZ. Consideration of volumes in LaharZ allows investigating multiple hazard scenarios with a gradation of their likelihood. It however also comes with the disadvantage of a binary discrimination between "safe/unsafe" zones which may reinforce the misperception of the hazard map as absolute, while Q-LavHA offers the possibility of constructing probabilistic hazard maps which are found to be usually better suited for communication with and between local stakeholders (e.g., Zerger, 2002; Smemoe et al., 2007; Darnell et al., 2012; Thompson et al., 2015). Note, however, that the volumes needed in LaharZ to obtain the most accurate simulation outputs were unrealistically high (usually 3×10^6 to 5×10^6 m^3) in comparison to the documented flows ($3 \pm 0.6\ 10^5$ – $1 \pm 0.2\ 10^6$ m^3).

Commonly highlighted LaharZ drawbacks include its sensitivity to the vertical accuracy of the DEM and the unrealistic shape of the modeled inundation zones, noticeable as jagged edges of the simulation results (e.g., Huggel et al., 2008; Castruccio and Clavero, 2015). Placing the simulation onsets at the foot of the Proximal Hazard Zone Boundary (PHZB) in a study area deprived of a clear drainage pattern implies that the different catchments have to be accurately delineated in advance. As shown in this study, the origin of the ravines may, however, be difficult to define in certain environments. When considering localized drainage disturbance, this can lead to confusion in the zonation of the future hazard. Another highlighted limitation of LaharZ is its impossibility to simulate a bifurcation of the flow path, despite its importance for simulations over gentle terrains and complex topographies (e.g., Darnell et al., 2012).

Q-LavHA overall simulation accuracies are lower than those of LaharZ, the first being regularly penalized by higher false negative. Q-LavHA has, however, features that allow getting around some limitations of LaharZ. Besides its ability to simulate flow path bifurcations, Q-LavHA generally offers a better distinction between channelized and unconfined flow zones. This characteristic is important over gently-sloping terrains. Another advantage is the high sensitivity of Q-LavHA to small topographic features, that can be fine-tuned by the use of the corrective factors (H_c and H_p). On the other hand, the absence of implemented relations between initial flow volume and potential runout length yield the need for a manual calibration with historic events or inundation scenarios. While for the sake of hazard zone delineation on volcanic islands a choice for selecting run-out distances that allow the simulated flows to reach the shoreline may be valid, it may be trickier for other environments, in particular in absence of historic events. The unrealistically high run-out length values needed in our simulations (up to 130 km while the maximal ravine length is 14 km) is a common flaw of iterative probabilistic flow models (Mossoux et al., 2016). These models being built from iterations of single flow lines, the higher the resolution, the less direct and more meandering, and thus longer, a flow line is before it reaches the actual physical head of the simulated flow. As an alternative to the use of maximal runout distance in Q-LavHA, an estimation of the lahar mobility could potentially be implemented by parameterizing a coefficient of friction along its flow path, such as proposed in the Modified Single Flow Model (MSF; Huggel et al., 2003). Such coefficient could be approximated using the Heim Coefficient, which is simply a measure of the tangent of the mean slope from the top of the source area to the most distal part of the flow (Charbonnier et al., 2018).

Finally, both models assume that lahars flow from a fixed and unique source and all at once. This assumption is not completely valid for lahars. Indeed, the incorporation of material through bulking and debulking processes and water integration from tributaries has to be considered. Both may lead to important volume changes along the flow path (Vallance and Iverson, 2015). The potential for repetition of lahar events is neither taken into account, while, as shown for Karthala, it may greatly affect the impacted zone due to incremental infilling of the channels with material deposits. Models that incorporate channel infilling, volume and concentration changes as well as bulking along the flow path (such as investigated by Fagents and Baloga, 2006; Castruccio and Clavero, 2015; Reid et al., 2016) are considered as particularly promising (Doyle et al., 2011).

Influence of DEM Modifications: Pertinence and Limitations

Despite its high original resolution, the 10 m TDX DEM incompletely represents the drainage system and ultimately leads to errors in the simulation of the lahar-prone areas. We suggest that those uncertainties were not associated with the intrinsic qualities of the DEM, but rather with the characteristics of the volcanic edifice. Karthala is a representative example of a young basaltic shield volcano not yet heavily dissected by erosion (Bachèlery et al., 2016). Its flank topography is therefore relatively smooth, with the presence of only few, low relief topographic features and no well-defined valleys. In addition, the dense and persistent forest canopy conceals large sections of Karthala's small-dimension ravines, making their identification difficult for the X-Band SAR sensor used for DEM creation (i.e., X-Band SAR has low vegetation penetrating capabilities, e.g., Dzurisin and Lu, 2006). These characteristics are less common on stratovolcanoes – where the topography is usually dominated by deeply incised valleys. The smooth topography and tropical forest make the simulation of flow trajectories on tropical shield volcanoes more subject to errors, in turn reducing the accuracy of hazard-zone delineations. Similar limitations were highlighted with LaharZ at other tropical volcanoes, motivating the design of our study (Muñoz-Salinas et al., 2009; Deng et al., 2019).

The implementation of detailed channel geometries into the DEM generally improved the delineation of lahar flow paths, and ultimately of modeled inundation areas. Small changes in the terrain morphology are known to modify the drainage course (Stevens et al., 2003; Hubbard et al., 2007; Schneider et al., 2008). The consequences of such hydrographic errors may be that the model misses the hazard-prone position of settlements actually affected by the hazard. This was especially noticeable in simulations initiating from source areas close to Karthala's summit. Changes in DEM particularly impacted Q-LavHA simulation results. In these simulations, the highest accuracies were obtained using an updated 5 m DEM in which channel geometries were edited. However, the change in DEM resolution (upsampling from 10 to 5 m) itself had a strong influence on the simulation outputs. Q-LavHA is known to be sensitive to differences in DEM resolution (Mossoux et al., 2016) and our results highlight that a careful selection of the DEM resolution is essential to ensure the most accurate simulations. Although the implementation of the drainage network within the DEM led to a clear increase in true positives, the upsampling strongly reduced the overall inundation area, ultimately leading to an increase of the false negatives. In our case, the small spatial scale of the ravines did not allow the use of an updated DEM with a lower spatial resolution, but it should be considered bearing in mind the size of the ravine.

Overall, our results highlight the importance of accurate terrain representation in the context of hazard assessment, as well as the differences in model sensitivity to the DEM quality and resolution (e.g., Davila et al., 2007; Hubbard et al., 2007; Huggel et al., 2008; Darnell et al., 2010, 2013). Updates of DEMs generally yield improved lahar simulation accuracies and could be considered in similar environments with unclear drainage systems such as other undissected basaltic shields or flat alluvial plains.

CONCLUSION

This study aims to gain insights in the recurrent formation of small-scale secondary lahars subsequent to the basaltic phreatic eruptions of Karthala volcano in 2005. Emplacement of unconsolidated volcanic material and damages to the summit vegetation caused important disturbances to water infiltration and drainage, ultimately leading to the repetitive formation of lahars on the flanks of the volcano. Exceptional rainfall events triggered the occurrence of the two largest lahar sequences in 2009 and 2012. The complete sequence of flows repetitively affected thousands of inhabitants living in settlements located at the foot of Karthala, becoming one of the primary hazards associated with the volcano. Our analysis allowed defining these flows as small-scale (volumes $\leq 10^5$ m^3), rain-triggered and predominantly low sediment concentration lahars.

Field measurements served to calibrate and compare numerical lahar simulations from the widely used LaharZ model with results from Q-LavHA, but were hindered by the time lag of several years between the occurrence of the events (2005–2012) and the field observations (2015). Our model comparison demonstrates that LaharZ outperforms Q-LavHA for small-scale lahar simulations. While Q-LavHA has features that mitigate some limitations of LaharZ, such as its ability to simulate flow bifurcations and the transition from constrained to unconstrained flow, it typically yielded lower simulation accuracies compared to LaharZ simulations (true positive values of 0.38 ± 0.04 vs. 0.47 ± 0.12). Such values represent a rather poor performance for both models compared to existing studies on larger-volume lahars. While the relatively small scale of Karthala lahars certainly played a role – e.g., by changing relationships between volume, cross sectional and planimetric inundation area compared to larger lahars – our results indicate the lower simulation accuracies to mostly result from errors arising from difficulties in delineating lahar flow trajectories on the smooth, poorly eroded topography of the volcanic edifice. Both models encountered difficulties delineating lahar flow paths. We showed that using a DEM updated on a small spatial

scale with detailed channel topography can lead to improved simulations with both models (increased true positive values of 1–10% for LaharZ and 13–77% for Q-LavHA simulations). This approach did not fully prevent simulations to sometimes miss the hazard-prone position of settlements which were actually affected by the hazard. Whereas we illustrate how the simulations can benefit from the integration of field observations, the rather poor performance of both simulation strategies demonstrates the need for careful investigation and evaluation of simulation outputs before their dissemination.

Although small flood events occurred in 2016, no lahars have occurred on Karthala since. The regrowth of vegetation on the upper flank of Karthala as well as the decline in the quantity of volcanic material which can potentially be mobilized decreases the occurrence probability of such lahar sequences. However, new (mildly) explosive eruption(s) may occur in the future. In this perspective, our study of the lahars that followed the 2005 eruptions, as well as our calibration data and study of models limitations, provides insights to better evaluate future lahar hazard, key for improving the risk mitigation strategies on this highly populated volcanic island (Mossoux et al., 2018). Our results indicate that accurate topographic representations and detailed documentation of spatial extent of the impacted area and lahar deposit thickness are essential to produce accurate lahar simulations, as well as the further adaptation of existing numerical simulation tools to better suit these particular environmental settings.

DATA AVAILABILITY STATEMENT

The datasets generated for this study are available on request to the corresponding author.

AUTHOR CONTRIBUTIONS

AD, SP, and MK conceived and designed the study. AD ran the simulations and analyzed the results. AD wrote the manuscript, with main inputs from MK, SP, and SM. AD, HS, and SP participated in the field data acquisition. All authors contributed to the final version of the manuscript.

FUNDING

AD was supported by the Belgian Science Policy Office (BELSPO) for RESIST (SR/00/305), MODUS (SR/00/358) and AfReSlide (BR/121/A2/AfReSlide) research projects (http://resist.africamuseum.be/, http://afreslide.africamuseum.be/). SP was financially supported by the Vocatio grant for field work on Karthala, and the FWO-Flanders Ph.D. Aspirant fellowship.

ACKNOWLEDGMENTS

We are extremely grateful to the "Centre National de Documentation et de la Recherche Scientifique" (CNDRS) of the Comores Union, and specifically the "Observatoire Volcanologique du Karthala" for their logistic support and providing field assistance from several students of the Université des Comores. Farid Hassane from the Comorian "Agence nationale de l'Aviation Civile de la Météorologie" (ANACM) kindly shared precipitation data available for Moroni. Elise Monsieurs assisted in the acquisition of the GPM IMERG data. Discussions with Julie Morin and Patrick Bachèlery helped planning and interpretation of field work. We thank the two reviewers and the associate editor for their comments that helped improving this manuscript.

SUPPLEMENTARY MATERIAL

The Supplementary Material for this article can be found online at: https://www.frontiersin.org/articles/10.3389/feart.2020.00369/full#supplementary-material

REFERENCES

Agence nationale de l'Aviation Civile de la Météorologie [ANACM] (2012).

Anderson, E. R., Griffin, R. E., and Irwin, D. E. (2016). "Implications of different digital elevation models and preprocessing techniques to delineate debris flow inundation hazard zones in el salvador," in *Natural Hazard Uncertainty Assessment: Modeling and Decision Support*, eds K. Riley, P. Webley, and M. Thompson (Hoboken, NJ: John Wiley & Sons, Inc), 167–177. doi: 10.1002/9781119028116.ch11

Bachelery, P., and Coudray, J. (1993). *Notice Explicative Carte Géologique de Grande Comore*.

Bachèlery, P., Morin, J., Villeneuve, N., Soulé, H., Nassor, H., and Ali, A. R. (2016). "Structure and eruptive history of Karthala Volcano," in *Active Volcanoes of the Southwest Indian Ocean: Piton de La Fournaise and Karthala*, eds P. Bachelery, J.-F. Lenat, A. Di Muro, and L. Michon (Berlin: Springer), 345–366. doi: 10.1007/978-3-642-31395-0_22

Blong, R. (2000). "Volcanic hazards and risk management," in *Encyclopedia of Volcano*, 1st Edn, ed. Academic Press (Berlin: Springer), 1215–1227.

Boreggio, M., Bernard, M., and Gregoretti, C. (2018). Evaluating the differences of gridding techniques for digital elevation models generation and their influence on the modeling of stony debris flows routing: a case study from rovina di cancia basin (North-eastern Italian alps). *Front. Earth Sci.* 6:89. doi: 10.3389/feart.2018.00089

Bourhane, A., Comte, J.-C., Join, J.-L., and Ibrahim, K. (2016). "Groundwater Prospection in Grande," in *Active Volcanoes of the Southwest Indian Ocean: Piton de La Fournaise and Karthala*, eds P. Bachelery, J.-F. Lenat, A. Di Muro, and L. Michon (Berlin: Springer), 385–401. doi: 10.1007/978-3-642-31395-0

Canuti, P., Casagli, N., Catani, F., and Falorni, G. (2002). Modeling of the guagua pichincha volcano (Ecuador) lahars. *Phys. Chem. Earth* 27, 1587–1599. doi: 10.1016/S1474-7065(02)00180-8

Carranza, E. J. M., and Castro, O. T. (2006). Predicting lahar-inundation zones: case study in West Mount Pinatubo, Philippines. *Nat. Hazards* 37, 331–372. doi: 10.1007/s11069-005-6141-y

Castruccio, A., and Clavero, J. (2015). Lahar simulation at active volcanoes of the Southern Andes: implications for hazard assessment. *Nat. Hazards* 77, 693–716. doi: 10.1007/s11069-015-1617-x

Charbonnier, S. J., Connor, C. B., Connor, L. J., Sheridan, M. F., Oliva Hernández, J. P., and Richardson, J. A. (2018). Modeling the October 2005 lahars at Panabaj (Guatemala). *Bull. Volcanol.* 80:4. doi: 10.1007/s00445-017-1169-x

Córdoba, G. A., Sheridan, M. F., and Pitman, B. (2018). Titan2F code for lahar hazard assessment?: derivation, validation and verification. *Bolet. Soc. Geol. Mex.* 70, 611–631. doi: 10.18268/BSGM2018v70n3a3

Darnell, A. R., Barclay, J., Herd, R. A., Phillips, J. C., Lovett, A. A., and Cole, P. (2012). Geographical information system approaches for hazard mapping of dilute lahars on Montserrat, West Indies. *Bull. Volcanol.* 74, 1337–1353. doi: 10.1007/s00445-012-0596-y

Darnell, A. R., Lovett, A. A., Barclay, J., and Herd, R. A. (2010). An application-driven approach to terrain model construction. *Int. J. Geogr. Inf. Sci.* 24, 1171–1191. doi: 10.1080/13658810903318889

Darnell, A. R., Phillips, J. C., Barclay, J., Herd, R. A., Lovett, A. A., and Cole, P. D. (2013). Developing a simplified geographical information system approach to dilute lahar modelling for rapid hazard assessment. *Bull. Volcanol.* 75:713. doi: 10.1007/s00445-013-0713-6

Davila, N., Capra, L., Gavilanes-Ruiz, J. C., Varley, N., Norini, G., and Vazquez, A. G. (2007). Recent lahars at Volcán de Colima (Mexico): drainage variation and spectral classification. *J. Volcanol. Geotherm. Res.* 165, 127–141. doi: 10.1016/j.jvolgeores.2007.05.016

Deng, F., Rodgers, M., Xie, S., Dixon, T. H., Charbonnier, S., Gallant, E. A., et al. (2019). High-resolution DEM generation from spaceborne and terrestrial remote sensing data for improved volcano hazard assessment — A case study at Nevado del Ruiz, Colombia. *Remote Sens. Environ.* 233:111348. doi: 10.1016/j.rse.2019.111348

Dezfuli, A. K., Ichoku, C. M., Huffman, G. J., Mohr, K. I., Selker, J. S., Van De Giesen, N., et al. (2017). Validation of IMERG precipitation in Africa. *J. Hydrometeorol.* 18, 2817–2825. doi: 10.1175/JHM-D-17-0139

Direction Générale de la Sécurité Civile [DGSC] (2012). *UNION OF COMOROS Early Recovery Plan*.

Doyle, E. E., Cronin, S. J., and Thouret, J.-C. (2011). Defining conditions for bulking and debulking in lahars. *Bull. Geol. Soc. Am.* 123, 1234–1246. doi: 10.1130/B30227.1

Dzurisin, D., and Lu, Z. (2006). "Interferometric synthetic-aperture radar (InSAR)," in *Volcano Deformation: New Geodetic Monitoring Techniques*, ed. D. Dzurisin (Cham: Springer Science & Business Media).

Fagents, S. A., and Baloga, S. M. (2006). Toward a model for the bulking and debulking of lahars. *J. Geophys. Res. Solid Earth* 111, 1–21. doi: 10.1029/2005JB003986

Favalli, M., Mazzarini, F., Pareschi, M. T., and Boschi, E. (2009). Topographic control on lava flow paths at Mount Etna, Italy: implications for hazard assessment. *J. Geophys. Res.* 114, 1–13. doi: 10.1029/2007JF000918

Hubbard, B. E., Sheridan, M. F., Carrasco-Núñez, G., Díaz-Castellón, R., and Rodríguez, S. R. (2007). Comparative lahar hazard mapping at Volcan Citlaltépetl, Mexico using SRTM, ASTER and DTED-1 digital topographic data. *J. Volcanol. Geotherm. Res.* 160, 99–124. doi: 10.1016/j.jvolgeores.2006.09.005

Huffman, G., Bolvin, D., Braithwaite, D., Hsu, K., and Joyce, R. (2019). *NASA Global Precipitation Measurement - Integrated Multi-satellite Retrievals for GPM, Algorithm Theoretical Basis Document v06*. Washington, DC: National Aeronautics and Space Administration.

Huggel, C., Kääb, A., Haeberli, W., and Krummenacher, B. (2003). Regional-scale GIS-models for assessment of hazards from glacier lake outbursts: evaluation and application in the Swiss Alps. *Nat. Hazards Earth Syst. Sci.* 3, 647–662. doi: 10.5194/nhess-3-647-2003

Huggel, C., Schneider, D., Miranda, P. J., Delgado Granados, H., and Kääb, A. (2008). Evaluation of ASTER and SRTM DEM data for lahar modeling: a case study on lahars from Popocatépetl Volcano, Mexico. *J. Volcanol. Geotherm. Res.* 170, 99–110. doi: 10.1016/j.jvolgeores.2007.09.005

Hutchinson, M., Xu, T., and Stein, J. (2011). Recent progress in the ANUDEM elevation gridding procedure. *Geomorphometry* 2011, 19–22.

Hutchinson, M. F. (1989). A new procedure for gridding elevation and stream line data with automatic removal of spurious pits. *J. Hydrol.* 106, 211–232. doi: 10.1016/0022-1694(89)90073-5

IFRC (2013). *Emergency Appeal Final Report Comoros?: Flash Floods*. Geneva: IFRC.

Iverson, R. M., Schilling, S. P., and Vallance, J. W. (1998). Objective delineation of lahar-inundation hazard zones. *Geol. Soc. Am. Bull.* 110, 972–984. doi: 10.1130/0016-76061998110<0972:odolih<2.3.co;2

Jones, R., Manville, V., Peakall, J., Froude, M., and Odbert, H. (2017). Real-time prediction of rain-triggered lahars: incorporating seasonality and catchment recovery. *Nat. Hazards Earth Syst. Sci. Discuss.* 17, 2301–2312. doi: 10.5194/nhess-2017-166

Korup, O., Seidemann, J., and Mohr, C. H. (2019). Increased landslide activity on forested hillslopes following two recent volcanic eruptions in Chile. *Nat. Geosci.* 12, 2–8. doi: 10.1038/s41561-019-0315-9

Lavigne, F., Thouret, J., Voight, B., Suwa, H., and Sumaryono, A. (2000). Lahars at Merapi volcano, Central Java: an overview. *J. Volcanol. Geotherm. Res.* 100, 423–456. doi: 10.1016/S0377-0273(00)00150-5

Lavigne, F., and Thouret, J. C. (2003). Sediment transportation and deposition by rain-triggered lahars at Merapi Volcano, Central Java, Indonesia. *Geomorphology* 49, 45–69. doi: 10.1016/S0169-555X(02)00160-5

Levandowsky, M., and Winter, D. (1971). Distance between sets. *Nature* 234, 34–35. doi: 10.1038/234034a0

Macías, J. L., Capra, L., Arce, J. L., Espíndola, J. M., García-Palomo, A., and Sheridan, M. F. (2008). Hazard map of El Chichón volcano, Chiapas, México: constraints posed by eruptive history and computer simulations. *J. Volcanol. Geotherm. Res.* 175, 444–458. doi: 10.1016/j.jvolgeores.2008.02.023

Maerker, M., Quénéhervé, G., Bachofer, F., and Mori, S. (2015). A simple DEM assessment procedure for gully system analysis in the Lake Manyara area, northern Tanzania. *Nat. Hazards* 79, 235–253. doi: 10.1007/s11069-015-1855-y

Major, J. J., Bertin, D., Pierson, T. C., Amigo, A., Iroume, A., Ulloa, H., et al. (2016). Extraordinary sediment delivery and rapid geomorphic response following the 2008-2009 eruption of Chaiten Volcano. *Chile. Water Resour. Res.* 52, 5075–5094. doi: 10.1002/2015WR018250

Manville, V., Major, J. J., and Fagents, S. A. (2012). "Modeling lahar behavior and hazards," in *Modeling Volcanic Processes The Physics and Mathematics of Volcanism*, eds S. A. Fagents, T. K. P. Gregg, and R. M. C. Lopes (Cambridge: Cambridge University Press), 300–330. doi: 10.1017/cbo9781139021562.014

Manville, V., Németh, K., and Kano, K. (2009). Source to sink: a review of three decades of progress in the understanding of volcaniclastic processes, deposits, and hazards. *Sediment. Geol.* 220, 136–161. doi: 10.1016/j.sedgeo.2009.04.022

Mead, S., Magill, C., and Hilton, J. (2016). Rain-triggered lahar susceptibility using a shallow landslide and surface erosion model. *Geomorphology* 273, 168–177. doi: 10.1016/j.geomorph.2016.08.022

Morin, J. (2012). *Gestion Institutionnelle et Réponses des Populations Face Aux Crises Volcaniques: Études de Cas á La Réunion et en Grande Comore*. La Réunion, France: Université de la Réunion.

Morin, J., Bachèlery, P., Soulé, H., Nassor, H., and Hamidi, N. (2016). "Volcanic risk and crisis management on Grande comore Island," in *Active Volcanoes of the Southwest Indian Ocean: Piton de La Fournaise and Karthala*, eds P. Bachèlery, J.-F. Lénat, A. Di Muro, and L. Michon (Berlin: Springer), doi: 10.1007/7854

Morin, J., Lavigne, F., Bachelery, P., Finizola, A., and Villeneuve, N. (2009). Institutional and social responses to hazards related to Karthala volcano, Comoros - PART II: the deep-seated root causes of Comorian vulnerabilities. *SHIMA Int. J. Res. Isl. Cult.* 3, 54–71.

Mossoux, S., Kervyn, M., and Canters, F. (2019). Assessing the impact of road segment obstruction on accessibility of critical services in case of a hazard. *Nat. Hazards Earth Syst. Sci.* 19, 1251–1263. doi: 10.5194/nhess-19-1251-2019

Mossoux, S., Kervyn, M., Soulé, H., and Canters, F. (2018). Mapping population distribution from high resolution remotely sensed imagery in a data poor setting. *Remote Sens.* 10:1409. doi: 10.3390/rs10091409

Mossoux, S., Saey, M., Bartolini, S., Poppe, S., Canters, F., and Kervyn, M. (2016). Q-LAVHA: a flexible GIS plugin to simulate lava flows. *Comput. Geosci.* 97, 98–109. doi: 10.1016/j.cageo.2016.09.003

Mothes, P. A., and Vallance, J. W. (2015). "Lahars at Cotopaxi and Tungurahua volcanoes, ecuador: highlights from stratigraphy and observational records and related downstream hazards," in *Hazards and Disasters Series: Volcanic Hazards*, eds J. F. Shroder and P. Papale (Amsterdam: Elsevier Inc), 141–168. doi: 10.1016/b978-0-12-396453-3.00006-x

Muñoz-Salinas, E., Castillo-Rodríguez, M., Manea, V., Manea, M., and Palacios, D. (2009). Lahar flow simulations using LAHARZ program: application for the Popocatépetl volcano. *Mexico. J. Volcanol. Geotherm. Res.* 182, 13–22. doi: 10.1016/j.jvolgeores.2009.01.030

Muñoz-Salinas, E., Renschler, C. S., Palacios, D., and Namikawa, L. M. (2008). Updating channel morphology in digital elevation models: lahar assessment for Tenenepanco-Huiloac Gorge, Popocatépetl volcano, Mexico. *Nat. Hazards* 45, 309–320. doi: 10.1007/s11069-007-9162-x

O'Brien, J. S., Julien, P. Y., and Fullerton, W. T. (2007). Two-Dimensional Water Flood and Mudflow Simulation. *J. Hydraulic Eng.* 119:2.

Perrotta, A., Scarpati, C., and Luongo, G. (2006). Volcaniclastic resedimentation on the northern slope of Vesuvius as a direct response to eruptive activity. *Landslides* 3, 295–301. doi: 10.1007/s10346-006-0057-9

Pierson, T. C. (2005). "Hyperconcentrated flow - transitional process between water flow and debris flow," in *Debris Flow Hazards and Related Phenomena*, eds M. Jakob and O. Hungr (Berlin: Springer), 159–202. doi: 10.1007/3-540-27129-5_8

Pierson, T. C., and Major, J. J. (2014) Hydrogeomorphic effects of explosive volcanic eruptions on drainage basins. *Ann. Rev. Earth Planet. Sci.* 42, 469–507. doi: 10.1146/annurev-earth-060313-054913

Pierson, T. C., and Scott, K. M. (1985). Downstream dilution of a lahar: transition from debris flow to hyperconcentrated streamflow. *Water Resour. Res.* 21, 1511–1524. doi: 10.1029/WR021i010p01511

Pistolesi, M., Cioni, R., Rosi, M., and Aguilera, E. (2014). Lahar hazard assessment in the southern drainage system of Cotopaxi volcano, Ecuador: results from multiscale lahar simulations. *Geomorphology* 207, 51–63. doi: 10.1016/j.geomorph.2013.10.026

Pitman, E. B., and Le, L. (2005). A two-fluid model for avalanche and debris flows. *Philos. Trans. A. Math. Phys. Eng. Sci.* 363, 1573–1601. doi: 10.1098/rsta.2005.1596

Reid, M. E., Coe, J. A., and Brien, D. L. (2016). Forecasting inundation from debris flows that grow volumetrically during travel, with application to the Oregon Coast Range, USA. *Geomorphology* 273, 396–411. doi: 10.1016/j.geomorph.2016.07.039

Rodolfo, R. S. (2000). "The Hazard from Lahars and Jokulhlaups," in *Encyclopedia of Volcano*, 1st Edn, eds H. Sigurdsson, B. F. Houghton, S. R. McNutt, H. Rymer, and J. Stix (London: Academic Press), 973–995.

Schilling, S. (2014). Laharz _ py: GIS tools for automated mapping of lahar inundation hazard zones. *U.S. Geol. Surv.* 78:1073. doi: 10.3133/ofr20141073

Schneider, D., Delgado Granados, H., Huggel, C., and Kääb, A. (2008). Assessing lahars from ice-capped volcanoes using ASTER satellite data, the SRTM DTM and two different flow models: case study on Iztaccíhuatl (Central Mexico). *Nat. Hazards Earth Syst. Sci.* 8, 559–571. doi: 10.5194/nhess-8-559-2008

Scott, K. M. (1988). *Origins, Behavior, and Sedimentology of Lahars and Lahar-Runout Flows in the Toutle-Cowlitz River System*. Professional Paper 1447- A. Washington, DC: UGSC.

Scott, K. M., Vallance, J. W., Kerle, N., Macías, J. L., Strauch, W., and Devoli, G. (2005). Catastrophic precipitation-triggered lahar at Casita volcano, Nicaragua: occurrence, bulking and transformation. *Earth Surf. Process. Landf.* 30, 59–79. doi: 10.1002/esp.1127

Skofronick-Jackson, G., Petersen, W. A., Berg, W., Kidd, C., Stocker, E. F., Kirschbaum, D. B., et al. (2017). The global precipitation measurement (GPM) mission for science and society. *Bull. Am. Meteorol. Soc.* 98, 1679–1696. doi: 10.1175/BAMS-D-15-00306.1

Smemoe, C. M., Nelson, E. J., Zundel, A. K., and Miller, A. W. (2007). Demonstrating floodplain uncertainty using flood probability maps. *J. Am. Water Resour. Assoc.* 43, 359–371. doi: 10.1111/j.1752-1688.2007.00028.x

Smietana, M., Bachelery, P., Boivin, P., and Boudon, G. (2007). *Etude Pétrologique et Volcanologique des Dépôts des Quatre Dernières Éruptions du Karthala*. Réunion: Université de la Réunion.

Smith, G. A., and Lowe, D. R. (1991). "Lahars: volcano-hydrologic events and deposition in the debris flow-hyperconcentrated flow continum," in *Sedimentation in Volcanic Settings*, eds R. V. Fisher and G. A. Smith (Tulsa: Society for Sedimentary Geology), 59–70. doi: 10.2110/pec.91.45.0059

Stevens, N., Manville, V., and Heron, D. (2003). The sensitivity of a volcanic flow model to digital elevation model accuracy: experiments with digitised map contours and interferometric SAR at Ruapehu and Taranaki volcanoes, New Zealand. *J. Volcanol. Geotherm. Res.* 119, 89–105. doi: 10.1016/S0377-0273(02)00307-4

Thompson, M. A., Lindsay, J. M., and Gaillard, J. C. (2015). The influence of probabilistic volcanic hazard map properties on hazard communication. *J. Appl. Volcanol.* 4:6. doi: 10.1186/s13617-015-0023-0

Thouret, J. C., Antoine, S., Magill, C., and Ollier, C. (2020). Lahars and debris flows: characteristics and impacts. *Earth Sci. Rev.* 201:103003. doi: 10.1016/j.earscirev.2019.103003

Vallance, J. W. (2000). "Lahars," in *Encyclopedia of Volcano*, eds H. Sigurdsson, B. F. Houghton, S. R. McNutt, H. Rymer, and J. Stix (Amsterdam: Elsevier), 601–616.

Vallance, J. W. (2005). "Volcanic debris flow," in *Debris Flow Hazards and Related Phenomena*, eds M. Jakob and O. Hungr (Berlin: Springer), 247–274. doi: 10.1007/3-540-27129-5_10

Vallance, J. W., and Iverson, R. M. (2015). "Lahars and their deposits," in *The Encyclopedia of Volcanoes*, 2nd Edn, eds H. Sigurdsson, B. F. Houghton, S. R. McNutt, H. Rymer, and J. Stix (Berlin: Springer), 650–664.

Wechsler, S. (2007). Uncertainties associated with digital elevation models for hydrologic applications: a review. *Hydrol. Earth Syst. Sci.* 11, 1481–1500. doi: 10.5194/hessd-3-2343-2006

Wessel, B. (2018). *TanDEM-X Ground Segment - DEM Products Specification Document*. Cologne: DLR.

Worni, R., Huggel, C., Stoffel, M., and Pulgarín, B. (2012). Challenges of modeling current very large lahars at Nevado del Huila Volcano, Colombia. *Bull. Volcanol.* 74, 309–324. doi: 10.1007/s00445-011-0522-8

Zerger, A. (2002). Examining GIS decision utility for natural hazard risk modelling. *Environ. Model. Softw.* 17, 287–294. doi: 10.1016/S1364-8152(01)00071-8

Conflict of Interest: The authors declare that the research was conducted in the absence of any commercial or financial relationships that could be construed as a potential conflict of interest.

frontiers in Earth Science

ORIGINAL RESEARCH
published: 02 September 2020
doi: 10.3389/feart.2020.00324

A Fluidisation Mechanism for Secondary Hydroeruptions in Pyroclastic Flow Deposits

M. A. Gilbertson[1], *A. Taylor*[2], *S. J. Mitchell*[2] *and A. C. Rust*[2]*

[1] School of Civil, Aerospace, and Mechanical Engineering, University of Bristol, Bristol, United Kingdom, [2] School of Earth Sciences, University of Bristol, Bristol, United Kingdom

Heating of water under hot pyroclastic flow deposits can drive hydroeruptions, forming craters and aprons of secondary deposits. According to the established conceptual model, steam pressure builds until failure of the pyroclastic overburden and a relatively low permeability (fine-grained) cap promotes secondary explosions. We explore a complementary model where the stress from drag related to gas flow up through the particle interstices is comparable in magnitude to the static pressure difference between the base and the top of the pyroclastic flow deposit. The drag force supports (part of) the weight of the particles and so reduces inter-particle friction; in a mono-sized bed this friction is effectively eliminated at the "minimum fluidisation velocity," which depends on the size and density of the particles. Through analogue experiments we show that violent outbursts can be generated when there are vertical variations in the minimum fluidisation velocities of granular materials. We ran experiments with layers of particles with different sizes or size distributions (bi-modal with different proportions of fine and coarse particles) in a tank with a porous base that allowed a distributed upward airflow through them. A finer-grained layer capping a coarser layer does not generate jets of particles or craters; rather, increased gas flux leads to fluidisation of first the fine and then the coarse (lower) layer. However, when the upper layer is coarser, the bed domes upward as a gas pocket grows within the finer layer for some combinations of layer thicknesses and grain sizes. When the gas pocket penetrates the top of the bed, it forms a crater and erupts particles. The gas velocity when doming initiates is greater than that calculated for the weight of the top layer to be balanced by drag and the pressure difference across that layer. This discrepancy is explained by the layers having a strength (from inter-particle friction), which is consistent with the observed dependence of the initiation velocity on the absolute thickness of the layer. Using data from Mt St Helens 1980 deposits, we show that the drag-related trigger observed in the laboratory is a feasible mechanism for secondary hydroeruptions through pyroclastic flow deposits.

Keywords: fluidisation, pyroclastic flow, secondary eruption, hydroeruption, drag, granular, jet, minimum fluidisation velocity

OPEN ACCESS

Edited by:
Stuart Mead,
Massey University, New Zealand

Reviewed by:
Sonia Calvari,
National Institute of Geophysics and Volcanology, Italy
Laura Pioli,
University of Cagliari, Italy

***Correspondence:**
A. C. Rust
alison.rust@bristol.ac.uk

Specialty section:
This article was submitted to Volcanology, a section of the journal Frontiers in Earth Science

Received: *16 March 2020*
Accepted: *13 July 2020*
Published: *02 September 2020*

Citation:
Gilbertson MA, Taylor A, Mitchell SJ and Rust AC (2020) A Fluidisation Mechanism for Secondary Hydroeruptions in Pyroclastic Flow Deposits. Front. Earth Sci. 8:324. doi: 10.3389/feart.2020.00324

1. INTRODUCTION

Pyroclastic flows are currents of hot particles and gases which travel down valleys and spread laterally under gravity, and so are often deposited in stream-valleys and near-shore environments. Steam generated by heating surface water or shallow groundwater under a pyroclastic deposit may escape passively via fumaroles or diffusively through the permeable deposit; however, under some conditions the steam can drive sudden secondary eruption(s) through the primary pyroclastic flow deposit leaving craters, surge deposits and fallout from ballistics and tephra fountaining (e.g., Moyer and Swanson, 1987; Keating, 2005).

The secondary eruption craters spatially associated with water sources in historic pyroclastic flow deposits including those of Mount St Helens 1980 (e.g., Moyer and Swanson, 1987), Redoubt 1990 (Gardner et al., 1994), Mount Pinatubo 1991 (Torres et al., 1996) and Katmai (Valley of Ten Thousand Smokes) 1912 (e.g., Hildreth, 1983), suggest that it is common to form secondary hydroeruptions when hot pyroclastic flows are deposited on a wet terrestrial environment. Not only are they a hazard to people near freshly emplaced pyroclastic flows, they are a potential trigger for destabilisation and remobilisation of pyroclastic material, forming secondary flows with more distal effects: the secondary ignimbrites after the main 1991 eruption of Mount Pinatubo travelled up to 10 km and generated ash clouds up to 10 km high (Torres et al., 1996). Their common occurrence and associated hazards motivate a better understanding of mechanisms for generating secondary explosive hydroeruptions in pyroclastic flow deposits. There are likely to be multiple mechanisms; here we only consider the scenario of a non-welded pyroclastic flow deposit with an underlying water source and not any mechanisms that involve welding nor cohesion nor water gulleying down into hot pyroclastic material (e.g., Torres et al., 1996).

When a fluid (e.g., steam) source is set under a layer of granular material then fluid will flow through the layer at a rate determined by the permeability of the layer and the pressure gradient across it. If the layer is not sufficiently permeable for the flow through it to match the rate of fluid generated at the source, then the source pressure will increase until fluid leaves the source at the same rate as it is generated. The forces exerted on the granular layer by the fluid are due to both the pressure difference generated across it, which pushes up on the base of the layer, and the drag caused by the flow through it, which pushes up on particles throughout the thickness of the layer (van der Hoef et al., 2005). These forces are opposed by the weight of the granular layer and the inter-particle friction within it. When these forces are exceeded by those generated by the source, then the layer will fail.

The modelling of secondary hydroeruptions has concentrated on the build-up of pressure. Moyer and Swanson (1987) proposed what we term a "static pressure build-up" model for secondary hydroeruptions in pyroclastic flow deposits (also discussed by Keating, 2005), building on their and other's (Rowley et al., 1981) observations from Mount St Helens 1980–1981. This remains the best-documented and most-studied set of secondary hydroeruptions. Most of the secondary craters formed within a few days of the emplacement of the May 18, and to a lesser degree the June 12 1980, pyroclastic flows that were deposited on top of May 18 debris avalanche material; however, there were some secondary eruptions much later, including one in May 1981 that was filmed (Moyer and Swanson, 1987). Photographs of craters dotting the landscape and a vertical section through a crater later exposed by fluvial erosion are found in Rowley et al. (1981) and Brand et al. (2014) respectively. The craters were generally near-circular in plan, 5–100 m diameter and 1–20 m deep. There is a clear spatial association of the craters with pre-1980 stream-valleys even though the streams were disrupted by the debris avalanche. Moyer and Swanson (1987) inferred that the source of steam driving the secondary eruptions was water ponded on the debris avalanche deposit at the base of the pyroclastic flows and not deeper groundwater because the secondary eruption products are lacking in clasts of the distinctive May 18 "blast dacite" (cryptodome) from the debris avalanche under the primary pyroclastic flow deposits.

The "static pressure build-up" model (Moyer and Swanson, 1987; Keating, 2005) involves steam generation at the base of the hot pyroclastic flow deposit at a rate faster than it escapes, until the steam pressure reaches some critical value slightly exceeding lithostatic pressure (Keating, 2005), causing failure of the deposit. This failure causes rapid rise of steam, including steam flashed from water that became superheated due to the sudden decompression when the pyroclastic overburden failed. Thus factors that should control explosive vs. passive steam release include the rate of steam generation (i.e., availability of water and rate of heat transfer) and the deposit permeability, which if not welded depends on the grain size distribution and packing. Moyer and Swanson (1987) emphasise the importance of the permeability of the pyroclastic overburden in regulating the eruptive phenomena, with finer-grained, lower permeability deposits more conducive to explosive steam release; Torres et al. (1996) even suggest that a confining layer of fine ashfall can significantly inhibit the release of pore pressure in pyroclastic flow deposits. Torres et al. (1996) note that increased pore pressure within the pyroclastic flow deposit would decrease its strength, and Moyer and Swanson (1987) discuss the possibility that increased pore pressure might expand (de-compact) the pyroclastic material and so increase its permeability (with potential complex feedback if localised). However, there is no consideration of the dynamic drag force pushing up on pyroclasts throughout the deposit that is related to gas flow up though the pore space between the particles.

In this paper we explore an alternative mechanism for secondary hydroeruptions where the drag force is critical, and variations in grain size distribution of the pyroclastic flow deposit matter not because grain size affects permeability but because it affects the gas flux at which the drag force supports the weight of the particles. Using analogue experiments we show how it is possible for violent eruptions to take place in layered beds where the top layer is more permeable than the bottom when gas is passed through them. We argue that the observed behaviour is a result of the interaction between the particles and the fluid, the flow pattern induced in the bed of particles, and the collective mechanical properties of the particles. The mechanism we propose for secondary hydroeruptions has many similarities

(and some differences) with that proposed by Nichols et al. (1994) to explain fluid escape structures in layered sediments in areas of rapid sedimentation in water. For both applications, it is important to understand the role of internal friction in the deformation and fluidisation of granular materials.

A granular layer can deform in response to a stress applied at a margin (e.g., pushing up on the base of the layer) because the particles transmit force to each other through friction, enabling them to behave collectively; however, it can also deform when there is a vertical fluid flow through the interstices of the granular layer owing to the drag exerted. In a bed with fluid flow up through the particles, the weight of the particles will be opposed by the drag, and so friction between particles decreases. If the particles are monosized and the flow rate is large enough to support the entire weight of the bed (the "minimum fluidisation velocity," u_{mf}) then friction between the particles will be eliminated and the layer does not deform collectively. For a simple bed of uniform particles, u_{mf} is greater (i.e., a greater fluid velocity is needed to support the weight of the particles) for larger and/or denser particles (e.g., Rhodes, 1998).

Nichols et al. (1994) suggested that fluidisation might be an important process for the violent breaching of a layer of particles subject to a fluid flow through them. In their laboratory experiments they observed water flow up through water-saturated layered beds in which a layer of larger (or denser) particles overlaid a layer of smaller (or less dense) particles in a tank with a solid porous base to provide a distributed water source. At water velocities greater than u_{mf} of the bottom layer but less than u_{mf} of the top layer, the bottom layer divided so that a void (i.e., a pocket of water) formed between a fluidised layer of small particles at the bottom of the tank and a static layer of small particles pressed up against the base of the layer of large particles above it. In this condition, the drag exerted on the static layer of small particles exceeded that necessary to support its weight, and so this excess drag allowed these small particles to support the layer of larger particles. If the fluid velocity was increased so that the total drag on the top, composite (coarse and fine) layer exceeded its weight, the composite layer deformed until it suddenly failed, releasing a plume of particles into the water above it. Unlike secondary hydroeruptions in pyroclastic deposits, the burst-out and jetting in these experiments did not generate conical craters in the top of the granular bed.

We present new experiments that, like those of Nichols et al. (1994), involve fluid flow up through layers of particles in a tank with a porous base. However, a key difference is that the fluid is gas (air) rather than liquid water. The associated difference in buoyancy and Reynolds number will affect inter-particle forces and drag, and so the mechanical response of the layers and the fluidisation dynamics. For example, it is well-established in chemical engineering that in gas-fluidised systems, when the gas velocity exceeds u_{mf}, the excess gas flow forms bubbles that rise through the bed, whereas in liquid-fluidised beds, bubbles do not form and the bed expands when the velocity exceeds u_{mf} (Davidson and Harrison, 1963). These differences make the new experiments more relevant to secondary hydroeruptions in pyroclastic deposits.

We have kept the experiments simple in order to identify the key physical processes involved and to isolate the effects of individual factors. The goal is to test whether a fluidisation mechanism for triggering secondary hydroeruptions is feasible and not to reproduce the full dynamics of the eruptions. For example we use room-temperature air and a bed thickness of order 10 cm rather than steam and a deposit thickness of tens of metres, which means the analogue eruptions are not boosted by sudden decompression-induced flashing of superheated water to steam as in nature. A more fundamental simplification is representing the primary pyroclastic flow deposit as layers of uniform-density spheres with narrow unimodal or bimodal size distributions. Pyroclastic flow deposits often have complex vertical and lateral facies changes and broad particle size distributions from ash to blocks, and a range of clast densities from lithics to pumice. However, due to multiple flow units and pulses, as well as changes in conditions with time as the deposit is progressively aggregated, there can be sub-horizontal layers defined by changes in grain size distribution and componentry (e.g., dense lithic content) on the scale of interest to this study (e.g., tens of metres). Such layering is present in the pyroclastic flow deposits of Mount St. Helens 1980, as shown in the photographs and data from vertical sections exposed by fluvial incision presented in Brand et al. (2014). In a fluidisation mechanism for secondary hydroeruption triggering, we hypothesise that what matters is vertical variations in u_{mf}, not whether the size (or density) distribution of particles is narrow or broad. We make use of a huge body of work on fluidised beds, mostly in chemical engineering (but also in volcanology), with particles of different size, density, shape, and packing in order to relate the results of our simplified experiments to more complicated natural conditions.

2. EXPERIMENTAL METHODS AND MATERIALS

The experiments were conducted with beds of particles in a transparent Perspex, vertical, planar (near-2D) container with a rectangular cross-section 300 mm by 8 mm as shown in **Figure 1**. The base was fitted with a porous plastic distributor (Vyon "D," pore size nominally 20 μm) to ensure uniform gas distribution into the base of the bed of particles, which was fluidised using air from a central supply, controlled and metered by rotameters to a maximum accuracy of 2 mm/s for superficial gas speed in the particle bed. The upstream pressure was set by a pressure regulating valve at 1 bar. The particles were glass spheres (ballotini) with density $\rho_p = 2,500$ kg/m^3, chosen for their known and uniform properties.

The ballotini were sieved and the nominal diameter (d) taken to be the centre of the sieved range. The Sauter mean diameter (e.g., Breard et al., 2019) is the most suitable diameter for considering the balance between particle weight and fluid drag, but as the samples are well-sorted, the arithmetic, geometric and Sauter means are within a few percent (based on measurements

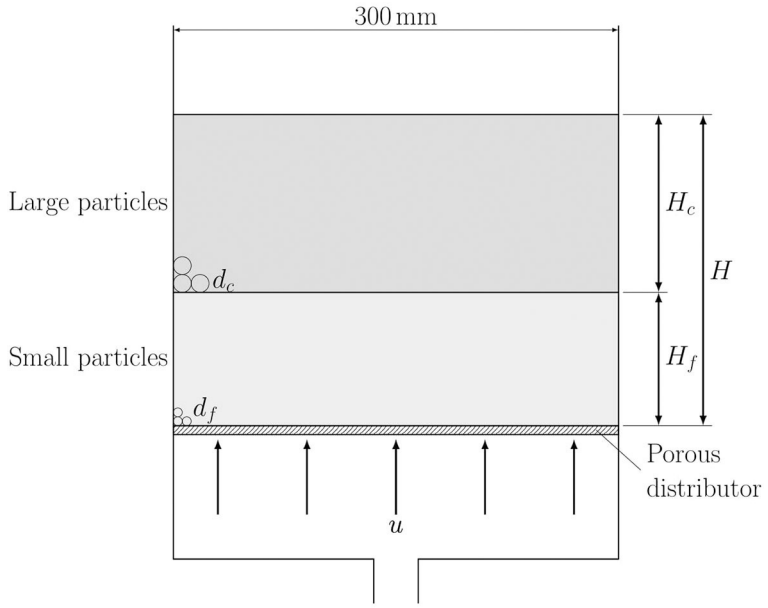

FIGURE 1 | Schematic diagram of the layered fluidised bed when there is a layer of large particles over a layer of small ones.

TABLE 1 | Particles used for two-layer beds with mono-sized particles.

r	Lower layer		Upper layer	
	Range (μm)	d_f (μm)	Range (μm)	d_c (μm)
2.67	125–250	188	400–600	500
5.63	45–75	60	250–425	338
8.33	45–75	60	400–600	500
10.08	45–75	60	510–700	605

r is the ratio of the diameter of the large particles in the top layer, d_c to that of the small particles in the bottom layer, d_f.

of other batches of ballotini in the same laboratory), and we have taken this into account in our errors.

The total bed depth (H) was varied, with a maximum of 12 cm; the thickness of the component layers of the bed, and the sizes of particles in those layers were also varied. In all experiments the superficial gas velocity u (the volume flow rate per unit cross-sectional area of the bed) was increased incrementally and the behaviour of the particle layers observed through the transparent container walls. For some experiments pressure in the air near the base of the bed was determined with a metal tube attached to a manometer.

Most experiments began with a two-layer bed with each layer consisting of single particle components. The combinations of particle sizes tested are shown in **Table 1**. In a subset of these experiments the total bed depth (H) was kept constant at 10 cm but the coarse layer thickness (H_c) was varied as well as particle sizes in the two layers and therefore the size ratio $r = d_c/d_f$, where the subscripts c and f refer to the coarse and fine particle layers respectively. A second subset of experiments consisted of a lower layer of 45–75 μm particles and an upper layer of particles with a diameter of 250–425 μm while H_c and H_c/H were varied systematically. A set of preliminary experiments explored the dynamics for three-layered beds with either a fine layer between two coarse layers or a coarse layer between two fine layers. In these experiments each layer contained a single particle size.

Experiments were also performed with two-layer beds consisting of mixtures of particles, where each layer contained two particle components, one large with a diameter d_l and one small, diameter d_s. The diameter for each layer was then determined by calculating the Sauter mean diameter, d_{av}, which preserves the ratio between volume and surface area for the particles. In general, for a bi-modal mixture this is given by

$$\frac{1}{d_{av}} = \frac{x_s/z_s}{d_s} + \frac{(1-x_s)/z_l}{d_l}, \tag{1}$$

where x_s is the mass fraction of the smaller component in the mixture, and the density ratio for component i is

$$z_i = \frac{\rho_i}{\rho_{av}}, \tag{2}$$

with the average density given by

$$\frac{1}{\rho_{av}} = \frac{x_s}{\rho_s} + \frac{1-x_s}{\rho_l}. \tag{3}$$

For particles of the same density, this reduces to

$$\frac{1}{d_{av}} = \frac{x_s}{d_s} + \frac{1-x_s}{d_l}. \tag{4}$$

TABLE 2 | Particles used for two-layer beds where each layer is a mixture of particles.

r	Lower layer					Upper layer				
	x_s	d_s	d_l	d_f	ϕ_f	x_s	d_s	d_l	d_c	ϕ_c
1.32	0.6	60	338	89	0.73	0.4	60	338	118	0.71
2.44	0.8	60	338	72	0.70	0.2	60	338	175	0.65
2.93	0.8	60	605	73	0.73	0.2	60	605	214	0.64
6.18	0.8	60	338	72	0.70	0.2	215	605	444	0.64

Particle volume fraction ϕ is calculated using the linear-mixture model of Yu and Standish (1991). x_s is the mass fraction of the smaller particles in each layer. d_s and d_l are the mean diameters of the small and large components in a layer, respectively. d_f and d_c are the Sauter mean diameter for the lower and upper layers, respectively. All diameters are in μm.

The particle volume fraction, ϕ, of mixtures was calculated with the linear-mixture method of Yu and Standish (1991) for randomly-packed mixtures of spherical particles; ϕ depends on the particle size ratio of the components of the mixture, d_s/d_l, and has better packing than mono-sized beds when $d_s/d_l < 0.741$. The mixtures used and the resulting values of d_{av} and ϕ for each layer are shown in **Table 2**.

3. OBSERVATIONS

3.1. Fine Particles on Top of Coarse Particles

When a layer of large particles (high permeability) is on the bottom and covered by a layer of small particles (low permeability), we were unable to find any experiment conditions (gas flow rate, layer thicknesses) with our apparatus and particles for which static-pressure failure or crater formation occurred. For this configuration, as the gas velocity was increased there was no particle motion until u_{mf} for the top layer was reached and the top layer fluidised. At this point all the small particles were in motion and gas bubbles rose through the fine-particle layer. However, these motions did not disturb the bottom (coarse) layer, which remained undeformed and acted as a type of distributor (i.e., the behaviour of the top layer was the same as if it were the only layer in the container and was directly on the distributor plate at the base of the container). Nothing further took place until u_{mf} for the large particles was reached and it was fluidised, causing mixing of the layers.

3.2. Coarse Particles on Top of Fine Particles

A much greater diversity of behaviour is seen for gas flows up through beds of particles with a layer of larger particles on top of a layer of smaller particles. The situation is shown schematically in **Figure 1**.

3.2.1. Jetting and Bubbling

For beds where $r(= d_c/d_f) < 6.5$, as u was increased, a velocity u_i is reached at which activity initiates. Initially, a longitudinal gas pocket formed within the bottom fine particle layer similar to those seen in the liquid-fluidised beds of Nichols et al. (1994). The

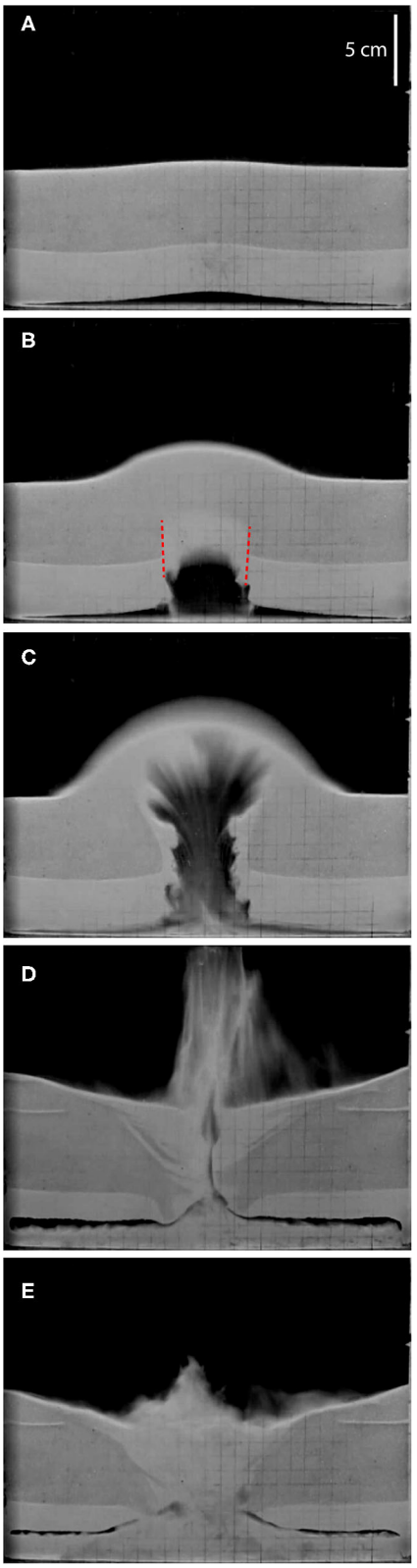

FIGURE 2 | An example of jetting behaviour in a two-layer bed. $r = 5.63$, $H_c/H = 0.6$, $H = 10$ cm, $d_f = 45$–75 µm, $d_c = 250$–425 µm. u = 3.3cm/s

(Continued)

FIGURE 2 | and photographs **(B–E)** were taken 0.5 s, 1.0 s, 3.0 s, and 5.0 s after **(A)**. The experiment started with a layer of coarser particles (darker) over a layer of finer particles (lighter grey); the lighter-grey at the top of **(A)** relates to lighting at the top of the coarser layer. The red lines in **(B)** indicate apparent planes of failure in the bed.

upper part of the layer of small particles was forced up against the layer of larger particles forming a double layer. This double layer deformed while maintaining the same thickness until the upper (coarse) layer of the bed is penetrated by the lower layer. This penetration could have the form of a jet or bubbles.

Jetting is shown in **Figure 2**. After initiation and the formation of a pocket, a column of fine particles intruded into the upper layer of large particles and a large cavity formed below it (both sometimes inclined). There appeared to be mechanical failure of the bed at the edges of the cavity. The top layer then suddenly failed and was penetrated and then broken through, causing particles to be projected above the bed and forming a jet of fine particles. While gas continued to be input at the base of the tank, the penetrating column of small particles widened and a stable, conical, bubbling pit of fine particles formed. In the example in **Figure 2**, before the breakthrough, the entire bottom layer was pushed up against the top layer and was not fluidised; however, after breakthrough only a portion of the fine layer pushed up on the base of the coarse layer, the rest formed a bubbling fluidised bed at the base of the tank.

An example of bubbling is shown in **Figure 3**. Many aspects of the bubbling regime were identical to jetting, but instead of a single cavity forming below the intruded column of small particles, smaller bubbles formed in the intrusion. When the top layer was breached, there was an overflow of small particles on top of the top layer, which broke up into blocks and sank. The crater area was dominated by bubbling. On some occasions this type of behaviour could be quite violent ("bubbles-jets") with a plume of particles being thrown above the bed.

When either of the layers was very thin compared with the other (H_c or $H_f = 1$ cm), the bed could just become wholly fluidised as for a bed of single-sized particles.

There was no evidence seen of a large-scale expansion of the layers with increasing u; instead structures largely void of particles—the pocket, jets, bubbles—formed, even for 45– 75 μm particles for which some expansion might be expected (Geldart, 1973). If the gas flow into the base of the apparatus was ceased while there was a gas pocket in the lower layer but before breakthrough, the pocket simply collapsed non-dramatically.

3.2.2. Strength of Breakthrough

The strength of the breakthrough of gas and fines through the top layer is important in connection with behaviour (jetting, bubbling, bubble-jets). The type of behaviour and its strength, based on the maximum height attained by the ejected particles, is plotted out for beds of a fixed depth (H) and different values of r in **Figure 4**. The type of activity observed is indicative, and repeat tests showed it could differ for the same nominal conditions

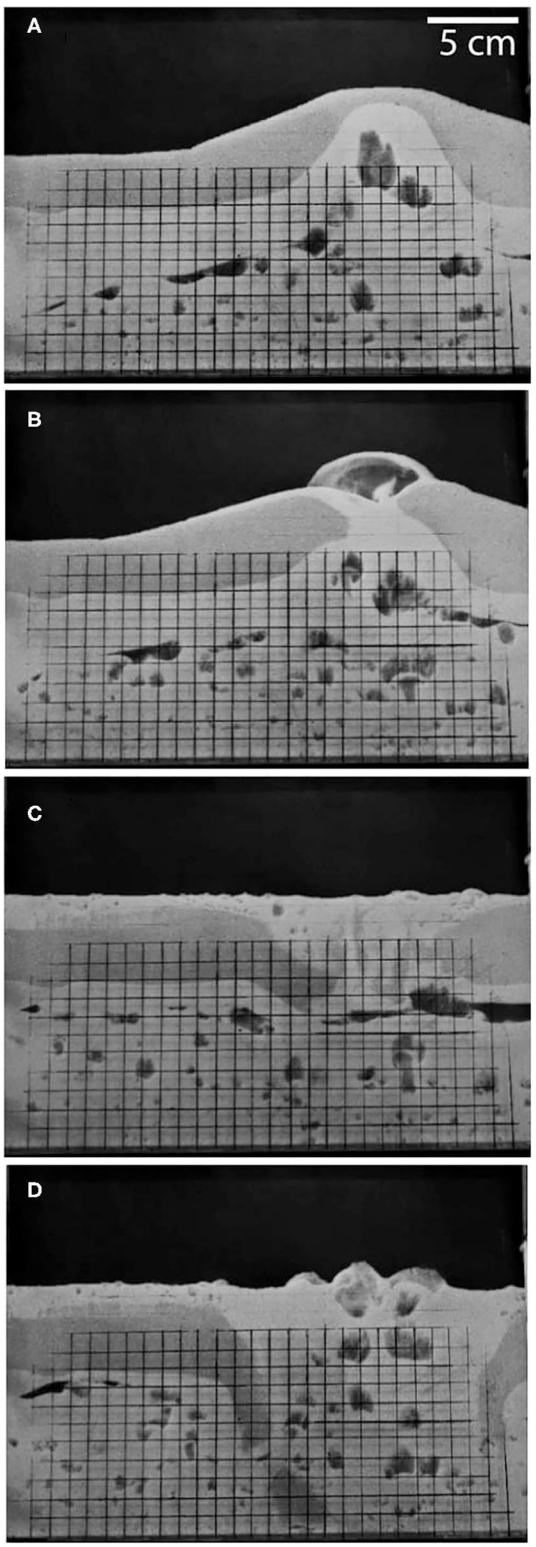

FIGURE 3 | An example of bubbling behaviour in a two-layer bed showing the progression with time from after initiation **(A)** to breakthrough **(B)** and further bubbling of fines (lighter grey) as gas continues to flow through the bed (**C** then **D**). $r = 2.67$, $H_c/H = 0.25$, $H = 12$ cm, $d_f = 125$–250 μm, $d_c = 400$–600 μm. The dark lines are a cm grid drawn on the front of the tank.

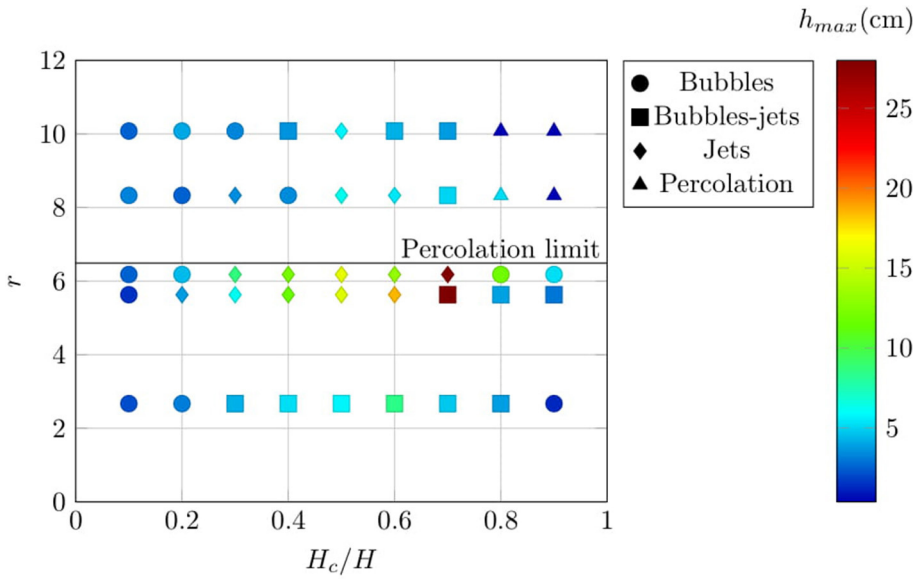

FIGURE 4 | The observed activity type in two-layer planar beds for different particle size ratios r, different coarse layer thicknesses (H_c) and constant total bed thickness (H) of 10 cm. Colours indicate the maximum height particles are ejected above the top of the bed (h_{max}). The nine points for $r = 6.18$ correspond to experiments where both layers were formed from a mixture of two particle sizes (bimodal); all other data are for experiments with unimodal layers. The percolation limit, i.e., the value for r above which small particles can move through the interstices of large particles, is 6.5 (Yu and Standish, 1991).

for some of the beds. However, jetting was more prevalent than bubbling for middling values of H_c/H and higher values of r. The strength of the breakthrough appeared to be highest for middling values of H_c/H but for all H_c/H it was diminished when r exceeded the percolation limit that permitted infiltration of fine particles into the coarse layer (see section 3.2.3 below) when jets could still take place but their vigour was significantly diminished. When the coarse layer was too thin then the void would not grow sufficiently to cause a jet to form; when it was too thick then the void could not grow sufficiently on its own to rupture the coarse layer.

After breakthrough, in the central part of the bed where breakthrough took place there appeared to be a region largely composed of fine particles which is fully fluidised. Away from this region, the layered structure of the bed was preserved though there might be some distortion and as for Nichols et al. (1994) some coarse particles passed downwards into the fluidised layer of fine particles below. A second layer of fine particles could form on top of the coarse layer owing to the fine particles that pass through the breakthrough region.

3.2.3. Percolation

A third type of behaviour occurred when a layer of large particles was over a layer of small ones when the small particles were sufficiently small relative to the large particles and $u_{mf_f} < u < u_{mf_c}$. In this case, the formation of the pocket after initiation did not take place, but the small particles travelled through the interstices between the large particles, percolating between them as shown in **Figure 5**. This would happen when $r > 6.5$ (Yu and Standish, 1991) for a packed bed. Vertical columns that were evacuated of small particles formed relatively slowly as for Gilbertson and Eames (2001) and Nermoen et al. (2010). These acted as high-permeability conduits for gas and so suppressed bubbling (Gilbertson and Eames, 2001) and there was no projection of particles above the bed. Small particles were transported through the spaces between the large particles to the top of the bed where they form a shallow pool.

3.2.4. Three-Layer Beds

Experiments were also performed in beds of three layers of unimodal spheres, always with $u < u_{mf_c}$. When a fine layer was between two coarse layers, the experiment proceeded in the upper two layers as if the bottom layer was not present: as u was incremented, a void formed in the fine layer and the top coarse layer was lifted until it failed. The particles in the bottom coarse layer did not move (i.e., the bottom layer acted as a distributor). When a coarse layer was between two layers containing the same fine particles, the upper layer behaved like an ordinary fluidised bed, and the behaviour of the lower-two layers was similar to the equivalent experiment with just those two layers.

4. FLUID FORCES ON LAYERED PARTICLE BEDS

Although uniform gas flow up through a layered bed of particles is a simple system, there is a rich variety of behaviour possible through the interaction between many different physical processes. Following the work of Nichols et al. (1994), the driving mechanism behind the deformation and rupture of the layers is the drag exerted on the particles by the passage of fluid past it.

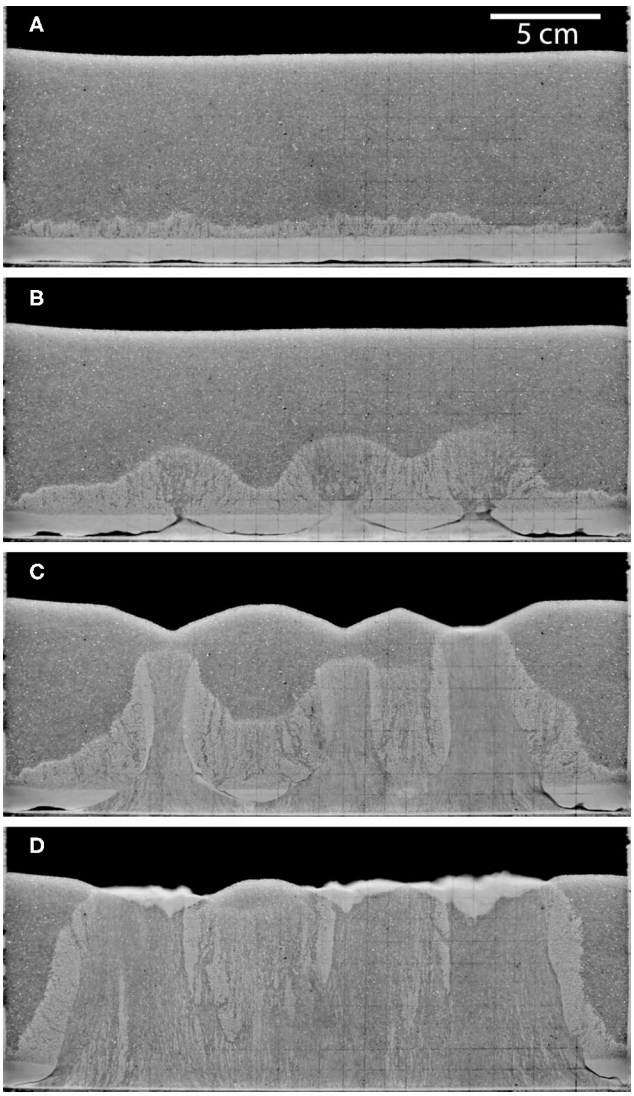

FIGURE 5 | Photographs of percolation behaviour in experiment with: $r = 10.08$, $^{H_f}/_{H} = 0.1$, $d_f = 45$–$75\,\mu m$, $d_c = 500$–$710\,\mu m$.u = 5.0 cm/s and photographs **(B–D)** were taken 10 s, 16 s, and 28 s after **(A)**.

This exerts a force on the particles directly, but also can change the interaction of particles.

4.1. Fluidisation in Beds of Particles of a Single Size

For a bed of uniform particles of diameter d and density ρ_p, when there is a flow of fluid of superficial velocity u through it, the forces on the bed are the particles' net weight and the drag exerted on them. The drag is considerably larger than that on a single isolated particle owing to the presence of nearby, surrounding particles. As the fluid flow through a bed of single-sized particles is increased, the drag on the particles increases. Eventually the minimum fluidisation velocity, u_{mf}, is reached when drag balances the net weight of the bed. For mono-sized particles, this is also the point at which the weight of individual particles is supported and inter-particle friction is eliminated so that the bed behaves in a similar manner to a fluid. A simple way of expressing this balance is the semi-empirical Ergun equation (Ergun, 1952)

$$\frac{1.75\phi}{(1-\phi)^3}\frac{\rho_f H}{d}u_{mf}^2 + \frac{150\phi^2}{(1-\phi)^3}\frac{\mu H}{d^2}u_{mf} = \phi\Delta\rho g H, \qquad (5)$$

where ϕ is the particle volume fraction of the bed, μ is the viscosity of the fluid, $\Delta\rho$ is the difference between the particle and the fluid densities, and H is the depth of the bed. u_{mf} is a superficial velocity and so the actual average velocity within the bed is $^{u_{mf}}/_{\phi}$. The left-hand side of the equation expresses the drag on the particles. A heuristic approach is taken summing the first term representing the inertial force to the second term representing the viscous force. The right-hand side of the equation is the net weight of the bed. It may be written in non-dimensional form as

$$PRe_{mf}^2 + QRe_{mf} - Ar = 0, \qquad (6)$$

where Re_{mf} is the particle Reynolds number (the ratio between inertial and viscous forces on a particle) at $u = u_{mf}$,

$$Re_{mf} = \frac{\rho u_{mf} d}{\mu},$$

and Ar is the Archimedes number

$$Ar = \frac{\Delta\rho\ \rho d^3 g}{\mu^2},$$

the ratio of net weight to viscous forces, and a function of particle and fluid properties only. P and Q define the effect that the close proximity of particles has on drag in the bed and so are functions of ϕ. They are defined by

$$P = \frac{1.75}{(1-\phi)^3}, \quad Q = \frac{150\phi}{(1-\phi)^3}.$$

They may be related to inertial permeability ($= d/P$) and viscous (Darcian) permeability ($= d^2/Q$).

Above the velocity of minimum fluidisation the net weight and the drag on the particles remain balanced. For particles that are not too small or light (Geldart, 1973), the excess gas flow is concentrated forming voids or "bubbles" in the bed that pass up through it (Davidson and Harrison, 1963). These bubbles can coalesce and divide, and also drive circulation currents of particles within the bed.

Fluidisation in a mono-sized bed of particles is idealised as a discrete event: it takes place at the gas velocity when at the bed scale the drag balances the net weight of the particles and at the particle scale inter-particle friction is practically eliminated. It is assumed that the drag on all the particles is the same for a given gas velocity and for each particle the only net vertical forces acting on it are its net weight and drag.

4.1.1. Fluidisation in a Two-Layer Bed

When a bed consists of two layers of particles, its fluidisation behaviour can be much more complicated. The minimum fluidisation velocity depends on the size and density of particles, and so from the point of view of individual particles, when there are two layers of different particles in a bed there will be an interval of fluid velocities over which the particles of one set will be fluidised and the other set will not be. The particles used in our experiments were differentiated by size only (density was constant) and so will be referred to as coarse and fine particles, but this is a proxy for referring to particles in a bed in which one set of particles has a higher value of u_{mf} than the other. In addition, the discussion below is for sets of particles for which r is not sufficiently large to allow particle percolation.

When a two-layer bed consists of a layer of coarse particles overlaid by a layer of fine particles, then the observed behaviour was straightforward as described in section 3.1.

More complex behaviour is seen when small u_{mf} particles form the lower layer and large u_{mf} particles the upper one. As for the opposite case (fine layer on top), as the fluid flow rate is increased it reaches the minimum fluidisation velocity for the fine particles; however, in this configuration the entire layer of small u_{mf} particles cannot be fluidised owing to the weight of the still unfluidised top layer of large u_{mf} particles. This causes a division of the fine-particle layer with a static upper part forced up against the upper layer and a lower part that is fluidised (Nichols et al., 1994): the drag exerted on the upper part of the fine-particle layer supports the weight of the small u_{mf} particles composing it and the excess drag (i.e., the total drag on the fine particles minus the drag to support the weight of the fine particles) supports the effective weight of the upper layer (Nichols et al., 1994). In this state, the weight of the upper layer of the bed (composed of coarser and so larger u_{mf} particles) is fully supported by the gas flow, but individual particles are not fluidised and there is significant friction between them; the same is true of the upper part of the layer of fine particles where the excess drag forces the particles together and so there is a frictional force between them. The particles in the lower part of the layer of fine particles (below the gas pocket) are fully fluidised i.e., the weight of the particles is fully supported and the inter-particle friction is insignificant.

A schematic diagram of the bed at the point at which the weight of the top layer is fully supported is shown in **Figure 6**. From the point of view of fluid drag, it is possible to estimate for a given gas velocity the thickness, H_f^*, of the upper part of the layer of low u_{mf} particles required to support the weight of the upper layer of large u_{mf} particles. From the Ergun equation, Equation (5), summing the pressure drop through the two parts of the composite layer gives

$$P\left(\frac{H_c}{d_c}+\frac{H_f^*}{d_f}\right)\rho_f {u_{mf}}^2_{bed} + Q\left(\frac{H_c}{d_c^2}+\frac{H_f^*}{d_f^2}\right)\mu u_{mf\,bed} = \Delta\rho_c g H_c + \Delta\rho_f g H_f^*, \quad (7)$$

where $u_{mf\,bed}$ is the superficial velocity at which the weight of the upper layer is supported, and $\Delta\rho$ is the difference between the density of the particles and that of the surrounding fluid. The

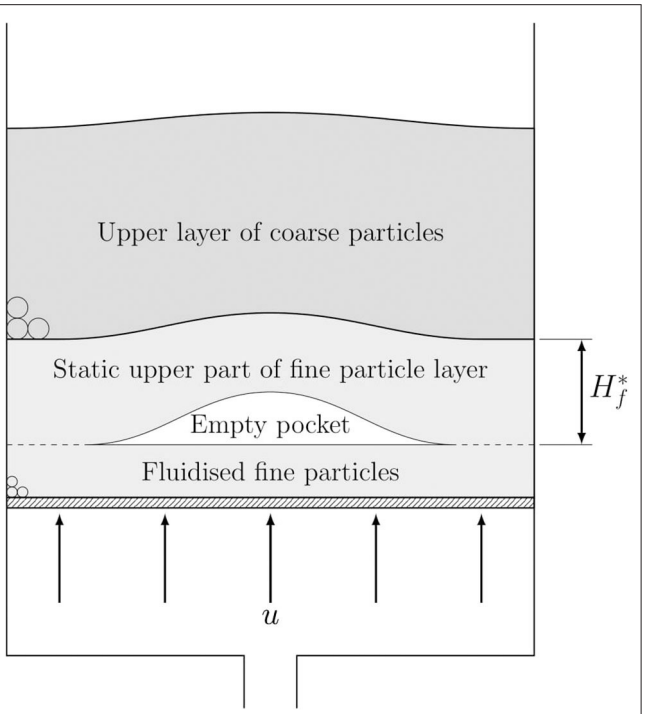

FIGURE 6 | Schematic diagram of a two-layered bed just after activity in the bed has initiated when the weight of the top layer is supported by the effects of fluid drag.

Ergun equation accommodates both drag and hydrostatic forces, the latter accounting for a factor of $(1-\phi)$ in the denominator of both P and Q. The particle volume fraction ϕ is assumed to be uniform throughout the composite layer. This expression includes the effects of inertia, which were neglected by Nichols et al. (1994).

Equation (7) may be non-dimensionalised so that

$$PRe_c^2\left(H_c'(1-r)+r\right) + QRe_c\left(H_c'(1-r^2)+r^2\right) - \left(H_c'\left(1-1/w\right)+1/w\right)Ar_c = 0, \quad (8)$$

where Re_c is calculated when $u = u_{mf\,bed}$, $H_c' = {}^{H_c}/_{H_c+H_f^*}$, the relative thickness of the layer of coarse particles, and the density difference ratio $w = \Delta\rho_c/\Delta\rho_f$.

For a given H_c', this equation may be solved implicitly to obtain the corresponding $u_{mf\,bed}$, the gas velocity at which the net weight of the upper layer is balanced by fluid flow drag. For a given $u_{mf\,bed}$ then

$$H_c' = \frac{{}^{Ar_c}/_w - rPRe_c^2 - r^2QRe_c}{PRe_c^2(1-r)+QRe_c(1-r^2)-\left((1-1/w)Ar_c\right)} \quad (9)$$

or, when all the particles have the same density so that $w = 1$,

$$H_c' = \frac{Ar_c - rPRe_c^2 - r^2QRe_c}{PRe_c^2(1-r)+QRe_c(1-r^2)}. \quad (10)$$

These equations are wholly in terms of the large particles: the properties of the small particle layer enter only through r. The

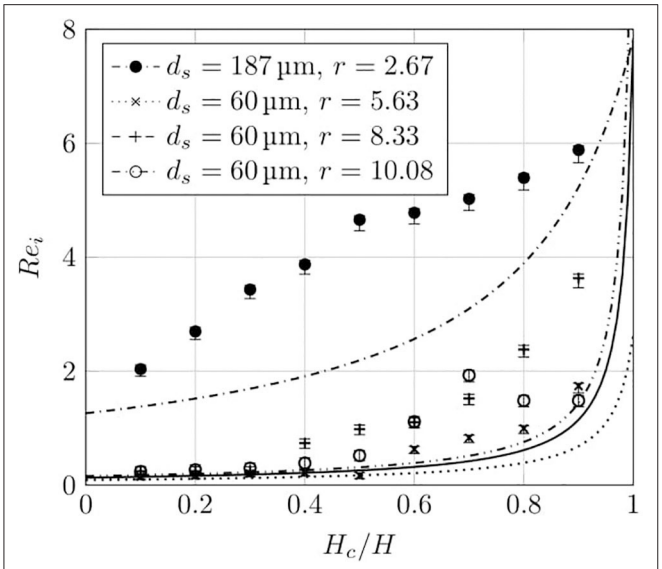

FIGURE 7 | Variation of the Reynolds number of the large particles at the point of initiation of the formation of a pocket in the lower, fine particle layer of the bed. The initial thickness of the bed was 10 cm for all the beds. Curves are Equation (10), which relates *Re* and H_c/H at $u = u_{mf}$; points are experimental measurements.

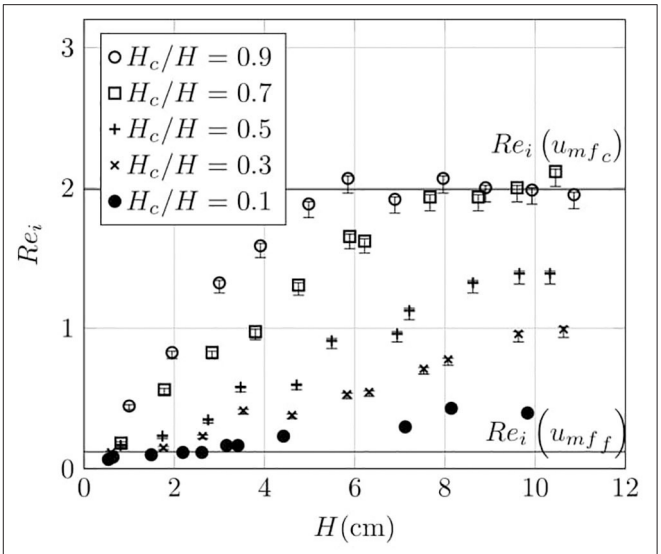

FIGURE 8 | Initiation Reynolds number as a function of *H* for the larger particles in two-layer fluidised beds consisting of a lower layer of particles with diameters 45–75 μm and an upper layer of particles with diameters of 250–425 μm for five H_c/H values. The two black horizontal lines indicate the two Reynolds numbers corresponding to the minimum fluidisation velocities, u_{mff} and u_{mfc}, determined experimentally with mono-sized fluidised beds of each component with a depth of 4 cm.

value of H_c' given by Equation (10) is a minimum value. In a system where u is steadily incremented, the value of H_c' required from Equation (10) will decrease as more of the weight of the coarse particles is supported directly by the flow through drag, but there is no mechanism by which fine particles can detach themselves from the double layer and so there will be a net upward force on the double layer.

4.2. Initiation of Activity in Layered Beds of Mono-Sized Particles

When the weight of the upper layer of the bed is supported, then it can start to deform, allowing the pocket to form in the lower layer of the bed. $u_{mf\,bed}$ can therefore be identified with the point at which deformation in the bed is first observed; we call this the initiation velocity u_i with corresponding particle Reynolds number, $Re_i = \rho_g u_i d_c/\mu$. Equation (10) is plotted out in **Figure 7** along with experimental data for the first sub-set of experiments (fixed $H = 10$ cm). For the small-scale experiments, H_f has been used to calculate H_c'. H_f^* was measured for the second sub-set of experiments (fixed $r = 5.63$). Neglecting the case when either layer was very thin (H_c or $H_f = 1$ cm), the mean relative thickness of the layer was $H_f^*/H_f = 0.87$ with a standard deviation of 0.10; therefore it is reasonable to identify H_c' with H_c/H. When $H_c' = 1$ then $Re_i = Re_{mf_c}$.

It is apparent that even a thin bottom layer of fine particles is sufficient to greatly increase the fluid force on the upper layer of large particles and cause a sharp drop in the expected value of Re_i. In the model, e.g., Equation (10), r controls the concavity of the curve, while the endpoints are controlled by the minimum fluidisation velocities for the fine and coarse particles alone. Many aspects of the theoretical curves are captured by the experimental measurements; however, the theory consistently under-predicts the Reynolds numbers at which initiation occurs in the experimental beds.

In the second sub-set of experiments there was a lower layer of 60 μm particles and an upper layer of particles with a diameter of 338 μm. Their particle size ratio $r = 5.63$ corresponded to some of the most energetic breakthroughs seen in the first sub-set of experiments. **Figure 8** shows the Reynolds number for the initiation of activity with overall bed depth for sets of experiments where H_c' was kept constant. It can be seen that Re_i depends strongly on H_c/H, as would be expected from Equation (7); however, if the activity in the bed was solely determined by the balance between weight and fluid drag then Re_i should be a constant for a given value of H_c/H; in fact there is a clear dependence on H, or perhaps $H_c + H_f^*$. There are signs that this levels out for deeper beds, but at values of Re_i that are significantly in excess of what would be expected from Equation (7). For the largest values of H_c/H, the levelling-off occurs when the value of $Re_{ic} = Re_{mf_c}$.

4.2.1. Initiation of Activity for Two Layers of Particle Mixtures

Geological materials are rarely composed of a single component. Two-layer beds where each layer was composed of a mixture of particles as detailed in **Table 2** were therefore examined. Each mixture consisted of a small component (subscript *s*) and a large component (subscript *l*). When calculating the drag, the Sauter mean diameter (4) is the most suitable diameter (van der Hoef

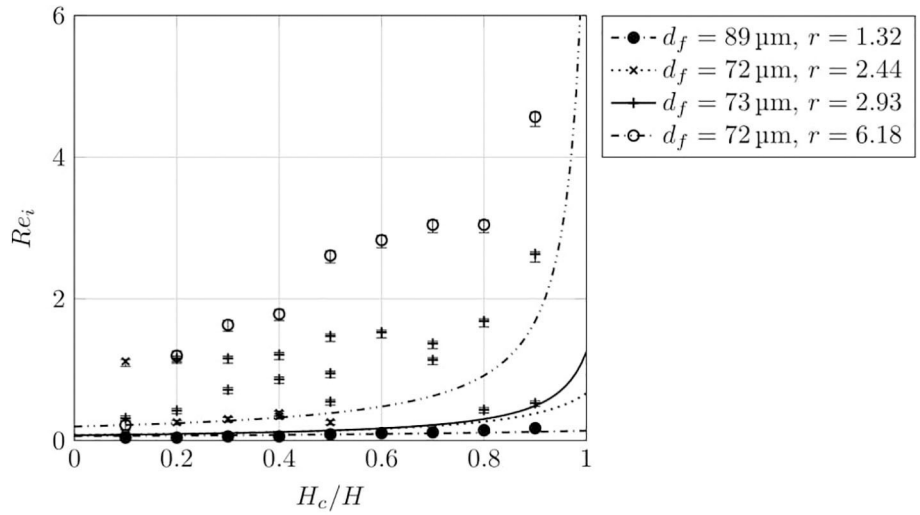

FIGURE 9 | Dependence of initiation Reynolds number on relative coarse layer thickness for several beds consisting of mixtures of particles as specified in **Table 2**. All the beds had an overall thickness $H = 10$ cm. The curves describe Equation 10 and the points are experimental measurements.

et al., 2005) and its value for the upper layer is the diameter that is used in Re_c and Ar_c. The mixing of particles can also allow better packing and so increase the drag experienced by the bed. The effect of packing in Equation (8) is determined by P and Q, and as ϕ will now be different in the upper and lower layers of the bed, then P and Q will also differ. Equation (8) therefore becomes

$$Re_c^2\left(P_f H_c'(1-r) + P_c r\right) + Re_c\left(Q_f H_c'(1-r^2) + Q_c r^2\right) - \left(H_c'\left(1 - 1/w\right) + 1/w\right) Ar_c = 0. \quad (11)$$

ϕ_f and ϕ_c can be estimated using a linear-mixture model (Yu and Standish, 1991; Yu and Zou, 1998), and the values for the mixtures used are listed in **Table 2**. From these, P and Q may be calculated for each layer and the equation solved for Re_c.

The same types of behaviour were seen for layers that are bi-modal mixtures of particles as for the layers of mono-sized particles, except that for the mixtures tested, jetting was seen more often than for the mono-sized layered beds. For $r = 6.18$, the maximum height of ejected particles was also measured and these results are plotted in **Figure 4**, and it can be seen that the types of activity and the strength of breakthrough were comparable to the beds of mono-sized layers.

Figure 9 shows the Reynolds number at which activity initiates. The trends are the same as for the mono-sized (non-mixed) layers shown in **Figure 7** including the significant under-prediction of the initiation Reynolds numbers by the theory based on fluidisation, Equation (10).

4.3. Breakthrough for Layered Beds

After initiation, H_f^* is maintained as there is no mechanism by which fine particles may be detached from it. This generates an excess drag on the layer of coarse particles and the immobile top part of the layer of fine particles, and so they are forced upwards to form the longitudinal air pocket. This pocket was typically centred within the tank, though on some occasions an asymmetrical pocket formed. A void above the pocket grew with increments of u until there was a sudden breakthrough of the lower layer through the upper layer in the form of bubbles or a jet.

For the set of experiments when H_c/H was kept constant, the breakthrough of the upper layer took place when $u \approx 1.2u_i$. In a conventional fluidised bed with a single layer of particles, the pressure drop over the bed would rise until it matched the weight of the bed and then level off (Davidson and Harrison, 1963); however, in our experiments for a two-layer bed with $u_{mf_c} > u_{mf_f}$ there was a steady pressure rise to a value significantly in excess of the weight of the bed until breakthrough. When breakthrough occurred, there was a sudden drop in pressure to a value close to that corresponding to the weight of the bed.

Figure 10 shows a typical pressure drop over a bed, recorded using a manometer with an outlet positioned at the bottom of the bed (i.e., just above the distributor plate). The pressures measured are steady pressures i.e., after each increment of u, the pressure was allowed to come to an equilibrium value. When u = 4 cm/s, the estimated pressure drop over the bed owing to drag calculated from terms equivalent to the first two terms of Equation (11) was 7200 Pa compared to the 6000 Pa measured. Some difference would be expected owing to the distortion of the particle layers at breakthrough, but this gives some confidence that the force exerted on the particles is dominated by drag.

The strength of breakthrough, as indicated by the maximum height of the particles ejected from the bed, is shown in **Figure 11** for five sets of experiments from the second sub-set for which H_c/H is constant. There is a similar dependency in the strength of the breakthrough on H_c/H with the strongest breakthroughs for middle values; however, there is a dependence on H in absolute terms as well.

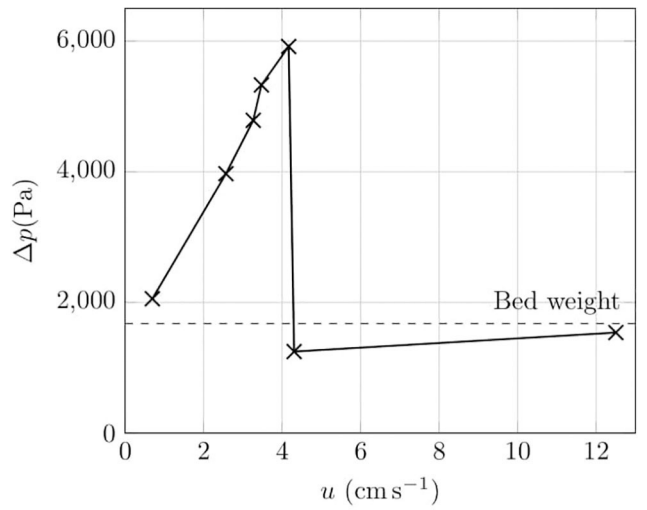

FIGURE 10 | Change of pressure drop over a two-layer bed as u is incremented. The sudden fall in pressure corresponds to the point at which breakthrough takes place. The total bed thickness was 10 cm and the bed layers conformed to $r = 2.44$ in **Table 2**. The dashed line is the bed weight calculated as $\phi_c \Delta\rho_c g H_c + \phi_f \Delta\rho_f g H_f$. $H_c/H = 0.6$.

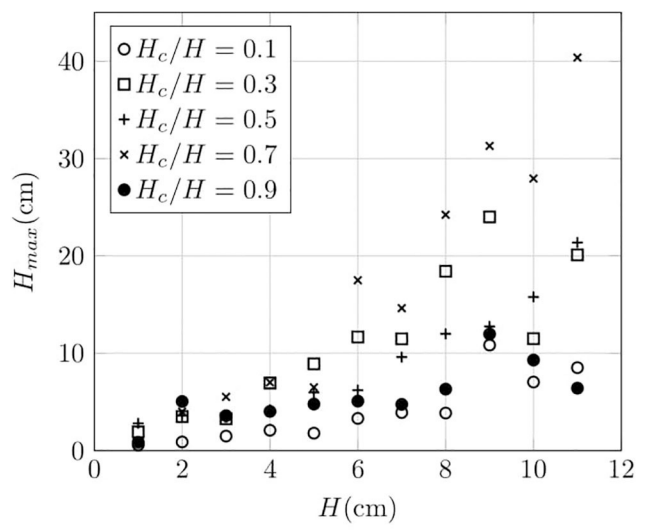

FIGURE 11 | Strength of breakthrough for a two-layer fluidised bed where H_{max} is the maximum observed height of particles ejected from the bed. Heights were measured to an accuracy of ±0.1 cm. The bed consisted of a lower layer of particles with diameters 45–75 μm particles and an upper layer of particles with a diameters 250–425 μm where H_c/H is kept constant over a range of H for five values of H_c/H.

5. DISCUSSION

The established conceptual model of secondary hydroeruptions through hot pyroclastic flow deposits (e.g., Moyer and Swanson, 1987) emphasises the role of permeability (fine grain size) in the primary deposit. In this model, which we term "static pressure build-up," the low permeability reduces the rate of steam escape enabling the underlying steam source to pressurise until the overburden fails, triggering the secondary eruption. However, for any non-zero permeability, if the pressure at the steam source increases, so will the flow up through the interstices of the deposit, increasing the drag force pushing upwards throughout the entire deposit thickness. We propose an alternative model where drag is fundamental to triggering secondary hydroeruptions. It is suitable for deposits that are effectively granular materials for which the permeability is high enough for the drag force to be comparable to the static pressure force; it is not relevant to secondary eruptions through welded deposits in which the particles will be stuck together regardless of the flow rate of gas. Our simple analogue experiments with uniform-density spherical particles demonstrate that upflow of gas from an underlying distributed source can cause localised violent outbursts of particles from the top of a bed of layered granular material.

Violent outbursts do not occur for single-layer beds or in two-layer beds where the capping layer is finer-grained (lower permeability) than the layer below it; however, if the layers are reversed so that the coarser-grained layer is on top, then jets of particles form for some gas fluxes and layer thicknesses and grain size contrasts. Our experiments and theoretical considerations, including those outlined in Nichols et al. (1994), indicate that what matters is not the permeability of the layers but the minimum gas velocity for drag to support the weight of the particles, u_{mf}. In the experiments we controlled u_{mf} through particle size and used spherical particles with unimodal or bimodal size distributions, which are well-studied in industrial applications and are the easiest to model and understand; however, in general u_{mf} will be determined by the size distribution, densities and shapes of particles making up a layer.

The violent breakthrough in layered systems where the top layer has a u_{mf} larger than that in the lower layer is enabled by the interaction between the two layers. The upper part of the lower layer of fine particles (above a gas pocket) supports the weight of the upper layer of coarse particles, forming a composite structure. In neither part of this composite are the particles individually fluidised because the gas flow is not large enough to fluidise the large particles, and the small particles are forced against the large ones by the excess drag on them. This ensures that there continues to be significant inter-particle friction and the composite has a strength so that the upstream pressure increases to a value in excess of the lithostatic. The theory based on fluidisation alone, Equation (10), underestimates Re_i for both mono-sized layers and mixed layers; this is consistent with the static strength of layers also playing a role in the initiation of activity. It is the arching of the bed (permitted by it having a strength) which forms a region with no particles. This gas pocket causes increased flow through its apex, locally fluidising the particles above. In this region where there is full fluidisation, jets and bubbles can form which further concentrate the flow. Once breakthrough is achieved, the central portion of the bed is fully fluidised and the pressure drop over it is suddenly reduced to that corresponding to the bed's weight, releasing the excess pressure. This transient, and the concentrated flow owing

to bubbles or a jet, generates the plume of particles expelled at breakthrough.

The analogue experiments and theoretical constraints indicate that the drag-induced triggering of secondary hydroeruptions pyroclastic deposits requires that:

- The deposit is a granular material with particles free to move relative to one another if the local gas flow is sufficient for the weights of particles to be supported. This means the primary deposit is not welded and has low cohesion.
- The deposit has some strength through friction in order to allow buildup of overpressure.
- The primary deposit is layered with vertical changes in u_{mf}.
- There is a layer with sufficiently low u_{mf} (e.g., it is sufficiently fine-grained) for the upwards velocity of steam generated by the thermal energy of the primary deposit to exceed it.
- This low-u_{mf} layer is overlaid by a layer with higher u_{mf} (e.g., due to coarser grain size and/or higher proportion of lithic clasts of high density).
- The low-u_{mf} layer is sufficiently thick compared to the thickness of the deposit above it to satisfy Equation (9).

5.1. Application to Deposits

To consider the above requirements and apply the insights from our analogue experiments to secondary hydroeruptions, we refer to the Mount St Helens (MSH) 1980 eruption. It has well-studied primary pyroclastic flow deposits (Kuntz et al., 1981; Rowley et al., 1981; Brand et al., 2014) and the best-documented secondary hydroeruptions (Rowley et al., 1981; Moyer and Swanson, 1987). That the deposits can be treated as low-strength granular materials that would fluidise with sufficiently fast upflow of gas is suggested by the "striking deformation" when people attempted to walk on the primary deposits in the weeks after emplacement (Wilson and Head, 1981) and the sloughing of the primary deposits into the secondary hydroeruption craters to form gentle slopes (Rowley et al., 1981). Based on the responses to loads on the top surface and shear vane tests in the upper channel deposit, Wilson and Head (1981) estimated a yield strength of $\sim$ 300–2,000 N/m^2 and 400–18,000 N/m^2, respectively. However, a degassed and compacted deposit (with degassing induced by loading experiments) was substantially stronger (e.g., it could support an adult standing on one foot), and they attributed much higher compressive strengths of 100,000–250,000 N/m^2 determined from cone penetration to the efficiency of degassing induced by the steadily increasing force applied during these tests. We hypothesise that for the drag-induced triggering of secondary hydroeruptions, the increased strength with compaction demonstrates how the portion of the (fine-grained) layer where $u_{mf} < u$ can gain an appreciable strength when it is pushed up and is compacted against the weight of the overlying material with $u_{mf} > u$. The pressure that builds in the gas pocket, which contributes to the intensity of the outburst when the overlying material is breached, depends on the bending strength of the material above the pocket, and so although most of the deposit would be weak and easily deformed, the compaction induced by excess drag in the low u_{mf} part of the composite layer above where the pocket initiated would allow greater pressure to accumulate.

Sections through the MSH May 18 pyroclastic flow deposits exposed along drainages by recent erosion that were studied by Brand et al. (2014) reveal that the primary deposits can be considered as layered with vertical changes in grain size and componentry, and so there are vertical variations in u_{mf}. Although the four main units (I, II, III, IV) of the May 18 pyroclastic flows have intricate vertical and lateral facies variations, the outcrop photographs and diagrams of Brand et al. (2014) show laterally continuous layering defined by grain size (and componentry) is common over distances of tens of metres. Lithofacies include: massive lapilli tuff; block-rich massive lapilli tuff, sometimes with block-rich basal breccia; pumice lens; fine-grained massive ash, up to tens of centimetres thick. There is considerable variation in median grain size and sorting (Kuntz et al., 1981; Brand et al., 2014): for example, the median of the samples sieved by Brand et al. (2014) 7.1–7.2 km from source vary from $<$ 100 µm to $>$ 10 cm. The stratigraphic logs show that there is commonly a sudden increase in grain size with stratigraphic height across unit boundaries (e.g., from units II to III and from III to IV), which would correspond to vertical increases in u_{mf}.

The preservation of layers in the primary deposits, including close to secondary hydroeruption sites, means that the steam flux after emplacement was not sufficient to exceed u_{mf} of most (or all) of the deposit. However, for the proposed drag-induced triggering of secondary eruptions, there must be layer(s) where the steam velocity exceeded u_{mf}. **Figure 12** shows u_{mf} as a function of particle diameter for three particle fractions ($\phi = 0.5, 0.6, 0.7$) and two end-member particle densities that correspond to the typical pumice density (750 kg/m^3) and the bubble-free (glass and crystals) juvenile clast density (2,550 kg/m^3) determined by Kuntz et al. (1981). It indicates that the effects of the expected variations in density and particle volume fractions would usually be much less important than variations in grain size in their effects on variations of u_{mf} in pyroclastic flow deposits. For beds with a range of particle sizes (e.g., pyroclastic deposits), if the property of interest relates to drag (e.g., u_{mf} and permeability, Breard et al., 2019), then the relevant particle diameter is the Sauter mean diameter (Equation 4). The Sauter mean diameter is sensitive to the finer grain sizes and is always smaller than the median (by mass) when all the particles are considered to have the same density (and also when the fine particles are relatively dense).

Most of the secondary hydroeruptions occurred within a few days of emplacement of the May 18 pyroclastic flows. Moyer and Swanson (1987) include data on the grain size distribution of one May 18 pyroclastic flow sample down to 9$\Phi \approx$ 2 µm, with just 0.12 wt.% finer than 9Φ. Applying Equation (4) and using the geometric mean for the diameter of each particle size bin gives a Sauter mean diameter of 110 µm. Breard et al. (2019) show how to estimate the Sauter mean diameter from the commonly reported Φ-scale based median (Md) and sorting (σ) parameters, assuming a log-normal particle size distribution. This gives a Sauter mean diameter of 97 µm for the same Moyer and Swanson (1987) sample, in good agreement with Equation (4). Applying

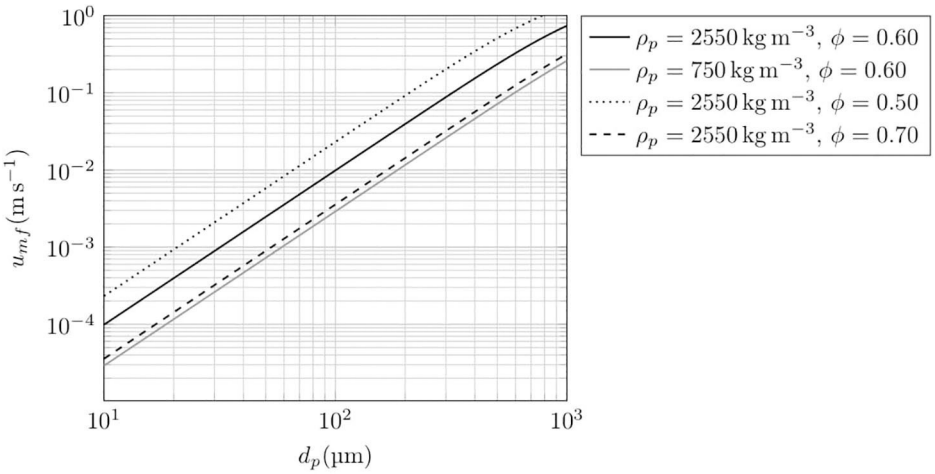

FIGURE 12 | Typical minimum fluidisation curves with particle diameter calculated from Equation (5) showing their sensitivity to particle density and particle volume fraction. The fluidising gas is superheated water vapour with a temperature of 250 °C: ρ =2.37 kg/m^3 and $\mu = 1.80 \times 10^{-5}$ kg/ms.

the Breard et al. (2019) approach to the nine May 18 pyroclastic flow size distributions in Kuntz et al. (1981) gives mean Sauter mean diameters of 55–206 μm. Data from the more extensive sampling of recent exposures of the May 18 units along drainages by Brand et al. (2014) suggest the Sauter mean diameter can range from $<$ 10 microns to $>$ 1 mm [c.f. Figure 4F of Brand et al. (2014) and Figure 9B of Breard et al. (2019)].

Figure 12 gives a sense of the implications of these grain size data for the ranges of u_{mf} in pyroclastic flow deposits. For example, for a density of 2,550 kg/m^3, Sauter mean diameters of 55, 200, and 1,000 μm correspond to u_{mf} values (and the volume flux of steam generated per unit area) of 3×10^{-3} m/s, 4×10^{-2} m/s, and 0.7 m/s, respectively. These steam rates suggest that it is feasible for upflow of steam to overcome u_{mf} of some, but not most, of a pyroclastic flow deposit succession as required to trigger secondary hydroeruptions and preserve layered deposits. However, the argument would clearly be strengthened by modelling of steam generation and data on grain size and density from samples collected at the roots of secondary hydroeruptions, which are beyond the scope of this study.

In our laboratory experiments with layers of mono-sized particles, the intensity of outbursts of particles was substantially diminished when the ratio of the particle diameters of the two layers was sufficient for the smaller particles to percolate through the interstices of the coarser layer above. For these experiments this meant that violent outbursts were abated when $r > 6.5$. This will be partly because excess drag on the particles in the lower layer causes percolation rather than it being exerted against the upper layer. Also the mixing of the small and large particles causes u_{mf} for the upper layer to be decreased (Gilbertson, 2019). For natural pyroclastic deposits with much broader size distributions we expect percolation to be much less important because of the more efficient packing and smaller interstices than in mono-sized beds. In fluidised beds of mixtures, segregation often takes place owing to the difference in u_{mf} of the components (Gilbertson, 2019); however, this was not apparent in experiments with mixtures of particles because the particles in the composite structure are not individually fluidised and they are not free to move. Thus we expect the intensity of outbursts to increase for greater r, even when $r > 6.5$, in pyroclastic deposits, with r based on the ratio of Sauter mean diameter of layers. Other factors that would affect intensity are the bending strength of the beds and the relative thickness of the layers; further work is required to make robust quantitative predictions of their roles.

The mechanism for triggering secondary hydroeruptions we have explored in this paper complements that proposed by Moyer and Swanson (1987) in that in both models steam pressure builds at depth before the deposit is breached causing a sudden pressure drop and eruption of steam and particles. The addition of the role of drag in our model means that the root of the secondary eruption is not necessarily at the depth of the steam source: it can, and generally would, be higher up in the deposit where there is a relatively low-u_{mf} layer. Moyer and Swanson (1987) proposed that the steam source for the MSH secondary hydroeruptions was pools of water on top of the May 18 debris avalanche deposit because of the dearth of the distinctive cryptodome dacite clasts from the debris avalanche in the secondary hydroeruption deposits. In our drag-related mechanism for secondary eruption triggering, the water could be in pools on top of the debris avalanche but could also be groundwater. Indeed, the secondary hydroeruptions that took place a year after emplacement of the pyroclastic flows are most likely to be related to seasonal recharge and a rising water table.

6. CONCLUSION

Secondary explosions through pyroclastic flow deposits have occurred in several historical eruptions, indicating they are a common hazard where hot pyroclastic flows are deposited on a wet environment. There has however been relatively little study of the phenomenon, perhaps because the explosion craters and

the associated surge and fallout deposits are readily modified and eroded, and so may often be poorly preserved or not recognized in the geological record.

Our laboratory experiments show that violent outbursts analogous to secondary eruptions can be generated by the drag induced by a distributed flow of gas through a granular material with vertical variations in the minimum fluidisation velocities. Notably, a low-permeability cap is not required to trigger a secondary eruption; in fact, the experiments demonstrate that distributed gas flow up through a granular layer capped with a finer-grained (and so lower permeability) layer made of particles of the same density does not generate jets of particles or craters. However, when the upper layer is coarser, a gas pocket may grow within the finer layer causing the bed to dome upwards until it fails forming a crater and erupting particles. Combining these results with theoretical considerations and constraints from the Mt St Helens 1980 sequence, we conclude that for sufficient steam flux, secondary eruptions can be triggered within pyroclastic flow deposits where there is a fine-grained layer with very low minimum fluidisation velocity under a layer that is coarser and/or contains more dense clasts so that a greater upward velocity of steam is required to fluidise it.

Our experiments with air flow up through layers of unimodal or bimodal glass spheres are very simple; however, the complex behaviour observed provides insights into even more complicated natural secondary eruptions. The experiments are intended only to elucidate the physical origins and triggers of eruptions and not the dynamics of the eruptions themselves, which will be strongly affected by the generation of the steam that drives them. When the eruption is triggered, the associated pressure drop will induce flashing of superheated water at depth to steam. Steam compressibility may also affect the eruption, which is not the case in the experiments due to the much smaller length-scale and pressure drop. These differences mean that once triggered, the natural secondary eruption is likely to be more energetic than predicted by the processes involved in the experiments.

DATA AVAILABILITY STATEMENT

All datasets generated for this study are included in the article/**Supplementary Material**.

AUTHOR CONTRIBUTIONS

AR conceived the project and supervised AT and SM, who did the experiments and analysis of data. MG re-analyzed and re-plotted the data, and developed some theoretical constraints. MG, AR, and SM created the figures. MG and AR wrote the manuscript. All authors contributed to the article and approved the submitted version.

FUNDING

The research was conducted by the authors in the ordinary course of their employment or education at the University of Bristol. Expenses were paid from academic discretionary accounts.

SUPPLEMENTARY MATERIAL

The Supplementary Material for this article can be found online at: https://www.frontiersin.org/articles/10.3389/feart.2020.00324/full#supplementary-material

REFERENCES

Brand, B. D., Mackaman-Lofland, C., Pollock, N. M., Bendaña, S., Dawson, B., and Wichgers, P. (2014). Dynamics of pyroclastic density currents: Conditions that promote substrate erosion and self-channelization - Mount St Helens, Washington (USA). *J. Volcanol. Geotherm. Res.* 276, 189–214. doi: 10.1016/j.jvolgeores.2014.01.007

Breard, E. C. P., Jones, J. R., Fullard, L., Lube, G., Davies, C., and Dufek, J. (2019). The permeability of volcanic mixtures-implications for pyroclastic currents. *J. Geophys. Res. Solid Earth* 124, 1343–1360. doi: 10.1029/2018JB016544

Davidson, J. F., and Harrison, D. (1963). *Fluidised Particles*. C.U.P.

Ergun, S. (1952). Fluid flow through packed beds. *Chem. Eng. Prog.* 48, 89–94.

Gardner, C. A., Neal, C. A., Waitt, R. B., and Janda, R. J. (1994). Proximal pyroclastic deposits from the 1989-1990 eruption of redoubt volcano, Alaska-stratigraphy, distribution, and physical characteristics. *J. Volcanol. Geotherm. Res.* 62, 213–250. doi: 10.1016/0377-0273(94)90035-3

Geldart, D. (1973). Types of gas fluidization. *Powder Technol.* 7, 285–292. doi: 10.1016/0032-5910(73)80037-3

Gilbertson, M. A. (2019). Estimation of the minimum fluidisation velocities in well-mixed bi-disperse fluidised beds. *Powder Technol.* 346, 433–440. doi: 10.1016/j.powtec.2019.02.019

Gilbertson, M. A., and Eames, I. (2001). Segregation patterns in gas-fluidized systems. *J. Fluid Mech.* 433, 347–356. doi: 10.1017/S0022112001003950

Hildreth, W. (1983). The compositionally zoned eruption of 1912 in the Valley of Ten Thousand Smokes, Katmai National Park, Alaska. *J. Volcanol. Geotherm. Res.* 18, 1–56. doi: 10.1016/0377-0273(83)90003-3

Keating, G. N. (2005). The role of water in cooling ignimbrites. *J. Volcanol. Geotherm. Res.* 142, 145–171. doi: 10.1016/j.jvolgeores.2004.10.019

Kuntz, M., Rowley, P., MacLeod, N., Reynolds, R., McBroome, L., Kaplan, A., et al. (1981). "Petrography and particle size distribution of pyroclastic flow, ash-cloud and surge deposits," in *The 1980 eruptions of Mount St. Helens*. U.S. Geological Survey Professional Paper 1250, 425–539.

Moyer, T. C., and Swanson, D. A. (1987). Secondary hydroeruptions in pyroclastic-flow deposits: examples from Mount St. Helens. *J. Volcanol. Geotherm. Res.* 32, 299–319. doi: 10.1016/0377-0273(87)90081-3

Nermoen, A., Raufaste, C., deVilliers, S. D., Jettestuen, E., Meakin, P., and Dysthe, D. K. (2010). Morphological transitions in partially gas-fluidized granular mixtures. *Phys. Rev. E* 81:061305. doi: 10.1103/PhysRevE.81.061305

Nichols, R. J., Sparks, R. S. J., and Wilson, C. J. N. (1994). Experimental studies of the fluidization of layered sediments and the formation of fluid escape structures. *Sedimentology* 41, 233–253. doi: 10.1111/j.1365-3091.1994.tb01403.x

Rhodes, M. (1998). *Introduction to Particle Technology*. Chichester: Wiley.

Rowley, P. D., Kuntz, M. A., and MacLeod, N. S. (1981). "Pyroclastic-flow deposits," in *The 1980 Eruptions of Mount St. Helens*. U.S. Geological Survey Professional Paper 1250, 489–512.

Torres, R. C., Self, S., and Martinez, M. M. L. (1996). "Secondary pyroclastic flows from the June 15, 1991, ignimbrite of Mount Pinatubo," in *Fire and Mud: Eruptions and Lahars of Mount Pinatubo, Philippines*, eds C. G. Newhall and R. S. Punongbayan (Seattle: University of Washington Press), 625–678.

van der Hoef, M. A., Beetstra, R., and Kuipers, J. A. M. (2005). Lattice-boltzmann simulations of low-Reynolds-number flow past mono- and bidisperse arrays of

spheres: results for the permeability and drag force. *J. Fluid Mech.* 528, 233–254. doi: 10.1017/S0022112004003295

Wilson, L., and Head, J. (1981). "Morphology and rheology of pyroclastic flows and their deposits, and guidelines for future observations," in *The 1980 Eruptions of Mount St. Helens*. U.S. Geological Survey Professional Paper 1250, 513–524.

Yu, A. B., and Standish, N. (1991). Estimation of the porosity of particle mixtures by a linear-mixture packing model. *Indus. Eng. Chem. Res.* 30, 1372–1385. doi: 10.1021/ie00054a045

Yu, A. B., and Zou, R. P. (1998). Prediction of the porosity of particle mixtures. *KONA Powder Part. J.* 16, 68–81. doi: 10.14356/kona.1998010

Conflict of Interest: The authors declare that the research was conducted in the absence of any commercial or financial relationships that could be construed as a potential conflict of interest.

frontiers in Earth Science

ORIGINAL RESEARCH
published: 15 September 2020
doi: 10.3389/feart.2020.557788

New Insights Into the 2070 cal yr BP Pyroclastic Currents at El Misti Volcano (Peru) From Field Investigations, Satellite Imagery and Probabilistic Modeling

S. J. Charbonnier[1], J.-C. Thouret[2], V. Gueugneau[1] and R. Constantinescu[1]*

[1] School of Geosciences, University of South Florida, Tampa, FL, United States, [2] Laboratoire Magmas et Volcans, CNRS, OPGC et IRD, Université Clermont-Auvergne, Aubière, France

Pyroclastic currents (PCs) are the most challenging volcanic hazards for disaster planners in populated areas around volcanoes. "El Misti" volcano (5,825 m above sea level), located only 17 km from the city center of Arequipa (>1.1 million inhabitants), South Peru, has produced small-to-moderate volume (<1 km^3) PCs with a frequency of 2,000–4,000 years over the past 50 kyr. The most recent Plinian eruption dated at 2070 cal yr BP (VEI 4) has been selected as one of the reference events for the hazard assessment and risk mitigation plan of Arequipa. Associated pumice- and lithic-rich PC deposits were emplaced from at least four phases of column-collapse into the radial valleys draining the volcano as far as 13 km toward the city. Field mapping and stratigraphic surveys conducted in seven valleys affected by the 2070 cal yr BP PCs were combined with a new high-resolution (2 m) digital surface model of the volcano to better estimate the distribution of individual PC volumes. Such data acquisition is particularly critical for two of these valleys (San Lázaro and Huarangal-Mariano Melgar) for which the medial and distal reaches now cross the suburbs of Arequipa. The total area covered by the PC deposits is estimated at 141 km^2 for a total bulk volume estimated at 406 ± 140 × 10^6 m^3. These volumes were used as input parameters to better calibrate probabilistic numerical simulations of future similar PC events using the two-layer VolcFlow model and assess the impacts of both the concentrated and dilute portions of these currents in the San Lázaro and Huarangal valleys. We discuss probability values of PC inundation obtained from these simulations both in terms of their implications for the dynamics of such hazardous PCs at El Misti and for their integration into its current multi-hazard assessment. Modeling results demonstrate that the risk of overbank processes and spreading of unconfined PCs inside Arequipa should be refined. This multi-disciplinary study aims to help the civil authorities' understanding of the likely effects of PCs associated with a similar VEI 4 eruption of El Misti on the urban area of Arequipa.

Keywords: El Misti volcano, pyroclastic currents, probabilistic modeling, field data acquisition, hazard assessment and mapping

OPEN ACCESS

Edited by:
Laura Sandri, National Institute of Geophysics and Volcanology (Bologna), Italy

Reviewed by:
Lucia Capra, National Autonomous University of Mexico, Mexico
Roberto Sulpizio, University of Bari Aldo Moro, Italy

****Correspondence:***
Sylvain Charbonnier
sylvain@usf.edu

Specialty section:
This article was submitted to Volcanology, a section of the journal Frontiers in Earth Science

Received: *30 April 2020*
Accepted: *24 August 2020*
Published: *15 September 2020*

Citation:
Charbonnier SJ, Thouret J-C, Gueugneau V and Constantinescu R (2020) New Insights Into the 2070 cal yr BP Pyroclastic Currents at El Misti Volcano (Peru) From Field Investigations, Satellite Imagery and Probabilistic Modeling. Front. Earth Sci. 8:557788. doi: 10.3389/feart.2020.557788

INTRODUCTION

Pyroclastic currents (PCs) are one of the most dangerous and least understood phenomena of explosive volcanism, leading to the highest number of fatalities during recent explosive eruptions. In the past decade alone, more than 1,000 people were killed by PCs around the world [e.g., Merapi (Indonesia) in 2010 (Surono et al., 2012), Sinabung (Indonesia) in 2014 and 2016 (Andreastuti et al., 2019), Fuego (Guatemala) in 2018 (Charbonnier et al., 2019), White Island (New Zealand) in 2019]. With more than 500 million people living in the proximity of an active volcano around the world and growing populations spreading over their flanks (Marti, 2017), improved methodologies and techniques for quantitative PC hazard assessment constitute a primary research objective in volcanology and volcanic hazard sciences. In this paper, we use the example of El Misti volcano (Peru) and its last Plinian eruption (~2070 calibrated ^{14}C years or "cal yr" BP) to demonstrate how robust field and laboratory work, along with high-resolution satellite imagery, can inform state-of-the-art computer models and drive a fully probabilistic PC hazard assessment at this high-risk volcano.

El Misti volcano (5,822 m), located in southern Peru within the northern segment of the Central Andes volcanic zone, is potentially one of the most active volcanoes in the region (Thouret et al., 2001; Harpel et al., 2011; Cobeñas et al., 2012). Arequipa, the second largest city and economic center of Peru with a population of 1,130,000 (as of 2017), is located at the foot of El Misti. The city center lies only 17 km southwest of El Misti's crater and approximately 3.5 km below the summit (**Figure 1**). In the past, El Misti has displayed a variety of eruptive styles, including Vulcanian and Plinian eruptions (**Table 1**).

From these, two eruptions have been selected as reference hazard scenarios (Sandri et al., 2014): 1) The small magnitude and high frequency VEI 2 (Volcanic Explosivity Index, Newhall and Self, 1982) Vulcanian eruption that occurred in 1440–1470 CE (Chávez Chávez, 1992) and emplaced an andesitic plug in the 400 m-wide vent, nested in the large 2070 cal yr BP crater, is the most likely scenario for renewed activity; 2) The VEI 4 2070 cal yr BP event (weighted mean age 2070 ± 20 ^{14}C cal yr BP, i.e., 1990–2060 cal yr BP; Cobeñas et al., 2014) because of its high recurrence rate, estimated between 2,000 and 4,000 years based on the chrono-stratigraphical dataset (see **Table 1** and Thouret et al., 2001; Sandri et al., 2014). The aim of Cobeñas et al. (2012, 2014) was to describe and explain how the 2070 cal yr BP tephra fallout and PC deposits were formed, and to understand the mechanisms that triggered the eruption with a rationale of providing civil authorities with a clear understanding of the likely effects of a major eruption of El Misti on Arequipa's urban area. With an increasing population and sprawling of developed area by ≥30% in the past 30 years, one of the goals of this study is to re-assess the PC extents, volumes and hazards around El Misti, using new high-resolution field-based, remote sensing, and numerical modeling tools.

Field mapping and stratigraphic surveys conducted in seven valleys affected by the 2070 years BP PCs were combined with a new high-resolution (2 m) digital surface model (DSM) of the volcano obtained by fusing a stereo-pair of Pleiades optical images with lower-resolution (10 m) TanDEM-X (TDX) radar

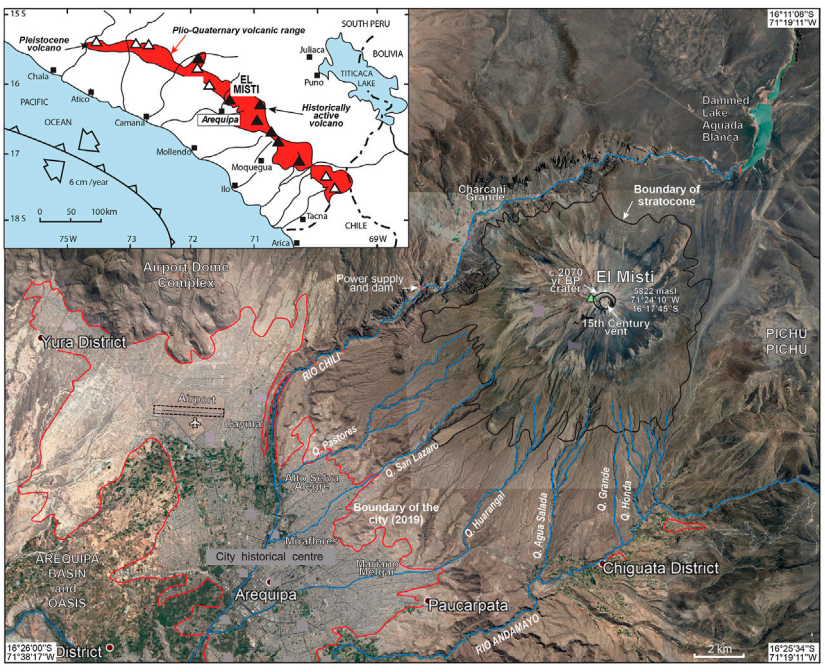

FIGURE 1 | Google Earth image of El Misti volcano showing the principal geological features, the drainage network in blue (Río Chili Valley and its tributaries Quebradas = seasonal ravines), and the urban area of the city of Arequipa (red line). The bold line indicates the boundary between El Misti stratocone and its ring plain. Inset: location of El Misti volcano in the central volcanic zone in south Peru.

TABLE 1 | Summary of magnitude and frequency data for each eruptive and non-eruptive phenomenon at El Misti volcano collected from eruptive records over the last 50 kyr of activity. Modified from Sandri et al. (2014).

Domain	Deposit type	Approximate thickness	Approximate volume	Examples	Rank according to estimated average frequency
Pyroclastic deposits	Ash fallout	1–20 cm	Several million m^3	Several ashfall layers over 10 ka, period 4-1	Every 400–1,000 years
	Sub-Plinian to Plinian fallout	20–50 cm, maximum 3 m	≤1 km^3	2070 years BP, "Autopista," Chachani road sequence	Every 2,000–4,000 years
	Small volume pumice- and/or ash-rich PCs	1–5 m each	<1 km^3	Period 3; Pastores	Three PC-producing periods over 50 ka, 3–6 PCs within each period (every 3,000 years?)
	Large volume pumice- and/or ash-rich PCs	5–10 m each	1–5 km^3	Many PCs between 50 and 40 ka and between 34–32 ka	At least 20,000 years, but frequent within caldera-forming period 3-3 and 3-1
	Scoriaceous PCs and fallout	3–7 m	1 km^3 each	Periods 3.3 and 3.4	Same pattern as BAFs, especially periods 3-3 and 3-4 (every 3,000–5,000 years?)
	Block-and-ash flows and lithic-rich PCs	5–10 m	<1 km^3	One or two units between 70 and >40 ka	Twice over 70 ka
	Bombs and ejecta of phreatomagmatic origin	1–2 m, in lower part of scoria PCs	1 to a few million m^3	Phreatomagmatic interactions in Late Glacial times	Infrequent except for period 3.4
Other deposits	Debris-avalanche deposits	20–50 m	Several km^3	At least 2, one is >50 ka, another is older >100 ka	Twice over >110 ka
	Lava flows	10–70 m	Several km^3 to 10 km^3	El Misti 1-2 and lava flows exist near summit between c.49 and 14 ka	Frequent during El Misti 1 and 2 growth, some during 3-1, then decrease. Lava flow dated 49 ± 3 ka, but youngest lava flows do exist

PC, pyroclastic current.

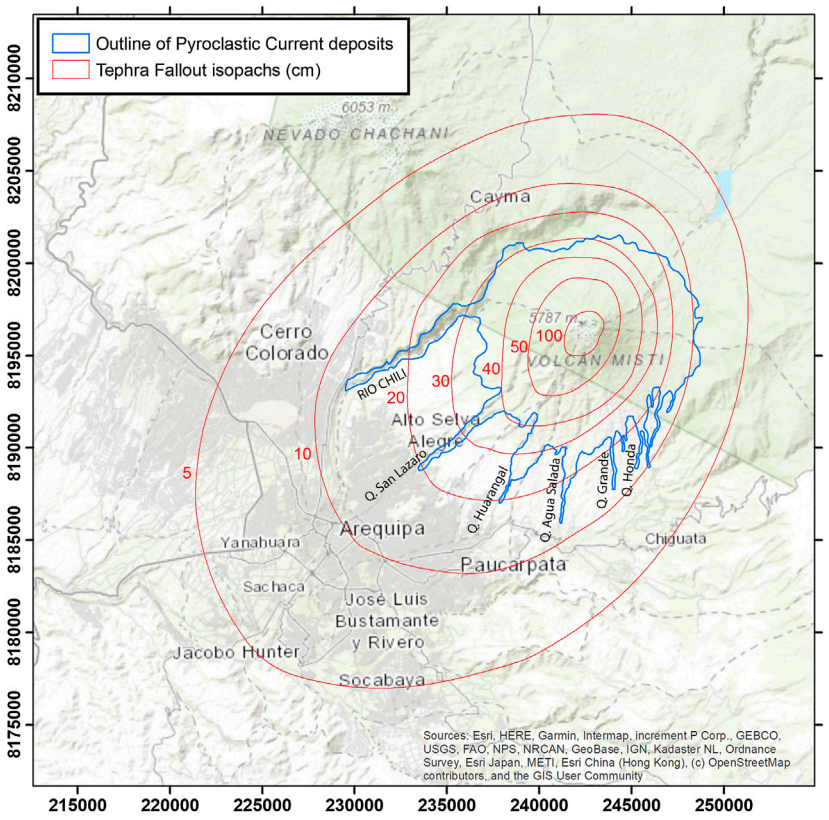

FIGURE 2 | Map of the 2070 cal yr BP eruptive deposits with pyroclastic current deposits outlined in blue and tephra fallout isopachs (in cm) delineated in red. Names of the studied valleys are indicated in black. Background map is from the ESRI World Topographic Map (source: ESRI). Modified from Cobeñas et al. (2012).

data. Surveys and DSM embedded in GIS tools allow to better estimate the distribution of individual PC volumes emplaced in each of the valleys impacted by this Plinian event. In addition, sedimentological analyses were performed on 16 samples collected during stratigraphic surveys to investigate the facies variations of the main valley-confined PC deposit units both longitudinally and laterally across the NW to SE flanks. Finally, this dataset was used to calibrate the source conditions (i.e., location, initial volume, and particle mean diameter) for probabilistic numerical simulations of potential similar PC events on the SW flank of the volcano using the two-layer VolcFlow model and assess the impacts of both the concentrated and dilute portions of these currents in Arequipa. We discuss probabilities of PC inundation both in terms of their implications for the dynamics of such highly mobile PCs and for their integration into the current multi-hazard assessment at this high-risk volcano. This multi-disciplinary study contributes to the current endeavor, led jointly by several national and international institutions, to revise the hazard-zone map of El Misti to be published in 2021.

THE 2070 CAL YR BP ERUPTION AND ASSOCIATED DEPOSITS

Pyroclastic deposits were identified in previous studies by Navarro Colque (1999), Suni Chambi (1999), Thouret et al. (1995, 1999, 2001), Legros (2001) and Harpel et al. (2011). The 2070 cal yr BP deposits are part of El Misti's fourth growth stage of Holocene age (Thouret et al., 2001; Cobeñas et al., 2012; Sandri et al., 2014), overly the 3,300–3,800 cal yr BP pyroclastic deposit and underlie the tephra fallout layer of the mid-15th Century event. The 2070 cal yr BP Plinian (VEI 4) eruption of El Misti is divided into five eruptive stages based on deposit stratigraphy: 1) a lower tephra layer deposited from a 21–24 km-high eruptive column, 2) a thin sand-sized, lithic-rich, middle tephra layer associated with the collapse of the crater walls and partial obstruction of the vent, 3) an upper tephra layer deposited when the Plinian eruption column resumed, 4) PC deposits produced by subsequent collapses of the column, 5) an uppermost unit made of a coarse, lithic-rich debris-avalanche deposit attributed to failure of the hydrothermally altered part of the crater rim toward the S and SE (Cobeñas et al., 2012). Tephra and PC deposits from the 2070 cal yr BP eruption were analyzed by Cobeñas et al. (2012), but their findings have been challenged by Harpel et al. (2011, 2013), in particular concerning the determination of the origin -PC vs. lahar- of some of the 2070 cal yr BP deposits. Subsequently, the characteristics of PCs and criteria for distinguishing all deposits associated to the 2070 cal yr BP event have been re-assessed by Cobeñas et al. (2014). We refer the reader to the aforementioned studies for a detailed description of the eruption source

parameters and associated tephra fallout deposits. To summarize, the Plinian column rose up to 21–24 km and associated tephra fallout deposits covered an area of at least 2,580 km^2 within the 5 cm-isopach line (**Figure 2**). Eruption duration was estimated between 0.6 and 2.3 h (yielding mass discharge rate between 6.3×10^7 and 1.1×10^8 kg/sec) for a total bulk volume estimated by Cobeñas et al. (2012) at 1.2 km^3, including between 0.2 and 0.6 km^3 of tephra fallout. The preserved lobe of the 2070 cal yr BP fallout deposit (about 30 cm thick at 9–15 km SW of source) extends as far as 28 km from the summit toward the south and southwest (**Figure 2**).

Pumice- and lithic-rich PC deposits were channeled along several radial ravines and the Río Chili, the main artery incising the west flank of El Misti (**Figure 2**). The PC deposits either form 5–8 m thick fans on the SW and south slopes or are confined in the pre-existing ravines: the thickness of the preserved valley-confined PC deposits reaches at least 5 m in the Río Chili canyon, and 10–20 m in the ravines draining the SW and south flanks [e.g., Quebradas (Q.) Pastores, San Lázaro, Huarangal also termed "Mariano Melgar (MM)," see **Figure 1** for locations] as far as 13 km from the vent. The preserved valley-confined PC deposits are thicker (10–40 m) toward the south and SE, particularly in the Q. Agua Salada, Q. Honda, and Q. Grande where they reached 8–11 km from the summit. Although tephra fallout deposits <10 cm was measured on the northern flank of El Misti, PC deposits have not been observed possibly due to the absence of deep ravines. However, PC deposits can be observed in the middle reach of the Río Chili canyon along with a thick debris avalanche deposit. Such deposits are also present near Charcani Grande upstream of the Río Chili canyon (**Figure 1**), suggesting that PCs also flowed down the NW flank.

The sharp erosional contact between the tephra fallout and the overlying PC deposits indicates that the currents were emplaced immediately after the pumice fallout, probably due to several episodes of column collapses (Harpel et al., 2011; Cobeñas et al., 2012). However, in the Q. Agua Salada, layers up to 5 cm thick of openwork pumices are intercalated within the lower unit of PC deposits (see *Stratigraphy and Mapping* and Cobeñas et al., 2014). Previous authors interpreted the intercalated pumice layers within PC deposits as follows: during the Plinian tephra fallout, whose dispersal axis was oriented toward the SW, the majority of PCs were emplaced toward the south in the Agua Salada valley, which is located 8 km off the main axis of the tephra dispersal to the East (**Figure 2**).

The abundance of lithic clasts and hydrothermal altered fragments in lithic-rich PC units, and the coarse debris avalanche deposit directly overlying the PC deposits toward the south and SE of El Misti suggest that PCs eroded and included parts of the instable uppermost south slope [above 4,800 m above sea level (asl)] during their emplacement. Presently, on the south rim of the 900 m-diameter summit crater, a notch cuts through the hydrothermal system and extends down toward a steep-sided flute and amphitheater carved in unstable rocks. The debris avalanche deposit is witness to the partial collapse of the hydrothermally altered summit above 5,400 m asl, perhaps as the consequence of removal of material by PCs flowing over the south and SE flanks (Cobeñas et al., 2014).

DATA ACQUISITION AND MATERIALS

Optical Imagery and Digital Surface Model Generation

A combination of optical and radar imagery were acquired and processed to generate an improved DSM of the El Misti-Arequipa area (**Figure 3**). Firstly, a stereo-pair of very high-spatial resolution panchromatic (0.5 m) and multispectral (2 m) Pleiades-1A images taken on March 28, 2013, which covered an area including the western part of the volcano as well as the entire city of Arequipa and its suburbs (**Figure 3**), was processed with the ERDAS Imagine software (Hexagon Geospatial). Using the Photogrammetry toolbox, a DSM of 2 m spatial resolution was extracted after performing an automatic tie point generation and triangulation. Different combinations of parameters for the photogrammetric processing were tested and we opted for those that maximized the number of matched points [see Bagnardi et al. (2016) for more details about this procedure]. In addition, the differential Global Positioning System solutions for the *X*, *Y*, and *Z* position of 58 selected ground control points (GCPs) measured in July 2010 were used to assess the horizontal and vertical accuracy of the new Pleiades DSM. The mean offsets between the selected GCPs and their clearly visible positions in a pansharpened image are <2.0 m (less than the size of one DSM cell) horizontally and 0.87 ± 2.86 m vertically, much lower than the nominal absolute location accuracy of Pleiades-1A imagery (8.5 m after Oh and Lee, 2014).

Secondly, in order to cover the summit area of the volcano and the eastern portion of the studied area (**Figure 3**), a digital elevation model (DEM) of 10 m spatial resolution was generated using a pair of bistatic synthetic aperture radar data taken from the TDX mission (German Aerospace Center, DLR) in 2011 and 2013. Details about the adaptive TDX DEM merging strategy employed, as well as statistical information on the TDX coherence and elevation difference maps generated, can be found in Charbonnier et al. (2018). To reduce the effect of geometric distortions inherent in synthetic aperture radar images, TDX DEMs generated from ascending and descending orbits were combined [see Charbonnier et al. (2018) for details]. The same assessment as for the Pleiades DSM was also performed, for completeness, on the 10 m resolution TDX DEM using the same 58 selected GCPs. Residual ramps remained in the elevation difference between the TDX DEM and Pleiades DSM, which could be due to processing errors of the TDX data. The ramp was fitted with a quadratic polynomial using the least-squares method (e.g., Poland, 2014; Arnold et al., 2017), and removed from the original TDX DEM.

Finally, the Pleiades and TDX DEMs were fused in order to close any remaining data gaps and obtain a single DSM of the entire study area. Using the grid mosaicking tool from the SURFER software (Golden Software, 2018), the fused DSM was generated using a bilinear interpolation resample method with a 9 × 9 pixel averaging window in order to smooth the transition at the edges of different data sets.

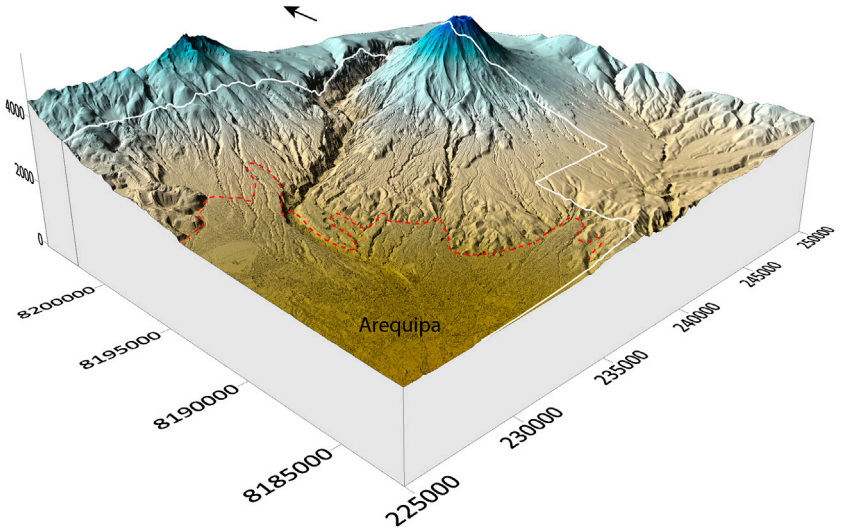

FIGURE 3 | 3-D view of the 2 m fused digital surface model oriented from Arequipa to the NE. The white outline defines the boundary between the coverage of the 2 m Pleiades digital surface model (on the west) and the 10 m TanDEM-X DEM (on the east). The red dashed outline defines the boundary of the urban area of Arequipa. The black arrow indicates the North direction. Coordinates are in UTM meters.

Field Data

Two field campaigns were carried out in May 2018 and 2019 to collect new data and samples from the 2070 cal yr BP PC deposits. Following the work done by Cobeñas et al. (2012, 2014) on the stratigraphy and sedimentology of these deposits, we focused our field mapping, stratigraphic survey and sampling in seven radial valleys (from northwest to southeast) affected by the various 2070 cal yr BP PCs: Río Chili, Q. Pastores, Q. San Lázaro, Q.

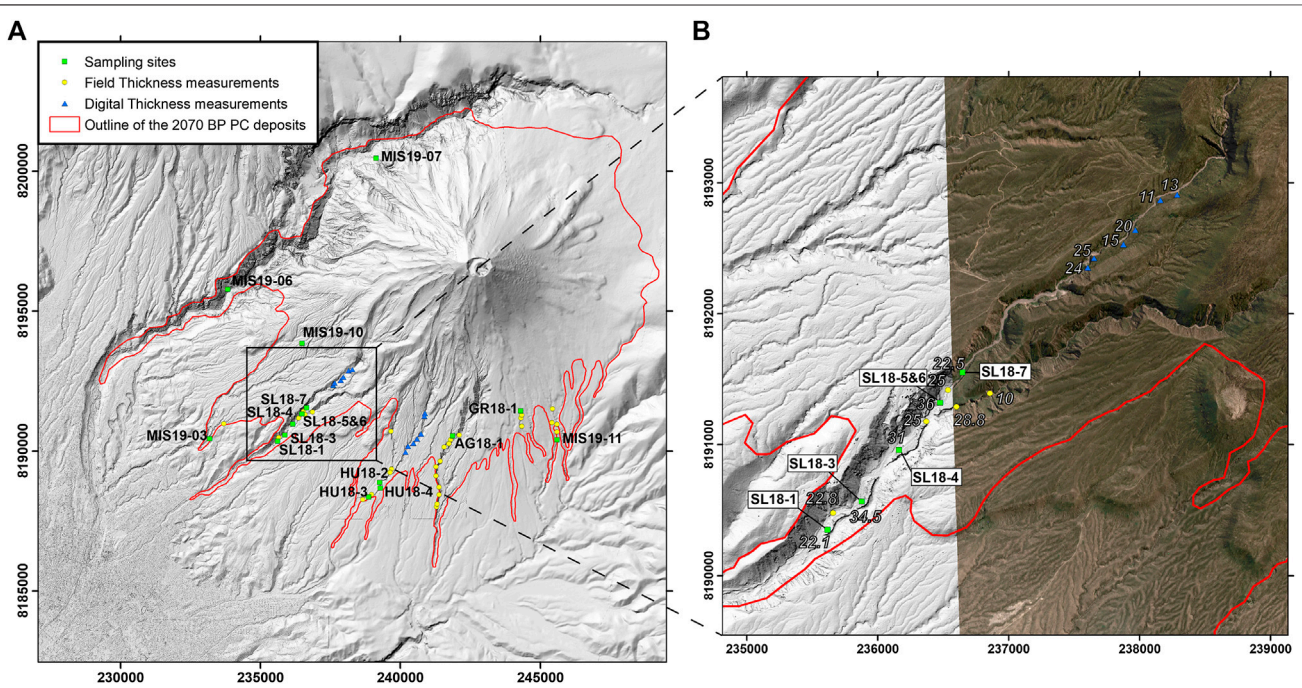

FIGURE 4 | (A) Revised extent of the preserved 2070 cal yr BP pyroclastic current deposits as mapped from new field data collected in 2018 and 2019. Sampling sites for sedimentological analyses and locations of field and digital thickness measurements are also included. **(B)** Close-up view of the sampling sites and thickness measurements along the San Lázaro river system. One of the 2 m resolution multispectral Pleiades 1A image used for digital thickness measurements in the proximal area of Q. San Lázaro has been superimposed on the digital surface model.

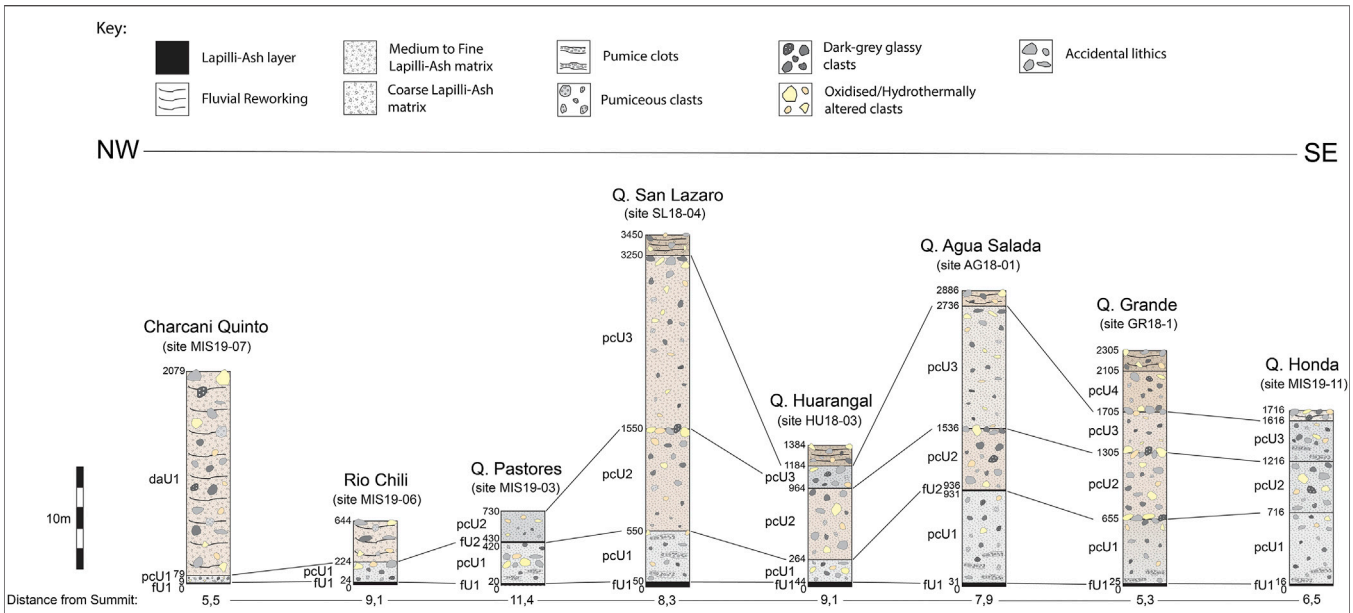

FIGURE 5 | Selected correlated stratigraphic sections with deposit facies characteristics (grain size, componentry) from the seven drainages affected by the 2070 cal yr BP pyroclastic currents. See **Figure 4** for the locations of the different sections and sampling sites.

Huarangal, Q. Agua Salada, Q. Grande and Q. Honda (**Figure 1**). In order to better estimate the volume of these deposits, 45 thickness measurements of the different PC units were collected using a TruePulse 360 laser rangefinder with a vertical accuracy of <0.3 m within the range of horizontal distances (<100 m) measured. Additional 15 thickness measurements were collected digitally, using the new elevation data acquired from the Pleiades DSM at 2 m spatial resolution with the VHR panchromatic Pleiades-1A images draped on top for clear visible recognition of the 2070 cal yr BP PC outcrops, along the different valleys surveyed in the field (**Figure 4**). Because distal valley-confined PC deposits have been eroded away, we focus our data collection on the proximal and medial channeled deposits at distances from 5.2 to 9.5 km to the summit. Stratigraphic logs were built at each location to identify and describe the different PC units and their facies, as well as tentatively correlate them longitudinally inside the same channel and laterally across the different radial valleys (**Figure 5**). Volumes of the different PC deposits were calculated using the ArcGIS software "Surface Analysis" toolbox (ESRI, Redlands, CA, United States) and the methods described in Charbonnier and Gertisser (2009, 2012). Based on our thickness measurements and the three different PC deposit facies recognized (valley-confined, overbank or veneer and surge), each drainage basin, interfluve and alluvial cone affected by the 2070 cal yr BP PCs has been divided into different zones of constant thicknesses. Volumes obtained for each polygon of the same geomorphic feature identified were added together to obtain the overall deposit volume.

To better identify the different PC units recognized during the stratigraphic survey and to characterize their deposit facies, a total of 16 samples were collected for sedimentological analyses. Due to the large range of particle sizes present in the PC deposits, grain size analyses were performed on the lapilli-ash ("matrix") fractions only (<16 mm or −4 phi). In order to avoid particle breakage and comminution, gentle wet sieving at 1 phi intervals down to 32 μm (5 phi) were carried out in the laboratory and each grain size fraction was weighed after drying in an oven for about 24 h. Estimates based on the loss of fines during wet sieving showed that the fraction smaller than 5 phi never exceeded 20 wt % of the total sample mass. The GRADISTAT software (Blott and Pyle, 2001) was used to compute statistics of the grain size distributions. A lithological component analysis of seven selected samples was performed under a binocular microscope by point counting of ~700 to 1,000 particles (converted to abundance % in **Table 2**) from the +2 phi fraction only. This grain size fraction was chosen because 1) it corresponds to the most abundant matrix fraction (by weight) according to the grain size analyses performed on these samples (**Table 2**), and 2) the size range (250–500 μm) is small enough to avoid particle clusters (i.e., with glass adhering to and/or crystals attached to other grains). Each particle was assigned to one of five lithological component categories: 1) white to brownish, banded-colored, and pumice fragments, 2) dark grey-colored to black, dense to vesiculated glassy fragments, 3) hydrothermally altered and oxidized clasts, 4) altered lava fragments and 5) free crystals.

Probabilistic Modeling

PCs are thought to be composed of two parts: a dense part formed by large blocks and particles that follow the drainage network (also called valley-confined or concentrated PCs) and a more dilute part, formed by small particles maintained in suspension by turbulent gases (also called ash-cloud surges or dilute PCs). Therefore, such complex currents are formed by a mixture of

TABLE 2 | Matrix grain size distribution (in weight %) of the studied samples and lithological component abundances [% with 700 < *N* (number of particles) < 1,000] of the +2 phi fraction of selected samples

Sample	Location	Unit	Matrix grain size distribution (wt%)					+2 phi fraction componentry (%)				
			Lapilli	Ash	Meanϕ	Mdϕ	$\sigma\phi$	Glassy	Pumices	Old lavas	Altered	Crystals
SL18-1	San Lazaro	pcU2	64.8	35.2	−1.4	−2.3	2.84	32.0	11.6	17.0	10.6	28.8
SL18-3	San Lazaro	pcU2	57.0	43.0	−0.9	−1.6	2.77	—	—	—	—	—
SL18-4	San Lazaro	pcU1	51.9	48.1	−0.5	−1.1	2.86	30.1	10.2	18.2	8.4	33.1
SL18-5	San Lazaro	pcU2	69.5	30.5	−1.8	−2.7	2.78	—	—	—	—	—
SL18-6	San Lazaro	pcU3	63.2	36.8	−1.4	−2.1	2.70	29.6	11.1	18.9	13.5	26.8
SL18-7	San Lazaro	pcU2	51.0	49.0	−0.5	−1.1	2.54	—	—	—	—	—
HU18-2	Huarangal	pcU2	49.0	51.0	−0.8	−0.9	2.66	—	—	—	—	—
HU18-3	Huarangal	pcU1	45.8	54.2	−0.6	−0.7	2.68	25.8	12.9	24.2	11.8	25.3
HU18-4	Huarangal	pcU2	50.6	49.4	−0.7	−1.0	2.72	—	—	—	—	—
AG18-1	Agua Salada	pcU1	35.0	65.0	0.7	0.4	2.96	—	—	—	—	—
GR18-1	Grande	pcU2	64.2	35.8	−1.6	−2.2	2.60	36.7	11.0	20.9	13.0	18.5
MIS19-03	Pastores	pcU1	39.1	60.9	0.1	0.2	2.70	—	—	—	—	—
MIS19-06	Rio Chili	pcU1	50.2	49.8	−0.8	−1.0	2.18	—	—	—	—	—
MIS19-07	Charcani	pcU1	60.5	39.5	−1.5	−2.0	2.85	23.2	5.8	23.6	11.2	36.1
MIS19-10	SW cone	Overbank	40.0	60.0	−0.3	0.1	2.61	—	—	—	—	—
MIS19-11	Honda	pcU3	51.0	49.0	−0.8	−1.1	2.85	—	—	—	—	—
M17	Agua Salada	fU1	85.2	14.8	−2.5	−2.6	1.49	1.4	12.1	26.9	14.2	45.3

Meanϕ, mean diameter; Mdϕ, median diameter; $\sigma\phi$, sorting; glassy, dark grey-colored to black, dense to vesiculated glassy fragments; pumices, white to brownish, banded-layered, pumice fragments; old lavas, altered lava fragments; altered, hydrothermally altered and oxidized clasts; crystals, free crystals.

particles and gases of various characteristics (grain sizes, densities, temperature, etc.) transported with a certain velocity. The basic concept of numerical simulation is to solve the balance equations of mass, momentum and energy according to simplified physical laws that model the real physics. A variety of approaches exists, depending on the degree of simplification of the physics and on the way chosen to solve the equations. To decrease the computation time, some approaches consider that the vertical variations of properties and the energy balance can be neglected, and they simplify the equations in 2D, with an isothermal, depth-averaged formulation of problem. A new version of VolcFlow has been developed especially for the simulation of PCs (Kelfoun, 2017). Unlike the previous version of VolcFlow (Kelfoun and Druitt, 2005), it couples two fluids: one for the concentrated part, another for the dilute part. Exchange laws allow the concentrated part to form the dilute part or, inversely, the dilute part to form a deposit or a concentrated current by sedimentation. Details about the two-layer VolcFlow code and its applications to PCs at Merapi and Soufriere Hills volcanoes can be found in Kelfoun (2017), Kelfoun et al. (2017) and Gueugneau et al. (2019).

PC hazard modeling and mapping approaches have developed and diversified in a number of ways. Methods can be subdivided into either deterministic (i.e., scenario-based) or probabilistic types. Probabilistic approaches are often the preferred technique as they are able to incorporate uncertainty in the physical phenomena by using numerous multiple numerical runs as in a "Monte Carlo" simulation approach (i.e., Wadge 2009; Tierz et al., 2016). This methodology, by varying input parameters across likely ranges, explores the effect of modifying key, but uncertain, variables. In some cases, probabilistic PC hazard mapping allows to represent the likelihood of PC inundation or the distribution of a specific hazard variable associated with the current (e.g., velocity, dynamic pressure, temperature, solid concentration).

Here, we propose to assess the uncertainty in PC hazard mapping at El Misti volcano using a fully probabilistic approach. The resulting probabilistic maps benefit from: 1) refined mapping and volume estimates of the 2070 cal yr BP PC deposits in all seven radial valleys affected by the eruption, 2) statistical/stochastic sampling of input parameters including PC volumes and mechanical properties [constant retarding stresses (CRS), mass exchange laws], 3) the new high-resolution (2 m) DSM of El Misti volcano, and 4) new computational capacities at the University of South Florida to perform up to 16 runs simultaneously. Using the Latin Hypercube Sampling method, a statistical method for generating a near-random sample of parameter values from a multidimensional distribution (McKay et al., 1979), 123 simulations were computed with the two-layer VolcFlow model at two locations from the apex of the two major drainage networks, which directly impact the city of Arequipa, the San Lázaro and Huarangal river valleys (**Figure 1**). Compilations of the 246 VolcFlow simulations were used to compute two probabilistic maps of PC inundation, one for the Q. San Lázaro and another for the Q. Huarangal, respectively. Due to the high computational resources and time used by the two-layer VolcFlow code, the ensemble runs had to be performed over a coarser (8 m spatial resolution) and smaller sample of the DSM, cropped in the East-West direction to cover only the drainage basins of interest. Each ensemble run of 123 simulations took about 720 computational hours with 16 parallel nodes. See *Probabilistic Modeling of the 2070 cal yr BP Pyroclastic Currents* for details about the procedure, model input parameters and the resulting probabilistic maps of PC inundation obtained.

TABLE 3 | Input parameters of the two-layer VolcFlow model used for all simulations. The first ten rows refer to fixed input values defined from previous numerical studies (Kelfoun et al., 2017; Gueugneau et al., 2019; Gueugneau et al., 2020). The last two rows refer to parameters which varied in the simulations within the range of values explored.

Input parameters	Symbols	Literature	Simulations
Particle mean diameter	D	0–3 ϕ	2 ϕ
Drag coefficient	C_d	1–35	1
Particle density	ρ_p	2,400 kg m^{-3}	2,400 kg m^{-3}
Atmosphere density	ρ_a	1–1.2 kg m^{-3}	1 kg m^{-3}
Concentrated PC density	ρ_d	1,600 kg m^{-3}	1,600 kg m^{-3}
Dilute PC gas density	ρ_g	0.6–0.8 kg m^{-3}	0.6 kg m^{-3}
Mixture density	ρ_m	3–50 kg m^{-3}	3 kg m^{-3}
Formation coefficient	c_1	10^{-4} to 10^{-2}	10^{-4}
Voellmy drag stress	c_2	0.01	0.01
Dilute PC drag stress	c_3	0.025–0.3	0.025
Constant retarding stress	T	—	3,500–9,000 Pa
Volume	V	—	10^6 to 50 10^6 m^3

PC, pyroclastic current.

FIELD OBSERVATIONS OF THE 2070 CAL YR BP PYROCLASTIC CURRENT DEPOSITS

Stratigraphy and Mapping

Figure 4 outlines the revised extent of the preserved 2070 cal yr BP PC deposits as mapped from new field data.

While we do not distinguish valley-confined deposits from overbank deposits on the valley margins and ash-cloud surge deposits beyond the valley margins, the analysis of additional stratigraphic sections has enabled us to delineate the approximate extent of the areas where overbank (veneer) and dilute PCs affected the margins of all valleys cutting the West, SW to SE slopes and piedmont (**Figure 4**). On interfluves and ridges, the PC deposits formed ash layers a few centimeters thick on the SW flanks, overbank deposits 2–4 m thick on the southern flank, and 1–3 m thick overbank and associated surge deposits on the SE flank of the volcano (see **Table 3** for thickness measurements). Thin layers of fine-grained, crystal-rich ash, that we assign to the distal settling of dilute PCs that stratigraphically correlate with the 2070 cal yr BP PC deposits, were observed >1 km outside the valleys toward the west, e.g., in the Cayma area and upstream of the airport between 9 and 15 km SW of the vent.

The non-welded, valley-confined PC deposits emplaced in the seven drainages around the volcano (see **Figure 1** for location) consist of one to four units (pcU1–pcU4 in **Figure 5**). Stratigraphic correlations across these drainages (**Figure 5**) show a general increase in both the numbers of units found and their individual thicknesses from northwest to south (between 0.7 and 17 m thick, totaling between 6 and 32 m in thickness), reaching a maximum between 3,400 and 2,800 m asl in the Q. San Lázaro and Q. Agua Salada, where they filled three quarters of the pre-existing valley up to 40–50 m deep. Thick stratigraphic sections (up to 21 m thick in the upper course of the Honda and Grande valleys and their tributaries on the eastern flank between 3,400 and 3,800 m asl) expose the maximum number of PC units, with up to four stacked units separated by lithic-rich, coarse-clast trains (pcU1–pcU4 units at Q. Grande section, **Figure 5**). Elsewhere, clots of pumice mark the boundary between PC units in the lowermost unit, a sharp change in grain size distribution and/or by thin fine ash layers between other units (i.e., fU2 unit in **Figure 5**). The boundary with the 2070 cal yr BP Plinian fallout deposit (fU1 unit in **Figure 5**) is sharp or erosional.

Pyroclastic Currents Unit1

The lowermost valley-confined PC unit (pcU1 in **Figure 5**) outcrops in all seven drainages studied. It consists of a massive, poorly sorted pumice rich unit with a light gray to beige, medium-to-fine grained lapilli-ash matrix and sub-angular to angular, dense lithic blocks. This unit is often reversely graded and contains abundant and coarse pumices with banded layers, sometimes over 10 cm in diameter, as well as several discontinuous pumice lenses or clots, suggesting shearing processes, e.g., in the upper reaches of Q. San Lázaro and Q. Agua Salada (**Figure 5**). The pcU1 unit shows strong thickness variations due to the infilling of the highly eroded, pre-existing valleys that dissected the cone before the 2070 cal yr BP eruption. While it outcrops only as a thin (0.7 m thick), fine-grained pumice rich PC unit near Charcani Grande in the northwest, unit thickness gradually increases in the southwestern and southern drainages to reach a maximum of 9 m in Q. Agua Salada at ~3,150 m asl. This lowermost unit is easily distinguishable from the other PC units due to: 1) its grey-colored and finer-grained matrix, 2) abundance of coarse and rounded, banded pumices, and 3) an often erosional contact with the top of the underlying 2070 cal yr BP Plinian fallout deposit.

Pyroclastic Currents Unit2

The second valley-confined PC unit (pcU2 in **Figure 5**) is missing in the Río Chili but outcrops from Q. Pastores in the southwest to Q. Honda in the southeast. It consists of a massive, poorly sorted lithic rich unit with a grayish to light-brown, medium-to-fine grained lapilli-ash matrix rich in hydrothermally altered fragments. This unit often shows a coarse-tail inverse grading and contains a few whitish-to-pinkish, pumice coarse lapilli as well as abundant sub-angular to sub-rounded, >20-cm sized accidental, lithic dense blocks, e.g., in the Q. Huarangal, Q. Agua Salada, and Q. Grande (**Figure 5**). Thicknesses of the pcU2 unit are variable across the different drainages, with a minimum of 3 m in Q. Pastores to a maximum of 10 m in Q. San Lázaro. The contact between pcU1 and pcU2 is sharp, and a fine ash fallout layer sometimes separates the two PC units (fU2 unit in **Figure 5**).

Pyroclastic Currents Unit3

The third valley-confined PC unit (pcU3 in **Figure 5**) outcrops in a relatively narrow sector between Q. San Lázaro in the southwest to Q. Honda in the southeast. It consists of a massive, poorly sorted, lithic-rich unit with a grayish to light-brown coarse-to-medium grained lapilli-ash matrix and abundant accidental lithics and sub-rounded hydrothermally altered blocks. The base of this unit is uneven and often hard to distinguish from the top of unit pcU2. The presence of an inverse coarse-tail grading and coarse clast trains (in Q. Pastores and Q. Grande) between the two units or discontinuous pumice lenses or clots at

the base of pcU3 (Q. Honda) help identify the gradational contact between these two stacked units. This unit has large variations in thickness ranging from ~2 to 4 m thick in Q. Huarangal and Q. Honda to >17 m thick in Q. San Lázaro at 2,980 m asl (**Figure 5**), but still represents the thickest unit of the PC deposits.

Pyroclastic Currents Unit4

A fourth valley-confined PC unit is present on top of pcU3 but outcrops are relatively scarce due to the strong erosion of the upper part of the eruptive sequence. The only two drainages where this pcU4 unit was found as a pristine PC unit was inside the upper courses of Q. San Lázaro and Q. Grande between ~3,200 and 3,650 m asl (**Figure 5**). Here, it consists of a massive, reversely graded lithic rich unit with a brownish coarse-to-medium grained lapilli-ash matrix and abundant accidental lithics blocks. A few rounded pumices up to 10 cm diameter are also present at the base of this unit. The contact with the pcU3 unit at the base is gradational with the presence of a coarse clast train. The upper part of this ~4 m thick unit is reworked and overlain by ~2 m thick post-eruption lahar deposits.

Sedimentology

Grain-size distributions (GSDs) and lithological components of the PC deposits are described in Harpel et al. (2011) and Cobeñas et al. (2012, 2014). However, our new analyses benefit from: 1) a high diversity (three PC units) and a larger geographic distribution (seven valleys) of PC deposits sampled, 2) a large range of matrix grain sizes investigated during laboratory GSD analyses (wide spectrum of lapilli and ash sizes from −4 to 5 phi but excluding blocks), and 3) a quantitative analysis of the lithological components of the PC samples using a binocular microscope. Our results (**Table 2**) are then used to refine the stratigraphic correlations of the four PC units recognized in the different valleys, re-estimate their runouts, calculate individual areas and volumes and finally calibrate the source conditions (location, input volumes, mean particle diameter) for our numerical simulations.

Most of the valley-confined PC samples analyzed for GSD show bimodal distributions with two modes between −4.5 and −1.5 phi for the coarse sub-population and between 1.5 and 4.5 phi for the fine sub-population. Only three samples have unimodal distributions with a mode between −3.5 and −2.5 phi. While all the samples are poorly sorted with a narrow range of sorting coefficients ($\sigma\varphi$ between 2.1 and 2.9), they also have very different matrix GSDs, with average mean diameters varying between −1.8 and 0.6 phi and median diameters from −2.6 to 0.1 phi (**Table 2**). The statistical parameters of the GSD curves show that the PC samples analyzed are fine skewed (spread out toward fine values) and platykurtic. No major differences in terms of matrix GSD were found between the samples from the three different stratigraphic units pcU1-pcU3, except for: 1) samples from pcU2 unit that exhibit the widest range of mean and median diameters, and 2) samples from pcU1 unit that are richer in ash size fractions (< −1 phi) than pcU2 and pcU3 (**Table 2**; **Figure 6**). The four samples from the pcU2 unit collected at various distances inside the Q. San Lázaro seem to show a down-flow increase in average median diameters (Mdφ averages from −1 to −2.3 phi), but more samples need to be collected and analyzed to confirm such longitudinal facies variations. Therefore, the variability in matrix GSD observed between the different samples could be due to a combination of topographic factors, variations in composition of the different PC deposits from different drainages (e.g., accidental lithic content, presence of pumices and/or dense glassy clasts) and/or fragmentation characteristics at the source.

Results from quantitative matrix component analyses performed on six valley-confined PC samples (from Río Chili, Q. San Lázaro, Huarangal, and Grande) and a tephra fallout sample collected at the base of the PC sequence in Q. San Lázaro, reveal significant textural variations (in terms of abundances of lithological components) within the 2070 cal yr BP deposit stratigraphy (**Table 2**; **Figure 6**). While the proportions of pumice clasts, old lava fragments and hydrothermally altered and oxidized clasts do not vary significantly among the samples analyzed, the abundance of free crystals (amphibole, pyroxene and plagioclase) differs significantly between the tephra fallout and PC deposit samples (**Table 2**). Moreover, the proportion of free crystals also decreases progressively both stratigraphically within the PC deposit sequence, from unit pcU1 to unit pcU3 (from 33 to 27% in the Q. San Lázaro), and geographically inside the basal unit pcU1 across valleys from the southwest to the southeast (from 36% in Río Chili to 18% in Q. Grande). Finally, the most substantial textural variations found between the tephra fallout and PC deposit samples lie in the abundance of dark gray to black colored, dense to micro-vesiculated glassy fragments (**Table 2**; **Figure 6**). While they are rare in the tephra sample (only ~1%), they constitute the most abundant lithological component inside the PC deposit samples analyzed with proportions between 23% (Río Chili) and 37% (Q. Grande). While the origin of the four other component categories has been documented and interpreted in previous studies (Harpel et al., 2011; Cobeñas et al., 2012, 2014), the source of these glassy fragments is conspicuous. The dark coloration and dense to vesiculated vitric textures suggest they are juvenile components.

Areas and Volume Estimation

Detailed volume calculations of the 2070 cal yr BP PC deposits are listed in **Supplementary Table S1**. A map of the distribution of 37 ArcGIS polygons of constant thicknesses drawn for each geomorphic feature affected by the PC deposits is shown in **Supplementary Figure S1**.

The total area covered by the PC deposits is estimated at 141 km^2, unevenly distributed between valley-confined (covering only ~20 km^2) and unconfined PC deposits (covering ~121 km^2). The total bulk volume of the 2070 cal yr BP PC deposits is estimated at 406 ± 140 × 10^6 m^3, equally distributed between valley-confined (~46%) and unconfined deposits (~54%). The uncertainty on each polygon volume calculation is calculated as the standard deviation of the mean thickness multiplied by the area. The uncertainty on the total volume is taken as the sum of the standard deviations of each mean polygon volume (**Supplementary Table S1**). Individual deposit volumes in each of the seven drainages vary by one order of magnitude between 4.4 ± 1 × 10^6 m^3 for Q. Grande to 38 ± 7 × 10^6 m^3 for Q.

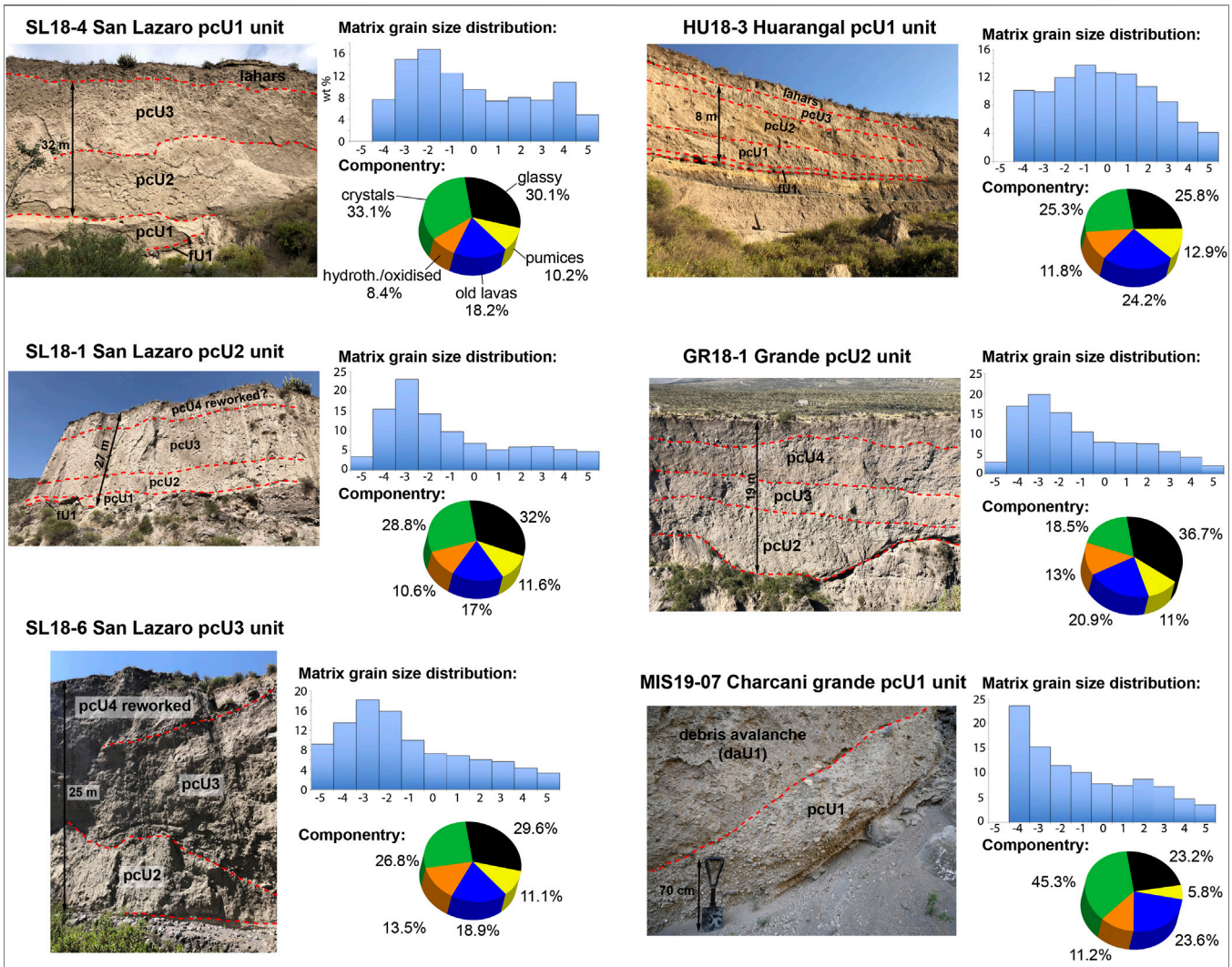

FIGURE 6 | Representative stratigraphic sections and sampling sites selected for grain size analyses and componentry. See **Figure 4** for the section location and sampling sites and **Table 2** for lithological component description. Dashed red lines indicate depositional unit boundaries or contacts between different facies.

Agua Salada, for which most of the total volume is distributed in the SW to SSW sectors of the cone. PC deposit volumes calculated for the two drainage basins for which the distal reaches now lie within the suburbs of Arequipa are $30 \pm 9 \times 10^6$ m^3 for Q. San Lázaro and its tributaries and $21 \pm 4 \times 10^6$ m^3 for Q. Huarangal and its branches (**Supplementary Table S1**). While our new areas and volume estimations are more accurate than those from previous studies (Harpel et al., 2011; Cobeñas et al., 2012; Cobeñas et al., 2014), the PC deposit volumes may still be underestimated and should be taken as minimum estimates for three reasons: 1) the proximal deposits on the high flanks of the cone have not been considered, as most of them have been removed, 2) ash-cloud surge and overbank deposits on the valley margins, although much thinner than valley-confined PCs, have not been mapped with accuracy, and 3) thicknesses of valley-confined deposits strongly vary along short distances due to the highly eroded channel geometries of the pre-existing valleys that dissected the cone prior to the 2070 cal yr BP eruption and the presence of several lahar terraces(e.g., along the Q. San Lázaro down valley as far as 12 km from the summit).

PROBABILISTIC MODELING OF THE 2070 CAL YR BP PYROCLASTIC CURRENTS

Procedure and Input Parameters

To generate the two PC probabilistic maps for the San Lázaro and Huarangal catchments, all the VolcFlow simulations were performed with the same source conditions, with the exception of PC input volume and the rheological parameter. The range of input volumes selected for the simulations is based on field estimates of the PC deposit volumes calculated for the two drainage networks, including the main channel, its tributaries and the interfluves (**Supplementary Table S1**; **Supplementary Figure S1**). Total PC deposit volumes are estimated at $30 \pm 9 \times$

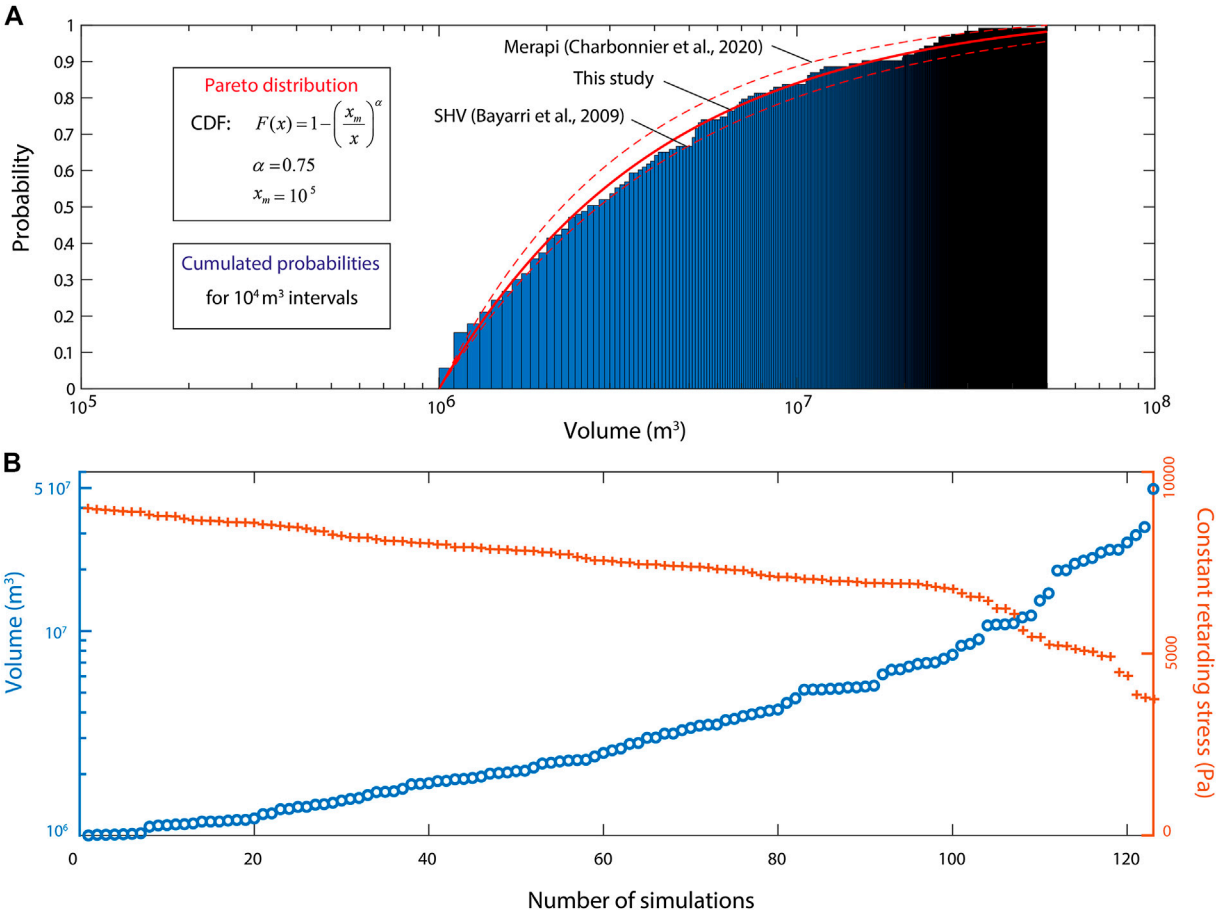

FIGURE 7 | Distribution of the 123 simulated pyroclastic current volumes sampled using a Pareto law. Graph **(A)** shows the cumulative probabilities of the pyroclastic current volumes (bars), obtained following the Pareto distribution for the volume range 1×10^6 to 50×10^6 m^3. The selected Pareto law with a shape parameter $\alpha = 0.75$ is represented by the solid red line and encircled by the Pareto laws from Bayarri et al. (2009) and Charbonnier et al. (in press) as dashed red lines, with a shape parameter $\alpha = 0.64$ and $\alpha = 0.83$, respectively. Graph **(B)** shows the distribution of the 123 volumes together with their associated constant retarding stress.

10^6 m^3 for the San Lázaro basin and $35 \pm 9 \times 10^6$ m^3 for the Huarangal basin. Given the uncertainties in these numbers, the fact that they are based on eroded deposits and are likely underestimated, the selected range of simulated volumes has been extended from 1×10^6 to 50×10^6 m^3 for a more accurate statistical exploration. Previous studies have shown that for such a range of PC volumes ($<100 \times 10^6$ m^3), the volume distribution is not uniform and follows a statistical distribution: Bayarri et al. (2009) demonstrated that the volume frequency of hundreds of PCs from Soufrière Hills Volcano at Montserrat fit well with a Pareto distribution, analogue to a decreasing power law, with a shape parameter $\alpha = 0.64$. More recently, Charbonnier et al. (in press) showed that the best statistical model describing the volume distribution of PCs at Merapi volcano is a Pareto type II law with a shape parameter $\alpha = 0.83$. Since PC volume distribution at El Misti is unknown but should follow the same statistical distribution as at Merapi or Soufrière Hills volcanoes, the 123 simulated volumes sampled here follow a Pareto distribution with a shape parameter $\alpha = 0.75$, corresponding to the mean value of the coefficient used in the studies mentioned above. With such a statistical sampling, the probability of a PC with a volume close to 10^6 m^3 is extremely high while the probability of a PC with a volume close to 50×10^6 m^3 is extremely low. The modeled cumulative density function of the Pareto law with $\alpha = 0.75$ is shown **Figure 7A** (solid red line) and the values of the 123 volumes sampled using this law are shown on **Figure 7B**. The Pareto law of Bayarri et al. (2009) and Charbonnier et al. (in press) was also added with dashed lines to better illustrate the role of the shape parameter. In addition, the resulting cumulative probabilities of the sampled volumes are represented as a bar diagram in **Figure 7A**.

The physical behavior of the concentrated PC is modeled with a plastic rheology, involving a CRS, considered as the most suitable rheology for the numerical simulation of concentrated PCs with a depth-averaged model (Kelfoun et al., 2009; Kelfoun, 2011; Charbonnier and Gertisser, 2012; Kelfoun et al., 2017; Ogburn and Calder, 2017; Gueugneau et al., 2019). When using such a broad range of simulated PC volumes for

probabilistic modeling, the CRS must vary to adapt the physical behavior of the concentrated PC to simulate such large variations in current mobility. Several studies have shown that the higher the volume and current mobility, the lower the CRS, indicating that the CRS seems to be inversely proportional to the volume and mobility of the PC (Charbonnier and Gertisser, 2012; Kelfoun et al., 2017; Ogburn and Calder, 2017), and the same empirical relation was applied here. A broad range of CRS values, comprised from 3,500 to 9,000 Pa, was defined according to the typical values used in previous numerical studies using similar PC volume ranges (Kelfoun, 2011; Charbonnier et al., 2012; Kelfoun et al., 2017; Ogburn and Calder, 2017; Gueugneau et al., 2019). Thus, for each volume, a value of the CRS is attributed as inversely proportional to the position of that volume in the range from 1×10^6 to 50×10^6 m^3. This means that the highest CRS is attributed to the smallest volume, and inversely, the smallest CRS is attributed to the highest volume. This yields 123 couples of volume-CRS with their distribution presented in **Figure 7B**.

The list of input parameters is presented in **Table 3**. The choice of using fixed values for these parameters over the full range of selected PC volumes and CRS is justified as: 1) other parameters acting on the concentrated PC rheology, the density ρ_d and the Voellmy drag stress c_2, do not vary significantly with different PC volumes and mobilities, as shown by previous numerical studies (Kelfoun, 2011; Charbonnier et al., 2012; Kelfoun et al., 2017; Ogburn and Calder, 2017; Gueugneau et al., 2019), 2) parameters that control the dilute PC formation and its emplacement are poorly constrained from field data and chosen empirically. These parameters are: the particle mean diameter d, the particle drag coefficient C_d, the particle density ρ_p, the atmosphere density ρ_a, the gas density of the dilute PC ρ_g, the density of the mixture transferred from the concentrated PC to the dilute PC ρ_m, the dilute PC production parameter c_1 and the dilute PC drag stress c_3 [see Kelfoun et al. (2017) and Gueugneau et al. (2019) for details about their calibration]. With such a large number of input parameters, a stochastic sampling may lead to poor calibration, and subsequently unrealistic simulations. Therefore, the empirical values selected for each of these input parameters are based on previous studies that have successfully reproduced PCs with the VolcFlow two-layer version, at Merapi (Kelfoun et al., 2017), Soufrière Hills Volcano (Gueugneau et al., 2019), and Mount Pelée (Gueugneau et al., 2020). When a range of values was already investigated by these previous studies, the lowest value is used here to obtain the least false negatives (i.e., areas inundated by the observed PCs where not simulated) as possible (**Table 3**).

For the simulated PCs, both valleys have identical source conditions, a 390 m diameter circular spot sets at the apex of the San Lázaro and Huarangal catchments and located ~600 m below the summit crater to ensure that most the simulated material flowed down the valley. A constant volumetric rate is supplied for 180 sec through the spot and calculated for each simulation by dividing the selected volume by the total number of time steps performed by the model in this timeframe. Because the time step is automatically adjusted by the model for each simulation, the amount of volume added in each time step is different. The concentrated PC begins at the source and remains in the main river channels whereas the dilute PC starts to form and spreads laterally according to the dilute PC formation law, which is also a function of the velocity of the concentrated PC (Kelfoun, 2017).

Probabilistic Maps

Probabilistic maps of PCs were built by combining the inundated areas of both PC components (dilute and concentrated PCs) from each simulation into a single map for each valley. For that, the number of hits (i.e., the number of times a DSM cell is inundated by a PC simulation) is computed at the end of the probabilistic run and divided by the total number of simulations (123 in our case). This yields a probability of inundation (expressed between 0 and 1) at each DSM cell, computed either for the 123 simulated dilute or concentrated PCs separately, or by combining the probability values (total number of hits) of the two parts of the 123 simulated PCs into integrated values. In order to better distinguish between the spatial distributions of each PC component, two different color scales are used. The resulting maps for the San Lázaro and Huarangal catchments are shown in **Figures 8** and **9**, respectively.

San Lázaro Valley

The integrated probabilistic map (**Figure 8A**) shows that the distribution of the PC probabilities exhibits a characteristic pattern, symmetrical to the San Lázaro valley, with a cluster of high probabilities inside the main channel (dark red area with values >0.6) and a sharp decrease in probability away from the main channel (yellow area with probabilities <0.3). This low probability zone is composed of two main lobes: 1) a proximal lobe from the source to the mid slope catchment, and 2) a distal lobe inside Arequipa city center, that extends to the south bank of the narrow San Lázaro channel, cutting through the city (**Figure 8A**). The unintegrated map (**Figure 8B**) shows that, as expected, the cluster of high probabilities is attributed to the valley-confined concentrated PCs that follow the main channel (pink area). However, the map also highlights the fact that the distal lobe of low probabilities inside the city (blue area) is attributed to the overspill of concentrated PCs when the San Lázaro channel narrows as it enters the suburbs and Miraflores district (**Figure 8B**). These overbank processes occur only during simulations with large PC volumes (>30×10^6 m^3), with low sampling frequency, explaining the low probability of events. In contrast, the proximal lobe of low probabilities is caused by large dilute PCs generated from fast and voluminous concentrated PCs, probably associated with the same simulations as those that shaped the large overbank areas in Arequipa further downstream.

Based on these probabilistic runs, we show that only the concentrated PCs are able to reach the city of Arequipa through the San Lázaro catchment. The probabilities of PCs entering the city is remarkably high (0.92), and almost every simulated PC reached the city, even though for only a few hundred meters for the lowest volumes (<10×10^6 m^3, **Figure 8B**). The probability of a PC entering the Q. Pastores and crossing the northern area of Arequipa (through the Alto Selva Alegre district, see **Figure 1**) is very high too, due to a major

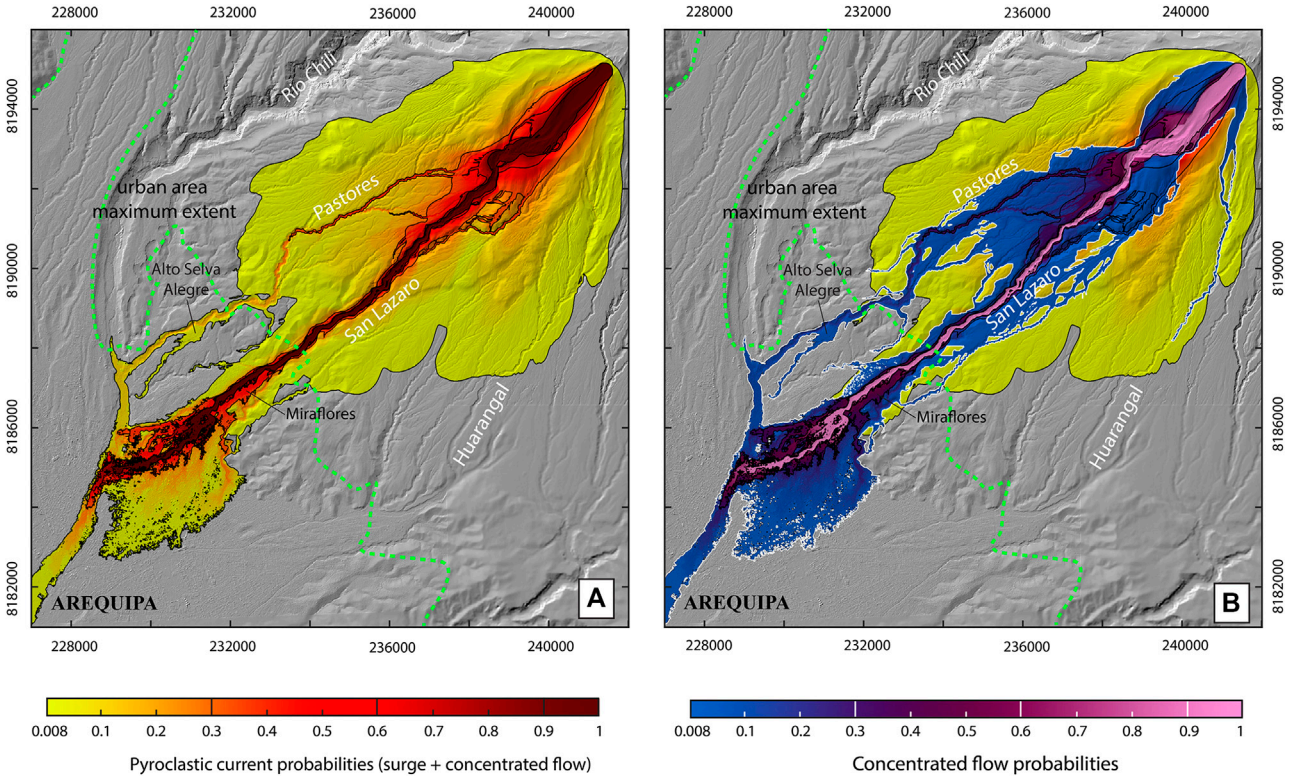

FIGURE 8 | VolcFlow probabilistic map for a pyroclastic current in the San Lázaro drainage basin, made by calculating the number of hits at each digital surface model cell for 123 numerical simulations. Map **(A)** shows the probabilities for the entire pyroclastic current (i.e., dilute + concentrated parts) with a yellow to red color scale. Map **(B)** distinguishes the probabilities of a concentrated pyroclastic current with a blue to pink color scale, from the dilute pyroclastic current, with a yellow to red color scale. Iso-probability contour lines at every 0.3 probability intervals are also included. The green dashed line corresponds to maximum extent of the Arequipa urban area.

source of overspill, at a sharp bend in the proximal San Lázaro western bank, where the simulated overbank PCs are voluminous enough to follow the former river path all the way to the Río Chili. The most remarkable aspect concerns the relatively high probabilities of overbank PCs that could inundate both the northern and central districts via the Q. San Lázaro (up to 10% of the simulations reached this distal area). Finally, arrival times of simulated PCs in the urban area of Arequipa vary between 9 and 12 min, depending on the input volumes, with current velocities between 11 and 14 m s^{-1}.

Huarangal–Mariano Melgar Valley

The same observations for the San Lázaro basin can be made for the probability distribution of simulated PCs along the Q. Huarangal-MM (**Figure 9A**). The same clustering of high probabilities is observed in the valley due to the channelization of concentrated PCs, contrasting with a wide zone of low probabilities on the south flank of the cone (yellow area) linked to the emplacement of voluminous dilute PCs. However, here the direction of the dilute PCs is not symmetrical to the Huarangal-MM channel and three large detachments can be observed, two proximal ones (<3 km from the starting location) toward the southwest entering the Pastores and San Lázaro catchments, and the third toward the east following a major bend in the valley at ~1 km further downstream (~4 km from the starting location). Moreover, the unintegrated map (**Figure 9B**) shows that simulated concentrated PCs are less constrained in the Huarangal-MM valley (slope gradient is lower, 3%) than they are in the San Lázaro (7%). Indeed, voluminous overbank PCs are observed at the middle section of the valley (~7 km from the starting location), creating a fan that separates the channelized PC into three main branches. These three PC branches merge back into the distal Huarangal-MM channel after a 90° bend in the valley (~10 km from the starting location) before entering Arequipa through the MM district (**Figure 9B**).

Beside the fact that the Huarangal-MM valley is longer than the San Lázaro (19 vs. 12 km from the initial confinement area, respectively), the probability of concentrated PCs reaching the eastern part of the city is still high due to re-channelization in the distal section of the valley. Again, simulations reach Arequipa with a relatively high probability (>0.3, first contour line in **Figure 9B**) with voluminous overflows that spread over the MM district down valley to the city center. In contrast to the San Lázaro, these large overbank PCs have a lower probability (~0.1) and never cross the city entirely. We notice that a few simulations generated major secondary PCs into the San Lázaro valley that flowed all the way down to Arequipa, stemming from

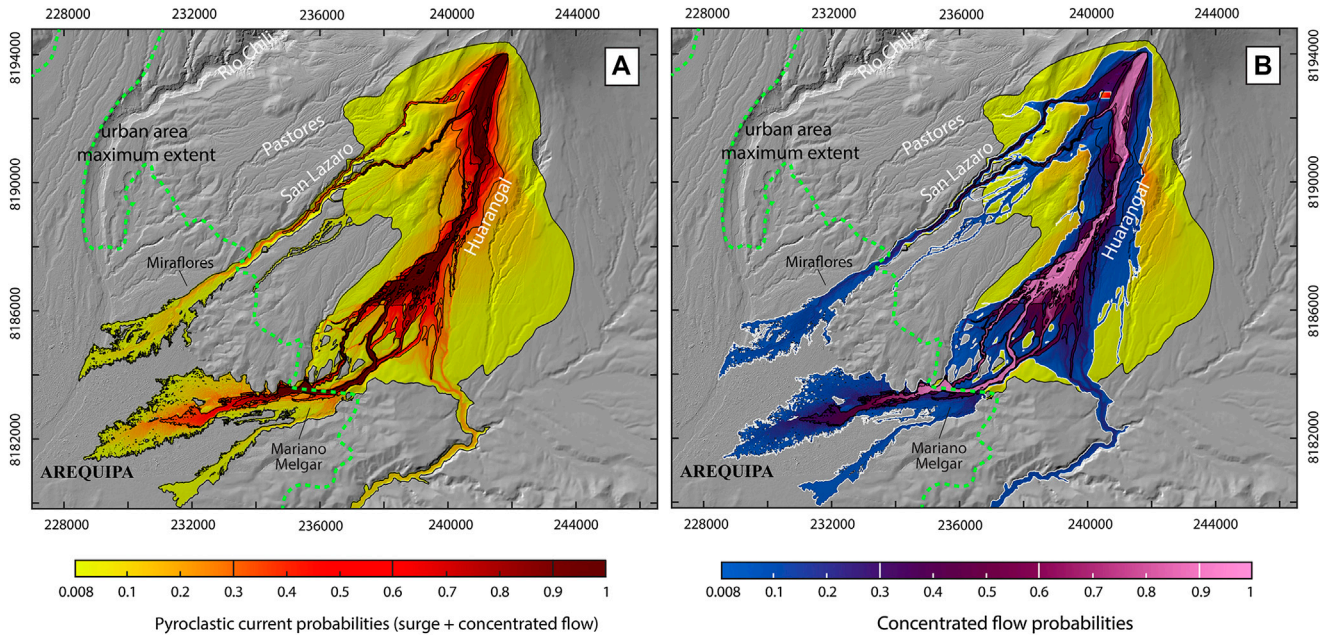

FIGURE 9 | VolcFlow probabilistic map for a pyroclastic current in the Huarangal-Mariano Melgar catchment, made by calculating the number of hits at each digital surface model cell for 123 numerical simulations. Map **(A)** shows the probabilities for the entire pyroclastic current (i.e., dilute + concentrated parts). Map **(B)** distinguishes the probabilities of a concentrated pyroclastic current with a blue to pink color scale, from the dilute pyroclastic current with a yellow to red color scale. Iso-probability contour lines at every 0.3 probability intervals are also included. The green dashed line corresponds to the maximum extent of the Arequipa urban area.

proximal overbank PCs and dilute PC detachments close to the source. However, the occurrence of such secondary PCs seems to depend on our source conditions and only shows that a voluminous (>10 × 10^6 m^3) PC entering the apex of the Huarangal-MM valley will most certainly reach and enter both valleys. Finally, arrival times of simulated PCs in the urban area of Arequipa and corresponding current velocities are estimated at ~10 min and 15 m s^{-1}, respectively.

DISCUSSION

New Insights Into the 2070 cal yr BP Pyroclastic Currents

Field Data and Optical Imagery

The revised extent of the preserved 2070 cal yr BP PC deposits (**Figure 4**) allows for the refinement of the runout of valley-confined PCs emplaced in the seven radial valleys affected by the eruption. These runout values should be taken as minimum values due to the intense erosion of the distal deposits. While the PC runouts in valleys from the S to SE flanks (Q. Agua Salada, Q. Grande, Q. Honda) do not change from the previous map proposed by Cobeñas et al. (2012), runout values from valley-confined PCs emplaced in the SW flank have increased, from <1 km in Q. San Lázaro and Q. Huarangual-MM to more than 5 km in Q. Pastores (**Figures 2** and **4**). The extent of unconfined PC deposits does not vary much between the two studies, except in the area between the Río Chili, Q. Pastores and Q. San Lázaro. Here, new evidence from field surveys allowed us to extend the area inundated by unconfined PCs (mostly overbank PCs) and increase runouts by ~4.2 km on the piedmont between Q. Pastores and Q. San Lázaro (**Figures 2** and **4**).

Results from stratigraphic surveys are in agreement with the stratigraphy proposed by Suni Chambi (1999) and Cobeñas et al. (2012, 2014) with up to four PC units recognized in Q. San Lázaro and Q. Grande while only three main PC units are exposed in other valleys (**Figure 5**). Facies variations also show an increase of matrix grain size (with a decrease of ash fractions), accidental lithics and hydrothermal alteration of the deposit matrices from pcU1 to pcU3 units, similar to previous observations made by the aforementioned authors. The coarser median diameters (from −2.6 to 0.1 phi) and narrower range of sorting (between 2 and 3) obtained in our grain size distributions compared to those from Cobeñas et al. (2012) may be due to the different methodology used for sieving and sampling of the PC deposits.

Significant textural variations (in terms of volume percentages of lithological components) are found within the 2070 cal yr BP deposit stratigraphy and differ quite substantially from similar component analyses performed by previous authors (Suni Chambi, 1999; Harpel et al., 2011; Cobeñas et al., 2012). While the differences in terms of proportions of pumices and free crystals found between the samples from valley-confined PC deposits are mainly due to different grain size fractions analyzed for point counting (+2 phi fraction only in this study), the abundance of dark gray to black colored, dense to micro-vesiculated glassy fragments shows the most significant variations between the tephra fallout and PC deposit samples (**Table 2**; **Figure 6**). The dark coloration and dense to micro-

vesiculated vitric textures of these glassy fragments suggest they are juvenile (cognate lithics). However, none of the aforementioned studies mentioned such micro-vesiculated glassy texture. We interpret these fragments as input from either a dense degassed magma batch (abundance of dense vitric texture) or the sudden depressurization of material from a gas-rich magma recharge batch (abundance of micro-vesicular texture). The dark coloration and the glassy texture of these clasts also suggest fast magma ascent during this period, as documented in the eruption chronology (Harpel et al., 2011; Cobeñas et al., 2012). Moreover, these glassy fragments are similar to other glassy components of rhyolitic composition found in other PC deposits dated at 31–34 ka at El Misti (group 3 of Thouret et al., 2001). Such glass and cognate lithics in the 2070 cal yr BP PC units may have been tapped from magma batches that remained at shallow level and/or near the conduit since the voluminous explosive eruptions of El Misti around 31–34 ka (Thouret et al., 2001; Rivera et al., 2017). These magma batches, when mixing with the fragmented superficial magma body, may have triggered instabilities in the plume that led to the first column collapse episode and emplacement of the first batch of PCs. Such rapid transitions in conduit/plume dynamics may explain the presence of the transitional, fined-grained pumice-rich pcU1 unit, which immediately overlies and/or erodes through the fU1 Plinian fallout deposit (**Figure 5**), confirming that only a short period of time elapsed between the end of the main Plinian phase and the emplacement of the first batch of PCs. Detailed petrological and geochemical analyses on these glassy fragments are needed to confirm this hypothesis. Finally, the large abundance of rhyolitic glass and cognate lithics in all the PC units analyzed confirms their pyroclastic nature, where such textural variations are directly linked to changes in dynamics of the plume and/or in the conduit during the eruption. This contradicts Harpel et al. (2011) who inferred that the upper three PC units (pcU2 to pcU4) were lahar deposits emplaced "wet and relatively cold."

Numerical Modeling

The multi-disciplinary approach taken here by combining field data and optical imagery to reconstruct the volume of past PC deposits is useful to better constrain the eruptive history at El Misti but is also limited by the poor exposure of the distal PC deposits. While this method is useful to constrain the range of input PC volumes used for probabilistic PC modeling, the choice of the Pareto distribution to statistically sample these PC volumes was made empirically and based on frequency-volume distribution of PCs from similar composite volcanoes, not El Misti. An improved frequency-volume distribution of similar PCs for the 2070 cal yr BP events would subsequently improve the hazard assessment performed by numerical modeling and demonstrate whether using a Pareto distribution was a realistic choice.

To our knowledge, the mapping of PC probabilities with the two-layer VolcFlow code represents the first attempt at using a two-phase depth-averaged model to generate probabilistic maps of PCs over natural terrain, where the concentrated PC can be modeled jointly with the dilute PC but mapped separately. The use of a physical-based model like VolcFlow to calculate the propagation of the currents gives more realistic outputs than an empirical model like the Energy Cone (EC) model previously used at El Misti by Harpel et al. (2011). Indeed, the EC model does not simulate the channelization of concentrated PCs, which is recognized here as a critical process in order to correctly assess the PC hazards at El Misti and Arequipa. With such an approach, we are also able to obtain the probability for the dilute and concentrated parts of a PC, in contrast with the TITAN2D model used by Constantinescu et al. (2011) and Sandri et al. (2014), which only simulates the concentrated layer in a deterministic framework. Indeed, the hazards and associated impacts of the concentrated PCs are different than those from the dilute PCs. These can be assessed separately while being parts of a single numerical model, which provides more robust outputs and significantly improves PC hazard assessment at El Misti. However, our PC probabilistic maps should not be considered as hazard maps because probabilities are "conditional" and computed only for the case when PCs generated by a future eruption similar to the VEI 4 2070 cal yr BP eruption enter the two main drainage networks threatening Arequipa (i.e., San Lázaro and Huarangal-MM). With the recurrence rate of similar sub-Plinian–Plinian eruptions at El Misti estimated to range between 2,000 and 4,000 years (see **Table 1**; Thouret et al., 2001; Sandri et al., 2014), the probability values obtained here may be converted into probabilities of occurrence for a PC of similar size to the 2070 cal yr BP to enter the city of Arequipa. Our maps demonstrate the suitability of a two-phase, depth-averaged numerical model to produce two probabilistic maps over an 8 m resolution DSM in a reasonable amount of time (~60 days for 246 simulations).

Another interesting result from our simulations stems from the strong channelization and longer runout of the concentrated PCs than those obtained by Constantinescu et al. (2011) and Sandri et al. (2014) with TITAN2D and Harpel et al. (2011) with the EC model. In our simulations, valley-confined PCs reach a maximum runout of 10–15 km in San Lázaro valley and 11–16 km in the Huarangal-MM valley, while the maximum runout obtained by Sandri et al. (2014) was 2–8 km (both valleys) with similar input volumes ($>10^6$ m^3), and 10 km for Harpel et al. (2011). While the 2070 cal yr BP mapped PC deposits in these two valleys (**Figure 4**) reach shorter runout distances than in our simulations, we know from the preserved thick deposits that PCs reached further distances; hence our field mapping suffers from poor exposures and intense erosion of the distal valley-confined deposits. The longer PC runouts obtained in our probabilistic simulations are due to the combined use of a broader range of selected input volumes associated with more realistic PC rheology. The strong channelization of the concentrated part of small-volume ($<100 \times 10^6$ m^3) PCs was demonstrated by numerous studies (e.g., Loughlin et al., 2002; Charbonnier and Gertisser, 2012; Charbonnier et al., 2013; Komorowski et al., 2013). The plastic rheology is considered more appropriate to simulate such channelized PCs (Kelfoun, 2011) because it allows the PC to either stay confined in the valley or spill over without losing momentum too rapidly (in contrast to the Mohr–Coulomb frictional rheology used in TITAN2D), providing a longer runout. When combined with an accurate,

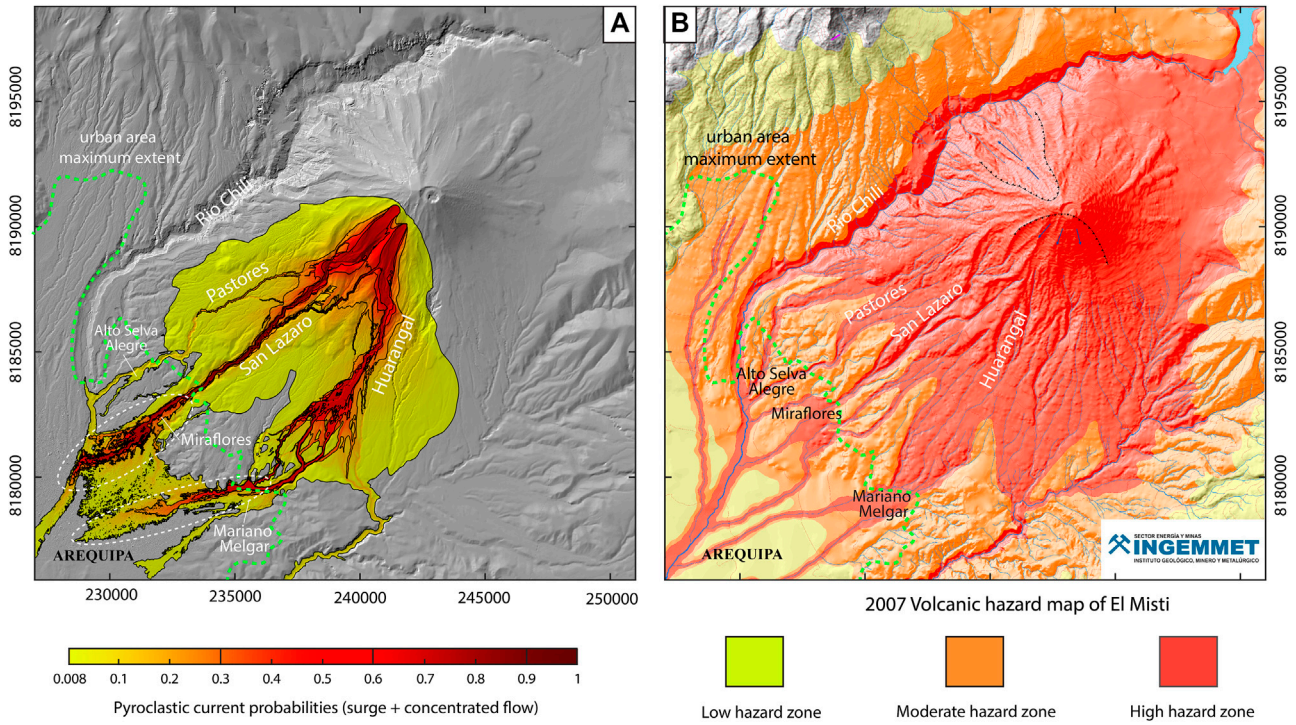

FIGURE 10 | Comparison of the map of cumulative pyroclastic current probabilities for both the San Lázaro and Huarangal valleys **(A)** to the 2007 hazard map of El Misti Volcano **(B)** published by INGEMMET (Mariño et al., 2007). White dashed ellipsoids indicate the main overbank pyroclastic current areas in the Arequipa urban area.

high-resolution DSM, this modeling approach enhances model accuracy and makes such numerical models a more robust tool for PC hazards reduction.

Considerations for Future Hazard Assessment of Pyroclastic Currents at El Misti

Results of the probabilistic runs performed in both the San Lázaro and Huarangal-MM valleys enable the identification of the principal areas inundated by future PCs with similar physical characteristics to those in 2070 cal yr BP. In order to investigate the potential PC hazards at Arequipa, the two ensemble runs computed for each valley were combined into a single probabilistic map (**Figure 10A**) which is then compared to the hazard map of El Misti volcano published by Mariño et al. (2007) (**Figure 10B**).

The discussion of hazards at the volcano scale is not pertinent here because our numerical simulations only cover in two drainage networks in the SW flank. The comparison will then focus only in the Arequipa urban area, where we discuss several features highlighted in our probabilistic maps in terms of considerations for future PC hazards and risk mitigation at El Misti:

1. The maximum extent of the dilute PCs obtained from the most voluminous VolcFlow runs (low probability yellow area in **Figure 10A**) outlines a single proximal lobe which covers the entire SW-SSW flanks before separating into two individual lobes at ~6 km from the crater (in the SW and SSW direction) following the main direction of the San Lázaro and Huarangal-MM valleys. The pattern of this modeled dilute PC inundation zone shares some similarities with the surge extent as outlined in the hazard map of Mariño et al. (2007), also discussed in Cobeñas et al. (2012). This zone is represented in their map by the "moderate hazard zone" (orange zone in **Figure 10B**) and is in accordance with the low probabilities obtained with VolcFlow for this area. However, while the maximum extent of the urban area as mapped in 2013 (green dashed line in **Figure 10**) coincides with the maximum extent of our modeled dilute PC inundation zone (**Figure 10A**), this zone extends further toward Arequipa in the 2007 hazard map (**Figure 10B**). Beside their low probability of occurrence in such distal areas, dilute PCs are responsible for the majority of deaths due to recent small-volume PCs elsewhere (Soufriere Hills, Loughlin et al., 2002; Unzen, Yamamoto et al., 1993; Merapi, Jenkins et al., 2013). Therefore, efforts must be made to maintain the current construction sprawl of Arequipa at a significant distance from the area of the SW flank between the green dashed line and the distal limit of the orange "moderate hazard zone" (**Figure 10**).
2. The maximum runout of simulated valley-confined PCs is high, even for small-volume PCs ($<10 \times 10^6$ m^3). Because of the strong channelization of the concentrated PCs, the probabilities remain high along both valleys down to Arequipa, where probabilities are still ~0.3 when simulated PCs reach the upper limit of the urban area (**Figure 10A**). This

valley-confined PC hazard is also included in the El Misti hazard map and represented by the "high hazard level" zone (in red, **Figure 10B**) that encompasses every valley reaching Arequipa. However, in the PC hazard maps of Harpel et al. (2011) and Sandri et al. (2014), for which no PC channelization is considered, such hazards from valley-confined PCs are not apparent. The channelization of such long-runout PCs at El Misti toward Arequipa should be considered for future mitigation plans, and the probability of such hazardous currents entering the city should not be underestimated.

3. The distal overspill of valley-confined PCs seems to be underestimated in previous studies on Arequipa's hazards. In our simulations, when PCs exit both valleys, they become unconfined and spread laterally, exposing the northern and eastern districts of Arequipa (Alto Selva Alegre, Miraflores, and MM) to massive overspills with a medium probability of occurrence (0.1–0.3 in **Figure 10A**). In case of voluminous PCs ($>30 \times 10^6$ m^3 in one valley), the overbank PCs merge and inundate the entire northern part of Arequipa (**Figure 10A**), reaching the central district. Some simulated overbank processes may be due to the relatively poor representation of the two narrow channels passing through the city in the DSM downgraded at 8 m spatial resolution. However, similar overbank PC phenomenon have repeatedly shown their danger and unpredictability, as witnessed during the Merapi 2006 and 2010 eruptions (Charbonnier and Gertisser, 2008; Lube et al., 2011; Gertisser et al., 2012; Charbonnier et al., 2013) and the Fuego 2018 events. Although the probabilities of these massive overspills are relatively low in our maps, the 2007 hazard-zone map of El Misti seems to disregard this phenomenon by only considering PC hazards along river paths (red zone in **Figure 10B**) that quickly become a low hazard zone (yellow) away from the river path in the city. The risk for such overbank processes and spreading of unconfined PCs inside Arequipa should then be refined and the "high hazard zone" of the hazard map extended accordingly. In order to help further investigate such overbank PC hazards in the city of Arequipa, future work will involve small-scale, high-resolution numerical modeling of valley-confined PCs performed over a very high resolution (<1 m) DSM along short reaches (few hundreds of meters long) of the San Lázaro and Huarangal-MM channels, similar to the recent work of Mead et al. (2017) to estimate building vulnerability from lahars in Q. Dahlia, a tributary to the latter channel. Robust estimates of the potential range of local mass fluxes and velocities of valley-confined PCs for each channel segment are critical for correctly assessing numerically overbank PC processes at such fine-scale level.

Results from our combined study using field data, optical imagery and numerical modeling at El Misti highlight the need to 1) calibrate model input parameters using quantitative and well-constrained geological data and 2) develop new high-resolution DSMs with high vertical accuracy together with a full probabilistic modeling approach in order to increase the confidence level in results from numerical simulations of small-volume PCs over complex volcanic terrains.

CONCLUSIONS

1. This multi-disciplinary study demonstrates the benefit of collecting and combining a quantitative dataset from field data and optical imagery to better calibrate the input parameters of a probabilistic ensemble run using a two-layer, depth averaged mass flow model like VolcFlow.
2. In the case of the 2070 cal yr BP PCs at El Misti volcano, new stratigraphic surveys, sedimentological analyses and thickness measurements of the different PC deposits, combined with a new high-spatial resolution (2 m) DSM of the volcano, allow to better estimate the distribution of individual PC volumes emplaced in each of the valleys impacted by this Plinian event. Such data acquisition is particularly critical for two of these valleys (San Lázaro and Huarangal-MM) for which the medial and distal reaches now cross the suburbs of Arequipa.
3. Volume estimates were used as input parameters to better calibrate probabilistic numerical simulations of future similar PC events using the two-layer VolcFlow model and assess the impacts (e.g., inundation, runout, thickness and velocity) of both the concentrated and dilute portions of these currents in the San Lázaro and Huarangal rivers.
4. Modeling results demonstrate that, while the hazards associated with widespread dilute PCs are in accordance with the extent of the "moderate hazard zone" from the 2007 EL Misti hazard map, the risk of overbank processes and spreading of unconfined PCs inside Arequipa are underestimated and should be refined.
5. Future work should focus on fine-scale studies combining field-based surveys and mapping with numerical modeling over very high resolution (<1 m) DSMs of small areas (<1 km^2) of the city at risk from PC overbanking, similar to recent studies focusing on building vulnerabilities from lahar avulsion. Such future work will provide civil authorities with a better understanding of the likely effects of PCs associated with a similar VEI 4 eruption of El Misti on the urban area of Arequipa.

DATA AVAILABILITY STATEMENT

The original contributions presented in the study are included in the article/**Supplementary Material**, further inquiries can be directed to the corresponding author.

AUTHOR CONTRIBUTIONS

SC wrote 80% of the manuscript and created 8 figures and 2 tables. JT wrote 10% of the manuscript, created 1 figure and 1 table. VG wrote 10% of the manuscript, created 3 figures and 1 table. RC did the grain size analyses and review the manuscript. SC, JT, and RC collected all field data presented in the manuscript during two field campaigns in 2018 and 2019. SC and VG performed the probabilistic modeling. SC built the DEM, did

the volume calculations and stratigraphy, and performed the component analyses.

FUNDING

This work was partially supported by the National Research Foundation (NSF) through the CAREER grant 1751905. JT acknowledges funding from CLERVOLC and I-Site Cap2025. This research was financed by the French Government IDEX-ISITE initiative 16-IDEX-0001 (CAP 20–25).

ACKNOWLEDGMENTS

The TanDEM-X data were provided by the German Aerospace Center (DLR) under proposals OTHER0653 and XTIGEOL6738. The VolcFlow simulation code is distributed and written by Karim Kelfoun at Laboratoire Magma et Volcans, Clermont-Ferrand, France. We thank our Peruvian colleagues from INGEMMET for their hospitality and support over the years and for kindly sharing their ideas about the 2070 cal yr BP of El Misti. SC would like to thank Apollo Mapping for their help with the Pleiades optical imagery and Fenghui Deng for processing the TanDEM-X data. JT acknowledges support from CLERVOLC.

SUPPLEMENTARY MATERIAL

The Supplementary Material for this article can be found online at: https://www.frontiersin.org/articles/10.3389/feart.2020.557788/full#supplementary-material

REFERENCES

Andreastuti, S., Paripurno, E., Gunawan, H., Budianto, A., Syahbana, D., and Pallister, J. (2019). Character of community response to volcanic crises at Sinabung and Kelud volcanoes. *J. Volcanol. Geoth. Res.* 382, 298–310. doi:10.1016/j.jvolgeores.2017.01.022

Arnold, D. W. D., Biggs, J., Anderson, K., Vallejo Vargas, S., Wadge, G., Ebmeier, S. K., et al. (2017). Decaying lava extrusion rate at El Reventador Volcano, Ecuador, measured using high-resolution satellite radar. *J. Geophys. Res. Solid Earth* 122 (12), 9966–9988. doi:10.1002/2017jb014580

Bagnardi, M., González, P. J., and Hooper, A. (2016). High-resolution digital elevation model from tri-stereo Pleiades-1 satellite imagery for lava flow volume estimates at Fogo volcano. *Geophys. Res. Lett.* 43, 6267–6275. doi:10.1002/2016gl069457

Bayarri, M. J., Berger, J. O., Calder, E. S., Dalbey, K., Lunagomez, S., Patra, A. K., et al. (2009). Using statistical and computer models to quantify volcanic hazards. *Technometrics* 51 (4), 402–413. doi:10.1198/tech.2009.08018

Blott, S. J., and Pye, K. (2001). GRADISTAT: a grain size distribution and statistics package for the analysis of unconsolidated sediments. *Earth Surf. Process. Landforms* 26, 1237–1248. doi:10.1002/esp.261

Chávez Chávez, J. A. (1992). *La erupción del Misti. Pasado, presente, futuro*. Arequipa: Impresiones Zenith. doi:10.2172/5420913

Charbonnier, S. J., Deng, F., Dixon, T. H., and Malservisi, R. (2018). "High-resolution DEMs of active volcanoes from TanDEM-X data: implications for flow modeling and hazard assessment," in IGARSS 2018, 2018 IEEE Int. Geosci. Remote Sens. Symp., Valencia, Spain, July 22–27, 2018 (IEEE), 399–402. doi:10.1109/igarss.2018.8518271

Charbonnier, S. J., and Gertisser, R. (2012). Evaluation of geophysical mass flow models using the 2006 block-and-ash flows of Merapi Volcano, Java, Indonesia: towards a short-term hazard assessment tool. *J. Volcanol. Geoth. Res.* 231–232, 87–108. doi:10.1016/j.jvolgeores.2012.02.015

Charbonnier, S. J., and Gertisser, R. (2008). Field observations and surface characteristics of pristine block-and-ash flow deposits from the 2006 eruption of Merapi Volcano, Java, Indonesia. *J. Volcanol. Geoth. Res.* 177, 971–982. doi:10.1016/j.jvolgeores.2008.07.008

Charbonnier, S. J., and Gertisser, R. (2009). Numerical simulations of block-and-ash flows using the Titan2D flow model: examples from the 2006 eruption of Merapi Volcano, Java, Indonesia. *Bull. Volcanol* 71, 953–959. doi:10.1007/s00445-009-0299-1

Charbonnier, S. J., Kelfoun, K., Widiwijayanti, C., Sayudi, D. S., and Putra, R. (In press). "Assessing the pyroclastic density current hazards at Merapi: from field data to numerical simulations and hazard maps," in *Merapi volcano*. Editors R. Gertisser, V. Troll, T. Walter, N. Nandaka and Ratdomopurbo (Berlin, Germany: Springer 'Active Volcanoes of the World' Book Series).

Charbonnier, S. J., Varner, L., Escobar Wolf, R., Rodriguez, L., Chigna, G., Chun, C., et al. (2019). "Unravelling the dynamics and hazards of the June 3rd, 2018 pyroclastic currents at Fuego volcano (Guatemala): a multi-parameter approach," in AGU Fall meeting Abstract #619589, San Francisco, CA, December 2019.

Cobeñas, G., Thouret, J.-C., et al. (2014). Reply to comment on: "Cobeñas, G., Thouret, J.-C., Bonadonna, C., Boivin, P., 2012. The c.2030yr BP Plinian eruption of El Misti volcano, Peru: eruption dynamics and hazard implications. Journal of Volcanology and Geothermal Research 241–242, 105–120." by Harpel et al., JVGR 2013 G., Thouret, J.-C., Bonadonna, C., and Boivin, P., 2012. The c.2030 yr BP Plinian eruption of El Misti volcano, Peru: eruption dynamics and hazard implications. J. Volc. Geoth. Res. 41–242,105–120." by Harpel et al., JVGR, 2013. *J. Volcanol. Geoth. Res.* 275, 103–113. doi:10.1016/j.jvolgeores.2014.02.014

Cobeñas, G., Thouret, J.-C., Bonadonna, C., and Boivin, P. (2012). The c.2030yr BP Plinian eruption of El Misti volcano, Peru: eruption dynamics and hazard implications. *J. Volcanol. Geoth. Res.* 241-242, 105–120. doi:10.1016/j.jvolgeores.2012.06.006

Constantinescu, R., Thouret, J-C., and Irimus, I. A. (2011). Computer modeling as tool for volcanic hazards assessment: an example of pyroclastic flow modeling at El Misti volcano, Southern Peru. *Geogr. Tech.* 2-2011, 1–14.

Gertisser, R., Cassidy, N. J., Charbonnier, S. J., Nuzzo, L., and Preece, K. (2012). Overbank block-and-ash flow deposits and the impact of valley-derived, unconfined flows on populated areas at Merapi volcano, Java, Indonesia. *Nat. Hazards* 60, 623–648. doi:10.1007/s11069-011-0044-x

Gueugneau, V., Kelfoun, K., Charbonnier, S. J., Germa, A., and Carazzo, G. (2020). Dynamic and impacts of the May 8th, 1902 pyroclastic current at Mount Pelée (Martinique): new insights from numerical modeling. *Front. Earth Sci* 8, 279. doi:10.3389/feart.2020.00279

Gueugneau, V., Kelfoun, K., and Druitt, T. (2019). Investigation of surge-derived pyroclastic flow formation by numerical modeling of the 25 June 1997 dome collapse at Soufrière Hills Volcano, Montserrat. *Bull. Volcanol.* 81 (4), 25. doi:10.1007/s00445-019-1284-y

Harpel, C., da Silva, S., and Salas, G. (2013). Comment on: "Cobeñas, G., Thouret, J.-C., Bonadonna, C., Boivin, P., 2012. The c.2030 yr BP Plinian eruption of El Misti volcano, Peru: eruption dynamics and hazard implications. J. Volcanol. Geoth. Res. 241–242, 105–120." *J. Volcanol. Geoth. Res.* 275, 103–113. doi:10.1016/j.jvolgeores.2014.02.014

Harpel, C., da Silva, S., and Salas, G. (2011). The 2 ka eruption of Misti volcano, southern Peru—the most recent Plinian eruption of Arequipa's iconic volcano. *Geol. Soc. Amer. Spec. Pap.* 484, 1–7. doi:10.1130/2011.2484

Jenkins, S., Komorowski, J.-C., Baxter, P. J., Spence, R., Picquout, A., Lavigne, F., et al. (2013). The Merapi 2010 eruption: an interdisciplinary impact assessment methodology for studying pyroclastic density current dynamics. *J. Volcanol. Geoth. Res.* 261 (1), 316–329. doi:10.1016/j.jvolgeores.2013.02.012

Kelfoun, K. (2017). A two-layer depth-averaged model for both the dilute and the concentrated parts of pyroclastic currents. *J. Geophys. Res. Solid Earth* 122, 1–19. doi:10.1002/2017jb014013

Kelfoun, K. (2011). Suitability of simple rheological laws for the numerical simulation of dense pyroclastic flows and long-runout volcanic avalanches. *J. Geophys. Res.* 116, B08209. doi:10.1029/2010JB007622

Kelfoun, K., and Druitt, T. H. (2005). Numerical modeling of the emplacement of Socompa rock avalanche, Chile. *J. Geophys. Res. Solid Earth* 112, B12202. doi:10.1029/2005JB003758

Kelfoun, K., Gueugneau, V., Komorowski, J.-C., Cholik, N., and Merciecca, C. (2017). Simulation of block-and-ash flows and ash-cloud surges of the 2010 eruption of Merapi volcano with a two-layer model. *J. Geophys. Res. Solid Earth* 122, 1–16. doi:10.1002/2017jb013981

Kelfoun, K., Samaniego, P., Palacios, P., and Barba, D. (2009). Testing the suitability of frictional behaviour for pyroclastic flow simulation by comparison with a well-constrained eruption at Tungurahua volcano (Ecuador). *Bull. Volcanol* 71, 1057–1075. doi:10.1007/s00445-009-0286-6

Komorowski, J.-C., Jenkins, S., Baxter, P. J., Picquout, A., Lavigne, F., Charbonnier, S., et al. (2013). Paroxysmal dome explosion during the Merapi 2010 eruption: processes and facies relationships of associated high-energy pyroclastic density currents. *J. Volcanol. Geoth. Res.* 261, 260–294. doi:10.1016/j.jvolgeores.2013.01.007

Legros, F. (2001). Tephra stratigraphy of Misti volcano, Peru. *J. S. Am. Earth Sci.* 14 (1), 15–29. doi:10.1016/s0895-9811(00)00062-6

Loughlin, S. C., Calder, E. S., Clarke, A., Cole, P. D., Luckett, R., Mangan, M. T., et al. (2002). Pyroclastic flows and surges generated by the 25 June 1997 dome collapse, Soufrière Hills Volcano, Montserrat. *Geol. Soc. Lond. Mem.* 21, 191–209. doi:10.1144/gsl.mem.2002.021.01.09

Lube, G., Cronin, S. J., Thouret, J.-C., and Surono, S. (2011). Kinematic characteristics of pyroclastic density currents at Merapi and controls on their avulsion from natural and engineered channels. *Geol. Soc. Am. Bull.* 123, 1127–1140. doi:10.1130/b30244.1

Mariño, J., Rivera, M., Cacya, L., Thouret, J.-C., Macedo, O., Salas, G., et al. (2007). Data from: Mapa de los peligros volcánicos del Misti. Ingemmet, Proyecto Multinacional Andino, IRD, LMV, Instituto de Geofísica UNAM, UNSA, Universidad Católica de Santa Maria, INDECI, Gobierno regional de Arequipa, Municipalidad provincial de Arequipa, PREDES, SENAMHI, Lima.

Martí, J. M. (2017). *Assessing volcanic hazard: a review*. Oxford University Press: Oxford.

McKay, M. D., Beckman, R. J., and Conover, W. J. (1979). Comparison of three methods for selecting values of input variables in the analysis of output from a computer code. *Technometrics* 21, 239–245. doi:10.1080/00401706.1979.10489755

Mead, S. R., Magill, C., Lemiale, V., Thouret, J-C., and Prakash, M. (2017). Examining the impact of lahars on buildings using numerical modelling. *Nat. Hazards Earth Syst. Sci.* 17, 703–719. doi:10.5194/nhess-17-703-2017

Navarro Colque, P. (1999). Cartografía geológica, historia eruptiva y evaluación de las amenazas volcánicas del estrato-volcán Misti. [dissertation's thesis]. Arequipa (Peru): Universidad Nacional San Agustin, Facultad de Geología, Geofísica y Minas.

Newhall, C. G., and Self, S. (1982). The volcanic explosivity index (VEI) an estimate of explosive magnitude for historical volcanism. *J. Geophys. Res.* 87, 1231–1238. doi:10.1029/jc087ic02p01231

Ogburn, S. E., and Calder, E. S. (2017). The relative effectiveness of empirical and physical models for simulating the dense undercurrent of pyroclastic flows under different emplacement conditions. *Front. Earth Sci.* 5, 1–26. doi:10.3389/feart.2017.00083

Oh, J., and Lee, C. (2014). Automated bias-compensation of rational polynomial coefficients of high resolution satellite imagery based on topographic maps. *ISPRS J. Photogramm. Remote Sens.* 100, 12–22. doi:10.1016/j.isprsjprs.2014.02.009

Poland, M. P. (2014). Time-averaged discharge rate of subaerial lava at Kīlauea Volcano, Hawai'i, measured from TanDEM-X interferometry: implications for magma supply and storage during 2011–2013. *J. Geophys. Res. Solid Earth* 119, 5464–5481. doi:10.1002/2014jb011132

Rivera, M., Martin, H., Le Pennec, J.-L., Thouret, J.-C., Gourgaud, A., and Gerbe, M.-C. (2017). Petro-geochemical constraints on the source and evolution of magmas at El Misti volcano (Peru). *Lithos*, 268-271, 240–259. doi:10.1016/j.lithos.2016.11.009

Sandri, L., Thouret, J.-C., Constantinescu, R., Biass, S., and Tonini, R. (2014). Long-term multi-hazard assessment for El Misti volcano (Peru). *Bull. Volcanol.* 76, 771. doi:10.1007/s00445-013-0771-9

Suni Chambi, J. (1999). Estudio geológico y vulcanológico del volcán Misti y sus alrededores. dissertation's thesis. Arequipa (Peru): Universidad Nacional San Agustin.

Surono, Jousset, P., Pallister, J., Boichu, M., Buongiorno, M. F., Budisantoso, A., et al. (2012). The 2010 explosive eruption of Java's Merapi volcano-A '100-year' event. *J. Volcanol. Geoth. Res.* 241–242, 121–135. doi:10.1016/j.jvolgeores.2012.06.018

Thouret, J.-C., Finizola, A., Fornari, M., Legeley-Padovani, A., Suni, J., and Frechen, M. (2001). Geology of El Misti Volcano near the city of Arequipa, Peru. *Geol. Soc. Amer. Bull.* 113 (12), 1593–1610. doi:10.1130/0016-7606(2001)113<1593:goemvn>2.0.co;2

Thouret, J.-C., Legros, F., Gourgaud, A., Salas, G., Juvigné, E., Gilot, E., et al. (1995). Un exemple de prévision des risques volcaniques au Pérou méridional (région d'Arequipa), fondé sur l'étude de l'activité éruptive récente du strato-volcan El Misti. *C.-R. Acad. Sci. Paris* 3, 923–929.

Thouret, J.-C., Suni, J., Eissen, J.-Ph., and Navarro, P. (1999). Assessment of volcanic hazards in the Arequipa area based on the eruptive history of Misti volcano, Southern Peru. *Z. Geomorphol* 114, 89–112.

Tierz, P., Sandri, L., Costa, A., Zaccarelli, L., Di Vito, M. A., Sulpizio, R., et al. (2016). Suitability of energy cone for probabilistic volcanic hazard assessment: validation tests at Somma Vesuvius and Campi Flegrei (Italy). *Bull. Volcanol.* 78, 1–15. doi:10.1007/s00445-016-1073-9

Wadge, G. (2009). "Assessing the pyroclastic flow hazards from dome collapse at Soufriere Hills Volcano, Montserrat," in *Studies in volcanology: the Legacy of George Walker*, Editors T. Thordarsson, S. Self, G. Larsen, S. K. Rowlands and A. Hoskuldsson (London, UK: Geological Society, London, Special Publications) 2, 211–224.

Yamamoto, T., Takarada, S., and Suto, S. (1993). Pyroclastic flows from the 1991 eruption of Unzen volcano, Japan. *Bull. Volcanol.* 55, 166–175. doi:10.1007/BF00301514

Conflict of Interest: The authors declare that the research was conducted in the absence of any commercial or financial relationships that could be construed as a potential conflict of interest.

frontiers in Earth Science

ORIGINAL RESEARCH
published: 16 September 2020
doi: 10.3389/feart.2020.542932

Identifying Pyroclastic Density Currents From Partial Outcrop Exposure on Mt. Ruapehu, New Zealand

Janina K. Gillies[1]*, *Ben M. Kennedy*[1], *Darren M. Gravley*[1], *Graham S. Leonard*[2] and *James Cowlyn*[1]

[1] School of Earth and Environment, University of Canterbury, Christchurch, New Zealand, [2] GNS Science, Lower Hutt, New Zealand

Pyroclastic density current (PDC) deposits, especially small to medium volume events, have low preservation potential at many volcanoes, particularly when unconsolidated or deposited on steep, glaciated slopes. This may lead to an underrepresentation of these events in the eruptive record, and consequently, in hazard management planning; leaving populations on and around the volcanoes unprepared for the threat of these smaller eruptions. Therefore, it is important to investigate and recognize these smaller events in the volcanic record to create more comprehensive plans for future eruptions. Mt. Ruapehu is one of New Zealand's most active volcanoes, last erupting in 2007. Few studies have investigated the PDC occurrence on this volcano, despite PDCs being one of the most hazardous volcanic processes. Poor preservation of PDC deposits, due to small volume, past glaciations, erosion, burial, and poor consolidation has left a significant gap in Mt. Ruapehu's eruptive record. By identifying and characterizing PDCs on Mt. Ruapehu this paper provides an updated account of PDC occurrence on this volcano, especially for smaller scale PDCs. Comprehensive field-mapping forms the basis for this study by identifying PDC deposits from partial outcrop exposures. We use field observations of these deposits to describe the lithofacies and infer PDC behavior. Relative stratigraphy and whole-rock geochemistry are used to correlate deposits with dated units from literature and provide approximate age ranges. This study describes 12 PDC deposits representing at least 10 previously unidentified flows. Combined with PDCs identified in previous studies there is a total of 23 PDC deposits found on Mt. Ruapehu, including the PDC observed during the 1945 eruption. These PDCs have been emplaced throughout Mt. Ruapehu's 250 ka eruptive history. The PDCs were concentrated and dominated by granular flow or granular fluid-based flow transport regimes. The lithofacies show PDCs forming from column collapse and dome collapse or explosion events. This demonstrates that Mt. Ruapehu is capable of producing a spectrum of PDC styles and sizes, something that must be considered during future hazard planning on the volcano.

Keywords: pyroclastic density currents, relative stratigraphy, Ruapehu volcano, hazard, lithofacies, column collapse, dome explosion, geochemistry

OPEN ACCESS

Edited by:
Laura Sandri,
National Institute of Geophysics and Volcanology, Italy

Reviewed by:
Claudio Scarpati,
University of Naples Federico II, Italy
Sylvain Charbonnier,
University of South Florida, United States

***Correspondence:**
Janina Gillies
janina.gillies@gmail.com

Specialty section:
This article was submitted to Volcanology, a section of the journal Frontiers in Earth Science

Received: *14 March 2020*
Accepted: *24 August 2020*
Published: *16 September 2020*

Citation:
Gillies JK, Kennedy BM, Gravley DM, Leonard GS and Cowlyn J (2020) Identifying Pyroclastic Density Currents From Partial Outcrop Exposure on Mt. Ruapehu, New Zealand. Front. Earth Sci. 8:542932. doi: 10.3389/feart.2020.542932

INTRODUCTION

With increasing populations, urbanization, and infrastructure over the last 50 years, natural hazards such as volcanic eruptions are posing a greater threat to society (Johnston et al., 2000). Therefore, it is crucial to fully understand these hazards in order to reduce the impact they have on society. This is especially important at volcanoes with large numbers of tourists, such as Mt. Ruapehu (New Zealand), or numerous residents living in the impact area. This was also highlighted by the tragic events at Whakaari/White Island (New Zealand) on December 9, 2019, where approximately 47 tourists were caught in a sudden-onset phreatic eruption, resulting in 21 deaths.

Pyroclastic density currents (PDCs) are one example of a volcanic hazard that threatens populations surrounding the volcano, contributing to 33% of fatalities during volcanic disasters since 1600 AD (Auker et al., 2013). PDCs can be generated by several different mechanisms: the collapse of an eruption column, boiling-over (Branney and Kokelaar, 2002), directed lateral blast (Waitt Jr., 1981), explosion or gravitational collapse of a lava dome (Dufek et al., 2015) or the toe of flowing lava (Valentine et al., 2000; Stinton and Sheridan, 2008; Buchwaldt, 2013; Dufek et al., 2015), or the collapse of accumulated Strombolian spatter (Valentine et al., 2000). These different mechanisms can produce different styles and sizes of PDCs.

Small to medium sized unconsolidated PDC deposits have a low preservation potential, especially when sedimented on steep slopes and in active drainages for water and ice (Manville et al., 2000; Cowlyn, 2016). This leads to an underrepresentation of these events in the volcanic record and, therefore, in hazard management plans. Recognizing and characterizing these types of PDCs is important in fully preparing for a range of eruption sizes and styles, not only large climactic events.

Lithofacies classifications are commonly used in literature to characterize deposits and infer emplacement mechanisms based on textural features. This is especially useful when describing PDC deposits due to the variety of generation, transport, and emplacement mechanisms that can influence the characteristics of the final deposit. Branney and Kokelaar (2002) provide an in-depth overview of ignimbrite lithofacies and interpretations for the processes that influenced them. Other work on ignimbrites includes Brown and Branney (2004) who characterized the lithofacies from the 273 ka Poris Formation on Tenerife. The ignimbrites from this eruption are composed of massive, diffuse bedded, and diffuse stratified lapilli tuff facies. These PDCs were density stratified and deposited massive, coarse ignimbrites in the valleys and finer-grained bedded tuff on topographic highs. Smaller pumiceous PDCs include the 1993 Lascar Volcano deposits, described by Calder et al. (2000). This pumice rich facies includes poorly sorted, reverse graded, ash rich deposits with elutriation pipes and fine-grained basal layers. Based on the lithofacies Calder et al. (2000) infers the PDC was a highly concentrated granular flow, and consisted of multiple flows. Pumice clasts are concentrated at the deposit margins due to flotation from their lower densities. Lube et al. (2011) and Charbonnier and Gertisser (2011) describe the lithofacies of small volume block-and-ash flows from the 2006 dome collapse events at Merapi. These include the massive, coarse, matrix supported, breccia channel facies, fine grained surge facies, and massive, matrix supported veneer facies. These flows were interpreted to have formed during unsteady granular PDCs dominated by particle interactions and segregation processes (Charbonnier and Gertisser, 2011). Torres-Orozco et al. (2018) also describe the lithofacies of block-and-ash flows deposits at Mt. Taranaki. This facies consisted of poorly sorted, matrix supported, dense blocks, and ash deposits. Torres-Orozco et al. (2018) used the reverse grading common in this facies to infer that dispersive pressure from grain collisions was the dominant process. These previous studies provide the basis for the lithofacies classifications used in this paper to characterize and interpret small, heavily eroded PDC deposits on Mt. Ruapehu.

Recent studies have highlighted in detail the PDC hazard at New Zealand volcanoes, such as Mt. Taranaki (Torres-Orozco et al., 2017a; Torres-Orozco et al., 2017b; Torres-Orozco et al., 2018). While the occurrence of PDCs on Mt. Ruapehu has been briefly mentioned in past literature (Hackett, 1985; Donoghue et al., 1995; Pardo et al., 2012a; Pardo et al., 2014; Townsend et al., 2017) little investigation has been conducted into their distribution, frequency, and subsequent hazard.

Poor consolidation, small eruptive events, and active drainages on a heavily glaciated volcano make it difficult to locate and identify PDC deposits on Mt. Ruapehu, leading to an unknown PDC hazard. A PDC was photographed during Mt. Ruapehu's 1945 eruption (Johnston and Neall, 1995; Cowlyn, 2016), illustrating that PDCs have historically occurred at Mt. Ruapehu. It has also been suggested that the 1996 eruption columns were likely to have collapsed to form PDCs if not for the presence of winds that increased the buoyancy of the plume during the eruption (Degruyter and Bonadonna, 2013).

Prior to the study conducted by Cowlyn (2016), who identified multiple PDC deposits on the eastern side of Mt. Ruapehu, the PDC hazard was generally overlooked. This is likely due to a lack of historic PDCs and the poor preservation of prehistoric PDC deposits. Houghton et al. (1987) noted the occurrence of pyroclastic surges during historical eruptions and speculated the occurrence of pyroclastic flows during future eruptions. Donoghue et al. (1995) described evidence for a magma mingling episode in the juvenile material of the Pourahu PDC within the Bullot Formation (27–10 ka; Pardo et al., 2012b). In more recent studies, Pardo (2012) and Pardo et al. (2014) found evidence of eruption columns that collapsed to form PDC deposits interspersed with fallout deposits. One PDC deposit, part of the Oruamatua Eruptive Unit (between 13 and 12 ka) was found up to 16 km from the source, Ruapehu's northern crater area (Pardo et al., 2014). Another PDC deposit, part of the Okupata-Pourahu Eruptive Unit (11.6 ka), was also found up to 16 km from the source, the southern crater area, which is still active today. PDC deposits were also identified in the Upper Waikato drainages, most likely formed from the partial collapse of an unsteady eruption column (Pardo, 2012; Pardo et al., 2014).

During these recent studies on Mt. Ruapehu, Pardo et al. (2014) hypothesized that pyroclastic flows accompanied some of Ruapehu's largest eruptions. Cowlyn (2016) later identified pumiceous PDC deposits from these eruptions and additional PDC deposits spanning a range of eruption styles and sizes. The

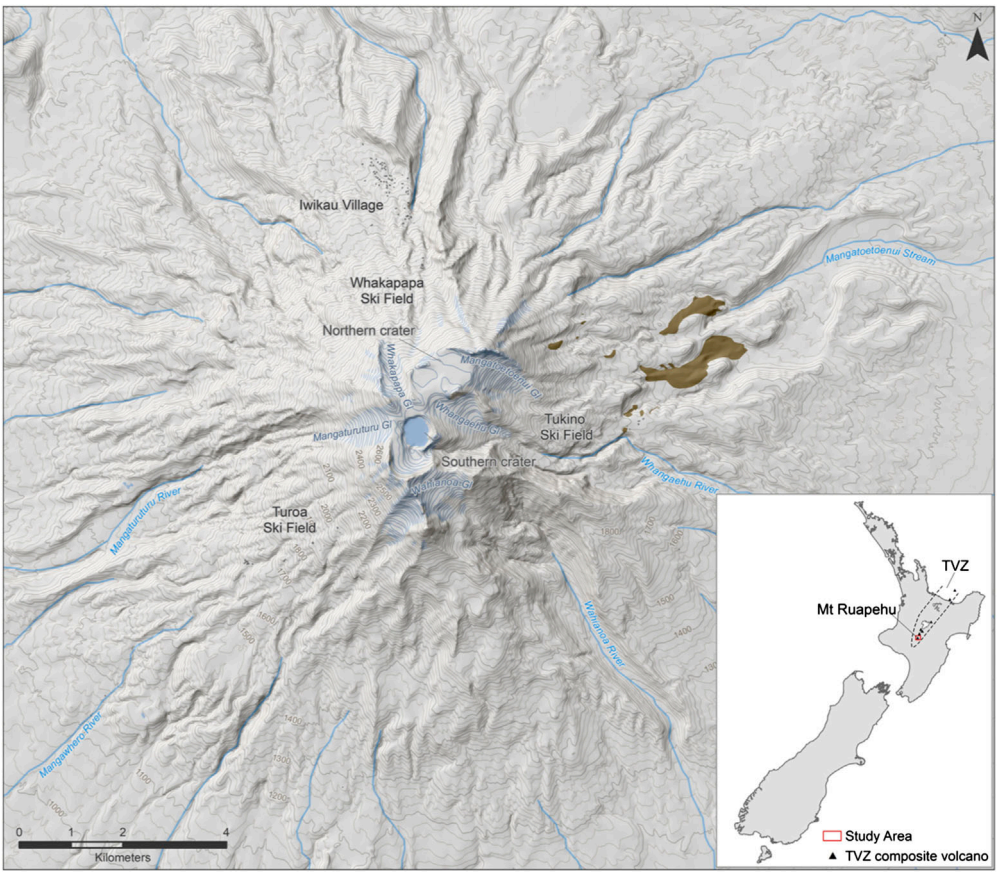

FIGURE 1 | Topographic map of Mt. Ruapehu with pyroclastic density current deposits identified by Cowlyn (2016) (brown areas). Inset shows location of Mt. Ruapehu within New Zealand and the Taupo Volcanic Zone (TVZ). Map data gathered from https://data.linz.govt.nz.

deposits described by Cowlyn (2016) fit three main categories: 1) Pumice-dominated PDC deposits, 2) Variably welded PDC deposits containing rounded clasts, and 3) Small volume PDC deposits containing dense primary clasts. The pumice-dominated PDC deposits described by Cowlyn (2016) were found to be geochemically similar to nearby Plinian fall deposits from the Taurewa (11.8–9.5 ka) and Ohinewairua (~13.6–11.6 ka) eruptive periods (Donoghue et al., 1999; Pardo et al., 2012b).

The study conducted by Cowlyn (2016) identified 12 previously unknown PDC deposits near the Tukino ski area on the eastern flank of Mt. Ruapehu. All of the deposits were estimated to have been emplaced within the last ~13.6 ka. However, that study did not investigate PDC occurrence in other sectors of Mt. Ruapehu, leaving a significant gap in the knowledge of PDCs on this volcano. The goal of this study is, therefore, to identify and characterize other poorly preserved PDC deposits throughout Mt. Ruapehu to better understand the overall hazard.

GEOLOGICAL SETTING

Mt. Ruapehu (2,797 m), located at the southern end of the Taupo Volcanic Zone (**Figure 1**), is an active, andesite-dacite composite volcano with a volume of approximately 150 km^3 (Hackett and Houghton, 1989). This volcano consists of four formations: Te Herenga (200–180 ka), Wahianoa (166–80 ka), Mangawhero (50–15 ka), and Whakapapa (<17 ka) (Hackett and Houghton, 1989; Conway et al., 2016).

A series of intense constructional events separated by periods of erosion, sector collapse, and minor volcanic activity characterize the formation of Mt. Ruapehu (Price et al., 2012). There is an apparent hiatus in eruptive activity from 80 to 50 ka (Townsend et al., 2017). Compositions range from basalt to dacite with predominantly medium *K* andesite (Hackett and Houghton, 1989). More evolved compositions have been erupted over time (Hackett and Houghton, 1989). The currently active vent is located in the southern portion of the broad summit, and forms the acidic Crater Lake/Te Wai-ā-moe (Hackett and Houghton, 1989).

Throughout its formation, eruptive activity at Mt. Ruapehu has included Plinian, sub-Plinian, Strombolian, phreatomagmatic, Vulcanian, dome-related activity, and the extrusion of lava flows (Houghton et al., 1987; Hackett and Houghton, 1989; Pardo et al., 2012b). Over the last 150 years the most frequently observed eruption types include phreatomagmatic and phreatic activity, with a larger lava-dome explosion event

in 1945 that occurred during an eruptive period also associated with sub-Plinian and Strombolian eruption styles (Johnston et al., 2000). More than 40 eruptions have occurred since then (Kilgour et al., 2013).

METHODS

Field Work

Field work formed the basis of this study, with three months spent on Mt. Ruapehu between November 2017 and March 2018. The targeted areas of the mountain were partly determined based on previous visits by other researchers. Other potential PDC deposits were identified in the field while accessing these targeted areas. While a broad area of the volcano was covered, logistics, and difficult terrain hindered access into some locations, especially the NW sector and the Wahianoa Valley.

Each location involved the sampling, identification, and textural description of PDC deposits. Permit restrictions within the National Park limited the quantity and size of samples. Clast and component percentages were quantified in the field using a percentage composition chart (Terry et al., 1955). Nearby units were also briefly described to correlate with mapped formations in Townsend et al. (2017).

Density

One to three lapilli, representative of the overall clast type at each outcrop, were selected from each deposit to measure indicative clast density using the methods of Houghton and Wilson (1989) and Barker et al. (2012). Sample size restrictions limited the quantity of lapilli of an appropriate size in each sample. Details about sample preparation and measurement are reported in **Appendix 1 in Supplementary Material**. The clast densities were calculated using the equation outlined in Houghton and Wilson (1989):

$$\rho_{\text{clast}} = \frac{W_{\text{clast (dry)}}}{S.G\left[W_{\text{clast (dry)}} + W_{\text{wax (wet)}} + W_{\text{cage (wet)}} - W_{\text{clast+ wax + cage (wet)}}\right]}$$

Where $W_{\text{clast (dry)}}$ is the weight of the clast measured while dry, $S.G$ is the specific gravity of water, and $W_{\text{cage (wet)}}$ the weight of the cage while in water. $W_{wax\,(\text{wet})}$ is the weight of the wax while being held underwater in the cage. The buoyancy of the wax resulted in a negative value.

It is important to note that the small quantity of lapilli clasts used for this method limits how representative the density values are for each deposit. However, these values are only used to give an approximation of the clast densities present in each deposit, not an extensive range.

Geochemistry

The geochemical analyses were conducted at Massey University (New Zealand) using a Bruker S8 TIGER Series WDXRF Spectrometer calibrated against international standards (OREAS 24c). Major and trace element geochemical data was measured for each sample. For complete sample preparation and analysis details, see **Appendix 2** in **Supplementary Material**.

Deposit Ages

The ages of deposits were estimated by geochemically correlating the deposits, through major and trace elements, with dated units (Pardo et al., 2012a; Conway et al., 2016). These correlations were also supported by comparing the relative stratigraphy of the deposits observed in the field to the surrounding units on a geological map of Mt. Ruapehu (Townsend et al., 2017). This approach allowed the age of the PDC deposits to be approximately bracketed.

RESULTS

A total of 12 new pyroclastic deposit outcrops were identified on Mt. Ruapehu on the northern, eastern, and south-western sectors of the mountain (**Figure 2**). Field descriptions of each deposit can be found in **Appendix 3** in **Supplementary Material**.

Pyroclastic Deposits

Pyroclastic Density Current 1

Located on the lower north-eastern slopes of Mt. Ruapehu 6.7 km away from the vent, this deposit is 5 m thick and located underneath approximately 50 m of lava flows. It is formed by two well indurated, poorly sorted, and matrix supported layers (**Figure 3A**). The lower layer is primarily massive, with ash to block-sized clasts. This layer grades into a 20 cm fines-rich bed of ash and lapilli. The upper layer truncates the lower layer and thickens toward the topographic low. This upper layer displays reverse grading where the base of the layer is primarily composed of ash and lapilli, and grades up to bomb-sized clasts in an ash matrix. The maximum clast size observed in the field was 40 cm. Juvenile clasts are vesicular, sub-rounded to sub-angular and comprise 20–30% of the outcrop. In both layers there are occasional dense, well rounded, and dark gray clasts. The average density of main clast type in this deposit is 1.3 ± 0.085 g/cm^3.

Pyroclastic Density Current 2

This deposit is located on the eastern side of Mt. Ruapehu between 3.7 and 4.3 km away from the vent and consists of a series of orange outcrops exposing a 0.3–1 m thick unit draping the surface (**Figure 3B**). The thinnest deposits were observed upslope, closer to the topographic highs. PDC 2 is well indurated, matrix supported, and display minor reverse grading. Grainsizes range from ash to bombs (~10 cm). The majority of the clasts are sub-rounded, black, and vesicular. There are occasional gray, dense, and angular lithic clasts. The average density of the dominant clasts is 1.2 ± 0.14 g/cm^3.

Pyroclastic Density Current 3

PDC 3 was found on the southern side of Mt. Ruapehu 3–3.5 km away from the vent as a bright red, 8 m thick, well indurated outcrop with a layer of unconsolidated material on top (**Figure 3C**). The outcrop is thickest in the center of the valley and appears to thin toward the valley sides. This deposit is poorly sorted, massive, and clast supported. Grain sizes range between ash and bomb. The deposit is rich in both vesicular, sub-rounded

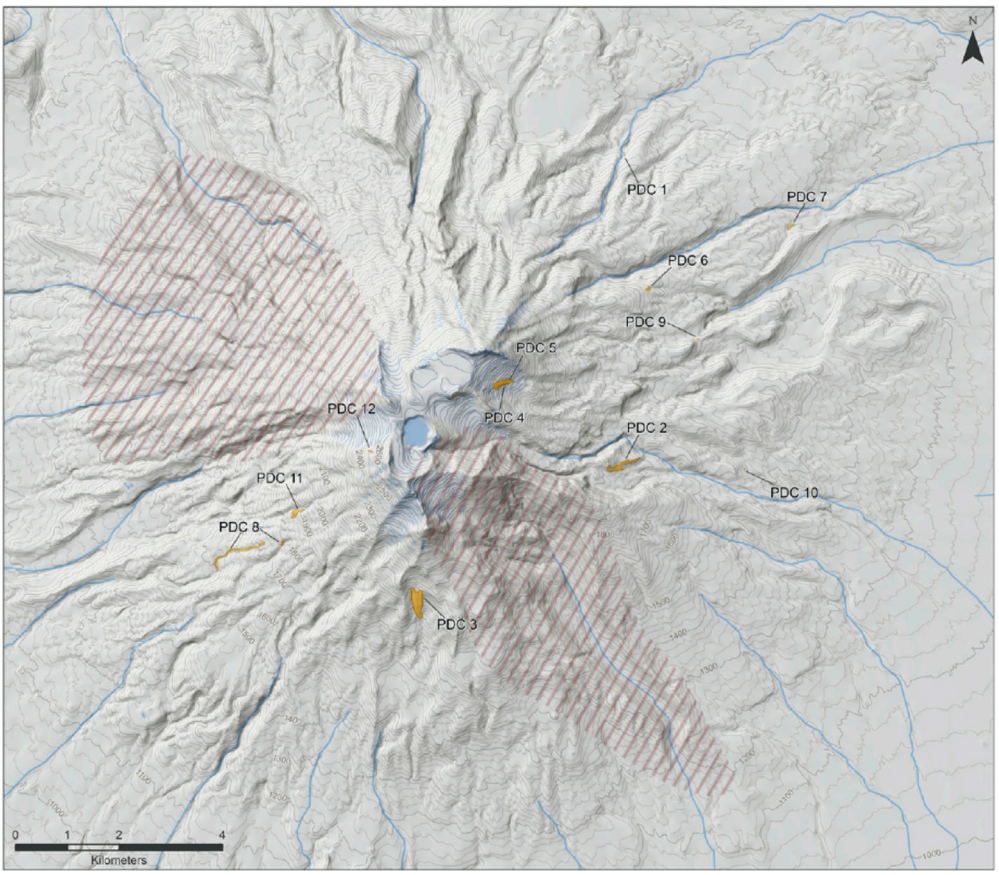

FIGURE 2 | Pyroclastic density current (PDC) deposits identified during this study. A total of 12 PDC deposits were identified. Red dashes indicate main areas that were unable to be accessed during this study due to time constraints or difficult terrain. Map data gathered from https://data.linz.govt.nz.

clasts and dense, angular to sub-angular clasts. The densities of these clasts range between 1.3 ± 0.0015 g/cm^3 for the vesicular clasts, and 2.3 ± 0.0016 g/cm^3 for the dense clasts.

Pyroclastic Density Current 4

This deposit was found below the Mangatoetoenui Glacier 1.9 km away from the vent as a 4 m thick, well indurated black outcrop (**Figure 3D**). The deposit can be seen outcropping across the entire valley with little variation in thickness. It is massive, poorly sorted, and matrix supported. Clasts comprise 40% of the visible outcrop. Grain sizes range from ash to bombs. The maximum observed grainsize is 50 cm. The clasts are sub-rounded to well-rounded and vesicular. The average density of the clasts in this group is 1.3 ± 0.18 g/cm^3.

Pyroclastic Density Current 5

PDC 5 is also located below the Mangatoetoenui Glacier 1.9 km from the vent, outcropping in two places across the valley. Overall it is a thick (~6 m), poorly sorted deposit, with multiple layers of reverse grading, and supported by an ash-rich matrix. The dominant clasts are pale yellow-grey and vesicular, or large black vesicular cauliflower bombs (<70 cm) (**Figure 3E**). These are primarily sub-rounded and constitute 25% of the outcrop. Occasional lithic clasts are distributed throughout the lower outcrop, though they appear to comprise less than 5% of the overall deposit. The average density of the vesicular clasts is 0.92 ± 0.080 g/cm^3.

This deposit is texturally similar to Package 1, part of the Ohinewairua eruptive period (~11.6–13.6 ka), identified by Cowlyn (2016) and was found topographically upslope of that package.

Pyroclastic Density Current 6

PDC 6 was found 5.2 km from the vent, on the north-eastern slopes of the mountain where a small channel has exposed a 1 m cross-sectional view of the deposit. This deposit is massive, matrix supported, and poorly sorted (**Figure 3F**). Grainsizes range from ash to lapilli, with occasional cauliflower bombs (<50 cm) that comprise 2% of the outcrop. The majority of the clasts are sub-angular and vesicular. There are also occasional angular, dense lapilli clasts. The average density of the vesicular clasts is 1.3 ± 0.16 g/cm^3.

Pyroclastic Density Current 7

This 1 m thick deposit was found 8.3 km from the vent in the valley of a small tributary to the Ohinepango stream on the north-

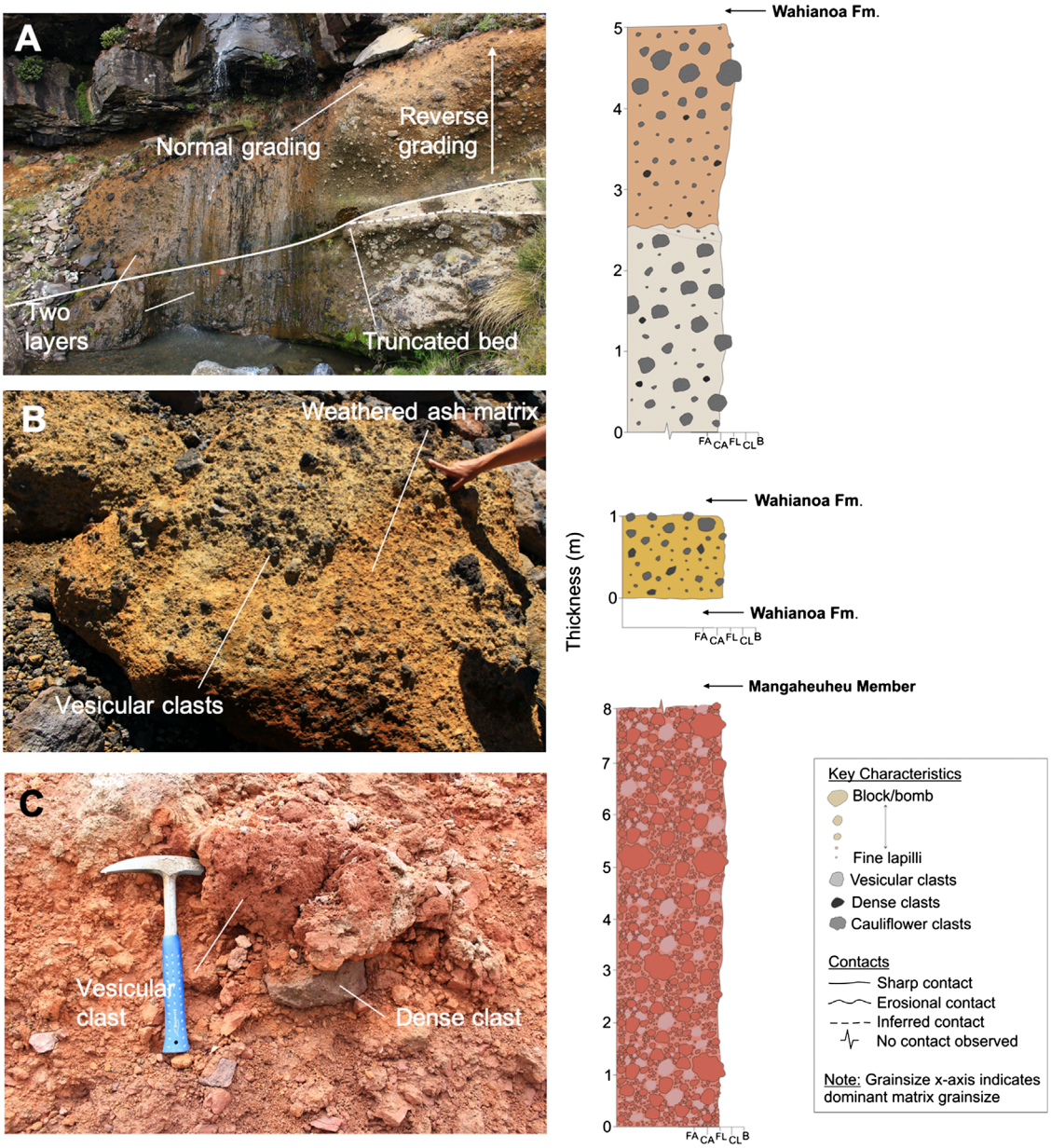

FIGURE 3 | Field photos of each deposit and corresponding stratigraphic columns illustrating main textural features. Grainsize axis on stratigraphic columns correspond to fine ash (FA), coarse ash (CA), fine lapilli (FL), coarse lapilli (CL), and blocks/bombs (B). **(A)** Pyroclastic density current (PDC) 1 underneath Wahianoa Formation lava flows. Two layers, the upper of which displays reverse and normal grading. The lower layer is primarily massive, but does have a fines-rich layer at the top of the flow. An erosional contact separates the two layers. **(B)** Weathered orange PDC 2 with black vesicular clasts concentrated on the surface. This deposit is found both above and below Wahianoa Formation units. **(C)** Close up image of PDC 3 showing the occurrence of both vesicular and dense clasts. The entire outcrop is bright red. **(D)** PDC 4 is black, well-indurated, and contains sub-rounded clasts. **(E)** PDC 5 is rich in ash and vesicular clasts. Large, black, vesicular bombs display multiple layers of reverse grading. **(F)** PDC 6 is primarily composed of vesicular ash and lapilli. Occasional dense lapilli clasts and vesicular bombs also occur. Above and below this layer is a series of ashfall deposits. **(G)** PDC 7 is situated between a series of airfall deposits and is bisected by a fault. This deposit is primarily composed of ash and lapilli, but does contain occasional blocks and bombs. **(H)** PDC 8 is well-indurated and contains sub-angular to well rounded clasts. The deposit is gray with pink areas dispersed throughout. Turoa Member lava flows were observed both above and below the deposit. **(I)** PDC 9 is thin and well-indurated. This deposit is primarily composed of ash and vesicular lapilli though it does contain occasional dense clasts. **(J)** PDC 10 is located on the surface of glacial till deposits and is ash supported and rich in vesicular lapilli, with occasional vesicular bombs. **(K)** PDC 11 is located on the surface of Turoa Member lava flows and is rich in ash and vesicular clasts (both lapilli and bombs). **(L)** PDC 12 is clast supported and is primarily composed of black cauliflower bombs. There is ash and black lapilli filling in the gaps between these clasts. Deposited above Turoa Member lava flows.

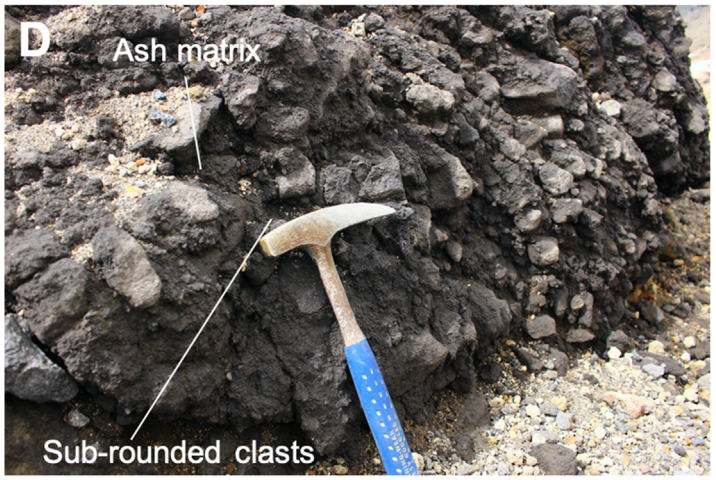

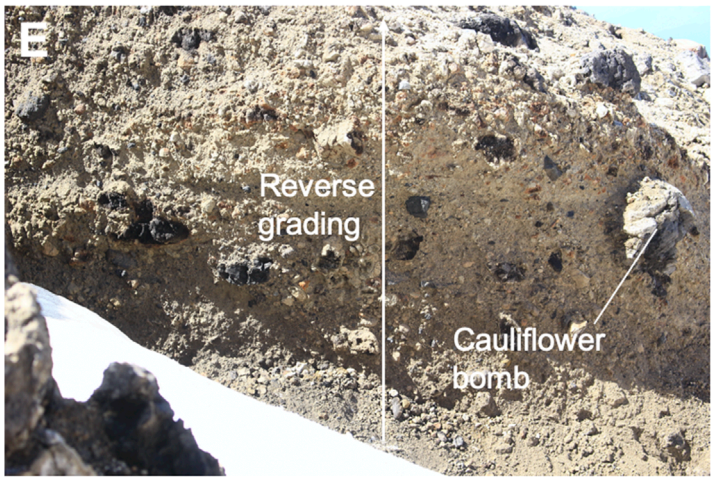

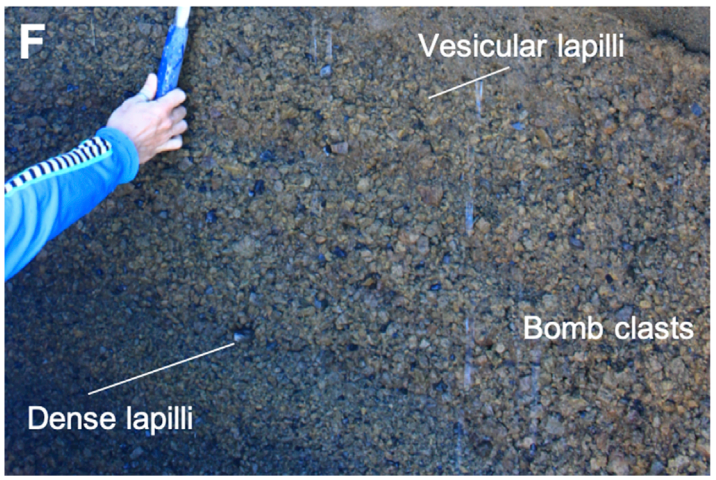

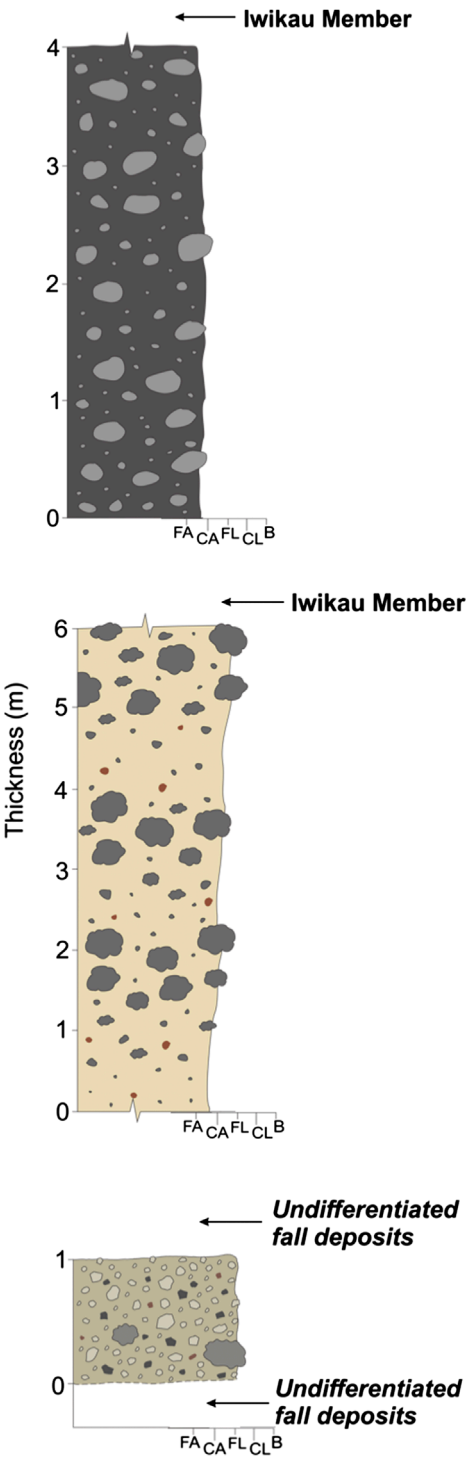

FIGURE 3 | (Continued).

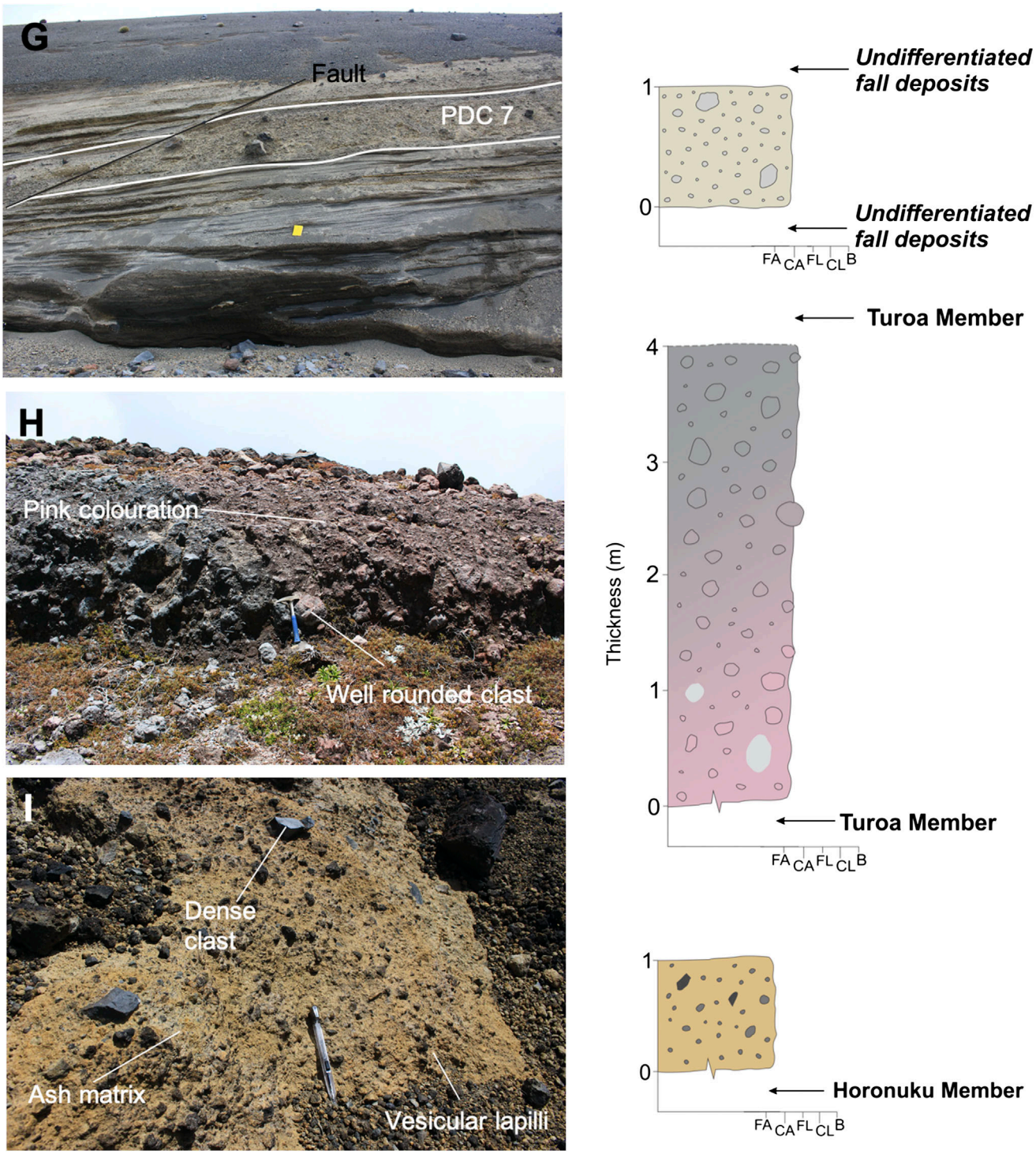

FIGURE 3 | (Continued).

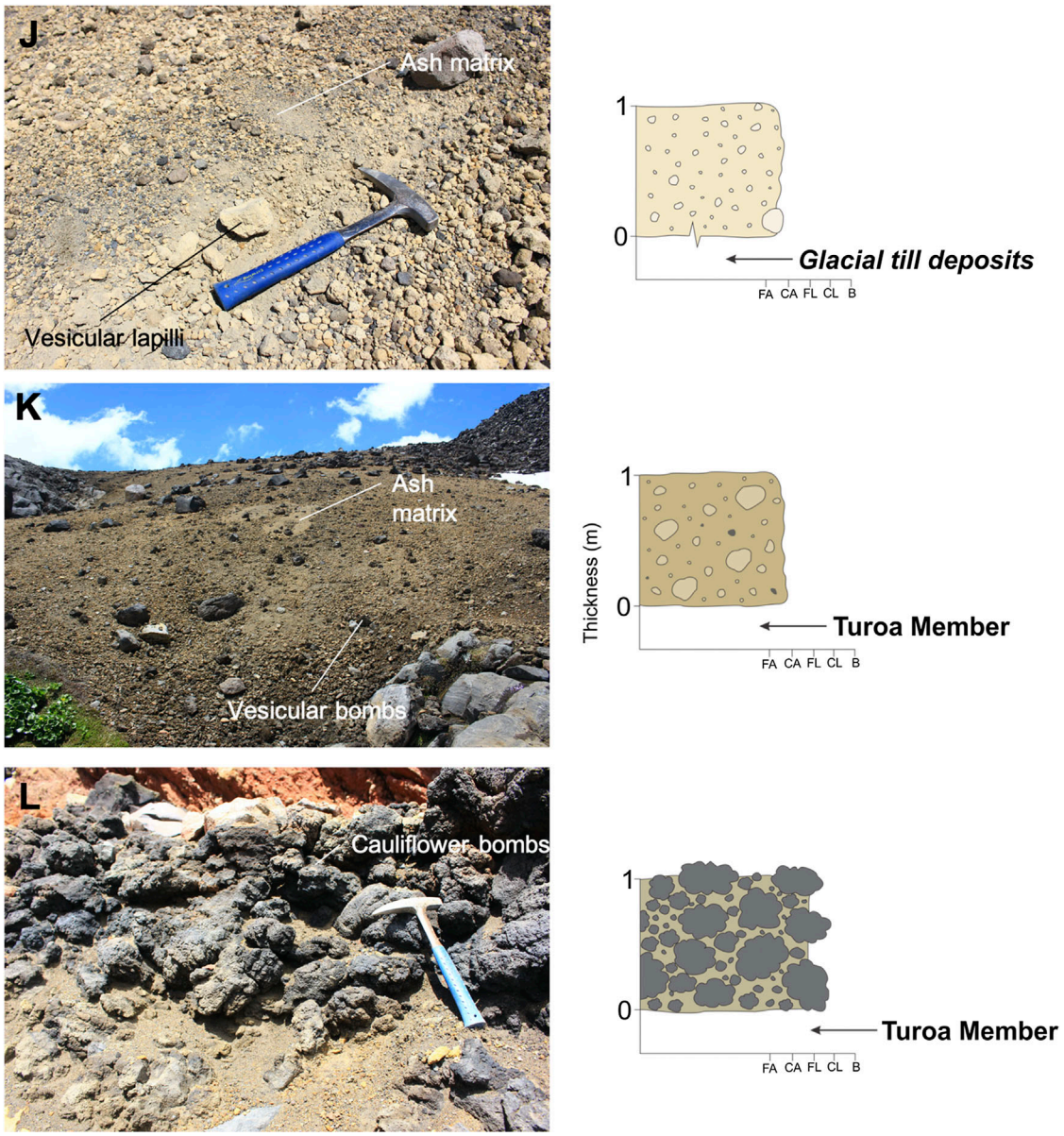

FIGURE 3 | (Continued).

eastern side of Mt. Ruapehu. PDC 7 is poorly sorted, massive, and matrix supported (**Figure 3G**). The grainsizes range from ash to lapilli, with occasional bombs (<15 cm) and angular blocks (<25 cm). These large blocks and bombs constitute for 5% of the outcrop. The clasts are angular to sub-angular, and dominantly vesicular. The average vesicular clast density is 1.3 ± 0.11 g/cm^3.

Pyroclastic Density Current 8

PDC 8 was found as two long outcrops down a small valley on the southwestern flanks of the volcano. The deposits are located between 3.3 and 4.7 km from the vent. These gray and light pink outcrops are well indurated and some reach 4 m in visible thickness (**Figure 3H**). The deposit is poorly sorted, massive, and matrix supported. Grain sizes range from ash to bombs (<65 cm). The majority of clasts are well-rounded and mildly vesicular. Occasional well-rounded, dense clasts also occur (<50 cm). The average density of the dominant clasts type is 1.5 ± 0.044 g/cm^3.

Pyroclastic Density Current 9

PDC 9 is a thin deposit found on the eastern side of Mt. Ruapehu 5.8 km from the vent. Only 1 m is exposed, which is well-indurated and massive. The deposit is supported by a pale ash matrix, with vesicular black lapilli (20%) and occasional dense lithic clasts (<2%) (**Figure 3I**). Vesicular clasts are sub-rounded,

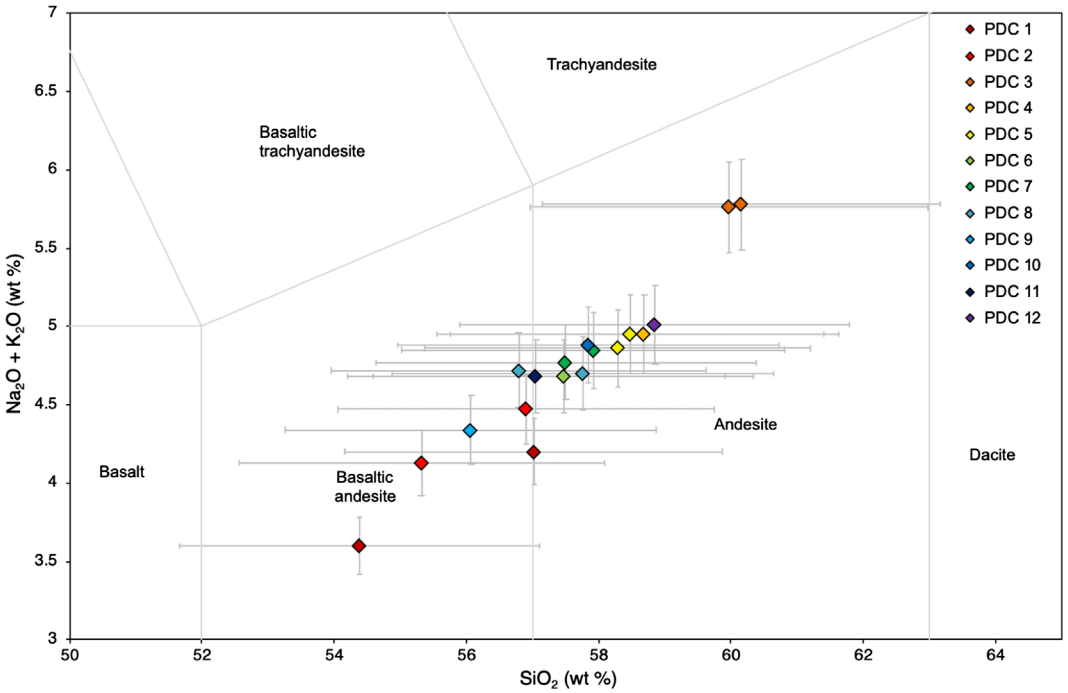

FIGURE 4 | Total alkali silica diagram showing the geochemical distribution of the pyroclastic density currents (PDCs) identified in this study. All samples fall within the basaltic andesite–andesite range, though the majority are andesite.

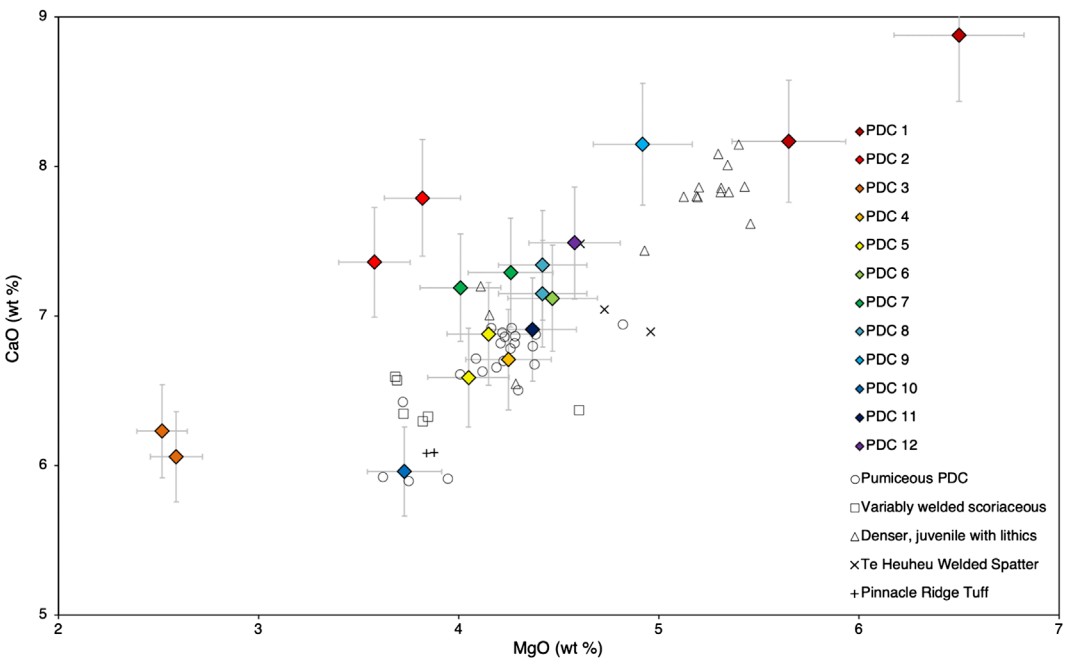

FIGURE 5 | MgO/CaO geochemical diagram comparing pyroclastic density currents (PDCs) identified by Cowlyn (2016) (black symbols), and those PDCs identified in this study (colored symbols). PDC 1, PDC 2, and PDC 3 are outside of the geochemical range identified by Cowlyn (2016). The majority of the other samples are within the range and follow the trend of increasing MgO/CaO. For raw geochemistry data, see Appendix 2 in **Supplementary Material**.

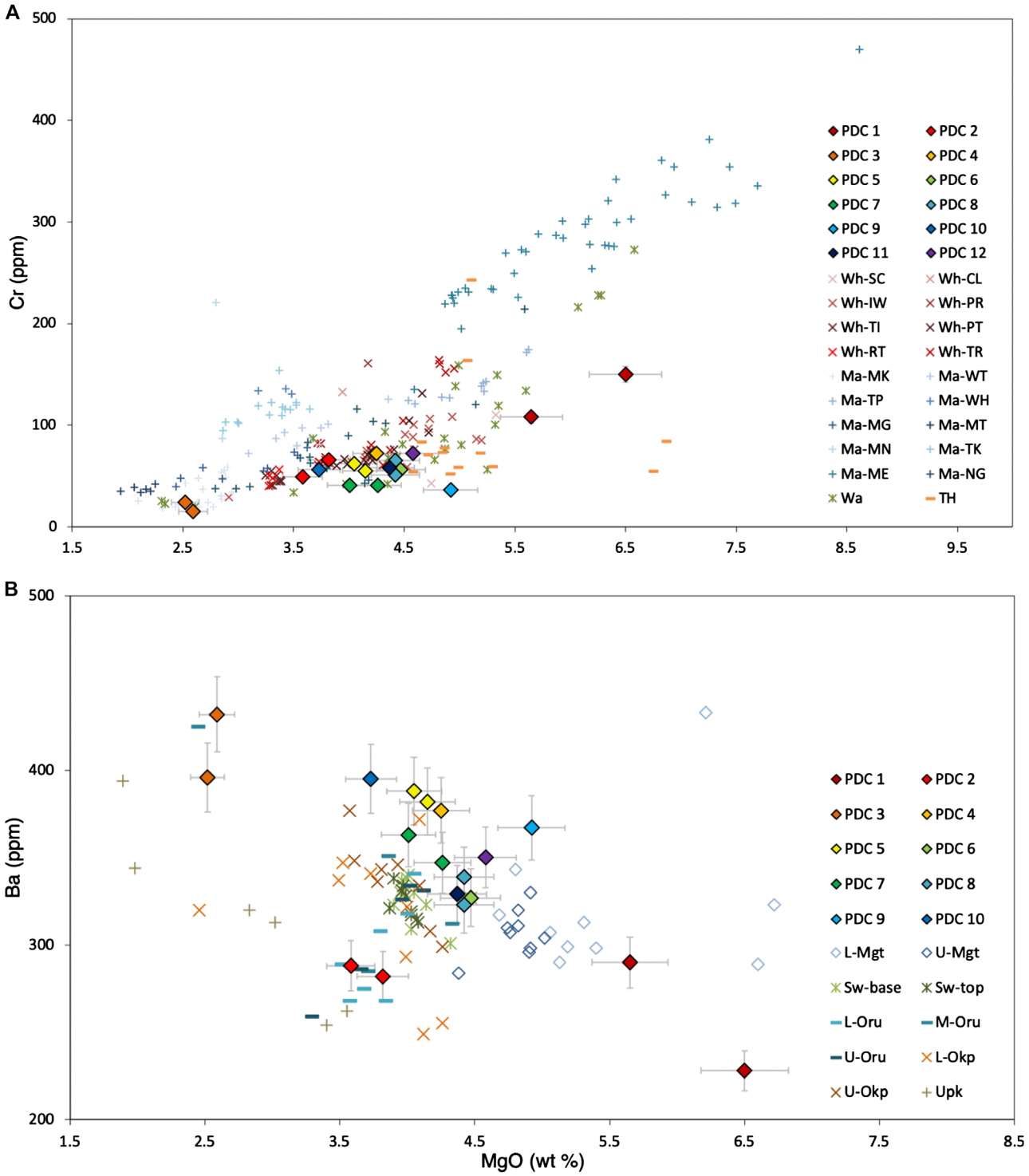

FIGURE 6 | Trace element graphs used to compare pyroclastic density current (PCD) deposits with formations identified by Conway et al. (2016) **(A)**, and Pardo et al. (2012a) **(B)**. For a summary of geochemical correlations between these formations and the PDC deposits, see **Table 1**. For raw trace element data see Appendix 2 in **Supplementary Material**.

TABLE 1 | Stratigraphic relationships of PDC deposits based on field observations and the geological map created by Townsend et al. (2017). Geochemical correlations for each deposit with formations and eruptive periods described by Conway et al. (2016) and Pardo et al. (2012a) are also summarized.

	Stratigraphic relationship			Geochemical correlations	
	Relative position	**Unit/formation**	**Age range**	**Pardo et al. (2012a)**	**Conway et al. (2016)**
PDC 1	Under	Wahianoa Fm	>160 ka	—	Wa TH
PDC 2	Within	Wahianoa Fm	160–115 ka	—	Wa
PDC 3	Under	Mangaheuheu member	>47 ka	—	Ma-MK, MG, NG Wa
PDC 4	Under	Iwikau member	>10 ka	Okp-U, L Oru, U, M, L	Wh-PT, TR Ma-NG Wa
PDC 5	Under	Iwikau member	>10 ka	Okp-U, L Oru-U, M, L	Wh-TR, PT Ma-NG Wa
PDC 6	Within	Undifferentiated fall deposits	<29 ka	Okp-U, L Oru-U, M, L	Wh-CL, IW, PT, TR
PDC 7	Within	Undifferentiated fall deposits	<29 ka	Okp-U, M, L Oru-U, L	Wh-IW, PT, TR
PDC 8	Within	Turoa member	17–10 ka	Okp-U, L	Wh-IW, PT, TR Ma-NG Wa
PDC 9	Above	Horonuku member	<16 ka	Okp-L	Wh-IW, PT, TR
PDC 10	Above	Glacial till deposits	< ~14.5 ka	Okp-U, L Oru-M, L	Wh-CL, IW, PT, TR
PDC 11	Above	Turoa member	<11.7 ka	Okp-U, L Oru-M	Wh-IW, TR
PDC 12	Above	Turoa member	<11.7 ka	Okp-U, L Oru-M	Wh-IW, PT, TR

PDC, pyroclastic density current; Okp, Okupata Eruptive Unit (~11.6 ka); Oru, Oruamatua Eruptive Unit (13.6–11.6 ka); Wh, Whakapapa Formation (<15 ka); IW, Iwikau eruptive package (<10 ka); PT, Paretetaitonga eruptive package (~15 ka); TR, Turoa eruptive package (17–10 ka); Ma, Mangawhero Formation (60–15 ka); MK, Makotuku eruptive package (24–16 ka); MG, Manganuitoteao eruptive package (30–22 ka); NG, Ngahuinga eruptive package (48–35 ka); Wa, Wahianoa Formation (160–115 ka); TH, Te Herenga Formation (250–180 ka).

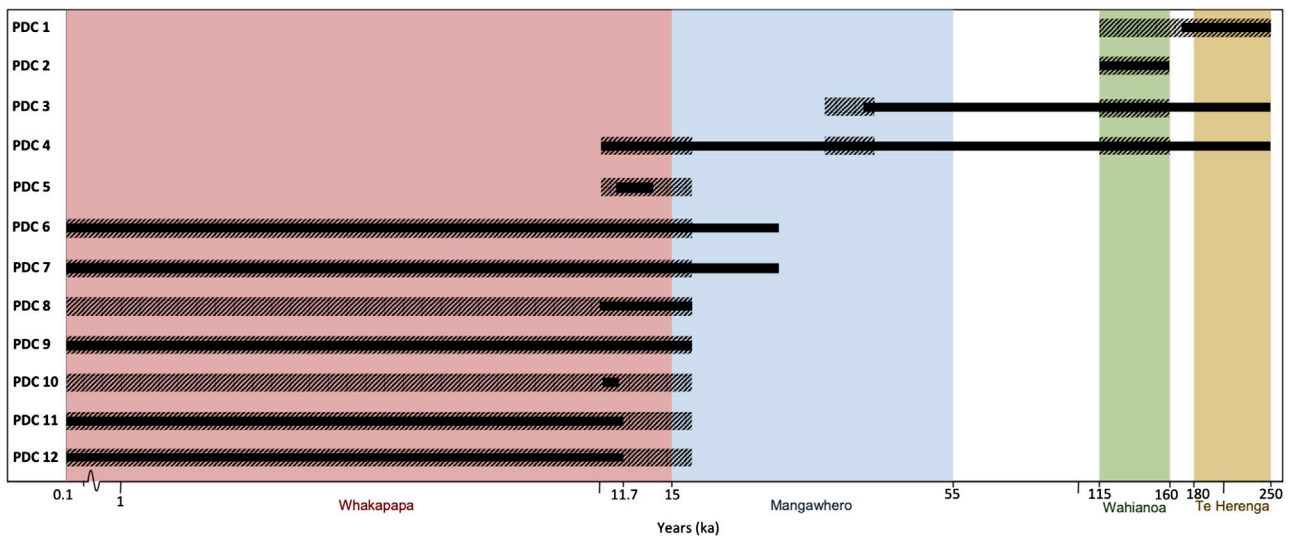

FIGURE 7 | Possible age ranges of pyroclastic density currents (PCDs) identified during this study. Age ranges are based on the relative stratigraphy (solid bars) with mapped units, and geochemical correlations to known eruptions (dashed bars). Trace element correlations that do not fall within the range of the stratigraphic age bracket have not been included. The stratigraphic constraints for PDC 5 and PDC 10 are based on the ages of Package 1 and Unit 4, respectively, as they are extensions of these PDC deposits identified by Cowlyn (2016). See **Table 1** for a summary of the stratigraphic relationships and geochemical correlations between the PDC deposits and known units and eruptive periods. Geological formations identified by Conway et al. (2016) are plotted along the age axis at a $\log_{10}$ scale. Geochemical data is from Pardo et al. (2014) and Conway et al. (2016). Relative stratigraphy is based on the geological map developed by Townsend et al. (2017).

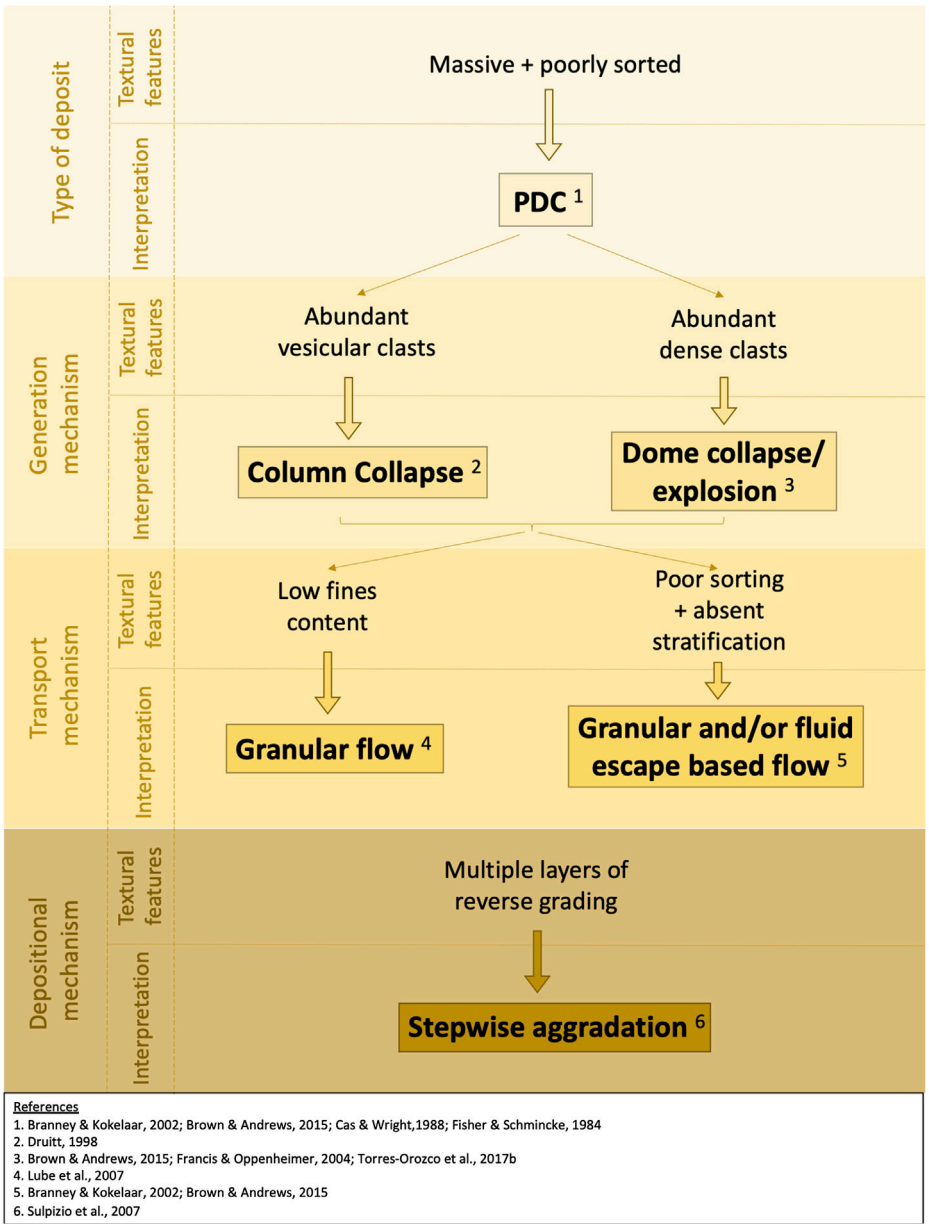

FIGURE 8 | Workflow chart outlining the textural characteristics used to interpret the deposit type, generation mechanism, transport mechanism, and depositional model for the lithofacies. Stepwise aggradation is attributed to one lithofacies as there was not enough textural data to interpret the depositional model in other facies. Interpretations are described in more detail in *Lithofacies*.

while the dense lithics are angular. The average vesicular clast density is 1.4 ± 0.036 g/cm^3.

Pyroclastic Density Current 10

Found in a small valley on the eastern flanks of the volcano, 6.3 km from the vent, this 1 m thick deposit is pale brown, and poorly indurated. The outcrop is poorly sorted, massive, matrix supported, and is primarily composed of ash and vesicular lapilli (**Figure 3J**). There are also occasional vesicular bombs within the deposit (<15 cm) that constitute 1% of the outcrop. The clasts are primarily sub-rounded, and the average density is 0.92 ± 0.089 g/cm^3.

PDC 10 is texturally similar to Unit 4 (Cowlyn, 2016), emplaced during the Taurewa eruptive period (~11.6 ka), and is located in a valley adjacent to this unit.

Pyroclastic Density Current 11

PDC 11, found 2.9 km from the vent, is a light brown, poorly indurated ~1 m thick deposit located as a single outcrop in a small depression on the south-western side of Mt. Ruapehu

TABLE 2 | Lithofacies classification system used to describe PDC deposits.

Volcanic facies	Blocks, lapilli, ash	Lapilli, ash
Clast supported	—	—
Pumice/scoria rich	—	—
1 massive	BLA1	—
Vesicular and dense clast rich	—	—
2 massive	BLA2	—
Matrix supported	—	—
Pumice/scoria rich	—	—
3 massive	BLA3	LA3
4 reverse	BLA4	—

Lithofacies type	PDC
BLA1	PDC 12
BLA2	PDC 3
BLA3	PDC 1, PDC 4, PDC 8, PDC 11
LA3	PDC 6, PDC 7, PDC 9, PDC 10
BLA4	PDC 1, PDC 2, PDC 5

PDC, pyroclastic density current.

(**Figure 3K**). The deposit has a small lobate front, and is massive, poorly sorted, and matrix supported. Clast sizes range between ash and blocks (<20 cm). The clasts are primarily sub-rounded though many are sub-angular where fragmentation has occurred. The entire deposit is rich in vesicular clasts, with only occasional dense lithic clasts appearing at the surface. The average vesicular clast density is 1.2 ± 0.043 g/cm^3.

Pyroclastic Density Current 12

This 1 m thick, 1 m wide deposit was found 1 km from the vent on the upper western side of Mt. Ruapehu, next to the Mangaturuturu Glacier. It is poorly sorted, massive, and clast supported. PDC 12 is primarily composed of black, vesicular, and sub-angular cauliflower bomb clasts (<50 cm) constituting for 60% of the deposit (**Figure 3L**). Vesicular lapilli and ash fill in the gaps between the larger clasts. The average clast density for this deposit is 1.1 ± 0.038 g/cm^3.

Geochemistry

We show the total alkali silica diagram for classification purposes (**Figure 4**) and follow Cowlyn (2016) by plotting CaO/MgO (**Figure 5**).

Figure 4 shows that all deposits fall within the basaltic andesite to andesite geochemical range. PDC 1 is basaltic andesite and has the lowest SiO_2 and $Na_2O + K_2O$ wt% values. The compositions increase linearly into andesite. PDC 3, an andesite, has the highest SiO_2 and $Na_2O + K_2O$ wt% values. The majority of the compositions are andesite and plot closely together near the boundary between basaltic andesite and andesite.

The compositional range of the samples in **Figure 5** is relatively small, with only 4 wt% SiO_2 separating the lowest and highest sample. PDC 3 shows the lowest CaO and MgO wt% values, while PDC 1 displays the highest values. PDC 5 has a similar composition to the pumiceous PDC group identified by Cowlyn (2016) especially samples from Package 1. PDC 10 correlates with Unit 4 of the pumiceous PDC group and is separate from the other deposit compositions. Many of the deposits in this study have marginally higher CaO values than most of those identified by Cowlyn (2016).

Figure 6 shows two examples of the trace elements graphs used to compare the PDC deposits in this paper against the lava flow units from Conway et al. (2016) (**Figure 6A**) and explosive eruptive units from Pardo et al. (2012a) (**Figure 6B**). **Figure 6A** displays an overall positive linear trend, where Cr (ppm) increases with increasing MgO (wt%). This figure also shows PDC 1 within the range of the Te Herenga and Wahianoa Formations. This similarity can also be seen when using other trace elements. The remaining PDC deposits frequently occur within the ranges of multiple formations. **Figure 6B** shows an overall negative linear trend, with decreasing Ba (ppm) as MgO (wt%) increases. The majority of the PDC deposits fall frequently within the range of the Okupata-Pourahu and Oruamatua Eruptive Units. Like **Figure 6A**, the PDC deposits in **Figure 6B** plot within the geochemical ranges of multiple eruptive units. This makes it difficult to geochemically correlate the PDC deposits with specific eruptive units.

Deposit Ages

Table 1 provides a summary of the relative stratigraphy and geochemical correlations with dated units used to provide an approximate age range for the deposits identified in this study. The pyroclastic deposits identified in this study have been erupted throughout Mt. Ruapehu's history. PDC 1, the oldest identified deposit, is located underneath thick lava flows from the Wahianoa Formation (115–160 ka). This suggests it was emplaced prior to 160 ka, and hence, within the Te Herenga Formation (180–250 ka) (**Figure 7**). This is supported by geochemical similarities between PDC 1 and the Te Herenga Formation (**Figure 6A**) (Conway et al., 2016; Townsend et al., 2017). The next oldest deposit, PDC 2, was observed above and below lava flows associated with the Wahianoa Formation (Conway et al., 2016; Townsend et al., 2017). Geochemically, this deposit also correlates with the Wahianoa Formation geochemistry (**Figure 6A**). Two other deposits, PDC 3 and PDC 4, were identified beneath lava flows from the Mangaheuheu Member (47–40 ka) in the Mangawhero Formation, and the Iwikau Member (<10 ka) in the Whakapapa Formation, respectively, (Conway et al., 2016; Townsend et al., 2017).

Eight (66%) of the deposits were emplaced during the Whakapapa Formation. Many of these deposits were found overlying lava flows from the Turoa (17–10 ka) and Horonuku (29–16 ka) Members. PDC 6 and PDC 7 were found within undifferentiated fall deposits (<29 ka) (Townsend et al., 2017). PDC 5 is texturally and geochemically similar to Package 1 (Cowlyn, 2016). This deposit is found above lava flows associated with the Turoa Member (17 and 10 ka). Based on the similarities in texture and geochemistry, and overlap in age ranges, the approximate age of PDC 5 is based on that of Package 1 (~13.6–11.6 ka) (Cowlyn, 2016). PDC 10 closely resembles Unit 4, texturally and geochemically (Cowlyn, 2016). This deposit was emplaced above glacial till deposits (14.5–45 ka) (Townsend et al., 2017). Due to the similarities in geochemistry and textures, and

the overlap in relative stratigraphic ages, the age range for PDC 10 is based on Unit 4 (~11.6 ka) (Cowlyn, 2016).

DISCUSSION

Lithofacies

Here we describe the lithofacies for each deposit (**Table 2**) based on the textural characteristics observed in the field and interpret the PDC behavior based on these facies. The lithofacies classification is based on techniques used by Torres-Orozco et al. (2018) and Németh and White (2003). In **Table 2**, deposits that were rich in grainsizes ranging from blocks to ash, were given the code BLA (blocks, lapilli, ash). Deposits that were primarily lapilli and ash rich (containing <3% blocks) have the code LA (lapilli, ash). The grouping method was further separated into clast supported and matrix supported deposits. In each of those groups, there are subgroups for the dominant clast type. This includes pumice/scoria-rich, or rich in both vesicular clasts and dense clasts. The matrix supported group only has one subgroup as there were no matrix supported deposits that were rich in dense and vesicular clasts. Grading is included in this classification scheme to help infer the PDC behavior at the locations they were deposited. The textural characteristics and interpretations of generation, transport, and deposition mechanism are collated in **Figure 8**.

BLA1

Description

This lithofacies was only found in PDC 12 in a topographic low. This facies is found proximally, 1 km from the vent. BLA1 is poorly sorted, massive, and clast supported. Less than 20% of ash was observed in this deposit. This facies consists of vesicular clasts with grainsizes ranging from blocks to ash. Clasts in this facies are black, sub-angular, and cauliflower bombs.

Interpretation

The proximity of the deposit to the vent (1 km) may indicate that this facies was deposited as proximal fall or ballistics. However, the presence of lapilli and ash infilling the gaps between the larger clasts indicates that this deposit may instead originate from a PDC (Branney and Kokelaar, 2002). The low fines content and large proportion of very coarse clasts suggest that this facies may have been transported by a granular flow regime where gas-fluidization was subordinate during transport and deposition (Lube et al., 2007). The absence of gas-escape structures also supports this interpretation.

BLA2

Description

BLA2 was only found in PDC 3 in a valley. This facies is found proximally, approximately 3 km from the vent. The deposit in this lithofacies is characterized as massive, clast supported, and rich in vesicular and dense clasts. Grainsizes range from blocks to ash. Vesicular clasts, which comprise approximately 30% of the deposit, are primarily sub-rounded, whereas the dense clasts are angular to sub-angular.

Interpretation

As this lithofacies is poorly sorted and massive, it has been inferred as a deposit from a concentrated PDC (Fisher and Schmincke, 1984; Branney and Kokelaar, 2002; Cas and Wright, 1988; Brown and Andrews, 2015). The scarcity of fine material, and absence of fluid-escape structures in this facies suggest that it may have been deposited under a granular flow regime where there was little fine ash to help facilitate gas-fluidization processes (Lube et al., 2007). The red and pink coloration observed in the deposit may have originated during PDC deposition. When freshly emplaced hot PDC deposits come into contact with water, steam is produced. As this steam rises through the deposit, it causes rapid thermal oxidation of iron within the deposit, resulting in a red coloration (Fisher and Schmincke, 1984; Francis and Oppenheimer, 2004; Cas and Wright, 1988). The abundance of dense clasts in this deposit indicates that it formed during a lava dome collapse or lava dome explosion PDC (Francis and Oppenheimer, 2004; Brown and Andrews, 2015; Torres-Orozco et al., 2017b). The significant proportion of vesicular clasts in this facies indicates that there may have been continued vesiculation of the erupted material after fragmentation of the lava dome (Brown and Andrews, 2015).

BLA3

Description

The BLA3 lithofacies was observed in four deposits (PDC 1, 4, 8, and 11), all of which occur in valleys. The facies is in the proximal to medial region, with deposits occurring between 3 and 7 km from the vent. The deposits are massive, matrix supported, and poorly sorted. This facies is rich in vesicular clasts, with few dense clasts. Grainsizes range from blocks (<65 cm) to ash. Clasts in this facies are primarily sub-rounded to well rounded.

Interpretation

The poorly sorted and massive characteristics suggests that this lithofacies was emplaced by PDCs (Fisher and Schmincke, 1984; Branney and Kokelaar, 2002; Cas and Wright, 1988; Brown and Andrews, 2015). The abundant vesicular clasts and scarcity of dense clasts indicates that the deposit may have been emplaced during a column collapse PDC (Druitt, 1998). The poor sorting and absence of stratification implies the PDC may have been concentrated with a granular fluid-based flow regime, where granular and/or fluid-escape processes may be predominant at different levels within the flow (Branney and Kokelaar, 2002; Brown and Andrews, 2015). Due to the lack of textural data we are unable to conclude that one transport mechanism was dominant over the other, so we include both mechanisms in these interpretations. No directional fabrics were observed in these facies which indicates that the grains in the flow did not experience significant shear as they were deposited, possibly due to deposition in a valley bottom or on low angle slopes (Branney and Kokelaar, 2002).

LA3

Description

This lithofacies was found in four deposits (PDC 6, 7, 9, and 10), which occur in small valleys and on topographic highs. LA3 is found in the upper medial region, with deposits occurring between 5 and 8 km from the vent. This facies is massive, matrix supported,

poorly sorted, and rich in vesicular clasts. Occasional dense clasts also occur. Grainsizes primarily range from ash to lapilli, with <3% blocks in the deposits. Clasts are sub-rounded to sub-angular.

Interpretation

Like BLA3, the poor sorting and massive nature of the deposits suggest that this lithofacies was emplaced during PDCs (Fisher and Schmincke, 1984; Branney and Kokelaar, 2002; Cas and Wright, 1988; Brown and Andrews, 2015). Based on the highly vesicular clasts, and scarcity of dense clasts, LA3 may have been deposited during a column collapse PDC (Druitt, 1998). The lack of stratification and poor sorting also suggest that this facies may have been emplaced from a granular fluid-based flow regime (Branney and Kokelaar, 2002; Brown and Andrews, 2015). The smaller average grainsize in this facies may be a result of the flow's inability to carry larger clasts, possibly due to a less energetic eruption or the distance traveled from the vent (Brown and Andrews, 2015), or a combination of both.

BLA4

Description

The BLA4 lithofacies is found in three deposits (PDC 1, 2, and 5), occurring in valleys and on valley sides. This facies is located in the proximal to medial region, found between 2 and 7 km from the vent. The deposits in this lithofacies are characterized as reverse graded, matrix supported, and poorly sorted. They are rich in vesicular clasts, and grainsizes range from blocks to ash. Occasional dense clasts also occur in this facies. Vesicular clasts are primarily sub-rounded.

Interpretation

The combination of poor sorting, and reverse grading suggests that this lithofacies was produced by a PDC (Branney and Kokelaar, 2002; Cas and Wright, 1988). The poor sorting and absence of stratification in this lithofacies indicate a potentially concentrated PDC with a granular fluid-based flow regime (Druitt, 1998; Branney and Kokelaar, 2002; Brown and Andrews, 2015). If transport was dominated by grain-to-grain interactions then reverse grading may have formed through kinetic sieving due to the dispersive pressure created during the flow (Sulpizio et al., 2014). Clast vibrations in the PDC generates pressure which inflates the granular mass. This dispersive pressure promotes the segregation of small particles downward into the gaps between larger particles, leaving the larger clasts toward the top of the flow-boundary zone. If this facies transport was instead dominated by fluid-escape processes the reverse grading may have been formed through floating processes due to the density contrast between the vesicular clasts and matrix of the flow (Branney and Kokelaar, 2002; Sulpizio et al., 2014). The presence of multiple layers of reverse grading in one of the deposits suggests that this lithofacies may have been emplaced through stepwise aggradation, where the main flow was deposited as several pulses, each displaying reverse grading (Sulpizio et al., 2007).

Limitations

In addition to the limitations associated with each individual method, there were other limitations that hindered the use of partial outcrops to make implications.

The short time frame, limited funds, and breadth of this study resulted in a restricted methodology, where some analyses, such as absolute age dating, were unable to be conducted. Age estimation based on stratigraphy and geochemistry had to be utilized instead. Due to the short time frame, only locations where PDC deposits were suspected were visited, leaving much of Mt. Ruapehu unexplored. Therefore, many PDC deposits may not have been located, leading to an underestimation of the PDC occurrence.

Most identified outcrops have been heavily eroded with little of the original deposit remaining. This limited the representativeness of field observations as the thickness and extent has been reduced over time. These small outcrops also made characterisation of the deposit difficult, as there was often not enough of the deposit exposed to see a cross-sectional view or spatial variations within the flow. This also hindered lithofacies interpretations. The scarcity of prehistoric PDC deposits also limits the estimation of PDC occurrence and frequency on Mt. Ruapehu.

Despite these limitations, this paper provides descriptions and characteristics of previously unstudied PDC deposits. This information acts as a foundation for further studies of PDCs on Mt. Ruapehu.

CONCLUSION

The updated PDC record presented here builds on previous work and extends the PDC history of Mt. Ruapehu. The main conclusions drawn from this study are as follows:

- Twelve new PDC deposits were identified. When combined with the deposits identified by Cowlyn (2016), taking into account some deposits that are extensions of their flows, and the known 1945 PDC, this is a total of 23 PDCs identified during these two studies. These were all emplaced during the past 250 ka years, and most in the past 15 ka years. Due to the poor preservation of pyroclastic material on glaciated volcanoes such as Mt. Ruapehu it is likely that many past PDCs deposits have been completely removed from the rock record. It is also likely that, due to the large field area of this project, other PDC deposits have been overlooked. These limitations have contributed to an underestimation of the PDC hazard on Mt. Ruapehu.
- PDC lithofacies at Mt. Ruapehu range from massive, clast supported deposits rich in vesicular and dense blocks and ash; to massive, matrix supported deposits dominated by vesicular lapilli and ash. Based on lithofacies characteristics the PDCs were identified as concentrated flows, with most dominated by granular fluid-based transport regimes. Two PDCs were dominated by granular flow regimes. These lithofacies also suggest that Mt. Ruapehu has erupted PDCs of varying styles, including column collapse and dome collapse or explosion. This proves that Ruapehu is capable of producing a wide spectrum of different PDCs, something that must be considered during future hazard planning on the volcano.

- This work extends the knowledge of PDCs on Mt. Ruapehu to >180 ka. Consistent with findings of Cowlyn (2016) and Pardo et al. (2012b) there is an abundance of PDCs after 15 ka. We conclude that this is likely due to poor preservation of deposits during glacial maximums on the mountain prior to this time. Poor preservation, particularly of small volume PDCs, needs to be considered in the future when attempting to quantify the frequency of PDCs at Mt. Ruapehu and at other volcanoes.
- This study highlights the importance of recognizing small to medium sized PDCs in the eruptive record at any volcano, especially where erosion or other processes may have played a substantial role in removing evidence of past events. Small PDC deposits may be heavily eroded, making them difficult to identify in the field. Techniques such as lithofacies classification may help in identifying and characterizing these PDC deposits and provide useful information for future hazard planning.

Overall, the evidence presented here necessitates continued comprehensive studies at Mt. Ruapehu to gain a better understanding of future PDC occurrence, and the threat they pose to nearby infrastructure and communities.

DATA AVAILABILITY STATEMENT

All datasets generated for this study are included in the article/ **Supplementary Material**.

AUTHOR CONTRIBUTIONS

BK conceptualized the study. JG and BK conducted field work. GL provided logistical support prior to field work and background knowledge on the field area. JC contributed knowledge of previous studies. JG completed analyses and wrote the first draft of the manuscript. All authors contributed to interpretations and manuscript revision.

FUNDING

This research was assisted through funding from the University of Canterbury Mason Trust Fund and the Project Tongariro Memorial Award which supported field work and logistical arrangements.

ACKNOWLEDGMENTS

We thank the NZ Department of Conservation and local iwi Ngāti Rangi and Ngāti Tuwharetoa for sampling permits, allowing access onto the land, blessing our samples, and introducing us to the cultural significance of Mt Ruapehu. Also Georg Zellmer and Anja Moebis from Massey University for assistance with geochemistry analyses, and the technical staff at the University of Canterbury for help with sample preparation and field work support. We also greatly appreciate the logistical support and detailed feedback of early versions of this manuscript from Dougal Townsend. BK also acknowledges GNS-RNC047, Resilience National Science Challenge: Volcanism theme. We would also like to thank the reviewers and editors for their time, patience and constructive feedback, which led to significant improvements in this paper.

SUPPLEMENTARY MATERIAL

The Supplementary Material for this article can be found online at: https://www.frontiersin.org/articles/10.3389/feart.2020.542932/full#supplementary-material

REFERENCES

Auker, M. R., Sparks, R. S. J., Siebert, L., Crosweller, H. S., and Ewert, J. (2013). A statistical analysis of the global historical volcanic fatalities record. *J. Appl. Volcanol.* 2, 1–24. doi:10.1186/2191-5040-2-2

Barker, S. J., Rotella, M. D., Wilson, C. J. N., Wright, I. C., and Wysoczanski, R. J. (2012). Contrasting pyroclast density spectra from subaerial and submarine silicic eruptions in the Kermadec arc: implications for eruption processes and dredge sampling. *Bull. Volcanol.* 74, 1425–1443. doi:10.1007/s00445-012-0604-2

Branney, M. J., and Kokelaar, B. P. (2002). *Pyroclastic density currents and the sedimentation of ignimbrites*. London, UK: Geological Society.

Brown, R. J., and Andrews, G. D. (2015). "Deposits of pyroclastic density currents," in *Encyclopedia of volcanoes*. 2nd Edn, Editors H. Sigurdsson, B. F. Houghton, S. Mcnutt, H. Rymer and J. Stix (San Diego, CA: Academic Press), 631–648.

Brown, R. J., and Branney, M. J. (2004). Event-stratigraphy of a caldera-forming ignimbrite eruption on Tenerife: the 273 ka Poris Formation. *Bull. Volcanol.* 66, 392–416. doi:10.1007/s00445-003-0321-y

Buchwaldt, R. (2013). "Pyroclastic flow," in *Encyclopedia of natural hazards*. Editor P. T. Bobrowsky (Dordrecht, The Netherlands: Springer).

Calder, E. S., Sparks, R. S. J., and Gardeweg, M. C. (2000). Erosion, transport and segregation of pumice and lithic clasts in pyroclastic flows inferred from ignimbrite at Lascar Volcano, Chile. *J. Volcanol. Geoth. Res.* 104, 201–235. doi:10.1016/s0377-0273(00)00207-9

Cas, R. A. F., and Wright, J. V. (1988). *Volcanic successions, modern and ancient: a geological approach to processes, products, and successions*. London, Boston: Allen & Unwin/Chapman & Hall.

Charbonnier, S. J., and Gertisser, R. (2011). Deposit architecture and dynamics of the 2006 block-and-ash flows of Merapi Volcano, Java, Indonesia. *Sedimentology* 58, 1573–1612. doi:10.1111/j.1365-3091.2011.01226.x

Conway, C. E., Leonard, G. S., Townsend, D. B., Calvert, A. T., Wilson, C. J. N., Gamble, J. A., et al. (2016). A high-resolution 40Ar/39Ar lava chronology and edifice construction history for Ruapehu volcano, New Zealand. *J. Volcanol. Geoth. Res.* 327, 152–179. doi:10.1016/j.jvolgeores.2016.07.006

Cowlyn, J. D. (2016). Pyroclastic density currents at Ruapehu volcano; New Zealand. PhD thesis. Christchurch: University of Canterbury.

Degruyter, W., and Bonadonna, C. (2013). Impact of wind on the condition for column collapse of volcanic plumes. *Earth Planet. Sci. Lett.* 377–378, 218–226. doi:10.1016/j.epsl.2013.06.041

Donoghue, S. L., Gamble, J. A., Palmer, A. S., and Stewart, R. B. (1995). Magma mingling in an andesite pyroclastic flow of the Pourahu Member, Ruapehu volcano, New Zealand. *J. Volcanol. Geoth. Res.* 68, 177–191. doi:10.1016/0377-0273(95)00012-j

Donoghue, S. L., Palmer, A. S., Mcclelland, E., Hobson, K., Stewart, R. B., Neall, V. E., et al. (1999). The Taurewa Eruptive Episode: evidence for climactic

eruptions at Ruapehu volcano, New Zealand. *Bull. Volcanol.* 61, 223–240. doi:10.1007/s004450050273

Druitt, T. H. (1998). "Pyroclastic density currents," in The Physics of Explosive Volcanic Eruptions: Geological Society of London Special Publication. Editors J. Gilbert, R. S. J. Sparks (Bath), Vol. 145, 145–182.

Dufek, J., Ongaro, T. E., and Roche, O. (2015). "Pyroclastic density currents: processes and models," in The Encyclopedia of Volcanoes. (Academic Press), 617–629.

Fisher, R. V., and Schmincke, H.-U. (1984). *Pyroclastic rocks*. Berlin, Germany: Springer.

Francis, P., and Oppenheimer, C. (2004). *Volcanoes*. Oxford, UK: Oxford University Press.

Hackett, W. R. (1985). Geology and petrology of Ruapehu volcano and related vents. PhD thesis. Wellington: Victoria University of Wellington.

Hackett, W. R., and Houghton, B. F. (1989). A facies model for a quaternary andesitic composite volcano: Ruapehu, New Zealand. *Bull. Volcanol.* 51, 51–68. doi:10.1007/bf01086761

Houghton, B. F., Latter, J. H., and Hackett, W. R. (1987). Volcanic hazard assessment for Ruapehu composite volcano, taupo volcanic zone, New Zealand. *Bull. Volcanol.* 49, 737–751. doi:10.1007/bf01079825

Houghton, B. F., and Wilson, C. J. N. (1989). A vesicularity index for pyroclastic deposits. *Bull. Volcanol.* 51, 451–462. doi:10.1007/bf01078811

Johnston, D. M., Houghton, B. F., Neall, V. E., Ronan, K. R., and Paton, D. (2000). Impacts of the 1945 and 1995-1996 Ruapehu eruptions, New Zealand: an example of increasing societal vulnerability. *Geol. Soc. Am. Bull.* 112, 720–726. doi:10.1130/0016-7606(2000)112<720:iotare>2.0.co;2

Johnston, D. M., and Neall, V. E. (1995). *Ruapehu awakens: the 1945 eruption of Ruapehu*. Issue 1 of Science Centre and Manawatu Museum Scientific Monograph. Palmerston North, New Zealand: Science Centre and Manawatu Museum.

Kilgour, G., Blundy, J., Cashman, K., and Mader, H. M. (2013). Small volume andesite magmas and melt-mush interactions at Ruapehu, New Zealand: evidence from melt inclusions. *Contrib. Mineral. Petrol.* 166, 371–392. doi:10.1007/s00410-013-0880-7

Lube, G., Cronin, S. J., Platz, T., Freundt, A., Procter, J. N., Henderson, C., et al. (2007). Flow and deposition of pyroclastic granular flows: a type example from the 1975 Ngauruhoe eruption, New Zealand. *J. Volcanol. Geoth. Res.* 161, 165–186. doi:10.1016/j.jvolgeores.2006.12.003

Lube, G., Cronin, S. J., Thouret, J.-C., and Surono, S. (2011). Kinematic characteristics of pyroclastic density currents at Merapi and controls on their avulsion from natural and engineered channels. *Geol. Soc. Am. Bull.* 123, 1127–1140. doi:10.1130/b30244.1

Manville, V., Hodgson, K. A., Houghton, B. F., Keys, J. R., and White, J. D. L. (2000). Tephra, snow and water: complex sedimentary responses at an active snow-capped stratovolcano, Ruapehu, New Zealand. *Bull. Volcanol.* 62, 278–293. doi:10.1007/s004450000096

Németh, K., and White, J. D. L. (2003). Reconstructing eruption processes of a Miocene monogenetic volcanic field from vent remnants: Waipiata volcanic field, South Island, New Zealand. *J. Volcanol. Geoth. Res.* 124, 1–21. doi:10.1016/s0377-0273(03)00042-8

Pardo, N. (2012). Andesitic Plinian eruptions at Mt. Ruapehu (New Zealand): from lithofacies to eruption dynamics. PhD in earth science. Palmerston North: Massey University.

Pardo, N., Cronin, S. J., Palmer, A., and Németh, K. (2012a). Reconstructing the largest explosive eruptions of Mt. Ruapehu, New Zealand: lithostratigraphic tools to understand subplinian-plinian eruptions at andesitic volcanoes. *Bull. Volcanol.* 74, 617–640. doi:10.1007/s00445-011-0555-z

Pardo, N., Cronin, S. J., Palmer, A., Procter, J., and Smith, I. (2012b). Andesitic Plinian eruptions at Mt. Ruapehu: quantifying the uppermost limits of eruptive parameters. *Bull. Volcanol.* 74, 1161–1185. doi:10.1007/s00445-012-0588-y

Pardo, N., Cronin, S. J., Wright, H. M. N., Schipper, C. I., Smith, I., and Stewart, B. (2014). Pyroclast textural variation as an indicator of eruption column steadiness in andesitic Plinian eruptions at Mt. Ruapehu. *Bull. Volcanol.* 76, 1–19. doi:10.1007/s00445-014-0822-x

Price, R. C., Gamble, J. A., Smith, I. E. M., Maas, R., Waight, T., Stewart, R. B., et al. (2012). The anatomy of an andesite volcano: a time-stratigraphic study of andesite petrogenesis and crustal evolution at Ruapehu volcano, New Zealand. *J. Petrol.* 53, 2139–2189. doi:10.1093/petrology/egs050

Stinton, A. J., and Sheridan, M. F. (2008). Implications of long-term changes in valley geomorphology on the behavior of small-volume pyroclastic flows. *J. Volcanol. Geoth. Res.* 176, 134–140. doi:10.1016/j.jvolgeores.2008.01.010

Sulpizio, R., Dellino, P., Doronzo, D. M., and Sarocchi, D. (2014). Pyroclastic density currents: state of the art and perspectives. *J. Volcanol. Geoth. Res.* 283, 36–65. doi:10.1016/j.jvolgeores.2014.06.014

Sulpizio, R., Mele, D., Dellino, P., and La Volpe, L. (2007). Deposits and physical properties of pyroclastic density currents during complex Subplinian eruptions: the AD 472 (Pollena) eruption of Somma-Vesuvius, Italy. *Sedimentology* 54, 607–635. doi:10.1111/j.1365-3091.2006.00852.x

Terry, R. D., Chilingar, G. V., and Hancock, A. (1955). Summary of "Concerning some additional aids in studying sedimentary formations," by M. S. Shvetsov. *J. Sediment. Res.* 25, 229–234. doi:10.1306/74d70466-2b21-11d7-8648000102c1865d

Torres-Orozco, R., Cronin, S. J., Damaschke, M., and Pardo, N. (2017a). Diverse dynamics of Holocene mafic-intermediate Plinian eruptions at Mt. Taranaki (Egmont), New Zealand. *Bull. Volcanol.* 79, 1–27. doi:10.1007/s00445-017-1162-4

Torres-Orozco, R., Cronin, S. J., Pardo, N., and Palmer, A. S. (2017b). New insights into Holocene eruption episodes from proximal deposit sequences at Mt. Taranaki (Egmont), New Zealand. *Bull. Volcanol.* 79, 1–25. doi:10.1007/s00445-016-1085-5

Torres-Orozco, R., Cronin, S. J., Pardo, N., and Palmer, A. S. (2018). Volcanic hazard scenarios for multiphase andesitic Plinian eruptions from lithostratigraphy: insights into pyroclastic density current diversity at Mount Taranaki, New Zealand. *Bull. Geol. Soc. Am.* 130, 1645–1663. doi:10.1130/b31850.1

Townsend, D. B., Leonard, G. S., Conway, C. E., Eaves, S. R., and Wilson, C. J. N. (2017). *Geology of the Tongariro National Park area*. GNS Science geological map 4. Lower Hutt, New Zealand: GNS Science.

Valentine, G. A., Perry, F. V., and Woldegabriel, G. (2000). Field characteristics of deposits from spatter-rich pyroclastic density currents at Summer Coon volcano, Colorado. *J. Volcanol. Geoth. Res.* 104, 187–199. doi:10.1016/s0377-0273(00)00206-7

Waitt, R. B., Jr. (1981). Devastating pyroclastic density flow and attendant air fall of May 18 - stratigraphy and sedimentology of deposits. Editors P. W., Lipman and D. R., Mullineaux, The 1980 eruptions of Mount St. Helens, (Washington: U.S. Geological Survey Professional Paper 1250), 439–460.

Conflict of Interest: GL was employed by the company GNS Science. The remaining authors declare that the research was conducted in the absence of any commercial or financial relationships that could be construed as a potential conflict of interest.

frontiers in Earth Science

ORIGINAL RESEARCH
published: 19 October 2020
doi: 10.3389/feart.2020.543399

The Magnitude of the 39.8 ka Campanian Ignimbrite Eruption, Italy: Method, Uncertainties and Errors

Aurora Silleni[1,2]*, *Guido Giordano*[1], *Roberto Isaia*[3] and *Michael H. Ort*[2]

[1]Dipartimento di Scienze, Università di Roma Tre, Rome, Italy, [2]School of Earth and Sustainability, Northern Arizona University, Flagstaff, AZ, United States, [3]Istituto Nazionale di Geofisica e Vulcanologia, Osservatorio Vesuviano, Naples, Italy

The calculation of the magnitude of an eruption needs the accurate estimate of its deposit volume. This is particularly critical for ignimbrites as no methods for their volume calculations and associated errors and uncertainties are consolidated in the literature, although invariably the largest magnitude eruptions on Earth are made of ignimbrites. The 39.8 ka Campanian Ignimbrite (CI) eruption is the largest of the Campi Flegrei caldera (Italy). The global cooling following the CI eruption and its widespread tephra affected the paleoenvironment and the migration of hominids in Europe at that time. Despite the large number of studies, the estimates of the Dense Rock Equivalent volume of the CI range between 60 and 300 km^3, because of the lack of clear and reproducible methods for its calculation. Here we present a new calculation of the volume of the CI, grounded on a clear and reproducible method that can be applied universally and which provides an accurate estimation of the volume of the deposits on ground and their uncertainties and errors, allowing a strong base for further estimates of the amount of deposits eroded, covered, elutriated, which are essential for the final computation of the eruption magnitude. In order to calculate the CI volume, we reconstructed the first total isopach map of the pyroclastic density current deposit preserved on land, developed through a method that reconstructs the paleo-topography during the eruption, which is reproducible for all topographically controlled ignimbrites and allows the calculation of well-defined uncertainties in the on-land ignimbrite deposits. The preserved total extra-caldera bulk volume of the ignimbrite is estimated at 68.2 ± 6.6 km^3. The total pyroclastic density current deposit volume is then corrected for erosion, ash elutriation, the intracaldera deposit volume, and the volume of tephra deposited in the sea, whereas volumes of the basal fallout deposits are taken from other studies. The total Dense Rock Equivalent volume of the eruption is 181–265 km^3, whose range accounts for errors and uncertainties. This value corresponds to a mass of 4.7–6.9 × 10^{14} kg, a magnitude (M) of 7.7–7.8 and a volcanic Explosivity Index (VEI) of 7.

Keywords: Campanian Ignimbrite, Campi Flegrei, isopach maps, ignimbrite volumes, pyroclastic density currents, super-eruption

OPEN ACCESS

Edited by:
Pablo Tierz,
British Geological Survey,
The Lyell Centre, United Kingdom

Reviewed by:
Colin J. N. Wilson,
Victoria University of Wellington, New Zealand
Biagio Giaccio,
Instituto di Geologia Ambientale e Geoingegneria (IGAG), Italy
Samantha Engwell,
British Geological Survey (BGS), United Kingdom

***Correspondence:**
Aurora Silleni
Aurora.Silleni@nau.edu

Specialty section:
This article was submitted to Volcanology, a section of the journal Frontiers in Earth Science

Received: *16 March 2020*
Accepted: *14 September 2020*
Published: *19 October 2020*

Citation:
Silleni A, Giordano G, Isaia R and Ort MH (2020) The Magnitude of the 39.8 ka Campanian Ignimbrite Eruption, Italy: Method, Uncertainties and Errors. Front. Earth Sci. 8:543399. doi: 10.3389/feart.2020.543399

INTRODUCTION

Pyroclastic density currents (PDCs) have large impacts on human communities and the environment; they can cause catastrophic environmental and property damage and loss of life, as well as accounting for a large proportion of deaths caused by direct volcanic activity. From 1500 to 2017 CE, 28% of volcano-induced mortality resulted from PDCs, second only to famine and epidemic disease (Auker et al., 2013 and references therein; Brown et al., 2017). Moreover, global and regional climatic effects can result from the injection of ash and sulfur aerosols into the stratosphere during large explosive eruptions, leading to a "volcanic winter" (Rampino and Self, 1992; Stuiver et al., 1995; Thordarson and Self, 1996; Robock, 2000). The quantitative computation of the size of explosive eruptions is essential to understand their potential impact on humans, climate and ecosystems (e.g., Mason et al., 2004). Calculating the volume of large volcanic eruptions is in fact necessary to define their size (e.g., Newhall and Self, 1982; Pyle, 2000; Crosweller et al., 2012; Pyle, 2015) and to model the climate effects of these natural phenomena that occurred in the past.

Caldera-forming eruptions produce both fall deposits and ignimbrites (Parfitt and Wilson, 2008), and typically the largest proportion of volcanic material is transported in PDCs and emplaced as ignimbrites (e.g., the Oruanui eruption; Wilson, 1991; the Otowi Member of the Bandelier Tuff; Cook et al., 2016). The tephra fall deposits are analyzed through field and statistical techniques to make isopach maps directly from thickness data (e.g., Walker and Croasdale, 1970; Walker, 1973; Rhoades et al., 2002; Burden et al., 2013; Engwell et al., 2015; Yang and Bursik, 2016; Cutler et al., 2020), from which numerical models can be used to calculate total volumes (Bonadonna et al., 1998; Bonadonna and Phillips, 2003; Bonadonna and Houghton, 2005; Folch et al., 2010; Costa et al., 2012; Folch, 2012). The resulting tephra volumes appear to be better constrained than ignimbrite volumes, where a clear "reference" method does not exist and uncertainties on such computations are significant (Mason et al., 2004).

Calculation of the volume of ignimbrites has been the subject of numerous studies (Walker, 1983; Aldiss and Ghazali, 1984; Henry and Price, 1984; Morgan et al., 1984; Ratté et al., 1984; Sparks et al., 1985; Scott et al., 1996; Wilson, 2001; Pérez et al., 2006; Giordano, 2010; Folkes et al., 2011; Best et al., 2013a; Best et al., 2013b; Cook et al., 2016; Pacheco-Hoyos et al., 2018; Takarada and Hoshizumi, 2020), but it remains difficult to evaluate due to the irregularity of the ignimbrite surface, the variable thickness (controlled by the paleotopography; e.g., Yokoyama, 1974; Wilson 1991; Broxton and Reneau, 1996; Daag and van Westen, 1996), the effect of erosion (e.g., Yokoyama, 1985), the presence of overlying deposits, the intracaldera deposits (e.g., Willcock et al., 2013) and the variable density of the deposits. The eruptive volume, and as a consequence the ignimbrite volume, is essential for computation of the magnitude (M; Pyle, 2000) and Volcanic Explosivity Index (VEI; Newhall and Self, 1982) of an eruption. The calculation of the volume of ignimbrites, which form the main part of eruptions with $M > 5$, remains one of the outstanding issues in volcanology [e.g., the collapse caldera database (CCDB) project, Geyer and Martí, 2008; the LAMEVE project, Crosweller et al., 2012].

The lack of a standardized accurate method for the calculation of ignimbrite volumes makes most of the existing figures for large-volume ignimbrites poorly constrained and, in many cases, unreproducible, resulting in a wide range of estimated volumes of the same ignimbrite [e.g., Cerro Galán, Folkes et al., 2011; Campanian Ignimbrite (CI), Scarpati et al., 2014]. The case study for this work is the CI (Barberi et al., 1978; Fisher et al., 1993; De Vivo et al., 2001; Fedele et al., 2008), associated with the most powerful caldera-forming eruption from the Campi Flegrei (CF) caldera (**Figure 1A**) (Rosi and Sbrana, 1987; Perrotta et al., 2006; Scarpati et al., 2013). It is one of the largest late Quaternary explosive events and has been considered as an example of a super-eruption (Sparks et al., 2005). The 39.8 ka CI tephra (Plinian and co-ignimbrite products; Giaccio et al., 2017) represents the most widespread volcanic deposit and one of the most important temporal/stratigraphic markers for the Early Upper Paleolithic of Western Eurasia (Fedele et al., 2003; Pyle et al., 2006; Giaccio et al., 2008). The eruption may have affected human residents in different ways: by destroying the animal and human populations, by altering the species composition and growth rhythm and by changing the availability of water (Fedele et al., 2002; Fedele et al., 2003; Fedele et al., 2007; Lowe et al., 2012). The abrupt volcanic cooling following the eruption produced a regional drop of 6–9°C in Eastern Europe and Northern Asia (Black et al., 2015). The cooling could have influenced the migration of the populations and have affected the daily life for Neanderthals and modern humans during the Middle to Upper Paleolithic transition (Fedele et al., 2002; Fedele et al., 2003; Black et al., 2015; Marti et al., 2016).

The first part of this work is a review of all articles that calculated the CI volume. In the second part, we present the most reliable method, up to now, to develop an isopach map and calculate the ignimbrite volume. Despite the large number of studies, the estimates of total Dense Rock Equivalent (DRE) volume of the CI eruption range from 60 to 300 km^3 (**Table 1**) (Thunell et al., 1979; Cornell et al., 1983; Rosi et al., 1983; Fisher et al., 1993; Civetta et al., 1997; Rosi et al., 1999; Fedele et al., 2003; Perrotta and Scarpati, 2003; Rolandi et al., 2003; Giaccio, 2006; Marianelli et al., 2006; Pyle et al., 2006; Pappalardo et al., 2008; Costa et al., 2012; Scarpati et al., 2014; Marti et al., 2016). Furthermore, none of these studies provides a solid method to determine the ignimbrite volume in the Apennine mountains. The volume of dispersed tephra (both Plinian and co-ignimbrite) was better defined due to the many measurements across the vast region blanketed by the CI ash and a recent improvement of computational methods (Costa et al., 2012; Marti et al., 2016), as well as by the simpler nature of its mantling deposition. In contrast, the volume of the ignimbrite deposits has never been calculated by accurate direct measurements, but only by approximate thicknesses (Thunell et al., 1979; Fisher et al., 1993; Civetta et al., 1997; Giaccio, 2006). Here, we assess the ignimbrite volume using precise thickness measurements and reporting those on an isopach map. We demonstrate a rigorous method to create a complete isopach map of the CI, with a similar approach to that normally applied to

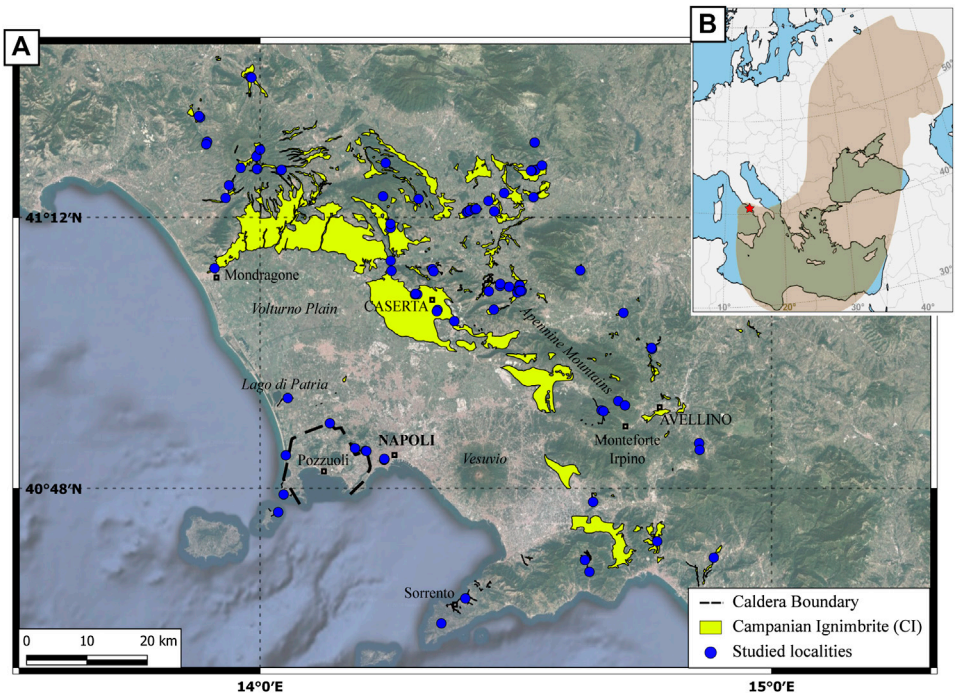

FIGURE 1 | The Campanian Ignimbrite distribution **(A)**. The Campanian Ignimbrite (CI) distribution in the Campanian region (the base map is from Google Satellite), defined merging fieldwork and geological maps (Servizio Geologico d'Italia, 1963; Servizio Geologico d'Italia, 1966; Servizio Geologico d'Italia, 1967; Servizio Geologico d'Italia, 1971a; Servizio Geologico d'Italia, 1971b; Servizio Geologico d'Italia, 1975; ISPRA, 2009; ISPRA, 2010; ISPRA, 2011a; ISPRA, 2011b; ISPRA, 2011c; ISPRA, 2011d; ISPRA, 2014a; ISPRA, 2014b; ISPRA, 2016; ISPRA, 2018). Blue dots indicate the location of the studied exposures (coordinates are reported in the **Supplementary Material**). **(B)** Dispersal area of the CI tephra from the Campi Flegrei caldera (red star), modified from Giaccio et al. (2017). The maps were generated using the QGIS Open-Source 3.4 (https://www.qgis.org/it/site/).

tephra-fall deposits (e.g., Engwell et al., 2015) and it can be easily used on other ignimbrites in the world. The map is based on the mapping of the preserved ignimbrite deposits, without the fall deposits, and reconstruction of the paleotopography, especially mountainous areas. This allows us to provide an accurate estimate of the volume of the extra-caldera deposits of the CI PDC preserved on land based on a verifiable method of calculation and with the relative uncertainties. Using this as a base, we correct for erosion, elutriation, intracaldera volume, and underwater deposits to calculate the, up to date, most reliable total bulk, and DRE volumes for this ignimbrite. We then estimate the co-ignimbrite volume and add the fallout volume from previous studies to calculate the total erupted volume for the eruption. The obtained eruptive volume significantly reduces the total uncertainty of the total volume calculation and should be used to better design and constrain the eruptive dynamics. Such data, well constrained and evaluated, from many volcanoes could help determine the frequency of eruptions of a given magnitude around the world.

VOLCANOLOGICAL BACKGROUND

Volcanic activity in the CF began prior to 80 ka (Pappalardo et al., 1999; Scarpati et al., 2013) and caldera collapses occurred during the eruptions of the CI, the ~15 ka Neapolitan Yellow Tuff (NYT) (Orsi et al., 1996; Perrotta et al., 2006; Acocella, 2008; Vitale and Isaia, 2014) and the 29 ka M 6.6 event Masseria del Monte Tuff correlated to the Y-3 marine tephra (Albert et al., 2019). Post-NYT activity in the caldera is well described by Di Vito et al. (1999), Isaia et al. (2009), and Smith et al. (2011).

The CI eruption emplaced both pyroclastic fall and PDC deposits in a complex sequence currently exposed in proximal, sporadic medial, distal and ultra-distal outcrops (**Figure 1**) (Barberi et al., 1978; Rosi et al., 1988; Fisher et al., 1993; Perrotta and Scarpati, 1994; Orsi et al., 1996; Rosi et al., 1996; Rosi et al., 1999; De Vivo et al., 2001; Cappelletti et al., 2003; Perrotta and Scarpati 2003; Perrotta et al., 2006; Fedele et al., 2008; Engwell et al., 2014; Scarpati et al., 2015a, Scarpati et al., 2015b; Sparice, 2015; Scarpati and Perrotta, 2016; Smith et al., 2016). The first phase of the eruption generated Plinian columns up to 44 km high (Rosi et al., 1999; Marti et al., 2016), producing a widespread fall deposit dispersed by winds to the east (Rosi et al., 1999; Perrotta and Scarpati, 2003; Marti et al., 2016; Scarpati and Perrotta, 2016). A PDC then spread over an area of 7,000 km^2 and surmounted ridges more than 1,000 m high (Barberi et al., 1978; Fisher et al., 1993). This stage caused the caldera collapse and the accumulation of lithic breccia deposits (Breccia Museo) in scattered outcrops along the caldera rim (Perrotta and Scarpati, 1994; Melluso et al., 1995; Rosi et al., 1996; Fedele et al., 2008). In distal outcrops, most of the CI is

TABLE 1 | Bulk and DRE (*) volume calculations proposed for the CI eruption by different authors. Y-5 refers to those studies that did not identify the co-Plinian and co-ignimbrite contribution. The methods are described in the text. The used density (kg/m^3) is reported bulk or DRE (*). *i*: ignimbrite, *a*: ash, *p*: pumices.

Volume calculations (km^3)							
Plinian fallout	**Co-Plinian ash**	**Pyroclastic density current**	**Co-ignimbrite ash**	**Y-5**	**Total**	**Authors**	**Used density (kg/m^3)**
5.33 (0.88*)	14.67 (6.88*)	–	–	–	–	Scarpati and Perrotta (2016)	1,000 (2,400*)
4	16	–	100	–	–	Perrotta and Scarpati (2003)	–
–	–	54 (25*)	100 (42*)	–	–	Scarpati et al. (2014)	2,600*
–	–	30–40*	–	100 (30–40*)	60–80*	Thunell et al. (1979)	–
15	–	–	–	–	–	Rosi et al. (1999)	–
–	–	–	–	73	>150	Cornell et al. (1983)	–
54 (22.6*)	–	–	153.9 (61.6*)	–	207.9 (84.2*)	Marti et al. (2016)	2,500*
–	–	–	72–120 (31–50*)	–	105–210*	Pyle et al. (2006)	2,400*
25*	–	120*	–	–	145*	Civetta et al. (1997)	–
20*	–	130*	–	–	150*	Marianelli et al. (2006)	–
–	–	–	–	–	200*	Fedele et al. (2003)	~1,250
–	–	180	–	140	320 (200*)	Rolandi et al. (2003)	–
20*	–	180*	–	–	200*	Pappalardo et al. (2008)	Average porosity: 0.58
–	–	–	–	250–300 (104–125*)	430–680 (180–280*)	Costa et al. (2012)	1,000
10 (3*)	–	385 (215*)	–	180 (86*)	575 (300*)	Giaccio (2006)	1,400–2,500 i, 1,200 a, 800 *p*
–	–	500	–	–	–	Fisher et al. (1993)	–

DRE, dense rock equivalent.

represented by a massive, gray ignimbrite (Barberi et al., 1978; Fisher et al., 1993; Scarpati and Perrotta, 2012; Scarpati et al., 2015a). Beyond about 80 km from the vent, deposits are made up of coarse to fine ash containing both co-Plinian and co-ignimbrite tephra (Thunell et al., 1979; Sparks and Huang, 1980; Engwell et al., 2014; Smith et al., 2016). The tephra marker related to this eruption is essential to correlate volcanological and archaeological sites in the Mediterranean area and Eastern Europe. Tephra-based correlations of human sites were used to date the Middle to Upper Paleolithic transition (Giaccio et al., 2008; Lowe et al., 2012; Giaccio et al., 2017).

The complex stratigraphy of this eruption differs between proximal and distal outcrops. Moreover, it is difficult to study the lateral correlations due to the absence of outcrops in medial areas (except for the Lago di Patria outcrop, **Supplementary Table S2**), because all quarry-pits have been refilled. The limited drill core data shows little evidence of lateral unit change. In our study, we refer to the stratigraphic units proposed by Fedele et al. (2008) (proximal area) and Cappelletti et al. (2003) (distal areas) (**Online Supplementary Material**). The first flow unit is the Unconsolidated Stratified Ash Flow (USAF) both in proximal and distal stratigraphy, which is followed by the main units of Piperno and Breccia Museo inside the caldera and the Welded Gray Ignimbrite (WGI) and Lithified Yellow Tuff (LYT) in medial and distal outcrops.

ESTIMATING ERUPTION VOLUME

Most studies of eruptive volume focus their attention on the Plinian fallout and the ignimbrite phases of volcanic eruptions, but the total volume calculation is a complex result of many different components. The total volume erupted during a caldera-forming eruption, like the CI, is composed of the mass ejected during the phases that produced Plinian columns (V_{Pcol}), and PDCs (V_{pdc}) **Eq. (1)**:

$$V = V_{Pcol} + V_{pdc} \quad (1)$$

Both V_{Pcol} and V_{pdc} refer to the primary deposits (respectively, the Plinian fallout V_{Pfall}, the proximal pumice lapilli deposit, and the ignimbrite V_{ign}) and their associated co-Plinian fall ($V_{coPfall}$) and co-ignimbrite ash fall (V_{coign}), respectively. Indeed, fine ash suspended in the atmosphere can be co-Plinian rather than co-ignimbrite (Fierstein and Hildreth, 1992). In this work, the co-Plinian ash is defined as the fine-grained Plinian ash, decoupled from the coarser fallout and subject to atmospheric turbulence (Fierstein and Hildreth, 1992). The co-ignimbrite ash is considered to be the buoyant material that rises from the PDC through the entrainment, heating, and expansion of ambient air (Woods and Wohletz, 1991), and may represent the counterpart to the crystal-enriched ignimbrite (Sparks and Walker, 1977). Consequently **Eq. (2)**:

$$V = \left(V_{Pfall} + V_{coPfall}\right) + \left(V_{ign} + V_{coign}\right) \quad (2)$$

The erosion and re-deposition can subsequently modify these components before measurement of the thicknesses occurs. In the

following sections, we discuss different methods used in the past to estimate the CI eruption volume. The CI is not a unique example and those methods have been applied to many eruptions (e.g., Pyle, 1989).

The Previous Estimates of the Campanian Ignimbrite Eruptive Volume

A synopsis of the previously determined estimates of the total volume is provided in **Table 1**.

Due to the difficulty to distinguish the contribution of the co-Plinian fall and the co-ignimbrite ash fall in ultra-distal locations, some authors simply refer to the widespread Y-5 ash layer, which comprises both (**Table 1**) (Thunell et al., 1979; Cornell et al., 1983; Rolandi et al., 2003; Costa et al., 2012). Other previous studies distinguished the co-Plinian and co-ignimbrite contribution (Sparks and Huang, 1980; Perrotta and Scarpati, 2003; Engwell et al., 2014; Marti et al., 2016; Smith et al., 2016), but only some of them calculated the relative volumes (Perrotta and Scarpati, 2003; Marti et al., 2016).

From Direct Measurements

The first volume estimate of the ignimbrite was presented by Thunell et al. (1979). Based on a geometrical method that considers a covered area of over 6,000 km^2 with a thickness up to 100 m and assuming radial flow of the PDC, they estimated the DRE volume was at least 30–40 km^3. The DRE volume of the Y-5 ash layer within the 1 cm isopach contour was also estimated at 30–40 km^3 (65 km^3 bulk). Their total DRE volume was 60–80 km^3 for the eruption.

Cornell et al. (1983) calculated the ash-fall layer volume of Y-5 from an isopach map derived by different cores drilled in the Mediterranean Sea (73 km^3 bulk). They then included the ignimbrite DRE volume proposed by Thunell et al. (1979) in their overall eruption volume estimate. On the other hand, the bulk volume of the original pyroclastic current deposit was estimated by Fisher et al. (1993) to be about 500 km^3 by circumscribing a circle of deposits with a radius of 100 km, 100 m thick at the center that thinned to zero at the perimeter of the circle, with no consideration of topography.

Rosi et al. (1999) calculated the bulk volume of the Plinian fallout as 15 km^3 based on the method proposed by Pyle (1989); in the CI eruption, the focus of the elliptical isopach distribution corresponds to a central vent located in the CF caldera center (town of Pozzuoli). The authors used thickness values from distal outcrops, up to 64 km from the vent. The same technique was used by Perrotta and Scarpati (2003), who estimated a bulk volume of about 4 km^3, the different value of this work being the result of a different isopach model compared to the one used by Rosi et al. (1999). In the same paper Perrotta and Scarpati (2003) attempted, for the first time, to discriminate between the volumes of the co-Plinian and co-ignimbrite components. The coarse ash of ultra-distal deposits was interpreted as the co-Plinian phase, while the fine ash represents the co-ignimbrite component. The authors evaluated the thicknesses of the two parts and estimated 16 km^3 bulk of co-Plinian ash and 100 km^3 bulk of co-ignimbrite ash.

These analyses were then improved by Pyle et al. (2006), who used ultra-distal thickness values all over Eastern Europe. The authors estimated the minimum bulk volume of the CI fallout at 74 or 31 km^3 DRE (using magma density of 2,400 and 1,000 kg/m^3 bulk deposit density) using Pyle's (1989) general observation that many fallout deposits show exponential decay of thickness. Pyle et al. (2006) compared these results with a second approach based on the rate of thinning of the distal ash sheets (based on Pyle, 1989; Pyle, 1990): given that the thickest ash layer in marine cores is in the order of 10–20 cm, it is most likely that the total bulk ash volume associated with the eruption was in the range 74–120 km^3 (31–50 km^3 DRE) (Pyle et al., 2006). Scarpati and Perrotta (2016) subdivided the fallout into five layers (A to E) on the basis of grain size, component variations and graded bedding. The volumes for each layer were calculated using the exponential fitting method of Pyle (1989), obtaining a primary fallout of about 5 km^3 (~1 km^3 DRE, using a magma density of 2,400 kg/m^3 proposed by Rosi et al., 1999) and a co-Plinian ash of about 15 km^3 (~7 km^3 DRE, using the same magma density as the primary fallout).

A first attempt to collate all the volume estimates was made by Fedele et al. (2003), who considered the sum of the conservative estimates reported in literature (the sum of the fallout, the PDC deposits, and the Y-5 ash layer volumes; Thunell et al., 1979; Civetta et al., 1997; Rosi et al., 1999). The total DRE volume they proposed is 200 km^3, using a bulk deposit density of around 1,250 kg/m^3. Rolandi et al. (2003) proposed the same volume (200 km^3 DRE, 320 km^3 bulk), consisting of 180 km^3 bulk of PDC (150 km^3 in proximal area and 30 km^3 in distal area, obtained by the analysis of seismic data, drill-holes, and considering the areal extent of the deposits) and 140 km^3 bulk of the distal ash (80 km^3 in the Mediterranean Sea and 60 km^3 as ultra-distal tephra, using an isopach map).

A similar value was proposed by Giaccio (2006), 215 km^3 DRE (385 km^3 bulk), who calculated the volume of the PDC using a complex truncated cone, with a concave surface and variable heights: 70 m up to 10 km from the center, 50 m up to 20 km, 20 m up to 45 km, and 0 m up to 100 km. At the same time, he proposed a revised isopach map for the fallout deposits, resulting in a volume estimate of 10 km^3 (3 km^3 DRE). Moreover, combining all available data on the distal tephra of CI from the literature (Cornell et al., 1983; Melekestsev et al., 1984; Paterne et al., 1986; McCoy and Cornell, 1990; Cini Castagnoli et al., 1995; Seymour and Christanis, 1995; Narcisi and Vezzoli, 1999; Ton-That et al., 2001; Upton et al., 2002; Seymour et al., 2004), Giaccio (2006) calculated the volume of the distal fraction as 180 km^3 (86 km^3 DRE) and thus estimated a bulk volume of 575 km^3 (300 km^3 DRE). The DRE volumes were calculated using a bulk density, ranging between 1,400 and 2,500 kg/m^3 for the ignimbrite, 1,200 kg/m^3 for the distal ash and 800 kg/m^3 for the fallout pumices.

From Petrological Data and Numerical Modeling

Civetta et al. (1997) is one of the first works that subdivided the volume of the CI eruption based on the pumices composition. The authors divided the magma into three different types: a most evolved one that consists of Plinian fallout and some ignimbrite up to 50 km from the vent (a volume of 25 km^3 DRE), a magma

with intermediate composition that includes some of the ignimbrite out to its farthest extent (100 km^3 DRE), and a least-evolved magma that includes much of the ignimbrite in the Campanian Plain (20 km^3 DRE). All the volume calculations were made by circumscribing circles with a radius similar to the maximum distance reached from the vent by that magma type and a thickness that goes from the maximum thickness of ignimbrite of that given composition at the caldera center to zero at the perimeter of the circle.

Marianelli et al. (2006) proposed different crystallization depths suggested by the results of CI melt inclusion studies and then estimated the volume of the eruption directly from a magma chamber model, attributing 20 km^3 DRE to the fallout deposits, and 130 km^3 DRE to the ignimbrite. The method was not explained with more details in the article (Marianelli et al., 2006). Pappalardo et al. (2008) used petrological data to constrain the pre-eruptive magma storage dynamics analyzing the different magma compositions for each eruptive phase. In agreement with Civetta et al. (1997), Pappalardo et al. (2008) proposed a total volume of 200 km^3 DRE based on a major and trace element modeling (20 km^3 for the fallout and 180 km^3 for the ignimbrite). The authors used the total porosity of each analyzed sample, which varies between 0.36 and 0.93, with an average of 0.58.

Costa et al. (2012) proposed a new tephra volume estimate based on the fit of an advection – diffusion tephra dispersion model to thickness data (more than 100 ultra-distal locations). They obtained a bulk volume of the tephra of 250–300 km^3 (104–125 km^3 DRE, the model assumes an average bulk deposit density of 1,000 kg/m^3) and a total volume of the eruption of 430–680 km^3 (180–280 km^3 DRE).

Scarpati et al. (2014) estimated the PDC volume applying **Eq. 3** (see below) assuming a co-ignimbrite volume (V_{coign}) of 100 km^3 obtained by Perrotta and Scarpati (2003) and a mean vitric loss of 0.65. The method is based on the enrichment factor of Walker (1972); Walker (1980) and the vitric loss of the ignimbrite proposed by Sparks and Walker (1977). The ignimbrite volume (V_{ign}) **Eq. (3)** is equal to:

$$V_{ign} = \frac{V_{coign}}{vitric\ loss} - V_{coign} \quad (3)$$

This method is strongly influenced by the mean value of vitric loss used, which is normally estimated from sporadic point measurements. The bulk volume of the PDC deposits thus estimated is 54 km^3 (25 km^3 DRE, using a density of 2,600 kg/m^3). In the same study, the authors proposed a review of the previous volume estimations (Scarpati et al., 2014).

The most recent work on the fallout volume was presented by Marti et al. (2016). The authors recognized two distinct plume phases: the Plinian (V_{Pcol}) and the co-ignimbrite fall. They applied a computational inversion method that explicitly accounts for the two phases and for gravitational spreading of the umbrella cloud. Dividing the modeling in two different eruptive phases provides the best estimate, as they are two different spreading and source phenomena. The Plinian fallout bulk volume thus calculated is 54 km^3 (22.6 km^3 DRE, using a magma density of 2,500 kg/m^3) and the co-ignimbrite bulk volume as 153.9 km^3 (61.6 km^3 DRE), for a total bulk volume of 207.9 km^3 (84.2 km^3 DRE).

To summarize, the range in volumes is wide (an order of magnitude, 54–500 km^3, in bulk volume) due to the different methods used, which is a problem in view of the importance of such figures in calculating the impact on climate and the environment. While the computational methods for the fallout deposits have improved significantly in the past ten years and the related figures for the CI fallout phase appear strong and solidly based on field data (Costa et al., 2012; Marti et al., 2016), the volume figures for the CI ignimbrite are still poorly constrained by field data and lack well-assessed (epistemic) uncertainties. The ignimbrite volume also affects the estimate of the volume of elutriated co-ignimbrite ash, which is the dominant fallout phase across Europe and the main fraction of ash injected into the stratosphere by the eruption (e.g., Costa et al., 2018).

METHODS

Investigated Campanian Ignimbrite Eruptive Unit

In order to reduce this wide range in volume estimates, we focus on constraining the volume of the ignimbrite deposits of the CI, as this is the most poorly constrained at present. We use volumes calculated by Perrotta and Scarpati (2003) and Marti et al. (2016) for the initial pyroclastic Plinian fall phase and the co-ignimbrite fallout to estimate the total erupted volume. Our CI isopach map is based on previous published data, new fieldwork, and the assessment of the paleo-topographic control exerted on the deposits thickness distribution.

Density Measurements

More than 40 samples from different outcrops scattered around the Campanian Plain were analyzed to determine their density. Samples were cut in cylinders (with radius between 0.9 and 2 cm and height between 0.8 and 5.7 cm) or cubes (sides from 0.8 to 2.5 cm) and analyzed using a Micromeritics AccuPyc II 1340 helium pycnometer. The instrument provides a standard deviation for each measurement that was used to evaluate the density errors. The resulting density was used to interpret total and open porosity. Open porosity was estimated with geometric (V_g) and matrix volume (V_{mx}): $100 \times (V_g - V_{mx})/V_g$, while closed porosity was determined using the DRE of the WGI and Piperno powder, which was obtained by the pycnometer. The total porosity (φ_t) was calculated directly by summing closed and open porosity. The density is used to determine the DRE volume.

Database and Fieldwork

Published data regarding CI thickness and outcrop locations were collected from 42 papers (presented in **Supplementary Table S1**). The data were inserted in a GIS Open-Source QGIS 3.4 (https://www.qgis.org/it/site/) database including 238 localized outcrops. The database includes the location name, the lithological description, the geographic coordinates, the elevation a.s.l., the thickness of the flow units (specifying whether total or minimum outcrop thickness), the maximum lithic dimensions and the

degree of welding. Where both base and top of the CI are exposed, the thickness is classified as total and elsewhere it is considered a minimum thickness. The database reports raw thickness data and adjustments due to erosion are explained later on.

This database has been augmented by our field data acquired in 97 locations (presented in **Supplementary Table S2**), both in proximal and distal areas (**Figure 1A**). At these new field sites, information on total or minimum thickness, to verify the local stratigraphy, and the relation of the ignimbrite to topography were collected.

Defining the Campanian Ignimbrite Pyroclastic Density Current Deposit Extent

The 0 m isopach is an outer limit beyond which the CI is not present, and it delimits the current areal distribution of the ignimbrite outcrops. The isopach was reconstructed through a first phase of revision of the geological maps already existing at the scale 1:50,000 or 1:100,000 (Servizio Geologico d'Italia, 1963; Servizio Geologico d'Italia, 1965; Servizio Geologico d'Italia, 1966; Servizio Geologico d'Italia, 1967; Servizio Geologico d'Italia, 1971a; Servizio Geologico d'Italia, 1971b; Servizio Geologico d'Italia, 1975; ISPRA, 2009; ISPRA, 2010; ISPRA, 2011a; ISPRA, 2011b; ISPRA, 2011c; ISPRA, 2011d; ISPRA, 2014a; ISPRA, 2014b; ISPRA, 2016; ISPRA, 2018). The contact was traced between the CI and older units and extrapolated where CI does not crop out. In this circumstance, the ignimbrite is generally covered by younger deposits, so it is necessary to assess if the CI was emplaced in these locations. To do this, a statistical and morphological analysis of the slope of the top of the CI was applied and a comparison between the topography and the average slope of the CI top was carried out. Where the slope angle is comparable, the area was included in the 0 m isopach, even if CI does not crop out. The underlying basement (mostly Meso-Cenozoic calcareous or flysch rocks) has generally higher slope angles than the CI (for example, the Apennine flanks), so the CI produces a morphologically distinct slope. The isopach was traced to leave out high-slope areas and no primary CI deposition was interpreted. The slope analysis was performed on a slope map developed using a 10 m resolution Digital Elevation Model (DEM; Tarquini et al., 2007; Tarquini et al., 2012; Tarquini and Nannipieri, 2017). The statistical and morphological analysis of the upper surface of the CI used 48,804 points distributed throughout the areal extent of the deposits (both in proximal and distal areas).

The Isopachs

To determine the isopach locations, two different methods were used, one in the proximal area to medial (from the caldera to the base of the Apennine Mountains, including the Campanian Plain) and one in the distal area. The almost complete lack of outcrops in the Campanian Plain and the valley-ponded depositional style in the ridge-valley topography of the Apennine Mountains (Rosi et al., 1983; Rosi et al., 1996; Perrotta et al., 2010; Langella et al., 2013; Scarpati et al., 2014; Scarpati et al., 2015a; Sparice, 2015; Fedele et al., 2016) make these different approaches necessary.

In the proximal-medial area, data from the literature (Ortolani and Aprile, 1985; Scandone et al., 1991; Bellucci, 1994; Rolandi et al., 2003; Milia and Torrente, 2007; Torrente et al., 2010; ISPRA, 2011d), consisting of more than 300 thickness values of CI from boreholes, outcrops, and geological sections were used to fit isopachs on the map (**Online Supplementary Material**). In the distal area, the isopach locations were based upon our field observations and a reconstruction of the pre-CI topography (**Figure 2**), which was a separate analysis based on series of ~150 profiles in the Apennine Mountains, drawn to outline the trend of the valleys (**Figure 2B**). The coastline of the Mediterranean Sea at the time of the CI emplacement (39.8 ka) was lower than today. Based upon limited sea-level correlation work in the Mediterranean basin (Lambeck and Bard, 2000; Antonioli et al., 2004; Antonioli, 2012), we assumed a sea level between 75 and 87 m below the present level.

Topographic cross-sections were traced orthogonally to the center of the valley and to the contour lines, including the flanks of the reliefs and the 0 m isopach. The slopes of the valley above the CI 0 m isopach were extended and gradually deepened toward the valley center in order to reconstruct the paleo-valley with an inclination of the sides similar to the current slope, always taking into consideration the geological and morphological features (**Figure 2B**), and assuming that the Meso-Cenozoic mountain slopes have not significantly changed since 40 ka. The base elevation of the paleo-valleys is constrained by field data where the CI base has been measured.

These reconstructed valleys culminate generally in a V shape, not considering the CI that filled them, with the bottom elevation, for each profile, representing the paleo-valley floor. All these elevations represent the ancient pattern of the valley bottom; for this reason, they were modified if they were inconsistent with the progressive downslope decrease in elevation toward the sea.

Finally, the neo-incision of rivers in the profiles was "filled in," so as to remove the linear erosion of the last 39.8 kyr, drawing a line that reproduces the original ignimbrite deposit before that the erosion occurred (**Figure 2B**). The CI thickness is calculated from these modified profiles, and it is from the top of the deposit obtained by the profiles into the paleo-valley slope. However, the thickness is always constrained by field data of the CI thickness and by the geological maps. These thickness values are then reported on the isopach map.

All the isopachs were traced in accordance with fieldwork, looking both to the base CI elevation and the CI thickness, the geology of Meso-Cenozoic valley sides and, finally, the present-day drainage network compared to the paleo-valleys during the eruption (**Figure 2**). Where these data were not consistent, an adjustment in some profiles was necessary. In some cases, a correction was made for an over-thickening in the valleys caused by an over-deepening of the extended valley sides, not consistent with field observations. In these cases, the thickness was modified in coherence with fieldwork.

We use, as a starting point for the volume estimate, the ignimbrite deposits volume obtained from the detailed isopach map. This information is lacking in previous estimates of the CI volume. We refer to all PDC units of the CI as the CI, without distinguishing them; in the medial and distal outcrops, the CI is mainly composed of WGI.

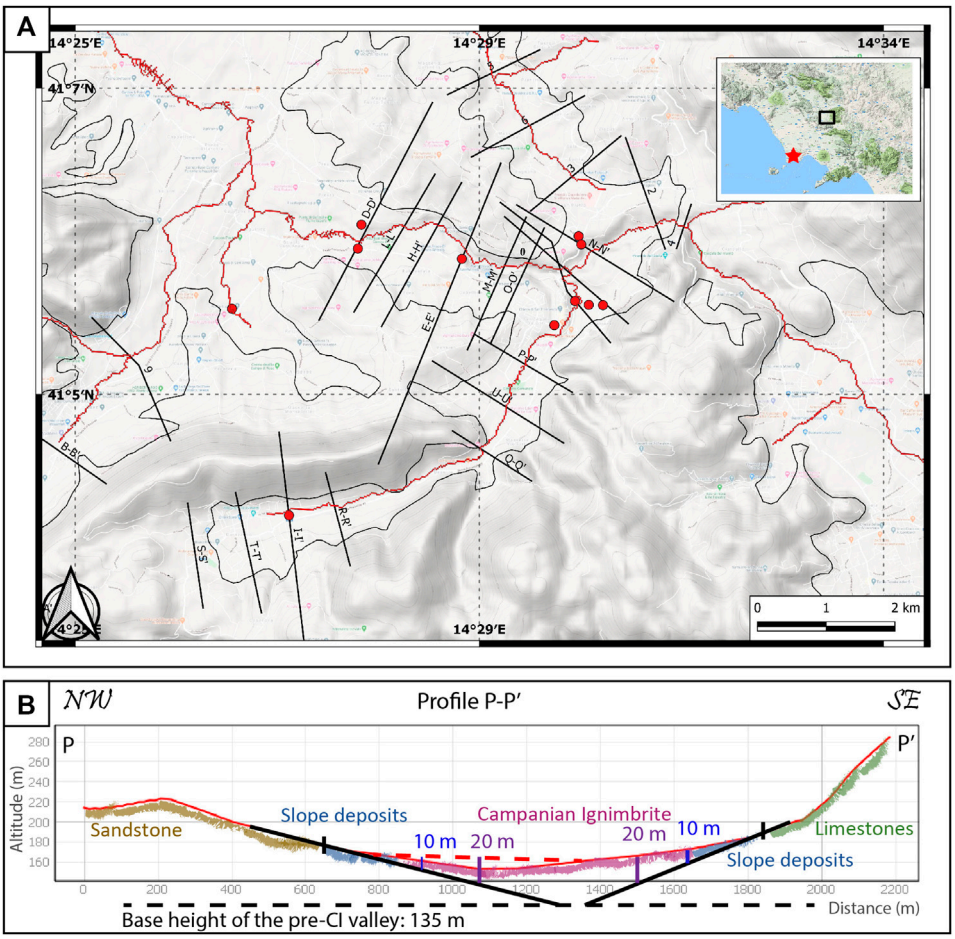

FIGURE 2 | The topographic reconstruction in the Sant'Agata dei Goti area (reported in the right corner, the red star is the vent). **(A)** A series of profiles traced to study the paleo-valley; the red dots are the studied outcrops where the Campanian Ignimbrite (CI) is exposed. The red lines represent the river network developed through the QGIS software, while the black line is the 0 m isopach. **(B)** Reconstruction of the paleo-valley in profile P-P', the base elevation is constrained to the CI base observed by fieldwork and to the current slope of the valley. The resulting thickness is coherent with fieldwork, so where thicknesses are too high, they were not considered and the isopachs were traced up to a realistic thickness. The numbers represent the thickness of the CI in meters. The different colors represent different types of deposits, while the dashed red line, is the linear erosion that occurred in 39 kyrs.

RESULTS

The Isopach map

The morphological analysis shows that 64% (31,057) of the points have slopes lower than 5°. Moreover, 88% of the points have slopes lower than 15° and 99% have a surface slope lower than 55° (**Figure 3**). The CI slope values are consistent with field observations during this work and in agreement with the observation on the slope of the top surface of the valley-ponded Taupo Ignimbrite, which is around 8° (Wilson and Walker, 1985).

Based on these results, the 0 m isopach was traced to enclose all the mapped CI and areas that probably have the CI below the recent sedimentary cover, they have a slope less than 15° and they are in contact with mapped CI outcrop. The 15° slope is consistent with the results, and it allows the inclusion of all the possible CI extent. With this approach, some CI-containing valleys are isolated from the main CI deposits (**Figure 4**). The isolated valleys contain some CI outcrops, but they are confined by high slope or basement deposits nearby, and they are separated from the main ignimbrite by post-emplacement erosion. The total area enclosed by the 0 m isopach of the CI is 3,216 km^2 (**Figure 4**). To understand also the total area of the region inundated by the PDC, and avoid underestimation, a shape was drawn comprising all the maximum areal extension of the isopach 0 m. The enveloped area is 6,095 km^2 (**Online Supplementary Material**), similar to the 6,000 km^2 estimate of Thunell et al. (1979).

The isopach map traced in the proximal area does not include the intracaldera deposits. The maximum thickness in proximal areas is 80 m (**Figure 5**), mainly based on outcrops near the caldera rim; the CI thins gradually away from the caldera margin. The detailed isopach maps show the areas of thickening or thinning in the Campanian Plain and in the Apennines (**Figure 6**). The isopach for the distal reaches has a maximum

thickness of 50 m in the Valle dei Maddaloni (**Figure 6C**). In distal areas, a series of confined valleys show local thickening.

Density of the Campanian Ignimbrite Deposits

The bulk density (ρ) of the WGI samples ranges from 745 ± 15 kg/m^3 to 1,330 ± 3 kg/m^3, with an average of 980 ± 11 kg/m^3 (see *Density Measurements* to methods on how the errors were calculated). Error-free measures for all samples follow a Gaussian distribution with a standard deviation of the Gaussian probability density function of 127 kg/m^3. The bulk density of the Piperno unit ranges from 1,275 ± 8 kg/m^3 to 1,302 ± 2 kg/m^3, with an average of 1,287 ± 4 kg/m^3 (presented in **Supplementary Table S3**). The total WGI porosity ranges from 49 ± 5% to 71 ± 5% and the average is 61.6 ± 5%. The average for the Piperno unit it is 50 ± 1%. The total porosity matches with the range used by Pappalardo et al. (2008). The ρ DRE is 2,607 ± 31 kg/m^3, which is in agreement with the magma density used by Scarpati et al. (2014). The DRE volume is determined multiplying the bulk volume by $(100 - \varphi_t)/100$.

Deposits Volume Calculation

Data were plotted in a semi-logarithmic plot (**Figure 7**) in which thickness (T) and area (A) follow the relation: $T = T_{max} \exp(-k_1 A)$ (Wilson, 1991). T_{max} of the CI from this relation is 71.3 m (the measured value in the field is 80 m), k_1 is equal to 10^{-9} m^{-2} and r^2 is 0.929. These values were obtained plotting thickness and area with the same unit (m).

Following this equation, the volume is the definite integral of the function, where the area of each isopach was calculated directly from the QGIS software. **Table 2** displays the values of the area and the volume for each isopach extrapolated by the function (**Figure 7**). Summing all the isopach volumes, the total volume of the preserved extra-caldera CI deposits on land is 68.2 ± 6.6 km^3 (26.8 ± 2.6 km^3 DRE). The sources of error and the uncertainties were calculated separately for the proximal and medial area and for the distal one; their calculation is explained in the **Online Supplementary Material**. The CI volume was compared to other ignimbrites, whose bulk volumes span three orders of magnitude: the Lund Ignimbrite (4,400 km^3; Best et al., 2013a), the Greens Canyon Tuff (GCT, 600 km^3; Best et al., 2013a), the Petroglyph Cliff (40 km^3; Best et al., 2013a), the Oruanui ignimbrite (300 km^3; Wilson, 1991) and the Pozzolane Rosse ignimbrite (RED, 35 km^3; Giordano, 2010; Giordano and Doronzo, 2017) (**Figure 7**).

To understand the extra-caldera volume subdivision in proximal and distal areas, the isopach map is divided into two parts, one comprising all the Campanian Plain, and the other from the first Apennine ridges to the final runout (**Figure 5**). The resulting extra-caldera volumes are 48.6 ± 1.7 km^3 in the proximal area (~70%) and 19.6 ± 4.9 km^3 in the distal area (~30%).

DISCUSSION

The linear relations between $\log_{10}$ thickness and area presented in **Figure 7** show all the ignimbrites have r^2 values above 0.9. k_1 varies between 10^{-10} m^{-2} and 10^{-9} m^{-2} for each ignimbrite, but it seems that bigger ignimbrites (Lund and Oruanui ignimbrites) have lower k_1 values. The concavity of this curve gives information on the aspect ratio of the deposits: concave-upward curves (i.e., convex) refer to low-aspect-ratio deposits while concave-downward curves apply to high-aspect-ratio ignimbrites (Wilson, 1991). The CI shows an intermediate aspect ratio, with the first part of the curve upward and the second downward, which reflects the field evidence, noticed during the fieldwork, of both low and high aspect ratio behavior of the CI. Greens Canyon Tuff and RED show a similar change in concavity. The RED shows similar features to the CI in the field: both ignimbrites encountered topographic barriers perpendicular to the flow, such that the RED climbed topographic barriers as high as 400 m (Giordano, 2010) while the CI overtopped 1,000 m barriers. Such interaction has an important role in the flow dynamics (e.g., Bursik and Woods, 2000; Andrews and Manga, 2011) and it is associated with a decrease in carrying capacity and an increase of the sedimentation rate (Giordano, 1998). The change of the curve concavity could directly show the sedimentation rate fluctuations.

Extracaldera Volume

The data from this work were compared with Ruberti et al. (2020), who proposed contour maps of the lower and the upper surfaces of the CI for the northwestern sector of the proximal-medial area, based on 1,000 lithostratigraphic logs from boreholes. The extrapolated thicknesses from their maps were

TABLE 2 | The values of thickness (m), area (km^2), cumulative area (km^2), volume (km^3), cumulative volume (km^3) and the percentage of volume for each isopach.

Thickness (m)	Area (km^2)	Cumulative area (km^2)	Volume (km^3)	Cumulative volume (km^3)	Volume (%)
>80	12.6	12.6	0.9	0.9	1.3
70–79	12.3	24.9	0.9	1.8	1.3
60–69	19.1	44.0	1.3	3.1	1.9
50–59	31.3	75.3	2.1	5.2	3.1
40–49	234.0	309.4	13.8	19.0	20.2
30–39	194.5	503.9	9.2	28.2	13.6
20–29	854.0	1,357.9	24.7	53.0	36.3
10–19	862.0	2,219.9	10.6	63.6	15.5
0–9	995.7	3,215.6	4.6	68.2	6.8
Total	3,215.6	—	68.2	—	—

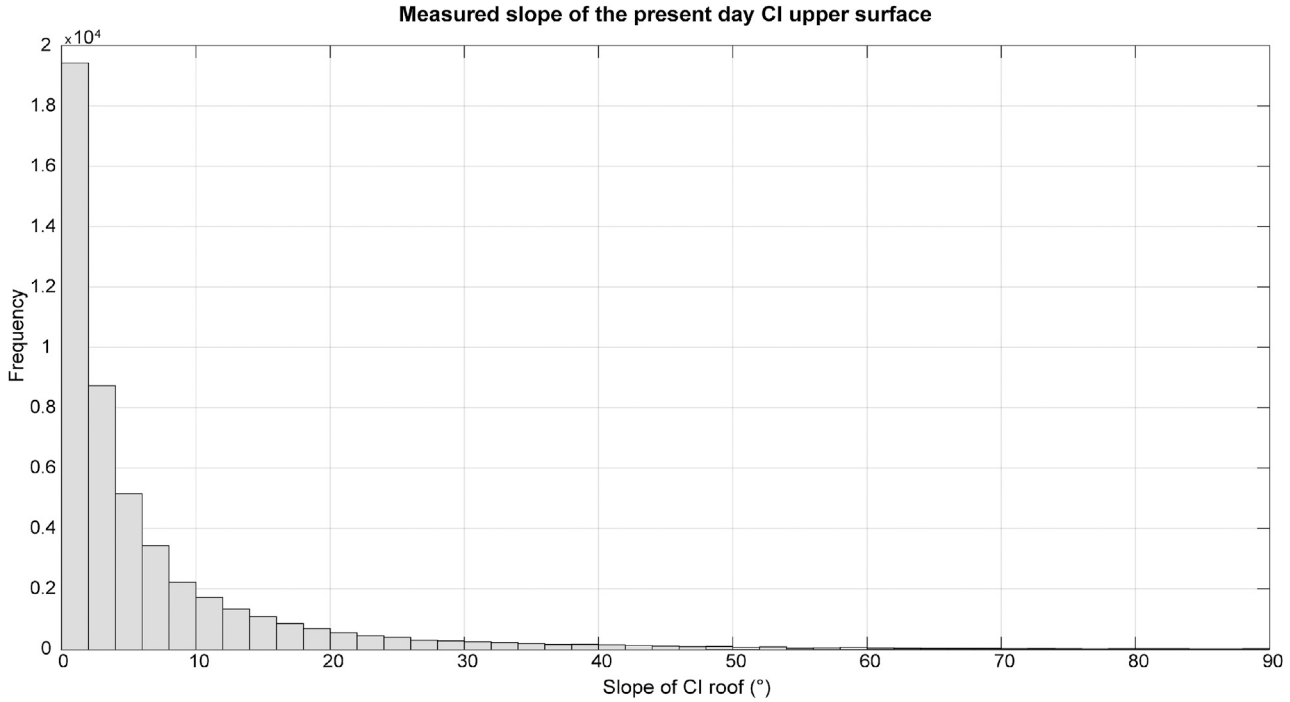

FIGURE 3 | Frequency of the slope of the upper surface of the Campanian Ignimbrite (CI). At least 80% of the exposed CI upper surface slopes less than 10°. The areas with slope greater than 35° are related to river incisions and CI escarpments.

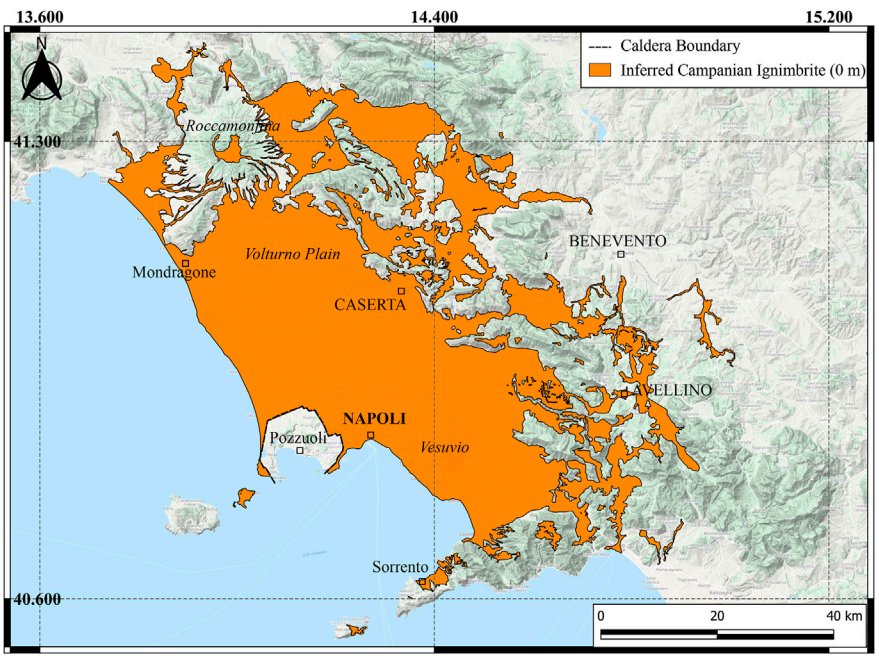

FIGURE 4 | Reconstruction of the areal extent of the ignimbrite deposits, enclosed within the 0 m isopach is shown in orange. The total area covered by the preserved deposits of CI is 3,216 km^2, the envelopment with a shape is equal to 6,095 km^2 (**Online Supplementary Material**). The isolated areas from the source are due to the erosion of veneer facies.

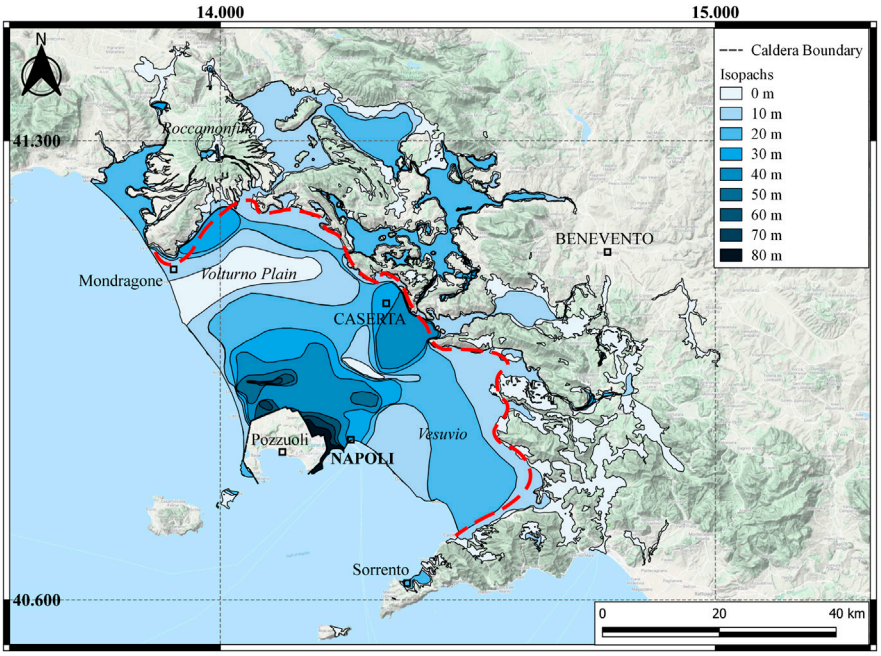

FIGURE 5 | Isopach map of the preserved extra-caldera deposits of the Campanian Ignimbrite. This map refers only to the ignimbrite deposits; it excludes the Plinian fallout and the co-ignimbrite ash. The different colors for each isopach are reported in the map key. The red dashed line divides the proximal and the distal area.

compared with the isopach map of this work by drawing a new proximal isopach map based on their contour maps. The volume calculated from this new isopach map is 46.5 km^3, 2.1 km^3 less than the volume we estimated. This difference is included in the 6.6 km^3 of the total volume error and uncertainties here presented. The data proposed by Ruberti et al. (2020) were not inserted in the isopach map reported in this work to avoid error propagation due to data coming from contour maps rather than deposit thickness measurements. However, a greater thickness in the Volturno Plain compared to this work could be considered, as proposed by Ruberti et al. (2020).

The error and uncertainties associated with our volume estimate of the terrestrial CI ignimbrite deposits (68.2 ± 6.6 km^3) are less than 10% (**Online Supplementary Material**), a good precision considering that many published estimates of eruption volume may be barely more precise than one order of magnitude (Mason et al., 2004). The accuracy of the applied method is also due to the development of the 0 m isopach areal extent. Cutler et al. (2020) demonstrated that the inclusion of zero values improved the modeling and the volume calculations for tephra layers of Mount St Helens. Moreover, the complexity of the isopach shapes, instead of simplified oblate shapes, allows better consideration of raw thickness data and lessens inaccurate volume estimates (Engwell et al., 2015). This method can now be applied to ignimbrite deposits, with a good parallelism between flow and fall volume calculations.

The volume we presented above is not the total volume of the CI PDC deposits, but the preserved extra-caldera ignimbrite volume and several corrections must be applied to this value (Mason et al., 2004; Folkes et al., 2011). Each factor has relative uncertainties, but here we constrain them to a well-defined preserved extra-caldera volume and we analyze each minimum and maximum volume. A significant amount of pyroclastic material was deposited in the sea and within the caldera, significant erosion has occurred in the last 39.8 kyrs, and a large amount of co-ignimbrite ash elutriated or rose into the air as a column.

The reconstructed isopachs do not consider the linear erosion due to river incision of the CI so the possible areal erosion must be calculated. The linear erosion is related to the selective erosion due to rivers, while the areal erosion comprises all the regional processes that occurred in the area. The deposits of WGI show a mainly valley-ponded deposit pattern; in many areas where the ignimbrite was deposited in narrow valleys (for instance near Roccamonfina), the only unit that mantles the topography is USAF, while the upper surface of WGI is mainly horizontal (**Figure 3**) (Sparice, 2015). This suggests that USAF is a facies emplaced over a wider area than WGI, comprising also topographic highs with mantling and veneer features, but was then subjected to significant areal erosion (Wilson, 1991). The thickness of USAF is mainly between 10 cm and 1 m; in rare cases, it can reach 3 m (Fedele et al., 2016). A median thickness of 1 m is assumed as eroded material for all the enveloped area (6,095 km^2, projected area) not covered by valley-pond facies, as a reference for the areal erosion. To calculate the erosion, we used the real surface of the enveloped area. The real surface is the actual surface of an area, not its projection, and it considers also the mountain slopes. From the Digital Elevation Model, the real surface was computed at 9,575 km^2. The volume associated with the areal erosion, on the real surface, is 9.6 km^3 (V_e) (3.7 km^3

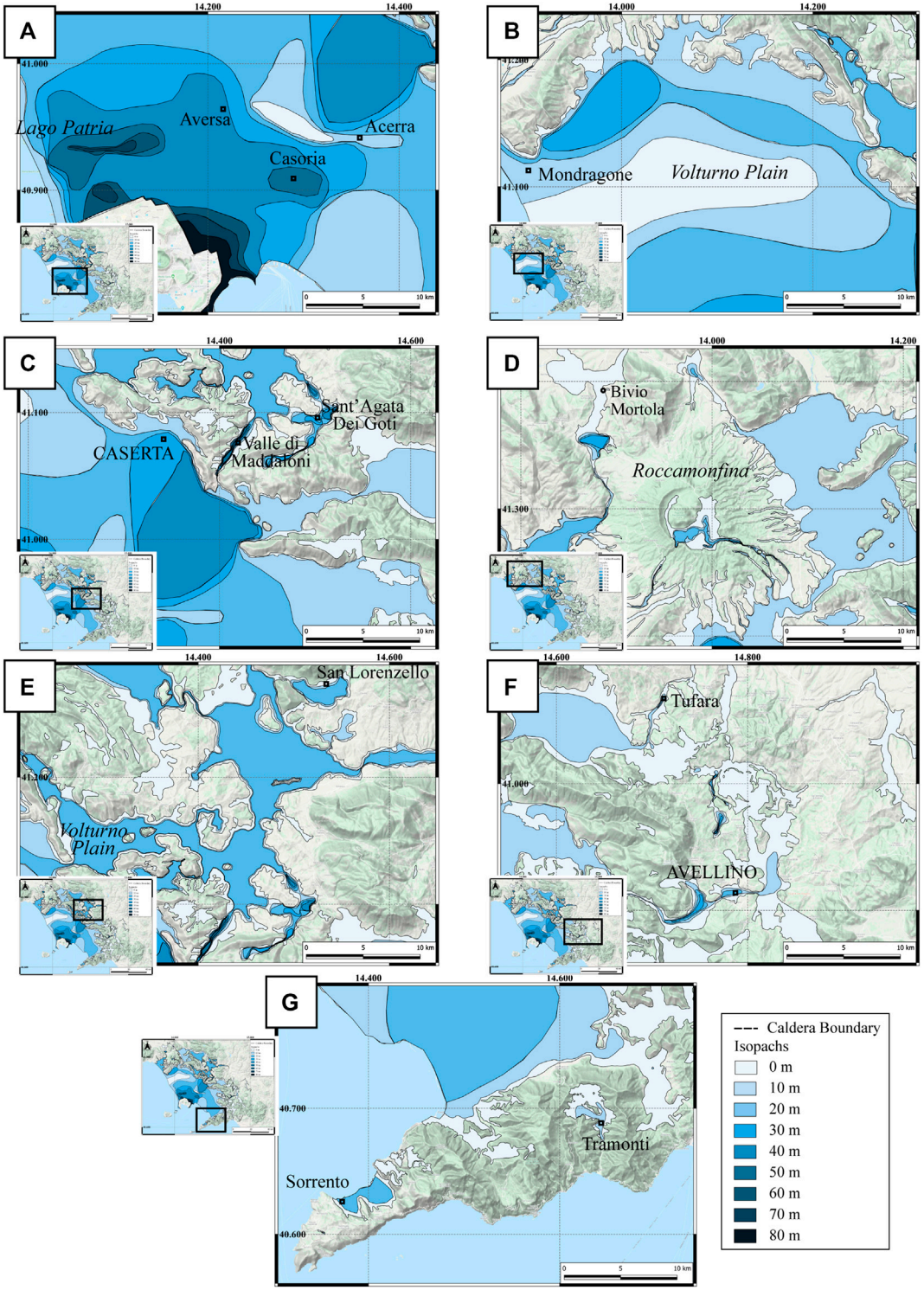

FIGURE 6 | Detailed isopach maps of selected areas of the Campanian Ignimbrite (excludes fallout): **(A)** north of the caldera, between Lago Patria and Acerra; **(B)** northern part of the Campanian Plain; **(C)** Apennine ridges east of the Campi Flegrei caldera and the Valley of Maddaloni; **(D)** Roccamonfina and Mortola, in the north of the studied area; **(E)** Volturno plain and San Lorenzello area, northeast of the caldera; **(F)** distal area of Avellino, southeast of the caldera; **(G)** Sorrento peninsula, in the southern part of the studied area. See *The Isopachs* to detailed methods on how the isopachs were traced.

TABLE 3 | The volume of the CI eruption. The various parts of the PDC volume estimate are explained in the text. The fallout volume considered in this work is the maximum and the minimum proposed in literature by Perrotta and Scarpati (2003) and Marti et al. (2016).

	Bulk volume (km^3)	DRE volume (km^3)
Preserved extra-caldera ignimbrite volume (V_{pr})	62–75	24–29
Marine volume (V_m)	62–75	24–29
Intracaldera volume (V_{intr})	16–43	8–21
Areal erosion volume (V_e)	10	4
Co-Ignimbrite ash volume (V_{coign})	294–394	116–155
Total PDC volume (V_{pdc})	453–606	179–243
Fallout volume (V_{Pfall}) (Perrotta and Scarpati, 2003; Marti et al., 2016)	4–54	2–22
Total CI volume (V)	457–660	181–265

PDC, pyroclastic density current.

DRE, using the average density of WGI). This is a correction based on field observations (USAF mantling the topography) and an average calculation (the thickness and the area) could vary if the eroded thickness, or involved area, are substantially different from those assumed here.

The CF caldera is located near and below the current sea-level but, about 40 ka, the coastline was farther to the southwest corresponding to a level between 75 and 87 m below its present position (Lambeck and Bard, 2000; Antonioli et al., 2004; Antonioli, 2012) (**Figure 8**). Based on the distribution on land of the ignimbrite, the assumed radial spreading (Thunell et al., 1979; Fisher et al., 1993; Ort et al., 2003), and the position of the CF caldera relative to the coastline (**Figure 8**), a roughly equal amount of material should be present both on land and offshore. The bathymetry offshore shows depressions and valleys south of the caldera that could be areas of ignimbrite deposit accumulation (**Figure 8**). Flow deposits of Kos and Krakatau demonstrate that PDCs can travel considerable distances above sea water (Carey et al., 1996; Allen and Cas, 2001; Dufek and Bergantz, 2007) and it is known the Campanian PDC flowed over the water of the Bay of Naples to deposit on the Sorrento Peninsula (~35 km from Pozzuoli Bay to Sorrento) (Fisher et al., 1993).

The occurrence of turbidity currents in the Mediterranean basin coeval with the eruption was confirmed by analyses of the core CT85-5 in the Tyrrhenian Sea (40°19′02″N, 11°15′42″E), more than

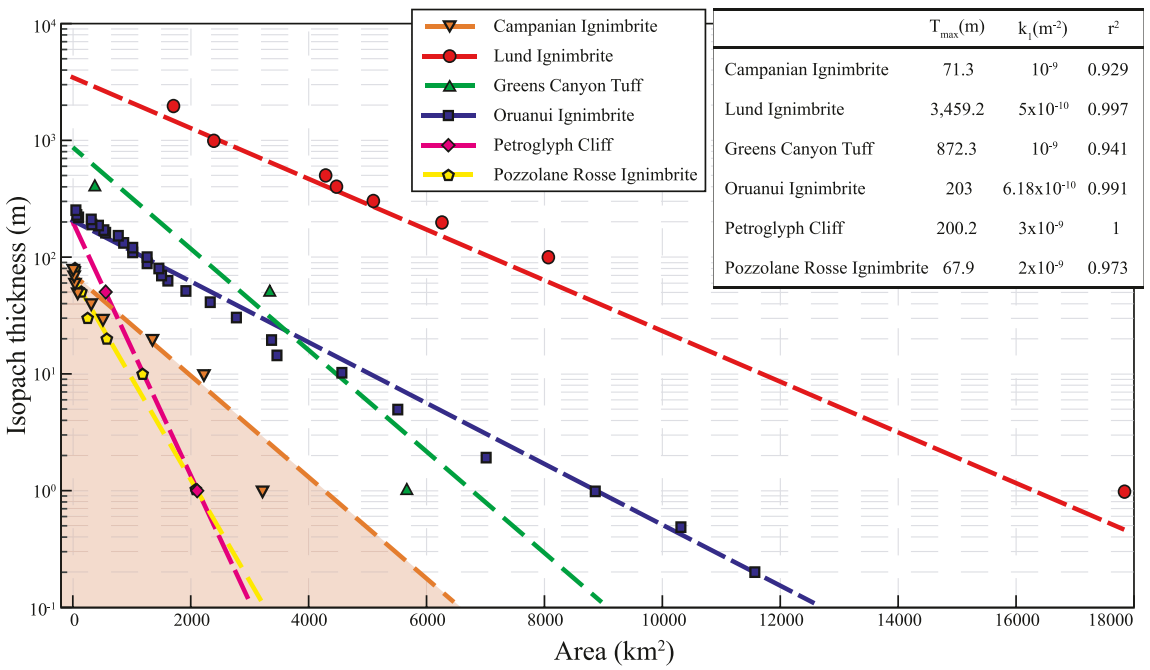

	T_{max}(m)	$k_1(m^{-2})$	r^2
Campanian Ignimbrite	71.3	10^{-9}	0.929
Lund Ignimbrite	3,459.2	$5x10^{-10}$	0.997
Greens Canyon Tuff	872.3	10^{-9}	0.941
Oruanui Ignimbrite	203	$6.18x10^{-10}$	0.991
Petroglyph Cliff	200.2	$3x10^{-9}$	1
Pozzolane Rosse Ignimbrite	67.9	$2x10^{-9}$	0.973

FIGURE 7 | Thickness (in log scale) vs. the cumulative area enclosed in that thickness of each isopach of different ignimbrites [the Campanian Ignimbrite (CI) in orange; the Lund Ignimbrite in red, Best et al., 2013a; the Greens Canyon Tuff in green, Best et al., 2013a; the Oruanui Ignimbrite in blue, Wilson, 1991; the Petroglyph Cliff in pink, Best et al., 2013a; and the Pozzolane Rosse Ignimbrite in yellow, Giordano and Doronzo, 2017]. The dashed lines represent the fit of each ignimbrite. The values of the fitting (T_{max}, k_1, and r^2) are reported in the upper right corner. The plotted CI points are those obtained by the isopach map. The CI volume is the integrated area displayed in orange.

200 km west of the CF caldera (Cini Castagnoli et al., 1995; Giaccio, 2006; Giaccio et al., 2006; Hajdas et al., 2011). The 45 cm-thick CI tephra recognized within the core was used as an important time marker. The nearby CT85-6 confirmed the presence of the CI tephra, but it was less studied as its record is shorter and the CI tephra is not reported fully (Hajdas et al., 2011). The CI layer contains shallow water gastropods and internal lamination, which indicate that at least 10 cm of the section are from turbiditic origin (Cini Castagnoli et al., 1995; Giaccio, 2006; Hajdas et al., 2011). These volcaniclastic currents related to the CI eruption are reported throughout the Tyrrhenian basin (McCoy and Cornell, 1990; Giaccio, 2006) and interpreted as the result of large syn-eruptive transport of the CI material as the PDCs entered the water. The turbidity currents can be reasonably considered as primary products of the eruption (Giaccio, 2006). Milia et al. (2020) report the presence of a debris flow related to the CI eruption in the CET2 core (39°55.23′N, 14°07.56′E) and an erosive surface in the nearby CET1 core (39°54.69′N, 14°06.65′E), both located in the lower bathyal zone offshore of the Campania margin. These authors recognized the CI's impact in the area and the possible generation of a tsunami related to the eruption.

For these reasons, a large amount of underwater material is realistic and, because of the nearly equal radial area covered by sea vs. on land, is considered equal to the on-land material, so each is considered to have a volume of 68.2 ± 6.6 km^3 (V_m). However, the total volume that entered the water during and after the eruption was equal to the preserved volume on land plus the eroded volume (68.2 + 9.6 km^3).

Intracaldera Volume

Wells have been drilled since the 1940s to understand the deep geothermal system in CF, reaching depths of 1,600–3,000 m below ground surface (Rosi and Sbrana, 1987). A strong hydrothermal alteration was recognized, with four main zones marked by distinctive mineral assemblages. These wells reached the CI units, but the extensive hydrothermal alteration prevented its identification. Due to the high uncertainties of correlating CI deposits inside the caldera, the isopach map was traced without the intracaldera area and the intracaldera volume was not estimated in this work.

More recently, a 506 m borehole was drilled west of Naples, penetrating both the NYT and CI (Mormone et al., 2015; De Natale et al., 2016). The hydrothermal alteration in the proximity of CI (around 439 and 501 m) was recognized and made the correlation with the deposits extremely difficult. However, through lithological, mineralogical and $^{40}Ar/^{39}Ar$ dating the authors recognized around 250 m of intracaldera CI (De Natale et al., 2016). This thickness value was previously observed through geological and geophysical features (Torrente et al., 2010). The ignimbrite volume inside the caldera was then estimated at less than 16 km^3, using a caldera area of 64 km^2 (De Natale et al., 2016).

There are some uncertainties due to the caldera's true shape. Vitale and Isaia (2014) proposed a 12 km-wide polygonal caldera, which corresponds to an area of 144 km^2, while De Natale et al. (2016) suggested a minimum area of 64 km^2. Considering an average thickness of 250 m of intracaldera deposits (De Natale et al., 2016), and an area varying from 64 to 144 km^2, the intracaldera volume (V_{intr}) ranges between 16 and 43.2 km^3 (7.9–21.4 km^3 DRE, using the proximal unit density of the Piperno).

Distal Tephra Volume

The CI tephra is an important correlation tool and time marker for Quaternary stratigraphy in different basins and archaeological sites in Western Eurasia. The tephra layer is visible in numerous sedimentary records, including marine (Keller et al., 1978; Paterne et al., 1986; Paterne et al., 1999; Ton-That et al., 2001), terrestrial sequences (Veres et al., 2013), cave-entrance environments (Fedele et al., 2003; Giaccio et al., 2008), lacustrine records (Narcisi, 1996) and archaeological sites (e.g., Badino et al., 2020). The occurrence of the CI tephra in archaeological sites helps to address the human bio-cultural evolution at the Middle-Upper Paleolithic transition in Italy (Castelcivita, Serino, and Grotta del Cavallo sites; Gambassini, 1997; Giaccio et al., 2008 and references therein; Lowe et al., 2012; Wood et al., 2012; Zanchetta et al., 2018), in Montenegro (Crvena Stijena; Morley and Woodward, 2011; Mihailović and Whallon, 2017), in Greece (Douka et al., 2014; Zanchetta et al., 2018) and in Russia (Kostenki; Giaccio et al., 2008 and references therein). In very distal sites, it can be found as a cryptotephra not visible to the naked eye, but clearly useful as an absolute and relative chronological and stratigraphic marker (Lowe et al., 2012).

Defining the distribution of the ultra-distal deposits is a difficult task due to the limitation of the field data available and to the thinning of the ash layers. Underestimation of the deposit volume can be result from simple extrapolation from proximal, medial, and distal data to the ultra-distal region. The case of the CI is complicated by the presence of both co-Plinian fallout ash and co-ignimbrite fallout ash, both transported far from the vent through to Eastern Europe and Russia (Thunell et al., 1979; Cornell et al., 1983; Narcisi and Vezzoli, 1999; Fedele et al., 2003; Giaccio et al., 2006; Pyle et al., 2006; Engwell et al., 2014; Smith et al., 2016).

Nevertheless, the ultra-distal tephra volume is necessary to define the total CI eruptive volume. Sparks and Huang (1980) recognized the bimodal grain-size of the ultra-distal deposits of the CI, interpreting the coarse lower unit as formed during the Plinian phase, and the finer upper unit as the co-ignimbrite phase. These features were also observed by Wulf et al. (2004) at Monticchio Lake. Sparks and Huang (1980) estimated that the fine layer represents, on average, 65% of the tephra volume and increases in proportion away from the vent, from 20% at 450 km to 95% of the deposit at 1,660 km from the vent. However, an absolute volume for each phase was not defined. The decreasing of Plinian material with distance from the source was also observed by Engwell et al. (2014), who used the grain-size data to investigate the dispersal of the co-Plinian and the co-ignimbrite phases. The authors calculated that 40 ± 5% of the volume of tephra within 850 km of the vent is related to the Plinian phase (as a consequence, around 60% relates to the co-ignimbrite phase, in agreement with Sparks and Huang, 1980). Furthermore, they recognized the difficulty in quantifying the absolute volume of the two phases, due to the complexity of separating the two layers in more distal deposits.

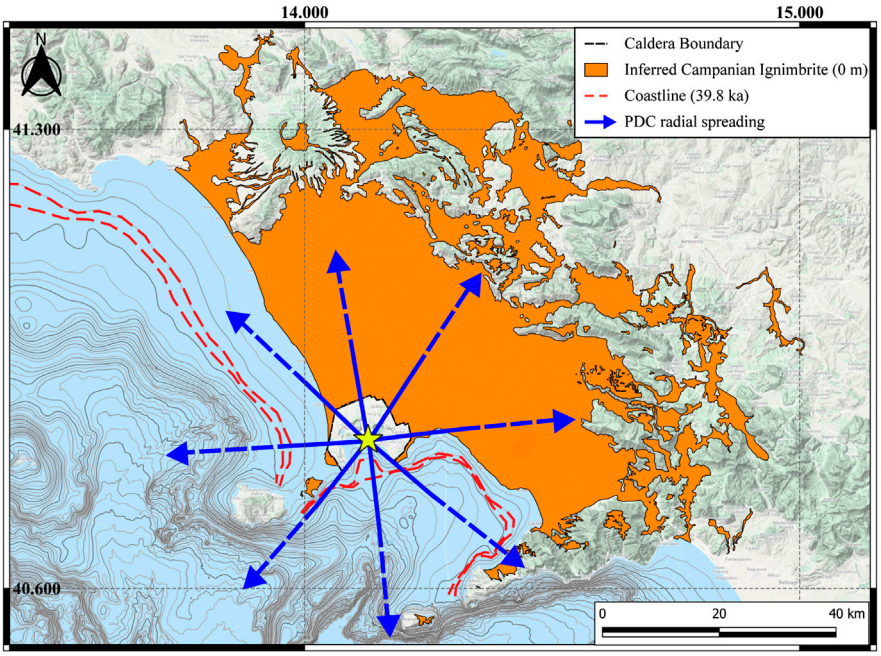

FIGURE 8 | Bathymetry of the submerged area of the Campi Flegrei caldera. The red line is the 40 ka coastline, equivalent to −75 to −87 m of the present one. The blue arrows indicate the possible radial spreading of the pyroclastic density current (PDC) based on outcrops disposed radially from the center of the caldera (yellow star) and turbidity currents in the Tyrrhenian Sea. Accumulation of volume south of the caldera is credible, due to the large submarine depressions and valleys.

Smith et al. (2016) used the CI tephra glass composition to map the dispersal of the Plinian and co-ignimbrite components over the dispersal region. Based on the glass composition, the authors recognized that the PDC component is dominant in the ultra-distal deposits, and the PDC produced the most voluminous deposits of the eruption.

Summarizing, a significant part of the pyroclastic current was elutriated or rose into the atmosphere as a co-ignimbrite cloud during the eruption and dispersed to the east (Thunell et al., 1979; Cornell et al., 1983; Perrotta and Scarpati, 2003; Pyle et al., 2006; Engwell et al., 2014; Scarpati and Perrotta, 2016). The co-ignimbrite phase was a substantial part of the total volume; but it remains difficult to define the associated absolute volume rather than as a percentage of the tephra layer.

The Volume, Mass, and Magnitude of the Campanian Ignimbrite Eruption

The bulk ignimbrite volume (V_{ign}) (**Eqs 4 and 5**) without the co-ignimbrite phase can be estimated as follows:

$$V_{ignmin} = V_{pr} + V_m + V_{intr} + 2V_e = 61.6 + 61.6 + 16 + 9.6 + 9.6 = 158.4\ km^3 \quad (4)$$

and

$$V_{ignmax} = V_{pr} + V_m + V_{intr} + 2V_e = 74.8 + 74.8 + 43.2 + 9.6 + 9.6 = 212.0\ km^3 \quad (5)$$

The total bulk PDC volume obtained using **Eqs 4 and 5** is 158.4–212.0 km^3 (**Table 3**). The co-ignimbrite volume (V_{coign}) is estimated using the formula **(6)** based on the crystal concentration method proposed by Scarpati et al. (2014) **Eq. (3)**:

$$V_{coign} = \frac{Vitric\ loss \times V_{ign}}{1 - Vitric\ loss} = \frac{0.65 \times V_{ign}}{1 - 0.65} = 294.2 - 393.7\ km^3 \quad (6)$$

The co-ignimbrite volume, using a vitric loss of 0.65, ranges between 294.2 and 393.7 km^3 (115.8–155.0 km^3 DRE), producing the highest of all previous estimates (**Table 1**). However, V_{coign} could change significantly based upon the value of vitric loss used. Walker (1972) proposed a vitric loss of 0.55 for a WGI outcrop at Altavilla, near Benevento. Using this datum, the co-ignimbrite bulk volume decreases to between 193.6 and 259.1 km^3. In this work, we use 0.65, as proposed by Scarpati et al. (2014), which is an average of more samples located in several distal sites all over the CI distribution, and from different units but it is not far from 0.55 proposed by Walker (1972). Because the calculation of the V_{coign} is beyond the purpose of this work, an alternative is to use the minimum and maximum co-ignimbrite volume reported in the literature, which are between 72 and 153.9 km^3 bulk (31–61.6 km^3 DRE; respectively, from Pyle et al., 2006 and Marti et al., 2016), but it is worth considering that this may be a significant underestimate.

The total volume of the material erupted during the PDC phase of the CI eruption ranges between 452.6 and 605.7 km^3 (179.5–242.6 km^3 DRE) (**Table 3**). This estimate is based on the preserved deposits of the CI. Among the previous estimates presented in the literature, the closest to our PDC volume are those proposed by Giaccio (2006) and Pappalardo et al. (2008) (**Table 1**).

Using the previously published fallout volume (the minimum and the maximum proposed; Perrotta and Scarpati, 2003; Marti et al., 2016), in combination with our PDC volume, gives a total eruptive volume of all eruptive phases of 456.6–659.7 km^3 (181.2–265.2 km^3 DRE) (**Table 3**). However, any of the previous estimates for the fallout volume could be used in our total volume estimate. These values are similar to some previously proposed total volumes (Cornell et al., 1983; Fedele et al., 2003; Giaccio, 2006; Pyle et al., 2006; Pappalardo et al., 2008; Costa et al., 2012), but they are constrained, for the first time, by direct thickness measurements of the ignimbrite deposit.

The mass associated with this volume, using our density estimate is **Eq. (7)**:

$$mass_{\min} = 181.2\,km^3 \times 2,608\,kg/m^3 = 4.72 \times 10^{14}\,kg \quad (7)$$

And **Eq. (8)**:

$$mass_{\max} = 265.2\,km^3 \times 2,608\,kg/m^3 = 6.91 \times 10^{14}\,kg \quad (8)$$

and the magnitude (M) **Eq. (9)** (Mason et al., 2004):

$$M = \log 10\,(mass) - 7 = 7.7 - 7.8 \quad (9)$$

This value is consistent with a VEI 7 and makes this eruption the largest Quaternary event in Europe. It is important to note, though, that while our volume calculation falls within the huge range of values previously proposed in the literature, it is in no way confirmative of any of such previous estimates, as nowhere was clarified the method for the calculation of the actual PDC deposits of the CI. We strongly state here that as the Magnitude of eruptions is essential for their classification and is the best proxy for the energy of the event, the volume calculation of PDC deposits has to be accurate and reproducible, and cannot be left to generic, averaged estimates, such as the common and usually undefined use of "average thickness" and "average area covered." Our approach to the estimate of the CI volume aims at contributing to the consolidation of a clear and reproducible method for the calculation of the deposits on ground which is the only real value onto which any other correction, such as extent of erosion and amount of ash elutriated, can be inferred.

The M and the VEI for the CI are herein calculated, for the first time, by the spatial variation of PDC thickness data, a method similar to that used to calculate tephra fallout volume, but much more complicated because of the topographic control on the PDC currents and deposits. By contrast, great errors result from using average thickness and inaccurate methods (e.g., conical shapes) instead of an accurate and reproducible isopach map for the ignimbrite deposits. The method to develop this map could be applied to any ignimbrite, including those that are mainly valley-filling and/or emplaced in complex topographic settings, such as the Andean ignimbrites (e.g., the Curacautín ignimbrite at Llaima; Naranjo and Moreno, 2005) or the Ito ignimbrite (Baer et al., 1997). A rigorous definition of the 0 m isopach, the isopachs, and each correction factor is necessary to avoid inaccurate volumes. The determination of precise errors in the ignimbrite volume (±6.6 km^3 in CI case; **Online Supplementary Material**), produced using a well-defined method to trace isopachs, is an important step forward in the study of these types of deposits.

CONCLUSIONS

The CI eruption is the largest eruptive event of the CF caldera and a fundamental chronological marker in all Central and Eastern Europe. Here we presented a review of previous estimates in the scientific literature and proposed a new method to trace ignimbrite isopachs based on the extrapolation of the paleo-topography. It works well in valley-ponded ignimbrites such as the CI, and allows the calculation of well-defined uncertainties in the on-land total volume. Before the present study, no complete isopach map of the ignimbrite was available, due to the high irregularities of the deposits. A new isopach map of the extracaldera sub-aerial CI pyroclastic flow deposits yields a volume of 68.2 ± 6.6 km^3, based directly on deposit thickness values. The greater part of this volume is in the proximal area (48.6 ± 1.7 km^3, ~70%) while only around the 30% of the volume is in the distal region within the Apennine Mountains (19.6 ± 4.9 km^3). The method, similar to those used for tephra deposits, can be used on other ignimbrites, to produce more accurate volume estimates.

Evidence suggests that the same amount of material should be both on land and offshore (assuming radial spreading of the flow). The generated submarine currents could have deposited a large amount of volcaniclastic deposits in all the submarine canyons in the Gulf of Naples and in the Tyrrhenian Sea and possibly had a strong impact on the underwater dynamics of that area. Combining separate estimates of the marine volume, the volume removed by erosion, the intracaldera volume, and the co-ignimbrite ash volume yields a total volume of 453–606 km^3 (179–243 km^3 DRE) for the PDC deposits. These values are in agreement with Giaccio (2006) and Pappalardo et al. (2008), although it is the first time that they are calculated by direct measurements with constrained error estimates. This work deals with the importance of constraining eruptive volume with field data, presenting a rigorous method to develop ignimbrite isopachs that avoids the inaccuracy of approximate techniques and defines step-by-step techniques for isopach construction and the error corrections. This is the first attempt to estimate ignimbrite volume in a comparable way to tephra fallout volume and by direct thickness data. The development of isopach maps for ignimbrite deposits, especially in complex topographic areas, is the most accurate instrument to calculate ignimbrite volumes, and is better than approximate techniques using average thicknesses or conical shapes. A rigorous definition of the 0 m isopach, the isopachs and each correction factor is necessary to avoid inexact volumes. Field data remain an essential tool to constrain primary properties of PDCs.

The total (including Plinian fallout) bulk volume estimate is 457–660 km^3 (181–265 km^3 DRE). This volume corresponds to a mass of 4.7–6.9 × 10^{14} kg, to a magnitude of 7.7–7.8 and to a VEI 7.

DATA AVAILABILITY STATEMENT

All datasets generated for this study are included in the article/ **Supplementary Material**.

AUTHOR CONTRIBUTIONS

AS conducted fieldwork, analysis, wrote the draft of this manuscript, and made the figures. GG designed the research and helped in the development of the method. RI contributed to data collection. All the authors contributed to the fieldwork, reviewed, and edited the draft.

FUNDING

The grant to the Department of Science, Roma Tre University (MIUR-Italy Dipartimenti di Eccellenza, ARTICOLO 1, COMMI 314–337 LEGGE 232/2016), is gratefully acknowledged. Partial support was provided by NSF EAR1761713 to MHO and AS.

ACKNOWLEDGMENTS

AS thanks Emanuele Sciarrino and Rose I. Gallo for their help in the fieldwork. We thank Danilo M. Palladino and Antonio Costa for discussions that improved an earlier version of this paper. Colin J. N. Wilson, Samantha Engwell, and Biagio Giaccio, as well as the editor Pablo Tierz and the chief editor Valerio Acocella are acknowledged for helpful comments that have highly improved the manuscript.

SUPPLEMENTARY MATERIAL

The Supplementary Material for this article can be found online at: https://www.frontiersin.org/articles/10.3389/feart.2020.543399/full#supplementary-material

REFERENCES

Acocella, V. (2008). Activating and reactivating pairs of nested collapses during caldera-forming eruptions: Campi Flegrei (Italy). *Geophys. Res. Lett.* 35, L17304. doi:10.1029/2008GL035078

Albert, P. G., Giaccio, B., Isaia, R., Costa, A., Niespolo, E. M., Nomade, S., et al. (2019). Evidence for a large-magnitude eruption from Campi Flegrei caldera (Italy) at 29 ka. *Geology* 47, 595–599. doi:10.1130/G45805.1

Aldiss, D. T., and Ghazali, S. A. (1984). The regional geology and evolution of the Toba volcano-tectonic depression, Indonesia. *J. Geol. Soc. London.* 141, 487–500. doi:10.1144/gsjgs.141.3.0487

Allen, S. R., and Cas, R. A. F. (2001). Transport of pyroclastic flows across the sea during the explosive, rhyolitic eruption of the Kos Plateau Tuff, Greece. *Bull. Volcanol.* 62, 441–456. doi:10.1007/s004450000107

Andrews, B. J., and Manga, M. (2011). Effects of topography on pyroclastic density current runout and formation of coignimbrites. *Geology* 39, 1099–1102. doi:10.1130/G32226.1

Antonioli, F., Bard, E., Potter, E. K., Silenzi, S., and Improta, S. (2004). 215-ka history of sea-level oscillations from marine and continental layers in Argentarola Cave speleothems (Italy). *Glob. Planet. Change.* 43, 57–78. doi:10.1016/j.gloplacha.2004.02.004

Antonioli, F. (2012). Sea level change in western-central Mediterranean since 300 kyr: comparing global sea level curves with observed data. *Alp. Mediterr. Quat.* 25, 15–23.

Auker, M. R., Sparks, R. S. J., Siebert, L., Crosweller, H. S., and Ewert, J. (2013). A statistical analysis of the global historical volcanic fatalities record. *J. Appl. Volcanol.* 2, 2. doi:10.1186/2191-5040-2-2

Badino, F., Pini, R., Ravazzi, C., Margaritora, D., Arrighi, S., Bortolini, E., et al. (2020). An overview of Alpine and Mediterranean palaeogeography, terrestrial ecosystems and climate history during MIS 3 with focus on the Middle to Upper Palaeolithic transition. *Quat. Int.* 551, 7–28. doi:10.1016/j.quaint.2019.09.024

Baer, E. M., Fisher, R. V., Fuller, M., and Valentine, G. (1997). Turbulent transport and deposition of the Ito pyroclastic flow: determinations using anisotropy of magnetic susceptibility. *J. Geophys. Res. Solid Earth.* 102, 22565–22586. doi:10.1029/96JB01277

Barberi, F., Innocenti, F., Lirer, L., Munno, R., Pescatore, T., and Santacroce, R. (1978). The Campanian Ignimbrite: a major prehistoric eruption in the Neapolitan area (Italy). *Bull. Volcanol.* 41, 10–31. doi:10.1007/BF02597680

Bellucci, F. (1994). Nuove conoscenze stratigrafiche sui depositi vulcanici del sottosuolo del settore meridionale della Piana Campana. *Boll. Soc. Geol. It.* 113, 395–420.

Best, M. G., Christiansen, E. H., Deino, A. L., Gromme, S., Hart, G. L., and Tingey, D. G. (2013a). The 36-18 Ma Indian Peak-Caliente ignimbrite field and calderas, southeastern Great Basin, USA: multicyclic super-eruptions. *Geosphere* 9, 864–950. doi:10.1130/GES00902.1

Best, M. G., Gromme, S., Deino, A. L., Christiansen, E. H., Hart, G. L., and Tingey, D. G. (2013b). The 36–18 Ma central Nevada ignimbrite field and calderas, Great Basin, USA: multicyclic super-eruptions. *Geosphere* 9, 1562–1636. doi:10.1130/GES00945.1

Black, B. A., Neely, R. R., and Manga, M. (2015). Campanian Ignimbrite volcanism, climate, and the final decline of the Neanderthals. *Geology* 43, 411–414. doi:10.1130/G36514.1

Bonadonna, C., Ernst, G. G. J., and Sparks, R. S. J. (1998). Thickness variations and volume estimates of tephra fall deposits: the importance of particle Reynolds number. *J. Volcanol. Geotherm. Res.* 81, 173–187. doi:10.1016/S0377-0273(98)00007-9

Bonadonna, C., and Houghton, B. F. (2005). Total grain-size distribution and volume of tephra-fall deposits. *Bull. Volcanol.* 67, 441–456. doi:10.1007/s00445-004-0386-2

Bonadonna, C., and Phillips, J. C. (2003). Sedimentation from strong volcanic plumes. *J. Geophys. Res.* 108, 2340. doi:10.1029/2002jb002034

Brown, S. K., Jenkins, S. F., Sparks, R. S. J., Odbert, H., and Auker, M. R. (2017). Volcanic fatalities database: analysis of volcanic threat with distance and victim classification. *J. Appl. Volcanol.* 6, 15. doi:10.1186/s13617-017-0067-4

Broxton, D., and Reneau, S. (1996). "Buried early Pleistocene landscapes beneath the Pajarito Plateau, northern New Mexico," in The Jemez Mountains region. New Mexico geological society 47th field conference guidebook, New Mexico, September 25–28, 1996. Editors F. Goff, B. S. Kues, M. A. Rogers, L. D. McFadden, and J. N. Gardner, 325–334.

Burden, R. E., Chen, L., and Phillips, J. C. (2013). A statistical method for determining the volume of volcanic fall deposits. *Bull. Volcanol.* 75, 707. doi:10.1007/s00445-013-0707-4

Bursik, M. I., and Woods, A. W. (2000). The effects of topography on sedimentation from particle-laden turbulent density currents. *J. Sediment. Res.* 70, 53–63. doi:10.1306/2DC408FE-0E47-11D7-8643000102C1865D

Cappelletti, P., Cerri, G., Colella, A., de'Gennaro, M., Langella, A., Perrotta, A., et al. (2003). Post-eruptive processes in the Campanian Ignimbrite. *Mineral. Petrol.* 79, 79–97. doi:10.1007/s00710-003-0003-7

Carey, S. N., Sigurdsson, H., Mandeville, C., and Bronto, S. (1996). Pyroclastic flows and surges over water: an example from the 1883 Krakatau eruption. *Bull. Volcanol.* 57, 493–511. doi:10.1007/BF00304435

Cini Castagnoli, G., Albrecht, A., Beer, J., Shen, C., Callegari, E., Taricco, C., et al. (1995). Evidence for enhanced ^{10}Be deposition in Mediterranean sediments 35 Kyr BP. *Geophys. Res. Lett.* 22, 707–710. doi:10.1029/95GL00298

Civetta, L., Orsi, G., Pappalardo, L., Fisher, R. V., Heiken, G., and Ort, M. H. (1997). Geochemical zoning, mingling, eruptive dynamics and depositional processes—the Campanian Ignimbrite, Campi Flegrei caldera, Italy. *J. Volcanol. Geotherm. Res.* 75, 183–219. doi:10.1016/S0377-0273(96)00027-3

Cook, G. W., Wolff, J. A., and Self, S. (2016). Estimating the eruptive volume of a large pyroclastic body: the Otowi Member of the Bandelier Tuff, Valles caldera, New Mexico. *Bull. Volcanol.* 78, 10. doi:10.1007/s00445-016-1000-0

Cornell, W., Carey, S. N., and Sigurdsson, H. (1983). Computer simulation of transport and deposition of the campanian Y-5 ash. *J. Volcanol. Geotherm. Res.* 17, 89–109. doi:10.1016/0377-0273(83)90063-X

Costa, A., Folch, A., Macedonio, G., Giaccio, B., Isaia, R., and Smith, V. C. (2012). Quantifying volcanic ash dispersal and impact of the Campanian Ignimbrite super-eruption. *Geophys. Res. Lett.* 39, L10310. doi:10.1029/2012GL051605

Costa, A., Suzuki, Y. J., and Koyaguchi, T. (2018). Understanding the plume dynamics of explosive super-eruptions. *Nat. Commun.* 9, 654. doi:10.1038/s41467-018-02901-0

Crosweller, H. S., Arora, B., Brown, S. K., Cottrell, E., Deligne, N. I., Guerrero, N. O., et al. (2012). Global database on large magnitude explosive volcanic eruptions (LaMEVE). *J. Appl. Volcanol.* 1, 4. doi:10.1186/2191-5040-1-4

Cutler, N. A., Streeter, R. T., Engwell, S. L., Bolton, M. S., Jensen, B. J. L., and Dugmore, A. J. (2020). How does tephra deposit thickness change over time? A calibration exercise based on the 1980 Mount St Helens tephra deposit. *J. Volcanol. Geotherm. Res.* 399, 106883. doi:10.1016/j.jvolgeores.2020.106883

Daag, A., and van Westen, C. J. (1996). Cartographic modelling of erosion in pyroclastic flow deposits of Mount Pinatubo, Philippines. *ITC J.* 2, 110–124.

De Natale, G., Troise, C., Mark, D., Mormone, A., Piochi, M., Di Vito, M. A., et al. (2016). The Campi Flegrei Deep Drilling Project (CFDDP): new insight on caldera structure, evolution and hazard implications for the Naples area (Southern Italy). *Geochem. Geophys. Geosyst.* 17, 4836–4847. doi:10.1002/2015GC006183

De Vivo, B., Rolandi, G., Gans, P. B., Calvert, A., Bohrson, W. A., Spera, F. J., et al. (2001). New constraints on the pyroclastic eruptive history of the Campanian Volcanic Plain (Italy). *Mineral. Petrol.* 73, 47–65. doi:10.1007/s007100170010

Di Vito, M. A., Isaia, R., Orsi, G., Southon, J., de Vita, S., D'Antonio, M., et al. (1999). Volcanism and deformation since 12,000 years at the Campi Flegrei caldera (Italy). *J. Volcanol. Geotherm. Res.* 91, 221–246. doi:10.1016/S0377-0273(99)00037-2

Douka, K., Higham, T. F., Wood, R., Boscato, P., Gambassini, P., Karkanas, P., et al. (2014). On the chronology of the Uluzzian. *J. Hum. Evol.* 68, 1–13. doi:10.1016/j.jhevol.2013.12.007

Dufek, J., and Bergantz, G. W. (2007). Dynamics and deposits generated by the Kos Plateau Tuff eruption: controls of basal particle loss on pyroclastic flow transport. *Geochem., Geophys. Geosystems.* 8, Q12007. doi:10.1029/2007GC001741

Engwell, S. L., Aspinall, W. P., and Sparks, R. S. J. (2015). An objective method for the production of isopach maps and implications for the estimation of tephra deposit volumes and their uncertainties. *Bull. Volcanol.* 77, 61. doi:10.1007/s00445-015-0942-y

Engwell, S. L., Sparks, R. S. J., and Carey, S. N. (2014). Physical characteristics of tephra layers in the deep sea realm: the Campanian Ignimbrite eruption. *Geol. Soc. London, Spec. Publ.* 398, 47–64. doi:10.1144/SP398.7

Fedele, F. G., Giaccio, B., Isaia, R., Orsi, G., Carroll, M. R., and Scaillet, B. (2007). "The Campanian Ignimbrite factor: towards a reappraisal of the Middle to Upper Palaeolithic 'transition'," in *Living under the shadow: cultural impacts of volcanic eruptions*. Editors J. Grattan and R. Torrence (Walnutt Creek, CA: Left Coast Press), 19–41.

Fedele, F. G., Giaccio, B., Isaia, R., and Orsi, G. (2002). Ecosystem impact of the Campanian Ignimbrite eruption in Late Pleistocene Europe. *Quat. Res.* 57, 420–424. doi:10.1006/qres.2002.2331

Fedele, F. G., Giaccio, B., Isaia, R., and Orsi, G. (2003). The Campanian Ignimbrite eruption, Heinrich Event 4, and Palaeolithic change in Europe: a high-resolution investigation. *AGU Geophys. Monogr.* 139, 301–325. doi:10.1029/139GM20

Fedele, L., Scarpati, C., Lanphere, M., Melluso, L., Morra, V., Perrotta, A., et al. (2008). The Breccia Museo formation, Campi Flegrei, southern Italy: geochronology, chemostratigraphy and relationship with the Campanian Ignimbrite eruption. *Bull. Volcanol.* 70, 1189–1219. doi:10.1007/s00445-008-0197-y

Fedele, L., Scarpati, C., Sparice, D., Perrotta, A., and Laiena, F. (2016). A chemostratigraphic study of the Campanian Ignimbrite eruption (Campi Flegrei, Italy): insights on magma chamber withdrawal and deposit accumulation as revealed by compositionally zoned stratigraphic and facies framework. *J. Volcanol. Geotherm. Res.* 324, 105–117. doi:10.1016/j.jvolgeores.2016.05.019

Fierstein, J., and Hildreth, W. (1992). The plinian eruptions of 1912 at Novarupta, Katmai National Park, Alaska. *Bull. Volcanol.* 54, 646–684. doi:10.1007/BF00430778

Fisher, R. V., Orsi, G., Ort, M. H., and Heiken, G. (1993). Mobility of a large-volume pyroclastic flow—emplacement of the Campanian ignimbrite, Italy. *J. Volcanol. Geotherm. Res.* 56, 205–220. doi:10.1016/0377-0273(93)90017-L

Folch, A. (2012). A review of tephra transport and dispersal models: evolution, current status, and future perspectives. *J. Volcanol. Geotherm. Res.* 235–236. doi:10.1016/j.jvolgeores.2012.05.020

Folch, A., Costa, A., Durant, A., and Macedonio, G. (2010). A model for wet aggregation of ash particles in volcanic plumes and clouds: 2. Model application. *J. Geophys. Res.* 115, B09202. doi:10.1029/2009JB007176

Folkes, C. B., Wright, H. M. N., Cas, R. A. F., de Silva, S. L., Lesti, C., and Viramonte, J. G. (2011). A re-appraisal of the stratigraphy and volcanology of the Cerro Galán volcanic system, NW Argentina. *Bull. Volcanol.* 73, 1427–1454. doi:10.1007/s00445-011-0459-y

Gambassini, P. (1997). *Il Paleolitico di Castelcivita: culture e ambiente*. Napoli, Italy: Electa.

Geyer, A., and Martí, J. (2008). The new worldwide collapse caldera database (CCDB): a tool for studying and understanding caldera processes. *J. Volcanol. Geotherm. Res.* 175, 334–354. doi:10.1016/j.jvolgeores.2008.03.017

Giaccio, B., Hajdas, I., Isaia, R., Deino, A. L., and Nomade, S. (2017). High-precision ^{14}C and $^{40}Ar/^{39}Ar$ dating of the Campanian Ignimbrite (Y-5) reconciles the time-scales of climatic-cultural processes at 40 ka. *Sci. Rep.* 7, 45940. doi:10.1038/srep45940

Giaccio, B., Hajdas, I., Peresani, M., Fedele, F. G., and Isaia, R. (2006). "The Campanian Ignimbrite tephra and its relevance for the timing of the Middle to Upper Paleolithic shift," in *When Neanderthals and modern humans met*. Editor N. J. Conard (Tübingen, Germany: Kerns Verlag), 343–375.

Giaccio, B., Isaia, R., Fedele, F. G., Di Canzio, E., Hoffecker, J. F., Ronchitelli, A., et al. (2008). The Campanian Ignimbrite and Codola tephra layers: two temporal/stratigraphic markers for the Early Upper Palaeolithic in southern Italy and eastern Europe. *J. Volcanol. Geotherm. Res.* 177, 208–226. doi:10.1016/j.jvolgeores.2007.10.007

Giaccio, B. (2006). L'eruzione dell'Ignimbrite Campana (c. 40 ka BP), oscillazioni climatiche sub-orbitali e i cambiamenti bioculturali dell'OIS 3 europeo. Doctoral dissertation/PhD thesis. Naples (IT): University of Naples Federico II.

Giordano, G.; The CARG Team (2010). "Stratigraphy and volcano-tectonic structures of the Colli Albani volcanic field," in *The Colli Albani Volcano*, Editors R. Funiciello and G. Giordano, (London: Geol. Soc. London, Special Publication of IAVCEI), Vol. 3, 43–97.

Giordano, G., and Doronzo, D. M. (2017). Sedimentation and mobility of PDCs: a reappraisal of ignimbrites' aspect ratio. *Sci. Rep.* 7, 4444. doi:10.1038/s41598-017-04880-6

Giordano, G. (1998). The effect of paleotopography on lithic distribution and facies associations of small volume ignimbrites: the WTT Cupa (Roccamonfina volcano, Italy). *J. Volcanol. Geotherm. Res.* 87, 255–273. doi:10.1016/S0377-0273(98)00096-1

Hajdas, I., Taricco, C., Bonani, G., Beer, J., Bernasconi, S. M., and Wacker, L. (2011). Anomalous radiocarbon ages found in Campanian Ignimbrite deposit of the Mediterranean deep-sea core CT85-5. *Radiocarbon* 53, 575–583. doi:10.1017/S0033822200039059

Henry, C. D., and Price, J. G. (1984). Variations in caldera development in the Tertiary volcanic field of Trans-Pecos Texas. *J. Geophys. Res.* 89, 8765–8786. doi:10.1029/JB089iB10p08765

Isaia, R., Marianelli, P., and Sbrana, A. (2009). Caldera unrest prior to intense volcanism in Campi Flegrei (Italy) at 4.0 ka B.P.: implications for caldera dynamics and future eruptive scenarios. *Geophys. Res. Lett.* 36, L21303. doi:10.1029/2009GL040513

ISPRA (2009). *Geological map n. 432 "Benevento"; scale 1:50,000*. Urbino, Italy: National Geological Survey of Italy, Università degli studi di Urbino, Istituto di Geologia Applicata.

ISPRA (2010). *Geological map n. 431 "Caserta Est"; scale 1:50,000*. Napoli, Italy: National Geological Survey of Italy, Regione Campania, Settore Difesa Suolo.

ISPRA (2011a). *Geological map n. 465 "Isola di Procida"; scale 1:50,000*. Napoli, Italy: National Geological Survey of Italy, Regione Campania, Settore Difesa Suolo.

ISPRA (2011b). *Geological map n. 448 "Ercolano"; scale 1:50,000*. Napoli, Italy: National Geological Survey of Italy, CNR Consiglio Nazionale delle Ricerche.

ISPRA (2011c). *Geological map n. 467 "Salerno"; scale 1:50,000*. National Geological Survey of Italy. Available at: https://www.isprambiente.gov.it/Media/carg/467_SALERNO/Foglio.html.

ISPRA (2011d). *Geological map n. 446-447 "Napoli"; scale 1:50,000*. Napoli, Italy: National Geological Survey of Italy, Regione Campania, Settore Difesa Suolo.

ISPRA (2014a). *Geological map n. 450 "S.Angelo dei Lombardi"; scale 1:50,000*. Napoli, Italy: National Geological Survey of Italy, CNR Consiglio Nazionale delle Ricerche.

ISPRA (2014b). *Geological map n. 466-485 "Sorrento-Termini"; scale 1:50,000*. Napoli, Italy: National Geological Survey of Italy, CNR Consiglio Nazionale delle Ricerche.

ISPRA (2016). *Geological map n. 449 "Avellino"; scale 1:50,000*. Napoli, Italy: National Geological Survey of Italy, Regione Campania.

ISPRA (2018). *Geological map n. 464 "Isola d'Ischia"; scale 1:25,000*. Napoli, Italy: National Geological Survey of Italy, Regione Campania, Settore Difesa Suolo.

Keller, J., Ryan, W. B. F., Ninkovich, D., and Altherr, R. (1978). Explosive volcanic activity in the Mediterranean over the past 200,000 yr as recorded in deep-sea sediments. *Bull. Geol. Soc. Am.* 89, 591–604. doi:10.1130/0016-7606(1978)89<591:EVAITM>2.0.CO;2

Lambeck, K., and Bard, E. (2000). Sea-level change along the French Mediterranean coast for the past 30000 years. *Earth Planet. Sci. Lett.* 175, 203–222. doi:10.1016/S0012-821X(99)00289-7

Langella, A., Bish, D. L., Calcaterra, D., and Cappelletti, P. (2013). "L'Ignimbrite Campana (IC)," in *Le pietre storiche della Campania dall'oblio alla riscoperta*. Editors M. De Gennaro, D. Calcaterra, and A. Langella (Napoli, Italy: Luciano Editore), 155–177.

Lowe, J., Barton, N., Blockley, S., Ramsey, C. B., Cullen, V. L., Davies, W., et al. (2012). Volcanic ash layers illuminate the resilience of Neanderthals and early modern humans to natural hazards. *Proc. Natl. Acad. Sci. U. S. A.* 109, 13532–13537. doi:10.1073/pnas.1204579109

Marianelli, P., Sbrana, A., and Proto, M. (2006). Magma chamber of the Campi Flegrei supervolcano at the time of eruption of the Campanian Ignimbrite. *Geology* 34, 937–940. doi:10.1130/G22807A.1

Marti, A., Folch, A., Costa, A., and Engwell, S. L. (2016). Reconstructing the plinian and co-ignimbrite sources of large volcanic eruptions: a novel approach for the Campanian Ignimbrite. *Sci. Rep.* 6, 21220. doi:10.1038/srep21220

Mason, B. G., Pyle, D. M., and Oppenheimer, C. (2004). The size and frequency of the largest explosive eruptions on Earth. *Bull. Volcanol.* 66, 735–748. doi:10.1007/s00445-004-0355-9

McCoy, F. W., and Cornell, W. (1990). "Volcaniclastic sediments in the Tyrrhenian Basin," in Proceedings of the ocean drilling program, scientific results 107, Editors K. A. Kastens, et al. (College Station, TX: Ocean Drilling Program), 291–305. doi:10.2973/odp.proc.sr.107.119.1990

Melekestsev, I. V., Kirianov, V. Y., and Praslov, N. D. (1984). Catastrophic eruption in the Phlegrean Fields region (Italy) - possible source for a volcanic ash in late Pleistocene sediments on the European part of the USSR. *Vulcanol. Seismol.* 3, 35–44.

Melluso, L., Morra, V., Perrotta, A., Scarpati, C., and Adabbo, M. (1995). The eruption of the Breccia Museo (Campi Flegrei, Italy): fractional crystallization processes in a shallow, zoned magma chamber and implications for the eruptive dynamics. *J. Volcanol. Geotherm. Res.* 68, 325–339. doi:10.1016/0377-0273(95)00020-5

Mihailović, D., and Whallon, R. (2017). Crvena Stijena revisited: the late Mousterian assemblages. *Quat. Int.* 450, 36–49. doi:10.1016/j.quaint.2016.12.026

Milia, A., Morabito, S., and Petrosino, P. (2020). Late Pleistocene–Holocene climatic and volcanic events in the bathyal area of the eastern Tyrrhenian Sea and the stratigraphic signature of the 39 ka Campanian Ignimbrite eruption. *Global Planet. Change.* 185, 103074. doi:10.1016/j.gloplacha.2019.103074

Milia, A., and Torrente, M. M. (2007). The influence of paleogeographic setting and crustal subsidence on the architecture of ignimbrites in the Bay of Naples (Italy). *Earth Planet. Sci. Lett.* 263, 192–206. doi:10.1016/j.epsl.2007.08.004

Morgan, L. A., Doherty, D. J., and Leeman, W. P. (1984). Ignimbrites of the Eastern Snake River Plain: evidence for major caldera-forming eruptions. *J. Geophys. Res.* 89, 8665–8678. doi:10.1029/JB089iB10p08665

Morley, M. W., and Woodward, J. C. (2011). The Campanian Ignimbrite at Crvena Stijena rockshelter in Montenegro. *Quat. Res.* 75, 683–696. doi:10.1016/j.yqres.2011.02.005

Mormone, A., Troise, C., Piochi, M., Balassone, G., Joachimski, M., and De Natale, G. (2015). Mineralogical, geochemical and isotopic features of tuffs from the CFDDP drill hole: hydrothermal activity in the eastern side of the Campi Flegrei volcano (southern Italy). *J. Volcanol. Geotherm. Res.* 290, 39–52. doi:10.1016/j.jvolgeores.2014.12.003

Naranjo, J. A., and Moreno, H. (2005). *Geología del volcán Llaima, región de La Araucanía, escala: 1: 50.000*, Santiago, Chile: Servicio Nacional de Geología y Minería, 88.

Narcisi, B. (1996). Tephrochronology of a late Quaternary lacustrine record from the Monticchio maar (Vulture volcano, southern Italy). *Quat. Sci. Rev.* 15, 155–165. doi:10.1016/0277-3791(95)00045-3

Narcisi, B., and Vezzoli, L. (1999). Quaternary stratigraphy of distal tephra layers in the Mediterranean - an overview. *Glob. Planet. Change.* 21, 31–50. doi:10.1016/S0921-8181(99)00006-5

Newhall, C. G., and Self, S. (1982). The volcanic explosivity index (VEI) an estimate of explosive magnitude for historical volcanism. *J. Geophys. Res. Oceans.* 87, 1231–1238. doi:10.1029/JC087iC02p01231

Orsi, G., de Vita, S., and Di Vito, M. A. (1996). The restless, resurgent Campi Flegrei nested caldera (Italy): constraints on its evolution and configuration. *J. Volcanol. Geotherm. Res.* 74, 179–214. doi:10.1016/S0377-0273(96)00063-7

Ort, M. H., Orsi, G., Pappalardo, L., and Fisher, R. V. (2003). Anisotropy of magnetic susceptibility studies of depositional processes in the Campanian Ignimbrite, Italy. *Bull. Volcanol.* 65, 55–72. doi:10.1007/s00445-002-0241-2

Ortolani, F., and Aprile, F. (1985). Principali caratteristiche stratigrafiche e strutturali dei depositi superficiali della Piana Campana. *Boll. Soc. Geol. It.* 104, 195–206.

Pérez, W., Alvarado, G. E., and Gans, P. B. (2006). The 322 ka Tiribí Tuff: stratigraphy, geochronology and mechanisms of deposition of the largest and most recent ignimbrite in the Valle Central, Costa Rica. *Bull. Volcanol.* 69, 25–40. doi:10.1007/s00445-006-0053-x

Pacheco-Hoyos, J. G., Aguirre-Díaz, G. J., and Dávila-Harris, P. (2018). Boiling-over dense pyroclastic density currents during the formation of the ~100 km^3 Huichapan ignimbrite in central Mexico: stratigraphic and lithofacies analysis. *J. Volcanol. Geotherm. Res.* 349, 268–282. doi:10.1016/j.jvolgeores.2017.11.007

Pappalardo, L., Civetta, L., D'Antonio, M., Deino, A. L., Di Vito, M. A., Orsi, G., et al. (1999). Chemical and Sr-isotopical evolution of the Phlegraean magmatic system before the Campanian Ignimbrite and the Neapolitan Yellow Tuff eruptions. *J. Volcanol. Geotherm. Res.* 91, 141–166. doi:10.1016/S0377-0273(99)00033-5

Pappalardo, L., Ottolini, L., and Mastrolorenzo, G. (2008). The Campanian Ignimbrite (southern Italy) geochemical zoning: insight on the generation of a super-eruption from catastrophic differentiation and fast withdrawal. *Contrib. Mineral. Petrol.* 156, 1–26. doi:10.1007/s00410-007-0270-0

Parfitt, L., and Wilson, L. (2008). *Fundamentals of physical volcanology*. Malden, MA: Blackwell.

Paterne, M., Guichard, F., Labeyrie, J., Gillot, P. Y., and Duplessy, J. C. (1986). Tyrrhenian Sea tephrochronology of the oxygen isotope record for the past 60,000 years. *Mar. Geol.* 72, 259–285. doi:10.1016/0025-3227(86)90123-4

Paterne, M., Kallel, N., Labeyrie, L., Vautravers, M., Duplessy, J. C., Rossignol-Strick, M., et al. (1999). Hydrological relationship between the north Atlantic Ocean and the Mediterranean Sea during the past 15–75 kyr. *Paleoceanography* 14, 626–638. doi:10.1029/1998PA900022

Perrotta, A., Scarpati, C., Luongo, G., and Morra, V. (2006). "Chapter 5 The Campi Flegrei caldera boundary in the city of Naples," in *Developments in volcanology*. Editor B. De Vivo (New York, NY: Elsevier), Vol. 9, 85–96. doi:10.1016/S1871-644X(06)80019-7

Perrotta, A., Scarpati, C., Luongo, G., and Morra, V. (2010). Stratigraphy and volcanological evolution of the southwestern sector of Campi Flegrei and Procida Island, Italy. *Geol. Soc. Am. Spec. Pap.* 464, 171–191. doi:10.1130/2010.2464(09)

Perrotta, A., and Scarpati, C. (1994). The dynamics of the Breccia Museo eruption (Campi Flegrei, Italy) and the significance of spatter clasts associated with lithic breccias. *J. Volcanol. Geotherm. Res.* 59, 335–355. doi:10.1016/0377-0273(94)90086-8

Perrotta, A., and Scarpati, C. (2003). Volume partition between the plinian and co-ignimbrite air fall deposits of the Campanian Ignimbrite eruption. *Mineral. Petrol.* 79, 67–78. doi:10.1007/s00710-003-0002-8

Pyle, D. M. (1989). The thickness, volume and grainsize of tephra fall deposits. *Bull. Volcanol.* 51, 1–15. doi:10.1007/BF01086757

Pyle, D. M. (1990). "New volume estimates for the Minoan eruption of Santorini," in *Thera and the Aegean world III*. Editors D. A. Hardy, J. Keller, V. Galanopoulos, N. C. Flemming, and T. H. Druitt (London, UK: The Thera Foundation), 113–121.

Pyle, D. M. (2000). "Sizes of volcanic eruptions," in *The encyclopedia of volcanoes*. Editors H. Sigurdsson, B. F. Houghton, S. R. McNutt, H. Rymer, and J. Stix (London, UK: Academic Press), 263–269.

Pyle, D. M. (2015). "Sizes of volcanic eruptions," in *The encyclopedia of volcanoes*. Editors H. Sigurdsson, B. F. Houghton, S. R. McNutt, H. Rymer, and J. Stix (London, UK: Academic Press), 257–264. doi:10.1016/B978-0-12-385938-9.00013-4

Pyle, D. M., Ricketts, G. D., Margari, V., van Andel, T. H., Sinitsyn, A. A., Praslov, N. D., et al. (2006). Wide dispersal and deposition of distal tephra during the Pleistocene "Campanian Ignimbrite/Y5" eruption, Italy. *Quat. Sci. Rev.* 25, 2713–2728. doi:10.1016/j.quascirev.2006.06.008

Rampino, M. R., and Self, S. (1992). Volcanic winter and accelerated glaciation following the Toba super-eruption. *Nature* 359, 50–52. doi:10.1038/359050a0

Ratté, J. C., Marvin, R. F., Naeser, C. W., and Bikerman, M. (1984). Calderas and ash flow tuffs of the Mogollon Mountains, southwestern New Mexico. *J. Geophys. Res.* 89, 8713. doi:10.1029/JB089iB10p08713

Rhoades, D. A., Dowrick, D. J., and Wilson, C. J. N. (2002). Volcanic hazard in New Zealand: scaling and attenuation relations for tephra fall deposits from Taupo Volcano. *Nat. Hazards.* 26, 147–174. doi:10.1023/A:1015608732356

Robock, A. (2000). Volcanic eruptions and climate. *Rev. Geophys.* 38, 191–219. doi:10.1029/1998RG000054

Rolandi, G., Bellucci, F., Heizler, M. T., Belkin, H. E., and De Vivo, B. (2003). Tectonic controls on the genesis of ignimbrites from the Campanian Volcanic Zone, southern Italy. *Mineral. Petrol.* 79, 3–31. doi:10.1007/s00710-003-0014-4

Rosi, M., and Sbrana, A. (1987). Phlegrean fields. *CNR Quad. La. Ricerca Sci.* 114, 1–175.

Rosi, M., Sbrana, A., and Principe, C. (1983). The Phlegraean Fields: structural evolution, volcanic history and eruptive mechanisms. *J. Volcanol. Geotherm. Res.* 17, 273–288. doi:10.1016/0377-0273(83)90072-0

Rosi, M., Sbrana, A., and Vezzoli, L. (1988). Correlazioni tefrostratigrafiche di alcuni livelli di Ischia, Procida e Campi Flegrei. *Mem. Soc. Geol. Ital.* 41, 1015–1027.

Rosi, M., Vezzoli, L., Aleotti, P., and Censi, M. (1996). Interaction between caldera collapse and eruptive dynamics during the Campanian Ignimbrite eruption, Phlegraean Fields, Italy. *Bull. Volcanol.* 57, 541–554. doi:10.1007/BF00304438

Rosi, M., Vezzoli, L., Castelmenzano, A., and Grieco, G. (1999). Plinian pumice fall deposit of the Campanian Ignimbrite eruption (Phlegraean Fields, Italy). *J. Volcanol. Geotherm. Res.* 91, 179–198. doi:10.1016/S0377-0273(99)00035-9

Ruberti, D., Vigliotti, M., Rolandi, R., and Di Lascio, M. (2020). "Effect of paleomorphology on facies distribution of the Campania Ignimbrite in the northern Campania Plain, southern Italy," in *Vesuvius, Campi Flegrei, and Campanian Volcanism*. Editors B. De Vivo, H. E. Belkin, and G. Rolandi (Amsterdam, Netherlands: Elsevier Inc.), 207–229. doi:10.1016/B978-0-12-816454-9.00009-2

Scandone, R., Bellucci, F., Lirer, L., and Rolandi, G. (1991). The structure of the Campanian Plain and the activity of the Neapolitan volcanoes (Italy). *J. Volcanol. Geotherm. Res.* 48, 1–31. doi:10.1016/0377-0273(91)90030-4

Scarpati, C., and Perrotta, A. (2012). Erosional characteristics and behavior of large pyroclastic density currents. *Geology* 40, 1035–1038. doi:10.1130/G33380.1

Scarpati, C., Perrotta, A., Lepore, S., and Calvert, A. (2013). Eruptive history of Neapolitan volcanoes: constraints from ^{40}Ar–^{39}Ar dating. *Geol. Mag.* 150, 412–425. doi:10.1017/S0016756812000854

Scarpati, C., and Perrotta, A. (2016). Stratigraphy and physical parameters of the Plinian phase of the Campanian Ignimbrite eruption. *Bull. Geol. Soc. Am.* 128, 1147–1159. doi:10.1130/B31331.1

Scarpati, C., Sparice, D., and Perrotta, A. (2014). A crystal concentration method for calculating Ignimbrite volume from distal ash-fall deposits and a reappraisal of the magnitude of the Campanian Ignimbrite. *J. Volcanol. Geotherm. Res.* 280, 67–75. doi:10.1016/j.jvolgeores.2014.05.009

Scarpati, C., Sparice, D., and Perrotta, A. (2015a). Facies variation in the Campanian Ignimbrite. *Rend. Online Soc. Geol. Ital.* 33, 83–87. doi:10.3301/ROL:2015.20

Scarpati, C., Sparice, D., and Perrotta, A. (2015b). The ground layer of the Campanian Ignimbrite: an example of deposition from a dilute pyroclastic density current. *Bull. Volcanol.* 77, 97. doi:10.1007/s00445-015-0985-0

Scott, W. E., Hoblitt, R. P., Torres, R. C., Self, S., Martinez, M. M. L., and Nillos, T. (1996). "Pyroclastic flows of the June 15, 1991, climactic eruption of Mount pinatubo," in *Fire and mud: eruptions and lahars of Mount Pinatubo, Philippines*. Editors C.G. Newhall and R. Punongbayan (Seattle, WA: University of Washington Press), 545–570.

Servizio Geologico d'Italia (1963). *Carta geologica d'Italia scala 1:100.000, foglio 174 – Ariano Irpino "Geological map of Italy at 1:100.000 scale, sheet number 174 – Ariano Irpino"*. Rome, Italy: Servizio Geologico d'Italia.

Servizio Geologico d'Italia (1965). *Carta geologica d'Italia scala 1:100.000, foglio 197 – Amalfi "Geological map of Italy at 1:100.000 scale, sheet number 197 – Amalfi"*. Rome, Italy: Servizio Geologico d'Italia.

Servizio Geologico d'Italia (1966). *Foglio Geologico no 172 - Caserta. Carta Geologica d'Italia, scala 1:100.000, II ediz.* Roma, Italy: Istituto Poligrafico e Zecca dello Stato.

Servizio Geologico d'Italia (1967). *Carta geologica d'Italia scala 1:100.000, fogli 160 – Cassino "Geological map of Italy at 1:100.000 scale, sheet number 160 – Cassino"*. Rome, Italy: Servizio Geologico d'Italia.

Servizio Geologico d'Italia (1971a). *Carta geologica d'Italia scala 1:100.000, foglio 171 – Gaeta e Vulcano di Roccamonfina "Geological map of Italy at 1:100.000 scale, sheet number 171 – Gaeta e Vulcano di Roccamonfina"*. Rome, Italy: Servizio Geologico d'Italia.

Servizio Geologico d'Italia (1971b). *Carta geologica d'Italia scala 1:100.000, foglio 161 – Isernia "Geological map of Italy at 1:100.000 scale, sheet number 161 – Isernia"*. Rome, Italy: Servizio Geologico d'Italia.

Servizio Geologico d'Italia (1975). *Carta geologica d'Italia scala 1:100.000, foglio 173 – Benevento "Geological map of Italy at 1:100.000 scale, sheet number 173 – Benevento"*. Rome, Italy: Servizio Geologico d'Italia.

Seymour, K. S., Christanis, K., Bouzinos, A., Papazisimou, S., Papatheodorou, G., Moran, E., et al. (2004). Tephrostratigraphy and tephrochronology in the Philippi peat basin, Macedonia, Northern Hellas (Greece). *Quat. Int.* 121, 53–65. doi:10.1016/j.quaint.2004.01.023

Seymour, K. S., and Christanis, K. (1995). Correlation of a Tephra Layer in Western Greece with a Late Pleistocene Eruption in the Campanian Province of Italy. *Quat. Res.* 43, 46–54. doi:10.1006/qres.1995.1005

Smith, V. C., Isaia, R., Engwell, S. L., and Albert, P. G. (2016). Tephra dispersal during the Campanian Ignimbrite (Italy) eruption: implications for ultra-distal ash transport during the large caldera-forming eruption. *Bull. Volcanol.* 78, 45. doi:10.1007/s00445-016-1037-0

Smith, V. C., Isaia, R., and Pearce, N. J. G. (2011). Tephrostratigraphy and glass compositions of post-15 kyr Campi Flegrei eruptions: implications for eruption history and chronostratigraphic markers. *Quat. Sci. Rev.* 30, 3638–3660. doi:10.1016/j.quascirev.2011.07.012

Sparice, D. (2015). Definizione delle litofacies e ricostruzione dell'architettura dell'Ignimbrite Campana. Doctoral dissertation/PhD thesis. Naples (Italy): University of Naples Federico II.

Sparks, R. S. J., Francis, P. W., Hamer, R. D., Pankhurst, R. J., O'Callaghan, L. O., Thorpe, R. S., et al. (1985). Ignimbrites of the Cerro Galan caldera, NW Argentina. *J. Volcanol. Geotherm. Res.* 24, 205–248. doi:10.1016/0377-0273(85)90071-X

Sparks, R. S. J., and Huang, T. C. (1980). The volcanological significance of deep-sea ash layer associated with ignimbrites. *Geol. Mag.* 117, 425–436. doi:10.1017/S0016756800028533

Sparks, R. S. J., Self, S., Grattan, J., Oppenheimer, C., Pyle, D. M., and Rymer, H. (2005). *Super-eruptions: global effects and future threats*. London, UK: The Geological Society. Report of a Geological Society of London Working Group.

Sparks, R. S. J., and Walker, G. P. L. (1977). The significance of vitric-enriched air-fall ashes associated with crystal-enriched ignimbrites. *J. Volcanol. Geotherm. Res.* 2, 329–341. doi:10.1016/0377-0273(77)90019-1

Stuiver, M., Grootes, P. M., and Braziunas, T. F. (1995). The GISP2 δ^{18}O climate record of the past 16,500 years and the role of the Sun, Ocean, and Volcanoes. *Quat. Res.* 44, 341–354. doi:10.1006/qres.1995.1079

Takarada, S., and Hoshizumi, H. (2020). Distribution and eruptive volume of Aso-4 pyroclastic density current and tephra fall deposits, Japan: a M8 super-eruption. *Front. Earth Sci.* 8, 170. doi:10.3389/feart.2020.00170

Tarquini, S., Isola, I., Favalli, M., Mazzarini, F., Bisson, M., Pareschi, M. T., et al. (2007). TINITALY/01: a new triangular irregular network of Italy. *Ann. Geophys.* 50, 407–425. doi:10.4401/ag-4424

Tarquini, S., and Nannipieri, L. (2017). The 10 m-resolution TINITALY DEM as a trans-disciplinary basis for the analysis of the Italian territory: current trends and new perspectives. *Geomorphology* 281, 108–115. doi:10.1016/j.geomprph.2016.12.022

Tarquini, S., Vinci, S., Favalli, M., Doumaz, F., Fornaciai, A., and Nannipieri, L. (2012). Release of a 10-m-resolution DEM for the Italian territory: comparison with global-coverage DEMs and anaglyph-mode exploration via the web. *Comput. Geosci.* 38, 168–170. doi:10.1016/j.cageo.2011.04.018

Thordarson, T., and Self, S. (1996). Sulfur, chlorine and fluorine degassing and atmospheric loading by the Roza eruption, Columbia River Basalt Group, Washington, USA. *J. Volcanol. Geotherm. Res.* 74, 49–73. doi:10.1007/s004450050136

Thunell, R., Federman, A., Sparks, R. S. J., and Williams, D. (1979). The age, origin, and volcanological significance of the Y-5 ash layer in the Mediterranean. *Quat. Res.* 12, 241–253. doi:10.1016/0033-5894(79)90060-7

Ton-That, T., Singer, B., and Paterne, M. (2001). $^{40}Ar/^{39}Ar$ dating of latest Pleistocene (41 ka) marine tephra in the Mediterranean Sea: implications for global climate records. *Earth Planet. Sci. Lett.* 184, 645–658. doi:10.1016/S0012-821X(00)00358-7

Torrente, M. M., Milia, A., Bellucci, F., and Rolandi, G. (2010). Extensional tectonics in the Campania Volcanic Zone (eastern Tyrrhenian Sea, Italy): new insights into the relationship between faulting and ignimbrite eruptions. *Boll. Soc. Geol. It.* 129, 297–315. doi:10.3301/IJG.2010.07

Upton, J., Cole, P. D., Shaw, P., Szakacs, A., and Seghedi, I. (2002). "Correlation of tephra layers found in southern Romania with the Campanian Ignimbrite (~37 ka)," in *The Quaternary research association and first postgraduate paleo-environmental symposium* (Amsterdam, Netherlands: Universiteit van Amsterdam), 36.

Veres, D., Lane, C. S., Timar-Gabor, A., Hambach, U., Constantin, D., Szakács, A., et al. (2013). The Campanian Ignimbrite/Y5 tephra layer–a regional stratigraphic marker for Isotope Stage 3 deposits in the Lower Danube region, Romania. *Quat. Int.* 293, 22–33. doi:10.1016/j.quaint.2012.02.042

Vitale, S., and Isaia, R. (2014). Fractures and faults in volcanic rocks (Campi Flegrei, southern Italy): insight into volcano-tectonic processes. *Int. J. Earth Sci.* 103, 801–819. doi:10.1007/s00531-013-0979-0

Walker, G. P. L., and Croasdale, R. (1970). Two plinian-type eruptions in the Azores. *J. Geolog. Soc.* 127, 17–55. doi:10.1144/gsjgs.127.1.0017

Walker, G. P. L. (1972). Crystal concentration in ignimbrites. *Contrib. Mineral. Petrol.* 36, 135–146. doi:10.1007/BF00371184

Walker, G. P. L. (1973). Explosive volcanic eruptions—a new classification scheme. *Geol. Rundsch.* 62, 431–446. doi:10.1007/BF01840108

Walker, G. P. L. (1980). The Taupo pumice: product of the most powerful known (ultraplinian) eruption? *J. Volcanol. Geotherm. Res.* 8, 69–94. doi:10.1016/0377-0273(80)90008-6

Walker, G. P. L. (1983). Ignimbrite types and ignimbrite problems. *J. Volcanol. Geotherm. Res.* 17, 65–88. doi:10.1016/0377-0273(83)90062-8

Willcock, M. A. W., Cas, R. A. F., Giordano, G., and Morelli, C., (2013). The eruption, pyroclastic flow behaviour, and caldera in-filling processes of the extremely large volume (> 1290 km^3), intra- to extra-caldera, Permian Ora (Ignimbrite) Formation, Southern Alps, Italy. *J. Volcanol. Geotherm. Res.* 265, 102–126. doi:10.1016/j.jvolgeores.2013.08.012

Wilson, C. J. N. (1991). Ignimbrite morphology and the effects of erosion: a New Zealand case study. *Bull. Volcanol.* 53, 635–644. doi:10.1007/BF00493690

Wilson, C. J. N. (2001). The 26.5 ka Oruanui eruption, New Zealand: an introduction and overview. *J. Volcanol. Geotherm. Res.* 112, 133–174. doi:10.1016/S0377-0273(01)00239-6

Wilson, C. J. N., and Walker, G. P. L. (1985). The Taupo eruption, New Zealand. 1. General aspects. *Philos. Trans. R. Soc. A Math. Phys. Eng. Sci.* 314, 199–228. doi:10.1098/rsta.1985.0019

Wood, R. E., Douka, K., Boscato, P., Haesaerts, P., Sinitsyn, A., and Higham, T. (2012). Testing the ABOx-SC method: dating known-age charcoals associated with the Campanian Ignimbrite. *Quat. Geochronol.* 9, 16–26. doi:10.1016/j.quageo.2012.02.003

Woods, A. W., and Wohletz, K. (1991). Dimensions and dynamics of co-ignimbrite eruption columns. *Nature*, 350, 225–227. doi:10.1038/350225a0

Wulf, S., Kraml, M., Brauer, A., Keller, J., and Negendank, J. F. W. (2004). Tephrochronology of the 100 ka lacustrine sediment record of Lago Grande di Monticchio (southern Italy). *Quat. Int.* 122, 7–30. doi:10.1016/j.quaint.2004.01.028

Yang, Q., and Bursik, M. (2016). A new interpolation method to model thickness, isopachs, extent, and volume of tephra fall deposits. *Bull. Volcanol.* 78. 68–21. doi:10.1007/s00445-016-1061-0

Yokoyama, S. (1974). Mode of movement and emplacement of Ito pyroclastic flow from Aira caldera, Japan. *Science Reports, Tokyo Kyoiku Daigaku.* 12, 17–62.

Yokoyama, S. (1985). Geomorphological aspects of large-scale pyroclastic flow deposits: a review. *Trans. Jpn. Geomorphol. Union.* 6, 131–152.

Zanchetta, G., Giaccio, B., Bini, M., and Sarti, L. (2018). Tephrostratigraphy of Grotta del Cavallo, Southern Italy: insights on the chronology of Middle to Upper Palaeolithic transition in the Mediterranean. *Quat. Sci. Rev.* 182, 65–77. doi:10.1016/j.quascirev.2017.12.014

Conflict of Interest: The authors declare that the research was conducted in the absence of any commercial or financial relationships that could be construed as a potential conflict of interest.

The reviewer BG declared a past co-authorship with one of the authors RI to the handling editor.

GLOSSARY

a.s.l.: above sea level

CCDB Collapse Caldera Database

CE Common Era

CF Campi Flegrei

CI Campanian Ignimbrite

DEM Digital Elevation Model

DRE Dense Rock Equivalent

ka thousands of years ago

kyrs thousand years

GCT Greens Canyon Tuff

LAMEVE Large Magnitude Explosive Volcanic Eruptions https://www.bgs.ac.uk/vogripa/view/controller.cfc?method=lameve

LYT Lithified Yellow Tuff

M Magnitude

NYT Neapolitan Yellow Tuff

PDC Pyroclastic Density Current

RED Pozzolane Rosse ignimbrite

USAF Unconsolidated Stratified Ash Flow

$\mathbf{V}$ total volume

$\mathbf{V_{coign}}$ co-ignimbrite ash fall volume

$\mathbf{V_{Pcol}}$ volume ejected during the phases that produced Plinian columns

$\mathbf{V_{coPfall}}$ co-Plinian fall volume

$\mathbf{V_e}$ areal erosion volume

VEI Volcanic Explosivity Index

$\mathbf{V_g}$ geometric volume

$\mathbf{V_{ign}}$ ignimbrite volume

$\mathbf{V_{intr}}$ intracaldera volume

$\mathbf{V_m}$ marine volume

$\mathbf{V_{mx}}$ matrix volume

$\mathbf{V_{pdc}}$ pyroclastic density current volume

$\mathbf{V_{Pfall}}$ proximal pumice lapilli deposits volume

$\mathbf{V_{pr}}$ preserved extra-caldera bulk volume

WGI Welded Gray Ignimbrite

$\boldsymbol{\rho}$ bulk density

$\boldsymbol{\varphi_t}$ total porosity.

frontiers in Earth Science

ORIGINAL RESEARCH
published: 09 December 2020
doi: 10.3389/feart.2020.542116

Insights Into the Internal Dynamics of Natural Lahars From Analysis of 3-Component Broadband Seismic Signals at Volcán de Colima, Mexico

Braden Walsh[1,2]*, *Velio Coviello*[3], *Lucia Capra*[4], *Jonathan Procter*[5] and *Victor Márquez-Ramirez*[4]

[1]Department of Earth Sciences, Uppsala University, Uppsala, Sweden, [2]Centre of Natural Hazards and Disaster Science, Uppsala University, Uppsala, Sweden, [3]Faculty of Science and Technology, Free University of Bozen-Bolzano, Bolzano, Italy, [4]Centro de Geociencias, Universidad Nacional Autónoma de México, Querétaro, Mexico, [5]Volcanic Risk Solutions, Institute of Agriculture and Environment, Massey University, Palmerston North, New Zealand

OPEN ACCESS

Edited by:
Elaine Spiller,
Marquette University, United States

Reviewed by:
Vern Manville,
University of Leeds, United Kingdom
Patricia Ann Mothes,
Escuela Politécnica Nacional, Ecuador
Mark Thomas,
University of Leeds, United Kingdom
Patrick J Smith,
Dublin Institute for Advanced Studies (DIAS), Ireland

***Correspondence:**
Braden Walsh
braden.walsh@geo.uu.se

Specialty section:
This article was submitted to Volcanology, a section of the journal Frontiers in Earth Science

Received: 11 March 2020
Accepted: 18 November 2020
Published: 09 December 2020

Citation:
Walsh B, Coviello V, Capra L, Procter J and Márquez-Ramirez V (2020) Insights Into the Internal Dynamics of Natural Lahars From Analysis of 3-Component Broadband Seismic Signals at Volcán de Colima, Mexico. Front. Earth Sci. 8:542116. doi: 10.3389/feart.2020.542116

Lahar monitoring on active volcanoes is challenging, and the ever changing environment leads to inconsistent results that hamper a warning systems ability to characterize the flow event properly. Therefore, more data, new methods, and the use of different sensors needs to be tested, which could lead to improvements in warning capabilities. Here, we present data from a 3-component broadband seismometer and video camera installed 3 m from the Lumbre channel on Volcán de Colima, Mexico to understand rheology differences within multiple lahar events that occurred in late 2016. We examine differences in frequency and directionality from each seismic component. Results indicate an increase in peak frequency above background in each component when a lahar nears the sensor, and a decrease in overall peak frequency when transitioning from a streamflow to a higher concentration flow. The seismic frequency distribution for the cross-channel component for the streamflow has a wider range compared with the lahar events. In contrast, the peak spectral frequency of the streamflow is narrower in comparison to the lahar events in the flow parallel and vertical directions. Estimated directionality ratios (cross-channel signal divided by flow parallel signal) yielded further evidence for a rheologic change between streamflow and lahars. Directionality ratios >1 were calculated for each lahar, and <1 for streamflow. Finally, we demonstrate from component analyses that channelization or freedom of movement in the cross-channel, bedload transport in the flow parallel, and bed composition in the vertical directions are possibly the main drivers in the peak spectral frequency output of lahars. The results described here indicate that using all three components may provide important information about lahar dynamics, which may be useful for automatic detection and warning systems, and using all three components should be encouraged.

Keywords: lahar dynamics, directionality, volcán de colima, peak spectral frequency, volcanic mass flow, 3-component seismic monitoring

INTRODUCTION

Seismic monitoring techniques are convenient for characterizing fluvial processes because they can provide continuous data at safe distances from the channel (Coviello et al., 2019; Hürlimann et al., 2019). However, correct interpretation of the seismicity induced by flow processes depends on many factors related to source and medium characteristics. Particularly, when describing what factors contribute to the frequency content generated by a flow, there are four main categories: dynamics of the suspended fraction, mechanics of the coarse fraction, properties of the solid-fluid mixture, and channel bed properties. The dynamics of the suspended fraction (e.g. size, concentration, distribution) have been shown to affect the frequency of the seismic signals in multiple ways (e.g. Tsai et al., 2012; Turowski et al., 2015). Doyle et al. (2010) noted when the concentration increases, the frequency will decrease. Furthermore, if there are larger clasts suspended in the flow, increasing the grain size distribution will produce a wide frequency range (Huang et al., 2004). Mechanics of coarse fraction factors (e.g. frictional effects, collisions, bedload) have varying effects on the frequency spectra (e.g. Doyle et al., 2011; Gimbert et al., 2014). It has been shown that the bedload is positively correlated with the amplitude of the frequency spectra, in that an increase in bedload transport will increase the amplitude of the frequency spectra (Coviello et al., 2018) and create higher peak frequencies (Schmandt et al., 2017). Furthermore, Huang et al. (2004) showed that frictional processes produce lower frequency ranges than particle collisions. Properties of the solid-fluid mixture (e.g. turbulence, velocity, viscosity, density) play a significant role in determining the frequency signature of flows (e.g. Cole et al., 2009; Barriere et al., 2015; Coviello et al., 2019). Huang et al. (2004) noted that the high frequency content dampens when the flow contains slurry, indicating that when the viscosity increases, the dominant frequency will be lower. Additionally, Doyle et al. (2010) showed that laminar high concentration flows have lower frequencies than turbulent ones. Similarly, Gimbert et al. (2014) found that turbulence has lower frequencies than bedload processes. Finally, channel bed properties (e.g. geometry, composition, wetted perimeter) can also have an impact on the spectral frequency of a flow (e.g. Doyle et al., 2010; Coviello et al., 2018). Kean et al. (2015) noted the composition of the channel bed can have significant impact on ground vibrations, which can lead to differences in the frequency spectra. For example, a bed made up of gravel or fine sediments will decrease the frequency of the seismic signal compared to a smooth surface (Huang et al., 2004). The density of the channel bed is important as well. Huang et al. (2007) showed that the frequency range will narrow when the bed surface is denser. Furthermore, the greater the wetted perimeter, the more effect the flow will have on the cross-channel signals (Doyle et al., 2010).

As mentioned above, seismic sensors have been used to estimate flow processes of mass flows many times previously. These studies have shown that inconsistent and non-universal results impede hazard assessment of mass flows. This indicates the need for new data processing techniques and more data to make interpretations more reliable. One such technique is to use all three components of the seismometer to study the seismic response of mass flows. Recently, others have used all three components while recording mass flows, including snow avalanches (Kogelnig et al., 2011), streamflow (Roth et al., 2016), hyperconcentrated flows (Walsh et al., 2016), landslides (Surinach et al., 2005), and snow-slurry lahars (Cole et al., 2009). By using all three components, full assessment of the overall properties of the flows can be completed to yield useful information about mass flow processes, particularly in the frequency domain, which may lead to better real-time monitoring and hazard evaluation.

Lahar monitoring on active volcanoes is a challenging task, and past work recording and characterizing the dynamics of natural lahars with 3-component seismometers base their conclusions off of only a few observed events at the same location in a limited time span. For example, Doyle et al. (2010) recorded eight events, only one of which was described seismically. Cole et al. (2009) recorded only two events, each with contrasting characteristics. Additionally, Doyle et al. (2011) describes only three events, which are the same as the events from Doyle et al. (2010). The reason for only a small amount of recordings is due to the limited amount of permanent monitoring stations that continually record lahars worldwide (e.g. Thouret et al., 2020). Conversely, natural lahar events are rarely recorded on channel side instrumentation in such robust detail as on Volcán de Colima. Nevertheless, even at Volcán de Colima, the continual installment of a 3-component seismometer is not possible, and the short duration of the monitoring in 2016 as shown here reinforces the idea that there is a need for a greater amount of lahar events recorded by 3-component broadband seismometers to adequately define either a detailed rheology classification of events or a robust quantification of internal dynamics. However, the identification of some unique features of flow events can still be theorized and shown with the limited amount of data presented here and in past publications.

Volcán de Colima (**Figure 1**) is one of the most active volcanoes in Mexico, which produces a wide range of primary eruptive and secondary non-eruptive hazards (Capra et al., 2018). The channels of the volcano often produce multiple flow events of different rheologies every rainy season that can travel great distances and cause damage to the surrounding infrastructure (Capra et al., 2010). These flow events are considered lahars and are defined as rapidly-flowing mixtures of poorly sorted rock, water, sediment, and mud flowing downslope from a volcano (Pierson, 1985; Calvari et al., 1998). Almost all of the lahars flow down one of the five main channels of Volcán de Colima (Cordobán, Arena, Lumbre, Montegrande, San Antonio), with Lumbre and Montegrande channels containing the most flow events (Coviello et al., 2018). Lumbre is the largest channel system on the volcano encompassing ~14 km^2 (Capra et al., 2018). Therefore, in 2014 a lahar monitoring station was installed (**Figure 1**) on the left bank of the channel (~7 m high) at ~1,580 m above sea level. The monitoring station is comprised of a vertical geophone and camera, where the channel is ~30 m across and slopes at ~6° (Coviello et al., 2018). Later, in

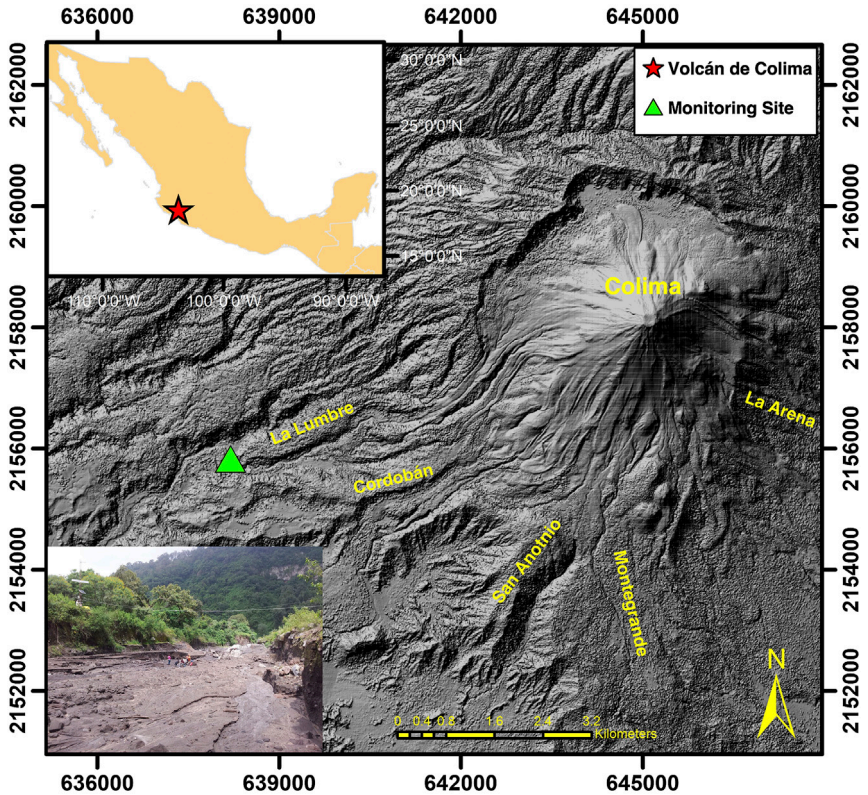

FIGURE 1 | Map of Vocán de Colima showing the five main lahar channels. Green triangle is the location of the monitoring site along the Lumbre channel used in this study, where a broadband 3-component seismometer and camera are installed. Inset picture shows the location of the monitoring station (pictured left) along the channel looking downstream.

2016, a 3-component broadband seismometer was installed for approximately three months at the same location.

2016 Lahar Events

In 2016 there were four lahar events that were recorded by the 3-component seismometer on Lumbre (August 26, 29, 30, September 9), with the larger two (August 26 and 30) contrasting in nature. The lahar on August 26 occurred during sunny conditions at the monitoring site with no precursory flow or sustained flowing water in the channel (these precursory conditions will henceforth be referred to as dry channel). The lahar passed the monitoring station at approximately 22:07:47 UTC (determined by video) and continued for ~40 min. The lahar started as a surge with a large frontal head (30 m wide with a velocity of ~12 m/s), which over time incised the channel bed creating a secondary channel, and was able to move and emplace large boulders up to 5 m in size.

The August 30 event differed from the other three lahars by the presence of a dilute precursory flow before the main lahar phase that lasted ~1.7 h altogether. The precursory streamflow started to pass the Lumbre station at approximately 22:52:53 UTC at a velocity of ~2.8 m/s with the lahar head arriving at 23:09:58 with a frontal velocity of ~9.6 m/s. Additionally, the August 30 event deposited fine-grained volcanic material in the channel, enough to cover the large boulders emplaced by the August 26 event.

The August 29 and September 9 events were smaller in size compared to the August 26 and 30 events. The August 29 lahar was a dry channel slow moving (frontal velocity of ~1.9 m/s) hyperconcentrated flow, which passed the monitoring station at 23:45:30 UTC, lasted ~1.5 h, and was contained within the August 26 incised channel. The September 9 event occurred overnight, reached the seismometer at 01:02:00 UTC and lasted ~1.4 h. The lahar event occurred in a dry channel with a frontal velocity of ~4.7 m/s and flowed over the fresh fine-grained material deposited by the August 30 event.

DATA

The seismic data for the 2016 lahars were recorded on a Nanometrics Trillium 120 s 3-component broadband seismometer, which was installed 3 m from the left bank (downstream) of the Lumbre channel. The station recorded data at 100 Hz sampling and had GPS time-stamps. The broadband seismometer axes were aligned with the lahar channel specifying the North-component pointed upstream as flow parallel (P) and the East-component as the cross-channel (T)

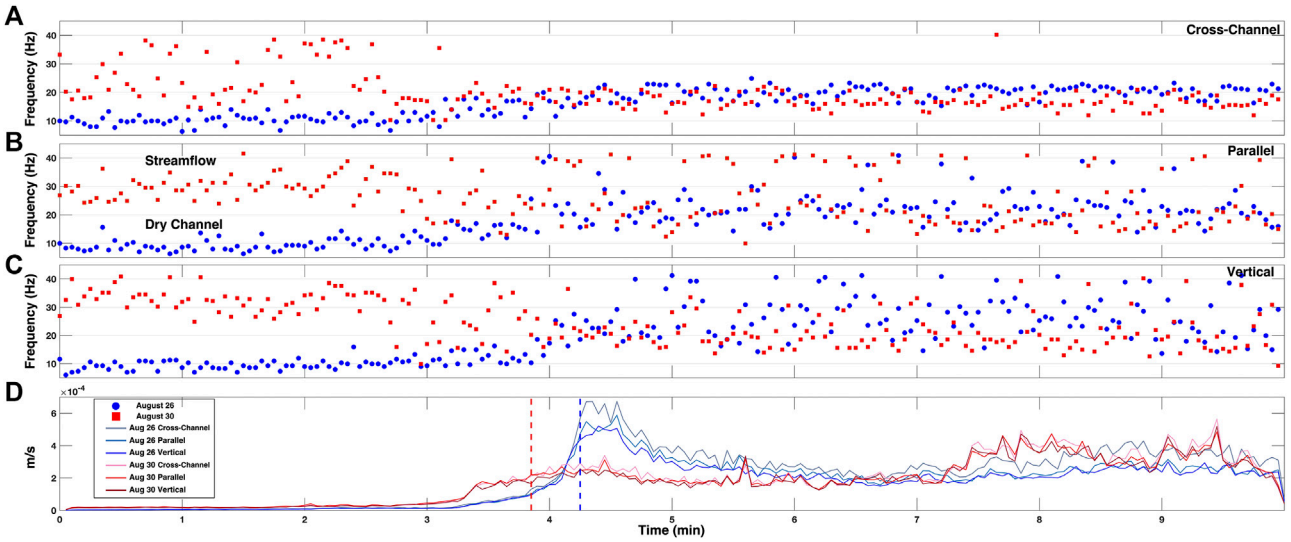

FIGURE 2 | (A–C) Peak spectral frequencies for both the August 26 (blue dots) and 30 (red squares) events containing pre-lahar (dry channel August 26, streamflow August 30) and first arrival. **(A)** cross-channel flow (E-component), **(B)** flow parallel (N-component), **(C)** vertical (Z-component), **(D)** RMS amplitude of the August 26 (blue lines) and 30 (red lines) events. Vertical ticks represent the time at which the first appearance of the lahar front is captured on the camera. All PSFs and RMS amplitudes were calculated using a 3 s time window.

direction. The installed video camera takes pictures every 3 s with 704 × 480 pixel resolution.

RESULTS

To examine the multi-component dynamics of the lahars, the recorded data were corrected for the instrument response before the maximum peak spectral frequency (PSF) amplitude, root mean squared (RMS) amplitude, and directionality ratios (DR) were estimated using a 3 s running time window. The 3 s time windows were acquired from a 10 min recording window around the head of the lahars as they passed the monitoring site (**Figures 2**, **3**) in each seismic component. Three second time windows were used to match the seismic data with the lapse time (3 s) between the camera imagery.

Multi-Component Peak Frequency Analysis

Examining PSFs in each flow direction, we use the frequency recorded at the maximum amplitude of the frequency spectra for each 3 s running time window. In this section, we describe only the August 26 and 30 events in detail, because of the differing nature of these events (dry channel/precursory flow) and their larger size compared to the other two events. For the August 26 lahar (**Figure 2**, blue plots) the dry channel/pre-lahar or background noise has a PSF around 10 Hz on average for all 3-components. When the lahar surge passes the monitoring station at ~4 min (**Figure 2D**, dashed lines) the PSF increases to above 15 Hz. Most notably, for the vertical (V) (**Figure 2C**) and the flow parallel directions (**Figure 2B**) there is a wide PSF range between 15 and 45 Hz. In the cross-channel direction (**Figure 2A**), the PSF distribution is more concentrated around 15–20 Hz.

The PSF for the August 30 lahar (**Figure 2**, red plots) contains two different flow types, with the precursory streamflow occurring before the lahar surge arrives. The streamflow cross-channel component (**Figure 2A**) has a range of PSFs between 15 and 40 Hz. The vertical (**Figure 2C**) and flow parallel (**Figure 2B**) directions have narrower PSF ranges between 25 and 40 Hz. When the lahar front is recorded seismically (~3 min, **Figure 2D**) the PSF of each component changes. The cross-channel PSF ranges between 15 and 20 Hz, which is similar to the August 26 lahar with the flow parallel and vertical components having PSFs between 10 and 40 Hz. In comparing the two types of flows on August 30, in the cross-channel direction the PSF changes from a wide (15–40 Hz) to a narrow range (15–20 Hz) when the lahar arrives. In contrast, the opposite is observed for the vertical and flow parallel directions, where the streamflow has a narrower (25–40 Hz) PSF range than the lahar (10–40 Hz).

In general, the differences between the lahars are small, the PSF ranges are similar for each component, where the cross-channel is 15–20 Hz (August 26, August 30), flow parallel is 15–45 Hz (August 26) and 15–40 Hz (August 30), as well as the vertical direction at 15–45 Hz (August 26) and 10–40 Hz (August 30). The most significant differences are seen at the range where the most dominant frequency bands or concentrations of PSF time windows exist for each component. The August 26 flow parallel direction (**Figure 2B**, blue dots) has a higher concentration of PSFs between 15 and 30 Hz with several time windows having PSFs up to 45 Hz. Moreover, the August 30 lahar (**Figure 2B**, red squares) has a PSF signature that is more bimodal than the August 26 event, where there is a lower range between 15 and 20 Hz and a higher range around 40 Hz. In the vertical component the August 26 event has a wide range of PSFs from 15

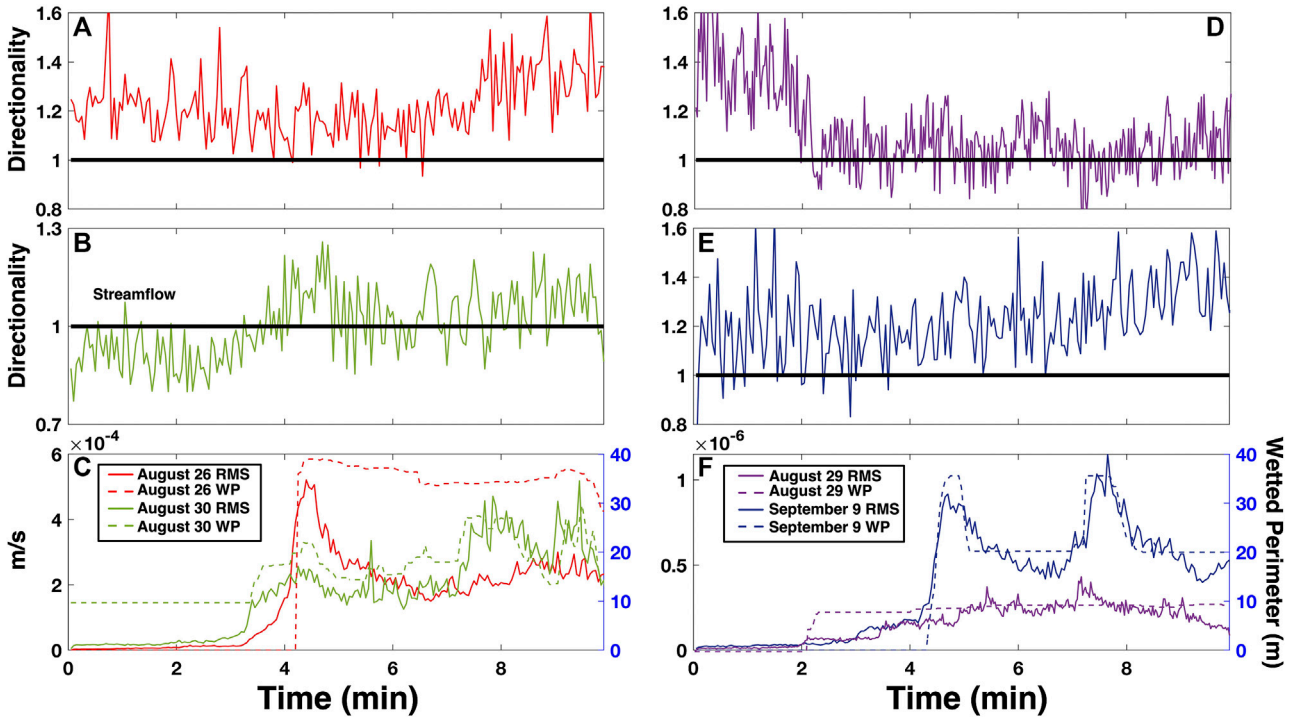

FIGURE 3 | Directionality ratio plots over time for the August 26 **(A)**, August 30 **(B)**, August 29 **(D)** and September 9 **(E)** events. Vertical RMS seismic signals and wetted perimeters for the August 26 and 30 events **(C)** and for the August 29 and September 9 events **(F)**. Wetted perimeters were estimated from video images and the known dimensions of Lumbre channel from digital elevation models (DEM). Video analyses used the imported measurements from the DEMs to estimate the height and width of each flow event for each 3 s lapse time of the camera.

to 45 Hz with no distinct pattern or concentration. The vertical component for the August 30 lahar on the other hand has a concentration of PSFs between ~15 and 25 Hz with several time windows encompassing PSFs up to 40 Hz. Finally, in the cross-channel direction, the PSF pattern for both lahars is similar with a narrow range between 15 and 20 Hz.

Directionality of Lahars

When analyzing mass flows using multiple component seismic data, one way to determine which flow direction has greater energy is through the directionality ratio (DR). The DR can be defined as the cross-channel divided by the flow parallel seismic amplitude. A $DR > 1$ indicates that the cross-channel energy is stronger than the flow parallel energy, and vice-versa for a $DR < 1$. The DR can be an indicator for many flow properties, including the wetted perimeter, amount of turbulent particle collisions, and sediment concentration (Doyle et al., 2010), which could yield evidence of flow rheology.

The DRs for a 3 s running time window for the 2016 events are shown in **Figure 3**. For the dense-front August 26 lahar (**Figure 3A**) the DR mostly stays above one for the entire 10 min recording duration. Furthermore, at ~7 min the DR increases to above 1.3. This increase late in the recording window is most likely becoming more positive due to an increase in concentration, amount of turbulent particle collisions and/or the channel beginning to incise (see **Supplemental Movie S1**), and not an increase in wetted perimeter, because the estimated wetted perimeter (**Figure 3C**, red dashed line) is less than when the lahar arrives. Furthermore, the dry channel bed/background noise also produces a $DR > 1$, indicating that the DR cannot be used for a potential real-time rheology change indicator for dry channels, at least for Lumbre.

For the August 30 event (**Figure 3B**), the precursory streamflow has a $DR < 1$, which then increases to a $DR > 1$ when the lahar surge passes the monitoring site. This switch from flow parallel to cross-channel dominance when the lahar arrives is possibly due to a larger wetted perimeter (**Figure 3C**, green dashed line) or an increase in sediment concentration (Doyle et al., 2010), and could be a potential real-time rheology change indicator for monitoring lahars. Additionally, even though the August 30 event has similar or increased seismic energy along with a lower wetted perimeter later in the recording window (after initial lahar front) than the August 26 event, the DR is ~0.2 less. This difference indicates that wetted perimeter cannot be the only factor in the determination of the DR.

During the August 29 event (**Figure 3D**) the DR remains around 1.0, which could indicate a smaller wetted perimeter or a lower concentration compared to the other events. From **Figure 3F** (purple lines), the amplitude and wetted perimeter are lower than the other events, but as also seen in the video analysis (**Supplementary Movie S2**) the lahar pulses show evidence of increased water content. When the second pulse occurs at ~7 min (**Figures 3D**,F, purple line) the $DR < 1$ indicates that the pulse may be a water wave with low particle

concentration. We also observe that the September 9 event (**Figure 3E**) is similar to the August 26 lahar in that the *DR* > 1 covers most of the duration and the wetted perimeters of the two pulses are comparable. Unlike the August 26 event, the September event is about two magnitudes smaller in seismic amplitude. Furthermore, the amplitude is smaller than the August 30 event, but has a larger DR. These differences could come from the fact that the September 9 event covered the entire width of the Lumbre channel which allowed for greater cross-channel compared to flow parallel seismic energy. Additionally, being able to flow over the entire channel width yielded a larger wetted perimeter than the August 30 event, which was mostly contained in the incised channel. Another possibility is that the sediment concentration could be higher for the September 9 event. The increased sediment conceivably came from erosion or entrainment of fine-grained material deposited by the August 30 event.

DISCUSSION

Comparing the PSF Response Between the August 26/30 Lahars

Examining the multi-component frequency content of the two main lahars in August 2016 shows that different flow types may play a significant role in the frequency spectra of the seismic signals. Additionally, each component details a different pattern in the frequency spectra, determined by many factors. As shown by others (e.g. Lai et al., 2018), the frequency range will increase as the lahar flows near and eventually passes the monitoring site. This can be seen for all three components (**Figures 2A–C**) in the dry channel scenario. As for the different flow types, each component has a differing frequency response and standard assessments from previous studies on just the vertical component cannot explain everything, but can help to understand what mechanisms may be causing these patterns.

As noted above, the August 26 lahar has a wider PSF range than the August 30 lahar in the vertical component (**Figure 2C**). This could be due to the August 26 lahar transporting larger clasts, which would make the bedload dominate the turbulent response, in turn creating higher frequencies (Schmandt et al., 2017). Furthermore, this same feature can be explained by the observations of Huang et al. (2004) who noted the PSF range increases with the mass of suspended clasts. Hence, the larger clasts of the August 26 event increases the PSF range because the grain size distribution becomes larger, thus creating a wider range within the flow from particle collisions to saltation effects. The vertical component of the streamflow has PSFs between 25 and 40 Hz where the flow is less turbulent and thus more capable of recording bedload transport produced frequencies (Doyle et al., 2010).

The difference in the flow parallel PSF pattern for the August 26 and 30 lahars (**Figure 2B**) may be explained by the flow parallel direction being more sensitive to flow processes, rather than bedload forces (Barriere et al., 2015), which would dampen the high frequencies of the August 26 event. Conversely, Coviello et al. (2018) showed that higher frequencies are more associated with fine-grained sediment transport. The August 30 event deposited fine-grained material all over the Lumbre channel (see **Supplementary Movie S3**) providing possible evidence for more time windows of higher PSF. Additionally, the August 30 lahar transported fewer large clasts compared to the August 26 event (see **Supplementary Movies S1, S3**), and PSFs created by particle collisions decreases with an increase in clast size (Huang et al., 2004; Burtin et al., 2009), which could be the cause of the August 30 event having a more bimodal PSF pattern than the August 26 event.

The PSF content in the cross-channel direction for the August 26 and 30 lahars (**Figure 2A**) could be due to the sizes of the lahars being similar or bedload processes having little to no influence on the frequency content. Conversely, the PSF signature for the streamflow may be due to the greater freedom of particle movement within the flow. When the sediment concentration decreases, the viscosity will decrease, creating a situation where fine grain particle collisions and interactions occur more, thus increasing the frequency content (Huang et al., 2004; Coviello et al., 2018). This opposing effect could also be due to the seismometer being installed according to the channel alignment, which could make the surface waves, in particular the Love wave nodes synchronize (lahar) or not (streamflow) with the location of the seismic station depending on flow type/energy. Furthermore, just the difference in the orthogonal forces on the channel walls could alter the frequency content.

The transition from streamflow to lahars (**Figures 2A–C**) shows a decrease in the PSF range, which could be caused by the transition from less solid to more solid content flowing by. If this were the case, the DR (**Figure 3B**) would increase from <1 to >1, because the cross-channel energy increases with an increase in sediment concentration (Doyle et al., 2010); which it does. This increase also suggests why the cross-channel frequency pattern is different from the other two directions. Doyle et al. (2010) showed that in the cross-channel direction, turbulence is more dominant than in the flow parallel direction, which could be why there is no scattering to higher frequencies seen in **Figure 2A** when the lahar arrives.

In the discussion above, we described many hypotheses of how differing flow processes or rheology may produce the recorded frequency response. Equally, other factors may also contribute to the seismic record of mass flows. Recently, others have shown (e.g. Coviello et al., 2019; Marchetti et al., 2019) that the energy of the source and the channel geometry play a significant role in the frequency response. High-friction channel beds, bends, and extreme elevation changes could all cause differing frequency responses produced by the same seismic source. Furthermore, background noise can cause "jumps" in PSFs, where each time window could be recording either the flow or background noise (Coviello et al., 2019). A potential cause for a bimodal response in the flow parallel direction can be produced by a moving source, where the seismometer records the flow before, as it passes, and after passing the sensor. Additionally, one of the more likely causes is the pulsatory nature of lahars, which could cause changes to the frequency spectra over the length of the event.

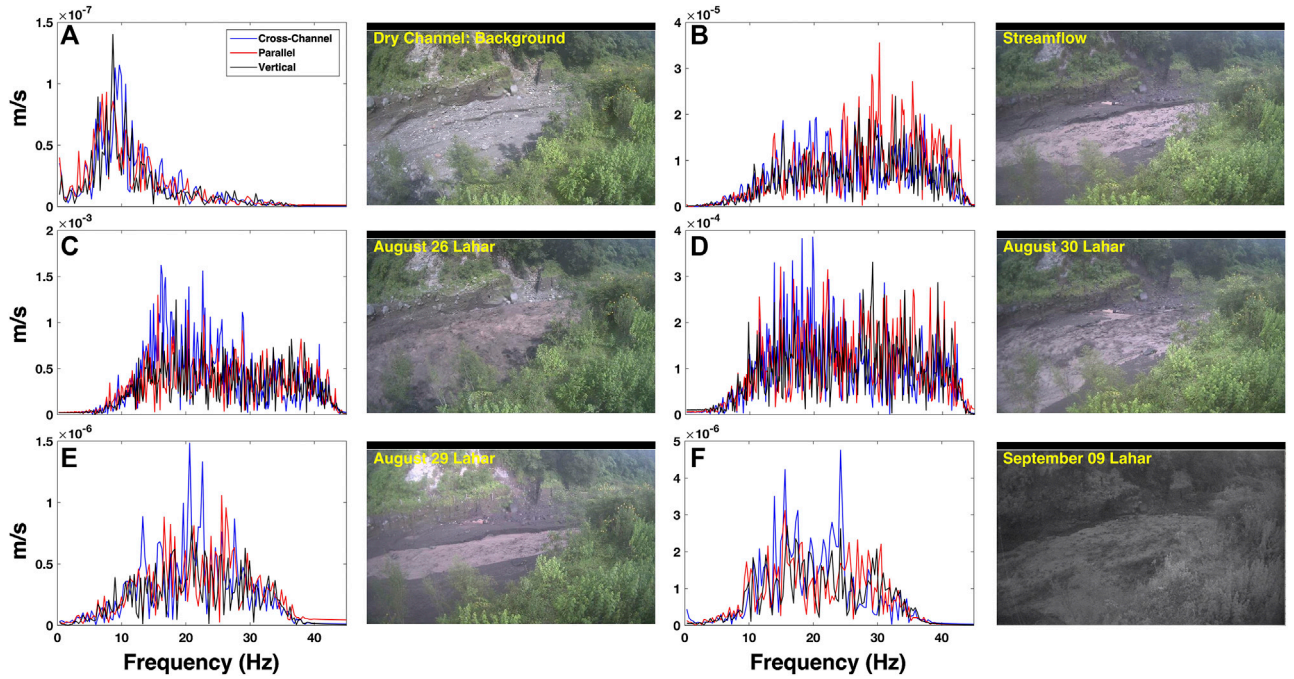

FIGURE 4 | Select 3 s multi-component frequency spectra with accompanying image of **(A)** dry channel, **(B)** streamflow, **(C)** August 26 lahar front, **(D)** August 30 lahar front, **(E)** August 29 lahar front, **(F)** September 9 lahar front for the cross-channel (blue), parallel (red) and vertical (black) directions. Note the amplitude difference between each frequency spectrum.

Spectral Analysis of Differing Regimes on Lumbre Channel

With a wide distribution of PSFs, we now investigate the entire frequency response of the flows by calculating full spectra for each 3 s time widow. For clarity, we only show a selected time widow for each event (**Figure 4**). From the full spectra, a pattern emerges from the different time windows during the 2016 events. The dry channel spectra (**Figure 4A**) depicts a low frequency (<10 Hz) response with little to no amplitude in the higher frequencies, typical of background noise (e.g. wind, environmental, etc.). The streamflow spectra (**Figure 4B**) has a shift to higher frequencies being more dominant. This is possible evidence that streamflow is more sensitive to bedload transport or less turbulent. Cole et al. (2009) showed that snow-slurry lahars on Ruapehu, New Zealand have higher flow parallel spectral amplitudes due to lower turbulence, and more lateral deposition, decreasing the cross-channel signal. Similarly, the streamflow on August 30 has increased amplitudes in the flow parallel direction, which suggests that the streamflow is less turbulent than the lahars. The August 26 frontal spectra (**Figure 4C**) is dominated by lower frequencies between 15 and 25 Hz with a drop in amplitude after this range. This effect may be caused by the lahar front being more sensitive to turbulence (Gimbert et al., 2014), sliding frictional effects of the front, creating lower frequencies (Huang et al., 2004), or higher sediment concentration (Doyle et al., 2010; Coviello et al., 2018). Conversely, the August 30 lahar front (**Figure 4D**) has a broad frequency spectra, which could be characterized as a combination of the low frequency August 26 event and the higher frequency August 30 streamflow. The broad frequency response of the August 30 lahar is similar to three lahars recorded on Mount Semeru, Eastern Java by Doyle et al. (2011), which was explained by the flows being less sensitive to flow properties (turbulence, viscosity), than to both frictional (lower frequency) and collisional (higher frequency) processes. If turbulence were dampened, the particles within the flow will have less influence on the basal shear stress, and the erosiveness of the flow would decrease (Doyle et al., 2011). This can be demonstrated by the August 30 lahar, which does not erode the channel but instead deposits fine grained material over the channel floor (**Supplemental Movie S3**). The August 29 event (**Figure 4E**) shows a dominant range of frequencies between 15 and 25 Hz, similar to the August 26 event. Differing, the August 29 event has a steep drop in amplitude at higher frequencies (>30 Hz), and the maximum peak frequency (~20 Hz) is higher than what was recorded for the August 26 event. The lack of higher frequency content is possibly from a smaller grain size distribution or a lower energy regime than the August 26 event, whereas the higher maximum frequency may be from a lower sediment concentration (e.g. Huang et al., 2004), as shown in **Figure 3D**, produced from a $DR \sim 1$. Furthermore, the September 9 event (**Figure 4F**) has a similar spectral pattern to the August 29 event, but with a bimodal peak frequency. The first peak frequency is at ~16 Hz and the second at ~22 Hz, which might signify two separate processes occurring. The lower peak could be related to flow processes such as freedom of particle movements (turbulence). The second peak at ~22 Hz may be a frictional process (bedload transport) similar to the August 26 event, in which a large block-rich front slides along a dry channel. Moreover,

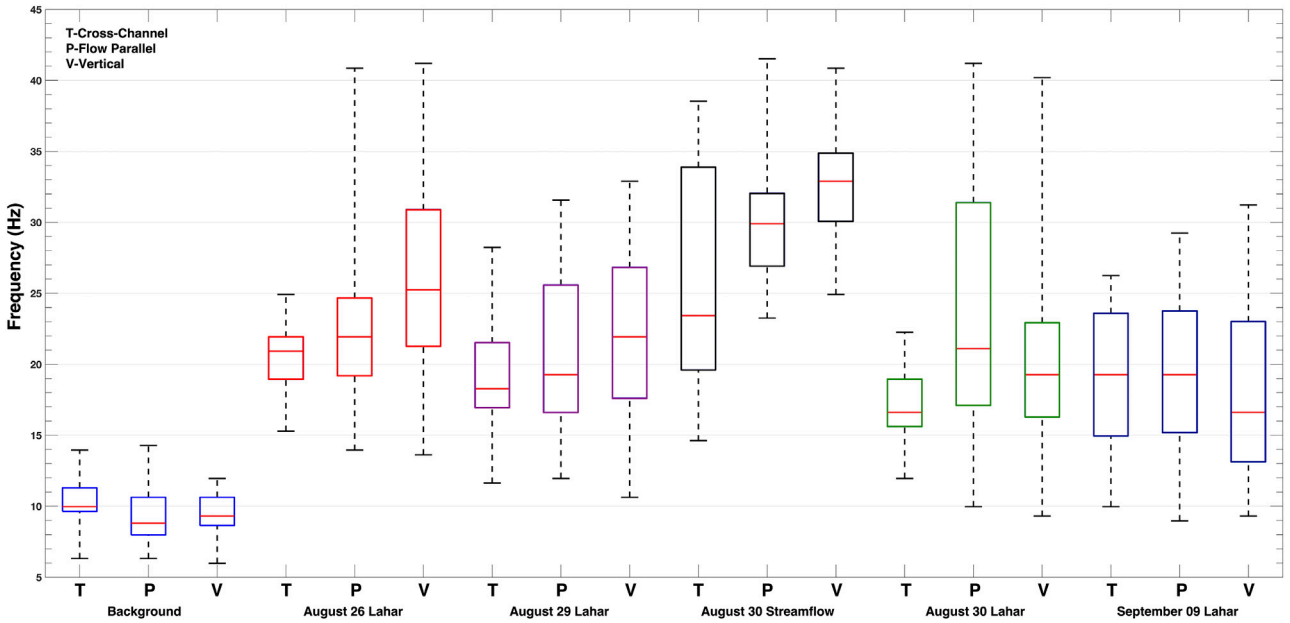

FIGURE 5 | Boxplots for peak spectral frequencies over the 10 min recording duration for each component for the background noise (blue), August 26 lahar (red), August 29 lahar (purple), August 30 streamflow (black), August 30 lahar (green), and September 9 lahar (navy).

the September 9 lahar has a high DR (**Figure 3E**) indicating a possible increase in concentration, which would decrease peak frequency as indicated by Huang et al. (2004). These two peaks are lower than the frequencies observed during passage of a hyperconcentrated flow in 2015, recorded with a geophone installed at the same location (Coviello et al., 2018). In that case, the high peak (70 Hz) was associated with sediment transport while the lower peak (30–40 Hz) was interpreted as flow turbulence. However, differing instruments, sampling frequencies, source energy, and channel conditions may have led to shifted spectral responses. The September 9 event flowed over the August 30 fine-grained deposits and was not channelized. The lahar was also smaller with less energy allowing the suspended grains more freedom to move and collide, producing higher frequency content, especially in the cross-channel direction.

The Implications of 3-Component PSF on Event Conditions

To obtain a more reliable comparison between each event, boxplots for each component and lahar event were created (**Figure 5**). The boxplots depict an evolution of the frequency content of the lahars over time at Lumbre. The cross-channel spectral content has a narrow interquartile range (IQR) for the August lahars, but becomes wider with the September lahar and the streamflow. This feature may be explained by channelization or freedom of movement, where the August 29 and 30 events were confined to the incised channel and the August 26 lahar was large enough to be confined to the Lumbre channel walls. Conversely, the lahar in September was not channelized and was free to flow side to side within the Lumbre channel. Compared to the streamflow, the September 9 event has a lower overall PSF IQR range, which could be explained by the freedom of fluid movement (channelization) as noted above, combined with higher turbulence and/or sediment concentrations compared to the streamflow shown by the increase in the DR (**Figure 3E**). Furthermore, since the streamflow was channelized, the wide IQR for the streamflow could instead be from the freedom of particle movement of smaller grain sizes within the flow, which would increase the overall PSF. The box plots for the flow parallel direction show that this component may be an indicator of erosiveness, i.e. where narrow IQRs may depict erosive regimes and wide IQRs indicate depositional regimes. The August 26 lahar has the smallest flow parallel IQR and eroded the channel bed creating the incised channel (**Supplemental Movie S1**), whereas the August 30 lahar deposited a layer of fine-grained sediment throughout the channel (**Supplemental Movie S3**). Furthermore, both the August 29 and September 9 events show a mix between depositional and erosional regimes, yielding similar IQR sizes between the extremes of the larger 2016 events. The vertical component boxplots for all the lahars have similar spreads, but **Figure 5** does show a decrease in median PSF over time. This pattern is possibly due to the change in channel bed composition by adding fine sediments (e.g. Huang et al., 2004). The August 26 and 29 events occurred on dry channels with little fine-grained material, whereas the August 30 event deposited fine-grained material, and the September 9 event flowed on top of these deposits decreasing the overall frequency.

Implications for Lahar Monitoring

The main goal of mass flow research is to progress the knowledge behind the properties and dynamics of flows for risk management and hazard warning. We show here that with

only one 3-component seismic station installed close to the channel (3 m) sufficient information was obtained for warning purposes. For example, the change in frequency distribution and DR when transitioning from streamflow to hyperconcentrated flow, the potential use of PSF to determine the depositional regime of a flow, and the increase in frequency when a lahar passes the monitoring station from a precursory dry channel. Using only one station does have its limitations, and installing more stations could benefit the results discovered here by showing whether or not these same features are universal in terms of both time and location. The seismic signals of mass flows are variable and strongly depend on where the station is, source-receiver distance, properties of the subsurface, properties of the channel, and flow properties and dynamics. For example, Schmandt et al. (2017) showed that there were differences in the seismic signals of stations installed on opposite sides of the channel from one another. This could affect not only the frequency response, but the amplitudes of the horizontal components, and thus the DR. Furthermore, flow dynamics and channel properties can and do change along the channel and having more stations along the channel could help to identify the characteristics of the flow. Doyle et al. (2011) used multiple stations along the same channel to show changes in lahars over time and station location at Semeru. Additionally, multiple stations along the channel allows the use of other techniques for detecting mass flows. Coviello et al. (2019) calculated the difference in seismic amplitudes of short and long period time windows to detect in real-time when a mass flow occurred.

The results from Volcán de Colima provide new data and show a practical application in using all three components, which can be used for monitoring, and that variabilities need to be accounted for before real world applications in systematic monitoring can be conducted. Using all three components for in depth frequency analysis and general hazard monitoring is beneficial in that there is important information in the horizontal components of the seismometer that should not be ignored. In earthquake hazards and geoengineering all seismic directions must be considered when building durable structures (e.g. buildings, bridges). Similarly, the construction of check dams and levees in flow channels should consider the horizontal energy from the mass flows. For risk management, using all available data needs to be considered by numerical modelers. Creating hazard models based on 3-component data could improve mass flow predictions due to the input of directional forces and patterns. Finally, in mass flow warning systems, we have shown that the DR and the distribution of PSFs can show regime changes within the channel, and that other information may be able to be obtained from the horizontal components (e.g. channelization, bedload transport). Overall, using all three components of the seismometer can enhance warning systems and yield results that single component instruments cannot.

CONCLUSION

Conducting a multi-component frequency analysis on lahars at Volcán de Colima, Mexico has yielded an understanding of which frequencies are dominant during differing flow types and processes. For the vertical and flow parallel directions, the transition from streamflow to a lahar coincides with a widening of the peak frequency distribution. This observation is reversed for the cross-channel frequency content, where the streamflow generates a wide frequency distribution, which then transitions to a narrow distribution as the lahars pass the seismometer. Furthermore, there is a drop in overall PSF when transitioning from streamflow to lahar. Component analyses demonstrated that channelization or freedom of movement in the cross-channel direction, bedload transport in the flow parallel direction, and channel bed composition in the vertical direction are possibly the main drivers in the PSF output of lahars. Conversely, with the number of variables that could affect the seismic signals produced by lahars, future assessments and data collection need to be conducted to solidify the observations discovered at Lumbre. Ultimately, the findings of this research may lead to better real-time monitoring of lahars, and lahar hazard assessment through the use of frequency analysis of all three components of the seismometer for dry channels, and especially channels with sustained flowing water.

DATA AVAILABILITY STATEMENT

The datasets generated for this study are available on request to the corresponding author.

AUTHOR CONTRIBUTIONS

BW performed seismic and video analyses and drafted the manuscript. LC and BW estimated wetted perimeter and frontal velocities of the flows. All participating authors contributed to the discussions and editing of the draft of the manuscript, as well as approving the final edition.

FUNDING

This work was supported by The Interdisciplinary Grant awarded by the Center of Natural Hazards and Disaster Science (CNDS), Sweden to BW, EARFLOW bilateral project granted to unibiz and CGEO-UNAM, funded by the MAECI (Ministero degli Affari Esteri e della Cooperazione Inernazionale) and the AMEXCID (Agencia Mexicana de Cooperación Internacional para el Desarrollo) to VC and the CONACyT-PN360 project to LC. We also recognize that this research would not be possible without support from the New Zealand Natural Hazards Research Platform and the Resilience to Natures Challenges (NSC), Volcano Program. We would also like to thank Kate Arentsen for editorial support.

SUPPLEMENTARY MATERIAL

The Supplementary Material for this article can be found online at: https://www.frontiersin.org/articles/10.3389/feart.2020.542116/full#supplementary-material

REFERENCES

Barriere, J., Oth, A., Hostache, R., and Krein, A. (2015). Bed load transport monitoring using seismic observations in a low-gradient rural gravel bed stream. *Geophys. Res. Lett.* 42, 2294–2301. doi:10.1002/2015GL063630

Burtin, A., Bollinger, L., Cattin, R., Vergne, J., and Nabelek, J. (2009). Spatiotemporal sequence of Himalayan debris flow from analysis of high-frequency seismic noise. *J. Geophys. Res.* 114, F04009. doi:F040090.1029/2008JF001198

Calvari, S., Tanner, L., and Groppelli, G. (1998). Debris-avalanche depostis of the Milo Lahar sequence and the opening of the Valle del Bove on Etna volcano (Italy). *J. Volcanol. Geoth. Res.* 87, 193–209. doi:10.1016/S0377-0273(98)00089-4

Capra, L., Borselli, L., Barley, N., Ruiz, J., Norini, G., Sarocchi, D., et al. (2010). Rainfall-triggered lahars at Volcan de Colima, Mexico: surface hydro-repellency as initiation process. *J. Volcanol. Geoth. Res.* 198, 105–117. doi:10.1016/j.jvolgeores.2009.10.014

Capra, L., Coviello, V., Borselli, L., Marquez-Ramirez, V., and Arambula-Mendoza, R. (2018). Hydrological control of large hurricane-induced lahars: evidence from rainfall-runoff modeling, seismic and video monitoring. *Nat. Hazards Earth Syst. Sci.* 18, 781–794. doi:10.5194/nhess-18-781-2018

Cole, S., Cronin, S., Sherburn, S., and Manville, V. (2009). Seismic signals of snow-slurry lahars in motion: 25 September 2007, Mt Ruapehu, New Zealand. *Geophys. Res. Lett.* 36, L09405. doi:10.1029/2009GL038030

Coviello, V., Capra, L., Vazquez, R., and Marquez-Ramirez, V. (2018). Seismic characterization of hyperconcentrated flows in a volcanic environment. *Earth Surf. Process. Landforms* 43, 2219–2231. doi:10.1002/esp.4387

Coviello, V., Arattano, M., Comiti, F., Macconi, P., and Marchi, L. (2019). Seismic characterization of debris flows: insights into energy radiation and implications for warning. *J. Geophys. Res.: Earth Surface* 124, 1440–1463. doi:10.1029/2018JF004683

Doyle, E., Cronin, S., Cole, S., and Thouret, J. (2010). The coalescence and organization of lahars at Semeru volcano, Indonesia. *Bull. Volcanol.* 72, 961–970. doi:10.1007/s00445-010-0381-8

Doyle, E., Cronin, S., Cole, S., and Thouret, J. (2011). Defining conditions for bulking and debulking in lahars. *GSA Bulletin* 123, 1234–1246. doi:10.1130/B30227.1

Gimbert, F., Tsai, V., and Lamb, M. (2014). A physical model for seismic noise generation by turbulent flow in rivers. *J. Geophys. Res.: Earth Surface* 119, 2209–2238. doi:10.1002/2014JF003201

Hürlimann, M., Coviello, V., Bel, C., Guo, X., Berti, M., Graf, C., et al. (2019). Debris-flow monitoring and warning: review and examples. *Earth Sci. Rev.* 102981. doi:10.1016/j.earscirev.2019.102981

Huang, C., Shieh, C., and Yin, H. (2004). Laboratory study of the underground sound generated by debris flows. *J. Geophys. Res.* 109, F01008. doi:10.1029/2003JF000048

Huang, C., Yin, H., Chen, C., Yeh, C., and Wang, C. (2007). Ground vibrations produced by rock motions and debris flows. *J. Geophys. Res.* 112, F02014.

Kean, J., Coe, J., Coviello, V., Smith, J., McCoy, S., and Arattano, M. (2015). Estimating rates of debris flow entrainment from ground vibrations. *Geophys. Res. Lett.* 42, 6365–6372. doi:10.1002/2015GL064811

Kogelnig, A., Surinach, E., Vilajosana, I., Hubl, J., Sovilla, B., Hiller, M., et al. (2011). On the complementariness of infrasound and seismic sensors for monitoring snow avalanches. *Nat. Hazards Earth Syst. Sci.* 11, 2355–2370. doi:10.5194/nhess-11-2355-2011

Lai, V. H., Tsai, V., Lamb, M., Ulizo, T., and Beer, A. (2018). The seismic signature of debris flows: flow mechanics and early warning at Montecito, California. *Geophys. Res. Lett.* 45 (11), 5528-5535. doi:10.1029/2018GL077683

Marchetti, E., Walter, F., Barfucci, G., Genco, R., Wenner, M., Ripepe, M., et al. (2019). Infrasound array analysis of debris flow activity and implications for early warning. *J. Geophys. Res.: Earth Surface* 124 (3), 567–587. doi:10.1029/2018JF004785

Pierson, T. (1985). *Initiation and flow behavior of the 1980 pine creek and muddy river lahars*. Mount St. Helens, Washington: Geological Society of America Bulletin, 1056–1069.

Roth, D., Brodsky, E., Finnegan, N., Rickenmann, R., Turowski, J., and Badoux, A. (2016). Bed load sediment transport inferred from seismic signals near a river. *J. Geophys. Res. Earth Surf.* 121, 725–747. doi:10.1002/2015JF003782

Schmandt, B., Gaeuman, D., Stewart, R., Hansen, S., Tsai, V., and Smith, J. (2017). Seismic array constraints on reach-scale bedload transport. *Geology* 45, 299–302. doi:10.1130/G38639.1

Surinach, E., Vilajosana, I., Khazaradze, G., Biescas, B., Furdada, G., and Vilaplana, J. (2005). Seismic detection and characterization of landslides and other mass movements. *Nat. Hazards Earth Syst. Sci.* 5, 791–798. doi:10.5194/nhess-5-791-2005

Thouret, J., Antoine, S., Magill, C., and Ollier, C. (2020). Lahars and debris flows: characteristics and impacts. *Earth Sci. Rev.* 201, 103003. doi:10.1016/j.earscirev.2019.103003

Tsai, V., Minchew, B., Lamb, M., and Ampuero, J. P. (2012). A physical model for seismic noise generation from sediment transport in rivers. *Geophys. Res. Lett.* 39, 2404. doi:10.1029/2011GL050255

Turowski, J., Wyss, C., and Beer, A. (2015). Grain size effects on energy delivery to the streambed and links to bedrock erosion. *Geophys. Res. Lett.* 42, 1775–1780. doi:10.1002/2015GL063159

Walsh, B., Jolly, A., and Procter, J. (2016). Seismic analysis of the 13 October 2012 Te Maari, New Zealand, lake breakout lahar: insights into flow dynamics and the implications on mass flow monitoring. *J. Volcanol. Geoth. Res.* 324, 144–155. doi:10.1016/j.jvolgeores.2016.06.004

Conflict of Interest: The authors declare that the research was conducted in the absence of any commercial or financial relationships that could be construed as a potential conflict of interest.

frontiers in Earth Science

ORIGINAL RESEARCH
published: 16 December 2020
doi: 10.3389/feart.2020.548251

Post-Caldera Eruptions at Chalupas Caldera, Ecuador: Determining the Timing of Lava Dome Collapse, Hummock Emplacement and Dome Rejuvenation

Marco D. Córdova, Patricia Ann Mothes, H. Elizabeth Gaunt and Josué Salgado*

Instituto Geofísico, Escuela Politécnica Nacional, Quito, Ecuador

Determining the lithology, extent, origin, and age of hummocks can be challenging, especially if these are covered by successive deposits and lush vegetation. At Chalupas caldera, a late-Pleistocene silicic center that lies astride the Eastern Cordillera of northern Ecuador, we have tried to overcome these difficulties by combining geological observations and sampling, laboratory analysis (geochemistry, scanning electron microscope analysis and radiometric dating) and remote sensing techniques. Chalupas is the second largest caldera in the Northern Volcanic Zone of South America and its VEI 7 eruption, which occurred ~0.21 Ma, has garnered the attention of the volcanological community. Our research highlights new observations of the post-caldera activity at Chalupas, beginning with the growth of Quilindaña stratovolcano (~0.170 Ma), followed by the formation of Buenavista dome that is located 5 km eastward of Quilindaña's summit. At the eastern foot of Buenavista dome we identify hummocky terrain covering an area of ~20 km^2. Collectively, the suite of techniques that we used helped to highlight geological features that shed light on the provenance of the hummocks and demonstrate that this topography may have originated from gravitational breccia flows from Buenavista lava dome. Numerical simulations were also performed to represent breccia flow transit and emplacement over the present caldera landscape and to view the potential hazard footprints of a future Buenavista dome collapse. For modeling we employed volumes of 20–120 Mm^3 to visualize the consecutive traces of mass flow deposition and how the traces correspond to the hummocky landscape. Following the partial collapse of Buenavista lava dome, its rejuvenation is represented by tephra layers of several small eruptions that are dated at about 40 ky BP. These tephras represent some of the youngest eruptive activity recognized at Chalupas caldera. Our results contribute to the overall knowledge about Chalupas and demonstrate that eruptions at this important caldera are more recent than was previously reported.

Keywords: Buenavista, Chalupas caldera, scanning electron microscope imaging, field mapping, volcanic hazards, dome collapse breccia

OPEN ACCESS

Edited by:
Pablo Tierz,
The Lyell Center, United Kingdom

Reviewed by:
Alessandro Tibaldi,
University of Milano-Bicocca, Italy
Jon J. Major,
United States Geological Survey (USGS), United States

****Correspondence:***
Patricia Ann Mothes
pmothes@igepn.edu.ec

Specialty section:
This article was submitted to Volcanology, a section of the journal Frontiers in Earth Science

Received: *01 April 2020*
Accepted: *18 November 2020*
Published: *16 December 2020*

Citation:
Córdova MD, Mothes PA, Gaunt HE and Salgado J (2020) Post-Caldera Eruptions at Chalupas Caldera, Ecuador: Determining the Timing of Lava Dome Collapse, Hummock Emplacement and Dome Rejuvenation. Front. Earth Sci. 8:548251. doi: 10.3389/feart.2020.548251

INTRODUCTION

As stated by Paguican et al. (2012) *"Hummocks are the morphological expression of brittle layer deformation due to spreading in landslides and avalanches. They are principally the stretched remains of tilted and rotated blocks of the original failure volume."* Sometimes it is difficult to know the processes that led to lava dome or sector collapse and subsequent hummock formation, especially if the hummocks were formed tens of thousands of years ago in a rainy environment, such as at Chalupas caldera.

Since the eruption of Mount St Helens in May 1980, in which the first well-observed debris avalanche deposits were emplaced (Voight et al., 1981; Voight et al., 1983; Glicken, 1996), researchers are more attuned to identifying hummocky morphologies around volcanoes. Also, it is now commonly accepted that hummocky morphologies are often indicative of the occurrence of lava dome collapse or flank collapses (van Wyk de Vries and Davies, 2015). Volcanic lava domes are characterized by highly viscous solidified or semi-solidified masses of extruded lava at a volcano. When lava domes collapse they often generate block-and-ash flows, sometimes with little warning (Calder et al., 2015). These block-and-ash flows may form hummocky terrain, such was the case at Soufriere Hills Volcano, Montserrat (Sparks et al., 2002).

On a larger scale, the failure of an entire volcanic flank can involve substantial volumes of lithic fragments, of one to tens of cubic kilometers, with runout distances of over 80 km from source, especially if the flow is channelized, as is the case at Raupehu volcano in New Zealand (Tost et al., 2014). Similarly, the runout for a 100 km long debris avalanche from Colima volcano, Mexico, reached the Pacific ocean (Stoopes and Sheridan, 1992). At Shasta volcano, United States, the collapse of a portion of the edifice provoked a debris avalanche which covered a broad plain and the angle of dispersion of the hummocks spanned approximately 40° (Crandell et al., 1984). Clast-rich hummocks originated from a sector collapse ~4,500 years BP on the northern flank of Cotopaxi volcano, Ecuador and upon deposition these hummocks were covered by a lahar deposit (Mothes et al., 1998). The latter example demonstrates the need to conduct careful fieldwork that considers all options that may have contributed to either create or modify hummocks. Local environmental conditions, past and present, play a key role in the preservation or destruction of the original characteristics and fabric of the avalanche deposit within hummocks.

While Chalupas caldera is best known for producing a large ignimbritic deposit (Hammersley, 2003) (**Figure 1**), an area stretching eastward from the foot of Buenavista lava dome on the Chalupas caldera also draws attention. There we observe a landscape with several hundred hummocks whose sizes range from a mere 10 m diameter and 10 m high to more than 200 m diameter and ~30 m high. The largest hummocks concentrate in the center area, while on the margins their dimensions are smaller. Our hypothesis is that the hummocks may be the product of a gravitational lava dome collapse. Their forms, distribution, clast homogeneity, varied sizes and lack of convincing evidence of heat set them apart from glacier or lahar deposits, planar pyroclastic density current deposits undergoing erosion and also from discrete block-and-ash flows originating from limited dome destruction. Thus, to gain an improved perspective on the hummocky terrain and to visualize and capture the distribution of flow emplacement, we apply remote sensing techniques, scanning electron microscope (SEM) image analysis and field mapping. Computational modeling also shows the footprint upon the terrain if the actual, but now inactive Buenavista lava dome collapsed, spreading out over the present topography.

There are a number of key issues we sought to resolve in this study, and these include:

What is the extent of the area covered by the hummocks?
What are the lithologies of the hummocks?
What is the approximate age of the hummock field and the subsequent eruptive activity of Buenavista lava Dome?
What volcanic event might have led to the formation of the hummocks at Chalupas caldera?
Can computational modeling, run on the present (modified since 40 ky) topography, produce hazard footprints that are comparable to the measured area of the hummock field?
Which mass-flow volumes, as an order of magnitude, can best represent the area covered by the hummock field?

THE ECUADORIAN ANDES AND THE CHALUPAS CALDERA

The Ecuadorian Andes mountain range is part of the "Northern Volcanic Zone" (NVZ) which is formed by subduction of the northern segment of the Nazca plate beneath the South American plate with a subduction rate of ~5–6 cm/year (Guillier et al., 2001; White et al., 2003; Nocquet et al., 2014; Yepes et al., 2016). The main volcanic arc consists of two parallel mountain ranges, called the Eastern and Western Cordilleras, which are separated by a structural depression known as the Inter-Andean Valley (Hall et al., 2008). The Western Cordillera consists of about 20 andesite to dacite volcanoes built upon mid-to late-Cretaceous accreted oceanic terrain (Vallejo et al., 2019), whereas the Eastern Cordillera has some 25 volcanoes, mainly andesitic, and its base is comprised of Paleozoic to early Cretaceous age metamorphosed rocks of continental affinity (Spikings et al., 2001; Baby et al., 2013; Spikings et al., 2015). The rear-arc is defined by four volcanoes: Pan de Azucar and Yanaurco (Pleistocene) and Sumaco and the Puyo cones (Holocene) (Hall et al., 2008).

Volcanism in the Ecuadorian Andes is mainly andesitic in nature (Hall et al., 2008; Hidalgo et al., 2012), and collapsed silicic calderas are infrequent. Several collapse caldera structures, including Chalupas, are recognized, lying astride the Eastern Cordillera backbone (Mothes and Hall, 2008). Chalupas caldera lies 80 km southeast of Quito and 15 km SE of the bimodal Cotopaxi volcano (Hall and Mothes, 2008) (**Figure 1**).

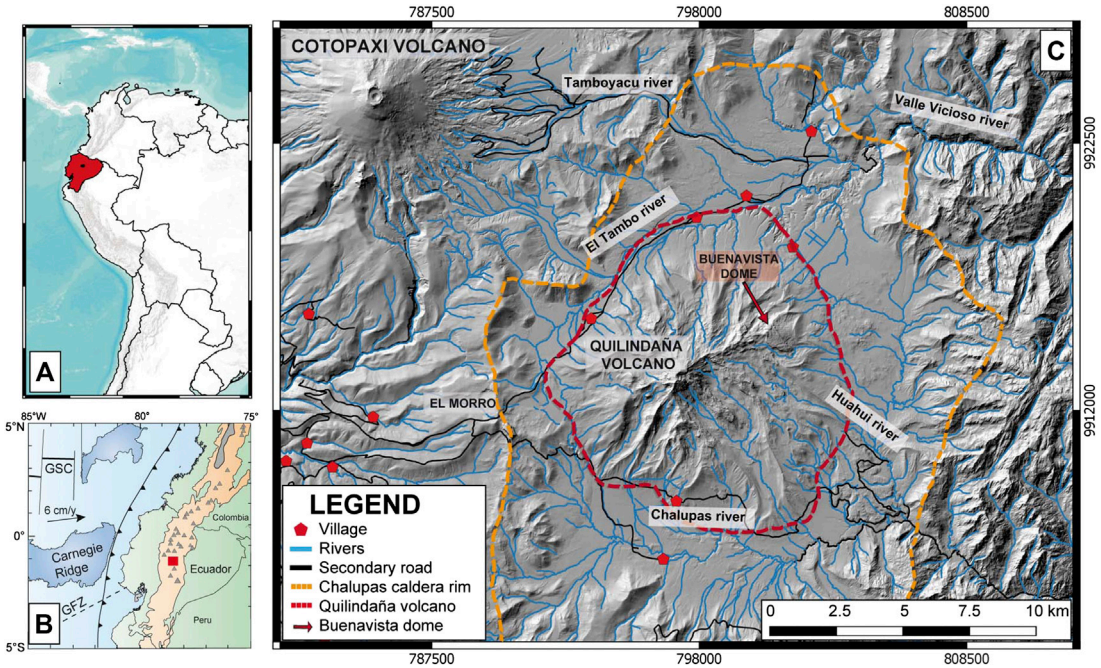

FIGURE 1 | Location of Chalupas caldera. **(A)** Ecuador. **(B)** Geodynamic framework of the Ecuadorian volcanic arc at the convergence of the Nazca and South American plates, converging eastward at 6 cm/years (White et al., 2003). The trench is represented by the black line with indents, GSC, Galápagos Spreading Center; GFZ, Grijalva Fracture Zone (modified from Robin et al., 2010). Chalupas caldera is represented by a red square. **(C)** Chalupas caldera in the local context with its topographic rim and the perimeter of Quilindaña volcano.

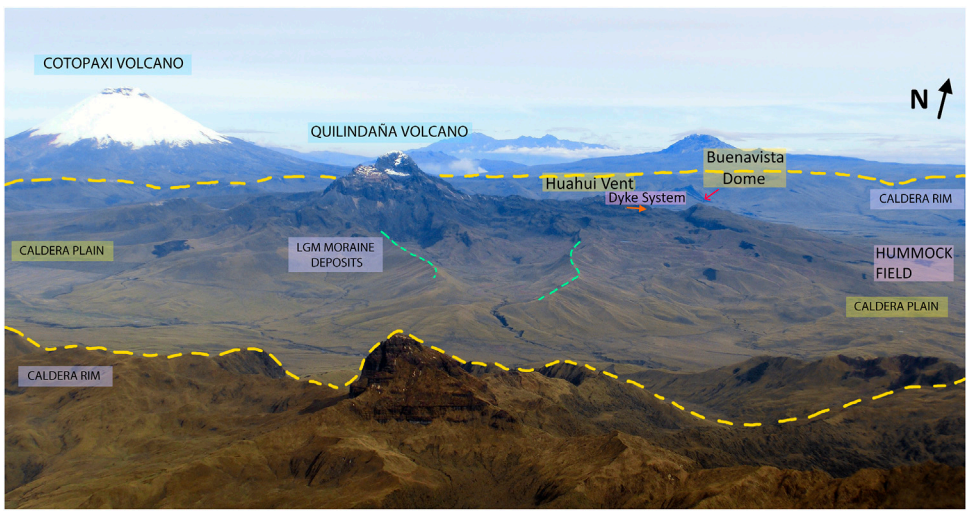

FIGURE 2 | Aerial view of the main structures of the Chalupas caldera, view toward W-NW, taken from above and slightly east of the caldera's eastern rim (yellow broken line). LGM refers to moraines of the Last Glacial Maximum period and are demarcated by green lines.

Chalupas caldera has an elongated SW-NE planform with an average diameter of ~17 km (**Figure 2**). Its formation followed one large rhyolitic eruption, causing foundering and inward collapse. Its most notable deposit is called "The Chalupas Ignimbrite" (Beate, 1989) and is dated with the $^{40}Ar/^{39}Ar$ method at 0.211 ± 0.014 Ma (Hammersley and DePaolo, 2002; Hammersley, 2003; Beate et al., 2006) and the K-Ar method at 0.216 ± 0.005 Ma (Bablon et al., 2020). The deposit has a radial distribution spreading out from the caldera rim into the Inter-andean Valley (IAV) (Beate, 1985), and related fine-grained layers are preserved on the coastal plain (Jackson et al., 2019) and in the eastern Amazon Basin.

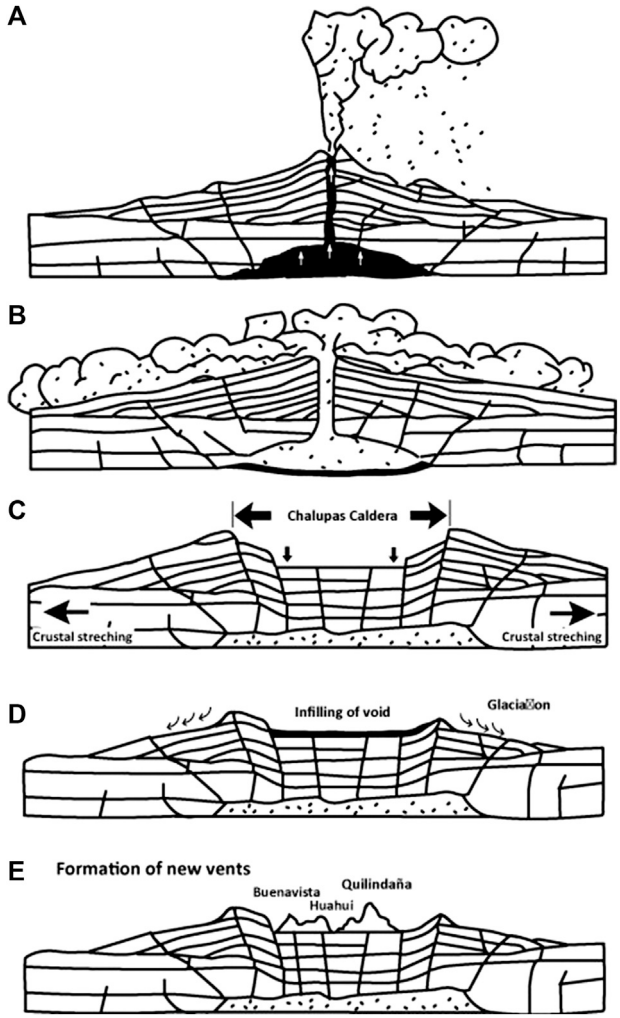

FIGURE 3 | Phases of formation of the Chalupas Caldera: **(A)** Upwelling of magma in center volcano, starting with a Plinian eruption column, with accompanying ring fracture andesitic cones forming outer boundary; **(B)** Magma evacuates the caldera and expulses ash-flow sheets to the E, W, S and N; **(C)** Collapse, foundering of caldera; **(D)** Erosion and infilling of void and glaciation; **(E)** Growth of Quilindaña peak, vent migration along dykes to the east and formation of Huahui vent and Buenavista lava dome.

Chalupas Ignimbrite

The ignimbrite deposit is a notable stratigraphic marker that contributes in determining relative ages within Ecuador's Inter-Andean Valley stratigraphy and in neotectonic studies (Fiorini and Tibaldi, 2010). The area covered by the ignimbrite is around 2,000 km^2 and the average thickness is approximately 30 m, providing an estimate of total bulk volume for the ignimbrite at around 100 km^3 (Beate, 1985; Hammersley, 2003). According to Bablon et al. (2020), the total bulk volume of both ignimbrite and associated co-ignimbrite deposits amounts to ~230 ± 30 km^3. The non-welded rhyolitic ignimbrite is crystal-poor, with scarce biotite and plagioclase crystals and typically displays large (25 cm diameter) pumice clasts with well-defined tubes. The magmas are highly evolved with SiO_2 values of 72–74 wt%.

The ignimbrite/co-ignimbrite volume ranks the eruption at a VEI 7, consistent with the associated caldera size of between 16 and 18 km diameter (INECEL, 1983; Beate, 1985; Lipman, 1997; Bablon et al., 2020). In the center of the caldera is the post-caldera andesitic volcano, Quilindaña (4,800 m), of which Buenavista lava dome (4,230 m) forms the eastern extreme (Hammersley, 2003; Córdova, 2018; Córdova et al., 2018).

Based on our fieldwork and that of Hammersley (2003), we suggest that the succession of formative events at Chalupas Caldera can be synthesized in the following stages (**Figure 3**):

Quilindaña Volcano

Shortly after the caldera collapse, a pulse of new magma began forming the andesitic stratovolcano, Quilindaña, located in the caldera's center. It has at least two main sub-phases are identified on its peak (**Figure 3E**):

(1) Quilindaña I (Initial phase), composed by amphibole andesite, which is altered due to past fumarolic activity of Quilindaña. Rocks from this phase are exposed on edges of glacial valleys (**Figure 4A**).
(2) Quilindaña II (Second phase) is composed of a pyroxene andesite which crops out at the top of the sequence and has glassier composition: an olivine-rich andesite is at the bottom of the sequence (**Figure 4B**).

$A^{40}Ar/^{39}Ar$ radiometric age, obtained on plagioclase from a sample taken from the center of Quilindaña I, is reported by Hammersley (2003). The date of 0.169 ± 0.001 Ma is interpreted as the age of the formation of Quilindaña peak and represents post-collapse activity of the caldera, following paroxysmal caldera formation about 40,000 years earlier. We recognize morphological traces of a probable sector collapse on the SE flank of Quilindaña peak. But due to glacial erosion and burial by lava flows, the collapse remains are obliterated (**Figure 5**).

Buenavista Lava Dome

Buenavista is a lava dome that formed at the northeast-east extreme of a propagating dyke system that extends 5 km east of Quilindaña peak. Between Quilindaña and Buenavista is another vent, Huahui, which emitted a 7 km long lava flow that flowed southeast to the caldera outlet carved out by the Chalupas river. Buenavista is dacitic and is more evolved than either Quilindaña or Huahui. The samples collected from Buenavista dome have compositions ranging from 61.6 to 69.5 wt% SiO_2. Petrographic descriptions and geochemical analysis show that the magma is one of the most acidic products of the post-caldera phase (Córdova, 2018).

Buenavista dome occupies about a 1.7 × 1.5 km area and has 700 m of relief above the eastern Chalupas plain. Our calculations give an approximate volume of 0.96 km^3 for the present-day Buenavista dome.

The Chalupas caldera has been affected by glacial processes both on its edges and at Quilindaña volcano (Hastenrath, 1981). We observe U-shaped valleys and sequences of both lateral and end moraines. The largest moraines, which were most active between ~36 and 13 ka (Clapperton, 1993), correspond to the

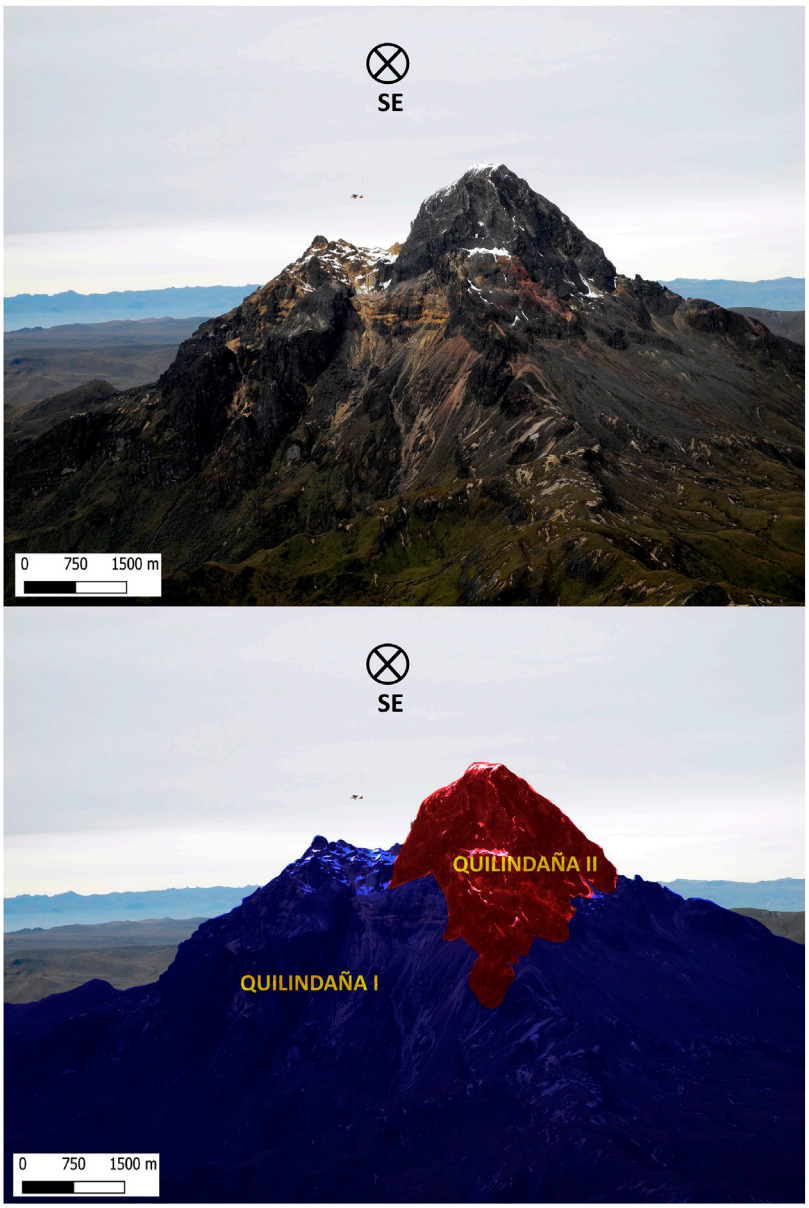

FIGURE 4 | (A) Quilindaña volcano view to the southeast. **(B)** Formation scheme of the two phases of Quilandaña. Ultralight plane is flying behind Quilindaña I.

Last Glacial Maximum (LGM) and can be found down to about 3,700 m elevation. Smaller Younger Dryas period moraines (12–10 ka) are found above 3,800 m elevation (Clapperton et al., 1997; Heine, 2004) (**Figure 2**). It is important to clarify that the hummock terrain on the eastern Chalupas plain lies below the LGM moraine limit and hummocks are not overridden by LGM moraines.

Our focus in this contribution is the study of the post-collapse phase of this potentially active caldera, aiming to account for the most recent eruptions through study of the hummocks at the base of Buenavista dome and the companion tephra layers. We elucidate the relative youthfulness of the post-caldera stage of the caldera and provide comment on potential hazards to downstream communities and projects, using our computational modeling results.

METHODS AND TECHNIQUES

Fieldwork

Our fieldwork was carried out from late 2016 to early 2020, over 7 trips of 5 days each. Access to most outcrops is by walking over high (3,600–4,400 m) alpine grasslands or riding on horseback, if swampy conditions permit. The best available stratigraphic exposures were along rivers or in road cuts. Our work concentrated on Buenavista dome and its feeder dikes,

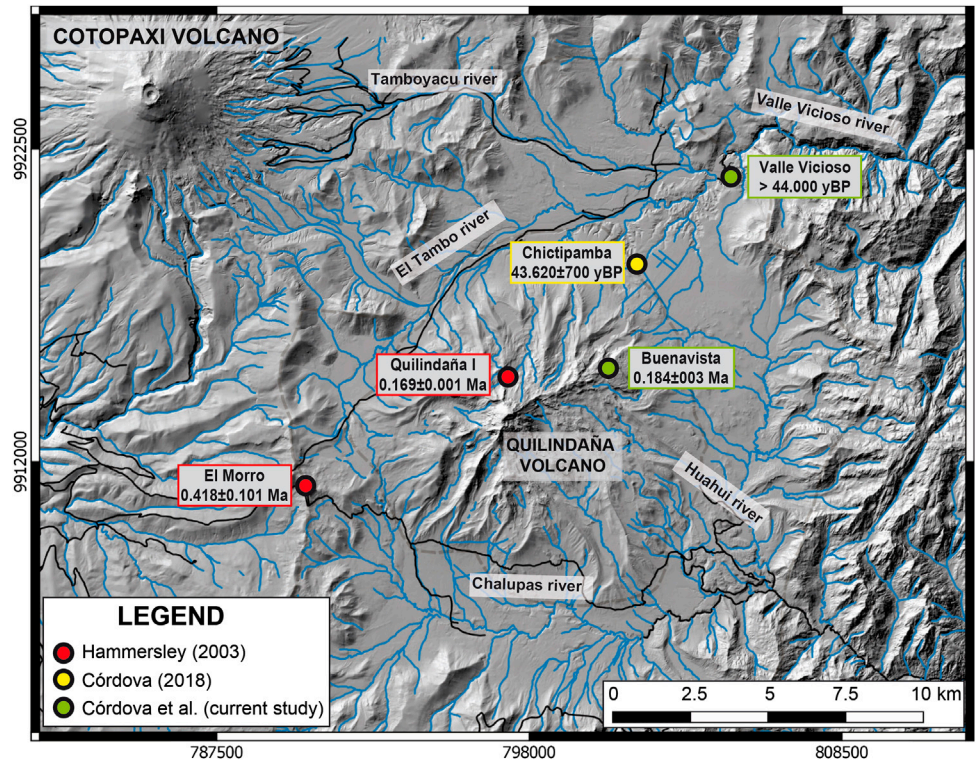

FIGURE 5 | Distribution of the radiometric ages from Hammersley (2003) (red circles), Córdova (2018) (yellow circle) and (current study) (green circle).

inspecting and mapping the hummocky terrain and identifying new ash layers that were thicker and had larger pumice and lithic sizes, compared to those emitted by other nearby volcanoes. Mineralogy is also a key factor to identify tephra origins. Based on our observations in the caldera, hornblende is present only in Buenavista dome rocks. Representative rock clasts were collected from all main lava flows and eruptive centers and analyzed for major and minor elements at the Peter Hooper GeoAnalytical Lab, Washington State University in Pullman, WA, United States. Samples of organic-rich material extracted from scarce peat layers were sent to Beta Analytic Laboratory in Miami, Florida, United States for radiometric dating (^{14}C and AMS).

Scanning Electron Microscope Image Analysis

Representative samples of rock were taken from Buenavista dome and from the interior of the hummocks and analyzed using a VEGA Tescan SEM. Samples were cut into thin wafers and polished prior to analysis. Backscatter electron images (BSE) were taken on representative areas of the samples using a 15 kV accelerating voltage, at ×100 and ×500 magnification.

Digital Elevation Map Analysis

All the geographic information was analyzed using Quantum GIS (Version 3.4) and ArcMap (Version 10.5) software. Initially, using a 3m/pix resolution DEM (Source: Instituto Geográfico Militar-Quito, 2015), which covers the entire caldera, we identified hummocky topography at the base of Buenavista Dome, spreading eastward over the caldera plain. Later we used *Topohazard*, a Linux script developed to calculate the vertical topographical differential between slopes, and which applies a color scale to smooth visual results (Marrero et al., 2019), visually enhancing the hummocky topography in the caldera.

Unmanned Aerial Vehicle Photography With a senseFly eBee Classic Drone and DEM Generation

Since the eastern Chalupas plain has difficult access due to swampy conditions, we designed a drone survey to take aerial photographs with the aim of making a higher-resolution DEM, specifically to model the emplacement of potential future breccia deposits borne off Buenavista Dome. We recognize that topography has likely undergone many modifications in 40 ka, therefore our approach is to use the present topography to model potential breccia flow emplacement. To perform the survey, we used an unmanned aerial vehicle (UAV), the eBee Classic, which is a fixed wing type drone, developed by SenseFly (**Figure 6**). To plan the survey and the flight path of the drone, we used the software eMotion 3 (designed for Windows) installed on a laptop which was used as a ground base station. The altitude of the area of interest is above 3,550 m a.s.l. with a maximum of nearly 3,800 m a.s.l. The chosen location for take-off and landing, as well as the ground station, has an elevation of 3,600 m a.s.l.

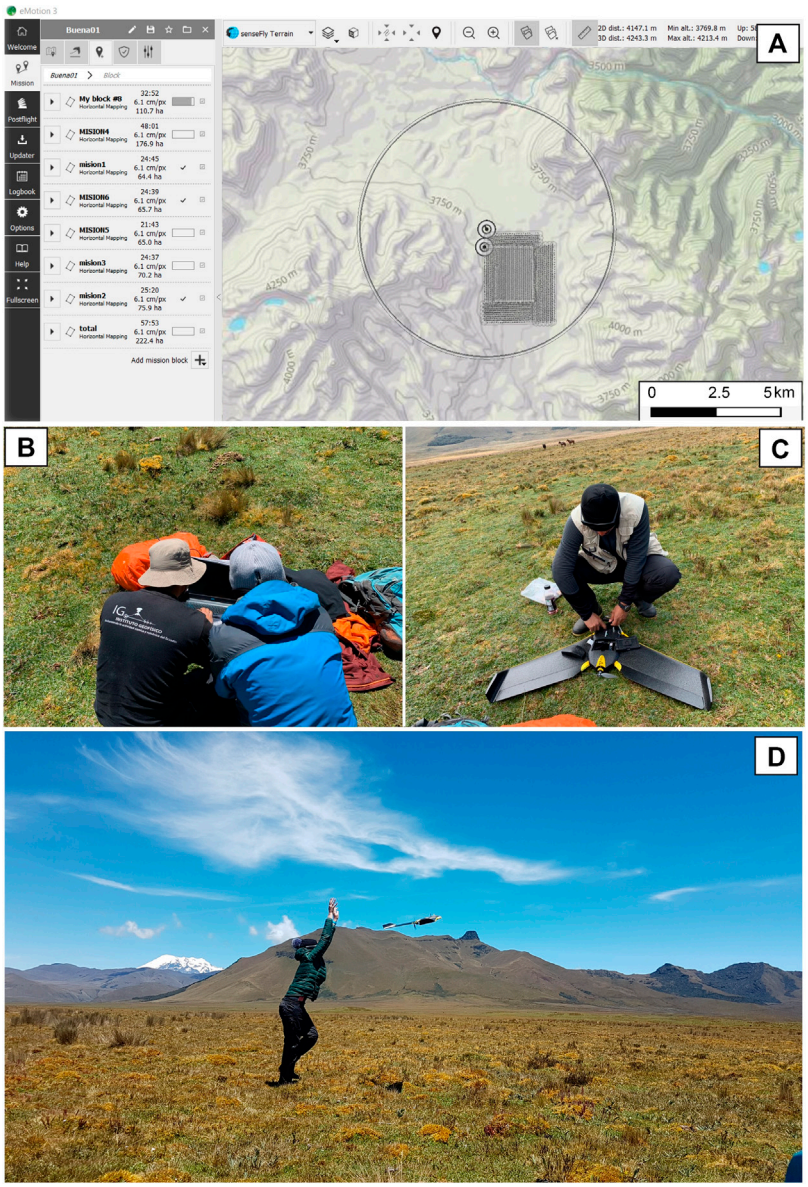

FIGURE 6 | Mosaic of the preparation for the drone survey. **(A)** Drone survey development on eMotion three software, **(B)** Ground station and flight planning on eMotion software. **(C)** Change of batteries after landing **(D)** Launching of the drone.

The survey area covered by the flights was approximately 12 km^2 and the average height of the flights was approximately 120 m above ground surface. More than 5,000 photos were taken with a Canon S110 Near-Infrared (NIR) camera with a resolution of 12 megapixels. This camera takes photos in the Near-Infrared band and red and green visual band. We used the NIR camera to avoid including clouds in the images and this type of camera also gives better results when conditions are foggy. While this may not be the main motivation to use a NIR camera, it provided images with excellent resolution to make the DEM. The dense sequence of photos recorded was processed using the software Agisoft Photoscan, version 1.5. This software works by building a dense mesh of points with a 70% lateral and longitudinal overlap on each photo in order to construct a high-resolution digital surface model and then a digital elevation model.

Geographic Data Analysis, Description of Hummocky Terrain Patterns, Volume Deposit Calculation

The result of the UAV survey over a 12 km^2 area produced a DEM with a spatial resolution of 1.5 m/pix, and produced a high quality hillshade in terms of the elevation data from the DEM (**Figures 7A–C**). The GPS of the eBee classic drone has an

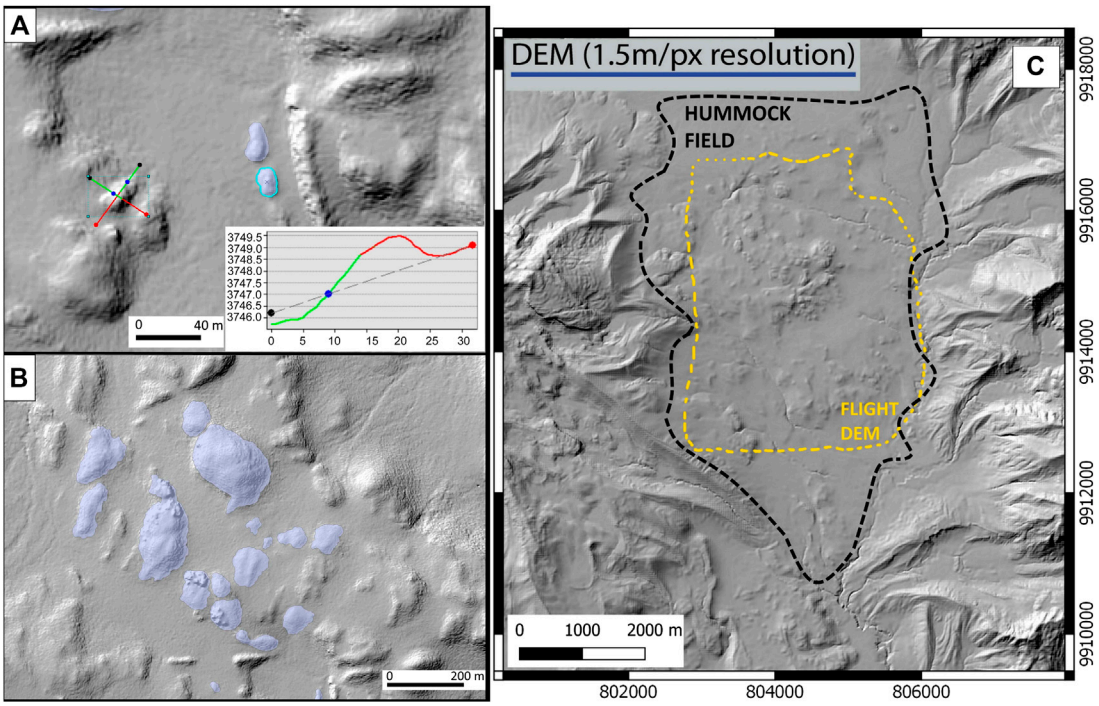

FIGURE 7 | DEM with a high spatial resolution of 1.5 m/pix which is a final result of the unmanned aerial vehicle survey. Insets **(A,B)** show polygons used to delimitate hummocks in order to derive their volume. **(C)**. The perimeter of the mapped hummock field is delimited by a broken black line, while the yellow line delimits the flight paths. BVD, Buenavista Dome.

accuracy of <3 m. Previous to our field campaign we made tests with ground control points with known coordinates, but found no significant difference between results.

Elevation profiles (**Figure 7A**) were useful to delimit each hummock with a polygon (shape files). Once we calculated the coordinates of the nodes from the borders of every polygon (**Figure 7B**), we were able to calculate the volume of the hummocks with a script written in MATLAB (Aguilar, 2013). The algorithm script calculates the volume of known polyhedrons using an interpolated grid between the coordinates of the polygons over the elevation data of a high-resolution DEM. A total of 168 representative hummocks which spread out on the east Chalupas plain were delimited, taking into consideration the relief of the hummock above its base. In earlier studies this method was used for calculating the volume of lava domes at Pululahua Volcanic Complex (Vásconez et al., 2015), hummock deposit volumes of Cotopaxi's debris avalanche (Encalada and Bernard, 2018) and the volume of eruptive vents on Wolf and Alcedo volcanoes in the Galapagos islands (Pérez, 2020).

Numerical Simulations

We ran numerical simulations of gravitational flows to compare the results to the mapped hummocky terrain draping the present landscape. We assume that the landforms of 40 ka were somewhat different than those of today due to modifications of the drainage networks. As commented upon by Özdemir et al. (2016), uncertainties in topography are a problem when trying to model older gravitational flows. Our modeling exercise helped to visualize where a future dome collapse breccia might reach onto the east Chalupas plain.

We used two numerical models: a modified version of LaharZ_py (Schilling, 2014), called *LaharZ/PFz* (Widiwijayanti et al., 2009) and VolcFlow (Kelfoun and Druitt, 2005). VolcFlow is a code which runs in MATLAB and is principally based on the depth-averaged approximation. It applies a topography-linked coordinate system, with x and y parallel to the local ground surface, h as vertical and with a depth-averaged set of equations of mass and momentum conservation. On the other hand, LaharZ_py (Schilling, 2014) is written in Python and is a tool used in conjunction with ArcMap, a Geographic Information System (GIS). Primarily, LaharZ_py is a computational model that employs statistical descriptions of areas inundated by past mass-flow events to forecast areas likely to be inundated by hypothetical future events (Iverson et al., 1998; Schilling, 2014).

We sought to simulate the flow and deposition of gravitational "dry" breccia flows. Therefore the modified version of LaharZ_py called *LaharZ/PFz*, described by Widiwijayanti et al. (2009) and developed to simulate block and ash-type PDCs, seemed the most suitable. In this case the area and cross sectional equations were modified in accordance with the semi-empirical equations A= (0.05 modified to 0.1) $V^{2/3}$, B= (35 modified to 40) $V^{2/3}$, as described by Widiwijayanti et al. (2009). The results give an objective means to assess cross sectional (A) and planimetric (B) areas to be inundated by block-and-ash pyroclastic flows of

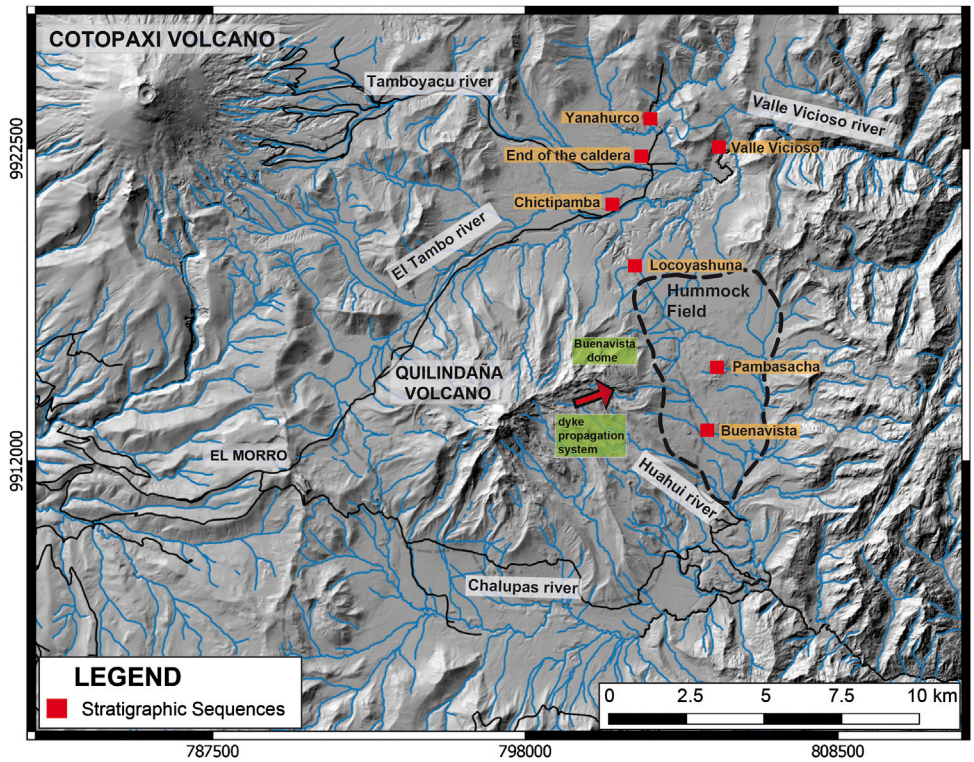

FIGURE 8 | Map showing hummock topography related to the Buenavista Dome fan on the eastern Chalupas plain, in the vicinity of Pambasacha and Buenavista stream cut sequences, and location of stratigraphic sequences discussed in the text. Mapped hummock field perimeter is delimited by broken black line and occupies the eastern Chalupas plain, which is confined between the Buenavista dome massif and steep - relief topography to the east.

various volumes (V). The program *LaharZ/PFz* does not provide information on deposit thickness. Hayashi and Self (1992) showed in a comparative study between parameters of deposits of 40 volcanic debris avalanches and pyroclastic flows that there is no discernible difference in H/L vs volume. Furthermore, they adduced that the emplacement mechanisms of the two flow types are probably very similar.

Before running VolcFlow, several inputs are required: the source location, time interval of the run, the eruptive and depositional phase of the phenomena, and other values that correspond to the particular rheological behavior of pyroclastic or avalanche flows. We applied the calibrated parameters used in VolcFlow flow modeling of two Ecuadorian volcanoes, Tungurahua (Kelfoun et al., 2009 and Sangay (Ordóñez et al., 2011). These parameters included designating values for the constant retarding stress (i.e. yield strength) variable. For example, a constant retarding stress of 50 kPa during flow was assigned for the emplacement of the Socompa debris avalanche (Chile), enabling a long runout and ample spreading of the avalanche (Kelfoun and Druitt, 2005) in the modeled results in order to match the actual trace of the deposit in the field. For the pyroclastic flows of Tungurahua's August 16, 2006 eruption, a constant retarding stress of 5 kPa was assigned for modeling the flows' emplacement, and gave very good results with regards to the mapped volcanic deposit (Kelfoun et al., 2009). For modeling Sangay's pyroclastic flows a constant retarding stress value of 4.5 kPa was employed in the VolcFlow modeling. Kelfoun et al. (2009) noted that flows with thick fronts must be modeled with a higher constant retarding stress value and at Socompa, the higher value (50 kPa) applied for this variable, represents adequately the thicker flow deposits of Socompa's avalanche deposit (Kelfoun and Druitt, 2005). For the two scenarios of our VolcFlow modeling we opted to employ the variables assigned to Tungurahua and Sangay, since our team had experience in these case studies and the similarity of rock chemistry. We acknowledge however that the yield strength values chosen may be too low, since the modeled Buenavista breccia flow did not spread out widely nor travel far enough compared to the mapped hummock trace.

Alternatively, running *LaharZ/PFz* only requires two initial parameters: a starting point and an estimated volume to begin simulating the flow phenomena. In our case, the starting point to simulate the dome collapse was the top of Buenavista dome (4,230 m.a.s.l), where the dyke propagation system which traverses from Quilindaña volcano may represent the source for new magma injection that led to dome growth. We also choose initiation at this high point because the unusually steep morphology on the eastern scarp of Buenavista lava dome suggests that there could have once been an appendage of the dome located immediately east of it (see **Figure 8**).

RESULTS

Tephra Layers From Buenavista Dome Complex

Study of stratigraphic sections in the river valleys near the base of Quilindaña volcano inform us about past activity of the local vents inside and around the caldera. Most stratigraphic sections are dominated by Holocene and earlier tephra fall deposits from rhyolitic eruptions of nearby volcanoes, Cotopaxi and Chaupiloma. Two lithic/tephra layers, here named A and B, which have angular dacitic clasts, scarce pumice and display a different mineral assemblage than that displayed at either of the two mentioned volcanoes, are deemed to be related to Buenavista dome complex. Also, a newly identified crystal-poor rhyolitic (73 wt% SiO_2) pumice lapilli layer provides possible evidence of an eruption of a silica-rich cap on top of a "crystalline mush" in the magmatic storage area (e.g., Bachmann and Bergantz, 2008). We derived a ^{14}C age of 43,620 ± 700 yBP from a peat layer beneath this siliceous ash layer. The source of this ash is also likely related to Buenavista dome and was discriminated from Cotopaxi and Chaupiloma volcanoes, based on different geochemistry and petrography (Hall and Mothes, 2008; Garrison et al., 2011; Córdova, 2018).

Stratigraphic Relationships of Tephra Layers, Breccia and Geochronology

Around the NE edge of Buenavista dome is an inclined fan with limited vertical exposure, except in stream cuts. The hummock field, shown in **Figure 8** with respect to the Buenavista and Pambasacha streams, represents higher topography initiating at the base of Buenavista dome.

Sections that we logged are generally comprised of sequences of Holocene tephras and soils, minor glacial outwash of Last Glacial Maximum age (~36,000 to 13,000 years BP) (Clapperton et al., 1997), peat layers, stream cobble bars, reworked and primary tephra layers, co-ignimbritic fine-grained ash layers that fell into a lacustrine environment, and limited debris flows. Here we will build the case for the stratigraphy associated with Buenavista dome activity, starting with evidence of breccia layers, which may be related to a collapse event or block-and-ash flows, and ascending the sequence through the younger post-collapse explosive activity represented by tephra layers.

At the bases of cuts in the Pambasacha and Buenavista stream valleys, where breccia exposures are 5–10 m below the east Chalupas plain surface (**Figure 8**) we observe units with angular to sub-angular porphyritic dacitic clasts containing large plagioclase and hornblende crystals in a glassy to ashy matrix. Some blocks are irregular size, with a diameter up to 5 m, homogeneous, monolithologic, with jigsaw-cracks. For the matrix, grain size ranges from fine to coarse gravel to medium sand size. Occasional white pumice clasts are observed but are rare. Mostly clasts are without a vesiculated rind. The sorting is generally poor, the deposit is unconsolidated and the matrix colors are off-grey to rosy pink (**Figure 9**) of the fresher outcrops, particularly for exposures in the Buenavista stream valley section (see photos, **Figures 9A**, **A2**). These clasts are akin to those rocks comprising Buenavista dome. Iron-staining of the finer-grained, matrix facies is common (**Figure 9**, photo E). A sequence of fine-grained co-ignimbritic ash and lithic fragments in an ash-rich matrix that has a massive appearance with no layering overlies the breccia layer.

We estimate that the breccia deposit is approximately 20+ m thick based on observations of the tallest hummocks that rear out of the slightly inclined surface. Hummocks are also observed several kilometers farther to the east on the plain's perimeter which is in contact with high-relief non-volcanic ridges, and southward to the incoming Hauhui stream valley (**Figure 8**).

In the Chictipamba section, along the Tambo river's right margin, (**Figure 9**, Photo B), starting at the top of the section, we first observe Holocene tephras and soil, then Last Glacial Maximum till and peat, down to layer CHL-MC-29, which is a white pumice lapilli with biotite and hornblende crystals and which has similar but more evolved chemistry of its pumice (73 wt% SiO_2) compared to Buenavista dome samples. An underlying peat almost immediately beneath the tephra layer (sample CHL-MC-29) provides a ^{14}C date of 43,620 ± 710 years BP. While there are few lithics in the ash-rich layer, its componentry and grain size suggest that it is from a local source. The underlying 5 m thick co-ignimbritic layers of fine silt-size ash display abundant biotite crystals with lathe-forms. A lack of hornblende crystals and the presence of obsidian shards suggest a distal source up-valley from Cotopaxi, however, interbedded are fine-grained lithic layers of fallout whose source is likely Buenavista dome explosions/collapse.

Both A and B tephra fallout layers cropping out 2 km S-SE at the higher elevation Locoyashuna cut (**Figures 8**, **9**, Photo C) have abundant lithic components of gray and rosy-colored dome-like rocks and scarce hornblende-bearing pumice. The angularity of the components, their similar petrography to Buenavista dome rocks and their dimensions (1–3 cm diameter) suggest that a local vent eruption is the probable source. The lower older Tephra A contains more altered clasts and overall has a more weathered appearance than the overlying Tephra B. Comparatively, the younger upper B layer is fresher and with more angular clasts, has scarce altered clasts and biotite crystals are coppery-colored. Both tephra layers are immersed in a massive deposit with faint centimeter thick laminations comprised of angular, tabular lithics in a coarse-sand-ashy matrix.

Lastly, two fallout layers, identical to the described Tephras A and B at Locoyashuna, are observed in the intermediate portion of a 100 m deep cut on the right margin of the Valle Vicioso River, on the far eastern limit of the Chalupas Caldera (**Figures 8**, **9**, Photos D and D2). In both fallout layers, fresh, angular hornblende-bearing lithics are prominent with scarce pumice content. An AMS date derived from analyzing an underlying peat layer, near the base of the Vicioso section, provides an indeterminate age of >44,000 yBP, which is older than the age of the peat (43,620 ± 700 yBP) beneath the Chictipamba tephra layer.

Our study provides a new $^{40}Ar/^{39}Ar$ date of 0.184 ± 0.003 Ma (sample CHL-MC-15). Dating was performed by Dr Brian Jicha of the Rare Gas Geochronology Lab, University of Wisconsin-

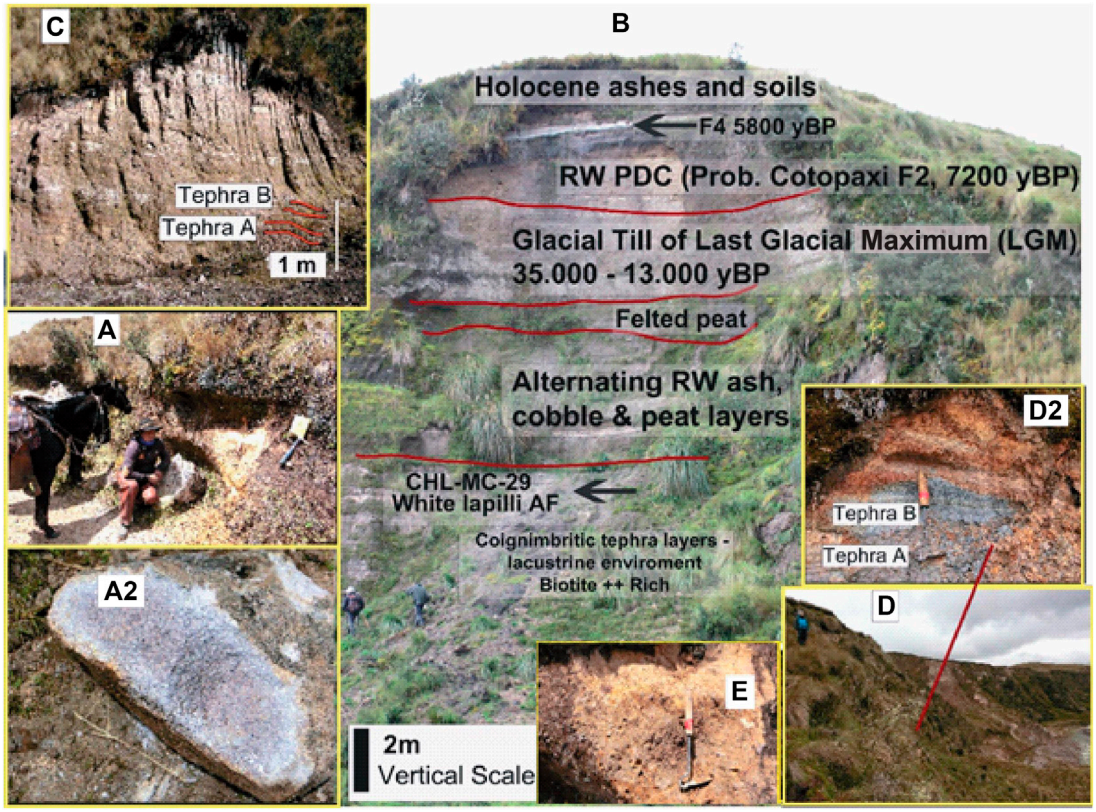

FIGURE 9 | Outcrops which display stratigraphic layers related to Buenavista dome complex. Photo **A** is of a cut in Buenavista stream valley, while **A2** is a close up of dacitic porphyritic, hornblende-bearing clast; (B) is section at Chictipamba, displaying the stratigraphic sequence, the tephra lapilli fallout layer CHL-MC-29, with a underlying date of 43,620 ± 710 years BP, and 5 m of underlying lacustrine/fine-grained layers; **(C)** is outcrop at Locoyashuna river valley where two fallout layers, **(A,B)**, predominantly of dacitic lithics, are hypothesized to be related to post dome collapse explosive activity of Buenavista dome complex; **(D)** is photo of 100 m deep cut on right margin of the Valle Vicioso River. At its base is a dated peat layer of >44 ky BP and at intermediate level are the two dacitic lithic fallout layers, **(A,B)** (photo **D2**), identical to the two layers logged at Locoyashuna cut (photo **C**). Photo E is of an iron-stained matrix facies of breccia deposit outcropping at the Buenavista stream cut. Here lithic matrix is >50%. An ashy co-ignimbritic layer caps the sequence.

Madison, on groundmass of a sample taken from the Buenavista dome summit (**Figure 5**). This age is contemporaneous with the first phase of Quilindaña I (0.169 ± 0.001 Ma), suggesting that both structures evolved more or less simultaneously in the early post-caldera phase and that the dyke feeder system has been active from the start.

Collapse of Buenavista's Eastern Flank?

Using the new 1.5 m/pix resolution DEM made from the drone flights and field observations, we identify a scar on the east limb of Buenavista dome where a possible appendage of Buenavista complex once extended and subsequently collapsed, thus forming the hummock field (**Figures 10**, **11**).

The scar left by the slide off the dome likely suffered subsequent glaciation and its morphology is now characterized by uneven terrain with numerous rock benches/ledges. LGM (Clapperton et al., 1997) moraines wrap around the Buenavista massif and descend to the base of the dome complex. Since we believe that the scar's morphology has been altered by erosional processes we did not compare our simulation volumes with an estimated volume of the scar. Additionally, in observations made by Voight et al. (2002) on the 1997 sector collapse and debris avalanche at Soufriere Hills volcano, Monserrat, the breccia deposit's volume was much greater than the volume estimated for the remnant scar due to volumetric bulking of the avalanche flow while in transit.

Moraines near to Buenavista dome are considerably shortened in their penetration onto the Chalupas plain, unlike at other sectors of the Quilindaña massif where robust LGM moraines extend down to 3,700 m elevation. This difference may reflect that the lava dome collapse destroyed or buried pre-existing moraines and that later glaciers around the Buenavista dome could not regrow and finally produce far-extending moraines. LGM moraines are present around Buenavista dome at 3700^{+} meters elevation, but are never seen over-capping hummocks.

During our field campaigns, our search on horseback along the Pambasacha and Buenavista streams (**Figures 8**, **10**), both of which originate on Buenavista dome, revealed outcrops of two different rocks types of possible dome origin. These rocks crop out some 5–8 m below the surface in a coarse sandy matrix. The

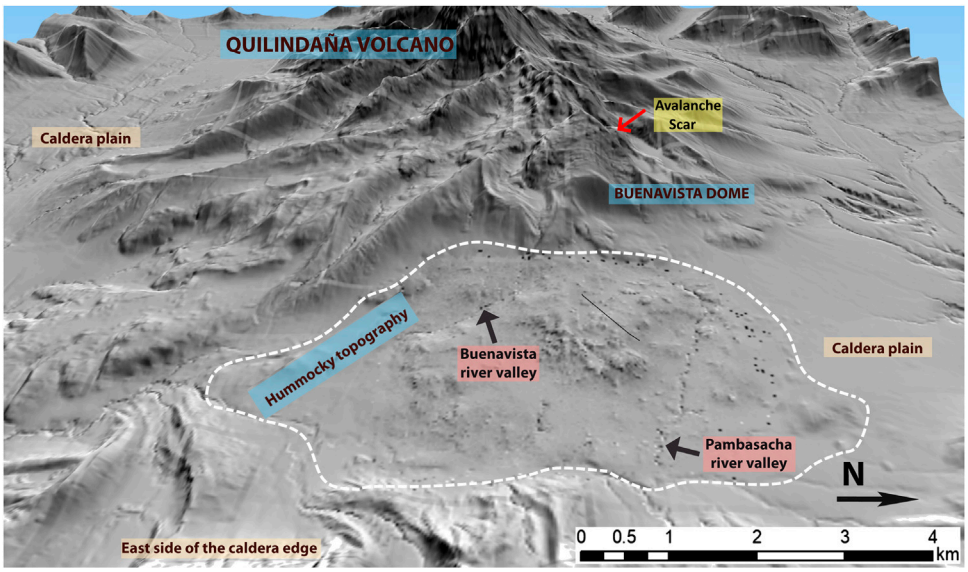

FIGURE 10 | 3D model of Buenavista dome, where hummocky topography spreads out from the eastern foot of Buenavista Dome. Top of scar indicated by red arrow. View to west.

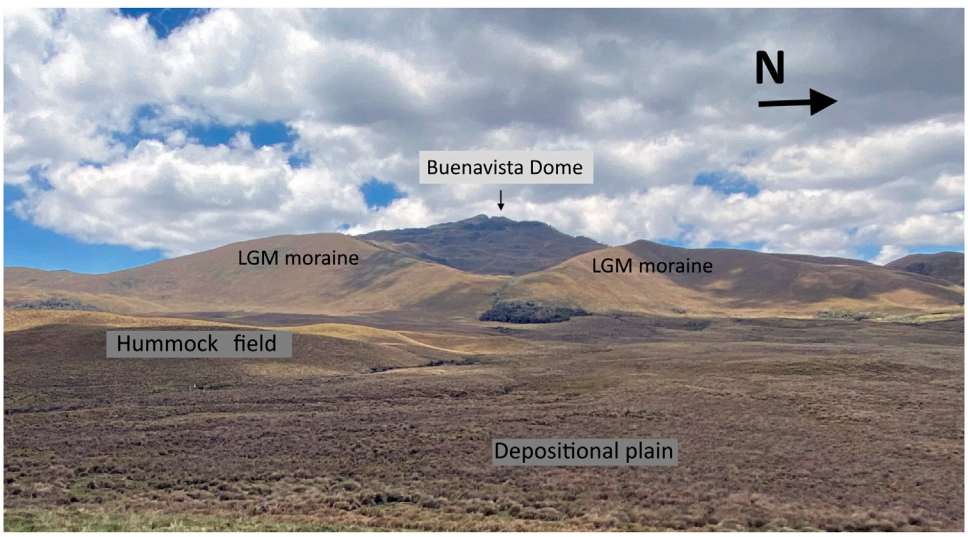

FIGURE 11 | Scar left by destruction of a portion of Buenavista dome's east flank whose resulting gravitational flow is hypothesized to have formed the hummock field, partially seen in the foreground. View west.

first category is a rose-grey colored, fresh, plagioclase-rich, semi-vesicular dacitic dome rock with crystals between 2–4 mm in size. This rock type represents the bulk of the deposit within the coarse sandy matrix which is of similar mineralogy. The second category is a dense, aphanitic black rock with large >2 mm sized plagioclase phenocrysts which are heavily altered and weathered. The first dacitic sample is most akin to present day Buenavista dome while the second sample does not have a recognizable modern cohort.

The upper Chalupas plain surface is not undergoing rapid incision by streams, attested to by swampy conditions, suggesting that the breccia may form an impermeable layer. The hummock field covers an area of about 20 km^2 and the farthest hummock cluster is located 7 km SE from the base of the dome. As mentioned, the east Chalupas plain is confined on the east by steep high-relief metamorphic ridges down to the intersection with the Huahui stream valley (**Figure 10**).

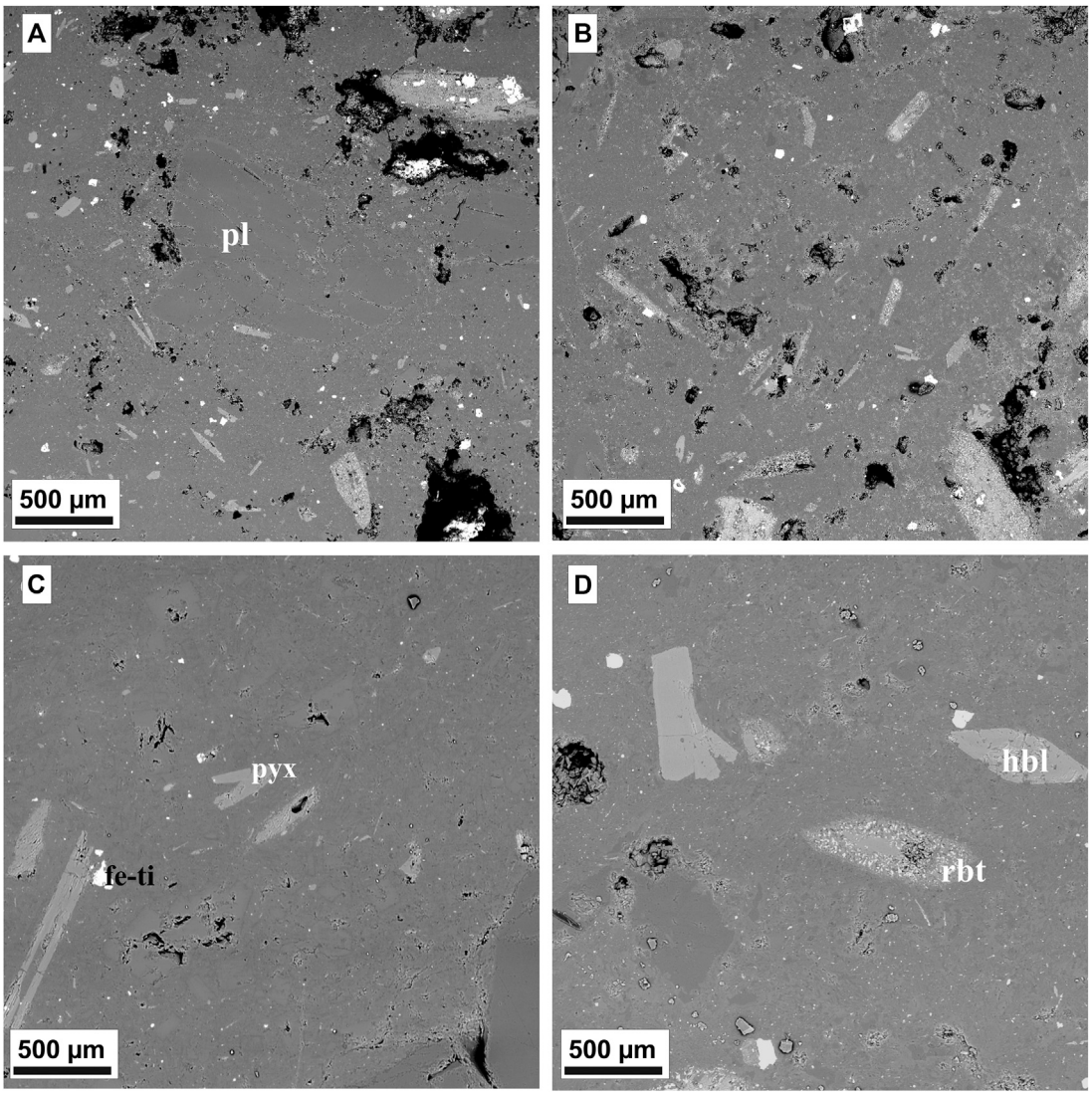

FIGURE 12 | A and **C** are of sample CHL-MC-15 (Buenavista Dome rocks) and **(B, D)** are of sample CHL-PIS-25 (Buenavista stream valley samples). Plagioclase (pL), hornblende (hbl), pyroxene (pyx) and Iron-Titanium oxides (Fe-Ti) are labeled in the images. **A** rim breakdown texture is also labeled in **D** (rbt).

Linking *In-Situ* Buenavista Dome Rocks to Breccia Samples From Pambasacha and Buenavista Stream Hummock Cuts

Samples of the Buenavista dome were collected during a field campaign in December 2016 when the remnant scar on the east flank was observed. More recently, during investigations in the Buenavista and Pambasacha stream valleys, samples of breccia were collected from outcrops in hummocks for comparison with the *in-situ* dome samples. This was done with the aim of confirming whether origin of the breccia deposit was derived from the Buenavista dome complex.

Samples taken from the Buenavista dome summit are massive, porphyritic dacite, light gray in color but often with a rosy hue. In thin section, they are hypocrystalline with phenocrysts of plagioclase (often with clay alteration products), clinopyroxene, amphibole, and metal-oxides. The matrix is microcrystalline and composed of plagioclase, orthopyroxene, and metal-oxides. SEM backscatter images were taken (**Figure 12**) of both the dome samples and samples collected from deposits in the hummocks. Samples from the breccia deposit show a marked resemblance to the samples from the dome both in appearance, composition and microstructure. As described in the stratigraphic section (**Figures 9A, A2**) the samples taken from a cut in Buenavista stream exposing the breccia deposits are light gray with a rosy hue and are porphyritic, with obvious plagioclase and hornblende crystals. The hand specimens of the two samples appear remarkably similar. Under the SEM, the similarities are even more obvious with both samples displaying large plagioclase, amphibole, pyroxene

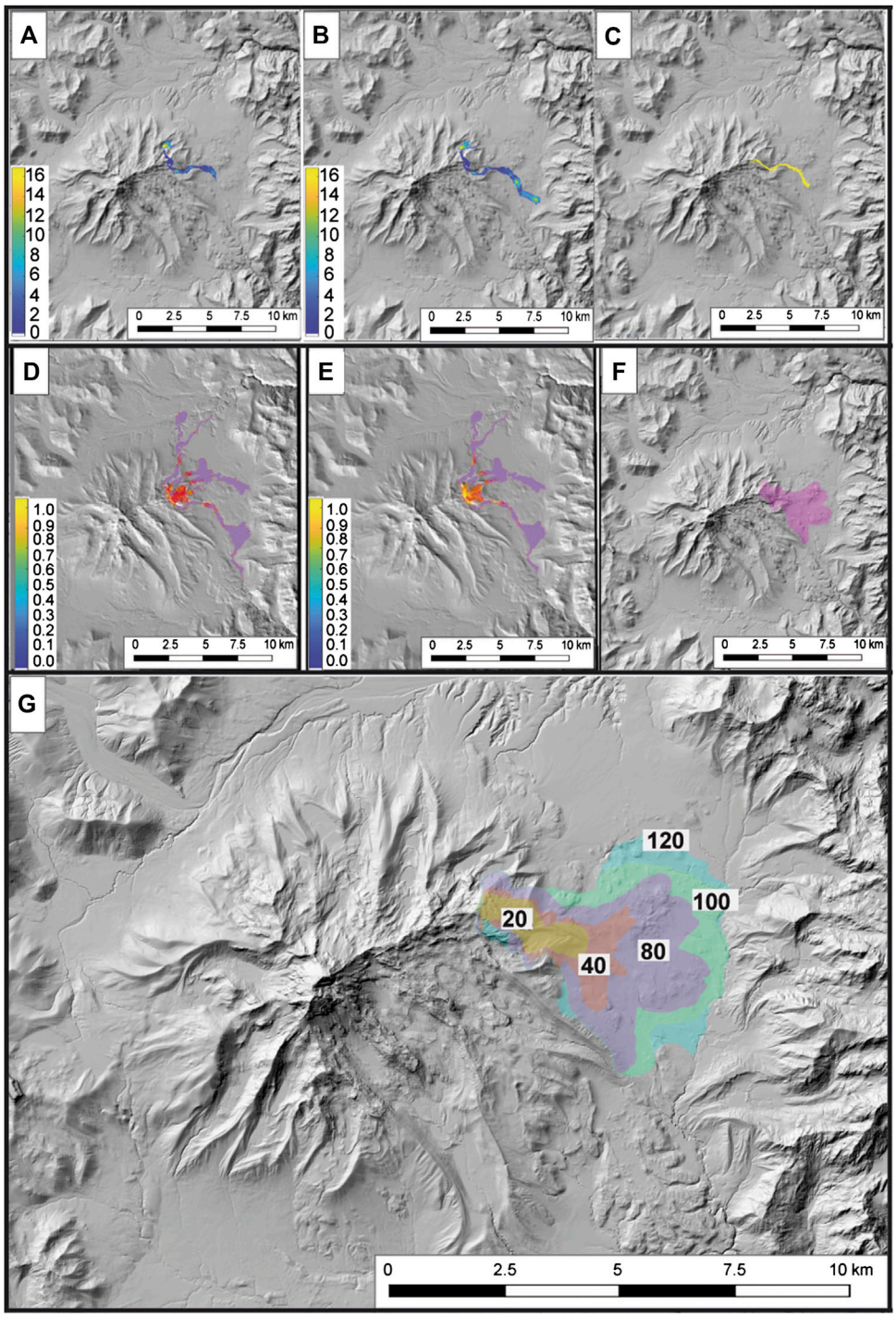

FIGURE 13 | Upper Panel **(A–C)**: Numerical results from modeling 10 million cubic meters for emplacement of a gravitational flow breccia. **(A)** Scenario I in VolcFlow, **(B)** Scenario II in VolcFlow; color bar represents thickness of deposit in meters. **(C)** *LaharZ/PFz* results (*LaharZ/PFz* does not provide thickness quantitative results). Middle Panel **(D–F)**: Numerical results from modeling a volume of 80 million cubic meters for emplacement of a breccia. **(D)** Scenario I in VolcFlow, **(E)** Scenario II in VolcFlow; **(F)** *LaharZ/PFz* results (*LaharZ/PFz* does not provide thickness quantitative results). Bottom Panel: **(G)** Nested inundation areas for 20–120 Mm^3 volumes, respectively, for emplacement of the breccia, modeled with *LaharZ/PFz*.

and metal oxide phenocrysts in a very fine ground mass composed of plagioclase, pyroxene and oxide mineral microlites (**Figure 12**). The phenocrysts present in both samples are of very similar size, shape and composition. Many of the pyroxene and amphibole phenocrysts, in both samples, also show signs of alteration and breakdown. Some of the phenocrysts

display alteration and breakdown of only the crystal rims (**Figure 12D**), while others display psuedomorph textures which result from a complete breakdown of the phenocryst (e.g., De Angelis et al., 2015). In the images of higher magnification (×500), the ground mass crystals are also extremely similar between the two samples and are dominated by plagioclase microlites with a very small quantity of glass in between.

Numerical Simulation Settings and Results

The main input data for the numerical simulations was the 3 m/pix resolution DEM. The output data of *LaharZ/PFz* is the representation of the flow footprint as a raster file. On the other hand, simulations with VolcFlow provide output data such as possible volume and velocity, based on rheological inputs. The outputs from each of the flow simulations are plotted as virtual phenomena on the initial DEM (3 m/pix special resolution) which was used since it covers the entire area of the caldera, while the higher resolution 1.5 m/pix DEM covers only the majority of the hummock field on the eastern Chalupas plain (**Figure 7C**). Neither software used for the numerical simulations can use "patched" or merged DEMs with different resolutions.

Employing the new high-resolution 1.5 m/pix DEM, we first calculated the volume of the deposit of the hummocky terrain from the polygon hummock shapes (**Figures 7A,B**), the results of which provided a total volume estimate of approximately 7 million cubic meters for the 168 identified hummocks. A limiting factor of this exercise is that only the relief of each hummock rising above the East Chalupas plain was tallied to provide the vertical component value. Therefore, this calculation gives a minimal volume of the deposit volume since it cannot estimate the buried subsurface volume, nor the volume that has been eroded. The hummock field was probably affected by post-emplacement erosion and stream reworking, which removed considerable portions of material, leaving the outstanding hummocks as testimony. In order to have a starting input volume for the modeling we increased the minimum volume of the hummocks to ~10 million cubic meters which was the volume that we applied to run the initial simulations of both *LaharZ/PFz* and VolcFlow programs (**Figure 13**). Still, this first-approximation volume is grossly under-calculated since it is not taking in consideration the volume of the deposit infilling between individual hummocks. We did not estimate this volume, given the long time that has elapsed since the collapse event, the modifications to topography and the mantling by soils and grasslands, which make detailed measurements of individual hummock profiles difficult. Hypothetically, if an average thickness of 20 m for the avalanche breccia deposit is assigned to cover the entire 20 km^2 hummock area, the total calculated volume would be on the order of 4×10^8 m^3. This is a value which we cannot vouch for, but which would also have suffered erosion and is about 40% of the actual Buenavista dome volume. Furthermore, it is unlikely that all areas of the east Chalupas plain had the same depositional thickness.

Initially, we ran the program *LaharZ/PFz* as this requires only two inputs (volume and starting point). This was a test to get initial results that would be plugged into the first simulations in VolcFlow. We summarize the two scenarios for running VolcFlow as follows with: T. represents time, T. Source is the time assigned for evacuation of mass flows from the source vent and T. Max is the duration of the flow moving over the terrain. The Cohesivity variable is the constant retarding stress (yield strength) that approximates rheological aspects of an avalanche and is also indicative of the spreading over the landscape of rock avalanches for a range of volumes (Kelfoun and Druitt, 2005).

Scenario I VolcFlow

Input parameters		References
Cohesivity	4.5 kPa	Sangay volcano, hazard map.
T. Source	3,000 s	Ordóñez et al. (2011)
T. Max	3,500 s	

Scenario II_VolcFlow

Input parameters		References
Cohesivity	5 kPa	Tungurahua volcano 2006 eruption.
T. Source	3,500 s	Kelfoun et al. (2009)
T. Max	3,500 s	

The results of running VolcFlow, applying both Scenario I and Scenario II, using different volumes, are shown in **Figures 13A,B,D,E**. The runs of *LaharZ/PFz* is shown in **Figures 13C,F,G**.

All flows reach the hummock plain, although each scenario gives slightly different, but similar results (**Figures 13A,B**). The higher cohesive value related to initial VolcFlow modeling of 10×10^6 m^3 (Scenario 1) gives a more limited reach compared to Scenario II and thickness values are on the order of 4–10 m. All flow paths, including those produced by *LaharZ/PFz*, are restricted in their lateral extent compared to the presently-observed Buenavista hummock field.

For VolcFlow results of modeling 8×10^7 m^3 we see that the flows' reach shown in **Figure 13** "d" and "e" is somewhat similar, with both scenarios taking a longer and wider path into three distinct drainages and showing very thin deposit thickness of 0.1–0.2 m. Given the considerable unknowns of the true dimensions of the hummock deposit when it was emplaced as well as the topography, we believe it is more honest and worthwhile to view our simulation exercises as forward modeling in order to understand where future flows may be directed.

Subsequently, we repeated the simulation with only *LaharZ/PFz*, incrementally increasing volumes within the range of 20–120 million cubic meters, in order to gain understanding of the extent of the inundation of future flows, should they occur at the now inactive dome (**Figure 13G**).

The results of the simulations with *LaharZ/PFz,* using 120 million cubic meters volume on the present-day landscape, take the flow out to the limit of the eastern Chalupas plain, nudging against the slopes of adjacent steep ridges and extending 7 km to the south. The modeling trace shows a reasonable association

with the perimeter of the mapped hummock field on the eastern Chalupas plain that we see today extending from Buenavista's base. It also well coincides with the densest remnant hummocky area. In sum, the mapped areas of highest concentration of hummocks are best represented by *LaharZ/PFz* simulations since they cover the full extent of the hummocky area, therefore we believe that the areal extent of the 20 km^2 hummocky zone is mostly invariable since deposition.

Hence in accordance with our fieldwork, the Buenavista hummock field as seen today is a good representative of the areal extent of the original deposit. However, the deposit thickness doubtless has experienced important variations and whatever volume is chosen will be a rough estimate. Therefore, modeling volumes based on reproducing the present extent of the deposits should be interpreted as an approximate, order-of-magnitude estimate. Our use of the 120 million m^3 volume in the modeling is defendable in general terms, as the results mantle the hummock field to its perimeter. Our results are also representative of a hypothetical new collapse of Buenavista's eastern flank using the actual topography provided by the high-resolution DEM.

Doubt is often expressed concerning remnant traces of avalanche deposits and how representative they are of when the event occurred. For the Socompa debris avalanche, researchers compared the pristinely preserved deposit (7 ka) outline of the avalanche with the modeled results (Kelfoun and Druitt, 2005); the results between the deposits on the ground and modeled results are very similar. Therefore, applying some precautions, both ground truth and modeling results can offer constraints on one another.

DISCUSSION

The VEI 7 Plinian eruption at 0.216 Ma that formed the Chalupas Ignimbrite evacuated between 100–230 km^3 of bulk volume of rhyolitic magma and provoked the collapse that formed the caldera. Then, reinjection of a more mafic magma into the magmatic reservoir formed Quilindaña stratovolcano, whose composition is andesitic to dacitic. Dyke propagation eastward of Quilindaña formed the Huahui and Buenavista vents. We identify a scar on the eastern side of Buenavista dome and observe topography on the caldera floor reminiscent of hummocky morphology generated by gravitational collapse (e.g., Crandell et al., 1984; Ui et al., 2000; Sparks et al., 2002). We suggest that the breccia deposit that comprises the hummocks is an avalanche deposit originated from a gravitational collapse on the eastern flank of Buenavista dome, resulting in a topographically well-confined 20 km^2 area covered with hummocks. This hummock field has undergone stream erosion and burial by younger ashfall layers and formation of young volcanic soils, but it has not been glaciated. The original area of hummock deposition was about 20 km^2, since broader spreading to the east was impeded by higher pre-existing topography.

From the new 1.5 m/pix DEM, created from our drone survey imagery, we determine that the hummock field has a variety of sizes and shapes. The heights of the hummocks, the steep sides on some of them, the presence of occasional large (>5 m) diameter lithic clasts that were eroded from hummock interiors and the overall lithic, non-vesicular nature of the matrix and clasts, suggest that a collapsing lava dome would be a more likely source rather than a PDC being erupted, where a more planar morphology usually results (Fruendt et al., 2000). The well-studied debris avalanche deposit laid down in December 1997 at Soufriere Volcano, Montserrat gives testimony to the chaotic nature of the interior of hummocks and the presence of megablocks which were deposited in several flow pulses during the avalanche breccia emplacement process at that volcano (Voight et al., 2002).

Through comparison of rock samples taken from Buenavista dome summit and of samples extracted from the breccia deposit within the hummock field we have shown that the origin of the deposit that forms the hummocks is most likely the Buenavista lava dome complex. The two sets of samples have the same petrological and textural characteristics (**Figure 12**). Specifically, analysis of SEM backscatter images of the collected samples show a striking similarity between the Buenavista lava dome samples and the hummock breccia deposit samples. Prevalence of similar breakdown features on amphibole and pyroxene crystals in both samples and other similarities provide significant evidence for the samples of the breccia deposit extracted from hummocks being the same as the Buenavista dome samples. These similarities therefore strongly suggest that the likely origin of the deposit that forms the hummocks was the collapse/slide of the eastern portion of Buenavista lava dome complex.

The partial collapse of the east flank of Buenavista lava dome may have been provoked by eruptive activity that involved dome growth and over steepening, leading to instability. The contribution of strong regional seismic activity could also have played a triggering role, since there is an active, shallow seismic source 30 km to the south which typically generates 6.5–7.0 M_w magnitude shallow (<15 km depth) earthquakes every couple hundred years (Beauval et al., 2013). This seismic activity has offset LGM moraines in the earthquake source area where the main strike-slip fault (Puna-Pallatanga-Cosanga-Chingual) passes through them.

Following the lava dome collapse, more explosive events likely occurred, generating small PDCs and this activity is represented by overcapping co-ignimbritic fine ash layer which has scarce vesicular pumiceous components as well as lithics from the Buenavista dome. However, there is no evidence of thick, massive PDC deposits at any of the studied outcrops.

We attribute the two lithic-rich/tephra layers (A and B) to eruptions that occurred after the collapse event and whose mineralogy corresponds to that of the breccia deposit in the hummocks. These tephra/lithic layers are younger than 44 ky BP, based on our stratigraphic investigations and radiometric dating and indicate rejuvenation of Buenavista dome. As such they represent the latest eruptive activity recognized at Chalupas Caldera involving magma from the Chalupas system. This is an important result, because dates of younger eruptive activity at Chalupas did not exist until now. The deposit of the Buenavista collapse event is not dated, but we hypothesize that it occurred before deposition of the tephra layers A and B. This assertion is

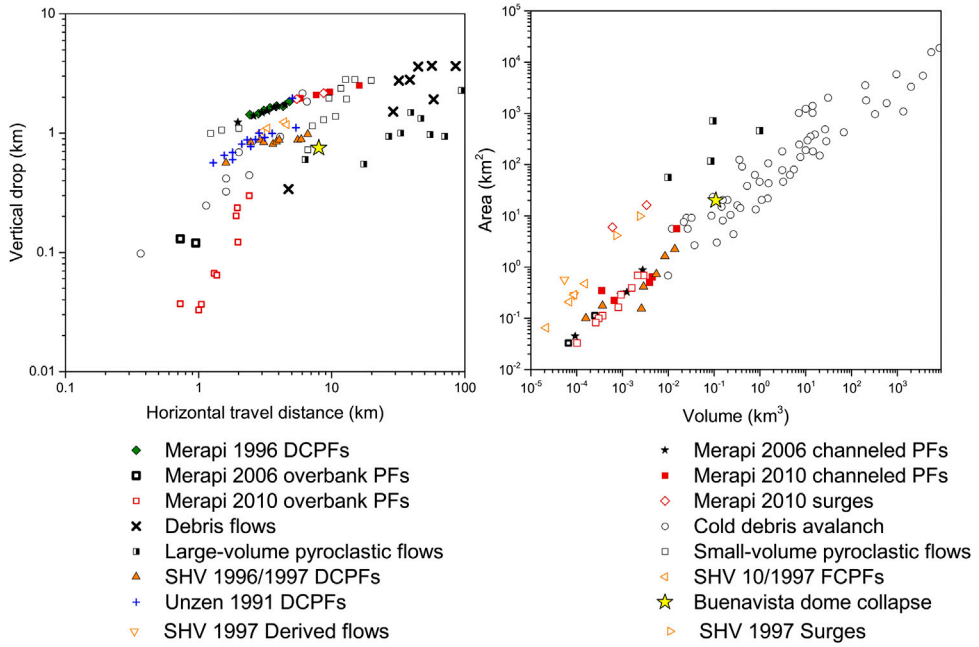

FIGURE 14 | Comparison between various types of flows of dome collapse origin (DCPFs), PFs, debris flows, and cold debris avalanche deposits (from Merapi volcano, Unzen volcano, Soufriere Hills volcano (SHV) and others) with regard to vertical drop over horizontal distance traveled (H/L), and Area (km^2) vs Volume (km^3). Buenavista data are represented with a yellow star, and are located within spaces represented by dome collapse block and ash flows, small-volume pyroclastic flows and cold debris avalanches. Modified from Charbonnier et al. (2013).

based on the presence of the dated tephra layer, CHL-MC-29 (43,620 ± 710 years BP) shown in **Figure 9**, photo B. Immediately beneath the dated tephra is a 5-m-thick fine–grained lithic ash and lacustrine sequence, which is indicative of fine materials being deposited in the local drainage for some time (months to years) in order to accumulate the fine ash lacustrine layers. We hypothesize that the fine lithic ashfall layers that also comprise the section are products of Buenavista lava dome activity. While interbedded layers of pumicious and obsidian shard-rich ash are likely a product of Cotopaxi eruptions.

The vertical drop (km) (H) (0.750 km) from the surmised highest point of the Buenavista collapse initiation to the horizontal distance that the flow traveled (L) (7,000 m) yields an H/L = 0.017. Block and ash flows from dome collapse at Soufriere Hills volcano had an H/L = 0.22 (Voight et al., 2002) and Unzen volcano is associated with H/L = 0.10 (Yamamoto et al., 1993). See also, Ogburn, (2012), for a comprehensive listing of mass flow data and earlier work by Hayashi and Self, (1992). By comparing deposit area to volume (using the 20 km^2 area of the mapped hummock field and the 120 Mm^3 volume derived from the *LaharZ/PFz* modeling), our Buenavista data fall in the category of a cold debris avalanche and also bear similarity to a block-and-ash flow from a lava dome collapse (**Figure 14**, see also Charbonnier et al., 2013). Nevertheless, it is noted that the volume estimate remains uncertain, as the basal topography over which the flow propagated is unknown. The estimate corresponds with simulations that mantle 90% of the hummock area but it can be considered a minimum value, since deposit thickness is highly variable. As observed by Carrasco-Nuñez (1999), the main driving force to obtain far-reaching emplacement of block-and-ash deposits at Citlaltépetl volcano (eastern Mexico) was gravitational collapse and not strong explosivity. We envision a similar situation for Buenavista, where a growing dome became progressively unstable on its eastern limb, and gravitational collapse may have happened successively, perhaps accompanied by some explosivity, but not enough to produce abundant vesicle-rich pyroclastic flows. Perhaps the hummocky nature of the resultant topography on the east Chalupas plain witnesses the contribution of a combination of components of a cold-avalanche and block-and-ash breccias, then later undergoing stream erosion.

Modeling the Buenavista collapse event helped us to appreciate the possible routes that the breccia flows may have taken to deposit the hummocks on the eastern plain and to envision where they might propagate in the future, should Buenavista dome reactivate. Essentially, evidence suggests that the flow propagated east to southeast, where it now outcrops, as our geological field investigations have found. Comparing simulations showed that the rheological parameter, represented by the yield strength values plugged into VolcFlow, can be an important input when trying to simulate the dispersion of dome collapse deposits. The VolcFlow results showed the mass flow heading down three drainages, more than what we can account for in our field mapping. Also this modeling did not show a good replication of the hummock field in the area of highest concentration of hummocks. This shortcoming could be the outcome of not applying an appropriate value for the cohesivity (constant retarding stress) variable

Results of running the *LaharZ/PFz* program covered the majority (~90%) of the area now occupied by the mapped hummock field on the eastern Chalupas plain, satisfactorily representing the final emplacement of the breccia flow on the present-day topography. We believe this is so, because the approximately 20 km^2 depositional area of the hummocks has basically remained the same, i.e., within the confines of the eastern Chalupas plain located between the massif of the dome and the high-relief structures to the east. What has undoubtedly changed is the basal topography over which the flow propagated and where it deposited its material. Using the limits of mapped hummocks is a constraint to help determine a reasonable volume for the deposit, which is the main unknown variable, since in this present study the area occupied by the hummock field has likely not changed significantly in the last 40 ky.

The starting volume of hummocks (10×10^6 m^3) that we initially estimated from the high-resolution DEM is an extreme lower limit. This first exercise led us to assume that the initial volume of hummocks was probably much greater, and that deposit modification was probably due to post-emplacement erosion, compaction, and the impossibility of incorporating all of the buried hummock portion concealed under the Chalupas plain. The modeled scenario that provided the closest approximation to replicating the deposit's footprint employed a volume of 12×10^7 m^3, and its inundation closely mantles (~90%) the mapped hummock area within the confines of the east Chalupas plain.

The remoteness of the eastern portion of the Chalupas caldera would greatly shield the local population in the Inter-Andean Valley (IAV) from strong impacts of gravitational flows should future dome collapse occur within the caldera. Tephra falls from VEI 3 to 5 eruptions would however cause impacts to buildings, public infrastructure and agricultural activities in the IAV, particularly since preferential wind direction generally directs tephra falls to this populated valley.

If there is renewed activity which could potentially include new dome growth in the future and collapse occurs, the route of the Buenavista stream takes it into the Chalupas river. This river is a principal tributary to the Jatunyacu-Napo rivers, located some 60 km downriver on the Amazonian plain. Aggradation by lithic deposits and probable secondary lahars would seriously affect many small villages built along river margins and road transport networks to these areas, located to the S and E of the provincial capital of Tena, in Napo Province. These areas have already been inundated by primary lahars born on Cotopaxi volcano (Sierra et al., 2019).

CONCLUSION

Our field mapping of hummocky terrain, sampling and radiometric dating of associated tephra layers in stream cuts, and analysis of SEM images suggest that the probable origin of hummocky terrain on the eastern plain of Chalpas caldera is a gravitational mass flow sourced from the Buenavista Dome. Stratigraphic constraints on the deposit provide a relative age for the most recent activity at Buenavista Dome, giving us insight into the youthfulness of the late stages of Chalupas activity.

Our study has shown that the last eruptive activity at Chalupas Caldera occurred about 40 ka ago and is represented by several post-collapse tephra layers, especially those named "A" and "B." Based on geochemistry, lithic componentry and the mineralogical suite of the tephra falls, the source vent likely belongs to the Buenavista dome complex. Antecedent to emission of the tephra falls was a collapse of the eastern flank of Buenavista lava dome complex. The collapse of the dome is represented by hummocky topography traceable from the eastern toe of Buenavista dome and spreading eastward upon a topographically-confined plain over a 20 km^2 area and extending southward at least 7 km. The area is basically hemmed in by older non-volcanic ridges and the parent dome. A minimal, order-of-magnitude estimate of the volume of the hummock field (120 Mm^3) is supported by numerical modeling using the present-day topography and achieving a reasonable overlay between modeling with the program *LaharZ/PFz* and the mapped limits of the hummock field on present-day topography. We believe that the basal topography has changed in the last 40 ka, but that the depositional area has experienced fewer changes.

The rocks and matrix collected from hummocks show strong similarities to samples taken from Buenavista dome. Given this similarity, the position of the hummock field at the base of the unbuttressed eastern flank of Buenavista, and visual recognition of a scar on the eastern shoulder of this dome, we believe that the most likely origin of the hummock field is a gravitational slide off of the Buenavista Dome Complex.

Comparison of the Buenavista H/L ratio and inundated area vs volume with cohorts of other volcanoes places the Buenavista breccia deposits in the categories of cold avalanche deposits and block-and-ash lava dome collapse breccia deposits (**Figure 14**). Therefore, we conclude that the provenance of the hummock field on the eastern Chalupas plain is a product of a gravitational slide off the eastern limb of Buenavista dome that occurred before 44 ky BP.

If a collapse occurred at Buenavista dome today with a volume of ~120 million m^3 or greater it would expand both eastward and southward to likely occupy the footprint left by the Buenavista event of ~40 ky. Breccia flows would also divulge into the Huahui and Chalupas rivers, and transform to secondary lahars over the 60 km distance to the Amazonian lowlands. Riverside-dwelling populations along the distal Napo river would be affected. At the moment, no geophysical indications (seismic or deformation) of unrest are detected by the instrumental monitoring carried out by the Instituto Geofísico of the Escuela Politécnica Nacional in Quito.

The modeling exercise as presented here is probably best considered as a reconnaissance-like first evaluation of potential breccia volumes to be modeled for future Buenavista dome collapse and assess which river channels would most likely be inundated by gravitational mass flows and subsequently, their possible transformation downstream to secondary lahars. On a broader scale, following lava dome collapse and regrowth cycles, river channels are often overloaded with lithic debris and the displaced water will occupy wider inundation zones, flooding the bottomlands. The aggradation of the lithic material may also infill channels and bury bridges and river-side infrastructure. These morphological changes may also occur far downstream as a result of lava dome activity, especially if it is long-lasting and voluminous.

DATA AVAILABILITY STATEMENT

The raw data supporting the conclusions of this article will be made available by the authors, without undue reservation, to any qualified researcher.

AUTHOR CONTRIBUTIONS

MC: Analysis of DEM and orthophotos, fieldwork, drone survey, computational simulations, investigation, petrography, geochemistry interpretation, writing—original draft, review and editing. PM: Investigation, conceptualization, fieldwork, stratigraphy, resources, writing—review and editing, supervision. JS: Analysis of DEM and orthophotos, fieldwork, drone survey, investigation, resources, writing—review and editing. HG: Investigation, fieldwork, drone survey, SEM analysis, resources, writing—review and editing.

FUNDING

The first phase of this project was funded by the Instituto Geofísico de la Escuela Politécnica Nacional through the project "SENPLADES- Generación de Capacidades para la Emisión de Alertas Tempranas" covering travel and logistics during fieldwork. In early 2019, the Escuela Politécnica Nacional awarded us the research project "Proyecto Semilla PIS-18-02" whose title is: *Geologic and petrological study of the eruptive products of the Chalupas Caldera*, which covered fieldwork expenses, some radiometric dates and publication costs. We kindly thank both institutions for providing financial and administrative support for this project.

ACKNOWLEDGMENTS

We thank the Instituto Geofísico of the Escuela Politécnica Nacional (IG-EPN) in Quito for logistical support and help with other intangibles. We kindly thank Lisa Hammersley for permitting us to use her extensive geochemical database from her doctoral dissertation at the University of California, Berkeley. We thank Ings. Bernardo Beate and Pedro Espin for kindly reviewing a draft of this manuscript. We would like to thank to Karim Kelfoun for providing the license of the numerical code VolcFlow, developed at the Laboratoire Magmas et Volcans, Clermont Ferrand, used for making the numerical simulations. We thank Silvia Vallejo for her help in VolcFlow modeling. And we thank USGS for their Lahar_Z open access software available on their web page. We would like to thank the project "Strengthening Resilience in Volcanic Areas" (STREVA), funded by the Natural Environment Research Council (NERC) and the Economic and Social Research Council (ESRC), (Great Britain), who provided the drone model eBee classic used to conduct this research. We thank Jorge Aguilar from the Instituto Geofísico de la Escuela Politécnica Nacional, for his continuous support in calculating the hummock volumes using his proposed script. We also thank the staff of DEMEX-EPN, particularly Ing. Evelyn Criollo, for assistance with the SEM analysis of the rock samples. The authors also especially thank Ing. Fernando Cobo, owner of Hacienda Yanahurco, and the local Chagras (Andean cowboys), for their enthusiastic help during the long days of fieldwork and horseback excursions in this beautiful caldera. Thanks to Jorge J. Anhalzer for his willingness to provide excellent photos and flying time in the caldera. Thanks to Jennifer Garrison and Ken Sims for assistance with sample processing, shared discussions and idea enrichment! Thanks to our two reviewers, and the editor Pablo Tierz, all who gave careful and demanding revisions that substantially improved our manuscript.

REFERENCES

Aguilar, J. (2013). *Cálculo del volumen de un volcán.* Quito, Ecuador: Instituto Geofísico de la Escuela Politécnica Nacional, 7.

Bablon, M., Quidelleur, X., Siani, G., Samaniego, P., Le Pennec, J.-L., Nouet, J., et al. (2020). Glass shard K-Ar dating of the Chalupas caldera major eruption: main Pleistocene stratigraphic marker of the Ecuadorian volcanic arc. *Quat. Geochronol.* 57, 101053. doi:10.1016/j.quageo.2020.101053

Baby, P., Rivadeneira, M., Barragán, R., and Christophoul, F. (2013). Thick-skinned tectonics in the oriente foreland basin of Ecuador. *Geolo. Soci., London, Spec. Publ.* 377, 59–76. doi:10.1144/SP377.1

Bachmann, O., and Bergantz, G. (2008). The magma reservoirs that feed supereruptions. *Elements.* 4, 17–21. doi:10.2113/GSELEMENTS.4.1.17

Beate, B. (1985). "El flujo piroclástico de Chalupas como causante de un desastre natural en el Cuaternario de los Andes Septentrionales del Ecuador," in *Primer simposio latinoamericano sobre desastres naturales.* Quito, Ecuador, 21–27.

Beate, B. (1989). IAVCEI – sta. Fe, New Mexico. abstract: the Chalupas ignimbrite. *N. M. Bur. Mines Mine. Resour. Bull.* 131, 18.

Beate, B., Hammersley, L., DePaolo, D., and Deino, A. (2006). La edad de la ignimbrita de Chalupas, Prov. de Cotopaxi, Ecuador, y su importancia como marcador estratigráfico. *Resúmenes Sex. J. Cienc. Tierra.* 1, 68–71.

Beauval, C., Yepes, H., Palacios, P., Segovia, M., Alvarado, A., Font, Y., et al. (20132013). An earthquake catalog for seismic hazard assessment in Ecuador. *Bull. Seismol. Soc. Am.* 103, 773–786. doi:10.1785/0120120270

Cardona, C., Pulgarín, B., Agudelo, A., Calvache, M., Ordoñez, M., and Manzo, O. (2015). Ajuste del método lahar-Z en el sector del volcán Nevado del Huila, con base en los flujos de escombros de 1994 y 2007. *Bol. Geol. Colomb.* 43, 63–74. doi:10.32685/0120-1425/boletingeo.43.2015.30

Carrasco-Núñez, G. (1999). Holocene block-and-ash flows from summit dome activity of Citlaltépetl volcano, Eastern Mexico. *J. Volcanol. Geoth. Res.* 88, 47–66. doi:10.1016/S0377-0273(98)00110-3

Charbonnier, S. J., Germa, A., Connor, C. B., Gertisser, R., Preece, K., Komorowski, J.-C., et al. (2013). Evaluation of the impact of the 2010 pyroclastic density currents at Merapi volcano from high-resolution satellite imagery, field investigations and numerical simulations. *J. Volcanol. Geoth. Res.* 261, 295–315. doi:10.1016/j.jvolgeores.2012.12.021

Clapperton, C. M. (1993). *Quaternary geology and geomorphology of South America.* Amsterdam, The Netherlands: Elsevier, 779.

Clapperton, C. M., Hall, M., Mothes, P., Hole, M. J., Still, J. W., Helmens, K. F., et al. (1997). A younger Dryas icecap in the equatorial Andes. *Quat. Res.* 47, 13–28. doi:10.1006/qres.1996.1861

Córdova, M. D. (2018). Identificación y caracterización de los últimos productos eruptivos de a fase resurgente de la Caldera de Chalupas. Quito, Ecuador: Escuela Politécnica Nacional, Vol. 133. Available at: http://bibdigital.epn.edu.ec/handle/15000/19286.

Córdova, M. D., Mothes, P. A., Hall, M. L., and Telenchana, E. (2018). "Identification and characterization of the youngest eruptive products of the Chalupas Caldera, Ecuador: an update on the caldera," in Abstract volume of the international meeting Cities on Volcanoes, 10, Naples, Italie, 682.

Crandell, D. R., Miller, C. D., Glicken, H. X., Christiansen, R. L., and Newhall, C. G. (1984). Catastrophic debris avalanche from ancestral Mount Shasta volcano, California. *Geology.* 12, 143–146. doi:10.1130/0091-7613(1984)12<143:CDAFAM>2.0.CO;2

De Angelis, S. H., Larsen, J., Coombs, M., Dunn, A., and Hayden, L. (2015). Amphibole reaction rims as a record of pre-eruptive magmatic heating: an experimental approach. *Earth Planet Sci. Lett.* 426, 235–245. doi:10.1016/j.epsl.2015.06.051

Encalada, M., and Bernard, B. (2018). "Dynamics of Cotopaxi volcano debris avalanche," in Abstract volume of the international meeting cities on volcanoes, 10, Naples, Italie, 682.

Fiorini, E., and Tibaldi, A. (2011). Quaternary tectonics in the central Interandean Valley, Ecuador: fault-propagation folds, transfer faults and the Cotopaxi Volcano. *Global Planet. Change.* 90–91, 87–103. doi:10.1016/j.gloplacha.2011.06.002

Fruendt, A., Wilson, C. F. N., and Carey, S. N. (2000). "Ignimbrites and block and ash flow deposits," in *Encyclopedia of volcanoes.* Editor H. Sigurdesson (San Diego, CA: Academic Press), 581–600.

Garrison, J. M., Davidson, J. P., Hall, M., and Mothes, P. (2011). Geochemistry and petrology of the most recent deposits from Cotopaxi volcano, NorthernVolcanic Zone, Ecuador. *J. Petrol.* 52, 1–38. doi:10.1093/petrology/egr023

Glicken, H. (1996). U.S. Geological Survey Open-File Report 96-677. Rockslide-debris Avalanche of May 18, 1980. Washington, DC: Mount St. Helens 983 Volcano, 90. Available at: https://pubs.usgs.gov/of/1996/0677/ (Accessed December 4, 2020).

Guillier, B., Chatelain, J. L., Jaillard, E., Yepes, H., Poupinet, G., and Fels, J. F. (2001). Seismological evidence on the geometry of the orogenic system in central-northern Ecuador (South America). *Geophys. Res. Lett.* 28 (19), 3749–3752. doi:10.1029/2001GL013257

Hall, M., and Mothes, P. (2008). The rhyolitic–andesitic eruptive history of Cotopaxi volcano, Ecuador. *Bull. Volcanol.* 70, 675–702. doi:10.1007/s00445-007-0161-2

Hall, M. L., Samaniego, P., Le Pennec, J.-L., and Johnson, J. B. (2008). Ecuadorian Andes volcanism: a review of Late Pliocene to present activity. *J. Volcanol. Geoth. Res.* 176, 1–6. doi:10.1016/j.jvolgeores.2008.06.012

Hammersley, L. C. (2003). Isotopic evidence for the relative roles of fractional crystallization, crustal assimilation and magma supply in the generation of large volume rhyolitic eruptions. Ph.D. Dissertation. Berkeley, (CA): University of California.

Hammersley, L., and De Paolo, D. J. (2002). "Oxygen isotope evidence for the role of crustal contamination in the evolution of the Chalupas caldera system, northern Andes, Ecuador," in AGU fall meeting, San Francisco, CA, December [abstract].

Hastenrath, S. (1981). *The glaciation of the Ecuadorian Andes.* Rotterdam, Balkema, 159.

Hayashi, J. N., and Self, S. (1992). A comparison of pyroclastic flow and debris avalanche mobility. *JGR: Solid Earth.* 97 (B6), 9063–109071. doi:10.1029/92JB00173

Heine, K., (2004). Late quaternary glaciations of Ecuador. *Dev. Quat. Sci.* 2, 165–169. doi:10.1016/S1571-0866(04)80121-0

Hidalgo, S., Gerbe, M. C., Martin, H., Samaniego, P., and Bourdon, E. (2012). Role of crustal and slab components in the northern Volcanic zone of the Andes (Ecuador) constrained by Sr–Nd–O isotopes. *Lithos.* 132 (133), 180–192. doi:10.1016/j.lithos.2011.11.019

INECEL (1983). Estudio de exploración de los recursos geotérmicos en Chalupas, Primera fase de prefactibilidad. Unpublished Technical Report, Quito Ecuador.

Iverson, R. M., Schilling, S. P., and Vallance, J. W. (1998). Objective delineation of lahar-inundation hazard zones. *GSA Bull.* 110, 972–984. doi:10.1130/0016-7606(1998)110<0972:ODOLIH>2.3.CO;2

Jackson, L. J., Horton, B. K., Beate, B. O., Bright, J., and Breecker, D. O., (2019). Testing stable isotope paleoaltimetry with quaternary volcanic glasses from the Ecuadorian Andes. *Geology.* 47, 1–4. doi:10.1130/G45861.1

Kelfoun, K., and Druitt, T. H. (2005). Numerical modeling of the emplacement of socompa rock avalanche, Chile. *J. Geophys. Res.* 110, B12202. doi:10.1029/2005JB003758

Kelfoun, K., Samaniego, P., Palacios, P., and Barba, D. (2009). Testing the suitability of frictional behaviour for pyroclastic flow simulation by comparison with a well-constrained eruption at Tungurahua volcano (Ecuador). *Bull. Volcanol.* 71, 1057–1075. doi:10.1007/s00445-009-0286-6

Lipman, P. W. (1997). Subsidence of ash-flow calderas: relation to caldera size and magma-chamber geometry. *Bull. Volcanol.* 59 (1997), 198–218.

Marrero, J. M., Vasconez, F., Espín, P., Ortiz, R., Yepes, H., García, A., et al. (2019). MDTanaliza: understanding digital elevation models when facing gravity-driven flows in a hazard assessment context. *Earth Sci. Inform.* 12, 257–274. doi:10.1007/s12145-018-0372-4

Mothes, P. A., Hall, M. L., and Janda, R. (1998). The enormous Chillos Valley Lahar: an ash-flow-generated debris flow from Cotopaxi volcano, Ecuador. *Bull. Volcanol.* 59, 233–244.

Mothes, P. A., and Hall, M. L. (2008). "Rhyolitic calderas and centers clustered within the active andesitic belt of Ecuador's eastern Cordillera," in IOP conference series: earth and environmental science. IOP Publishing, 012007.E Available at: https://iopscience.iop.org/article/10.1088/1755-1307/3/1/012007.

Nocquet, J., Villegas-Lanza, J., Chlieh, M., Mothes, P. A., Rolandone, F., Jarrin, P., et al. (2014). Motion of continental slivers and creeping subduction in the northern Andes. *Nat. Geosci.* 7, 287–291. doi:10.1038/ngeo2099

Ogburn, S. E. (2012). FlowDat: mass flow database v2.2. On Vhub. Available at: https://vhub.org/groups/massflowdatabase (Accessed December 4, 2020).

Ordoñez, J., Vallejo, S., Bustillos, J., Hall, M., Andrade, D., Hidalgo, S., et al. (2011). *Volcan Sangay, Mapa de Peligros Volcánicos Potenciales. 1:50,000.* Quito, Ecuador: Instituto Geofisico, Escuela Politécnica Nacional. Available at: https://www.igepn.edu.ec/sangay-mapa-de-peligros.

Özdemir, Y., Akkaya, İ., Oyan, V., and Kelfoun, K. (2016). A debris avalanche at Süphan stratovolcano (Turkey) and implications for hazard evaluation. *Bull. Volcanol.* 78 (2), 1–13.

Paguican, E. M. R., van Wyk de Vries, I. B., and Lagmay, I. A., (2012). Hummocks: how they form and how they evolve in rockslide-debris avalanches. *Landslides.* 11, 67–80. doi:10.1007/s10346-012-0368-y

Pérez, G. (2020). *Caracterización de las fisuras eruptivas y morfologías de los volcanes Wolf y Alcedo del Archipiélago de Galápagos: aporte a la evaluación de amenaza volcánica.* Quito, Ecuador: Escuela Politécnica Nacional. Available at: https://bibdigital.epn.edu.ec/handle/15000/20686.

Robin, C., Samaniego, P., Le Pennec, J.-L., Fornari, M., Mothes, P., and van der Plicht, J. (2010). New radiometric and petrological constraints on the evolution of the Pichincha volcanic complex (Ecuador). *Bull. Volcanol.* 72, 1109–1129. doi:10.1007/s00445-010-0389-0

Schilling, S. P. (2014). Laharz_py: GIS tools for automated mapping of lahar inundation hazard zones. US Department of the Interior, Geological Survey doi:10.3133/ofr20141073

Sierra, D., Vasconez, F., Andrade, D., Almeida, M., and Mothes, P. (2019). Historical distal lahar deposits on the remote eastern-drainage of Cotopaxi volcano, Ecuador. *J. S. Am. Earth Sci.* 95, 102251. doi:10.1016/j.jsames.2019.102251

Sparks, R. S. J., Barclay, J., Calder, E. S., Herd, R. A., Komorowski, J. C., Luckett, R. G., et al. (2002). "Generation of a debris avalanche and violent pyroclastic density current on 26 December (Boxing Day) 1997 at Soufriere Hills Volcano, Montserrat," *The eruption of Soufriere Hills volcano, Montserrat, from 1995 to 1999. Geological society, London, memoirs, 21.* (London, England: Editors T. H. Druitt and b. P. KokelaarThe Geological Society of London), 409-434. 0435-4052/02/S15 r.

Spikings, R. A., Cochrane, R., Villagomez, D., Van Der Lelij, R., Vallejo, C., Winkler, W., et al. (2015). The geological history of northwestern South America: from Pangaea to the early collision of the Caribbean large igneous province (290–75Ma). *Gondwana Res.* 27 (1), 95–139. doi:10.1016/j.gr.2014.06.004

Spikings, R. A., Winkler, W., Seward, D., and Handler, R. (2001). Along-strike variations in the thermal and tectonic response of the continental Ecuadorian Andes to the collision with heterogeneous oceanic crust. *Earth Planet Sci. Lett.* 186, 57–73. doi:10.1016/S0012-821X(01)00225-4

Stoopes, G. R., and Sheridan, M. F. (1992). Giant debris avalanches from the Colima Volcanic Complex, Mexico, Implication for long runout landslides (>100 km). *Geology.* 20, 299–302. doi:10.1130/0091-7613(1992)020<0299:GDAFTC>2.3.CO;2

Tost, M., Cronin, S. J., and Procter, J. N. (2014). Transport and emplacement mechanisms of channelized long-runout debris avalanches, Ruapehu volcano, New Zealand. *Bull. Volcanol.* 76 (12), 1–14.

Ui, T., Takarada, S., and Yosimoto, M. (2000). "Debris avalanches,"in *Encyclopedia of volcanoes.* Editor H. Sigurdsson (San Diego, CA: Academic Press), 617–626.

Vásconez, F. J., Andrade, D., and Valverde, V. (2015). The deposits of Pululahua Volcanic Complex (PVC), Ecuador: estimation of the erupted magma mass/volume. Prague, The Czech Republic. Available at: https://www.researchgate.net/publication/289994184_The_deposits_of_Pululahua_Volcanic_Complex_PVC_Ecuador_estimation_of_the_erupted_magma_massvolume (Accessed December 4, 2020).

Vallejo, C., Spikings, R. A., Horton, B. K., Luzieux, L., Romero, C., Winkler, W., et al. (2019). Late Cretaceous to Miocene stratigraphy and provenance of the coastal forearc and Western Cordillera of Ecuador: evidence for accretion of a single oceanic plateau fragment," in *Andean Tectonics.* Elsevier, 209–236.

van Wyk de Vries, B., and Davies, T. (2015). "Landslides, debris avalanches, and volcanic gravitational deformation," in *Encyclopedia of volcanoes.* Editors H. Sigurdsson, B. Houghton, S. McNutt, H. Rymer, and J. Stix, 2nd Edn. (665–684). Available at: http://dx.doi.org/10.1016/B978-0-12-385938-9.00038-9.

Voight, B., Glicken, H., Janda, R. J., and Douglas, P. M. (1981). "Catastrophic rockslide avalanche of May 18," in *The 1980 eruptions of Mount St. Helens.* Editors P. W. Lipman and D. R. Mullineaux (Washington, DC: US Geological Survey). Professional Paper, 1250, 347–377.

Voight, B., Glicken, H., Janda, R. J., and Douglass, P. M. (1983). Nature and mechanics of the Mount St Helens rockslide-avalanche of 18 May 1980. *Geotechnique.* 33, 243–273.

Voight, B., Komorowski, J.-C., Norton, G., Belousov, A., Belousova, M., Boudon, G., et al. (2002). The 26 december (boxing day) 1997 sector collapse and debris avalanche at Soufriere Hills volcano, Montserrat. London, UK: Geological Society, 21. doi:10.1144/GSL.MEM.2002.021.01.17

White, S. M., Trenkamp, R., and Kellogg, J. N. (2003). Recent crustal deformation and the earthquake cycle along the Ecuador–Colombia subduction zone. *Earth Planet Sci. Lett.* 216, 231–242. doi:10.1016/S0012-821X(03)00535-1

Widiwijayanti, C., Voight, B., Hidayat, D., and Schilling, S. P. (2009). Objective rapid delineation of areas at risk from block-and-ash pyroclastic flows and surges. *Bull. Volcanol.* 71, 687–703. doi:10.1007/s00445-008-0254-6

Yamamoto, T., Takarada, S., and Suto, S. (1993). Pyroclastic flows from the 1991 eruption of Unzen volcano. *Japan. Bull. Volcanol.* 55, 166–175. doi:10.1007/BF00301514

Yepes, H., Audin, L., Alvarado, A., Beauval, C., Aguilar, J., Font, Y., et al. (2016). A new view for the geodynamics of Ecuador: implication in seismogenic source definition and seismic hazard assessment. *Tectonics.* 35 (5), 1249–1279. doi:10.1002/2015TC003941

Conflict of Interest: The authors declare that the research was conducted in the absence of any commercial or financial relationships that could be construed as a potential conflict of interest.

frontiers in Earth Science

ORIGINAL RESEARCH
published: 16 December 2020
doi: 10.3389/feart.2020.535567

Volcanic Hazard Assessment for an Eruption Hiatus, or Post-eruption Unrest Context: Modeling Continued Dome Collapse Hazards for Soufrière Hills Volcano

Elaine T. Spiller[1], Robert L. Wolpert[2], Sarah E. Ogburn[3], Eliza S. Calder[4], James O. Berger[2], Abani K. Patra[5] and E. Bruce Pitman[6]*

[1]Department of Mathematical and Statistical Sciences, Marquette University, Milwaukee, WI, United States, [2]Department of Statistical Science, Duke University, Durham, NC, United States, [3]United States Geological Survey (USGS)/United States Agency for International Development (USAID) Volcano Disaster Assistance Program, Cascades Volcano Observatory, Vancouver, WA, United States, [4]School of Geosciences, University of Edinburgh, Edinburgh, United Kingdom, [5]Departments of Mathematics and Computer Science, and Director, Data Intensive Studies Center (DISC), Tufts University, Medford, MA, United States, [6]Department of Materials Design and Innovation, University at Buffalo, Buffalo, NY, United States

OPEN ACCESS

Edited by:
Conrad Daniel Lindholm, Norsar, Norway

Reviewed by:
Joern Lauterjung, German Research Centre for Geosciences, Germany
Hugo Delgado Granados, National Autonomous University of Mexico, Mexico

***Correspondence:**
Elaine T. Spiller
elaine.spiller@marquette.edu

Specialty section:
This article was submitted to Geohazards and Georisks, a section of the journal Frontiers in Earth Science

Received: 16 February 2020
Accepted: 21 August 2020
Published: 16 December 2020

Citation:
Spiller ET, Wolpert RL, Ogburn SE, Calder ES, Berger JO, Patra AK and Pitman EB (2020) Volcanic Hazard Assessment for an Eruption Hiatus, or Post-eruption Unrest Context: Modeling Continued Dome Collapse Hazards for Soufrière Hills Volcano. Front. Earth Sci. 8:535567. doi: 10.3389/feart.2020.535567

Effective volcanic hazard management in regions where populations live in close proximity to persistent volcanic activity involves understanding the dynamic nature of hazards, and associated risk. Emphasis until now has been placed on identification and forecasting of the escalation phase of activity, in order to provide adequate warning of what might be to come. However, understanding eruption hiatus and post-eruption unrest hazards, or how to quantify residual hazard after the end of an eruption, is also important and often key to timely post-eruption recovery. Unfortunately, in many cases when the level of activity lessens, the hazards, although reduced, do not necessarily cease altogether. This is due to both the imprecise nature of determination of the "end" of an eruptive phase as well as to the possibility that post-eruption hazardous processes may continue to occur. An example of the latter is continued dome collapse hazard from lava domes which have ceased to grow, or sector collapse of parts of volcanic edifices, including lava dome complexes. We present a new probabilistic model for forecasting pyroclastic density currents (PDCs) from lava dome collapse that takes into account the heavy-tailed distribution of the lengths of eruptive phases, the periods of quiescence, and the forecast window of interest. In the hazard analysis, we also consider probabilistic scenario models describing the flow's volume and initial direction. Further, with the use of statistical emulators, we combine these models with physics-based simulations of PDCs at Soufrière Hills Volcano to produce a series of probabilistic hazard maps for flow inundation over 5, 10, and 20 year periods. The development and application of this assessment approach is the first of its kind for the quantification of periods of diminished volcanic activity. As such, it offers evidence-based guidance for dome collapse hazards that can be used to inform decision-making around provisions of access and reoccupation in areas around volcanoes that are becoming less active over time.

Keywords: pyroclastic density current, uncertainty quantification, hazard assessment, non-stationarity, Bayesian analysis

INTRODUCTION AND MOTIVATION

The ability for communities around volcanoes to recover from volcanic unrest hinge on well-judged and timely decisions about land use, as well as access to some areas around volcanoes for reasons of work, attending personal property, and/or potential reoccupation. However, identifying and defining, as such, "the end" of an eruption is notoriously difficult (Siebert et al., 2011; Ogburn et al., 2015). Furthermore, hazard assessments that account for diminishing activity, cessation in eruptive activity and/or the establishment of new post-eruption background activity levels are hard to develop given that the processes involved are poorly understood, and are necessarily characterized by high uncertainties. To our knowledge no such hazard assessments have been carried out for any eruptions so far.

This work is motivated by the need for reassessing the hazards from the Soufrière Hills Volcano (SHV), Montserrat, given the now extended state of quiescence of the volcano since 2010.

Recent Eruptive History at Soufrière Hills Volcano

The eruption has been characterized throughout by alternating periods of active lava dome extrusion (months–years), punctuated by sequences of Vulcanian explosions (up to VEI 3) (Wadge et al., 2014b). The last phase of dome growth ended on February 11, 2010 after an explosion removed about 20% of the $248 \cdot 10^6\,m^3$ dome (Stinton et al., 2014; Cole et al., 2015). Sporadic, small dome collapse PDCs and rockfalls generated by progressive collapse of the remaining dome and crater area occurred until 2013, and have subsequently phased out almost entirely. In the period 2016–2020 there were typically less than 10 rockfalls/year. The volcanic activity therefore, as observed at the surface, has been very low since 2010. This quiescence now represents the longest pause since the 1995 eruption began. Deep but low-level residual seismicity, low level degassing and slow inflation (**Figure 1**) indicates that the volcanic system is still in a state of unrest. The causal processes for this continued unrest are hard to elucidate. Although for a while it was interpreted as representing continued pressurization of the system, it is now considered possible that current unrest is at least in part the manifestation of ongoing visco-elastic response to the initial emplacement of magma in the crust (Scientific Advisory Committee of the Montserrat Volcano Observatory, 2019).

In this work we try to address the issue of hazard assessment, specifically tuned for the current situation within this long hiatus period or potentially (still to be shown) post-eruption scenario. We focus specifically on hazards associated with lava dome collapse as these are recognized to be a key high-impact hazard that could still occur with little or no warning. We recognize that in the case of a re-start of eruptive activity, other precursory activity might be the first to manifest—such as ash venting or explosive activity. This work does not address the question of forecasting *which* events are most likely to occur, either during a continued hiatus period or after a re-start. Instead we address the question of how likely are dome collapse hazards to occur and, if so, where and when.

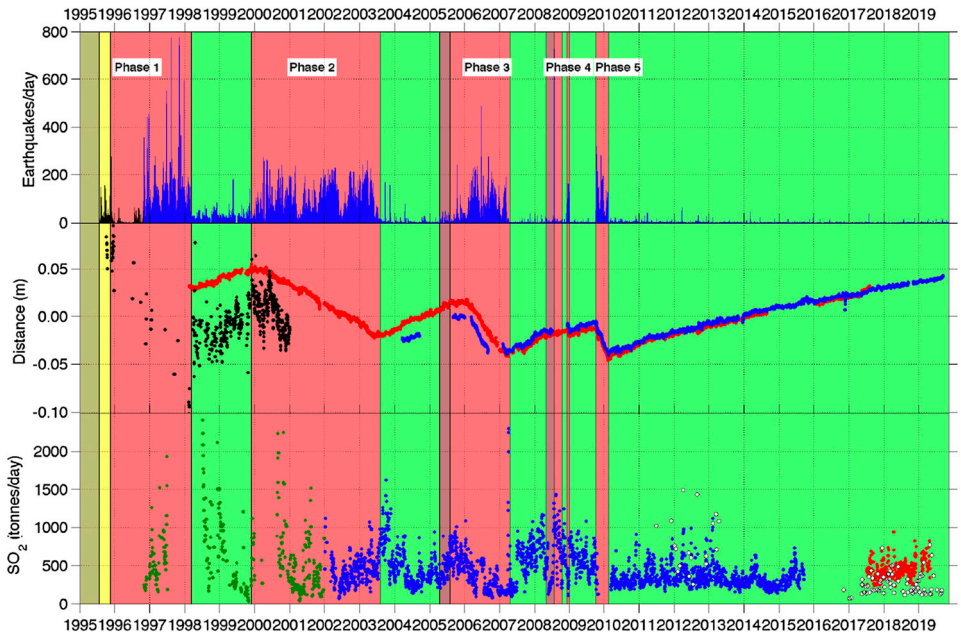

FIGURE 1 | Seismic, Global Positioning System (GPS), and SO_2 monitoring data for the period January 1, 1995–November 7, 2019. Extrusive phases and pauses are in shown red and green, respectively. Top: Number of seismic events detected by the seismic system. Middle: Radial ground displacement of continuous GPS (cGPS) stations MVO1 (red) and GERD (blue) smoothed with 7-days running mean filter, Black: GPS Height of HARR. Bottom: Measured daily SO_2 flux, filtered with 7-days running median filter. Green: Correlation Spectrometer (COSPEC), Blue: Differential Optical Absorption Spectroscopy (DOAS), White: Traverse data, Red: new DOAS network (Adapted from MVO activity report; MVO OFR 18-02-draft).

The broader rationale for this hazard assessment is provided by the following risk management questions which are currently being considered on island: **To what extent is it safe to work in, visit, or re-inhabit the flanks of the Soufrière Hills Volcano and surrounding area in the south of Montserrat?** And, in balancing the long term continued exposure (albeit now to very low levels of activity) with short-term development gains; for example, by supporting the extractive (sand mining) and tourist industries which might be key to the island's economic recovery: **To what extent are re-investments in this area possible and prudent?** Ultimately these questions are for civil protection authorities, the Government of Montserrat, and the Montserrat Volcano Observatory to consider but they also weigh on the Scientific Advisory Committee (SAC) of the UK Government's Foreign and Commonwealth Office Montserrat. It is under that auspice that this work is undertaken.

It is noted that the conditions and mechanisms for PDC generation are different now from those during the main eruptive period. During periods of active lava dome extrusion, the first-order control on PDC generation is by lava dome extrusion and associated dome instability and collapse (Calder et al., 2002). In the absence of dome growth during pauses, a long hiatus (such as the current one), or post-eruption unrest, other collapse mechanisms can come into play. Lava domes can collapse years, decades, or millennia after volcanic activity is over, triggered by bouts of intense rainfall, new seismic activity, and/or weakening by hydrothermal activity and structural instabilities (Ball et al., 2013; Harnett et al., 2019). Post-eruption collapses of lava domes, or more extensive parts of volcanic edifices are known as *sector collapses* and they generate debris avalanches. There is substantial evidence across the Lesser Antilles volcanic arc (e.g., Boudon et al., 2007; Sampler et al., 2008) and elsewhere, for the generation of modest to extensive debris avalanches sourced from collapses of lava dome complexes. At the volcano-scale these can be considered "extreme events," and as such, for any given volcano, there is little data to constrain the frequency of occurrence and anticipated time-scale post-eruption until one of these post-eruption events might occur. One can consider the different types of collapse events on a spectrum where debris avalanches represent the larger volume, lower recurrence rate collapses, and where typical dome-collapse PDCs during eruptions are the smaller volume, higher frequency events. Our consideration of "collapses" in this work, implicitly considers this spectrum of plausible scenarios.

We use the catalog of previous collapse events at SHV, and how that has changed over time, to inform our analysis. Over the course of the SHV eruption more than 900 PDCs with runout over 1 km were produced. Most PDCs were the result of dome collapse events, but column-collapse PDCs were also common. Dome-collapse PDCs show a first-order correlation with periods of dome growth as seen in **Figure 2**, and there is a known association between high dome-extrusion rates and frequent dome-collapses (Calder et al., 2002; Wadge et al., 2010). Calder et al. (2002) also noted that many larger-volume collapses were associated with periods of elevated dome extrusion, intense seismicity, and/or deformation cycles. Lava extrusion mechanically destabilizes growing domes by increasing internal shear stress, increasing loading on support structures, and by over-steepening dome structures (Calder et al., 2002; Pallister et al., 2013). High extrusion rates are also frequently associated with gas pressurization (Voight and Elsworth, 2000) and explosive activity that can cause dome-collapse events or produce column-collapse PDCs. The dominant mechanisms controlling the size and frequency of dome-collapse PDCs during dome growth thus include the volume of the dome, the extrusion rate, and associated explosive activity that can cause large, violent dome-collapse events. The collapses from this period are dominantly gravitationally induced dome collapse events, but a number of other causes contribute (Calder et al., 2002). The slope of the cumulative count of PDCs in **Figure 2** episodically steepens and shallows, reflecting intervals of higher and lower rates of PDC production associated with dome growth phases. Wolpert (2018) estimate the annual rate to range between a high level of roughly 260 events/year and a low level of about 30 events/year, based on evidence from the period 1995–2012. Including the quiescent period from 2013 to 2020 (in which no PDCs were recorded) reduces the estimated low-frequency PDC expected annual rate to roughly 17 event/year. Even this reduced rate, however, is inconsistent with the current behavior—the probability of a PDC gap of seven or more years is almost zero for a Poisson model with rate as high as 17/year. This indicates that a different model is required to explain the current hiatus in PDC activity. That is, with respect to dome collapse events, the activity levels during this extended pause is significantly quieter than that during the previous pauses. A Poisson model will still fit the data well, but the annual rate must be much lower (below 0.20/year or so) for a seven year PDC gap to be plausible. We now take this into account in our forward modeling for future collapse hazards.

The work developed here presents a defensible, evidence-based approach to PDC forecasting, in a post-eruption context, which accounts for attendant uncertainties and assesses specifically the threat posed by inundation of infrequent post-eruption-unrest flows that could affect southern Montserrat. To do so, we develop a new statistical model for forecasting the probability of post-eruption-unrest flows occurring over the next s years, for a range of possible forecast periods. The model is based on considering a very low-frequency background level of activity that is balanced with the chance that activity has already completely ceased or will cease at some point in the future (Wolpert et al., 2016). More precisely, PDC events are modeled using a homogeneous Poisson process with constant expected rate λ events per year up to an uncertain time T at which the eruption ends. The absence of observed PDC events prior to the present time t suggests that either the eruption has *already* ended, i.e., that $T < t$, or else that $T \geq t$ but the rate λ is very small. The distribution for the end-of-eruption time T is based on observations of hundreds of dome-collapse volcano histories (Wolpert et al., 2016). This is the key, and novel contribution in this work, which we believe to be the first of its kind. The model is then combined with a simulation-based strategy to assess the impact on a specific area of interest from flows corresponding to different scenarios (e.g., flow

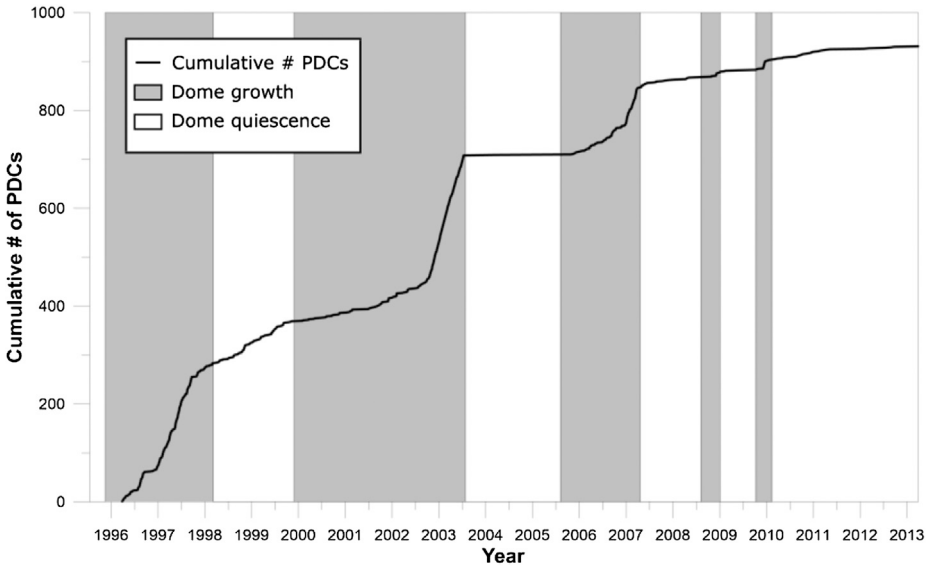

FIGURE 2 | Cumulative number of recorded, dome-collapse PDCs, beginning July 18, 1995 and ending with the last recorded PDC on March 28, 2013. Data are from FlowDat (Ogburn and Calder, 2012; Ogburn and Calder, 2017).

volume, initial direction) (Spiller et al., 2014; Bayarri et al., 2015). In its own right, the new statistical method for forecasting the probability of post-eruption flows is a potentially powerful approach that could readily be applied to other volcanoes. Likewise, the combined statistical-simulation modeling approach could be undertaken at other volcanoes and used as a tool to inform decisions about land use planning for communities situated near volcanoes prone to PDCs, during or after eruptive periods or during prolonged low-level unrest.

Post-Eruptive Pyroclastic Density Currents and Debris Avalanches

Currently, neither lava dome growth nor explosive activity has occurred at SHV since February 11, 2010, and no PDCs have been produced since 2013. However, the large lava dome remaining at the summit means that dome-collapse PDCs can still be generated. While frequency-volume statistics exist for dome-collapse PDCs during eruptions, only very sparse information exists for PDC-generating collapses of inactive lava domes (e.g., Ball et al., 2015; Harnett et al., 2019). However, collapses during low to no eruptive activity do occur, both from the collapse of still hot lava domes to produce PDCs and from collapse of unstable, older domes and volcanic flanks to produce colder debris avalanches and rockfalls.

Statistical analysis of rockfall activity at SHV led Calder et al. (2002) to suggest that, during periods of low dome extrusion or pauses in dome growth, external forces, such as extreme rainfall, seismic activity, and talus apron erosion more strongly control failure of lava domes. For example, following heavy rainfall, the July 3, 1998 dome collapse removed 20% of a $110 \cdot 10^6$ m^3 metastable dome that developed between November 1995 and February 1998, but which was no longer actively extruding (Norton et al., 2002; Elsworth et al., 2004). Shallow or intense seismic activity at SHV was shown to destabilize unconsolidated talus aprons and the dome itself *via* direct shaking of the edifice and to contribute to collapses (Calder et al., 2002).

Dome growth also contributes to the instability of adjacent hydrothermally altered volcanic edifices, which may remain unstable and prone to failure in the form of debris avalanches for decades after dome growth has ceased. Hydrothermal alteration and partial flank and talus collapse triggered the December 26, 1997 debris avalanche at SHV. Though this collapse did occur during active dome-growth, evidence suggests (Ball et al., 2013; Ball et al., 2015; Harnett et al., 2019) that dome and flank collapses caused by instability due to hydrothermal alteration pose a significant, and difficult to anticipate hazard. For example, debris avalanches of lava domes have occurred at La Soufrière, Guadeloupe (Salaün et al., 2011); Cerro Chascon-Runtu Jarita Complex, Bolivia (Watts et al., 1999); and Las Derrumbadas Dome Complex, Mexico (Capra et al., 2002).

Several mechanisms are known to generate post-eruptive PDCs and/or debris avalanches:

Rainfall-Triggered Collapses of Lava Domes

Especially heavy rainfall occurred before and during the SHV collapse of July 3, 1998 (Norton et al., 2002), and this has been recognized elsewhere as an important collapse-triggering mechanism (Mastin, 1994; Yamasato et al., 1998; Ratdomopurbo and Poupinet, 2000; Voight, 2000; Matthews et al., 2002; Barclay et al., 2006). Although rainfall-triggered collapses may also occur during active growth periods, they are likely to represent a more important forcing mechanism during

the months to years following cessation of extrusion. Barclay et al. (2006) examined rainfall and PDC data between 1998 and 2003 and found that, given a rainfall event of more than 20 mm, the probability of producing a multiple dome-collapse PDC episode increased by up to 9.2%. In fact, several of the largest dome-collapses at SHV were associated with extreme rainfall events (Matthews et al., 2002; Barclay et al., 2006).

Sector Collapse Associated With Hydrothermally Altered Systems

Lava domes and lava dome complex volcanoes, with mature hydrothermal systems are frequently associated with sector collapses (Vallance et al., 1995; Capra et al., 2002; Clavero et al., 2004). Lava dome and/or flank failures are often attributed to hydrothermally altered and weakened edifices [e.g., Mount Rainier in the United States (Reid et al., 2001); Casita volcano in Nicaragua (Opfergelt et al., 2006); and Santa María volcano (Ball et al., 2013)].

Two pertinent examples are the 1998 debris flow at Casita in Nicaragua (Sheridan et al., 1998; Voight et al., 2002; Opfergelt et al., 2006) and the 1997 debris avalanche at Soufrière Hills, Montserrat (Sparks et al., 2002; Voight et al., 2002). At Casita, an ~8 ka dacite lava dome complex, a $1.6 \cdot 10^6\,m^3$ collapse generating a debris flow on October 30, 1998 was triggered by intense rainfall associated with Hurricane Mitch, resulting in more than 2,500 fatalities (Sheridan et al., 1998; Kerle, 2002). It was found that intense hydrothermal activity had altered the rocks to smectite clays (Opfergelt et al., 2006). For the December 26, 1997 debris avalanche at Soufrière Hills Volcano, Montserrat, hydrothermal alteration of the retaining crater wall was implicated as a major contributor to the destabilization and subsequent collapse and depressurization of the lava dome (Sparks et al., 2002; Voight et al., 2002). In both these cases low-strength, low-permeability, fines-rich alteration materials were thought to have helped to concentrate water along and lubricate structural discontinuities, thereby reducing the shear strength of the rocks and ultimately leading to destabilization of the edifice (Voight et al., 2002; Opfergelt et al., 2006).

Volcanic Island Flank Collapses

Large scale flank collapses are recurring processes in the Lesser Antilles volcanic arc (Deplus et al., 2001; Le Friant et al., 2004; Boudon et al., 2007; Sampler et al., 2008). Horseshoe-shaped structures within Dominica, Saint Lucia and Martinique consistently open toward the Grenada basin. The recurrence rate of flank collapse events in the Lesser Antilles may be linked to tectonic activity, and/or magma production rate, with intervals as high as 10^4 years to several 10^5 years (Sampler et al., 2008). There have been 15 flank collapses in the last 12,000 years in the Lesser Antilles (Boudon et al., 2007). In the northern arc, the potential for future flank collapse is high. Boudon et al. (Boudon et al., 2007) stress that edifice collapse can trigger laterally directed explosions and are often associated with tsunamis (Boudon et al., 2007). The same authors state that collapse of La Soufrière, Guadeloupe, is a "highly plausible geological scenario, whose risks must be taken into account."

Downward Propagation of Cooling Fractures

At Mount St. Helens, this appeared to be the most likely mechanism that caused dome collapse-explosions in 1989–1991 that were associated with rainfall (Mastin, 1994).

Few forecasting models exist for eruption durations (Sparks and Aspinall, 2004; Wolpert et al., 2016); this in part is difficult because the definition of "end" for the catologue of long-duration eruptions is not very precise. It could refer to the end of *any* activity, such as dome collapse PDCs or post-eruption debris avalanches [which we can broadly consider as a spectrum from small to large mass flow events which can defensibly be modeled by flow simulators like TITAN2D (Patra et al., 2005)]. Likewise, as we define *level of activity* we do not distinguish among different types of collapse events, but merely focus on their average frequency or recurrence rate. As we will see, precise knowledge of the activity rate is not needed, as for any forecast window we can find the most conservative frequency (i.e., the one leading to the highest forecast probability) to find an upper bound on the probability of a collapse event whatever the actual frequency might be.

METHODOLOGY

Probabilistic hazard forecasting and analysis as we present here hinge on probabilistic modeling of aleatory scenarios, and combining those scenario models with physical models. A road block for that combination is the computational burden of exercising physical models for Monte Carlo calculations. As such, we advocate utilizing statistical emulators of computationally expensive simulators to overcome that burden, an approach that we have developed since 2009. In the section titled *Forecasting and Planning With Dynamic Probabilistic Hazard Maps*, we present a summary of our previously published statistical emulator methodology for efficient hazard calculations and walk through the process we advocate for creating probabilistic hazard maps. [Detailed descriptions of emulator-based probabilistic hazard methodology are available in Spiller et al. (2014) and Bayarri et al. (2015)]. In the section titled *Forecasting With a Chance of Ending*, we expand upon the previous approaches for the specific application to the current activity level, a protracted hiatus in eruptive activity, or a potentially post-eruption scenario. To do so, we present a new probabilistic model that balances a low-level of potential volcanic activity with the possibility that the eruptive phase has actually ended. In the section titled *Quantifying Uncertainty in Hazard Forecasts*, we describe how to quantify epistemic uncertainties associated with probabilistic (aleatoric) scenario descriptions.

As before (Spiller et al., 2014; Bayarri et al., 2015), we explore potential inundation footprints by future PDCs as modeled by TITAN2D. The TITAN2D computational environment simulates large, dry mass flows over terrain. TITAN2D solves depth-averaged mass and momentum conservation equations (Patra et al., 2005). A digital elevation model (DEM) provides a local coordinate system, yielding normal, down-slope, and

cross-slope directions. A fixed mass of material is released with sampled dissipation parameters (internal and basal friction angles). Simulations were performed on a 1 m 2010 LiDAR-based digital elevation model with a vertical resolution of 15 cm m^{-2} (Cole et al., 2010; Scientific Advisory Committee of the Montserrat Volcano Observatory, 2011) obtained from the MVO. The original DEM was smoothed to 10 m grid spacing to eliminate spurious features at high spatial frequency which can degrade the flow simulations.

FORECASTING WITH A CHANCE OF ENDING

Sparks and Aspinall (2004) fit a generalized Pareto probability distribution to data consisting of the recorded durations of a subset of 137 dome-building eruptions taken from the Smithsonian Institution Global Volcanism Program Volcanoes of the World database (Simkin and Siebert, 1994) (note that all the distributions used in this work are described in Appendix 1). In this model the probability that the duration τ of an eruption exceeds any time $t > 0$ is given by

$$\mathrm{P}[\tau > t] = \left(1 + t/\beta\right)^{-\alpha} \quad (1)$$

for some constants $\alpha > 0$ and $\beta > 0$, to be estimated from the data (we used maximum likelihood methods to estimate $\alpha \approx 0.58$ and $\beta \approx 0.60$ years). Wolpert et al. (2016) applied an extension of that model to a more recent collection of 177 dome-building eruptions taken from the DomeHaz database (Ogburn et al., 2012; Ogburn et al., 2015); in this extension, the parameters α, β (and hence the survival distribution) may depend on the magma composition. (Note, data used to fit this model and extension, including estimation of α and β, is available within (Wolpert et al., 2016).) This led in Wolpert et al. (2016) to a median forecast of 35–47 years of additional activity at SHV, under the explicit assumption of stationarity—i.e., assuming that by 2016 the volcano remained in the same active state it had begun in 1995. The present work is intended to remove that assumption, and make forecasts of future activity that reflect the likely possibility that the eruption has already subsided, or will soon do so.

Wolpert (2018) constructed and fit a dynamic model for volcanic activity in which the activity level λ (measured in expected PDCs per year) and preferred (i.e., most likely) direction could change over time. The best fit activity level function alternated between two values: a high activity of $\lambda_{\mathrm{hi}} = 261.3$ events/year, and a low level of $\lambda_{\mathrm{lo}} = 30.9$ events/year (see slope of **Figure 2**).

During the seven-year period from March 2013 through March 2020 there have been no PDC events large enough to be reflected in these models (the threshold was a volume of $0.15 \cdot 10^6\ \mathrm{m}^3$). The probability that a volcano remaining active at a rate as high as $\lambda \geq \lambda_{\mathrm{lo}} = 30.9$ events/year would exhibit no PDC in ten years is negligible (below 10^{-100}), so it is statistically untenable that SHV has remained at the same activity level up to the present.

Two possibilities remain: that SHV remains active, but at a much lower rate λ (perhaps once in a decade, or once in a century); or that PDC generation from the 1995 eruption has ended. In this work we explore variations on those two possibilities.

Results

Three Possibilities

probability of no PDC occurring over the time frame including t years since the last recorded PDC and s years of forecast can be broken down into three cases:

(1) Eruptive activity may have ceased sometime between the last recorded PDC and time t, and hence we will see no PDCs through the forecast window.
(2) Eruptive activity may cease at some point during the forecast period, and until that time we get "lucky" that no PDC happens to occur.
(3) Eruptive activity may not cease until after the forecast window, and we get "lucky" that no PDC happens to occur during the forecast window.

We explore several cases for different activity levels, λ, and visualize the probability of PDCs occurring (or not) through a series of figures.

The thick solid lines in **Figures 3A–C** (see **Eq. 3** for their derivation) indicate the forecast probability of at least one PDC at SHV in the next s years, as a function of s, for $0 \leq s \leq 20$ years, assuming that the volcano remains active but at a much lower rate than in the decade 1995–2005: a rate of once annually in **Figure 3A**, once a decade in **Figure 3B**, and once a century in **Figure 3C**. The thin dashed and dotted lines (see figure legend) show the probability of no PDC in that same period (dashed black line), broken down into three possible cases: that the 1995 SHV eruption has already subsided (red dotted line); that it has not yet subsided, but will before s years have passed (blue dash-dot line); or that it has not yet subsided and will not during the next s years (green dashed line). Mathematical expressions for these curves are given in **Eq. 3** below. Evidently the forecast PDC probability is lower for *both* a rate as high as $\lambda \approx 1.0 \gg 0.10$, because with such a high annual rate λ it is overwhelmingly likely that a PDC would have occurred during these $t = 7$ years, unless the eruption had paused; and also for $\lambda \approx 0.01 \ll 0.10$, in which case the rate is so low that any PDC would be unlikely, even if the eruption is continuing. **Figure 4** shows that the highest possible forecast probability of a PDC in the next $s = 5$ years would be $P = 0.0947$, achieved at an annual rate of $\lambda = 0.085$, about one event per decade. Thus even without any knowledge of the rate λ, the forecast probability of a PDC at SHV in the next $s = 5$ years is bounded above by about 9.5%. Similar results are available for any forecast period s.

The Model Behind the Plots

Let us begin by measuring time starting at the onset of eruption, and take the recorded event times of PDC events with volume exceeding $0.15 \cdot 10^6\ \mathrm{m}^3$ to be $\mathrm{t} = \{t_1, \ldots, t_n\}$ with $0 \leq t_1 \leq \cdots \leq t_n$ for some positive integer n (the number of recorded PDCs), all in

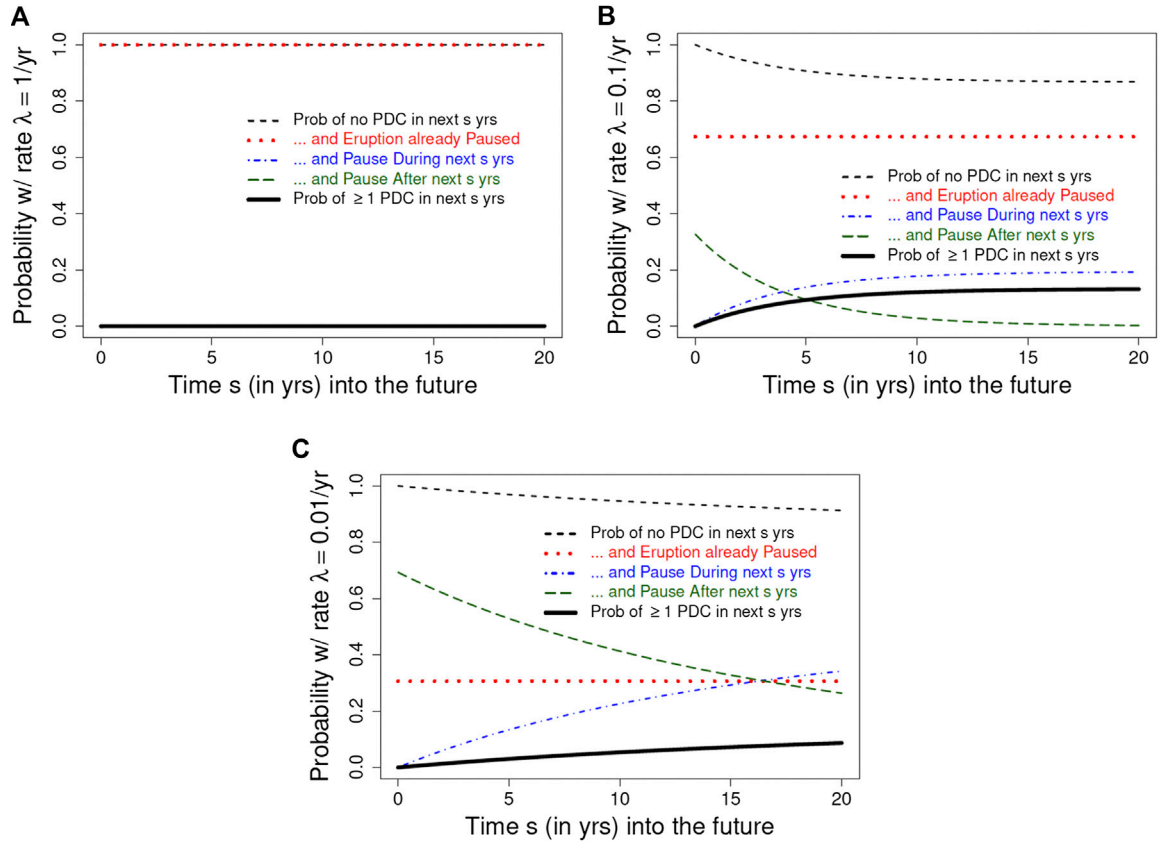

FIGURE 3 | Solid black curve shows forecast probability (nearly zero) of at least one PDC in s years, for $0 \le s \le 20$, starting $t = 7$ years after the most recent eruption. Assumed activity rates are **(A)** $\lambda = 1$ event per year, **(B)** $\lambda = 0.1$ yr^{-1} (once per decade), and **(C)** $\lambda = 0.01$ yr^{-1} (once per century), on average, until the uncertain time T the eruption ends. Thin dashed black curve shows probability of the complimentary event, zero PDCs in s years, as the sum of three parts: the probability the eruption has already paused by time t (red curve); and the probabilities that the eruption pauses during the next s years (blue dash-dot curve) or after the next s years (green dashed curve) without an intervening PDC.

the interval $[0, t]$ from the eruption onset 0 to the present time t. Our data (Ogburn and Calder, 2012; Ogburn and Calder, 2017) currently include $n = 931$ PDCs with runout of at least 1 km, ending $t = 7$ years ago. Denote by T the uncertain time of the eruption's end; necessarily $T > t_n$ but we don't know whether or not T exceeds the present time t, i.e., whether or not the eruption remains active. We suppose that PDC events arrive at a Poisson rate of $\lambda > 0$ during $(0, T]$, and zero outside that interval. Then the likelihood function for T is

$$f(T|\mathrm{t}, \lambda) \propto \lambda^n e^{-\lambda T} 1_{\{T > t_n\}}$$

(where the notation 1_E denotes the indicator function of an event E, the function that is one if E occurs—here, if $T > t_n$—and otherwise zero.) Utilizing the generalized Pareto $GPa(\alpha, \beta)$ prior distribution of (1), the posterior probability density function for T is

$$p(T|\mathrm{t}, \alpha, \beta, \lambda) = c\lambda^n e^{-\lambda T} (1 + T/\beta)^{-\alpha - 1} 1_{\{\mathrm{T} > \mathrm{t_n}\}}$$

with normalizing constant (to ensure that $p(T|\cdot)$ integrates to one, as any pdf must) given by

$$c = \beta^{-\alpha-1} \lambda^{-\alpha-n} e^{-\beta\lambda} \big/ \Gamma[-\alpha, \lambda(\beta + t_n)].$$

Here the function $\Gamma(z, x) := \int_x^\infty t^{z-1} e^{-t}\, dt$ of two variables $z \in \mathbb{R}$ and $x > 0$ denotes the incomplete Gamma function [Abramowitz and Stegun, 1964, §6.5.3]. Simplifying a little, the posterior density function for T, given $\mathrm{t} = \{t_j\}$ (the vector of observed PDC times), (α, β) (parameters of the $GPa(\alpha, \beta)$ distribution), and $\lambda > 0$ (the PDC mean annual event rate), is:

$$p(T|\mathrm{t}, \alpha, \beta, \lambda) = \frac{e^{-\lambda(\beta+T)} (1 + T/\beta)^{-\alpha-1}}{\lambda^\alpha \beta^{\alpha+1} \Gamma[-\alpha, \lambda(\beta + t_n)]} 1_{\{T > t_n\}}. \qquad (2)$$

The values of α, β are estimated in Wolpert et al. (2016) from the entire DomeHaz data set (Ogburn and Calder, 2012; Ogburn et al., 2012; Ogburn and Calder, 2017).

At any time $t > t_n$ the probability of no PDC in the next $s > 0$ years under this model, given none in $(t_n, t]$, is given by a sum of three simple integrals over different time intervals, each available in closed form:

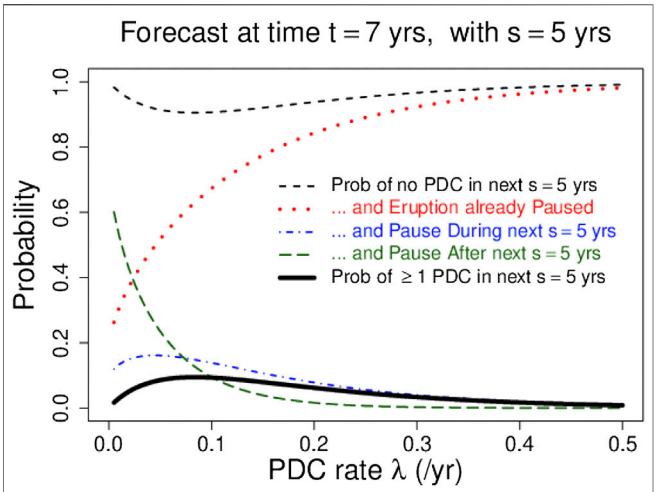

FIGURE 4 | Solid black curve shows forecast probability of at least one PDC in $s = 5$ years, starting $t = 7$ years after the most recent eruption and assuming an activity rate of λ events per year (on average) until the uncertain time T when the eruption ends, plotted for $0 \le \lambda \le 0.5$. Peak probability of $P = 0.0947$ is achieved at $\lambda = 0.085$, about one event per decade. Results are similar for other choices of s in the range $0 \le s \le 20$ years. Other curves have same meaning as in **Figure 3**.

$$\begin{aligned} &\mathrm{P}\left[\text{No PDC in first } s \text{ years after present time } t \middle| \mathrm{t}, \alpha, \beta, \lambda\right] \\ &= \int_{t_n}^{t} 1 p\left(T|\mathrm{t}, \alpha, \beta, \lambda\right) dT + \int_{t}^{t+s} e^{-\lambda(T-t)} p\left(T|\mathrm{t}, \alpha, \beta, \lambda\right) dT \\ &\quad + \int_{t+s}^{\infty} e^{-\lambda s} p\left(T|\mathrm{t}, \alpha, \beta, \lambda\right) dT, \end{aligned} \tag{3}$$

where each integrand is the product of the *conditional probability* of no PDC in s years (given the uncertain value of T) and the conditional pdf for T. The first of these three terms, shown as a red dotted curve in **Figures 3A–C**, covers the range $T \le t$, in which the eruption has completed (or paused) before the current time t (and so the conditional probability of no PDC in s years is one). The second, shown as a blue dash-dot line, covers the range $t < T \le t + s$, in which the eruption is still active at the present time t but ends before an additional s years transpire. The third, shown as a green dashed line, covers the range in which $T > t + s$, so the eruption remains active throughout the period of interest. The dashed black line shows their sum (see **Eq. 3**), the probability $S(s, t)$ of *no* PDC in the first s years after the present. Finally, the solid black line shows the probability $1 - S(s, t)$ of the complimentary event, i.e., the forecast probability of at least one PDC event in the next s years, given none in the t years since the last recorded PDC.

As time passes without additional PDCs, the forecast probability that the 1995 SHV eruption has paused or ended will rise, and the forecast probabilities of future events will fall. **Figure 5** shows the forecast probability that SHV has paused or ended as a function of the time t since the last PDC, for $7 \le t \le 20$ (note $t = 7$ in 2020). Forecast probability that the eruption has already paused or ended (shown as a dotted red curve) rises from 67% at $t = 7$ years up to 95% at $t = 20$, with the forecast probability of a PDC in the next century (solid black curve) dropping to below 2%.

FORECASTING AND PLANNING WITH DYNAMIC PROBABILISTIC HAZARD MAPS

Now that we have probabilistic forecasts of future flow events occurring at SHV, one may ask:

If a flow event happens at SHV, what locations might be affected?

It is still useful to think of this question probabilistically, as the flow scenario—flow volume, valleys affected, hot vs. cold flows etc. — are governed by aleatoric uncertainty.

Many locations surrounding SHV have not been inundated by any flows to date, or by just one or two of the several hundred on record since 1995. This does not, however, imply that these locations are immune from inundation by future flows. To study the effect of future flows we will rely on flow simulations [in this work using TITAN2D, see (Patra et al., 2005)] at scenarios consistent with activity at SHV in a probabilistic sense. That is, we can probe scenarios that have some reasonable probability of occurring and exercise TITAN2D at those scenarios to approximate which locations would be inundated by such flows. The approach taken in this work follows (Bayarri et al., 2009; Spiller et al., 2014; Bayarri et al., 2015) and for clarity we summarize important aspects of those contributions in the next subsection.

Probabilities of Pyroclastic Density Current Inundations and Emulator-Based Calculations

Bayarri et al. (2009) explored this question of potential PDC inundation under the assumption that PDC event times follow a stationary Poisson point process [Note, one can consider non-stationary models of event timing in a similar fashion, but for

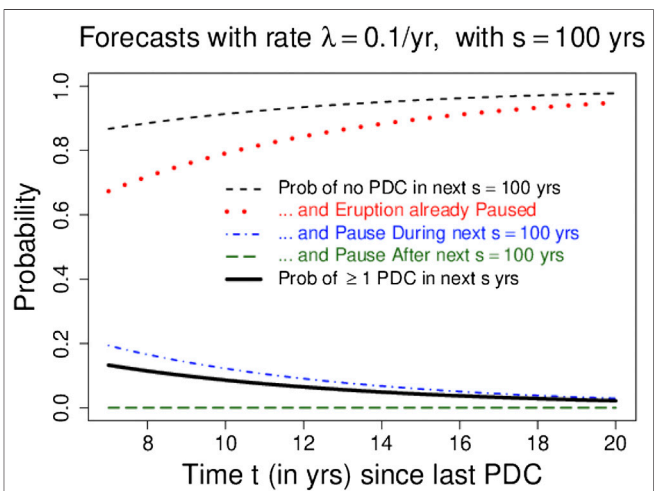

FIGURE 5 | Solid black curve shows forecast probability of at least one PDC in $s = 100$ years, assuming an activity rate of $\lambda = 0.1$ event per year, starting t years after the most recent eruption for $7 \le t \le 20$. Dotted red curve shows forecast probability that the eruption has already ended by time t, rising from 67% at $t = 7$ years (i.e., in 2020) up to 95% at $t = 20$ years.

purposes of elucidating our approach, we will follow (Bayarri et al., 2009)]. Let us further consider the case where the aleatory uncertainty in volume and initial angle is described by a probability density function (pdf), $p(V,\phi)$. (Note, we intentionally leave $p(V,\phi)$ unspecified at this point, so that we can consider different functions and explore the impacts of uncertainty in these functions). Under these assumptions, the expected number of flows in s years that inundate a specific location, $(x,y)_k$, is given by

$$\begin{aligned}&\mathrm{E}\left[\#\text{ flows that inundate } (x,y)_k|\lambda\right]\\&\quad=\lambda s\int_{(-180,180]\times\mathbb{R}_+}1_{\{h_k>h_{\mathrm{crit}}\}}\,p(V,\phi)\,dV\,d\phi\end{aligned}\tag{4}$$

where h_k is the maximum flow depth at map location $(x,y)_k$, h_{crit} is the critical threshold whose exceedance indicates "inundation," and 1_E is again the indicator function that takes on the value one if the event E occurs (here, that location $(x,y)_k$ is inundated) and otherwise zero. The probability of inundation is then given by one minus the probability that *no* flow leads to inundation at $(x,y)_k$ in s years, namely

$$\begin{aligned}&\mathrm{P}\left[\text{location } (x,y)_k \text{ is inundated over } s \text{ years}\,|\lambda\right]\\&\quad=1-\exp\left[-\lambda s\int_{(-180,180]\times\mathbb{R}_+}1_{\{h_k>h_{\mathrm{crit}}\}}\,p(V,\phi)\,dV\,d\phi\right].\end{aligned}\tag{5}$$

From a practical standpoint, evaluating the indicator function is a significant barrier to calculating **Eq. 5**. Maximum simulated flow height h_k is not available in closed form (for TITAN2D or other partial differential equation based models solved over digital elevation models), so such integrals must typically be approximated using Monte Carlo (MC) simulation. A straightforward MC simulation may require thousands to millions of unique samples and hence indicator function evaluations (e.g., $h_k(V_j,\phi_j)$ with $V_j,\phi_j\sim p(V,\phi)$). This approach is a prohibitive computational expense, as a single TITAN2D run takes O(mins–hours) on a super-computer.

To overcome this obstacle, Spiller et al. (2014) and Bayarri et al. (2015) built statistical models of the physical model of flowing mass. Specifically they fit Gaussian process (GP) emulators to TITAN2D output at each location $(x,y)_k$. This approach requires an initial set of N training runs, typically several hundred to several thousand. (Note that all map locations share this common set of N training runs, and the following approach can be applied in parallel at each location). Input values $\{\mathrm{V},\phi\}$ for these TITAN2D runs, called design points, are sampled in a space-filling manner to cover the support of any potential pdf $p(V,\phi)$. The responses, $h_k(\cdot)$ of the *design points* are collected into an $N\times 1$ response vector, y_k. Then a Gaussian process is fit to these training runs, yielding

$$\tilde{h}_k(V^*,\phi^*)\sim\mathrm{MVN}\left[\mu(V^*,\phi^*),\mathrm{R}|\mathrm{y}_k,\mathrm{V},\phi\right],$$

where MVN denotes the multivariate-normal distribution, (V^*,ϕ^*) are an untested input pair, $\mu(\cdot)$ is the mean of the GP, and R is an $N\times N$ covariance matrix for the GP at the design points. "Fitting" a GP entails finding good choices of the mean function, correlation structure, and correlation parameters; further details can be found in the references we cite (additionally, and in a more general context, (Rasmussen and Williams, 2006; Santner et al., 2018; Welch et al., 1992) provide an excellent background on this topic). It is worth mentioning that $\tilde{h}_k$ acts as an interpolator, so at all design points $\tilde{h}_k(\mathrm{V},\phi)=h_k(\mathrm{V},\phi)$. For an untested input scenario, (V^*,ϕ^*), $\tilde{h}_k(V^*,\phi^*)$ is a draw from a GP whose variance reflects the uncertainty we introduce by emulation, i.e., by taking $\tilde{h}_k(\cdot)$ as a surrogate for $h_k(\cdot)$. The benefit of utilizing this approximation in **Eq. 5** is that each indicator function evaluation in a MC sample is now a computationally "free" function evaluation available in milliseconds, instead of a O(min–hours) computation. Additionally, once the GP has been fit, no additional runs of TITAN2D are necessary.

Dynamic Probabilistic Pyroclastic Density Current Inundation Forecast Maps

To address the motivating question—of the extent to which the area surrounding the flanks of SHV in southern Montserrat could be impacted by PDC hazards—we now seek not just a probability of a PDC occurring in the next s years, but the probability of a PDC occurring that is big enough, and oriented close enough toward a specific location $(x,y)_k$, to inundate that location in the next s years. Effectively this means combining **Eqs 3 and 4**. In particular, the expected number of PDCs in s years with annual rate λ is $s\lambda$, and the expected number of PDCs in s years that lead to inundation at location $(x,y)_k$ is given by **Eq. 4**. Thus, the arguments of the exponential functions in the second and third integrals in **Eq. 3** get replaced by **Eq. 4**, and we have

$$\begin{aligned}&\mathrm{P}\left[\text{A flow inundates}\,(x,y)_k\text{ in the s years after present time } t|\mathrm{t},\alpha,\beta,\lambda\right]\\&=1-\Bigg[\int_{t_n}^{t}1p(T|\mathrm{t},\alpha,\beta,\lambda)\,dT\\&\quad+\int_{t}^{t+s}\exp\Big(-\lambda(T-t)\int_{(-180,180]\times\mathbb{R}_+}1_{\{h_k>h_{\mathrm{crit}}\}}p(V,\phi)\,dV\,d\phi\Big)\\&\quad\times p(T|\mathbf{t},\alpha,\beta,\lambda)\,dT+\int_{t+s}^{\infty}\exp\Big(-\lambda s\int_{(-180,180]\times\mathbb{R}_+}1_{\{h_k>h_{\mathrm{crit}}\}}\\&\quad\times p(V,\phi)\,dV\,d\phi\Big)p(T|\mathbf{t},\alpha,\beta,\lambda)\,dT\Bigg].\end{aligned}\tag{6}$$

We now consider various probabilistic scenarios for flow volume and initial orientation. In Wolpert (2018), motivated by the near-linearity of a log-log plot of the number of observed PDCs of volume exceeding v vs. v, we fit a Pareto probability distribution to PDC volumes at SHV, $\mathrm{V}=\{V_1,\ldots,V_n\}$ at or exceeding volume $5\cdot10^6\,\mathrm{m}^3$. We further assume that this holds for flows down to the smallest considered, $\varepsilon=0.15\cdot10^6\,\mathrm{m}^3$—a reasonable approximation, since small volume flows are only hazardous to areas very near the source. Now we consider the aleatory scenario model for the volume of flows at SHV, given by

$$p(V|\alpha_V)=\frac{\alpha_V}{\varepsilon}\left(\frac{V}{\varepsilon}\right)^{-(\alpha_V+1)}1_{\{V>\varepsilon\}}\tag{7}$$

where the uncertain "shape" parameter $\alpha_V>0$ must be estimated from the data (see below). Further, in Wolpert et al. (2018), we show that there is not strong evidence against independence for volumes and initial directions of flow events. Thus we take $p(V,\phi)=p(V)\,p(\phi)$ to be of product form and here we

consider three cases for $p(\phi)$: that flows are distributed uniformly over all possible angles; that flows are initiated exactly to the east; or that they are initiated exactly to the northwest, i.e., we take $p(\phi)$ to be uniform on $(-180, 180]$, or a point mass at 0°, or one at 135°, respectively, for angles ϕ increasing counter-clockwize from due east. These three choices represent 1) no preference for a particular collapse direction, or high uncertainty about the directionality, here represented by a uniform distribution of initial angles; 2) collapse direction and flow due east, down the Tar River Valley to the sea, which has been the dominant flow direction throughout the eruption (in part due to the substrate topography slope); and 3) collapse direction and flow toward the northwest, in order to understand the worst-case scenarios for the Belham Valley where there is proximity to population and to sand mining activities.

Note that **Eq. 6** depends on the choice of the shape parameter α_V through the Pareto probability density function. Likewise it depends on α, β, and λ from the posterior distribution of eruption duration. Although there is very little data (from SHV or other volcanoes) to constrain the low-level frequency λ, we see the maximum probability of an event occurs for $\lambda \approx 0.10$ flows per year for any combination of current time, t, and forecast length, s (see **Figure 4** for $t = 7$ years and $s = 5$ years). Thus we use $\lambda = 0.10$ flows per year for all forecasts as probabilities calculated with that value will offer a conservative bound for all forecasts even if the "true" frequency is as high as 1 flow per year or as low as 1 flow per 50 years. This leaves choices for α_V, α, and β which, respectively, have maximum likelihood estimates of $\alpha_V = 1.01$, $\alpha = 0.58$, and $\beta = 0.60$ years. One can imagine plugging these numbers into **Eq. 6**, and proceeding with a Monte Carlo simulation to estimate **Eq. 6**; this will reflect the aleatoric uncertainty associated with the randomness of volcanic processes, but not the epistemic uncertainty arising from our lack of certainty about model parameter values. Alternately, one can account for aleatoric and epistemic uncertainty in the models for T and V by treating the parameters in the associated probability distribution functions as random variables. Following the Bayesian paradigm we use probability theory to describe both kinds of uncertainty. To help distinguish them, we systematically use "$p(\cdot)$" to denote probability density functions (pdfs) describing aleatoric uncertainty associated with the inherent randomness of the governing physical processes, and "$\pi(\cdot)$" to denote pdfs describing epistemic uncertainty associated with our imperfect knowledge of model parameters describing these processes. Details of this approach are explored in the next subsection.

We create dynamic probabilistic hazard maps by repeating the calculation in **Eq. 6** for every location on the map (in the maps presented here, we do this for each point on a 200 m grid covering roughly the southern half of Montserrat). We then repeat it for different choices of angle distribution $p(\phi)$ and forecast time length s. Again, the key to making these calculations tractable is that we rely on a single initial design set of roughly 2,000 TITAN2D runs at different scenarios covering the support of $p(V, \theta)$ and build emulators for each location, e.g., $\hat{h}_k(V, \phi) \approx h_k(V, \phi)$. With these emulators in hand and by running MC simulations for **Eq. 6** at each location in parallel, the computational cost of our MC simulations is very low (roughly 1 min per map on a laptop computer).

Results

Choice of appropriate forecast timescale should be linked directly to the types of decisions that need to be made. Decisions around short-term access to sites of interest—for example, tourist access or sand mining, both of which have significant economic and livelihood implications—could be based on short-term, annual, forecasts. Such forecasts can be updated to reflect the extending time frame of relative quiescence, and should provide a defensible quantification of background hazard level for visitors. We would recommend this approach over using a longer-term forecast map in this context. Alternatively, for decisions such as investment in infrastructure and longer term development, a time scale consistent with a return on the investment might be more appropriate. In these circumstances it might be more appropriate to use 5 or even 20 years forecast maps.

Figure 6 assumes a uniform probability density function for $p(\phi)$, $t = 7$ years since the most recent PDC. The three panels show forecast snapshots in time, with $s = 1, s = 5$ and, $s = 20$ years, respectively, in panels (**A–C**). Directionality of a potential flow event is random in an aleatoric sense and should be described by a probability density function (pdf). It is a useful exercise to think about different possible probabilistic descriptions of directionality depending on available data, expert elicitation, or interest in worst-case scenarios. To that end, we have illustrated this process for three separate choices of initiation angle pdfs: uniform (**Figure 6**), east (**Figure 7**), and northwest (**Figure 8**).

Quantifying Uncertainty in Hazard Forecasts

Equation 3 presents the probability of no PDC in the next s years starting t years after the eruption onset, for a specific value of the uncertain parameter vector θ that determines the prior distribution of T (here $\theta = (\alpha, \beta)$). To reflect epistemic uncertainty in hazard forecasts, we integrate this with respect to a density function $\pi(\theta)$ governing prior uncertainty about θ, then subtract from one, to get:

$$\begin{aligned} &\mathrm{P}\left[\text{At least one PDC in first } s \text{ years after present time t}|t, \lambda\right] \\ &= 1 - \int_{\mathbb{R}_+^2} \left\{ \begin{array}{l} \displaystyle\int_{t_n}^{t} 1p\left(T|\mathrm{t}, \alpha, \beta, \lambda\right) dT \\ \displaystyle + \int_{t}^{t+s} e^{-\lambda(T-t)} p\left(T|\mathrm{t}, \alpha, \beta, \lambda\right) dT \\ \displaystyle + \int_{t+s}^{\infty} e^{-\lambda s} p\left(T|\mathrm{t}, \alpha, \beta, \lambda\right) dT \end{array} \right\} \pi(\theta)\, d\theta. \end{aligned} \tag{8}$$

Results

Here we explore the effects of epistemic uncertainty on both forecasting the probability of a PDC occurring and on the probability of a PDC inundating a particular location. **Figure 9A** shows a scatter plot of samples from $\pi(\theta)$. Using these samples in a MC simulation of **Eq. 8** yields an estimate for the probability of a future flow as a function of time, as is plotted by the pink curve in **Figure 9B**. This curve is analogous to the thick black curve in **Figure 3B**. Another approach to explore the impacts of epistemic uncertainties on forecasts is to again sample $\theta \sim \pi(\theta)$, but instead of averaging over the probabilities of a PDC corresponding to each θ (e.g., the term

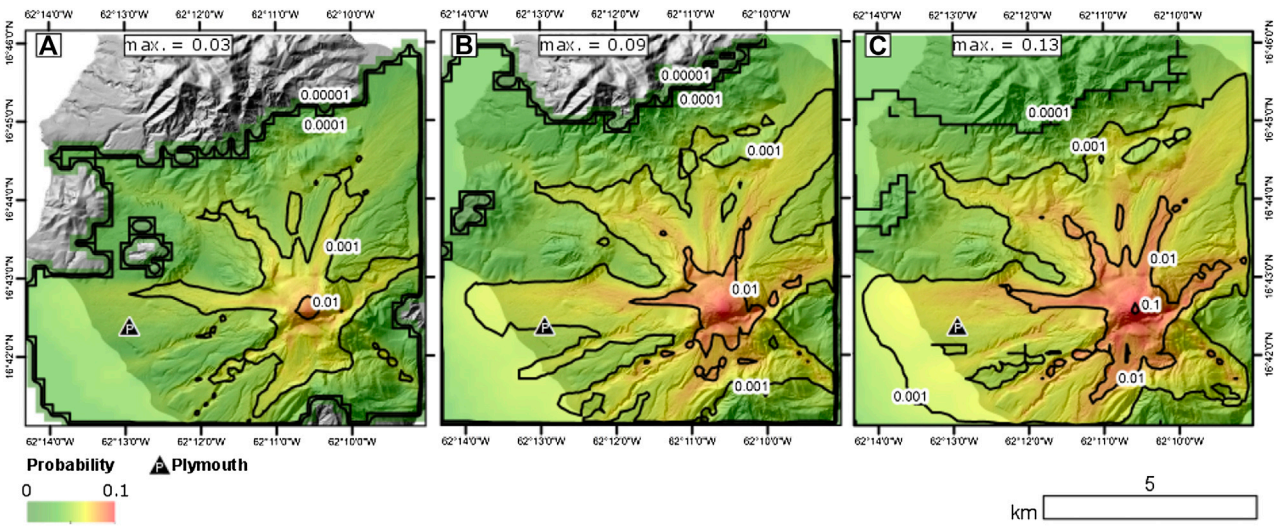

FIGURE 6 | Probability of PDC inundation forecasts plotted on a $\log_{10}$ color scale, under the assumption of a uniform distribution for $p(\phi)$ over the entire range $-180^\circ < \phi \leq 180^\circ$. Inundation probability contours are plotted for visual reference. Panel **(A)** is a forecast for s = 1 year, **(B)** for s = 5 years, and **(C)** for s = 20 years into the future. Location of Plymouth is indicated by small triangle due west of SHV.

calculated within the large brackets on the right hand side of **Eq. 8**) as one would for MC, collect those probabilities and visualize them as a histogram. To explore how these histograms of probabilities evolve in time, we calculate one for each forecast year and fit a kernel density estimate to each histogram. These posterior probabilities reflect the epistemic uncertainty in eruption duration on PDC forecasts and are plotted as a color map in **Figure 9**; the mode of this posterior is also plotted in time as a white curve. For the first five years, the spread of PDC forecasts is rather narrow and the mean of this posterior distribution lines up its mode. This behavior then transitions to a steady state forecast after about 20 years. At that point, the spread of PDC forecasts reflecting epistemic uncertainties in the duration model goes from a probability of roughly 0.06–0.16, and this posterior distribution is skewed to the left (see **Figure 9C**), resulting in slightly larger forecasts when using the posterior mode rather than when using the posterior mean.

To understand how epistemic uncertainty affects the forecast of inundation probabilities, we will focus on forecasts for the Plymouth area, take $\theta = \{\alpha, \beta, \alpha_V\}$, and integrate **Eq. 6** against $\pi(\theta)$. This approach yields:

$$\begin{aligned}
&\mathrm{P}\left[\text{A flow inundates Plymouth in the s years after present time t}\,\middle|\,\mathrm{t}, \lambda\right] \\
&= 1 - \int_{\mathbb{R}_+^3} \Bigg[\int_{t_n}^{t} 1 p(T \mid \mathrm{t}, \alpha, \beta, \lambda) dT \\
&+ \int_{t}^{t+s} \exp\Big(-\lambda (T - t) \int_{(-180,180]\times\mathbb{R}_+} 1_{\{h_k > h_{\mathrm{crit}}\}} p(V \mid \alpha_V) p(\phi) dV\, d\phi \Big) p(T \mid \mathrm{t}, \alpha, \beta, \lambda) dT \\
&+ \int_{t+s}^{\infty} \exp\Big(-\lambda s \int_{(-180,180]\times\mathbb{R}_+} 1_{\{h_k > h_{\mathrm{crit}}\}} p(V \mid \alpha_V) p(\phi) dV\, d\phi \Big) p(T \mid \mathrm{t}, \alpha, \beta, \lambda) dT \Bigg] \pi(\theta) d\theta.
\end{aligned} \tag{9}$$

Just as in the flow forecasting case, we calculate the probability of a flow inundating Plymouth by sampling $\theta \sim \pi(\theta)$, computing the probability in the bracket on the right hand side of **Eq. 9** for each sample, and averaging over those probability forecasts in a Monte Carlo simulation. This approach was followed at Plymouth and all locations on the 200 m grid of South Montserrat to produce **Figures 6–8** which account for both aleatoric and epistemic uncertainty. Location of Plymouth is indicated by small triangle, due west of SHV. Again, as in the flow forecasting case, we can calculate histograms and kernel approximations to the posterior density of inundation probabilities—these are plotted in a color map in **Figure 10C**. The mean inundation forecast posterior probability is plotted against time as a pink curve, and the mode posterior is plotted as a white curve. The mean curve gives inundation forecasts more than twice as high as those corresponding to the mode posterior curve indicating that the posterior probability distributions are strongly skewed to the right.

To explore the effect of epistemic uncertainties in the volume model vs. those in the duration model, we take $\pi(\theta)$ to be of product form $\pi(\theta) = \pi(\alpha, \beta)\pi(\alpha_V)$ and explore uncertainty in α_V. We find posterior histograms reflecting uncertain in $\pi(\alpha_V)$ by repeating the process of calculating probability histograms from samples of $\pi(\alpha_V)$, but marginalizing **Eq. 9** over $\pi(\alpha, \beta)$. The resulting marginal posterior density is plotted as a color map in **Figure 10A** along with the mode posterior for the marginal posterior in white and the mean in pink. We also look at the other case where we calculate histograms of inundation probabilities based on samples of $\pi(\alpha, \beta)$ with **Eq. 9** marginalized over $\pi(\alpha_V)$. For this case, the resulting marginal posterior is plotted as a color map in **Figure 10B** along with the corresponding mode posterior in white and the mean in pink. Note, the mean for each of the three cases is identical, but it is insightful to plot the marginalized mode posterior curves on the full inundation posterior color map. We do this with the two black dashed curves in **Figure 10C**: the upper one corresponding to the mode posterior from **10B**, and

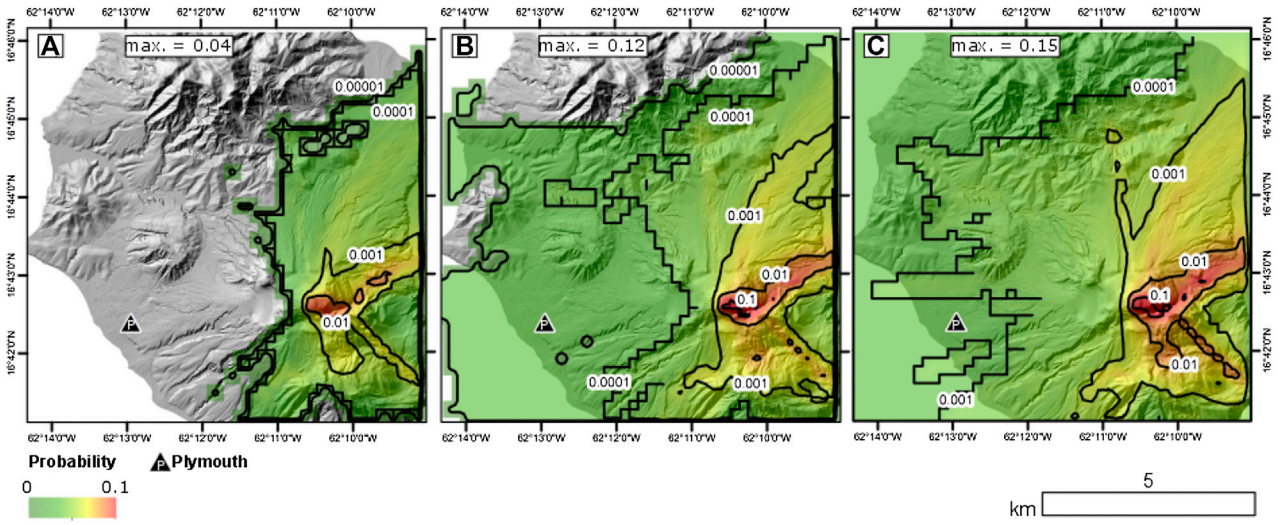

FIGURE 7 | Probability of PDC inundation forecasts plotted on a $\log_{10}$ color scale, under the assumption of a distribution for $p(\phi)$ that is a point mass at $\phi = 0°$, i.e., due east *via* the Tar River Valley to the sea. Inundation probability contours are plotted for visual reference. Panel **(A)** is a forecast for $s = 1$ year, **(B)** for $s = 5$ years, and **(C)** for $s = 20$ years into the future.

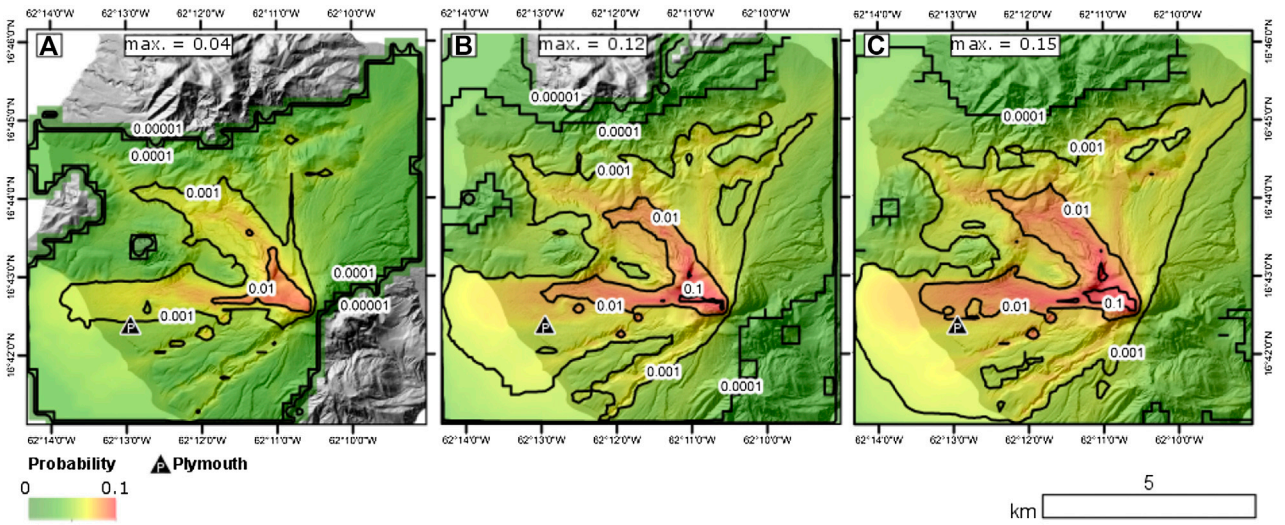

FIGURE 8 | Probability of PDC inundation forecasts plotted on a $\log_{10}$ color scale, under the assumption of a distribution for $p(\phi)$ that is a point mass at $\phi = 135°$, i.e., northwest toward the Belham Valley. Inundation probability contours are plotted for visual reference. Panel **(A)** is a forecast for $s = 1$ year, **(B)** for $s = 5$ years, and **(C)** for $s = 20$ years into the future.

the lower from **10A**. Note over the first 10 or so years, the color map of the full posterior suggests that the posterior is bimodal with a dominant lower mode corresponding to the epistemic uncertainty in the volume model $\pi(\alpha_V)$ and a secondary mode dominated by the epistemic uncertainty in the duration model $\pi(\alpha, \beta)$.

DISCUSSION

In this work, we present an evidence-based approach for probabilistic hazard assessment that combines available data on flow events from SHV, statistical modeling, and flow simulations while also accounting for attendant uncertainties. We develop and apply this methodology to assess threats posed by inundation from infrequent, possibly post-eruption unrest flows that could affect the flanks of SHV and parts of southern Montserrat. To do so, we consider a very low-frequency background level of activity that is balanced with the chance that the activity has completely ceased or will cease at some point in the future. Under these assumptions, we can forecast the probability of a post-eruption unrest flow occurring over the next s years, for a range of possible values of s. We then

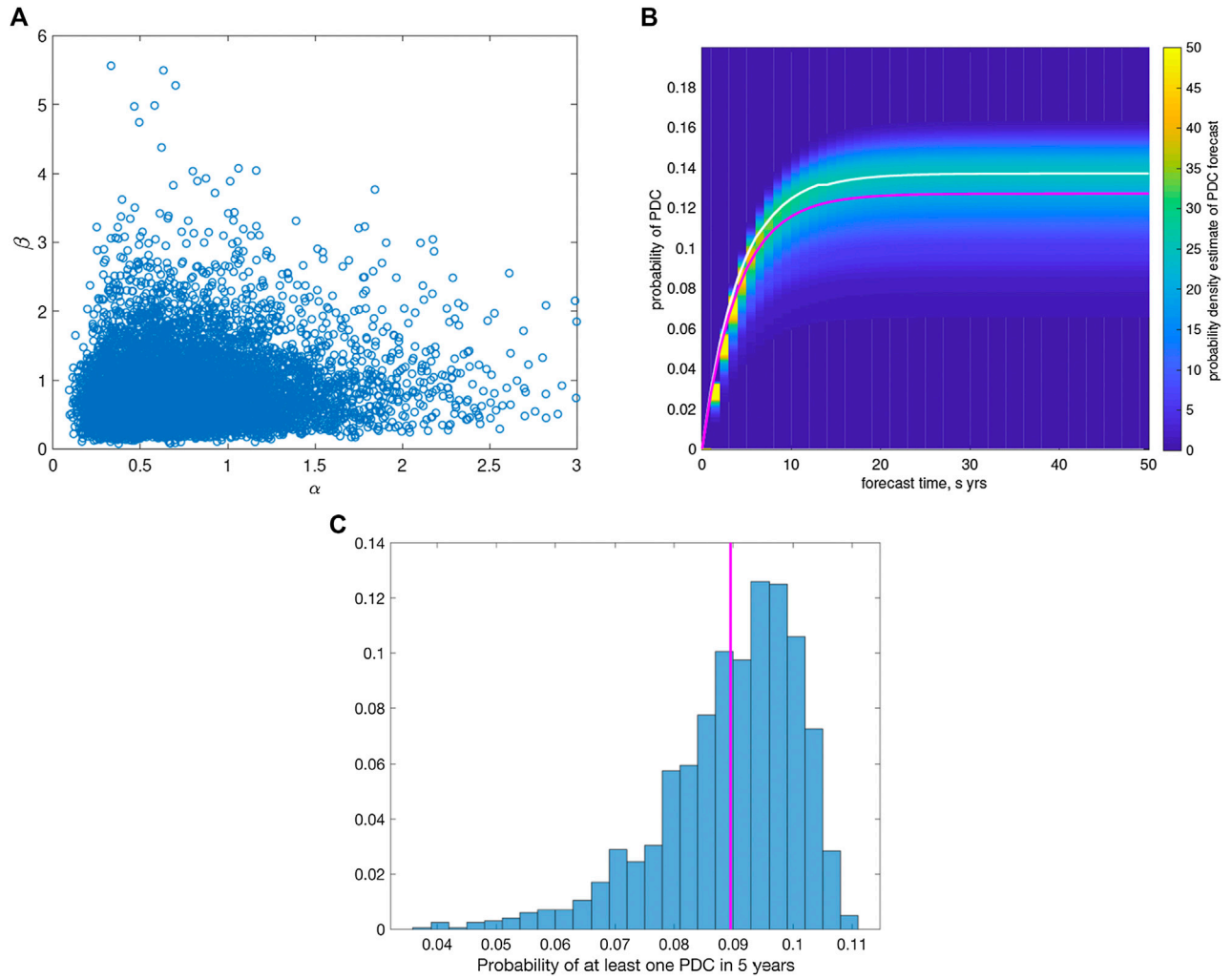

FIGURE 9 | Top Left **(A)**: a scatter plot of posterior Monte Carlo samples from $\pi(\alpha, \beta)$ reflecting uncertainty in the duration model, i.e., samples from the posterior probability distribution for T (Wolpert et al., 2016). Each sample (plotted point) of (α, β) represents a single possible shape for the duration distribution. Top Right **(B)**: Probability density function estimates (in color) of flow forecast probabilities (left axis) as they evolve in forecast time s (bottom axis). Uncertainty in these forecasts reflects uncertainty in the duration model. Bottom **(C)**: Histogram of (normalized) pdf for probability of at least one PDC in next s = 5 years, following s = 7 years of quiescence—a slice from panel **(B)** at abscissa s = 5. Note left skewness [also visible in **(B)**].

combine this model with simulation-based strategies to glean understanding about how different probabilistic scenarios (e.g., flow volume, initial direction) would impact hazard assessment at specific locations of interest on the flanks of SHV.

This work provides direct information on which relevant stakeholders and/or decision-makers could base practical decisions about managing risk including decisions about livelihoods, and to some extent reoccupation and development around the SHV Montserrat. The context for doing this is that lava domes can remain unstable, or become unstable by various mechanisms during eruptive pauses, or even post eruption. Here we assess collapse hazards related to both rare pyroclastic density currents from an inactive lava dome to debris avalanches from flank or sector collapse. Wisdom gained from other Lesser Antilles lava dome complexes indicate that such events are infrequent but are "highly plausible geological scenarios, whose risks must be taken into account" (Boudon et al., 2007). Our approach provides a means for decision-support by helping to address questions regarding the risk associated with short-term accessibility as well as long-term land-use planning, and infrastructure investments. This method is being used by MVO and SAC to determine the residual level of hazard and associated risk around the volcano and to develop a new micro-zonation hazard map for the island, but it could also be used to address questions of risk around still active volcanoes elsewhere.

Of note, the probabilities of inundation for 1 year forecast windows as determined by this method are also in line with those determined independently through the expert estimates and the expert elicitation process undertaken during SAC meetings (Scientific Advisory Committee of the Montserrat Volcano Observatory, 2011; Scientific Advisory Committee of the Montserrat Volcano Observatory, 2019). Although this cannot

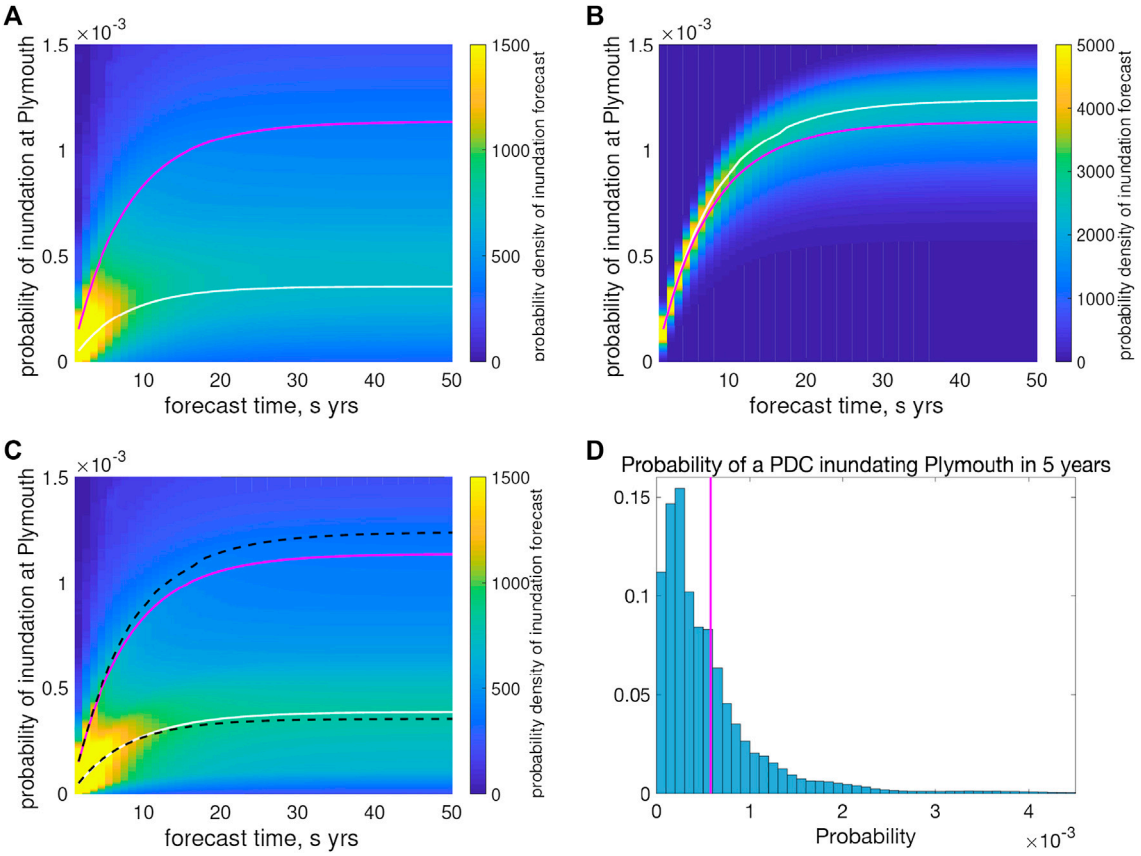

FIGURE 10 | Probability density function estimates (in color) of forecast inundation probabilities at Plymouth (left axis) as they evolve in forecast time *s* (bottom axis). In **(A)** uncertainty in these estimates reflects only uncertainty in the posterior probability distribution for the flow volume *V*. In **(B)** uncertainty in these estimates reflects only uncertainty in the posterior probability distribution for *T*, the eruption duration. In **(C)** uncertainty in these estimates reflects uncertainty in both the posterior probability distribution for the eruption duration *T* and the flow volume *V*. Evidently the dominant uncertainty is that in *V*. In all cases, the pink curve represents the mean of the probability density function estimates, and the white curves represent the mode of the mode of the posterior distribution of the inundation forecasts. In Panel **(C)** the modes from **(A)** and **(B)** are plotted as black dashed curves for reference (Note, color scales are truncated for visualization). Panel **(D)** shows histogram of posterior pdf for probability of inundation of Plymouth within next $s = 5$ years, reflecting uncertainty in both volume *V* and end-of-eruption time *T*—a slice from panel **(C)** at abscissa $s = 5$. Mean and 95% credible appear in bold on **Table 1**.

be considered a validation as the two assessment methods are so different, it is reassuring that the differing methodologies offer similar forecast probabilities.

In its own right, this new statistical method for forecasting the probability of a post-eruption-unrest flows is a potentially powerful approach that could readily be applied to other volcanoes. This model provides a robust and defensible approach for long term hazard assessment as it treats both the eruption duration and flow frequency as uncertain. The model combines a heavy-tailed duration model introduced in Wolpert et al. (2016), based on an extensive record of dome collapse PDC producing volcanoes worldwide, with a low-level background frequency of activity. Results of the model indicate that the background frequency need not be constrained or inferred by volcano or episode specific data, but instead that a conservative "worst-case" frequency can be found, and that rate only varies with the period of quiescence (t in the model) for the volcano under study and the forecast period s. For the current situation at SHV, the conservative frequency is roughly one PDC event in 10 years.

Further, with the use of statistical emulators, this low-frequency model can readily be folded into a simulation-based probabilistic hazard mapping approach as presented here. With

TABLE 1 | Numbers in the table (note division by one million on the left) are mean probabilities of inundating Plymouth within *s* years for flows with initial direction $\phi = 0^\circ$ (due east), $\phi = 135^\circ$ (northwest), or ϕ drawn uniformly from $(-180^\circ, 180^\circ)$, along with 95% posterior credible intervals. Middle column of bottom row (in bold) corresponds to the histogram shown in **Figure 10D** below, with mean $5.8 \cdot 10^{-4}$ and 95% credible interval $(3.8 \cdot 10^{-5}, 2.4 \cdot 10^{-2})$. Note intervals are asymmetric due to skewness of the distribution. Probabilities increase with interval duration *s* and are highest for flows directed NW toward Plymouth and lowest for flows directed due east down the Tar River Valley toward the sea.

Direction ϕ	**s = 1 year**		**s = 5 years**		**s = 20 years**		
East	8.6	(0.012, 62)	32	(0.044, 240)	60	(0.071, 440)	$\times 10^{-6}$
Northwest	260	(11, 1,100)	980	(43, 4,200)	1800	(80, 7,600)	
Uniform	150	(9.4, 630)	**580**	**(38, 2,400)**	1,100	(66, 4,400)	

this approach, one can efficiently develop a suite of probabilistic hazard maps under different aleatoric scenario models as there is no need for further time-consuming flow simulations. Additionally, the emulator-based strategy for developing probabilistic hazard maps allows one to explore the effect of epistemic uncertainties. Specifically, at SHV, this has allowed us to compare the uncertain "tail" effects for both the eruption duration and flow volumes, each of which follows a heavy-tailed distribution. To this end, we compared histograms of forecast probabilities whose spread occurs as a result of uncertainty in fitting those probabilistic models.

Although the probabilistic models for flow volume, as well as DEMs, are volcano specific, the general combined statistical-simulation modeling approach is entirely transferable to PDC hazard assessment at other volcanoes worldwide. It is also entirely adaptable for use and application to other geohazards (tephra, tsunamis, etc.).

CONCLUSION

In summary, we presented a new statistical model for assessing pyroclastic density current (PDC) hazards during conditions of post-eruption-unrest and have combined that with flow simulations to develop a probabilistic hazard assessment and uncertainty quantification for rare, but plausible dome and edifice collapses during periods of quiescence at Soufrière Hills Volcano (SHV), Montserrat. The primary takeaways include:

(1) We introduced a new statistical model for forecasting the probability of post-eruption flow events that is a potentially powerful approach that could readily be applied to other volcanoes.
(2) We combined multiple probabilistic models describing aleatory uncertainty with flow simulations by utilizing statistical emulators. As such, we can rapidly create probabilistic hazard maps for a number of scenarios of interest.
(3) This approach enables efficient uncertainty quantification of both aleatoric and epistemic uncertainties associated with a probabilistic hazard forecast.
(4) We focused on PDC hazard assessment over timescales of 1, 5, and 20 years at SHV. Assuming a uniform distribution of a flow's initial direction, over 1 year the probability of inundation at Plymouth is $150/10^6$. Over 5 years the probability of inundation nearly quadruples to $580/10^6$. Yet in 20 years, the probability of inundation is $1,100/10^6$—not quite double the 5 years forecast window level.
(5) This approach has the potential to be transferable to other locations, other hazards, and different times scales. Of course details—data collection, aleatoric modeling, hazard process simulations, etc.—are specific to the hazard and location, but building a flexible framework for rapid probabilistic hazard assessment utilizing statistical emulators is a compelling and widely applicable approach to hazard assessment that can help inform decision making.

DATA AVAILABILITY STATEMENT

The raw data supporting the conclusions of this article will be made available by the authors, without undue reservation, to any qualified researcher. Additionally, the data are available at the following locations: 1) DomeHaz data are available in spreadsheet snapshot format at Ogburn et al. (2012). DomeHaz: Dome-forming eruptions database v2.4 (https://vhub.org/groups/domedatabase). 2) FlowDat data are available in spreadsheet snapshot format at: Ogburn and Calder (2012). FlowDat: Mass flow database v2.2 (https://vhub.org/groups/massflowdatabase).

AUTHOR CONTRIBUTIONS

ES: overall project management, co-developer of our dynamic modeling framework, led code development efforts. RW: stochastic modeling of PDC events and eruption durations, co-developer of our dynamic modeling framework, assisted in code development. SO: volcanology and geology expertise, data acquisition and curation, figure generation. EC: motivated project; volcanology expertise, deep familiarity with SHV eruption, interaction with stakeholders (MVO). JB: statistical modeling and uncertainty quantification expertise. AP: high-performance computer expertise, co-developer of TITAN2D flow simulator. EP: granular flow expert, co-developer of TITAN2D flow simulator.

FUNDING

US National Science Foundation grants DMS-1821289-1821311-1821338, DMS-1621853-1622403-1622467, DMS-1638521, and SES-1521855 covered travel expenses, PhD student support, and some researchers' compensation. UK NRC grants EP/K032208/1 and NERC Standard Grant NE/R011001/1 covered some travel and subsistence. Duke University will contribute some Open Access publication fees through their CODA program.

ACKNOWLEDGMENTS

Any opinions, findings, and conclusions or recommendations expressed in this material are those of the authors and do not necessarily reflect the views of the NSF. ES would like to thank the Isaac Newton Institute for Mathematical Studies, Cambridge, United Kingdom, for support and hospitality during the program Mathematical and statistical challenges in landscape decision making where work on this paper was undertaken. The authors would like to thank MVO scientists, in particular Paul

Cole, Victoria Miller, and Graham Ryan, for discussions which have helped to direct this work. The authors would further like to thank the reviewers including Larry Mastin who performed a U.S. Geological Survey internal review.

REFERENCES

Abramowitz, M., and Stegun, I. A. (Editors) (1964). *Handbook of mathematical functions with formulas, graphs, and mathematical tables*, Washington, DC: National Bureau of Standards, 1046.

Ball, J. L., Calder, E. S., Hubbard, B. E., and Bernstein, M. L. (2013). An assessment of hydrothermal alteration in the Santiaguito lava dome complex, Guatemala: implications for dome collapse hazards. *Bull. Volcanol.* 75, 676. doi:10.1007/s00445-012-0676-z

Ball, J. L., Stauffer, P. H., Calder, E. S., and Valentine, G. A. (2015). The hydrothermal alteration of cooling lava domes. *Bull. Volcanol.* 77, 102. doi:10.1007/s00445-015-0986-z

Barclay, J., Johnstone, J. E., and Matthews, A. J. (2006). Meteorological monitoring of an active volcano: implications for eruption prediction. *J. Volcanol. Geoth. Res.* 150, 339–358. doi:10.1016/j.jvolgeores.2005.07.020

Bayarri, M. J., Berger, J. O., Calder, E. S., Dalbey, K., Lunagómez, S., Patra, A. K., et al. (2009). Using statistical and computer models to quantify volcanic hazards. *Technometrics* 51, 402–413. doi:10.1198/TECH.2009.08018

Bayarri, M. J., Berger, J. O., Calder, E. S., Patra, A. K., Pitman, E. B., Spiller, E. T., et al. (2015). Probabilistic quantification of hazards: a methodology using small ensembles of physics-based simulations and statistical surrogates. *Int. J. Uncertainty Quantif.* 5, 297–325. doi:10.1615/Int.J.UncertaintyQuantification.2015011451

Boudon, G., Le Friant, A., Komorowski, J.-C., Deplus, C., and Semet, M. P. (2007). Volcano flank instability in the Lesser Antilles Arc: diversity of scale, processes, and temporal recurrence. *J. Geophys. Res.* 112, B08205. doi:10.1029/2006JB004674

Calder, E. S., Luckett, R., Sparks, R. S. J., and Voight, B. (2002). Mechanisms of lava dome instability and generation of rockfalls and pyroclastic flows at Soufrière Hills Volcano, Montserrat. *Geol. Soc. London Mem.* 21, 173–190. doi:10.1144/GSL.MEM.2002.021.01.08

Capra, L., Macías, J. L., Scott, K. M., Abrams, M., and Garduño-Monroy, V. H. (2002). Debris avalanches and debris flows transformed from collapses in the Trans-Mexican Volcanic Belt, Mexico - behavior, and implications for hazard assessment. *J. Volcanol. Geoth. Res.* 113, 81–110. doi:10.1016/S0377-0273(01)00252-9

Clavero, J. E., Sparks, R. S. J., Pringle, M. S., Polanco, E., and Gardeweg, M. C. (2004). Evolution and volcanic hazards of Taapaca Volcanic Complex, Central Andes of Northern Chile. *J. Geol. Soc. London.* 161, 603–618. doi:10.1144/0016-764902-065

Cole, P. D., Bass, V. A., Christopher, T. E., Eligon, C., Murrell, C., Odbert, H. M., et al. (2010). Report No.: OFR 10-02a. Report to the scientific advisory committee on volcanic sctivity at Soufrière Hills Volcano, Montserrat: Report on activity between 28 February 2010 and 31 October 2010, 50.

Cole, P. D., Neri, A., and Baxter, P. J. (2015). "Hazards from pyroclastic density currents," in *The encyclopedia of volcanoes*. New York, NY: Elsevier, 943–956. doi:10.1016/B978-0-12-385938-9.00054-7.

Deplus, C., Le Friant, A., Boudon, G., Komorowski, J.-C., Villemant, B., Harford, C., et al. (2001). Submarine evidence for large-scale debris avalanches in the Lesser Antilles Arc. *Earth Planet Sci. Lett.* 192, 145–157. doi:10.1016/S0012-821X(01)00444-7

Druitt, T. H., and Kokelaar, B. P. (Editors) (2002). The eruption of Soufrière Hills Volcano, Montserrat from 1995 to 1999. *Geol. Soc. London Mem.* 21, 71–91, doi:10.1144/GSL.MEM.2002.021

Elsworth, D., Voight, B., Thompson, G., and Young, S. R. (2004). Thermal-hydrologic mechanism for rainfall-triggered collapse of lava domes. *Geology*. 32, 969. doi:10.1130/G20730.1.

Harnett, C. E., Thomas, M. E., Calder, E. S., Ebmeier, S. K., Telford, A., Murphy, W., et al. (2019). Presentation and analysis of a worldwide database for lava dome collapse events: the Global Archive of Dome Instabilities (GLADIS). *Bull. Volcanol.*, 81 (3), 1–17. doi:10.1007/s00445-019-1276-y

Kerle, N. (2002). Volume estimation of the 1998 flank collapse at Casita volcano, Nicaragua: a comparison of photogrammetric and conventional techniques. *Earth Surf. Process. Landforms.* 27, 759–772. doi:10.1002/esp.351

Le Friant, A., Harford, C. L., Deplus, C., Boudon, G., Sparks, R. S. J., Herd, R. A., et al. (2004). Geomorphological evolution of Montserrat (West Indies): importance of flank collapse and erosional processes. *J. Geol. Soc. London.* 161, 147–160. doi:10.1144/0016-764903-017

Mastin, L. G. (1994). Explosive tephra emissions at Mount St. Helens, 1989-1991: the violent escape of magmatic gas following storms? *Geol. Soc. Am. Bull.* 106, 175–185. doi:10.1130/0016-7606(1994)106<0175:eteams>2.3.co;2

Matthews, A. J., Barclay, J., Carn, S., Thompson, G., Alexander, J., Herd, R., et al. (2002). Rainfall-induced volcanic activity on Montserrat. *Geophys. Res. Lett.* 29, 1644. doi:10.1029/2002GL014863

Norton, G. E., Watts, R. B., Voight, B., Mattioli, G. S., Herd, R. A., Young, S. R., et al. (2002). Pyroclastic flow and explosive activity at Soufrière Hills Volcano, Montserrat, during a period of virtually no magma extrusion (March 1998 to November 1999). *Geol. Soc. London Mem.* 14, 467–481. doi:10.1144/GSL.MEM.2002.021.01.21

Ogburn, S. E., and Calder, E. S. (2012). FlowDat–Mass flow database. Available at: https://vhub.org/groups/massflowdatabase.

Ogburn, S. E., and Calder, E. S. (2017). The relative effectiveness of empirical and physical models for simulating the dense undercurrent of pyroclastic flows under different emplacement conditions. *Front. Earth Sci.* 5, 83. doi:10.3389/feart.2017.00083

Ogburn, S. E., Loughlin, S. C., and Calder, E. S. (2015). The association of lava dome growth with major explosive activity (VEI ≥ 4): DomeHaz, a global dataset. *Bull. Volcanol.* 77, 40. doi:10.1007/s00445-015-0919-x

Ogburn, S. E., Loughlin, S. C., and Calder, E. S. (2012). DomeHaz: Dome-forming eruptions database. Available at: https://vhub.org/groups/domedatabase.

Opfergelt, S., Delmelle, P., Boivin, P., and Delvaux, B. (2006). The 1998 debris avalanche at Casita volcano, Nicaragua: investigation of the role of hydrothermal smectite in promoting slope instability. *Geophys. Res. Lett.* 33, L15305. doi:10.1029/2006gl026661

Pallister, J. S., Schneider, D. J., Griswold, J. P., Keeler, R. H., Burton, W. C., Noyles, C., et al. (2013). Merapi 2010 eruption-chronology and extrusion rates monitored with satellite radar and used in eruption forecasting. *J. Volcanol. Geoth. Res.* 261, 144–152. doi:10.1016/j.jvolgeores.2012.07.012

Patra, A. K., Bauer, A. C., Nichita, C. C., Pitman, E. B., Sheridan, M. F., Bursik, M., et al. (2005). Parallel adaptive numerical simulation of dry avalanches over natural terrain. *J. Volcanol. Geoth. Res.* 139 (1–2), 1–21. doi:10.1016/j.jvolgeores.2004.06.014

Rasmussen, C. E., and Williams, C. K. I. (2006). *Gaussian processes for machine learning. Adaptative computation and machine learning series*. Boston, MA: The MIT Press, 266.

Ratdomopurbo, A., and Poupinet, G. (2000). An overview of the seismicity of Merapi volcano (Java, Indonesia), 1983-1994. *J. Volcanol. Geoth. Res.* 100, 193–214. doi:10.1016/S0377-0273(00)00137-2

Reid, M. E., Sisson, T. W., and Brien, D. L. (2001). Volcano collapse promoted by hydrothermal alteration and edifice shape, Mount Rainier, Washington. *Geology* 29, 779–782. doi:10.1130/0091-7613(2001)029<0779:vcpbha>2.0.co;2

Salaün, A., Villemant, B., Gérard, M., Komorowski, J.-C., and Michel, A. (2011). Hydrothermal alteration in andesitic volcanoes: trace element redistribution in active and ancient hydrothermal systems of Guadeloupe (lesser Antilles). *J. Geochem. Explor.* 111, 59–83. doi:10.1016/j.gexplo.2011.06.004

Sampler, A., Quidelleur, X., Boudon, G., Le Friant, A., and Komorowski, J.-C. (2008). Radiometric dating of three large volume flank collapses in the lesser antilles arc. *J. Volcanol. Geoth. Res.* 176, 485–492. doi:10.1016/j.jvolgeores.2008.04.018

Santner, T. J., Williams, B. J., and Notz, W. I. (2018). *The design and analysis of computer experiments*. 2nd Edn. New York, NY: Springer-Verlag, 436, doi:10.1007/978-1-4939-8847-1

Scientific Advisory Committee of the Montserrat Volcano Observatory (2011). Assessment of the hazards and risks associated with the Soufrière Hills Volcano, Montserrat: 16th report of the scientific advisory committee on Montserrat volcanic activity. Technical report, MVO. November 14–16, 2011, Montserrat Volcano Observatory.

Scientific Advisory Committee of the Montserrat Volcano Observatory (2019). Assessment of the hazards and risks associated with the Soufrière Hills Volcano, Montserrat: 24th report of the scientific advisory committee on Montserrat volcanic activity. Technical report, MVO.

Sheridan, M. F., Bonnard, C., Carreno, R., Siebe, C., Strauch, W., Navarro, M., et al. (1998). Report on the 30 October 1998 rock fall/avalanche and breakout flow of Casita Volcano, Nicaragua, triggered by Hurricane Mitch. *Landslide News.*, 12, 2–4.

Siebert, L., Simkin, T., and Kimberly, P. (2011). *Volcanoes of the world*. 3rd Edn. Oakland, CA: University of California Press, 568.

Simkin, T., and Siebert, L. (1994). *Volcanoes of the world: a regional directory, gazetteer, and chronology of volcanism during the last 10,000 years*. 2nd Edn. Tucson, AZ: Geoscience Press, 349.

Sparks, R. S. J., and Aspinall, W. P. (2004). "Volcanic activity: frontiers and challenges in forecasting, prediction and risk assessment," in *The state of the planet: frontiers and challenges in geophysics, volume 19 of IUGG monograph*. Editors R. S. J. Sparks and C. J. Hawkesworth, New York, NY: AGU, 359–373. doi:10.1029/150GM28. Geophysical Monograph 150

Sparks, R. S. J., Barclay, J., Calder, E. S., Herd, R. A., Komorowski, J.-C., et al. (2002). Generation of a debris avalanche and violent pyroclastic density current on 26 December (Boxing Day) 1997 at Soufrière Hills Volcano, Montserrat. *Geol. Soc. London Mem.* 21, 409–434. doi:10.1144/gsl.mem.2002.021.01.18

Spiller, E. T., Bayarri, M. J., Berger, J. O., Calder, E. S., Patra, A. K., Pitman, E. B., et al. (2014). Automating emulator construction for geophysical hazard maps. *SIAM/ASA J. Uncertain. Quantif.* 2, 126–152. doi:10.1137/120899285

Stinton, A. J., Cole, P. D., Stewart, R. C., Odbert, H. M., and Smith, P. (2014). The 11 February 2010 partial dome collapse at Soufrière Hills Volcano, Montserrat. *Geol. Soc. London Mem.* 29, 133–152. doi:10.1144/M39.7

Vallance, J. W., Siebert, L., Rose, W. I., Girón, J. R., and Banks, N. G. (1995). Edifice collapse and related hazards in Guatemala. *J. Volcanol. Geoth. Res.* 66, 337–355. doi:10.1016/0377-0273(94)00076-S

Voight, B. (2000). Structural stability of andesite volcanoes and lava domes. *Philos. Trans. R. Soc. London Ser. A* 358, 1663–1703. doi:10.1098/rsta.2000.0609

Voight, B., and Elsworth, D. (2000). Instability and collapse of hazardous gas-pressurized lava domes. *Geophys. Res. Lett.* 27(1), 1–4. doi:10.1029/1999GL008389

Voight, B., Komorowski, J.-C., Norton, G. E., Belousov, A. B., Belousova, M., Boudon, G., et al. (2002). The 26 December (Boxing Day) 1997 sector collapse and debris avalanche at Soufrière Hills Volcano, Montserrat, *Geol. Soc. London Mem.* 21, 363–407. doi:10.1144/GSL.MEM.2002.021.01.17

Wadge, G., Herd, R., Ryan, G., Calder, E. S., and Komorowski, J.-C. (2010). Lava production at Soufrière Hills Volcano, Montserrat: 1995-2009. *Geophys. Res. Lett.*, 37, L00E03. doi:10.1029/2009GL041466

Wadge, G., Robertson, R. E. A., and Voight, B. (Editors) (2014a). *The eruption of Soufri`ere Hills Volcano, Montserrat from 2000 to 2010*. London, UK: Geological Society, 501.

Wadge, G., Voight, B., Cole, P. D., Loughlin, S. C., and Robertson, R. E. A. (2014b). The eruption of Soufrière Hills Volcano, Montserrat from 2000 to 2010. *Geol. Soc. London Mem.* 39, 1–40. doi:10.1144/M39.1

Watts, R. B., De Silva, S. L., Jimenez de Rios, G., and Croudace, I. (1999). Effusive eruption of viscous silicic magma triggered and driven by recharge: a case study of the Cerro Chascon-Runtu Jarita Dome Complex in Southwest Bolivia. *Bull. Volcanol.* 61, 241–264. doi:10.1007/s004450050274

Welch, W. J., Buck, R. J., Sacks, J., Wynn, H. P., Mitchell, T. J., and Morris, M. D. (1992). Screening, predicting, and computer experiments. *Technometrics* 34, 15–25. doi:10.2307/1269548

Wolpert, R. L., Ogburn, S. E., and Calder, E. S. (2016). The longevity of lava dome eruptions. *J. Geophys. Res. Solid Earth.* 121, 676–686. doi:10.1002/2015JB012435

Wolpert, R. L., Spiller, E. T., and Calder, E. S. (2018). Dynamic statistical models for pyroclastic density current generation at Soufrière Hills Volcano. *Front. Earth Sci.* 6, 55. doi:10.3389/feart.2018.00055

Yamasato, H., Kitagawa, S., and Komiya, M. (1998). Effect of rainfall on dacitic lava dome collapse at Unzen volcano, Japan. *Pap. Met. Geophys.* 48, 73–78. doi:10.2467/mripapers.48.73

Conflict of Interest: The authors declare that the research was conducted in the absence of any commercial or financial relationships that could be construed as a potential conflict of interest.

APPENDIX 1: DISTRIBUTIONS

This short appendix describes the probability distributions used in this work.

Generalized Pareto

The $\mathrm{GPa}(\alpha,\beta)$ is a continuous distribution for positive random variables T, with probability density function (pdf), survival function (or inverse cumulative distribution function (CDF)), and mean given by:

$$\begin{aligned} f(t) &= (\alpha/\beta)(1+t/\beta)^{-\alpha-1}, & t>0 \\ \overline{F}(t) &= \mathrm{P}[T>t] = (1+t/\beta)^{-\alpha}, & t>0 \\ \mathrm{E}[T] &= \begin{cases} \beta/(\alpha-1) & \text{if } \alpha>1 \\ \infty & \text{if } \alpha\le 1 \end{cases} \end{aligned}$$

for parameters $\alpha>0$, $\beta>0$. For large values of α,β these are close to those of an Exponential distribution $\mathrm{Ex}(\lambda)$ with

$$\begin{aligned} f(t) &= \lambda\exp(-\lambda t), & t>0 \\ \overline{F}(t) &= \mathrm{P}[T>t] = \exp(-\lambda t), & t>0 \\ \mathrm{E}[T] &= 1/\lambda \end{aligned}$$

with parameter $\lambda=(\alpha/\beta)$, but for modest values of α,β the Generalized Pareto has much heavier tails than the exponential—i.e., $\mathrm{P}[T>t]$ falls off much more slowly with increasing t, so very large values of T are more likely. The unitless "shape" parameter α governs the weight of the tails—for large α (say, larger than 10 or 20) the distribution is almost indistinguishable from the light-tailed exponential distribution, while for values smaller than $\alpha\le 2$ the tails are so heavy that the distribution has infinite variance, and for $\alpha\le 1$ even the mean is infinite. This distribution is commonly used to model incomes, long durations, and other phenomena exhibiting heavy tails. We first use it in this paper in the subsection titled *Forecasting with a Chance of Ending*. Evidence is very strong that heavy-tailed distributions like the $\mathrm{GPa}(\alpha,\beta)$ fit observed eruption durations much better than "light tailed" distributions (exponential, gamma, etc.) do. It was used by Sparks and Aspinall (2004) for a similar purpose. Frequently the Generalized Pareto is introduced as a three parameter distribution family, $\mathrm{GPa}(\alpha,\beta;\varepsilon)$, taking values in $[\varepsilon,\infty)$ for some $\varepsilon\in\mathbb{R}$, with survival function

$$\mathrm{P}[T>t] = (1+(t-\varepsilon)/\beta)^{-\alpha}, \qquad \mathrm{t}>\varepsilon;$$

this is simply our $\mathrm{GPa}(\alpha,\beta)$ distribution plus a constant offset ϵ.

Pareto

A close relative of the Generalized Pareto is the Pareto distribution $\mathrm{Pa}(\alpha,\beta)$ with pdf, survival function, and mean given by:

$$\begin{aligned} f(t) &= (\alpha/\beta)(t/\beta)^{-\alpha-1}, & t>\beta \\ \overline{F}(t) &= \mathrm{P}[T>t] = (t/\beta)^{-\alpha}, & t>\beta \\ \mathrm{E}[T] &= \begin{cases} \alpha\beta/(\alpha-1) & \text{if } \alpha>1 \\ \infty & \text{if } \alpha\le 1 \end{cases} \end{aligned}$$

It is a special case of the three-parameter $\mathrm{GPa}(\alpha,\beta;\beta)$, or simply the $\mathrm{GPa}(\alpha,\beta)$ plus a constant offset of β. In this work it is used to model PDC volumes V, beginning in the subsection *Dynamic probabilistic Pyroclastic Density Current Inundation Forecast Maps*.

Poisson

The $\mathrm{Po}(\mu)$ is a discrete distribution for integer-valued count data $N\in[0,1,2,\ldots]$, with probability mass function (pmf) and mean given by

$$\begin{aligned} \mathrm{p}(k) = \mathrm{P}[N=k] &= \frac{\mu^k}{k!}e^{-\mu}, k\in\{0,1,2,\ldots\} \\ \mathrm{E}[N] &= \mu \end{aligned}$$

for a single parameter $\mu>0$. It is commonly used for modeling the number of events occurring in some specified time interval or spatial area. In that case one often considers a Poisson process N_t, the number of events occurring in time interval $[0,t]$, under an assumption that event counts in disjoint time intervals $(t_{j-1},t_j]$ are independent. In that case the mean is an increasing function of t,

$$\mu_t := \mathrm{E}[N_t].$$

The process is called "homogeneous" if $\mu_t=\lambda t$ for some constant average event rate $\lambda>0$. In this case the joint pmf for counts $\{N_j\}$ of events in J intervals $(t_{j-1},t_j]$ has the simple form

$$\mathrm{P}\left[N_j=n_j, 1\le j\le J\right] = \lambda^{n_+}e^{-\lambda(t_J-t_0)}\prod_{j=1}^{J}\left(t_j-t_{j-1}\right)^{n_j}/n_j!$$

where $n_+ := \sum n_j$ is the total number of events in the entire time range $(t_0,t_J]$.In this work Poisson models are first mentioned in the *Recent Eruptive History at Soufrière Hills Volcano* section, but are used more extensively in the section *The Model Behind the Plots*.

Circular Distributions

We consider two possible distributions for the initial angle ϕ (measured in degrees counter-clockwize from due east, from the interval $(-180^\circ,180^\circ]$):

- Uniform on $(-180^\circ,180^\circ]$, with pdf

$$f(\phi) = \begin{cases} 1/360 & -180<\phi\le 180 \\ 0 & \text{else.} \end{cases}$$

This indicates that flows in all directions are equally likely.

- Point mass at a specific value ϕ_0 in $(-180^\circ,180^\circ]$. This indicates certainty that $\phi=\phi_0$ (specifically, we consider $\phi_0=0^\circ$, due east toward the Tar River Valley, and $\phi_0=135^\circ$, northwest toward the Belham valley).

These are both limiting special cases of von Mizes distribution, a flexible family of circular distributions used to model angles and defined in Wolpert et al., 2018. We discuss these angular distributions in the subsection entitled *Dynamic probabilistic Pyroclastic Density Current Inundation Forecast Maps*.

Multivariate Normal

The $\mathrm{MVN}(\mu,\Sigma)$ is the probability distribution of a random vector $Y\in\mathbb{R}^d$ for some integer dimension d, with $\mathbb{R}^d$-valued mean $\mu=E[Y]$ and $d\times d$-dimensional variance matrix $\Sigma=E(Y-\mu)(Y-\mu)^T$. It is ubiquitous in statistical modeling of multi-variate data. In particular, it is the joint probability distribution for the values $y_k=Y[x_k]$ of a Gaussian Process (GP) Y, evaluated at any finite collection of design points. We use it in that context, beginning in the subsection *Probabilities of Pyroclastic Density Current Inundations and Emulator-Based Calculations*.

Advantages of publishing in Frontiers

OPEN ACCESS
Articles are free to read for greatest visibility and readership

FAST PUBLICATION
Around 90 days from submission to decision

HIGH QUALITY PEER-REVIEW
Rigorous, collaborative, and constructive peer-review

TRANSPARENT PEER-REVIEW
Editors and reviewers acknowledged by name on published articles

Frontiers
Avenue du Tribunal-Fédéral 34
1005 Lausanne | Switzerland

Visit us: www.frontiersin.org
Contact us: frontiersin.org/about/contact

REPRODUCIBILITY OF RESEARCH
Support open data and methods to enhance research reproducibility

DIGITAL PUBLISHING
Articles designed for optimal readership across devices

FOLLOW US
@frontiersin

IMPACT METRICS
Advanced article metrics track visibility across digital media

EXTENSIVE PROMOTION
Marketing and promotion of impactful research

LOOP RESEARCH NETWORK
Our network increases your article's readership